DPM
DIGITAL PRECISION MEDICINE

CHINESE ACADEMY OF SCIENCES

Fluorescence
Image-guided Surgery

Edited by: Jie Tian, AAAS Fellow



CONTENTS

Review

002 NIR-II Light in Clinical Oncology: Opportunities and Challenges

021 Fluorescence Image-Guided Tumour Surgery

Neurosurgery

039 Near-Infrared Window II Fluorescence Image-Guided Surgery of High-Grade Gliomas Prolongs the Progression-Free Survival of Patients

052 Real-Time Intraoperative Glioma Diagnosis Using Fluorescence Imaging and Deep Convolutional Neural Networks

063 First-in-Human Study of PET and Optical Dual-Modality Image-Guided Surgery in Glioblastoma Using ^{68}Ga-IRDye800CW-BBN

Ophthalmology

075 First-in-human Orbital Tumor Surgery Guided by Near-Infrared II Window Fluorescence Imaging: A Feasibility Study

Stomatology

084 Near-Infrared Fluorescence Imaging With an MET-Targeting Probe for Biopsy Site Selection in Patients with Oral Potentially Malignant Disorders

100 Multispectral Fluorescence Imaging of EGFR and PD-L1 for Precision Detection of Oral Squamous Cell Carcinoma: A Preclinical and Clinical Study

116 A c-MET-Targeted Topical Fluorescent Probe cMBP-ICG Improves Oral Squamous Cell Carcinoma Detection in Humans

Thoracic Surgery

127 Efficacy of Near-Infrared Fluorescence Video-Assisted Thoracoscopic Surgery for Small Pulmonary Nodule Resection with Indocyanine Green

138 Near-Infrared Intraoperative Imaging of Thoracic Sympathetic Nerves: From Preclinical Study to Clinical Trial

147 The Identification of Sub-Centimetre Nodules by Near-Infrared Fluorescence Thoracoscopic Systems in Pulmonary Resection Surgeries

Breast Surgery

155 Comparison Between the Indocyanine Green Fluorescence and Blue Dye Methods for Sentinel Lymph Node Biopsy Using Novel Fluorescence Image-Guided Resection Equipment in Different Types of Hospitals

Hepatobiliary Surgery

162 NIR-II Fluorescence Image-Guided Surgery Prolongs the Relapse-Free Survival of Hepatocellular Carcinoma Patients

166 Efficacy of Near-Infrared Fluorescence-Guided Hepatectomy for the Detection of Colorectal Liver Metastases: A Randomized Controlled Trial

174 First-in-Human Liver-Tumour Surgery Guided by Multispectral Fluorescence Imaging in the Visible and Near-Infrared-I/II Windows

Gynecology

189 Intraoperative Near-Infrared Fluorescence Imaging Can Identify Pelvic Nerves in Patients with Cervical Cancer in Real Time During Radical Hysterectomy

197 Visualisation of Pelvic Autonomic Nerves Using NIR-II Fluorescence Imaging

Urology

200 A Clinical Study of a CD44v6-Targeted Fluorescent Agent for the Detection of Non-Muscle Invasive Bladder Cancer

211 Intraoperative Near-Infrared II Window Fluorescence Imaging-Assisted Nephron-Sparing Surgery for Complete Resection of Cystic Renal Masses

Colorectal Surgery

216 Blood Perfusion Assessment by Near-Infrared Fluorescence Angiography of Epiploic Appendages in Prevention of Anastomotic Leakage after Laparoscopic Intersphincteric Resection for Ultra-Low Rectal Cancer: A Case-Matched Study

228 Clinical Value of Fluorescence Laparoscopic Surgery on Anastomotic Leakage Prevention in Ultra-Low Rectal Cancer: Real-World Multicenter Retrospective Evidence with Neoadjuvant Chemoradiotherapy Stratification

238 Prediction of Lymph Node Metastasis in Colorectal Cancer Using Intraoperative Fluorescence Multi-Modal Imaging

Pediatric Surgery

252 Indocyanine Green Localization for Laparoscopic Duodenal Web Excision

Fluorescence Imaging Standard

256 Harmonized Technical Standard Test Methods for Quality Evaluation of Medical Fluorescence Endoscopic Imaging Systems

Review Article

NIR-II Light in Clinical Oncology: Opportunities and Challenges

Zeyu Zhang[1,11,*], Yang Du[2,11,*], Xiaojing Shi[2,11,*], Kun Wang[2], Qiaojun Qu[3], Qian Liang[2], Xiaopeng Ma[4], Kunshan He[2], Chongwei Chi[2], Jianqiang Tang[5], Bo Liu[6], Jiafu Ji[7] ✉, Jun Wang[8] ✉, Jiahong Dong[9] ✉, Zhenhua Hu[2] ✉ & Jie Tian[1,2,10] ✉

Abstract

Novel strategies utilizing light in the second near-infrared region (NIR-II; 900–1,880 nm wavelengths) offer the potential to visualize and treat solid tumours with enhanced precision. Over the past few decades, numerous techniques leveraging NIR-II light have been developed with the aim of precisely eliminating tumours while maximally preserving organ function. During cancer surgery, NIR-II optical imaging enables the visualization of clinically occult lesions and surrounding vital structures with increased sensitivity and resolution, thereby enhancing surgical quality and improving patient prognosis. Furthermore, the use of NIR-II light promises to improve cancer phototherapy by enabling the selective delivery of increased therapeutic energy to tissues at greater depths. Initial clinical studies of NIR-II-based imaging and phototherapy have indicated impressive potential to decrease cancer recurrence, reduce complications and prolong survival. Despite the encouraging results achieved, clinical translation of innovative NIR-II techniques remains challenging and inefficient; multidisciplinary cooperation is necessary to bridge the gap between preclinical research and clinical practice, and thus accelerate the translation of technical advances into clinical benefits. In this Review, we summarize the available clinical data on NIR-II-based imaging and phototherapy, demonstrating the feasibility and utility of integrating these technologies into the treatment of cancer. We also introduce emerging NIR-II-based approaches with substantial potential to further enhance patient outcomes, while also highlighting the challenges associated with imminent clinical studies of these modalities.

[1] Key Laboratory of Big Data-Based Precision Medicine of Ministry of Industry and Information Technology, School of Engineering Medicine, Beihang University, Beijing, China.

[2] CAS Key Laboratory of Molecular Imaging, Beijing Key Laboratory of Molecular Imaging, Chinese Academy of Sciences, Beijing, China.

[3] Department of Radiology, First Hospital of Shanxi Medical University, Taiyuan, China.

[4] School of Control Science and Engineering, Shandong University, Jinan, China.

Nat Rev Clin Oncol. 2024.21: 449-467 Published online: 1 May 2024

[5] Department of Colorectal Surgery, National Cancer Center/National Clinical Research Center for Cancer/Cancer Hospital, Chinese Academy of Medical Sciences and Peking Union Medical College, Beijing, China.

[6] Department of General Surgery, The Third Affiliated Hospital of Sun Yat-sen University, Guangzhou, China.

[7] Department of Gastrointestinal Surgery, Peking University Cancer Hospital and Institute, Beijing, China.

[8] Thoracic Oncology Institute/Department of Thoracic Surgery, Peking University People's Hospital, Beijing, China.

[9] Hepatopancreatobiliary Center, Beijing Tsinghua Changgung Hospital, School of Clinical Medicine, Tsinghua University, Beijing, China.

[10] Engineering Research Center of Molecular and Neuro Imaging of Ministry of Education, School of Life Science and Technology, Xidian University, Xi'an, China.

* These authors contributed equally: Zeyu Zhang, Yang Du, Xiaojing Shi.

Key points

- Extending the clinical imaging spectrum to the second near-infrared (NIR-II) window offers greatly improved visualization of multiple features of cancer, providing a promising approach for enhancing surgical quality and facilitating oncological research.
- The efficacy of phototherapy can be substantially improved through the use of NIR-II irradiation, with the potential to improve therapeutic selectivity for cancer and facilitate the development of innovative combination therapies.
- Early phase clinical studies of NIR-II image-guided surgery and phototherapy for solid tumours have demonstrated promising potential to improve resection rates, reduce complications and prolong survival.
- Facilitating clinical application will be the primary objective for the future development of NIR-II techniques; a cyclical flow from bench to bedside and back again is necessary to promote this clinical translation.
- Emerging NIR-II techniques should aim to complement and enhance existing approaches rather than replace them; exploiting incremental value is essential to translating these novel approaches into clinical practice.
- Advances in NIR-II techniques might greatly facilitate a paradigm shift in cancer imaging, surgery and phototherapy, ultimately improving patient outcomes.

Introduction

Eliminating cancer while optimally protecting non-malignant tissues is a crucial requirement for successful precision oncology[1–3]; this clinical imperative has fostered technical advances in cancer diagnosis and treatment. Harnessing the power of light, optical technologies have been extensively used to image and treat solid tumours[4–6]. Tumours can be visualized using optical labelling techniques, enabling surgeons to perform precise resections[5]. Additionally, for inoperable lesions, light can be utilized as a therapeutic tool — namely, phototherapy[6]. Optical technologies have consistently advanced so that enhanced performance can be achieved in a variety of oncological applications[7,8].

Expanding the utilizable spectrum of light from the visible region to the near-infrared (NIR) window has greatly facilitated the clinical application of optical technologies[9,10]. Although optical imaging with visible light is intuitive to humans, its clinical use is limited by various factors, including shallow penetration depths and high background noise (mainly caused by autofluorescence and ambient interference)[11–13]. With NIR light, however, these limitations are substantially reduced, resulting in improved image quality and enhanced therapeutic efficacy[4,14,15]. Indeed, various innovative clinical imaging techniques and highly selective phototherapies have been developed utilizing the light spectrum between 700 nm and 900 nm, also known as the first NIR region (NIR-I)[6,16]. Moreover, since 2009, increasing research interest has been focused on the second, NIR-II, spectral region (wavelengths in the range 900–1,880 nm)[17–20]. Distinct subregions of the NIR-II window have been defined based on differential bio-optical characteristics, including NIR-IIa (1,300–1,400 nm)[21], NIR-IIx (1,400–1,500 nm)[20], NIR-IIb (1,500–1,700 nm)[22] and NIR-IIc (1,700–1,880 nm)[20]. Generally, imaging in the NIR-II window offers various advantages, including enhanced contrast, improved spatial resolution and increased imaging depth without an increase in excitation power or probe dose[23] (Fig. 1). Furthermore, phototherapy using NIR-II irradiation offers higher maximum permissible exposure and reduced photon scattering, resulting in enhanced therapeutic activity against solid tumours[24].

Over the past decade, numerous promising NIR-II-based techniques for precision cancer imaging and therapy have been proposed[25–27] (Fig. 2). NIR-II imaging enables the visualization of various molecular and cellular processes in vivo from macroscopic to mesoscopic, and to microscopic levels, and artificial intelligence (AI) could potentially be used to further improve image quality, providing a powerful tool to decipher biological heterogeneity of cancer[19,28]. Utilizing novel NIR-II probes, multiple characteristics of cancers (such as abnormal expression of biomolecules and a low extracellular pH microenvironment) can be observed with high resolution in living organisms, and many promising biomedical applications have been explored[11]. These probes have shown great potential for visualizing small tumours, tumour margins and tiny anatomical structures (such as nerves and microvessels), which might improve the identification and resection or ablation

of neoplastic lesions[29–31]. Through a microscopic view, the spatial distribution of and interaction between multiple cell types have been distinguished in vivo using NIR-II imaging probes, aiding research on the development of tumours and their microenvironment[32,33]. In addition to imaging, NIR-II light can be used to provide energy to perform photothermal therapy (PTT) and/or photodynamic therapy (PDT) with high selectivity for cancer cells[6,34,35]. When applied for PTT, the focal irradiation of cancerous regions with NIR-II light generates local hyperthermia that induces cancer cell death[6]. Notably, photothermal transduction agents (PTAs), that absorb NIR-II light and convert it into heat energy, can effectively improve the photothermal conversion efficiency (PCE) in the irradiated regions, and further enhanced therapeutic selectivity can be achieved by integrating PTAs with tumour-targeting moieties[6,34]. In the context of PDT, NIR-II irradiation is used for the local activation of a photosensitizer that converts O_2 into reactive oxygen species (ROS) to efficiently kill cancer cells[35]. NIR-II-based PTT and PDT have been extensively studied in preclinical models and found to have a favourable therapeutic index, demonstrating that precise targeting of tumour areas and the use of PTAs or photosensitizers enhances therapeutic activity while minimizing damage to non-malignant tissues and, thus, adverse effects[6,35–37].

Substantial preclinical research is facilitating efforts to exploit the advantages of NIR-II-based imaging and therapy in clinical practice. Indeed, several clinical studies have demonstrated the feasibility and effectiveness of NIR-II image-guided cancer surgery, with the exceptional sensitivity of NIR-II imaging enabling the detection of clinically occult small lesions and thus improving resection rates, which results in a lower risk of recurrence and prolonged survival[29,38,39]. Clinical implementation of NIR-II PTT in the treatment of various cancers is also advancing progressively[40–42]. Hence, improving cancer treatment with the power of NIR-II light is expected and is eagerly awaited by both scientists and clinicians. Nonetheless, many challenges to the clinical integration of NIR-II techniques remain to be addressed. For example, only surgical open-field imaging systems and ex vivo NIR-II back-table imaging systems have thus far been tested in humans (Table 1), and the systems used in clinical studies have relied on the tail of the fluorescence emission spectra of indocyanine green (ICG) or IRDye800CW, which predominantly produce NIR-I fluorescence.

Herein, we review important advances in NIR-II imaging and phototherapy of cancer, including preclinical and clinical studies of emerging technologies such as multispectral imaging, cross-scale imaging (from open-field macroscopic to mesoscopic and microscopic techniques) and combination phototherapy, and summarize the potential clinical utility of such modalities. We also discuss the challenges and opportunities to broaden the application of NIR-II light in oncology and promote the translation from bench to bedside.

Clinical applications of NIR-II

Fluorescence image-guided surgery

High sensitivity and resolution make NIR-II fluorescence molecular imaging (FMI) a promising and practical tool for visualizing small lesions and subtle non-malignant structures. Notably, the clinically applicable fluorophores ICG and IRDye800CW have proved effective for NIR-II FMI[43–45], offering an opportunity to explore NIR-II image-guided surgery in patients with cancer. Several clinical studies have explored potential applications of NIR-II FMI, with preliminary results suggesting the potential to enhance surgical quality and thus improve patient outcomes (Fig. 3 and Table 1).

Achieving radical resection

Radical tumour resection is crucial for the curative treatment of many patients with solid tumours. Ideally, the primary and metastatic lesions should be completely removed with a safety margin of surrounding non-malignant tissue. Yet, achieving this goal remains challenging with conventional approaches, such as visual inspection and palpation. NIR-II FMI has shown remarkable utility in visualizing malignant lesions and thus enhancing tumour excision[46].

The first-in-human study of NIR-II fluorescence image-guided surgery was reported in 2020 (ref. 29). This study involved 23 patients with liver cancer and used an integrated visible, NIR-I and NIR-II multi-spectral imaging instrument, with ICG as a dual NIR-I/II imaging probe. The results of the trial not only verified the feasibility of clinical NIR-II FMI, but also demonstrated improved cancer detection. In comparison with NIR-I FMI, NIR-II imaging had substantially greater sensitivity (100% versus 90.6%) and accuracy (91.4% versus 82.9%)[29]. Notably, NIR-II imaging revealed five small malignant lesions (including two detected in vivo, the smallest with a diameter of 0.3 cm) that were missed by preoperative imaging, three of which were also undetectable with intraoperative in vivo and ex vivo NIR-I FMI[29]. The clinical data also highlighted the importance of imaging depth, given that the in vivo tumour detection rates were 56.4% and 46.2% with NIR-II and NIR-I imaging, respectively, when deep-seated tumours were not exposed through incisions in the liver[29]. Therefore, intraoperatively combining NIR-II imaging and other modalities (for example, ultra- sonography) might further improve surgical decision-making and enable more complete excision of malignant lesions, which might lead to better

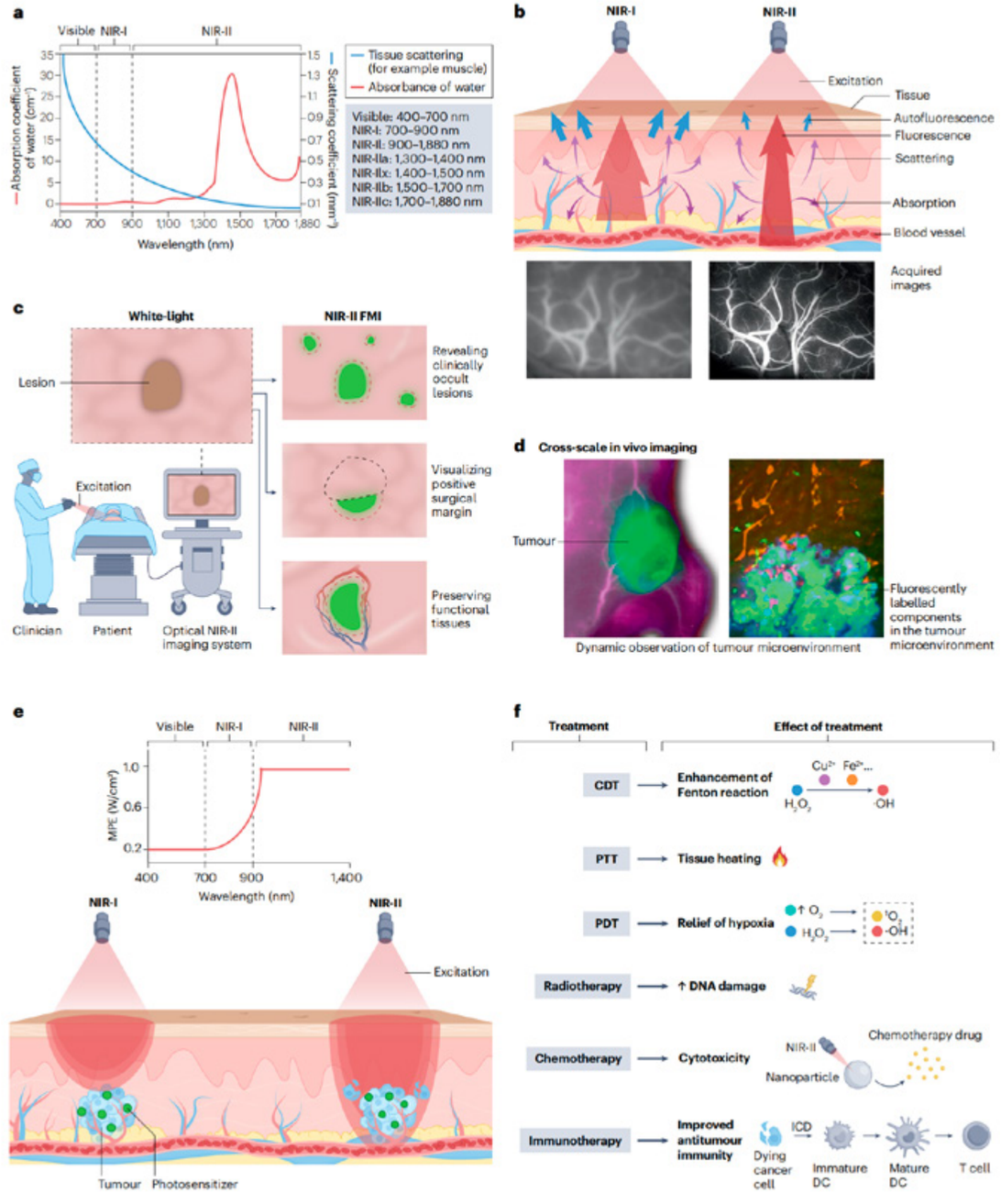


Fig.1 Fundamental principles and applications of NIR-II imaging and phototherapy. a, Key bio-optical characteristics of light in the second near- infrared region (NIR-II) include a lower level of scattering in tissues compared with visible and light in the first NIR region (NIR-I), which provides improved imaging resolution, although imaging performance might be reduced in the 1,400–1,500 nm subregion owing to high absorption of these wavelengths by water. **b,** In comparison with imaging using NIR-I light, reduced autofluorescence and scattering by tissues and increased tissue penetration depth empower NIR-II fluorescence molecular imaging (FMI) with a greater ability to visualize cancer and tiny anatomical structures in vivo. **c,** NIR-II imaging can, therefore, improve tumour resection and avoid surgical complications. **d,** Cross-scale, macroscopic and microscopic NIR-II imaging can also enable dynamic assessment of the tumour microenvironment during cancer development and therapy. **e,** With regard to phototherapy, the increased tissue penetration depth and higher maximum permissible exposure (MPE) of NIR-II versus NIR-I light offer improved phototherapeutic activity. f, Novel combinations of NIR-II phototherapies and other therapeutic modalities can exploit the advantages of the various therapies for synergistic effects. CDT, chemodynamic therapy; DC, dendritic cell; ICD, immunogenic cell death; PDT, photodynamic therapy; PTT, photothermal therapy.

Nat Rev Clin Oncol. 2024.21: 449-467 Published online: 1 May 2024

survival outcomes (Fig. 3a). Nevertheless, false-positive findings were observed with NIR-II imaging (overall specificity 88.5%)[29], which might have reflected the accumulation of ICG in cirrhotic nodules[47]. To enhance the imaging accuracy of malignant hepatic lesions in patients with cirrhosis, a negative imaging strategy using an intravenous nanoscale NIR-II fluorophore consisting of IRDye800CW conjugated to IgG (IgG–IRDye800CW) has been proposed[48]. Although the IgG–IRDye800CW conjugate used did not possess molecular targeting capabilities towards tumours, this probe enabled the differentiation of malignant and benign tissues based on their differing permeability to nanoscale materials. In a patient with hepatitis B-related cirrhosis and a single hepatocellular carcinoma lesion, most of the injected IgG–IRDye800CW accumulated in the hepatic parenchyma, while the tumour remained non-fluorescent, which might be attributable to the generally high retention of nanoscale materials in the non- malignant liver[49–51]. Consequently, the boundary between the hepatic parenchyma and tumour could be clearly distinguished, with a high contrast ratio of >10.4, to ensure a clear surgical margin during hepatectomy[48]. Although not specific to cancerous cells, this NIR-II FMI strategy presents an effective and practical approach to achieve the clinical objective of preserving hepatic function in patients with cirrhosis.

In 2022, data from a study evaluating the feasibility of NIR-II imageguided glioma surgery were reported[39]. This new surgical approach was tested in 15 patients with glioblastoma and four with WHO grade III glioma, with in vivo tumour detection rates of 100% and 75%, respectively, using ICG as the FMI probe[39]. The complete resection rate in patients with lesions detected on FMI was 100% (excluding two patients with glioblastoma who had fluorescence signal infiltrating eloquent areas that could not be safely resected)[39]. Traditional white-light surgery was performed for comparison in a separate group comprising 18 patients with glioblastoma and four with WHO grade III glioma, with complete resection rates of 50% and 25%, respectively[39]. Moreover, among the patients with glioblastoma, NIR-II image-guided surgery was associated with significant improvements in 6-month progression-free survival (PFS) (100% versus 66.7% with white-light surgery; P = 0.013), median PFS (9 months versus 7 months; P < 0.0001) and median overall survival (OS) (19.0 months versus 15.5 months; P = 0.0002)[39]. Notably, no iatro- genic effects on neurological function were observed in the patients who underwent NIR-II image-guided surgery, according to evaluations using the National Institute of Health Stroke Scale and the Karnofsky Performance Scale[39].

Both radical resection and functional preservation are also crucial but challenging objectives of surgery for cystic renal cell carcinoma, and the use of intraoperative NIR-II imaging to guide nephron-sparing surgery has been proved feasible in this context[52]. In a study involving nine patients with benign or malignant cystic renal masses, ICG was injected intravenously after exposing the lesion and NIR-II negative imaging was then used to visualize and mark the tumour margins, with the non-malignant renal parenchyma being illuminated and the lesion area remaining non-fluorescent owing to lower permeability of the cancerous tissues to ICG[52] (Fig. 3b). The fluorescence intensity ratios between the non-malignant tissue and the lesion reached values as high as 6.37, which is ideal for delineating the tumour boundaries, and radical tumour resection with pathological verification of clear margins (R0) was achieved in all enrolled patients[52].

Currently, clinical studies on NIR-II FMI primarily utilize non-specific probes, particularly ICG, and novel probes with greater tumour specificity are needed. A cancer-targeted probe conjugating IRDye800CW to a single-chain variable fragment (scFv) of an anti-EGFR antibody has been used to evaluate the margin status of primary lung tumours. Fresh resection specimens from ten patients undergoing surgery owing to high suspicion of lung cancer were incubated with the EGFR–IRDye800CW probe for 20 min and then analysed with NIR-II imaging during the surgical procedure[53]. The results demonstrated a sensitivity of 85.7% and a specificity of 100% for identifying the tumour area (all subsequently confirmed as invasive adenocarcinomas, 60% of which were stage I), reflecting upregulation of EGFR expression in the malignant cells (EGFR mutation status was not assessed); a total of 60 lymph nodes from these patients were also analysed and lymph node metastases were detected with 77.8% sensitivity and 92.1% specificity[53]. Notably, the same research team has demonstrated that NIR-based imaging of lung cancers using intravenously administered ICG can yield different quantitative characteristics depending on the CT features and histopathological subtype of the tumour[54]. Using an ex vivo dual NIR-I/II imaging system, they found that the signal-to-background ratio was higher for CT-identified solid nodules than for ground-glass nodules and also for squamous cell carcinomas compared with adenocarcinoma. These findings suggest that intraoperative NIR-II FMI will have greater accuracy and thus utility in detecting solid nodules and squamous cell carcinomas. Regardless, this ex vivo imaging approach might complement intraoperative pathology by enabling rapid evaluation of safety margins and detection of potential metastases to improve surgical decision-making.

Several clinical studies using other tumour-targeted probes comprising IRDye800CW conjugated to various antibodies have revealed outstanding performance in the detection of brain[55], head and neck[56], breast[57], pancreatic[58] and rectal cancers[59] under NIR-I imaging. These efforts will expedite the development and clinical translation of novel NIR-II probes, and the IRDye800CW-based probes themselves are also promising candidates for NIR-II FMI.

Mitigating complications

In the upcoming era of precision surgery, achieving an optimal balance between complete resection of malignant lesions and preservation of the surrounding non-malignant tissues will be imperative. NIR-II FMI has substantial potential to avoid iatrogenic injuries by improving the visualization of vital structures, such as blood vessels and nerves.

Results of clinical trials reported over the past 5 years demonstrate that NIR-II FMI can effectively reduce surgical complication rates, thereby enhancing surgical quality. In a first-in-human study with results reported in 2022, in vivo intraoperative ICG-based NIR-I/II/IIa/ IIb multispectral FMI was used to visualize glioma, tumour-feeding arteries and tumour-draining veins simultaneously in seven patients[60] (Fig. 3c). This multispectral imaging technique enabled the surgeon to precisely block the tumour-feeding arteries, resulting in a 38% reduction in mean blood loss volume compared with a retrospective control group (n = 15)[60] (Table 1). Although not directly assessed in this study, the substantial reduction in blood loss could potentially decrease the incidence of complications such as cranial haematoma. In addition, the potential of NIR-II FMI to improve surgical decision-making has been demonstrated in the setting of microsurgery for orthopaedic trauma[61]. In this study involving 39 patients, NIR-II FMI following intravenous injection of ICG enable clear and prompt visualization of anastomotic vessels and ischaemic areas, which might lead to lower rates of re-operation and thromboembolic complications. This NIR-II FMI approach could potentially be generalized to many surgical oncology settings, as exemplified by data indicating that intraoperative fluorescence angiography decreases the risk of anastomotic leakage in patients undergoing resection of gastrointestinal cancers[62].

Iatrogenic nerve injury is an often serious surgical complication and a major source of postoperative morbidity[63]. For example, up to 76% of patients with cervical cancer have bladder dysfunction after radical hysterectomy, owing to iatrogenic injuries affecting the pelvic autonomic nerves; therefore, nerve-sparing radical hysterectomy is recommended as a novel surgical strategy to preserve neural function while ensuring effective tumour resection[64]. This strategy relies on complete discrimination of the nerves intraoperatively, which is difficult to achieve with visual inspection and palpation only. The feasibility of ICG-based NIR-II FMI of nerves has been assessed in a patient with cervical cancer[65] (Fig. 3d). Benefitting from the enhanced resolution and contrast afforded by NIR-II FMI, this approach is effective for visualizing pelvic autonomic nerves including the superior hypogastric plexus, hypogastric nerves and inferior hypogastric plexus bladder branch[65]. NIR-II FMI enabled the surgeons to identify nerves <1 mm thick, which are difficult to see with the naked eye under white light alone[65]. Although these studies remain preliminary, NIR-II imaging has demonstrated notable performance in identifying vital structures such as microvessels and nerves, indicating potential clinical utility in a range of surgical applications.

AI-aided decision-making

AI holds great promise for enhancing the clarity of medical images and for improving the analysis of such images[66–68]. In comparison with conventional analytical tools, AI can provide more precise and efficient results, consequently improving clinical decision-making[69,70]. Existing data demonstrate that various tumour characteristics, including biomarker overexpression, can be extracted from clinical ICG-based NIR-II images using AI algorithms to more accurately identify malignant lesions during surgery[71,72] (Fig. 3e).

In one study, a deep convolutional neural network (CNN) model was designed to classify surgical specimens from patients with glioma in real time, based on intraoperative NIR-II FMI data[71]. This study involved 23 patients who were injected with ICG for fluorescence image-guided glioma resection; NIR-II fluorescence images of 1,874 surgical tissue samples from these patients were collected for training and validation of the model. The AI model achieved an area under the curve (AUC) of 0.945 for

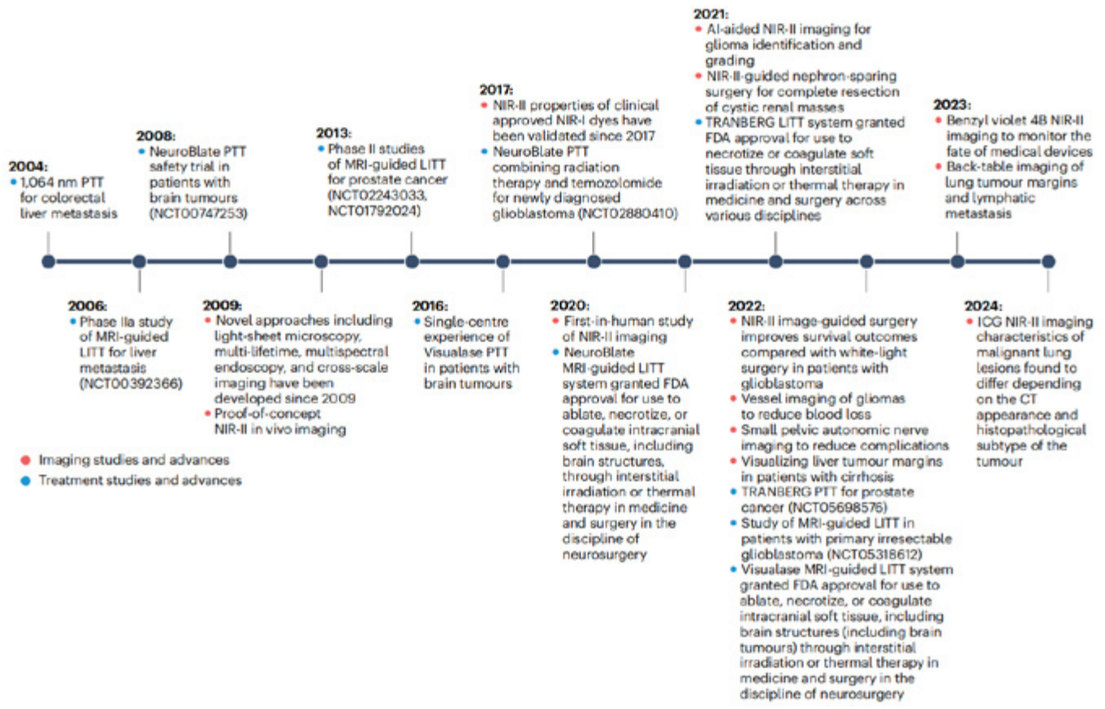


Fig.2 Key advances in NIR-II imaging and phototherapy of cancer. Important progress in medical imaging using light with wavelengths in the second near-infrared (NIR-II) window has been made since 2009, when the first-in-human study of NIR-II imaging was completed after a decade of preclinical development. Subsequently, a number of clinical trials investigating the various advantages of NIR-II imaging in the field of oncology have been reported. With regard to NIR-II phototherapy for cancer, clinical achievements to date have predominantly involved photothermal therapy (PTT). Several NIR-II laser interstitial thermal therapy (LITT) systems, including NeuroBlate78, Visualase79 and TRANBERG80, have been approved by the FDA. Additional clinical reagents and applications for NIR-II imaging and phototherapy of cancer are anticipated in the upcoming decade. AI, artificial intelligence; ICG, indocyanine green; NIR-I, first near-infrared region.

Table 1 Published early phase studies of NIR-II imaging and phototherapy in patients with cancer

Cancer type	Patients (*n*)	Technical approaches used	Clinical outcomes	Ref.
NIR-II-based imaging				
Liver cancer (mostly HBV-related HCC)	23	ICG (0.5 mg/kg) intravenously 1–7 days before surgery with open-field in vivo visible-light, NIR-I and NIR-II imaging	NIR-II FMI was associated with a higher sensitivity for ex vivo tumour detection (100% vs 90.6%) and increased tumour detection rate in vivo (56.41% vs 46.15%) compared with NIR-I FMI, and enabled the detection of some tumours that were not detected on preoperative imaging	29
HCC	1	IgG-conjugated IRDye800CW (10 mg) intravenously 6 days before surgery guided by in vivo open-field visible-light and NIR-II imaging	NIR-II FMI clearly delineated the tumour boundaries on a background of cirrhosis, thus enabling precise tumour resection with negative margins and maximal sparing of the parenchyma	48
Glioblastoma or grade III glioma	41 (33 with glioblastoma)	ICG (1.5 mg/kg) intravenously 24 h before surgery guided by open-field visible-light, NIR-I and NIR-II imaging, with gross tumour resection in the FGS group guided primarily by the NIR-II images	The complete resection rate was 100% in both the 15 patients with glioblastoma and the 3 patients with grade III glioma who underwent FGS[a] vs 50% and 25%, respectively, in the patients who underwent WGS; FGS was associated with prolonged PFS (median 9 months vs 7 months; 100% vs 66.7% at 6 months; $P<0.0001$) and OS (median 19.0 months vs 15.5 months; $P=0.0002$) in the patients with glioblastoma; no recurrence was detected in the patients with grade III glioma	39
Grade III or IV glioma	7	ICG (2.5 mg/ml, 10 ml) bolus intravenously during surgery, followed by open-field in vivo visible-light, NIR-I and NIR-II imaging, including separate imaging of the NIR-IIa and NIR-IIb subregions	Capillaries as small as 182 μm in diameter could be visualized using NIR-IIb FMI; tumour-feeding arteries were precisely blocked and maximal tumour resection was achieved in all patients; vascular injury (mean blood loss volume 283.3 ml vs 453.3 ml; $P=0.0366$) was reduced compared with that in a retrospective control group ($n=15$)	60
Lung cancer (stage I–III adenocarcinoma)	10	Fresh resection specimens were incubated with anti-EGFR scFv-conjugated IRDye800CW (1 mg/ml) for 20 min, followed by back-table visible-light and NIR-II imaging	NIR-II FMI was used to assess tumour margins (achieving 85.7% sensitivity and 100% specificity in identifying the tumour area) and lymph node metastases (77.8% sensitivity and 92.1% specificity in a total of 60 nodes)	53
Lung cancer	102	ICG (5.0 mg/kg) intravenously 24 h before surgery, with back-table NIR-I and NIR-II imaging	ICG FMI characteristics differed depending on the CT manifestations and histopathological subtype of the tumour; solid nodules had superior FMI qualities compared with ground-glass nodules	54
Cervical cancer	1	ICG (5.0 mg/kg) intravenously 24 h before surgery with open-field in vivo visible-light and NIR-II imaging	NIR-II FMI visualized small pelvic autonomic nerves for functional preservation through nerve-sparing surgery	65
Cystic renal masses (including ccRCC)	9 (4 with ccRCC)	ICG (0.5 mg/kg) intravenously during surgery, followed by open-field in vivo visible-light and NIR-II imaging	NIR-II FMI clearly visualized tumour margins enabling precise nephron-sparing surgery with negative margins and no tumour rupture	52
NIR-II-based phototherapy				
Colorectal cancer liver metastases	603 with a total of 1,801 liver metastases (≤5 each, all ≤5 cm)	MRI-guided 1,064 nm LITT without photosensitizer	6-month local recurrence rates of 1.2–4.4% depending on the diameter of the metastases; 5-year OS 37%, with median and mean durations of 3.5 years and 4.4 years from diagnosis, respectively (2.9 years and 3.8 years after the first LITT treatment)	41
Recurrent glioblastoma	10	MRI-guided 1,064 nm LITT without photosensitizer, using the NeuroBlate system	Median OS 316 days; neurological function improved in 3 patients, remained stable in 6 and worsened in 1; steroid-responsive treatment-related oedema occurred in all but one patient; three patients had grade 3 adverse events at the highest dose	83
Glioma or recurrent brain metastases	102 (87 with brain tumours)	MRI-guided 980 nm LITT without photosensitizer, using the Visualase system	The average durations of ICU and hospital stays were 1.8 days and 3.6 days, respectively; by postoperative day 1, 54% of the patients were neurologically stable for discharge; however, 13.7% developed new deficits after LITT, and although these deficits resolved completely within 1 month in 64.3% of these patients, 7.1% had only partial resolution of symptoms, 14.3% had no resolution of symptoms at the most recent follow-up, and 14.3% died without resolution of symptoms	75
Prostate cancer	130 (198 cancer foci)	MRI-guided 980 nm LITT without photosensitizer, using the Visualase system	27 of 131 of evaluable treated lesions (21%) in 20 of 95 men (21%) were positive for clinically significant neoplasia in 6-month biopsy samples, while 83 of 131 of lesions (63%) in 61 of 95 men (64%) were negative; a 40% decrease in mean serum prostate-specific antigen levels was observed at 12 months after treatment, with no statistically significant change in IPSS and SHIM scores; no serious adverse events or morbidity were reported	76

Table 1 (continued) Published early phase studies of NIR-II imaging and phototherapy in patients with cancer

Cancer type	Patients (*n*)	Technical approaches used	Clinical outcomes	Ref.
NIR-II-based phototherapy (continued)				
Prostate cancer	27	MRI-guided 980 nm LITT without photosensitizer, using the Visualase system	At 3 months, 26 patients (96%) had no evidence of cancer on MRI-guided biopsy of the ablation zone; no statistically significant change in IPSS; SHIM scores were reduced at 1 month ($P=0.03$) and at 3 months ($P=0.05$), but showed no significant difference at 12 months ($P=0.38$); at 12-month biopsy sampling, cancer was detected in 10 patients (37%), including in the ablation zones in 3 (11%), outside the ablation zones in 8 (30%), and both in and outside the ablation zone in 1 (3.7%)	77

ccRCC, clear-cell renal cell carcinoma; FGS, fluorescence-guided surgery; FMI, fluorescence molecular imaging; HBV, hepatitis B virus; HCC, hepatocellular carcinoma; ICG, indocyanine green; ICU, intensive care unit; IPSS, International Prostate Symptom Score; LITT, laser interstitial thermal therapy; NIR-I, first near-infrared region (wavelengths in the range 700–900 nm); NIR-II, second near-infrared region (wavelengths in the range 900–1,880 nm); OS, overall survival; PFS, progression-free survival; SHIM, Sexual Health Inventory for Men; WGS, white light-guided surgery.
[a]One patient without detection of grade III glioma by NIR-II imaging was omitted from this analysis.

discriminating cancerous from non-cancerous tissues (compared with 0.873 for a CNN model based on white light images; $P < 0.001$) in the validation set. Importantly, >70% of all classification errors made by neurosurgeons were corrected by the FMI-based CNN algorithm. Remarkably, the CNN models also had the ability to predict tumour grade (AUC 0.810) and Ki-67 expression levels (AUC 0.625)[71], which could potentially assist surgeons in selecting optimal samples for further intraoperative pathological evaluation.

Similarly, an AI algorithm using multimodal imaging was developed to increase the precision of glioma grading[72]. The multimodal dataset was constructed using white-light, NIR-I and NIR-II images that were simultaneously obtained during surgery. In total, 1,115 tissue specimens from 24 patients with glioma were analysed; all patients had received ICG intravenously 48 h prior to surgery. The AI algorithm was able to predict the histopathological grade of each specimen within 1 s with an AUC of 0.843 (ref. 72), demonstrating the considerable potential of this approach for use in prompt diagnosis.

Phototherapy

Phototherapy is mostly used to treat tumours that are deemed unresectable or that are not cured after surgery and/or other therapies. The deeper tissue penetration of NIR-II light, with a penetration distance≥1 cm greater than that of NIR-I light in the same tissues[15], enables effective phototherapy of deep-seated tumours. The advantages of NIR-II irradiation for PTT have been studied in mouse models of liver cancers[73] and breast cancer bone metastases[74], demonstrating deeper tissue penetration and greater temperature enhancement compared with NIR-I irradiation. Therefore, NIR-II irradiation can enhance phototherapeutic efficacy against deep-seated tumours. Clinical NIR-II PTT studies have primarily utilized contrast-free laser ablation systems (Table 1). For example, neodymium-doped yttrium aluminium garnet (Nd:YAG) lasers have a wavelength of 1,064 nm that can be used to generate photothermal energy to eliminate cancer cells. These lasers can also be integrated into MRI-guided laser interstitial thermal therapy (LITT) systems[75]. In a study evaluating MRI-guided LITT for the treatment of 1,801 colorectal cancer liver metastases in 603 patients, this approach was found to be safe and effective in preventing local recurrence (1.2–4.4% of metastases recurred, depending on their size), and was also associated with a prom- ising median OS duration of 3.5 years, 5-year OS of 37% and complication rate of 1.5%[41]. Clinical trials have also evaluated the use of MRI-guided LITT for the treatment of localized prostate cancers. A phase II study (NCT02243033) was conducted to evaluate outpatient, transrectally delivered MRI-guided laser focal therapy of prostate cancer in 130 men, with a total of 198 cancer foci treated[76]. The results indicate that this approach is safe and feasible, and a 40% decrease in mean serum prostate-specific antigen levels was observed at 12 months after MRI- guided LITT[76]. In another phase II study (NCT01792024), MRI-guided LITT in 27 patients with prostate cancer had an acceptable morbidity profile and was associated with encouraging short-term oncological outcomes, although longer follow-up is needed to further assess efficacy[77]. In 2022, a single-centre, phase I pilot study with a planned enrolment of 20 patients (NCT05698576) was initiated to assess the safety and tolerability of ablation of low-risk or intermediate-risk prostate cancers using an MRI–ultrasonography fusion imaging-guided LITT system incorporating the TRANBERG 25 W, 1,064 nm diode laser. The findings from these trials demonstrate the potential of NIR-II PPT to treat a range of solid tumours safely and effectively, with the promise to improve long-term outcomes.

LITT systems including NeuroBlate (12 W, 1,064 nm laser)[78], Visualase (15 W, 980 nm laser)[79] and TRANBERG (25 W, 1,064 nm laser)[80] have been approved for clinical use by the FDA, facilitating their testing in largescale trials. Encouraging results have been demonstrated utilizing the NeuroBlate and Visualase systems for the treatment of glioma[81,82]. The first-in-human trial of the NeuroBlate system was designed to assess safety and efficacy in patients with recurrent glioblastoma, with thermal dose escalation. This system enabled controlled thermal ablation of deep glioblastoma lesions in the ten patients enrolled (the mean percentage of tumour treated was 78%, range 57–90%) (Fig. 3f), leading to a median OS duration of 316 days; all but one patient had steroid-responsive treatment-related oedema, although

neurological function improved in three patients and remained stable in six others[83]. A phase I trial testing the NeuroBlate PTT system in combination with standard-of-care radiation therapy and temozolomide in patients with newly diagnosed glioblastoma was initiated in 2017 (NCT02880410); however, this trial was terminated after recruiting only three patients, owing to slow enrolment. The effectiveness of MRI-guided LITT using the Visualase system for the treatment of intracranial tumours was demonstrated in a single-centre study involving 102 patients, with a low incidence of complications observed; most patients were discharged within 1 day and the 30-day re-admission rate was 5.6%[75]. However, damage to crucial and eloquent structures occurred despite MRI guidance, with morbidity reported in 27 of 102 patients, including new-onset neurological deficits in 14, as well as two perioperative deaths[75] (Table 1). Furthermore, a prospective controlled pilot study demonstrated the feasibility and safety of adding MRI-guided LITT to biopsy sampling in patients with primary irresectable glioblastoma, with no delay observed in referring patients for standard chemoradiotherapy compared with biopsy sampling alone[40]; the efficacy and cost-effectiveness of this approach is currently being tested in the ongoing multicentre, randomized phase III EMITT trial (NCT05318612). These initial clinical data suggest the potential of NIR-II phototherapy to improve patient outcomes, and further multicentre randomized controlled trials are expected. In terms of NIR-II-based PDT, despite demonstrating promise preclinically, no clinical studies have been reported to date.

Emerging NIR-II technologies

Although NIR-II-based imaging and PTT have shown

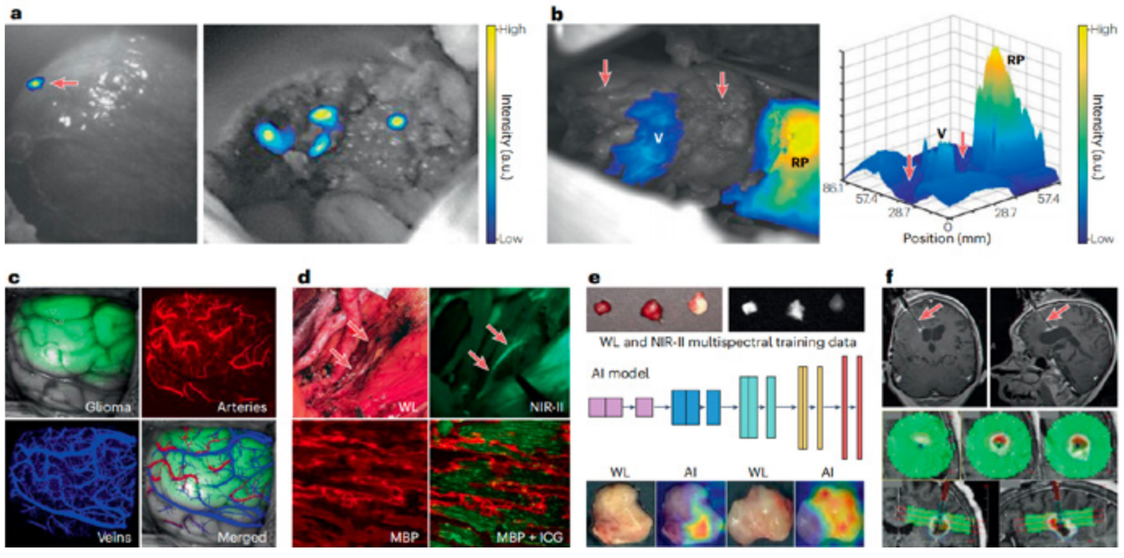


Fig.3 NIR-II image-guided surgery and PTT. a, In vivo second near infrared (NIR-II) imaging during surgery in a patient with liver cancer enabled the detection of clinically occult lesions (left panel, red arrow) not detected on preoperative imaging as well as the residual lesions (right panel)29. **b,** For nephron-sparing surgery in a patient with renal cell carcinoma, the tumour margins were clearly visualized through in vivo quantitative NIR-II imaging, using a negative imaging approach (red arrows indicate the cancerous region; 'v' indicates vessels and 'RP' indicates the renal parenchyma that needed to be preserved)52. **c,** Multispectral NIR-II imaging in a patient with glioblastoma enabled the simultaneous visualization of the tumour, tumour- feeding arteries and tumour-draining veins, providing clear guidance to resect the tumour while preserving the functional tissues60. **d,** In a patient with cervical cancer, intraoperative NIR-II imaging with indocyanine green (ICG) visualized pelvic autonomic nerves (red arrows), facilitating the avoidance of iatrogenic injury through nerve-sparing surgery65. **e,** Artificial intelligence (AI) methods can be applied to analyse cancer imaging data, extracting abundant diagnostic information to aid clinical decision-making71,72. The white light (WL) and NIR-II images of glioma specimens (top panel) were utilized to train an AI model (middle panel) for predicting tumour grade and Ki-67 index; the bottom panel displays a heatmap of the data used for predicting tumour grade. **f,** MRI-guided NIR-II laser interstitial thermal therapy (LITT) can enable effective treatment of glioma with minimal neurological deficits231,232. The red arrows (top panels) indicate the laser fibre used to deliver therapeutic energy into a brain tumour, guided by MRI. The axial images (middle panel) demonstrate three LITT treatment slices, and the sagittal and coronal images (bottom panel) illustrate the ablation area of cumulative LITT. The tumour contour is indicated by the light blue lines and the deep blue lines indicate the thermal damage threshold that is equivalent to exposure to 43 °C for at least 10 min. The green areas represent the limits of temperature detection via magnetic resonance thermometry. MBP, myelin basic protein. Part a adapted from ref. 29, Springer Nature Ltd. Part b adapted from ref. 52, CC BY 4.0 (https:// creativecommons.org/licenses/by/4.0/). Part c adapted with permission from ref. 60, IEEE. Part d adapted from ref. 65, Springer Nature Ltd. Part e, top and middle panels, adapted from ref. 71, CC BY 4.0 (https://creativecommons.org/ licenses/by/4.0/). Part e, bottom panel, adapted with permission from ref. 72, IEEE. Part f, top row, adapted from ref. 231, Springer Nature Ltd; middle and bottom rows, adapted with permission from ref. 232, JNS

Nat Rev Clin Oncol. 2024.21: 449-467 Published online: 1 May 2024

Table 2 Summary of emerging NIR-II-based approaches for cancer imaging and therapy

Approaches	Oncological applications	Primary advantages	Stage of development	Current limitations	Refs.
Imaging					
Open-field (in vivo) FMI	Visualizing tumours and their margins and vital structures intraoperatively	High sensitivity, decimetre FOV, real-time imaging	Clinical trials	Lack of clinical standard systems	29,39
Endoscopic FMI	Minimally invasive diagnosis and surgery	Minimal invasive, millimetre FOV, real-time imaging	Preclinical	Lack of clinically applicable systems	143
Back-table (ex vivo) FMI	Rapid analysis of tissue specimens during surgery	High sensitivity, decimetre FOV, applicable to novel probes with an unknown in vivo safety profile	Clinical trials	Requires a convenient approach for probe administration	53,54
Wide-field microscopy	Visualizing multiple oncological or pharmaceutical processes	Millimetre FOV, in vivo imaging, real-time imaging	Preclinical	Limited resolution for imaging cellular processes	20,21,145
Light-sheet microscopy	3D analysis of dynamic processes with cellular resolution in vivo	Sub-millimetre FOV, 3D imaging, in vivo imaging, real-time imaging	Preclinical	Need for high-specificity probes to label multiple cells	33
Confocal microscopy	3D visualization of characteristics of cancer or organ dysfunction with high resolution	Sub-micrometre resolution, 3D imaging, high signal-to-background ratio, low phototoxicity	Preclinical	Limited speed and small FOV	36,93,230
Photoacoustic imaging	Dynamic 3D visualization of cancer progression, vascular abnormalities and drug delivery	Millimetre depth, in vivo imaging, 3D functional imaging	Preclinical	Clinical translation of probes is difficult	165,170,171
Dual NIR-II FMI and CT or MRI	Multimodal imaging without depth limitation that can provide structural information	Excellent imaging depth, decimetre FOV, 3D tomography	Preclinical	Lack of multimodal clinically applicable probes	151–156
Dual NIR-II FMI and PET	Localizing multiple lesions with high sensitivity before or during surgery	Improved imaging depth (compared with FMI alone), decimetre FOV, enhanced tumour detection rate	Preclinical	Lack of multimodal clinically applicable probes	158–160
Phototherapy					
PTT	Local tumour ablation	Improved tissue depth (compared with NIR-I PTT) and therapeutic efficacy, high selectivity	Clinical trials	Lack of clinically applicable agents	41,81,181, 182,189
PDT	Localized treatment of tumours	Improved tissue depth and better efficacy (compared with NIR-I PTT), high selectivity	Preclinical	Lack of clinically applicable agents	186,187
PTT and/or PDT+immunotherapy	Enhancing the antitumour immune response and thus improving the efficacy of immunotherapy	Ability to convert immunologically 'cold' tumours into 'hot' tumours	Preclinical	Lack of clinically applicable agents	196,197
PTT and/or PDT+chemotherapy	Localized sensitization of cancer cells to chemotherapy, thus enhancing therapeutic selectivity	Improved therapeutic selectivity, fewer adverse effects	Preclinical	Lack of clinically applicable agents	198
PTT and/or PDT+radiotherapy	Sensitizing cancer cells to radiotherapy by inhibiting DNA damage repair	Improved therapeutic efficacy, fewer adverse effects	Preclinical	Lack of clinically applicable agents	199,200
PTT and/or PDT+CDT	Generate synergistic effects by accelerating the generation of hydroxyl radicals and other ROS	Improves CDT effect by enhancing Fenton reaction efficiency and depleting glutathione	Preclinical	Lack of clinically applicable agents	202–204
PTT and/or PDT+SDT	PTT can promote the ultrasound-triggered cavitation effect, and photosensitizers can mediate ultrasound-triggered ROS generation to enhance therapeutic efficacy	Improved therapeutic efficacy against deep-seated tumours	Preclinical	Lack of clinically applicable agents	206

CDT, chemodynamic therapy; FMI, fluorescence molecular imaging; FOV, field of view; NIR-I, first near-infrared region (wavelengths in the range 700–900 nm); NIR-II, second near-infrared region (wavelengths in the range 900–1,880 nm); PDT, photodynamic therapy; PTT, photothermal therapy; ROS, reactive oxygen species; SDT, sonodynamic therapy.

substantial promise in clinical studies, continuous effort is being dedicated to further improving the precision of these technologies. Data from preclinical studies underscore the possibilities of exploiting NIR-II light in a diverse range of oncological applications (Table 2).

Novel imaging techniques

Revealing occult lesions

Increasing imaging contrast and improving the targeting efficiency of NIR-II probes might enhance our ability to visualize clinically occult cancerous lesions. A variety of nanoparticle and small-molecule fluorophores have been synthesized to achieve such objectives[84–86].

Inorganic nanomaterials such as quantum dots and rare earth-doped nanoparticles have been widely applied in NIR-II-based cancer imaging preclinically. These nanofluorophores possess the benefitsof high quantum yield, great versatility and immunity to quenching effects[23,27]. Typically, these nanoprobes passively accumulate in tumours owing to the enhanced permeability and retention effect, and do not require targeting modifications[87,88]. Following intravenous injection into cancer-bearing mice, such nanoprobes enabled the high-contrast visualization of tiny cancer lesions (reportedly as small as 90 μm in diameter) intraoperatively with a penetration depth of approximately 8 mm, enabling the detection of previously occult lesions[89–91]. In the past 5 years, aggregation-induced emission has emerged as a cutting-edge strategy to develop ultrabright NIR-II imaging probes, which may further improve the detection rate of tiny lesions[92–95]. Nonetheless, concerns relating to long clearance times and potential toxicity (for example, impaired liver and kidney function)[96–98] present considerable obstacles to the clinical translation of these nanoprobes[50].

Small molecules that are rapidly renally excreted are deemed favourable for surgical applications[25,43,99]. Rapid clearance not only improves the safety of small-molecule probes, but also enables the probes to be administered and to accumulate at tumour sites within a few hours of surgery, providing greater flexibility in clinical practice. Since the first small-molecule NIR-II fluorophore, namely CH1055, was reported in 2016 (ref. 25), a series of novel small molecules designed for use in NIR-II imaging, including DPP-BDT[100], SCH1100 (ref. 101) and IR-FEP[102], have shown great potential for clinical translation[103,104].Nevertheless, the fluorescence quantum yields of most small-molecule probes are lower than those of inorganic nanoprobes, and their low molecular weight necessitates the use of conjugative binders for tumour targeting[7,23,105,106]. For these reasons, comprehensive assessment of the combined impact of small molecules, binders and conjugation approaches is crucial to achieve optimal tumour imaging outcomes[7].

The varied properties of nanomaterials and small molecules offer great versatility to NIR-II imaging that can be exploited to visualize occult lesions in different organs, including tiny metastases in the liver and lungs[89,91], primary colorectal cancers and peritoneal

Glossary

Aggregation-induced emission
A photophysical phenomenon whereby certain organic fluorescent dyes have enhanced electron-donating and donor–acceptor abilities and, thus, increased emission efficiency when aggregated compared to when they are in a dispersed state.

Ambient interference
Background fluorescence originating from sources outside the field of view, for example, the reflected light from shadowless lamps and the light emitted by nearby light-emitting diode monitors.

Autofluorescence
Intrinsic emission of light by biological structures when excited by external light, primarily within the visible spectrum.

Back-table imaging systems
Imaging systems typically comprising a lightproof imaging chamber and movable frame, intended for pathological examination of fresh tissue samples in the operating room during the surgical procedure.

Cerenkov radiation
A form of electromagnetic energy emitted by charged subatomic particles travelling faster than light in a dielectric medium such as biological tissue.

Enhanced permeability and retention
Phenomenon in which non-targeted high molecular weight compounds accumulate in tissues with high levels of vascular permeability, such as tumours with a characteristically abnormal vasculature.

Lifetime imaging
A quantitative imaging approach that captures and analyses the duration of fluorescence emission.

Maximum permissible exposure
The highest power or energy density of a light source that is considered safe, with negligible probability of causing damage to the eye or skin.

Open-field imaging systems
Imaging systems tailored for use during open surgery, enhancing visualization of tissues with decimetre-scale size of the field of view and metres-long working distances.

Photoacoustic imaging
A biomedical imaging modality that utilizes the photoacoustic effect to produce wideband ultrasonic emission through transient thermoelastic expansion, and that is expected to combine the strengths of deep ultrasound penetration with high optical contrast.

Photon scattering
During bio-optical imaging, scattering occurs when the directional motion of photons is altered owing to their interaction with tissue or other materials, potentially affecting image quality and imaging depth.

Pyrolysis
The thermal decomposition of materials, often in an inert atmosphere, resulting in volatile products.

Quantum yield
The ratio of the number of photons emitted relative to the number of photons absorbed.

Quenching
Decreased fluorescence intensity owing to various features of fluorophores, such as excited state reactions, energy transfer, complex formation and collisional deactivation.

Ratiometric imaging
An imaging method that involves measuring fluorescence intensities at multiple emission wavelengths, which can differ under different physiological conditions, to monitor changes in the surrounding tissue microenvironment.

Ultrasound-triggered cavitation
Phenomenon in which high-frequency sound waves create tiny bubbles in a liquid, which then rapidly collapse, releasing energy.

Nat Rev Clin Oncol. 2024.21: 449-467 Published online: 1 May 2024

metastases[107], abdominal metastases from ovarian cancer[90,108] and lymph node metastases from breast cancer[109]. These achievements have considerably improved the ability to detect small lesions with diameters of <1 mm in animal models, lesions that are typically undetectable with current clinical diagnostic imaging technologies[91,108].

In the past few years, advanced biosensing imaging strategies have also been developed to further improve the sensitivity and accuracy of tumour NIR-II FMI[110,111]. The engineered probes can sense tumour-associated changes in physiological characteristics, causing variations in fluorescence intensity and spectral range that aid in lesion identification[112,113]. For example, novel chemiluminescent and phosphorescent biosensing probes have demonstrated substantial capability to detect cancer-associated physiological features (such as high levels of H_2S production or an acidic microenvironment) to produce images with a high contrast ratio (>100)[114–116]. Moreover, NIR-II signals can be quantified through lifetime imaging or ratiometric imaging[117,118]. In these approaches, specific physiological features of cancer can be linearly correlated with the lifetime or ratiometric intensity of NIR-II signals. A major advantage of lifetime and ratiometric imaging approaches is that the results are independent of the probe concentrations[119,120]; therefore, the influence of probe uptake and clearance is reduced, leading to higher precision in quantitatively identifying lesions and their margins[32,118,121]. These emerging approaches are smoothing the path to precision quantitative cancer imaging with increased contrast and specificity.

Visualizing for preservation

Optimally preserving functional anatomical structures is an important topic in precision surgery. Great efforts have been made to visualize structures including blood vessels, the biliary tract, ureters and nerves with NIR-II imaging[21,65,122,123]. The merits of NIR-II imaging in terms of contrast, resolution and depth make it an ideal tool to reveal such small and vulnerable structures[94,124,125].

Utilizing probes with high photochemical stability, NIR-II imaging especially in the NIR-IIb and NIR-IIc subregions can substantially improve the ability to map the vascular system and thus reduce the risk of vascular injury and blood loss during surgery in animal models[25,122,126,127]. Similarly, evidence from studies in animal models indicates that intraoperative visualization of the biliary tract[128,129] and ureters[130] using novel NIR-II FMI techniques might result in reduced surgical com- plication rates and training times. Therefore, these approaches have the potential to facilitate a paradigm shift towards precision cancer surgery. In the interim before novel NIR-II probes are integrated into routine practice, ICG could serve as an alternative in proof-of-principle clinical studies, albeit as a non-targeted probe[131].

Nerves are more difficult to visualize during surgery than the aforementioned anatomical structures, and iatrogenic nerve injury is strongly associated with postoperative complications[63,132]. Clinical studies have revealed that in vivo NIR-I imaging using ICG enables visualization of thoracic sympathetic nerves and pelvic nerves during thoracoscopic surgery and radical hysterectomy, respectively[133,134]. Under NIR-II imaging, the ICG-labelled nerves can be identified with higher clarity[65] (Fig. 3d); however, the imaging specificity remains lower than expected. Despite the development of a variety of novel FMI technologies designed to specifically image nerves[135–137], this field faces many ongoing challenges. Advances in the development of nerve-specific fluorescent probes, their routes of administration, as well as considerations for future clinical translation efforts, have been reviewed in detail elsewhere[132]. In preclinical models, important improvements in fluorescence-guided nerve-sparing surgery have been realized through the application of low molecular weight probes[136,138] or dyes conjugated to nerve-binding peptides (such as NP41 and HNP41) identified using phage display screens[135,137,139,140]. Moreover, data from clinical studies using near-ultraviolet light systems demonstrate the potential to exploit the autofluorescence of nerves for real-time intraoperative imaging[141,142]. Although few of these studies have used the NIR-II window[137], they have laid the groundwork for utilizing NIR-II-based neural imaging as a potentially revolutionary tool for more precise cancer surgery in the future.

Using these high-performance functional probes, simultaneously imaging vital structures and malignancies is achievable and represents an important future direction for FMI-guided surgery. Indeed, integrated multispectral NIR-II imaging is expected to become a powerful tool to improve the precision of cancer surgery.

Crossing scales

Aiming to discern multiple anatomical structures or cellular processes at higher levels of spatial resolution, research efforts have been extended to integrating NIR-II FMI into endoscopy and microscopy. In 2019, an initial study verified the feasibility of performing endoscopic NIR-II image-guided surgery in small animals[143]. A prototype endoscope with a dichroic design was used to capture visible and NIR-II light simultaneously, providing an adjustable view at millimetre scale (smallest area 4 mm^2) and micrometre resolution (~20 μm)[143]. This imaging system enabled successful delineation of orthotopic colorectal tumours using ICG conjugated to the anti-VEGFA antibody bevacizumab as a targeted probe, although an impediment was observed owing to the strong attenuation of NIR-II light within endolaparoscopes[143]. Most existing clinical endolaparoscopes are primarily tailored for high-resolution imaging of visible light, with limited transmittance of NIR light. Therefore, future progress in this field would be facilitated by the development of high NIR transmittance devices to ensure superior imaging quality.

Regarding NIR-II fluorescence microscopy, various techniques including wide-field, light-sheet and confocal imaging have been developed[144]. Wide-field microscopy offers the largest field of view (FOV) and the highest time resolution among these microscopic techniques (Table 1). In preclinical studies, in vivo wide-field NIR-II fluorescence microscopy has micrometre resolution, millimetre imaging depths and real-time imaging capabilities[20,144]. This technique holds promise for visualizing the cancer-related vessels and monitoring the retention effects of cancer drugs[145]. Additionally, wide-field NIR-II microscopy could facilitate bedside evaluation of tissues to improve cancer treatment by enabling the analysis of various oncological features. For example, the status of tumour margins and lymph nodes could be promptly assessed through bedside microscopy of the resected tissues using molecularly targeted NIR-II probes[146,147], enabling intraoperative optimization of the surgical plan. Light-sheet microscopy is advantageous in performing 3D imaging of multiple oncological processes with cellular resolution in real time[28,33]. This technique involves the use of planar excitation and acquisition devices that are arranged orthogonally to decrease background noise, with only signals in the focal plane being obtainable, with image acquisition performed section-by-section. Utilizing NIR-II light-sheet microscopy, in vitro and in vivo volumetric imaging with

a sub-millimetre FOV and enhanced contrast can be achieved, which is beneficial for observing various cellular activities in the tumour microenvironment (TME)[33,148]. NIR-II confocal microscopy offers superior, sub-micrometre resolution and improved imaging depths (up to 2.5 mm) with less phototoxicity or photobleaching in vitro[149]. The point-by-point signal acquisition inherent to this imaging technique can attenuate background fluorescence and thus maximize the signal-to-background ratio. However, this approach is unsuitable for real-time imaging and the FOV is commonly limited to <1 mm^2 (ref. 150) (Table 1). Therefore, NIR-II confocal microscopy is typically applied to the analysis of biological features of tumour and other tissue specimens ex vivo[150]. By combining these NIR-II technologies with different FOVs, cross-scale multispectral in vivo FMI — from macroscopic to mesoscopic and to microscopic levels — can be achieved with improved imaging resolution and depth, which will surely facilitate a deeper understanding of tumour biology, thereby advancing cancer research.

Combining modalities

Despite the numerous demonstrated merits of NIR-II imaging, exploration of strategies to leverage the complementary advantages of this approach in conjunction with other imaging modalities is imperative for improved clinical outcomes. A typical strategy involves combining NIR-II FMI with CT or MRI to overcome the depth limitations of optical imaging. Using innovative dual-modality probes for NIR-II–CT, combinatorial benefits, including exceptional sensitivity, superior spatiotemporal resolution and unlimited imaging depth, can be achieved[151]. MRI is also combinable with NIR-II imaging, and NIR-II–MRI dual-modality imaging has shown potential for improving the management of patients with cancer. For example, NIR-II imaging can be used to evaluate the expression of therapeutic targets as well as drug delivery and accumulation in tumours, while MRI enables non-invasive long-term monitoring of the treatment response[152–154]. Thus, the combination of NIR-II and CT or MRI might enable more precise and guided therapy, potentially minimizing damage to non-malignant tissues. Furthermore, these structural imaging modalities could pro- vide anatomical data as a reference standard to facilitate the process of NIR-II tomography[155,156]. Indeed, 3D images can be derived from planar NIR-II images of tumours through tomographic processing[155,156]. Studies in mouse models have demonstrated that NIR-II tomography can be used to delineate small tumours with morphological precision of up to 80%[157]. With the integration of molecularly targeted probes, this technique is expected to facilitate monitoring and understanding of the processes mediating tumour growth.

In addition to structural imaging, functional imaging exemplified by PET can be combined with in vivo NIR-II imaging using bimodal nanoprobes to pursue precision tumour delineation and resection[158,159]. Specifically, radiolabelled NIR-II probes can specifically accumulate in lesions through enhanced permeability and retention effects[158] or molecular targeting[159,160], enabling the use of PET to non-invasively locate deep-seated tumours preoperatively and NIR-II imaging to provide real-time intraoperative guidance for tumour resection, after the radioactivity has decayed to safe levels. The intriguing discovery that Cerenkov radiation can produce NIR-II emission[161] has inspired the use of radiation beams from clinical linear accelerators or medical radioisotopes to perform dual-modality radio-optical imaging[162,163]. Imaging of NIR-II Cerenkov luminescence can contribute to assessments of geometric accuracy in external beam radiotherapy[161,162], with the aim of reducing unintended injury to non-malignant tissues. The ability of medical radioisotopes to generate Cerenkov luminescence provides a readily available source of probes for use in dual PET–NIR-II imaging, while also presenting a novel class of utilizable NIR-II probes.

Photoacoustic imaging (PAI) in the NIR-II window provides enhanced spatial resolution and greater penetration depth[164]. Different from FMI, PAI involves the use of NIR-II pulse lasers to irradiate tissues or probes, resulting in the emission of acoustic waves that can be visualized through ultrasonographic imaging[164]. Moreover, diverse agents (for example, semiconducting polymer nanoparticles) have been developed to amplify PAI signals, providing excellent imaging performance for tumours and vasculatures in vivo[165–167]. Especially, the 3D multispectral optoacoustic tomography technique can be used not only to visualize primary and metastatic tumours, but also to assess features of the tumour and its TME, such as the vasculature, acidity and hypoxia[168,169]. By combining both NIR-II FMI and PAI, the vision of clinicians could potentially be further extended. In preclinical studies, tumour margins and metastases could be visualized more precisely during surgery guided by dual FMI–PAI utilizing NIR-II[170,171], which might ultimately translate into a reduced risk of disease recurrence. With regard to phototherapy, FMI–PAI enables monitoring of delivery and release of the drug, assessing therapeutic response after drug administration, and thus facilitating timely improvements to the treatment plan[172–174]. Specifically, the biodistribution of nanoprobes integrating imaging agents with anticancer drugs can be tracked under FMI–PAI, which aids in evaluation of the selectivity of drug delivery[175,176]. Further- more, the therapeutic effects can be assessed by monitoring changes in tumour physiological features and size[177,178]. For example, FMI–PAI can be used to visualize dynamic immunological changes in the TME during immunotherapy, aiding in the development of personalized treatment plans[179,180]. As research in this field continues to advance, therapy guided by NIR-II FMI–PAI is anticipated to provide innovative strategies to revolutionize cancer treatment paradigms.

Novel NIR-II-based phototherapies

Enhanced PTT and PDT

Emerging technologies with improved performance demonstrated in preclinical studies have the potential to further increase the clinical efficacy of NIR-II phototherapy. A diverse range of PTAs have been demonstrated to improve the PCE of NIR-II PTT, achieving more complete tumour elimination in preclinical models. The maximum permissible exposure of NIR-II radiation is three times that of NIR-I (1 W/cm^2 versus 0.33 W/cm^2)[15], consequently enabling the exploration of more efficient PTAs over a wider range of laser power densities. Dual acceptor[181] and acceptor–donor acceptor[182] engineering strategies have been used to produce NIR-II-absorbing PTAs with high PCEs. Moreover, high-PCE hybrid semiconducting nanozymes (HSNs) have been designed not only to increase the direct thermal cytotoxicity of NIR-II PTT, but also to photothermally enhance the generation of cytotoxic hydroxyl radicals by an iron-chelating Fenton reaction catalyst component of the HSN[183]. NIR-II irradiation of these HSNs effectively inhibits breast tumour growth and metastasis to the lung and liver in mouse models[183]. In addition, phase engineering of nanomaterial PTAs such as transition metal dichalcogenide nanodots (for example, MoS_2) can be used to further improve their PCE, by facilitating the identification of crystal and/or amorphous phases associated with optimal NIR-II absorption[184].

With regard to NIR-II PDT, efficacy can be improved by alleviating hypoxia in the TME. Hypoxia is a common feature of tumours that promotes the proliferation, invasion and metastasis of cancer cells and substantially restrains the activity of PDT, owing to the limited availability of O_2 for conversion into ROS by photosensitizers[6]. This hypoxia can be overcome or alleviated using novel hypoxia-tolerant or O_2-producing photosensitizers, resulting in enhanced PDT efficacy. For example, a nanoparticle photosensitizer containing COi6-4Cl enables hypoxia-tolerant NIR-II PDT (using an 880 nm laser) via the less O_2-dependent 'type I' pathway (through a photochemical reaction with H_2O), as well as the O_2-dependent 'type II' pathway[185]. Moreover, this agent also generates high levels of NIR-II fluorescence (1,035 nm) that can be exploited for image-guided PDT[185]. By contrast, LSCaFPCe6, a novel TME-responsive O_2 self-supplying nanoparticle photosensitizer, enables efficient alleviation of tumour hypoxia as well as enhanced production of cytotoxic ROS when activated in the acidic TME, resulting in selective suppression of tumour growth without notable systemic toxicity in mouse models; like COi6-4CL nanoparticles, this nanosystem was also designed to emit NIR-II light for imaging guidance of PDT[186]. Furthermore, a probiotic-based TME-responsive platform, involving the use of Lactobacillus acidophilus for in situ amorphization of 2D CoCuMo layered double-hydroxide nanosheets in the acidic TME, has also demonstrated promising preclinical utility for precision NIR-II PDT by enhancing the generation of singlet oxygen ($^1O_2$)[187].

More precise NIR-II PTT and PDT might be achieved by combining targeting and image-guidance strategies. Active targeting relies on the modification of PTAs or photosensitizers with moieties that can bind to specific target molecules expressed on cancer cells. The potential of such an approach has been exemplified in a preclinical study in which a bi-orthogonal labelling system was used to enhance the tumour-specific retention of theranostic nanoparticles, which enabled precise NIR-II image-guided PTT[188]. Another study demonstrated preferential binding of biomimetic aggregation-induced emission-based DHTDP nanoparticles coated with cancer cell membrane to homologous cancer cells, resulting in tumour enrichment that maximized the therapeutic outcomes of NIR-II PTT guided by FMI, PAI as well as photothermal imaging[189]. Subcellular targeting strategies, including nucleus-targeted[190] and mitochondria-targeted strategies[191], might also improve efficacy of NIR-II phototherapy. Furthermore, physical forces such as magnetic fields can be used to improve the targeting of phototherapy agents to tumours, thus enhancing NIR-II PDT or PTT and imaging[192].

Combination therapy

PTT or PDT alone is likely to be suboptimal for the treatment of large and inoperable lesions, and incomplete elimination of cancer increases the risk of local recurrence and distant metastasis. However, combining phototherapy with other therapeutic modalities might result in enhanced antitumour efficacy. Indeed, increasing research focus is being placed on using NIR-II PTT and PDT to reverse immunosuppression and alleviate hypoxia in the TME, thereby sensitizing cancer cells to immunotherapy, chemotherapy, radiotherapy, chemodynamic therapy (CDT) and sonodynamic therapy (SDT)[15,193].

The integration of NIR-II phototherapy with immunotherapy has shown substantial potential to enhance the antitumour response in various preclinical models. For example, PTT can induce immunogenic cell death via the generation of tumour-associated antigens, damagerelated molecular patterns and pro-inflammatory cytokines, thus increasing T lymphocyte infiltration to enhance the efficacy of immunecheckpoint inhibitors as well as Toll-like receptor agonists[193–197]. Theoretically, NIR-II phototherapy can reprogramme immune networks in the TME by inducing immunogenic cell death and maturation of dendritic cells, thereby activating the immune response to prevent local tumour recurrence and distant metastasis[197].

Data indicate that NIR-II phototherapy can sensitize cancer cells to chemotherapy, thereby improving therapeutic efficacy and potentially selectivity. For example, in preclinical models, upon NIR-II irradiation, doxorubicin included in a platinum nanocrystal-tipped gold nanorod zeolitic imidazolate framework-8 (DOX-Pt-tipped Au@ZIF-8) nanoplatform could be precisely released within the tumour area[198]. Moreover, heat generated through NIR-II irradiation of the gold nanorods can enhance the catalase-like activity of the platinum nanocrystals and thereby relieve tumour hypoxia, resulting in increased PTT and PDT activity compared with that of gold nanorods lacking platinum tips[198]. Collectively, these stimulus-responsive properties of the DOX-Pt-tipped Au@ZIF-8 nanoplatform improved the efficacy of chemophototherapy with negligible adverse effects[198].

The combination of NIR-II phototherapy with radiotherapy is expected to reduce adverse effects while improving therapeutic efficacy. NIR-II PTT can inhibit DNA damage repair to sensitize cancer cells to radiotherapy, and PDT can synergize with radiotherapy by generating ROS[15]. Furthermore, NIR-II light can trigger the surface plasmon resonance effect to increase O_2 release, consequently relieving tumour hypoxia and thus enhancing radiosensitivity and achieving satisfactory efficacy with reduced levels of non-malignant tissue damage[199]. Hence, NIR-II irradiation might enable precise control over radiation sensitivity in the treatment field while sparing surrounding non-malignant tissues, thereby improving the tumour selectivity of radiotherapy. Besides external X-ray radiation, combination therapy with radioisotopes (such as iodine-131) conjugated to NIR-II PTT nanomaterials (for example, gold nano-frameworks) has been demonstrated to enhance radiotherapeutic efficacy in mouse models[200].

Similarly, the combination of NIR-II phototherapy with CDT can further improve therapeutic efficacy. CDT is a Fenton-type reaction- mediated cancer treatment strategy. In the mildly acidic TME, metal ions (such as Fe^{2+}, Cu^{2+} and Mn^{2+}) can be released from phototherapeutic agents to promote the catalysis of H_2O_2 into $^{\cdot}OH$, thereby inducing cancer cell death. Moreover, the thermal energy from PTT can improve the TME and accelerate $^{\cdot}OH$ production for enhanced CDT, and the ROS generated during PDT can kill cancer cells and produce a synergistic effect. The NIR-II photothermal enhancement of Fenton reaction efficiency and CDT activity has been demonstrated in mouse models of cervical cancer[201] and breast cancer[202]. TME-activated NIR-II phototheranostic agents designed to enhance phototherapy and CDT by increasing ROS generation and glutathione depletion have provided evidence of such synergy in preclinical models[203,204].

Although NIR-II light exhibits deeper tissue penetration than NIR-I light, this physical limitation still restricts the utility of NIR-II phototherapy. Combining NIR-II phototherapy with other deeperpenetrating therapeutic methods, such as SDT, can improve therapeutic activity against deep-seated and/or large tumours. Similar to PDT, SDT involves the activation of sonosensitizers to generate toxic ROS, including $^{\cdot}OH$, H_2O_2, $^1O_2$

Nat Rev Clin Oncol. 2024.21: 449-467 Published online: 1 May 2024

and superoxide anions ($O_2^{\bullet-}$), to kill cancer cells, as well as pyrolysis of sonosensitizers induced by heat generated through ultrasound-triggered cavitation[205]. The cavitation effect can be promoted by the thermal energy from NIR-II PTT, and NIR-II photosensitizers can also enhance ultrasound-triggered ROS generation for improved therapeutic effects against deep-seated tumours. For example, a defect-rich, gadolinium-doped zinc oxide (D-ZnOx:Gd) semiconductor sonosensitizer and PTA has been designed for synergistic NIR-II PTT and SDT therapy. This 'nanobullet' agent has demonstrated good photothermal conversion performance, while the abundant oxygen defect of D-ZnOx:Gd promotes separation of the electron (e^-) and hole (h^+) of this agent under ultrasound irradiation, which establishes a strong electric field that promotes ROS generation and thereby enhances the SDT effect[206].

Outlook and challenges

Despite the substantial promise of NIR-II-based cancer imaging and therapy, these techniques remain in the early stages of clinical translation. The primary objectives in the future development of such techniques should be to facilitate their clinical application and improve clinical outcomes. To attain these objectives, several challenges must be met. For example, the discrepancy between the goals of preclinical research and clinical needs must be addressed. Most preclinical studies prioritize technological and performance improvements, exemplified by the pursuit of ultra-high quantum efficiency probes. However, clinical applications necessitate a comprehensive consideration of safety, practicality and technical performance[207]. Therefore, multidisciplinary efforts are necessary in the early stages of clinical translation to establish a cyclical flow from bench to bedside and back again, bridging the gap between clinical requirements and technical developments[208,209]. This flow will help to translate clinical demands into technical solutions, spawning more clinically oriented studies. Meanwhile, increasing knowledge of NIR-II techniques among clinicians could potentially inspire them to suggest and explore new promising applications for such techniques. Crucially, the aim of NIR-II-based techniques should not be to compete with existing approaches being tested in phase II/III trials, but rather complement and enhance them by adding incremental value. Moreover, another crucial determinant of successful translation is whether the technical merits can lead to clinical benefit. Therefore, during both preclinical and clinical stages, investigators should design and structure studies in a way that maximizes the likelihood of achieving meaningful improvements in important end points, such as decreasing recurrence risk, reducing complications and prolonging survival.

Another practical challenge relates to the limited availability of clinical NIR-II systems and agents. Even if various imaging systems have been developed in preclinical studies, only open-field and backtable surgical imaging systems have been tested in clinical studies to date. More crucially, none of the novel tumour-targeted NIR-II probes, PTAs and photosensitizers have been tested clinically. To overcome this challenge, 'incremental innovation' is strongly recommended. Indeed, innovative NIR-II imaging approaches could serve as an incremental patch to existing clinical systems. Although the composite materials of NIR-II detectors and illuminators typically differ from visible-light or NIR-I imaging devices, the structure of these systems is largely the same; therefore, existing systems could potentially be upgraded to become multispectral by incorporating a NIR-II channel. Presently, the financial costs of NIR-II cameras are slightly higher than those of NIR-I-based models, potentially affecting accessibility temporarily. As technologies become standardized, however, the cost–benefit ratio of clinical NIR-II systems will improve progressively, similar to the development trajectory of NIR-I-based platforms. With regard to NIR-II imaging and therapeutic agents, the current shortage could be partially addressed by utilizing compounds clinically approved for use in NIR-I-based systems, such as ICG, IRDye800CW and methylene blue[44,45,210]. Indeed, these probes have already facilitated the implementation of NIR-II imaging in patients with cancer, and their functionalization for improved tumour targeting can further enhance imaging specificity[39,48]. Current experience indicates that probes with a stable chemical structure, rapid excretion and a high level of tumour specificity are preferable for oncological imaging[5,211,212]. Therefore, small-molecule probes such as CH1055 (ref. 25), DPP-BDT[100] and SCH1100 (ref. 101) are prime candidates for future clinical trials testing NIR-II imaging systems; medical radioisotopes associated with NIR-II Cerenkov luminescence are also notable candidates, if the radiation-related concerns can be adequately addressed, given that numerous radiotracers have been applied widely in cancer diagnosis with excellent performance. Initial trials in patients with cancer have provided valuable insights into how NIR-II imaging can be implemented to enhance clinical decision-making[29,53], reduce complications[60,61,65] and improve survival outcomes[39]. As NIR-II imaging approaches mature and are standardized, the quality of cancer imaging and surgery are expected to be further enhanced. Regarding phototherapy, NIR-II LITT systems such as NeuroBlate and Visualase have demonstrated impressive efficacy with minimal complications[75,81–83]. The availability of these clinical PTT systems might stimulate the investigation of novel NIR-II PTAs and photosensitizers, perhaps prioritizing those that hold potential for combination therapy[213,214]. Furthermore, innovation in the design of theranostic drugs might enable image-guided surgery and phototherapy to be performed simultaneously, improving efficiency and precision[88,215–217]. These advances are expected to pave the way for more successful NIR-II phototherapy in clinical practice.

Additionally, clinical investigations of novel NIR-II agents might be facilitated by optimizing their route of administration. Besides intravenous injection, probes, PTAs and photosensitizers can be administered locally by many methods that have a lower risk of toxicity, such as topical spraying[218,219], transcatheter arterial embolization[220] and oral gargling[221,222]. Ingeniously utilizing these methods could not only avert adverse effects, but also strongly promote the implementation of multitarget imaging and combination therapies, given that these emerging applications typically require simultaneous administration of multiple different agents.

The aforementioned 'bench to bedside and back' flow is likely to be important in optimizing NIR-II imaging and phototherapy strategies, by fostering the development of clinically useful NIR-II agents. Unquestionably, increasing numbers of first-in-human studies of novel NIR-II imaging and phototherapy technologies will emerge in the next few years. A broadened adoption of NIR-II light in clinical oncology, integrating more standardized systems and reagents, should be anticipated.

Looking to the future, ideal cancer imaging techniques will provide quantifiable, multitarget, adjustable FOV, 3D resolvable and real-time images; cancer therapy might be revolutionized with exceptional selectivity for cancer cells and thus fewer adverse effects. Numerous emerging NIR-II techniques such as multitarget cross-scale imaging[33], biosensing imaging[118] and combination therapy (for example, PTT or PDT plus radiotherapy under NIR-II image guidance)[223] are being developed to realize these future aims, thereby reshaping cancer treatments. Cancer surgery can benefit from the use of these novel imaging techniques to visualize multiple different anatomical structures with high resolution and in real-time[224,225]; thus, both precise radical tumour resection and function preservation can be achieved with NIR-II image guidance. Advanced surgical interventions (for example, nerve-sparing resections) might become less complicated, leading to enhanced surgical quality and improved patient outcomes, as well as shortened surgical training times. Moreover, the interpretation of optical images might be transformed by exploiting specific properties of NIR-II fluorescence. Current intensity-based quantification of imaging data is susceptible to interference from ambient light and the nonspecific distribution of probes. Quantification based on the lifetime or ratiometric intensity of NIR-II fluorescence might be immune to these artefacts and therefore holds tremendous potential for the precise analysis of complex oncological features[32,118]. Furthermore, AI methods will probably enable further enhance image quality and the integration of a wider range of physiological information[28,71,72,226]. For inoperable lesions, combination therapy has become a promising and practical trend in cancer treatment, and NIR-II phototherapy has substantial potential to synergize with other therapeutics[227,228]. The integration of NIR-II phototherapy with emerging CDT[201,202], SDT[206] and magnetothermal therapy[229] approaches also offers the possibility to optimize cancer therapies through complementary mechanisms.

Conclusions

NIR-II imaging and therapeutic techniques have contributed significantly to preclinical research and have entered the clinical translation stage of development. These advances have shown the benefits of such techniques in the treatment of operable and inoperable solid cancers. During surgery, multispectral imaging integrating NIR-II can be used to simultaneously visualize lesions and anatomical structures with improved contrast and resolution, thus enhancing surgical quality. Multiple molecular processes in cancer can be clearly observed through a cross-scale view afforded by the macroscopic, mesoscopic and microscopic NIR-II-based imaging techniques. The efficacy of phototherapy for inoperable lesions can also be enhanced by utilizing NIR-II light, and the combination of NIR-II phototherapies with other treatment modalities presents novel therapeutic strategies. Future development of successful NIR-II imaging and phototherapy approaches will require multidisciplinary efforts from the early stages of designing clinical systems to the development of imaging methods and cancer-targeted agents. If these challenges are addressed, NIR-II light has substantial potential to enhance cancer treatments and improve clinical outcomes.

Acknowledgements

The authors acknowledge grant support from the National Natural Science Foundation of China (62027901, 81930053 and 81227901 to J. Tian, 92359301 to J.D., 92259302 to J.J., 92259303 to J.W., 92059207 to Z.H.) and the CAS Youth Interdisciplinary Team (JCTD-2021-08 to Z.H.), as well as research support from the National Key Laboratory of Kidney Diseases (China).

Author contributions

Z.Z., Y.D. and X.S. researched data for the article and wrote the manuscript. All authors made a substantial contribution to discussions of content and reviewed and/or edited the manuscript prior to submission.

Competing interests

The authors declare no competing interests.

References

1. 20 years of precision medicine in oncology. Lancet. 2021;397: 1781.
2. Dell'Oglio, P. et al. Precision surgery: the role of intra-operative real-time image guidance – outcomes from a multidisciplinary European consensus conference. Am. J. Nucl. Med. Mol. Imaging. 2022;12:74–80.
3. Wahida, A. et al. The coming decade in precision oncology: six riddles. Nat. Rev. Cancer. 2023; 23: 43–54.
4. Rowe, S. P. & Pomper, M. G. Molecular imaging in oncology: current impact and future directions. CA Cancer J. Clin. 2022;72: 333–352.
5. Wang, K. et al. Fluorescence image-guided tumour surgery. Nat. Rev. Bioeng.2023 ;1:161–179.
6. Li, X., Lovell, J. F., Yoon, J. & Chen, X. Clinical development and potential of photothermal and photodynamic therapies for cancer. Nat. Rev. Clin. Oncol.2020 ;17: 657–674.
7. Mieog, J. S. D. et al. Fundamentals and developments in fluorescence-guided cancer surgery. Nat. Rev. Clin. Oncol.2022 ;19: 9–22.
8 Kang, H., Kang, M.-W., Kashiwagi, S. & Choi, H. S. NIR fluorescence imaging and treatment for cancer immunotherapy. J. Immunother. Cancer .2022;10: e004936.
9 Vahrmeijer, A. L., Hutteman, M., van der Vorst, J. R., van de Velde, C. J. H. & Frangioni, J. V. Image-guided cancer surgery using near-infrared fluorescence. Nat. Rev. Clin. Oncol. 2013;10, :507–518.
10. Chi, C. et al. Intraoperative imaging-guided cancer surgery: from current fluorescence molecular imaging methods to future multi-modality imaging technology. Theranostics.2014; 4: 1072–1084.
11. Hong, G., Antaris, A. L. & Dai, H. Near-infrared fluorophores for biomedical imaging. Nat. Biomed. Eng.2017; 1:0010.
12. Hu, Z., Chen, W.-H., Tian, J. & Cheng, Z. NIRF nanoprobes for cancer molecular imaging: approaching clinic. Trends Mol. Med.2020; 26: 469–482.
13. Bruns, O. T. et al. Next-generation in vivo optical imaging with short-wave infrared quantum dots. Nat. Biomed. Eng.2017; 1: 0056.
14. Andreou, C., Weissleder, R. & Kircher, M. F. Multiplexed imaging in oncology. Nat. Biomed. Eng. 6, 527–540 (2022).
15. Xu, C. & Pu, K. Second near-infrared photothermal materials for combinational nanotheranostics. Chem. Soc. Rev. 2021;50: 1111–1137 (2021).
16. Zhang, Z., He, K., Chi, C., Hu, Z. & Tian, J. Intraoperative fluorescence molecular imaging accelerates the coming of precision surgery in China. Eur. J. Nucl. Med. Mol. Imaging .2022;49:2531–2543.
17. Smith, A. M., Mancini, M. C. & Nie, S. Bioimaging: second window for in vivo imaging. Nat. Nanotechnol.2009;4: 710–711.
18. Welsher, K. et al. A route to brightly fluorescent carbon nanotubes for near-infrared imaging in mice. Nat. Nanotechnol.2009; 4: 773–780.
19. Li, C., Chen, G., Zhang, Y., Wu, F. & Wang, Q. Advanced fluorescence imaging technology in the near-infrared-II window for biomedical applications. J. Am. Chem. Soc. 2020;142:14789–14804.
20. Feng, Z. et al. Perfecting and extending the near-infrared imaging window. Light. Sci. Appl.2021; 10: 197.
21. Hong, G. et al. Through-skull fluorescence imaging of the brain in a new near-infrared window. Nat. Photonics.2014; 8: 723–730.
22. Diao, S. et al. Fluorescence imaging in vivo at wavelengths beyond 1500 nm. Angew. Chem. Int. Ed. Engl. 2015; 54: 14758–14762.
23. He, S., Song, J., Qu, J. & Cheng, Z. Crucial breakthrough of second near-infrared biological window fluorophores: design and synthesis toward multimodal imaging and theranostics. Chem. Soc. Rev. 2018; 47: 4258–4278.
24. Dai, H. et al. NIR-II organic nanotheranostics for precision oncotherapy. Small. 2021;17: e2102646.
25. Antaris, A. L. et al. A small-molecule dye for NIR-II imaging. Nat. Mater. 2016;15: 235–242.
26. Wang, S., Li, B. & Zhang, F. Molecular fluorophores for deep-tissue bioimaging. ACS Cent. Sci. 2020; 6: 1302–1316.
27. Lei, Z. & Zhang, F. Molecular engineering of NIR-II fluorophores for improved biomedical detection. Angew. Chem. Int. Ed. Engl.2021; 60: 16294–16308.
28. Ma, Z., Wang, F., Wang, W., Zhong, Y. & Dai, H. Deep learning for in vivo near-infrared imaging. Proc. Natl Acad. Sci. USA .2021;118: e2021446118.
29. Hu, Z. et al. First-in-human liver-tumour surgery guided by multispectral fluorescence imaging in the visible and near-infrared-I/II windows. Nat. Biomed. Eng. 2020;4: 259–271.
30. Qu, Q. et al. Novel multifunctional NIR-II aggregation-induced emission nanoparticles-assisted intraoperative identification and elimination of residual tumor. J. Nanobiotechnol. 2022;20: 143.
31. Yang, J. et al. In vivo multifunctional fluorescence imaging using liposome-coated lanthanide nanoparticles in near-infrared-II/IIa/IIb windows. Nano Today. 2021; 38: 101120.
32. Zhong, Y. et al. In vivo molecular imaging for immunotherapy using ultra-bright near-infrared-IIb rare-earth nanoparticles. Nat. Biotechnol. 2019;37: 1322–1331.
33. Wang, F. et al. Light-sheet microscopy in the near-infrared II window. Nat. Methods .2019;16: 545–552.

34. Liu, Y., Bhattarai, P., Dai, Z. & Chen, X. Photothermal therapy and photoacoustic imaging via nanotheranostics in fighting cancer. Chem. Soc. Rev. 2019; 48: 2053–2108.
35. Chen, Q. et al. NIR-II light activated photodynamic therapy with protein-capped gold nanoclusters. Nano Res. 2018;11: 5657–5669.
36. Feng, Z. et al. Excretable IR-820 for in vivo NIR-II fluorescence cerebrovascular imaging and photothermal therapy of subcutaneous tumor. Theranostics. 2019; 9: 5706–5719.
37. Li, Y. et al. Biologically excretable AIE nanoparticles wear tumor cell-derived “exosome caps” for efficient NIR-II fluorescence imaging-guided photothermal therapy. Nano Today .2021;41: 101333.
38. Chen, Y., Wang, S. & Zhang, F. Near-infrared luminescence high-contrast in vivo biomedical imaging. Nat. Rev. Bioeng. 2023;1: 60–78.
39. Shi, X. et al. Near-infrared window II fluorescence image-guided surgery of high-grade gliomas prolongs the progression-free survival of patients. IEEE Trans. Biomed. Eng. 2022; 69: 1889–1900.
40. Viozzi, I., Overduin, C. G., Rijpma, A., Rovers, M. M. & Laan, M. T. MR-guided LITT therapy in patients with primary irresectable glioblastoma: a prospective, controlled pilot study. J. Neurooncol. 2023;164: 405–412.
41. Vogl, T. J., Straub, R., Eichler, K., SöIlner, O. & Mack, M. G. Colorectal carcinoma metastases in liver: laser-induced interstitial thermotherapy – local tumor control rate and survival data. Radiology. 2004; 230: 450–458.
42. Schwarzmaier, H.-J. et al. MR-guided laser-induced interstitial thermotherapy of recurrent glioblastoma multiforme: preliminary results in 16 patients. Eur. J. Radiol. 2006; 59: 208–215.
43. Antaris, A. L. et al. A high quantum yield molecule-protein complex fluorophore for near-infrared II imaging. Nat. Commun. 2017; 8: 15269.
44. Zhu, S. et al. Repurposing cyanine NIR-I dyes accelerates clinical translation of near-infrared-II (NIR-II) bioimaging. Adv. Mater. 2018; 30: 1802546.
45. Carr, J. A. et al. Shortwave infrared fluorescence imaging with the clinically approved near-infrared dye indocyanine green. Proc. Natl Acad. Sci. USA. 2018; 115: 4465–4470.
46. Lauwerends, L. J. et al. Real-time fluorescence imaging in intraoperative decision making for cancer surgery. Lancet Oncol.2021; 22: e186–e195.
47. Wang, X. et al. Consensus guidelines for the use of fluorescence imaging in hepatobiliary surgery. Ann. Surg. 2021; 274: 97–106.
48. Zhang, Z. et al. NIR-II nano fluorescence image guided hepatic carcinoma resection on cirrhotic patient. Photodiagnosis Photodyn. Ther. 2022; 40: 103098.
49. Tsuchikama, K. & An, Z. Antibody-drug conjugates: recent advances in conjugation and linker chemistries. Protein Cell. 2018; 9: 33–46.
50. Yu, W., Liu, R., Zhou, Y. & Gao, H. Size-tunable strategies for a tumor targeted drug delivery system. ACS Cent. Sci. 2020; 6: 100–116.
51. Zhang, Y.-N., Poon, W., Tavares, A. J., McGilvray, I. D. & Chan, W. C. W. Nanoparticle-liver interactions: cellular uptake and hepatobiliary elimination. J. Control. Rel. 2016; 240: 332–348.
52. Cao, C. et al. Intraoperative near-infrared II window fluorescence imaging-assisted nephron-sparing surgery for complete resection of cystic renal masses. Clin. Transl. Med. 2021; 11: e604.
53. Li, C. et al. New and effective EGFR-targeted fluorescence imaging technology for intraoperative rapid determination of lung cancer in freshly isolated tissue. Eur. J. Nucl. Med. Mol. Imaging. 2023; 50: 494–507.
54. MI, J. et al. Comparative study of indocyanine green fluorescence imaging in lung cancer with near-infrared-I/II windows. Ann. Surg. Oncol. 2024;31: 2451–2460.
55. Miller, S. E. et al. First-in-human intraoperative near-infrared fluorescence imaging of glioblastoma using cetuximab-IRDye800. J. Neurooncol. 2018;139: 135–143.
56. Rosenthal, E. L. et al. Sensitivity and specificity of cetuximab-IRDye800CW to identify regional metastatic disease in head and neck cancer. Clin. Cancer Res. 2017;23: 4744–4752.
57. Lamberts, L. E. et al. Tumor-specific uptake of fluorescent bevacizumab–IRDye800CW microdosing in patients with primary breast cancer: a phase I feasibility study. Clin. Cancer Res. 2017; 23: 2730–2741.
58. Lu, G. et al. Tumour-specific fluorescence-guided surgery for pancreatic cancer using panitumumab-IRDye800CW: a phase 1 single-centre, open-label, single-arm, dose-escalation study. Lancet Gastroenterol. Hepatol. 2020; 5: 753–764.
59. de Jongh, S. J. et al. Back-table fluorescence-guided imaging for circumferential resection margin evaluation using bevacizumab-800CW in patients with locally advanced rectal cancer. J. Nucl. Med. 2020; 61: 655–661.
60. Cao, C. et al. First clinical investigation of near-infrared window IIa/IIb fluorescence imaging for precise surgical resection of gliomas. IEEE Trans. Biomed. Eng. 2022; 69: 2404–2413.
61. Wu, Y. et al. First clinical applications for the NIR-II imaging with ICG in microsurgery. Front. Bioeng. Biotechnol. 2022;10: 1042546.
62. Slooter, M. D. et al. Defining indocyanine green fluorescence to assess anastomotic perfusion during gastrointestinal surgery: systematic review. BJS Open. 2021; 5: zraa074.
63. Walsh, E. M. et al. Fluorescence imaging of nerves during surgery. Ann. Surg.2019; 270: 69–76.
64. Rob, L., Halaska, M. & Robova, H. Nerve-sparing and individually tailored surgery for cervical cancer. Lancet Oncol. 2010; 11: 292–301.
65. Qu, Q. et al. Visualisation of pelvic autonomic nerves using NIR-II fluorescence imaging. Eur. J. Nucl. Med. Mol. Imaging. 2022; 49: 4752–4754.
66. Wang, S. et al. Mining whole-lung information by artificial intelligence for predicting EGFR genotype and targeted therapy response in lung cancer: a multicohort study. Lancet Digit. Health. 2022; 4: e309–e319.
67. Dong, D. et al. Development and validation of an individualized nomogram to identify occult peritoneal metastasis in patients with advanced gastric cancer. Ann. Oncol. 2019; 30: 431–438.
68. Wang, S. et al. Predicting EGFR mutation status in lung adenocarcinoma on computed tomography image using deep learning. Eur. Respir. J. 2019; 53: 1800986.
69. Cahill, R. A. et al. Artificial intelligence indocyanine green (ICG) perfusion for colorectal cancer intra-operative tissue classification. Br. J. Surg. 2021;108: 5–9.
70. Kitaguchi, D. et al. Artificial intelligence for the recognition of key anatomical structures in laparoscopic colorectal surgery. Br. J. Surg. 2023110: 1355–1358.
71. Shen, B. et al. Real-time intraoperative glioma diagnosis using fluorescence imaging and deep convolutional neural networks. Eur. J. Nucl. Med. Mol. Imaging .2021;48: 3482–3492.
72. Xiao, A. et al. Intraoperative glioma grading using neural architecture search and multi-modal imaging. IEEE Trans. Med. Imaging. 2022; 41: 2570–2581.
73. Sun, T. et al. Tailor-made semiconducting polymers for second near-infrared photothermal therapy of orthotopic liver cancer. ACS Nano. 2019; 13: 7345–7354.
74. Zeng, Y. et al. Inhibiting osteolytic breast cancer bone metastasis by bone-targeted nanoagent via remodeling the bone tumor microenvironment combined with NIR-II photothermal therapy. Small. 2023; 19: e2301003.
75. Patel, P., Patel, N. V. & Danish, S. F. Intracranial MR-guided laser-induced thermal therapy: single-center experience with the Visualase thermal therapy system. J. Neurosurg. 2016;125: 853–860.
76. Feller, J. et al. A phase II study to evaluate outpatient, transrectally-delivered, MRI-guided laser focal therapy of prostate cancer: 9 year interim results (NCT02243033) [abstract MP78-17]. J. Urol. 2019; 201(4S):e1149 .
77. Eggener, S. E., Yousuf, A., Watson, S., Wang, S. & Oto, A. Phase II evaluation of magnetic resonance imaging guided focal laser ablation of prostate cancer. J. Urol. 2016; 196: 1670–1675.
78. US Food & Drug Administration. https://www.accessdata.fda.gov/cdrh_docs/pdf19/K193375.pdf (2020).
79. US Food & Drug Administration. https://www.accessdata.fda.gov/cdrh_docs/pdf21/K211269.pdf (2022).
80. US Food & Drug Administration. https://www.accessdata.fda.gov/cdrh_docs/pdf20/K201466.pdf (2021).
81. Mohammadi, A. M. & Schroeder, J. L. Laser interstitial thermal therapy in treatment of brain tumors – the NeuroBlate system. Expert. Rev. Med. Devices. 2014; 11: 109–119.
82. Belykh, E. et al. Laser application in neurosurgery. Surg. Neurol. Int. 2017; 8: 274.
83. Sloan, A. E. et al. Results of the NeuroBlate System first-in-humans phase I clinical trial for recurrent glioblastoma: clinical article. J. Neurosurg. 2013; 118: 1202–1219.
84. Zhou, H.-J. & Ren, T.B. Recent progress of cyanine fluorophores for NIR-II sensing and imaging. Chem. Asian J. 2022; 17: e202200147.
85. Lin, H. et al. Near-infrared-II nanomaterials for fluorescence imaging and photodynamic therapy. Adv. Opt. Mater. 2021; 9: 2002177.
86. Li, C. et al. Near-infrared metal agents assisting precision medicine: from strategic design to bioimaging and therapeutic applications. Chem. Soc. Rev. 2023; 52: 4392–4442.
87. Liu, S., Xu, W., Li, X., Pang, D.-W. & Xiong, H. BOIMPY-based NIR-II fluorophore with high brightness and long absorption beyond 1000 nm for in vivo bioimaging: synergistic steric regulation strategy. ACS Nano. 2022; 16: 17424–17434.
88. Sun, Y. et al. Rhomboidal Pt(II) metallacycle-based NIR-II theranostic nanoprobe for tumor diagnosis and image-guided therapy. Proc. Natl Acad. Sci. USA. 2019; 116: 1968–1973.
89. Ren, Y. et al. An NIR-II/MR dual modal nanoprobe for liver cancer imaging. Nanoscale 12, 11510–11517 (2020).
90. Wang, P. et al. NIR-II nanoprobes in-vivo assembly to improve image-guided surgery for metastatic ovarian cancer. Nat. Commun. 2018; 9: 2898.
91. Lou, H. et al. A novel NIR-II nanoprobe for precision imaging of micro-meter sized tumor metastases of multi-organs and skin flap. Chem. Eng. J. 2022; 449: 137848.
92. Sheng, Z. et al. Bright aggregation-induced-emission dots for targeted synergetic NIR-II fluorescence and NIR-I photoacoustic imaging of orthotopic brain tumors. Adv. Mater. 2018; 30: 1800766.
93. Yu, W. et al. NIR-II fluorescence in vivo confocal microscopy with aggregation-induced emission dots. Sci. Bull. 2019; 64: 410–416.
94. Feng, Z. et al. Engineered NIR-II fluorophores with ultralong-distance molecular packing for high-contrast deep lesion identification. Nat. Commun. 2023; 14: 5017.
95. Feng, Z. et al. Biologically excretable aggregation-induced emission dots for visualizing through the marmosets intravitally: horizons in future clinical nanomedicine. Adv. Mater. 2021; 33: e2008123.
96. Isoda, K. et al. Toxicity of gold nanoparticles in mice due to nanoparticle/drug interaction induces acute kidney damage. Nanoscale Res. Lett. 2020; 15: 141.
97. Cornu, R., Béduneau, A. & Hélène Martin, H. Influence of nanoparticles on liver tissue and hepatic functions: a review. Toxicology .2020; 430, 152344.
98. Yao, Y., Zang, Y., Qu, J., Tang, M. & Zhang, T. The toxicity of metallic nanoparticles on liver: the subcellular damages, mechanisms, and outcomes. Int. J. Nanomed. 2019; 14; 8787–8804.
99. Sun, Y. et al. Novel bright-emission small-molecule NIR-II fluorophores for in vivo tumor imaging and image-guided surgery. Chem. Sci. 2017; 8: 3489–3493.
100. Wang, Q. et al. Biocompatible small organic molecule phototheranostics for NIR-II fluorescence/photoacoustic imaging and simultaneous photodynamic/photothermal combination therapy. Mater. Chem. Front. 2019; 3: 650–655.
101. Sun, Y. et al. Novel benzo-bis(1,2,5-thiadiazole) fluorophores for in vivo NIR-II imaging of cancer. Chem. Sci. 2016; 7: 6203–6207.
102. Yang, Q. et al. Rational design of molecular fluorophores for biological imaging in the NIR-II window. Adv. Mater. 2017; 29(12).
103. Dai, H. et al. Small molecular NIR-II fluorophores for cancer phototheranostics. Innovation. 2021; 2: 100082.
104. Su, Y., Yu, B., Wang, S., Cong, H. & Shen, Y. NIR-II bioimaging of small organic molecule. Biomaterials. 2021; 271: 120717.
105. Ding, F., Zhan, Y., Lu, X. & Sun, Y. Recent advances in near-infrared II fluorophores for multifunctional biomedical imaging. Chem. Sci. 2018; 9: 4370–4380.
106. Miao, Q. & Pu, K. Organic semiconducting agents for deep-tissue molecular imaging: second near-infrared fluorescence, self-luminescence, and photoacoustics. Adv. Mater. 2018; 30: e1801778.
107. Guo, X. et al. NIR-II fluorescence imaging-guided colorectal cancer surgery targeting CEACAM5 by a nanobody. EBioMedicine. 2023; 89: 104476.
108. Xu, Y. et al. In situ albumin-hitchhiking NIR-II probes for accurate detection of micrometastases. Nano Lett. 2023; 23: 5731–5737.
109. Zhu, Y.-Y. et al. Development of a rare earth nanoprobe enables in vivo real-time detection of sentinel lymph node metastasis of breast cancer using NIR-IIb imaging. Cancer Res. 2023; 83: 3428–3441.
110 Zhang, X. et al. Activatable NIR-II organic fluorescent probes for bioimaging. Theranostics. 2022; 12: 3345–3371.
111. Zhao, M., Li, B., Zhang, H. & Zhang, F. Activatable fluorescence sensors for in vivo bio-detection in the second near-infrared window. Chem. Sci. 2020; 12: 3448–3459.
112. Lu, L. et al. NIR-II bioluminescence for in vivo high contrast imaging and in situ ATP-mediated metastases tracing. Nat. Commun. 2020; 11: 4192.
113. Ling, S. et al. Tumor microenvironment-activated NIR-II nanotheranostic system for precise diagnosis and treatment of peritoneal metastasis. Angew. Chem. Int. Ed. Engl. 2020; 59: 7219–7223.
114. Shen, H. et al. Rational design of NIR-II AIEgens with ultrahigh quantum yields for photo- and chemiluminescence imaging. J. Am. Chem. Soc. 2022; 144: 15391–15402.
115. Chen, Z. et al. Design and synthesis of a small molecular NIR-II chemiluminescence probe for in vivo-activated H2S imaging. Proc. Natl Acad. Sci. USA. 2023;120: e2205186120.
116. Chang, B. et al. A phosphorescent probe for in vivo imaging in the second near-infrared window. Nat. Biomed. Eng. 2022; 6: 629–639.
117. Li, M. et al. Near-infrared-II ratiometric fluorescence probes for non-invasive detection and precise navigation surgery of metastatic sentinel lymph nodes. Theranostics. 2022;12: 7191–7202.
118. Fan, Y. et al. Lifetime-engineered NIR-II nanoparticles unlock multiplexed in vivo imaging. Nat. Nanotechnol. 2018;13: 941–946.
119. Liao, N. et al. In vivo tracking of cell viability for adoptive natural killer cell-based immunotherapy by ratiometric NIR-II fluorescence imaging. Angew. Chem. Int. Ed. Engl. 2021; 60: 20888–20896.
120. Wang, S. et al. In vivo high-resolution ratiometric fluorescence imaging of inflammation using NIR-II nanoprobes with 1550 nm emission. Nano Lett. 2019; 19: 2418–2427.
121. Wang, S. et al. Anti-quenching NIR-II molecular fluorophores for in vivo high-contrast imaging and pH sensing. Nat. Commun. 2019; 10: 1058.
122. Hong, G. et al. Multifunctional in vivo vascular imaging using near-infrared II fluorescence. Nat. Med. 2012; 18: 1841–1846.
123. Wu, D. et al. Organic dots with large π-conjugated planar for cholangiography beyond 1500 nm in rabbits: a non-radioactive strategy. ACS Nano. 2021; 15: 5011–5022 (2021).
124. Yu, X. et al. Aggregation-induced emission dots assisted non-invasive fluorescence hysteregraphy in near-infrared IIb window. Nano Today. 2021; 39: 101235.
125. Fan, X. et al. Nanoprobes-assisted multichannel NIR-II fluorescence imaging-guided resection and photothermal ablation of lymph nodes. Adv. Sci. 2021; 8: 2003972.
126. Chang, Y. et al. Bright Tm3+-based downshifting luminescence nanoprobe operating around 1800 nm for NIR-IIb and c bioimaging. Nat. Commun. 2023;14: 1079.
127. Wang, F. et al. In vivo non-invasive confocal fluorescence imaging beyond 1,700 nm using superconducting nanowire single-photon detectors. Nat. Nanotechnol. 2022; 17: 653–660.
128. He, M. et al. Protein-enhanced NIR-IIb emission of indocyanine green for functional bioimaging. ACS Appl. Bio Mater. 2020; 3: 9126–9134.
129. Wu, D. et al. Extrahepatic cholangiography in near-infrared II window with the clinically approved fluorescence agent indocyanine green: a promising imaging technology for intraoperative diagnosis. Theranostics. 2020; 10: 3636–3651.
130. Du, J. et al. Highly stable and bright NIR-II AIE dots for intraoperative identification of ureter. ACS Appl. Mater. Interfaces. 2020; 12: 8040–8049.
131. Wang, F. et al. In vivo NIR-II fluorescence imaging for biology and medicine. Nat. Photon.2024; 18:535–547.
132. Wang, L. G. & Gibbs, S. L. Improving precision surgery: a review of current intraoperative nerve tissue fluorescence imaging. Curr. Opin. Chem. Biol. 2023; 76: 102361.
133. He, K. et al. Near-infrared intraoperative imaging of thoracic sympathetic nerves: from preclinical study to clinical trial. Theranostics. 2018; 8: 304–313.
134. He, K. et al. Intraoperative near-infrared fluorescence imaging can identify pelvic nerves in patients with cervical cancer in real time during radical hysterectomy. Eur. J. Nucl. Med. Mol. Imaging. 2022; 49: 2929–2937.
135. Whitney, M. A. et al. Fluorescent peptides highlight peripheral nerves during surgery in mice. Nat. Biotechnol. 2011; 29: 352–356.
136. Wang, L. G. et al. Near-infrared nerve-binding fluorophores for buried nerve tissue imaging. Sci. Transl. Med. 2020; 12: eaay0712.
137. Feng, Z. et al. In vivo and in situ real-time fluorescence imaging of peripheral nerves in the NIR-II window. Nano Res. 2019; 12: 3059–3068.
138. Barth, C. W. et al. Nerve-sparing gynecologic surgery enabled by a near-infrared nerve-specific fluorophore using existing clinical fluorescence imaging systems. Small, 2023; 14:e2300011.
139. Hingorani, D. V. et al. Nerve-targeted probes for fluorescence-guided intraoperative imaging. Theranostics.2018; 8: 4226–4237.
140. Glasgow, H. L. et al. Laminin targeting of a peripheral nerve-highlighting peptide enables degenerated nerve visualization. Proc. Natl Acad. Sci. USA. 2016; 113: 12774–12779.
141. Dip, F., Falco, J., White, K. & Rosenthal, R. Fluorescence imaging to visualize the recurrent laryngeal nerve during thyroidectomy procedures: analysis of 65 cases and 81 nerves. Surg. Endosc. 2024; 38: 1406–1413.
142. Dip, F. et al. Nerve autofluorescence under near-ultraviolet light: cutting-edge technology for intra-operative neural tissue visualization in 17 patients. Surg. Endosc. 2022; 36: 4079–4089.
143. Suo, Y. et al. NIR-II fluorescence endoscopy for targeted imaging of colorectal cancer. Adv. Healthc. Mater. 2019; 8: e1900974.
144. Wang, T., Chen, Y., Wang, B. & Wu, M. Recent progress of second near-infrared (NIR-II) fluorescence microscopy in bioimaging. Front. Physiol. 2023; 14: 1126805.
145. Qi, J. et al. Real-time and high-resolution bioimaging with bright aggregation-induced emission dots in short-wave infrared region. Adv. Mater. 2018; 30: e1706856.
146. Zhan, Y. et al. Rapid unperturbed-tissue analysis for intraoperative cancer diagnosis using an enzyme-activated NIR-II nanoprobe. Angew. Chem. Int. Ed. Engl. 2021; 60: 2637–2642.
147. Fan, X. et al. NIR-II and visible fluorescence hybrid imaging-guided surgery via aggregation-induced emission fluorophores cocktails. Mater. Today Bio. 2022; 16: 100399.
148. Wang, F. et al. In vivo NIR-II structured-illumination light-sheet microscopy. Proc. Natl Acad. Sci. USA. 2021; 118: e2023888118.
149. Zhu, S. et al. Molecular imaging of biological systems with a clickable dye in the broad 800- to 1,700-nm near-infrared window. Proc. Natl Acad. Sci. USA. 2017; 114: 962–967.
150. Wan, H. et al. A bright organic NIR-II nanofluorophore for three-dimensional imaging into biological tissues. Nat. Commun. 2018; 9: 1171.
151. 151.Li, B. et al. Noninvasive gastrointestinal tract imaging using BSA-Ag2Te quantum dots as a CT/NIR-II fluorescence dual-modal imaging probe in vivo. ACS Biomater. Sci. Eng. 2023; 9: 449–457.
152. 152.Zhang, N. et al. DNA-functionalized liposomes in vivo fusion for NIR-II/MRI guided pretargeted ferroptosis therapy of metastatic breast cancer. ACS Appl. Mater. Interfaces. 2022; 14: 20603–20615.
153. 153.Liu, W.-L. et al. Novel dual-mode NIR-II/MRI nanoprobe targeting PD-L1 accurately evaluates the efficacy of immunotherapy for triple-negative breast cancer. Int. J. Nanomed. 2023; 18: 5141–5157.
154. Zheng, Z. et al. Biodegradable silica-based nanotheranostics for precise MRI/NIR-II fluorescence imaging and self-reinforcing antitumor therapy. Small. 2021; 17: e2006508.
155. Cai, M., Zhang, Z., Shi, X., Hu, Z. & Tian, J. NIR-II/NIR-I fluorescence molecular tomography of heterogeneous mice based on gaussian weighted neighborhood fused lasso method. IEEE Trans. Med. Imaging. 2020; 39: 2213–2222.
156. Shi, X., Guo, L., Liu, J., Tian, J. & Hu, Z. NIR-IIb fluorescence molecular tomography of glioblastomas based on heterogeneous mouse models and adaptive projection match pursuit method. IEEE Trans. Biomed. Eng. 2023; 70:2258–2269.
157. Cao, C. et al. Excitation-based fully connected network for precise NIR-II fluorescence molecular tomography. Biomed. Opt. Express. 2022; 13: 6284–6299.
158. Zhang, Q. et al. Hierarchically nanostructured hybrid platform for tumor delineation and image-guided surgery via NIR-II fluorescence and PET bimodal imaging. Small. 2019; 15: e1903382.
159. Shi, X. et al. PET/NIR-II fluorescence imaging and image-guided surgery of glioblastoma using a folate receptor α-targeted dual-modal nanoprobe. Eur. J. Nucl. Med. Mol. Imaging. 2022; 49: 4325–4337.
160. Zhang, X. et al. A thiopyrylium salt for PET/NIR-II tumor imaging and image-guided surgery. Mol. Oncol. 2020; 14:1089–1100.
161. Cao, X. et al. Cherenkov excited short-wavelength infrared fluorescence imaging in vivo with external beam radiation. J. Biomed. Opt. 2018; 24: 1–4.
162. Meng, X. et al. Cherenkov excited luminescence imaging induced by megavolt X-ray beams in the second near-infrared window. Opt. Commun. 2019; 452: 417–421.
163. Mc Larney, B. E. et al. Detection of shortwave-infrared cerenkov luminescence from medical isotopes. J. Nucl. Med. 2023; 64: 177–182.
164. Zhen, X., Pu, K. & Jiang, X. Photoacoustic imaging and photothermal therapy of semiconducting polymer nanoparticles: signal amplification and second near-infrared construction. Small 17, e2004723 (2021).
165. Jiang, Y. et al. Metabolizable semiconducting polymer nanoparticles for second near-infrared photoacoustic imaging. Adv. Mater. 2019; 31: e1808166.
166. Huang, J. & Pu, K. Activatable molecular probes for second near-infrared fluorescence, chemiluminescence, and photoacoustic imaging. Angew. Chem. Int. Ed. Engl. 2020; 59: 11717–11731.
167. Li, Z. et al. NIR-II functional materials for photoacoustic theranostics. Bioconjug. Chem. 2022; 33: 67–86.
168. Lin, L. & Wang, L. V. The emerging role of photoacoustic imaging in clinical oncology. Nat. Rev. Clin. Oncol. 2022; 19: 365–384.
169. Jin, L. & Liang, Y. Fiber laser technologies for photoacoustic microscopy. Vis. Comput. Ind. Biomed. Art. 2021; 4: 11.
170. Chen, J., Chen, L., Zeng, F. & Wu, S. Aminopeptidase N activatable nanoprobe for tracking lymphatic metastasis and guiding tumor resection surgery via optoacoustic/NIR-II fluorescence dual-mode imaging. Anal. Chem. 2022; 94: 8449–8457.
171. Ouyang, J. et al. Nanoaggregate probe for breast cancer metastasis through multispectral optoacoustic tomography and aggregation-induced NIR-I/II fluorescence imaging. Angew. Chem. 2020; 59: 10111–10121.
172. Chen, Y.-S., Zhao, Y., Yoon, S. J., Gambhir, S. S. & Emelianov, S. Miniature gold nanorods for photoacoustic molecular imaging in the second near-infrared optical window. Nat. Nanotechnol. 2019; 14: 465–472.
173. Chen, T. et al. Dual activated NIR-II fluorescence and photoacoustic imaging-guided cancer chemo-radiotherapy using hybrid plasmonic-fluorescent assemblies. Nano Res. 2020; 13: 3268–3277.
174. Dai, Y. et al. NIR-II excitation phototheranostic nanomedicine for fluorescence/photoacoustic tumor imaging and targeted photothermal-photonic thermodynamic therapy. Small. 2021; 17: e2102527.
175. Nguyen, A., Kumar, S. & Kulkarni, A. A. Nanotheranostic strategies for cancer immunotherapy. Small Methods. 2022; 6: e2200718.
176. Zhou, T. et al. A hepatocellular carcinoma targeting nanostrategy with hypoxia-ameliorating and photothermal abilities that, combined with immunotherapy, inhibits metastasis and recurrence.ACS Nano.2020;14:12679–12696.
177. Sun, W. et al. Synergistic triple-combination therapy with hyaluronic acid-shelled PPy/CPT nanoparticles results in tumor regression and prevents tumor recurrence and metastasis in 4T1 breast cancer. Biomaterials. 2019; 217: 119264.
178. Wang, Q. et al. All□in□one phototheranostics: single laser triggers NIR□II fluorescence/photoacoustic imaging guided photothermal/photodynamic/chemo combination therapy. Adv. Funct. Mat. 2019; 29: 1901480.
179. Ji, Y. et al. Near-infrared fluorescence imaging in immunotherapy. Adv. Drug. Deliv. Rev. 167, 121–134 (2020).
180. Du, Y., Qi, Y., Jin, Z. & Tian, J. Noninvasive imaging in cancer immunotherapy: the way to precision medicine. Cancer Lett. 2019; 466: 13–22.
181. Li, J. et al. Synchronously manipulating absorption and extinction coefficient of semiconducting polymers via precise dual-acceptor engineering for NIR-II excited photothermal theranostics. Angew. Chem. 2023; 62: e202301617.
182. Li, C. et al. Fluorination enhances NIR-II emission and photothermal conversion efficiency of phototheranostic agents for imaging-guided cancer therapy. Adv. Mater. 2023; 35: e2208229.
183. Jiang, Y. et al. Transformable hybrid semiconducting polymer nanozyme for second near-infrared photothermal ferrotherapy. Nat. Commun. 2020; 11: 1857.
184. Zhou, Z. et al. Metallic 1T phase enabling MoS2 nanodots as an efficient agent for photoacoustic imaging guided photothermal therapy in the near-infrared-II window. Small. 2020; 16: e2004173.
185. Li, L. et al. An NIR-II-emissive photosensitizer for hypoxia-tolerant photodynamic theranostics. Adv. Mater. 2020; 32: e2003471.
186. Li, W. et al. NIR-II fluorescence imaging-guided oxygen self-sufficient nano-platform for precise enhanced photodynamic therapy. Small. 2022; 18: e2205647.
187. Yang, Y. et al. Coupling probiotics with 2D CoCuMo-LDH nanosheets as a tumor-microenvironment-responsive platform for precise NIR-II photodynamic therapy. Adv. Mater. 2023; 35: e2211205.
188. Zhang, W. et al. Bioorthogonal-targeted 1064 nm excitation theranostic nanoplatform for precise NIR-IIa fluorescence imaging guided efficient NIR-II photothermal therapy. Biomaterials. 2020; 243: 119934.
189. Cui, J. et al. ‘Trojan Horse’ phototheranostics: fine-engineering NIR-II AIEgen camouflaged by cancer cell membrane for homologous-targeting multimodal imaging-guided phototherapy. Adv. Mater. 2023; 35: e2302639.
190. Cao, Y. et al. Engineered exosome-mediated near-infrared-II region V2C quantum dot delivery for nucleus-target low-temperature photothermal therapy. ACS Nano. 2019; 13:

Nat Rev Clin Oncol. 2024.21: 449-467 Published online: 1 May 2024

1499–1510.
191. Zhuang, J. et al. Efficient NIR-II type-I AIE photosensitizer for mitochondria-targeted photodynamic therapy through synergistic apoptosis-ferroptosis. ACS Nano. 2023; 17: 9110–9125.
192. Liu, Y., Liang, Y., Lei, P., Zhang, Z. & Chen, Y. Multifunctional superparticles for magnetically targeted NIR-II imaging and photodynamic therapy. Adv. Sci. 2023; 10: e2203669.
193. Jiang, Y., Huang, J., Xu, C. & Pu, K. Activatable polymer nanoagonist for second near-infrared photothermal immunotherapy of cancer. Nat. Commun. 2021; 12: 742.
194. Ma, Y. et al. Near-infrared II phototherapy induces deep tissue immunogenic cell death and potentiates cancer immunotherapy. ACS Nano. 2019; 13: 11967–11980.
195. Wen, M. et al. Artificial enzyme catalyzed cascade reactions: antitumor immunotherapy reinforced by NIR-II light. Angew. Chem. 2019; 58: 17425–17432.
196. Lan, P. et al. NIR-II responsive molybdenum dioxide nanosystem manipulating cellular immunogenicity for enhanced tumor photoimmunotherapy. Nano Lett. 2022; 22: 4741–4749.
197. Yan, D. et al. Multimodal imaging-guided photothermal immunotherapy based on a versatile NIR-II aggregation-induced emission luminogen. Angew. Chem. Int. Ed. Engl. 2022; 61: e202202614.
198. Chen, M.-M. et al. A plasmon-enhanced theranostic nanoplatform for synergistic chemo-phototherapy of hypoxic tumors in the NIR-II window. Chem. Sci. 2021; 12: 10848–10854.
199. Yang, Y. et al. NIR-II driven plasmon-enhanced catalysis for a timely supply of oxygen to overcome hypoxia-induced radiotherapy tolerance. Angew. Chem. 2019; 58: 15069–15075.
200. Cheng, D. et al. 131I-Labeled gold nanoframeworks for radiotherapy-combined second near-infrared photothermal therapy of cancer. J. Mater. Chem. B. 2021; 9: 9316–9323.
201. Liu, Y. et al. One-dimensional Fe2 P acts as a Fenton agent in response to NIR II light and ultrasound for deep tumor synergetic theranostics. Angew. Chem. Int. Ed. Engl. 2019; 58: 2407–2412.
202. Yang, C. et al. Programmable NIR-II photothermal-enhanced starvation-primed chemodynamic therapy using glucose oxidase-functionalized ancient pigment nanosheets. Small. 2020; 16: e2001518.
203. Dai, Y. et al. An activatable phototheranostic nanoplatform for tumor specific NIR-II fluorescence imaging and synergistic NIR-II photothermal-chemodynamic therapy. Small. 2023; 19: e2206053.
204. Chen, T. et al. Singlet oxygen generation in dark-hypoxia by catalytic microenvironment-tailored nanoreactors for NIR-II fluorescence-monitored chemodynamic therapy. Angew. Chem. Int. Ed. Engl. 60, 15006–15012 (2021).
205. Liu, X., Wang, J., Wu, Y., Wu, M. & Song, J. Ultrasound activated probe for disease imaging and therapy in-vivo. Adv. Drug. Deliv. Rev. 2024; 205: 115158.
206. Liu, Y. et al. Defect modified zinc oxide with augmenting sonodynamic reactive oxygen species generation. Biomaterials. 2020; 251: 120075.
207. James, M. L. & Gambhir, S. S. A molecular imaging primer: modalities, imaging agents, and applications. Physiol. Rev. 2012; 92: 897–965.
208. Hampton, T. Bench to bedside and back again may be key to clinical breakthroughs. JAMA. 2017; 318: 16–17 .
209. Mitchell, M. J., Jain, R. K. & Langer, R. Engineering and physical sciences in oncology: challenges and opportunities. Nat. Rev. Cancer. 2017; 17: 659–675.
210. Xue, D. et al. Structural and functional NIR-II fluorescence bioimaging in urinary system via clinically approved dye methylene blue. Engineering. 2023; 22: 149–158.
211. Hernot, S., van Manen, L., Debie, P., Mieog, J. S. D. & Vahrmeijer, A. L. Latest developments in molecular tracers for fluorescence image-guided cancer surgery. Lancet Oncol. 2019; 20: e354–e367.
212. Barth, C. W. & Gibbs, S. L. Fluorescence image-guided surgery – a perspective on contrast agent development. Proc. SPIE Int. Soc. Opt. Eng. 2020; 11222: 112220J.
213. Bozinov, O., Yang, Y., Oertel, M. F., Neidert, M. C. & Nakaji, P. Laser interstitial thermal therapy in gliomas. Cancer Lett. 2020; 474: 151–157.
214. Overchuk, M., Weersink, R. A., Wilson, B. C. & Zheng, G. Photodynamic and photothermal therapies: synergy opportunities for nanomedicine. ACS Nano. 2023; 17: 7979–8003.
215. Roy, S., Bag, N., Bardhan, S., Hasan, I. & Guo, B. Recent progress in NIR-II fluorescence imaging-guided drug delivery for cancer theranostics. Adv. Drug. Deliv. Rev. 2023; 197: 114821.
216. Zheng, Y. et al. All-in-one mitochondria-targeted NIR-II fluorophores for cancer therapy and imaging. Chem. Sci. 2020; 12: 1843–1850.
217. Tao, W. & Farokhzad, O. C. Theranostic nanomedicine in the NIR-II window: classification, fabrication, and biomedical applications. Chem. Rev. 2022; 122: 5405–5407.
218. Nagengast, W. B. et al. Near-infrared fluorescence molecular endoscopy detects dysplastic oesophageal lesions using topical and systemic tracer of vascular endothelial growth factor A. Gut. 2019; 68: 7–10.
219. Chen, J. et al. Multiplexed endoscopic imaging of Barrett's neoplasia using targeted fluorescent heptapeptides in a phase 1 proof-of-concept study. Gut. 2021; 70: 1010–1013.
220. 220.He, P. et al. An exploratory human study of superstable homogeneous lipiodol-indocyanine green formulation for precise surgical navigation in liver cancer. Bioeng. Transl. Med. 2022; 8: e10404.
221. Wang, J. et al. A c-MET-targeted topical fluorescent probe cMBP-ICG improves oral squamous cell carcinoma detection in humans. Ann. Surg. Oncol. 2023; 30: 641–651.
222. Kossatz, S. et al. Validation of the use of a fluorescent PARP1 inhibitor for the detection of oral, oropharyngeal and oesophageal epithelial cancers. Nat. Biomed. Eng. 2020; 4: 272–285.
223. Huang, J. et al. Molecular radio afterglow probes for cancer radiodynamic theranostics. Nat. Mater. 2023; 22: 1421–1429.
224. Li, B., Zhao, M., Lin, J., Huang, P. & Chen, X. Management of fluorescent organic/inorganic nanohybrids for biomedical applications in the NIR-II region. Chem. Soc. Rev. 2022; 51: 7692–7714.
225. Mu, J. et al. The chemistry of organic contrast agents in the NIR-II window. Angew. Chem. Int. Ed. Engl. 2022; 61: e202114722.
226. Zhang, H., Meng, Z., Ru, J., Meng, Y. & Wang, K. Application and prospects of AI-based radiomics in ultrasound diagnosis. Vis. Comput. Ind. Biomed. Art. 2023; 6: 20.
227. Ng, C. W., Li, J. & Pu, K. Recent progresses in phototherapy-synergized cancer immunotherapy. Adv. Funct. Mater. 2018; 28: 1804688.
228. Xie, Z. et al. Emerging combination strategies with phototherapy in cancer nanomedicine. Chem. Soc. Rev. 2020; 49: 8065–8087.
229. Song, G. et al. Carbon-coated FeCo nanoparticles as sensitive magnetic-particle-imaging tracers with photothermal and magnetothermal properties. Nat. Biomed. Eng. 2020; 4: 325–334.
230. Yu, X. et al. Deciphering of cerebrovasculatures via ICG-assisted NIR-II fluorescence microscopy. J. Mater. Chem. B. 2019; 7: 6623–6629.
231. Parikh, B. B. & Neil, E. C. Evolving strategies to potentially further optimize surgical interventions in brain cancer. Curr. Oncol. Rep. 2020; 22: 32.
232. Missios, S., Bekelis, K. & Barnett, G. H. Renaissance of laser interstitial thermal ablation. Neurosurg. Focus. 2015; 38: E13.

Review Article

Fluorescence Image-Guided Tumour Surgery

Kun Wang [1,2,3,4,11,*], Yang Du [1,2,3,4,11,*], Zeyu Zhang [5,11,*], Kunshan He [6,7], Zhongquan Cheng [8], Lin Yin [1,2,3,4], Di Dong [1,2,3,4], Changjian Li [5], Wei Li [1,3,4,9], Zhenhua Hu [1,2,3,4], Chong Zhang [10], Hui Hui [1,2,3,4], Chongwei Chi[1,3,4] & Jie Tian [1,3,4,5]

Abstract

Intraoperative fluorescent imaging can provide real-time identifcation of tumours, lymph nodes, nerves and other healthy and malignant tissues during oncological surgery, contributing to better surgical outcomes. Various fluorescent probes have been clinically approved for surgical applications, improving tumour resection precision and preventing iatrogenic injury. In this Review, we discuss the development and application of fuorescent probes for image-guided surgery, including systemically and locally applied probes that are either nontargeted or targeted to specifc tumours and tissues. We discuss the optimization and clinical potential of these probes, and highlight their current and future applications in oncological surgery. In addition, we examine the hardware of fuorescence imaging equipment, and discuss how artifcial intelligence can enable real-time quantifcation to guide surgical decision-making. Finally, we highlight the remaining challenges in the feld of image-guided surgery, including the need for standardization to achieve regulatory approval of new probes, and the required team effort for new probe development.

[1] CAS Key Laboratory of Molecular Imaging, Institute of Automation, Chinese Academy of Sciences, Beijing, China.

[2] School of Artificial Intelligence, University of Chinese Academy of Sciences, Beijing, China.

[3] Beijing Key Laboratory of Molecular Imaging, Institute of Automation, Chinese Academy of Sciences, Beijing, China.

[4] State Key Laboratory Management and Control for Complex Systems, Institute of Automation, Chinese Academy of Sciences, Beijing, China.

[5] Beijing Advanced Innovation Center for Big Data-Based Precision Medicine, School of Engineering Medicine, Beihang University, Beijing, China.

[6] State Key Laboratory of Computer Science, Institute of Software, Chinese Academy of Sciences, Beijing, China.

[7] Beijing Key Laboratory of Human–Computer Interaction, Institute of Software, Chinese Academy of Sciences, Beijing, China.

[8] Department of General Surgery, Capital Medical University, Beijing Friendship Hospital, Beijing, China.

[9] Medical Imaging Center, the First Affiliated Hospital, Jinan University, Guangzhou, China.
[10] Department of Big Data Management and Application, School of International Economics and Management, Beijing Technology and Business University, Beijing, China.
* These authors contributed equally: Kun Wang, Yang Du, Zeyu Zhang.

Key points

- Fluorescence image-guided surgery offers real-time intraoperative visualization of tumours and/or nearby healthy tissues, enabling high-precision tumour resection and prevention of iatrogenic injury.
- Several fluorescence imaging probes have been clinically approved for oncological surgery, including non-targeted and tumour-targeted probes, and various new probes are being explored at the preclinical stage.
- Hardware improvements and artificial intelligence software of intraoperative fluorescence imaging systems have improved imaging quality and enable image quantification, optimized ergonomics and straightforward human–machine interaction.
- The clinical translation of new fluorescent imaging probes will require equipment standardization, interdisciplinary cooperation and technological development.

Introduction

Surgical resection of solid tumours always aims at complete removal of cancerous tissue and maximum preservation of healthy tissue, which requires the accurate identification of the tumour (including the primary tumour and metastases) and nearby healthy tissue (such as nerves, blood vessels and lymph nodes) during the operation[1,2]. However, the difference between tumour and healthy tissue is often unrecognizable by the naked eye and non-palpable by hands[3,4]. Alternatively, fluorescence image-guided surgery[2–4] offers real-time intraoperative visualization of tumours and nearby healthy tissues.

In intraoperative fluorescence imaging, a fluorescent probe is first preoperatively or intraoperatively administered into the tissues of interest. An external light source then illuminates the tissues during surgery, and the emitted light is captured by a specialized camera system, providing an optical contrast for surgical resection[4]. In clinical practice, fluorescent wavelengths in the near-infrared (NIR) region are preferred, including the first (NIR-I, 700–900 nm) and second (NIR-II, 1,000–1,700 nm) NIR windows. Compared with visible light, NIR light can visualize deep tissue (up to 1 cm or more), because it has less optical scattering and less autofluorescence[5,6]. However, limited imaging depth remains an issue for deep tissue tumours. Importantly, fluorescence image-guided surgery depends on the effectiveness (such as targeting ability, emission spectra and quantum efficiency) of fluorescent probes, the quality of the intraoperative imaging system and the cooperation between those two.

Several fluorescent probes, including indocyanine green (ICG) and methylene blue (MB), are currently approved for fluorescence image-guided surgery by the US Food and Drug Administration (FDA), the National Medical Products Administration (NMPA) in China and the European Medicines Agency (EMA)[3,7] (Table 1). In addition, various fluorescent probes are being explored preclinically and in clinical trials, including targeted, activatable and hybrid (combining optical with radionuclide or magnetic signals) probes, with better optical properties, compared with ICG and MB (Fig. 1). Moreover, fluorescent imaging devices have been developed that allow intraoperative navigation in open and minimally invasive surgeries, including devices operating with artificial intelligence (AI)[8].

In addition to fluorescence imaging, ultrasonography, X-ray imaging, computer tomography, magnetic resonance imaging (MRI), γ-radiation imaging and Cerenkov luminescence are clinically used for intraoperative imaging; however, these techniques can interfere with the surgery as they require direct contact with the tissue, and they are also limited by low sensitivity and/or specificity, lack of real-time guidance, long radiation exposure and high costs[2,9].

In this Review, we discuss the clinical potential of fluorescence image-guided surgery, examining the design of intraoperative imaging probes, imaging equipment and the use of AI, in tumour resection and for iatrogenic injury reduction.

Intraoperative imaging probes

Intraoperative fluorescence imaging probes can be classified into nontargeted and targeted probes. Non-targeted fluorescence imaging probes, mainly fluorophores without further modification, are passively transported in interstitial fluids and non-specifically accumulate in tumours, facilitating sentinel lymph node (SLN) mapping[10], blood flow assessment[11] and tumour imaging3. Targeted probes contain fluorophores and targeting molecules, such as antibodies, peptides, small molecules and nanoparticles, which bind to overexpressed targets in the tumour microenvironment (TME)[2]. Importantly, they show low or non-detectable off-target accumulation in benign tissues[2]. Their specificity contributes to the identification of tumour margins, micro- satellite lesions and vital structures (Fig. 2). Various fluorescence imaging probes are currently applied in the clinic (Table 1), which can be administered systemically or locally.

Systemically applied imaging probes

Systemic administration involves direct introduction of imaging probes into the body through intravenous injection or infusion, which is typically performed minutes, hours or days[12] before surgery. Here, a predetermined dose of imaging probe is administered into the circulation and maintains a stable concentration in blood for intraoperative imaging.

Nat Rev Bioeng. 2023. 1(3): 161-179 Published online: 3 February 2023

Table 1. Clinically applied intraoperative imaging probes

Type	Imaging principle	Administration routes	Applications	Advantages	Disadvantages
ICG	~780–1,700 nm fluorescence imaging	Intravenous injection, peritumoural injection, inhalation	Liver tumour imaging, lymph node mapping, nerve imaging, cholangiography, angiography, constructive surgery[3,14–16]	Optimal tissue penetration, low light scattering, minimal levels of autofluorescence interference, low toxicity	Non-specific targeting, in vivo instability, rapid body clearance, self-quenching, low quantum yield
MB	~685–705 nm fluorescence imaging	Intravenous injection, subcutaneous injection	Ureter imaging, thyroid and parathyroid gland localization, pancreatic neuroendocrine tumour visualization, surgical margin evaluation of the breast, lymphatic vessel mapping[15,70,77]	Deep tissue visualization, obvious colour difference between tumours and surrounding tissues	Low tissue penetration, high autofluorescence interference, toxicity considerations Not usable for patients with hypersensitivity reaction or renal insufficiency, non-specific targeting
Fluorescein	~530–570 nm fluorescence imaging	Intravenous injection	Malignant glioma imaging and resection, retinal angiography[28–30]	Widely available, cheap, low rate of adverse events, high imaging contrast, low administration doses	Non-specific targeting, surgical margins difficult to define, incidence of allergic reactions
5-ALA	620–710 nm fluorescence imaging	Oral administration, intravenous injection	Malignant glioma, bladder cancer intraoperative imaging and image-guided resection[31–33]	FDA-approved, obvious contrast between tumour and surrounding tissues, simple administration method, optimal safety properties, tumour margin evaluation	Long time interval between local administration and anaesthesia induction, high rate of skin photosensitivity, high costs
SGM-101	~685–705 nm fluorescence imaging	Intravenous administration	Intraoperative detection of colorectal cancer[36]	Specific to CEA, improves intraoperative surgical decision-making, deep lesion identification, high sensitivity	Small clinical sample size (26 patients), lack of evaluation of different doses and timings for fluorescence imaging, lack of quantitative analysis
Cetuximab-IRDye800CW	780–850 nm fluorescence imaging	Intravenous administration	Ex vivo detection of malignant lymph nodes of head and neck cancer[34]	Specifically targeted to EGFR, high TBR, high sensitivity, detection of lesions in deep sections (1mm), no severe adverse events	Small clinical sample size (12 patients), lack of thorough analysis of interval time effects
Panitumumab-IRDye800CW	780–850 nm fluorescence imaging	Intravenous administration	Intraoperative imaging of primary lesions, metastatic lymph nodes and micro-metastasis of pancreatic cancer[37]	Specifically targeted to EGFR, no severe adverse events, high TBR, high specificity, improves intraoperative surgical decision-making	Possibility of false uptake by healthy pancreatic cells, small clinical sample size (16 patients), lack of quantitative analysis of surgical margin detection and metastasis identification, patient prognosis has not been evaluated
Bevacizumab-IRDye800CW	780–850 nm fluorescence imaging	Intravenous administration	Intraoperative imaging of peritoneal metastasis of colorectal cancer[35]	Specifically targeted to VEGFR, no severe adverse events, high TBR, successful detection on additional lesions	High false positive ratio, small clinical sample size (7 patients), insufficient data on accuracy evaluation
cRGD-ZW800-1	~788–850 nm fluorescence imaging	Intravenous administration	Intraoperative imaging of colon cancer[45]	Specifically targeted to integrins, no severe adverse events, rapid elimination through urine, high TBR, minimal doses required	Small clinical sample size (12 patients), lack of experimental data on margin evaluation in lower rectal tumour cases, further evaluation needed in other cancer types
PLSWT7-DMI	780–850 nm fluorescence imaging	Intravesical administration	Intraoperative detection of non-muscle invasive bladder cancer[166]	Specifically targeted to CD44V6, no severe adverse events, simple administration (intravesical), short administration time	Small clinical sample size (22 patients)
BLZ-100	~760–841 nm fluorescence imaging	Intravenous administration	Ex vivo detection of cancerous tissues in skin cancer samples[47]	Specifically targeted to Annexin A2 and MMP2, no severe adverse events	Long reaction time, small clinical sample size (21 patients), lack of experimental data on real-time imaging, low specificity
EC17	520 nm fluorescence imaging	Intravenous administration	Targeted imaging and image-guided resection of ovarian cancer[49]	Targeted to folate receptor, non-toxic, inexpensive, easy production, easy modification	Limited light penetration, high autofluorescence, non-specific signals in collagen-rich healthy tissue

Table 1(continued). Clinically applied intraoperative imaging probes

Type	Imaging principle	Administration routes	Applications	Advantages	Disadvantages
OTL38	~790–815 nm fluorescence imaging	Intravenous administration	Targeted imaging and image-guided resection of ovarian cancer[50]	High affinity and specificity to folate receptor, short terminal half-life, long retention in the tumour, rapid clearance from plasma	Limited light penetration, lack of overall survival evaluation, small clinical sample size (30 healthy volunteers and 12 patients)
cRGDY-PEG-Cy5.5 nanoparticles	~690–710 nm fluorescence imaging	Intravenous administration	SLN biopsy of head and neck melanoma[62]	Highly specific to integrins, safe, deep lymph node detection, low-dose administration, high TBR	Lack of quantitative analysis, low spatial resolution, depth-dependent sensitivity, high rate of signal saturation
ONM-100	~785–830 nm fluorescence imaging	Intravenous administration	Targeted imaging of breast cancer, gastrointestinal cancer, oral cancer and head and neck cancer[51]	Well tolerated, highly specific to low extracellular pH, high contrast ratio	Activation by inflammatory tissues, long administration time interval before surgery, lack of higher-dose evaluation
LUM015	675 nm fluorescence imaging	Intravenous administration	Ex vivo imaging of breast cancer specimens[63]	Activated by cathepsin, high TBR, high sensitivity, no obvious adverse events	Small clinical sample size (15 patients), lack of in vivo analysis of imaging performance, low positive margin detection rate
AVB-620	~620–800 nm fluorescence imaging	Intravenous administration	Intraoperative imaging of primary tumours and metastatic lymph nodes of breast cancer[52]	Activated by MMPs, high TBR, no obvious adverse events, high sensitivity	Small clinical sample size (27 patients), lack of quantitative analysis of fluorescence thresholds for differentiating malignant tissues from normal tissues
^{111}In-DOTA-girentuximab-IRDye800CW	SPECT/CT and 780–850 nm fluorescence imaging	Intravenous administration	Intraoperative imaging and surgical guidance of renal carcinoma resection[71]	Specifically targeted to CAIX, high specificity, high TBR, no obvious adverse events	Small clinical sample size (15 patients), lack of evaluation of surgical strategy changes and patient prognosis, laborious and time-consuming probe preparation, high cost
^{68}Ga-IRDye800CW-BBN	PET and 780–850 nm fluorescence imaging	Intravenous administration	Intraoperative imaging and surgical guidance of glioblastoma resection[72]	Specifically targeted to GRPR, high specificity, improved patient prognosis	Small clinical sample size (14 patients), low penetration depth, high cost, laborious and time-consuming probe preparation
PARPi-FL	~510–520 nm fluorescence imaging	Topical administration	Intraoperative imaging of oral cancer and cervical cancer, ex vivo imaging of oral, oesophageal, oropharyngeal specimens[74–76]	Specifically targeted to PARP, short administration time, high sensitivity, simple administration (spraying or gargling), high TBR, safe	Small clinical sample sizes (12 patients[74], 7 human surgical biospecimens[75], 4 patient cone-biopsy biospecimens[76]), lack of quantitative analysis of margin detection, low spatial resolution
QRHKPRE-Cy5, KSPNPRE-IRDye800CW	780–850 nm fluorescence imaging	Topical administration	Intraoperative imaging of oesophageal cancer and Barrett's neoplasia[77]	Specifically targeted to EGFR and ErbB2, short administration time, simple administration (spraying), no severe adverse events, high sensitivity, low cost, high imaging contrast	Small clinical sample size (22 patients), lack of quantitative analysis
Anti-CD47-FITC, anti-CD47–Qdot$_{605}$	625 nm fluorescence imaging	Intravesical administration	Intraoperative imaging and surgical guidance of bladder cancer resection[78]	Specifically targeted to CD47, simple administration (intravesical), short administration time, high sensitivity, high TBR	Small clinical sample size (26 patients), low penetration, high cost
EMI-137	670 nm fluorescence imaging	Topical administration	Ex vivo evaluation of squamous cell carcinoma of tongue specimens[79]	Specifically targeted to c-Met, simple administration (incubation), short administration time, high contrast, high specificity	Small clinical sample size (10 patients), lack of in vivo analysis and systemic TBR statistics
EP-HMRG	~520–600 nm fluorescence imaging	Topical administration	Ex vivo evaluation of oesophageal squamous cell carcinoma and head and neck cancer specimens[80,81]	Specifically activated by DPP-IV, simple administration (incubation and spraying), short administration time, high sensitivity	Small clinical sample sizes (44 and 17 resected human specimens[80,81]), lack of in vivo analysis before resection, unknown safety profile

Table 1(continued) Clinically applied intraoperative imaging probes

Type	Imaging principle	Administration routes	Applications	Advantages	Disadvantages
GB119	665 nm fluorescence imaging	Topical administration	Ex vivo evaluation of non-melanoma skin cancer specimens[82]	Specifically activated by cathepsin, high specificity, simple administration (incubation), short administration time, accurate evaluation of peripheral margins	Small clinical sample size (55 human skin specimens), lack of in vivo analysis
6qc-NIR	799 nm fluorescence imaging	Topical administration	Ex vivo evaluation on the keratinocyte carcinoma specimen[83]	Specifically activated by active cathepsin, simple administration (incubation), short administration time, high sensitivity	Small clinical sample size (90 human skin specimens), lack of in vivo analysis, background fluorescence in benign tissues, low penetration depth

5-ALA, 5-aminolevulinic acid; AVB, Avelas Biosciences; CEA, carcinoembryonic antigen; DOTA, tetraazacyclododecane-1,4,7,10-tetraacetic acid; DPP-IV, dipeptidyl peptidase IV; EC, folate fluorescein isothiocyanate; EGFR, epidermal growth factor receptor; EMI, Edinburgh Molecular Imaging; FDA, US Food and Drug Administration; FITC, fluorescein isothiocyanate; GRPR, gastrin-releasing peptide receptor; ICG, indocyanine green; LUM, Lumicell; MB, methylene blue; MMP, matrix metalloproteinase; NIR, near-infrared; ONM, Onconano Medicine; OTL, On Target Laboratories; PARP, poly(ADP-ribose) polymerase; PARPi, poly(ADP-ribose) polymerase inhibitor; PEG, polyethylene glycol; PET, photon emission tomography; SLN, sentinel lymph node; SPECT/CT, single-photon emission computed tomography/computed tomography; SGM, Surgimab; TBR, tumour to background ratio; VEGFR, vascular endothelial growth factor receptor.

Clinically approved non-targeted imaging probes

Non-targeted imaging probes currently approved by the FDA, EMA and NMPA include ICG, MB, fluorescein and 5-aminolevulinic acid (5-ALA). These probes are applied in the majority of clinical applications, with fluorescein being in clinical use since 1948 (ref. [13]) (Fig. 1).

ICG, a water-soluble tricarbocyanine fluorophore, is a cyanine compound with a hydrodynamic diameter of 1.2 nm and a molecular weight of 751.4 Da[4]. The first medical application of ICG was in 1955, and it was FDA-approved for retinal angiography in 1956 (ref. [14]). With deep tissue penetration (approximately 1 cm in depth), low light scattering, minimal autofluorescence and low toxicity, ICG can be applied for liver tumour imaging[3], SLN mapping[15] and cholangiography[16], among other fluorescence-guided medical uses[17,18].

MB is a phenothiazine salt with an excitation at 668 nm and an emission at 688 nm wavelength[19], and is safe to use at therapeutic doses below 2 mg kg^{-1} (ref. [20]). It has a distinct biodistribution profile that can be exploited to identify several types of cancers, such as parathyroid adenomas, paragangliomas and neuroendocrine insulinomas, as well as vital healthy structures, including ureters and the parathyroid gland, by fluorescence imaging[19]. Therefore, MB allows intraoperative detection of certain tumours and healthy structures[21–25]. Compared with ICG, MB is limited by low tissue penetration depth and high auto-fluorescence of background tissues. In addition, the administration of MB may cause pain, and possibly fat necrosis, serotonin syndrome and other complications (for example, rash, coronary vasoconstriction, decreased renal function and hypertension)[26,27].

Fluorescein is a visible fluorophore with excitation and emission wavelengths at 494 nm and 521 nm, respectively. Since 1961, fluorescein has been safely used for retinal angiography[28] and brain tumour margin imaging[29], because it accumulates in specific cerebral regions owing to the disrupted blood–brain barrier in the brain tumour TME, with an average intravenous injection dose of 3–5 mg kg^{-1} (ref. [30]).

5-ALA and its derivative 5-aminolevulinic acid hexyl ester promote the synthesis of fluorescent protoporphyrin IX in the heme biosynthesis pathway. Owing to the optical properties of protoporphyrin IX (excitation at 380–440 nm and emission at 620–640 nm), and its selective accumulation in malignant glioma cells, 5-ALA can serve as a diagnostic agent[31]. 5-ALA was first used in 1998 for surgical guidance in malignant glioma excision, and was approved by the FDA for glioma treatment in 2017. In addition, 5-ALA fluorescence cystoscopy outperforms conventional white-light cystoscopy for the detection of bladder cancer[32]. However, several disadvantages limit its widespread application, including a long waiting time before induction of anaesthesia (on average 2.5–3.5 h), high risk of skin sensitization when exposed to sunlight and high costs[33].

Although in clinical use, these non-targeted probes often show low tissue uptake and fluorescent signalling, because they were not originally designed for tumour or specific tissue targeting. Moreover, their optical properties are not ideal for tumour imaging; for example, imaging with 5-ALA can be affected by photobleaching and by the tumour vessel conditions[2]. Therefore, imaging probes with higher binding affinities and improved pharmacokinetic features are being clinically tested.

Targeted imaging probes

Antibody-based fluorescence imaging probes have dominated the field of fluorescence image-guided surgery[34] (Fig. 1). By conjugating fluorophores to an antibody (for example, bevacizumab[35], cetuximab[36], panitumumab[37] and Surgimab (SGM)-101 (ref. [38])) that specifically binds to molecules overexpressed in tumour cells (for example, epidermal growth factor receptor (EGFR), vascular endothelial growth factor receptor (VEGFR), carcinoembryonic antigen (CEA))[1], and that has been clinically evaluated for in vivo cancer detection and ex vivo specimen analysis[39], probes can be targeted to tumours. Antibody-based imaging probes have high binding affinities to cancer cells and enable high imaging contrast ratios; for example, cetuximab-IRDye800CW achieved a mean fluorescence contrast ratio of 4.0 for the detection of glioblastoma in a first-in-human study[40]. In addition, only a single, low-dose administration is required for intra-operative imaging in the clinic; for example, doses of up to 62.5 mg

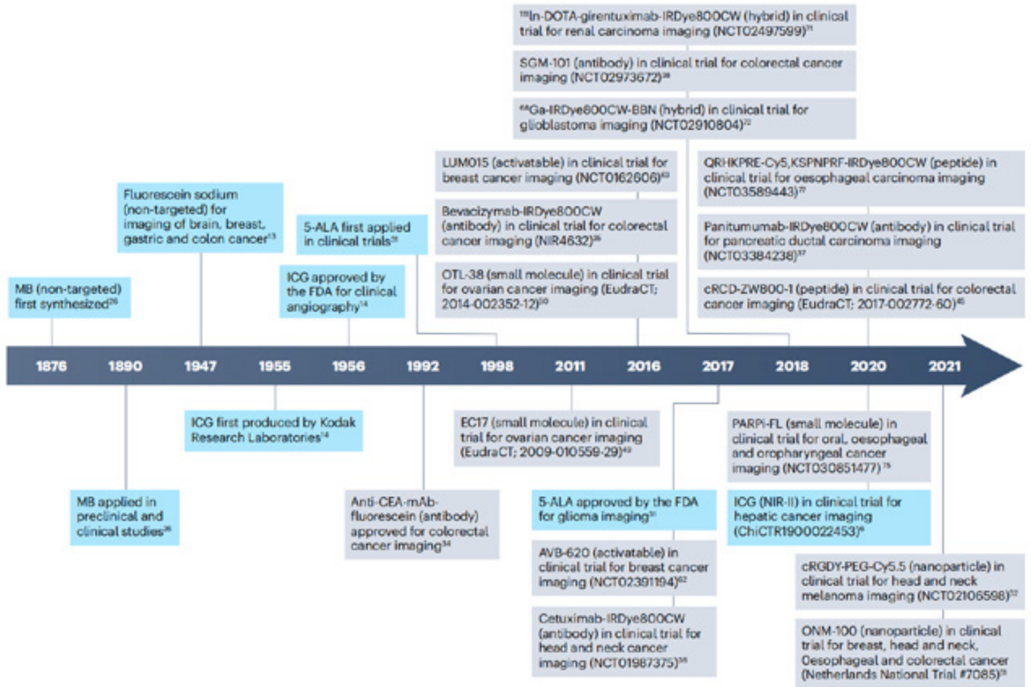


Fig.1 Major milestones in fluorescent probe development for oncological surgery. Blue boxes represent non-targeted probes, and gray boxes represent targeted probes. 5-ALA, 5-aminolevulinic acid; AVB, Avelas Biosciences; CEA, carcinoembryonic antigen; DOTA, tetraazacyclododecane-1,4,7, 10-tetraacetic acid; EC, folate fluorescein isothiocyanate; FDA, US Food and Drug Administration; ICG, indocyanine green; LUM, Lumicell; MB, methylene blue; NIR, near-infrared; ONM, Onconano Medicine; OTL, On Target Laboratories; PARPi, poly(ADP-ribose) polymerase inhibitor; PEG, polyethylene glycol; SGM, Surgimab.

m^{-2} ofcetuximab-IRDye800CW correspond to 25% of the therapeutic dose of cetuximab[41], and 0.5 mg kg^{-1} or 1 mg kg^{-1} panitumumab-IRDye800CW allow in situ imaging of head and neck cancer[42]. Furthermore, therapeutic monoclonal antibodies possess a long circulation half-life and, thus, may promote uptake of imaging probes by tumours, benefiting the sensitivity and specificity of cancer detection; for example, panitumumab-IRDye800CW achieves a sensitivity of 91% for clinical ex vivo cancer detection[42]. Nevertheless, antibody-based fluorescence imaging probes are limited by their large size and long circulation time, leading to high background signals and poor tumour penetration, as well as high costs, restricting their widespread application[43].

Alternatively, peptides have low immunogenicity, various binding sites and simple production methods[44]. For example, the RGD peptide (<1 kDa), consisting of three amino acids, shows excellent binding affinity for a subset of integrins (for example, αvβ1, αvβ3 and αvβ6) expressed in multiple types of cancers. The targeted probe cRGD-ZW800-1, which consists of a cyclic pentapeptide and a zwitterionic NIR fluorophore, allows colon cancer detection in the clinic, and its rapid renal clearance also enables intraoperative imaging of the ureter, preventing accidental iatrogenic injuries of the ureter while performing colon cancer resections[45]. BLZ-100, consisting of chlorotoxin (CTX) and ICG, has been preclinically applied to differentiate malignant from benign tissues of adenocarcinoma, soft tissue sarcoma and fibrosarcoma[46]. In a clinical trial, BLZ-100 achieved 80% basal cell carcinoma and 100% melanoma detection rates (NCT02097875)[47]. In addition, bombesin targeting the gastrin-releasing peptide receptor (GRPR), Edinburgh Molecular Imaging (EMI)-137 targeting c-Met, gastrointestinal heptapeptide targeting human epidermal growth factor receptor 2 (HER2) and LS301 targeting integrins are being evaluated in clinical trials[48].

Imaging probes can also be conjugated to small molecules with short half-lives. For example, fluorescein isothiocyanate (FITC)-labelled folate (folate-FITC) is used in the clinic for targeted imaging of ovarian cancer. Using an intraoperative multispectral fluorescence imaging system, the probe achieves a mean tumour to background ratio (TBR) of 3.1, detecting significantly more tumour deposits, compared with conventional visible light observation[49]. Similarly, On Target Laboratories (OTL)-38, a folate analogue conjugated to an NIR fluorescence dye, has high binding affinity to folate receptor-α (FRα), achieving the identification of 29% additional malignant ovarian cancer lesions that were undetectable through conventional inspection and palpation[50]. OTL38 is also being clinically evaluated for lung cancer (NCT02602119 and NCT02769156) and bladder cancer (NCT02852252)[48]. Demeclocycline (NCT02740933), IRDye800BK (NCT03387410), IS-001 (NCT03937505), HS-196 (NCT03333031), TMVP1-ICG (NCT03320772) and Prosense/VM110 (NCT03286062) are also being clinically tested[48].

Nat Rev Bioeng. 2023. 1(3): 161-179 Published online: 3 February 2023

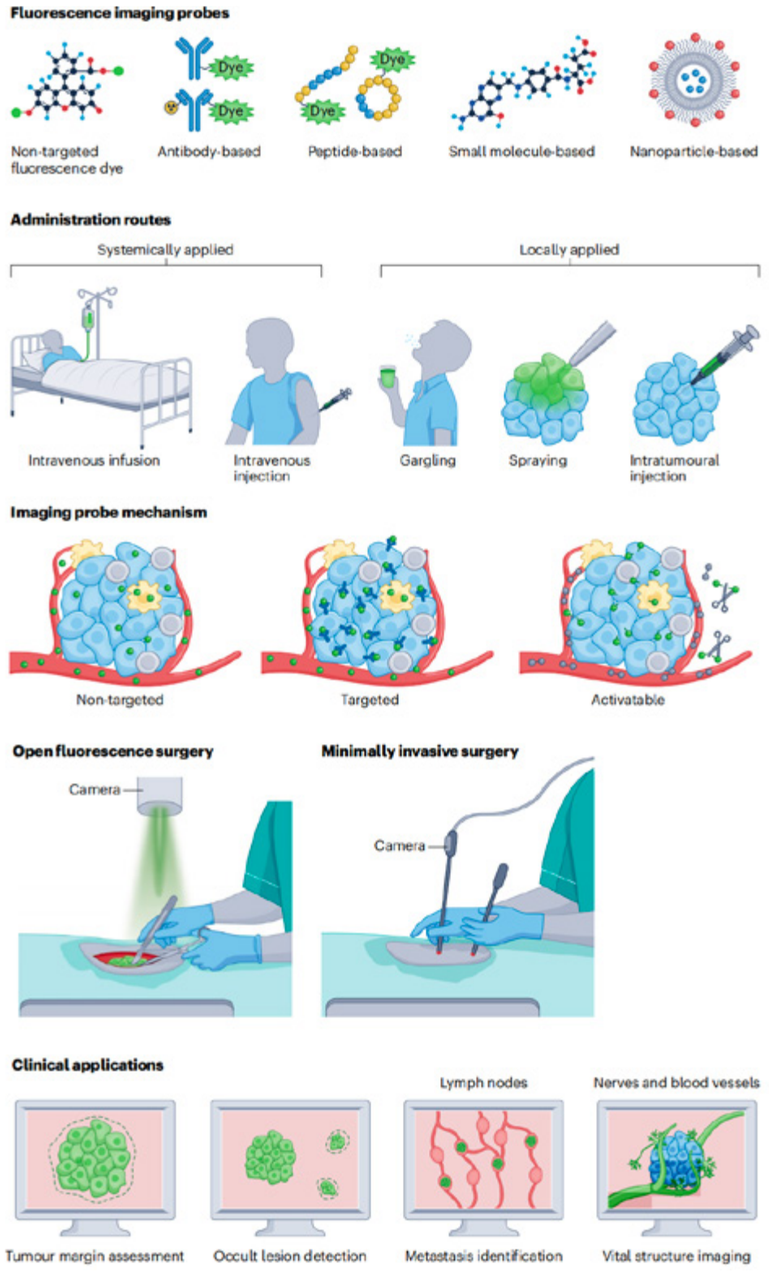


Fig.2 Fluorescent imaging probes in image-guided surgery. Clinically used fluorescence imaging probes include non-targeted and targeted probes. Non-targeted imaging probes are typically fluorescent dyes without further modification. Targeted probes can be antibody-based, peptide-based, small molecule-based and nanoparticle- based. Through systemic (for example, intravenous injection or infusion) or local (for example, gargling, spraying or intratumoural injection) administration, fluorescent imaging probes can target cancer lesions. Within tumours, the probes accumulate in malignant tissues through diffusion, receptor binding or activation. In open or minimal-invasive surgery, fluorescence imaging allows tumour margin assessment, occult lesion detection, metastasis identification and healthy tissue imaging.

Nanoparticle-based imaging probes are also being explored for the detection of cancerous tissue; for example, Onconano Medicine (ONM)-100, which consists of a pH-sensitive amphiphilic polymer bound to ICG, can detect tumour resection margins and occult lesions that are not detectable by conventional clinical methods[51]. cRGDY-PEG-Cy5.5 nano-particles target αvβ3 integrin, thereby allowing SLN visualization with a maximum SLN signal to background ratio of 40, thus enabling reliable SLN biopsy in the clinic[52]. Other nanoparticle-based imaging probes are being explored in clinical trials, including ^{64}Cu-NOTA-prostate-specific membrane antigen inhibitor (PSMAi)-polyethylene glycol (PEG)-Cy5.5-C′ for prostate cancer (NCT04167969)[48] and cRGDY-PEG- Cy5.5-C′ for breast and colorectal cancer (NCT02106598)[48]. However, the clinical translation of nanoparticle-based imaging probes is more time-consuming, laborious and expensive compared with other types of imaging probes, because they typically contain inorganic compounds, micelles, polymers and other nanomaterials that require more comprehensive investigations in terms of pharmacokinetics, biodistribution and effectiveness to ensure sufficient evaluation of biocompatibility and long-term toxicity[53].

Activatable imaging probes

Activatable imaging probes, or 'turn-ON' probes, can be specifically activated through chemical reactions with highly expressed enzymes in the TME[54–57] or by specific TME conditions[58–61]. Activatable imaging probes consist of linkers, quenchers and fluorophores. Cleavage of the linkers by enzymes causes the release of the quenched fluorescence signal, allowing the imaging of cancer lesions. For example, Avelas Biosciences (AVB)-620 and Lumi-cell LUM015 are activated by matrix metalloproteinases (MMPs) and cathepsin, respectively, and are clinically used for breast cancer detection with a high TBR[62,63]. These probes are also currently investigated in clinical trials for brain cancer (NCT03717142), prostate cancer (NCT03441464) and Barret's oesophagus (NCT02584244) detection[48]. Protease-activatable imaging probes are also preclinically tested for visualization of tumour margins[64] to avoid resection of benign tissues.

Hybrid imaging probes

Limited tissue penetration depth remains a key challenge in fluorescence imaging[65], in particular for the detection of deep-lying tumour lesions, which can be addressed by optical multimodality cancer imaging. Nuclear imaging has unlimited tissue penetration, and can serve as a complementary tool for fluorescence imaging[66]. For example, ICG-^{99m}Tc-nanocolloids enable radio-guided SLN biopsies[67] for various cancers[68–70], with a better detection rate and a fivefold lower administration dose compared with a single ICG application. However, ICG-^{99m}Tc-nanocolloids are not targeted to tumours, limiting tumour-specific imaging. Alternatively, monoclonal antibodies co-labelled with radionuclides and NIR dyes allow clinical intraoperative cancer imaging with a high contrast ratio, enabling delineation of tumour margins, for example[111]. In-DOTA-girentuximab- IRDye800CW for renal carcinoma[71,68]Ga-IRDye800CW-BBN for glioblastoma[72] and ^{111}In-Labetuzumab-IRDye800CW for colorectal cancer (NCT03699332) detection[48]. Furthermore, a prostate-specific membrane antigen (PSMA)-targeted imaging probe allows both fluorescence and radionuclide imaging, which has been demonstrated in a preclinical study using metastatic mouse models for detecting prostate cancer metastases intraoperatively[73].

Locally applied imaging probes

Alternative to systemic administration, imaging probes can be locally applied by spraying, smearing, gargling or intratumoural injection. Local administration has the benefits of shorter administration times (a few seconds to a few hours), simpler administration and less adverse effects compared with systemic administration. However, local administration is mainly suitable for superficial tumours or lesions located in cavity organs, but not for deep tumours or distant metastatic lesions. Both targeted and activatable imaging probes have been designed for local administration.

Targeted local imaging probes

Poly(ADP-ribose) polymerase inhibitor (PARPi)-FL, a fluorescently labelled inhibitor of poly(ADP-ribose) polymerase 1 (PARP1), which is a key enzyme in cancer invasion path- ways, can be applied for the diagnosis of oral cancer[74]. Gargling a PARPi-FL solution for 60 s allows the clinical detection of cancerous tissues in the mouth with a TBR > 3 (ref. [74]). PARPi-FL has also been used for the diagnosis of oropharyngeal and oesophageal epithelial cancers. Here, the fluorescence signal of PARPi-FL can be correlated to the expression of PARP1 in tumour tissues[75]. In addition, locally applied PARPi-FL can be imaged with a hand-held confocal microscope to enable immediate detection of invasive cervical carcinomas in situ at the cellular level for the assessment of cervical cancer tissues in both preclinical and clinical applications[76]. Moreover, fluorescent heptapeptides have been designed that specifically target both EGFR and human epidermal growth factor 2 (ErbB2) for Barrett's neoplasia diagnosis[77]. Here, the diagnostic performance and accuracy of the dual-target multiplex probe were quantitatively compared with single-target (EGFR or ErbB2) imaging using a support vector machine algorithm and receiver operating characteristic curve analysis, showing that the area under curve (AUC) reaches 0.97 for multiplex imaging, which is more accurate than imaging EGFR (AUC = 0.95) or ErbB2 (AUC = 0.94) separately in diagnosing Barrett's neoplasia[77]. In addition, anti-CD47–FITC has been explored for in vivo bladder cancer diagnosis, showing minimal systemic toxicity, and EMI-137 has been tested for ex vivo oral tumour detection. Anti-CD47–FITC and EMI-137 specifically bind to CD47 (90.5% specificity) and c-Met (90% specificity), respectively, improving resection efficiency[78,79].

Activatable local imaging probes

Glutamylprolylhydroxy methyl rhodamine green (EP-HMRG) can undergo structural changes from a fluorescent 'off' state to an 'on' state within several minutes by exposure to dipeptidyl peptidase IV (DPP-IV). The expression levels of DPP-IV are significantlyh igherinvarioushumancancersthaninhealthytissues[2], and thus EP-HMRG has been used for in situ detection of oesophageal[80] and head and neck squamous cell carcinomas[81], with a high detection accuracy of more than 90%, allowing the diagnosis of 12 out of 17 patients with head and neck cancer[81]. Following local administration, the quenched activity-based imaging probe GB119 is activated by cysteine cathepsin in tumour tissues, and thus enables discrimination between malignant and healthy skin tissue to accurately identify tumour margins and reduce the re-excision rate, with a specificity of 89%[82]. Similarly, the NIR-quenched, protease-activatable probe 6qc-NIR, in combination with a fluorescence imaging system that has minimal optical scattering, allows precise tumour margin evaluation, addressing the limitations of bread-loaf histology[83]. However, locally applied, activatable fluorescent imaging probes have mainly been used for ex vivo specimen evaluation thus far.

Locally applied imaging probes are also being explored in preclinical animal studies for specifically identifying malignant lesions. For example, the tumour-activatable fluorescence probe BMV109 can reliably detect small polyps in mice for in vivo optical pathology using a 1 mm wide-field fibrescope[84]. Similarly, the γ-glutamyltranspeptidase (GGT)-activatable imaging probe gGlu-HMRG can guide colon tissue biopsy. After 5 min of local administration, cancerous lesions show higher fluorescent signals (approximately tenfold) compared with inflammatory tissues, indicating the potential of gGlu-HMRG for clinical biopsies[85].

Optimization of imaging probes

Increasing wavelength

Fluorescence imaging in the NIR-I (excitation at 700–900 nm) window is limited by poor tissue penetration depth (<1 cm) and strong photon scattering, which may interfere with fluorescence image-guided surgery. Alternatively, probes emitting in the NIR-II window (1,000–1,700 nm), that is, short-wave infrared probes, show less autofluorescence interference and reduced photon scattering[65]. Combined with nanomaterials, NIR-II fluorophores can be made biocompatible and designed with reasonable pharmacokinetics (such as rapid clearance and minimal accumulation in the reticuloendothelial system). Shortwave infrared probes are particularly useful for non-invasive imaging of blood and lymphatic vessels, hepatobiliary clearance, as well as fluorescence image-guided surgical navigation in EGFR-positive breast cancer, human HER2-amplified breast cancer and other applications[86–89]. For example, ICG has been used for intraoperative NIR-II fluorescence imaging of hepatic cancer, achieving a better tumour detection rate (56.41%) compared with imaging in the NIR-I window (46.15%), allowing the identification of intrahepatic metastasis, which cannot be detected in the NIR-I window[6]. Importantly, short-wave infrared probes can be imaged under ambient light conditions, because the sensor of the imaging system is insensitive to the visible spectrum. Thus, the lighting inside the operating room does not need to be controlled[87]. NIR-II fluorescence imaging has the potential to substantially improve imaging quality and meet the requirements for precise surgery.

Improving tumour to background ratio

Tumour contrast in fluorescence imaging can be improved by increasing the imaging agent dose or detector sensitivity; however, this approach does not take into account the spatially and temporally heterogeneous expression levels of targets in the TME. To increase the TBR, high selectivity between malignant and benign tissues is required. For example, a multivariate 'AND-gate' probe is activated by the coexistence of lysosomal cysteine cathepsins, executioner caspases and fibroblast activation protein (FAP) within tumours, producing a tumour-specific fluorescence signal. This highly selective 'AND-gate' probe achieves high imaging contrast for primary breast cancer and lung metastasis lesions (<1 mm diameter) in 4T1 breast tumour-bearing mouse models, and could thus serve as a useful tool for surgical guidance[90]. Similarly, the fluorescence imaging probe Ir-Im-PEG, consisting of a macromolecular NIR-I poly(ethylene glycol)-conjugated iridium(III) complex, responds to both tumour hypoxia and acidity, allowing intraoperative detection of primary liver tumours and metastatic breast tumour lesions as small as 1 mm in tumour-bearing mouse models, and reporting metabolic information (tissue acidity and oxygen levels) with minimal background signal. Therefore, Ir-Im-PEG may enable ultrasensitive intraoperative identification of cancer lesions with high tumour to background contrast[91].

Implementing quantification

Fluorescence image analysis has mainly focused on qualitative assessment thus far, which is influenced by the expression levels of epitopes (of note, epitope expression may vary in different tumour regions and across tumour types[92]), tissue conditions (tumour grade, location, blood and lymphatic conditions can impact probe uptake[93]) and camera performance (pixel size, quantum efficiency, noise and other technical factors affect sensitivity[94]). Therefore, quantitative analysis — that is, determining the absolute concentration of imaging probes — is required to allow objective and accurate intraoperative decisions. Magnetic particle imaging (MPI), which has high sensitivity and unlimited imaging depth, enables quantitative imaging owing to the linear correlation between the MPI signal and iron concentration. MPI could thus serve as a complementary tool for intraoperative fluorescence imaging[95]. For example, the magnetic, fluorescent hybrid nanoparticle Fe_3O_4@PFODBT-COOH can specifically label cancer cells, which can then be visualized by both fluorescence imaging and MPI in cervical tumour-bearing mouse models, enabling the accurate quantification of tumour cells[96]. Similarly, the fluorescence and MPI dual-modality imaging probe SPIO@A-T enables specific detection and quantitative analysis of metastatic cancer cells in lymph nodes in 4T1 breast tumour- bearing mice, and could thus be applied for intraoperative guidance of metastatic lymph node dissection[97].

Clinical potential

Ideally, tumour-targeted imaging probes have high binding affinity to cancer-specific targets, remain stable after administration, emit fluorescence according to their actual concentration in tumours, rapidly penetrate the tumour, have low off-target binding or no detectable background signal in healthy tissue, are rapidly cleared (in particular, non-binding imaging probes) and do not cause short-term or long- term adverse events[1,98]. Nanoparticle-based imaging probes allow selective targeting, deep tumour penetration and high retention, and they exhibit low toxicity. In particular, noble metal quantum clusters, which possess fixed finite atoms in an ultra-small size, can be used for cancer imaging and drug distribution evaluation. For example, a gold quantum cluster encapsulating α-lactalbumin (α-LA) enables multimodal imaging, including X-ray imaging, MRI and fluorescence imaging, for the image-guided resection of breast tumours in mice, as well as activation of antitumour immunity through rapid surface trans-location of calreticulin in tumour cells and infiltration of macrophages into breast tumours[99]. This imaging probe retains the imaging signal within the tumour, enabling preclinical image-guided surgery[99]. Acyclic octapeptide emitting NIR light (LS301) targets overexpressed phosphorylated annexin A2 (pANXA2), which promotes cancer-associated post-translational modifications in many solid tumours. LS301 specifically accumulates in tumours (for example, breast cancer, fibrosarcoma, pancreatic adenocarcinoma), and its intratumoural distribution correlates

Nat Rev Bioeng. 2023. 1(3): 161-179 Published online: 3 February 2023

Box 1

Regulatory considerations

The following considerations are key to the clinical translation of new fluorescent imaging probes intended for preoperative and intraoperative oncological surgery[95].

Production methods and quality assurance. Good manufacturing practices include the production process (for example, synthetic materials, environmental conditions and synthetic manufacturing steps)[172], stability assessment (for example, pH, osmolality and sterility)[198] and physicochemical, biopharmaceutical and pharmacokinetic properties[199]. Complying with good manufacturing practices is a prerequisite for the clinical translation of imaging probes[72].

Safety evaluation. Safe operation with imaging probes[200] requires in vitro cytotoxicity evaluation, acute and long-term toxicity monitoring (for example, blood routine, blood biochemistry analysis and histological examination) in animal models, and clinical phase I and II trials to confirm safety profiles (for example, mass dose, administration routes, administration frequency and biological half-lives). Notably, the design of clinical trials using new fluorescent imaging probes must meet US Food and Drug Administration (FDA) standards and investigational new drug application recommendations to confirm safety and patient benefits.

Effectiveness. The effectiveness of imaging probes is based on their binding affinity to cancer targets, which can be evaluated by surface plasmon resonance imaging, biofilm interference technology, polarization-modulated oblique-incidence reflectivity difference and cell-binding tests. In addition, cell-specific uptake and preclinical imaging of animal models allow evaluation of imaging probe specificity. Effectiveness also has to be proven in small-scale clinical trials[201].

Approval. Clinically used imaging probes need to be formally approved by the local institutional review board and hospital pharmacists according to FDA and European Medicines Agency (EMA) regulations. Prior to their application in patients, imaging probes must be stored and recorded according to specific guidelines (including quantity, production time, expiration date and storage conditions)[49].

Long-term monitoring. Following clinical approval, the performance of imaging probes (including clinical outcome and cost-effectiveness) is continuously assessed by the Centers for Medicare & Medicaid Services, which influences investment by industry and widespread use of imaging probes[202].

well with pANXA2 expression, highlighting the potential of this low molecular weight imaging probe for targeting pANXA2- expressing cancer[100]. In addition, antibody fragments (diabodies) and Fab fragments specifically bind their targets, which can be exploited for probe targeting and to achieve deeper tumour penetration and faster clearance from non-targeted tissues, compared with antibodies[2]. Various molecular imaging probes have shown promise in preclinical studies. However, even if they fulfil all the aforementioned requirements, safety and effectiveness in the clinic remain a concern. Ultimately, to enable clinical translation, fluorescence image-guided surgery should outperform conventional white-light approaches, with minimal risk to the patient. Extensive preclinical experiments should establish manufacturing quality, optical properties, metabolism, pharmacokinetics, acute and chronic toxicities, possible side effects, and short-term and long-term characteristics of new fluorescence probes[43,101]. Furthermore, their production has to meet the standards of good manufacturing practices, and adequate characterization standards need to be established to assess their structure, function and stability. Targeting ability, safety and pharmacokinetics need to be evaluated in preclinical studies, providing the basis for regulatory approval, which requires assessment of effectiveness, clinical viability and patient benefit. Small-scale clinical phase I studies can then be performed to monitor in vivo targeting, short-term and long-term adverse events, patient prognosis and survival rate, followed by large-scale, multicentre clinical phase II and III trials[102] (Box 1).

Intraoperative imaging technologies

Intraoperative fluorescent image-guided surgery also relies on the imaging equipment[103–105], imaging processing and analysis algorithms[106] to enable high image quality, various imaging capabilities, optimized ergonomics and intelligent human–machine interaction. Fluorescence imaging systems typically contain one or more light sources, collection and delivery optics, specialized cameras and dedicated display devices (Fig. 3a). Furthermore, multimodal intraoperative imaging systems can incorporate fluorescent imaging components to improve the depth and sensitivity of lesion detection[107,108], for example NIR fluorescence and MPI hybrid imaging (Fig. 3b). Surgeons interact with both the hardware and AI software algorithms in real time during the entire operation (Fig. 3c).

Hardware

Various types of imaging equipment have been developed to achieve intraoperative images with high resolution and signal to background ratio (SBR).

Single-channel and multi-channel imaging

Single-channel imaging devices are typically designed and optimized for NIR fluorescence signals and can only provide monochrome images; for example, the Photodynamic Eye (PDE; Hamamatsu Photonics, Japan)[109]. Although single-channel imaging can confirm tumour location, it may temporarily halt the surgical procedure owing to the lack of anatomical context[110]. Alternatively, a dual-channel imaging system typically consists of a white-light imaging channel for anatomical information and an NIR imaging channel for visualizing the fluorescence signal of the region of interest. Through dual-image integration, often called 'image fusion' or 'image overlay', visualization is improved for intraoperative decision-making[111]. For example, dichroic beam-splitters can separate NIR and white-light images in a video-rate imaging system[112]. Alternatively, the PINPOINT system sequentially measures white-light and NIR channels using a camera sensitive to both visible and NIR light[113]. Furthermore, multi-channel imaging systems with more than two channels enable multi-probe imaging, either simultaneously or by switching between channels using a filter wheel. For example, the FLARE imaging system provides real-time three-channel imaging, including white light, 700 nm NIR and 800 nm NIR[114].

Minimally invasive operation

Open surgery allows direct visual and tactile feedback, as well as flexible degrees of freedom; however, it requires surgeons to make an incision before performing any surgical task[115]. Open fluorescence imaging systems can either be compact and portable, such as the Iridium[116] and Fluobeam[117], or mounted on robotic arms with wheels, such as the Solaris[118] and FIRE system[119]. Portable systems provide more flexible access to tissues with complex geometries, such as the neck and abdominal cavity, whereas wheel-based systems have larger surgical fields of view, longer working distances and more complex functions.

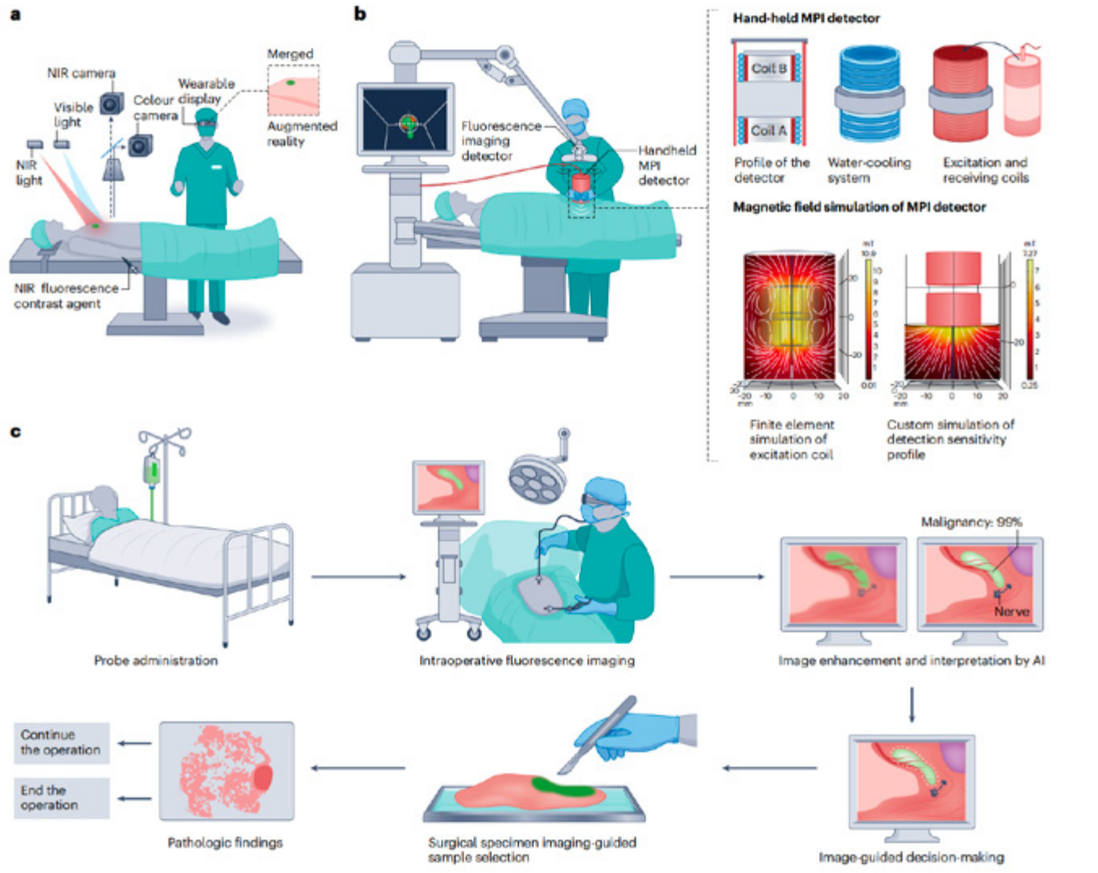


Fig.3 Intraoperative imaging in oncological surgery. a, A near-infrared (NIR) fluorescence imaging system consists of excitation light sources (NIR and visible), dedicated cameras and optics (NIR and colour), as well as the display unit (such as augmented reality goggles). **b,** Fluorescent imaging can be combined with a hand-held magnetic particle imaging (MPI) system. The MPI detector can locate deep tissue tumours beyond a centimetre depth. When tissues above the tumour are gradually removed, fluorescence imaging can detect the tumour with high resolution and, in combination with MPI, can provide information for intraoperative guidance. A hand-held MPI system mainly consists of twin magnet coils, a water-cooling unit, and excitation and receiving magnet coils. The magnetic field simulation shows the space for receiving magnetic excitation, and the corresponding space, where MPI probes can be detected. **c,** The workflow of imaging-guided surgery includes intraoperative imaging and sampling. Assessment of the resulting images relies on artificial intelligence (AI) to quantify and identify malignant tissue to guide decision-making (margin identification) and preserve nearby nerves. In addition, postoperative patient samples are assessed by fluorescence imaging, enabling pathological diagnosis.

Minimally invasive surgery results in less trauma, fewer perioperative complications and shorter hospitalization, compared with invasive surgery[120]. Unlike in open surgery, where fluorescence imaging is disturbed by ambient light, minimally invasive surgery is performed in the dark, resulting in a higher SBR[121]. Minimally invasive fluorescence imaging devices include laparoscopic, endoscopic and robotic systems[122,123]. For example, in a pilot clinical study, fluorescence molecular endoscopy has been applied to evaluate VEGFA-targeted, locally advanced rectal cancer[124]. Notably, such systems typically have lower fluorescence yields, compared with open systems, owing to safety limitations of the excitation intensity and light loss[125].

Cutting-edge intraoperative imaging systems

The ultra-high resolution of 4K imaging can be exploited to improve imaging in laparoscopic choledochal cyst surgery[126]. In addition, NIR-II imaging has higher optical resolution than NIR-I imaging, which benefits liver cancer surgery[6]. To improve intraoperative visual perception and navigation for surgeons, wearable imaging systems have been developed, such as the fluorescence goggle system and the head-mounted display system[127,128]. Moreover, 3D intraoperative imaging provides real-time depth information of tissue or tumour structures[129]. Such hardware developments provide the basis for applying augmented reality (Fig. 3a).

Multimodal intraoperative imaging devices are required to integrate different imaging modalities. For example, a real-time fluorescence imaging topography scanning system[130] enables optical and computer tomography imaging. Similarly, freehand MPI and fluorescence can be combined for surgical guidance[131]. Such a multimodal device has been demonstrated in porcine surgery, providing intraoperative 3D quantitative visualization of the distribution of superpara-magnetic iron-oxide nanoparticles, thus allowing magnetic guidance in SLN surgery[131]. Here, fluorescence imaging using ICG optimizes visualization and provides additional confirmation of probe distribution (Fig. 3b). MPI has also been proposed for intraoperative margin analysis in breast-conserving surgery. Here, a hand-held magnetic particle detector is used to identify residual tumours in the breast, and a small-calibre MPI scanner can rapidly image tumour distribution in resected specimens[132] (Fig. 3b).

Multimodal, multiscale intraoperative fluorescence imaging was also proposed for fresh specimen evaluation (back-table fluorescenceguided imaging)[133]. For example, the fluorescence imaging system SurgVision (Bracco, Milan, Italy) enables evaluation of the circumferential resection margins status of locally advanced rectal cancer in fresh surgical specimens, tissue slices and tissue sections. Here, areas with high fluorescence accurately correlate with histopathology[133].

AI in intraoperative imaging

AI is being explored for preoperative and intraoperative multimodality imaging to improve the imaging quality in real time, and, more importantly, to allow real-time, quantitative analysis and interpretation of intraoperative images (Fig. 3c).

AI-based image registration and fusion

Preoperative images can be registered and fused with intraoperative images. For example, the registration of a preoperative 3D surgical plan with intraoperative fluorescence imaging enables the precise localization of intraoperative lesions in liver surgery[134]. In real-time fluorescence imaging topography scanning, preoperative computer tomography images and intraoperative fluorescence images can be registered using a point cloud-based alignment method[130]. Such multimodal image registration can provide both functional and structural information for surgical guidance.

In addition to multimodal image registration, AI-based fusion algorithms were developed for intraoperative white-light and fluorescence images. Using an attention-based deep learning method, multi- channel images can be fused in real time, and the overall brightness of the overlay images is automatically adjusted[135]. An image feature- based fusion method can also enable intraoperative augmented reality[136]. Here, instead of hardware-based spectroscopy, AI algorithms are applied for white-light and fluorescence image fusion, which could also be implemented in wearable devices.

AI-based image enhancement

Intraoperative fluorescence imaging quality is limited by the hardware, ambient noise, optical scattering, weak emission signal and many other factors. AI algorithms can address these issues, and thus improve imaging quality. NIR-II fluorescence imaging, in particular, in the wavelength range of 1,500–1,700 nm (the NIR-IIb window), has higher resolution compared with the NIR-I window and the NIR-IIa window (1,000–1,300 nm). However, NIR-IIb imaging requires nanoprobes that have not yet been approved for clinical applications. To generate a higher-definition NIR-IIb image from a given NIR-IIa image, a deep learning method adopting the cycle generative adversarial network (CycleGAN) was developed by training the network with in vivo NIR-IIa and NIR-IIb images of mice[137]. Similarly, AI algorithms can also be applied for NIR-I image improvement using regular images and fluorescence microscopy images as training data sets, which has been demonstrated in intraoperative NIR-I images acquired in the clinic[8]. The imaging SBR can be improved by an optical flow that accumulates fluorescence signals[138]. Real-time background subtraction and delineation of target fluorescence from non-target autofluorescence can be achieved using a multispectral open-air fluorescence imaging system and a special algorithm[118]. This combination of hardware and software addresses the limitations of weak fluorescence, autofluorescence and ambient light, resulting in a high SBR and nanomolar imaging sensitivity. Furthermore, a noise-suppressed multi-focus fusion method can improve intraoperative imaging[139].

AI-based image quantification

AI can also be applied for the quantitative analysis of white-light and NIR images (NIR-I and NIR-II). For example, for white-light images, AI allows the identification of 'dangerous' and 'safe' zones during dissection in cholecystectomy with a laparoscope[140]. Here, experienced surgeons were first asked to identify these zones in 290 surgical videos; the intersection over union of AI for identifying dangerous and safe zones was 0.71 (± 0.29) and 0.53 (± 0.24), respectively. In addition, the AI model adopting a specially designed pyramid scene parsing network (PSPNet) could identify anatomical landmarks, including the hepatocystic triangle, gallbladder and liver, yielding an intersection over union of 0.65 (± 0.22), 0.72 (± 0.19) and 0.86 (± 0.12), respectively. Therefore, AI has the potential to identify important anatomic structures within the operative field and assist surgeons in dissection.

Nat Rev Bioeng. 2023. 1(3): 161-179 Published online: 3 February 2023

NIR-I intraoperative imaging can also be applied to implement an automated suturing method for robotic soft tissue surgery[141] to guide the surgical robot in suturing and intestinal anastomosis. During surgery, a mix of ICG, acetone and cyanoacrylate are placed in the operative field, serving as probes for white-light images and NIR-I images (845 ± 55 nm), which are then collected and analysed to allow navigation. Interestingly, in ex vivo tissues and living pigs, the automated algorithm performs better than experienced surgeons with regards to five metrics of anastomosis. AI also allows intraoperative tissue classification of colorectal lesions, based on NIR-I images[142]. Here, colonoscopy videos, including white-light and NIR-I images, from 24 patients (11 with cancer), who were administered ICG, were first collected. The pathological results were then used as the gold standard for classifying malignant, benign and healthy tissue. A total of 435 lesion regions of interest could be identified from the videos of 20 selected patients. The mean accuracy of AI was 86.4% at the lesion level, showing the potential value of AI in intraoperative screening of colorectal cancer.

A deep convolutional neural network model allows real-time tissue classification of surgical samples in open surgery of glioma[143], based on NIR-II intraoperative images. Here, 23 patients with glioma were injected with ICG before tumour dissection. NIR-II images (1,000–1,700 nm) of 1,874 surgical samples from these patients were then used for training and validation of the model. The AI model achieved an AUC of 0.945 in discriminating cancer from non-cancer tissue. More interestingly, AI could also predict the Ki-67 level (a cellular marker for cell proliferation, often correlated with cancer) and tumour grade from the NIR-II images. This method could help surgeons select optimal samples for intraoperative frozen sections.

Clinical application of image-guided surgery

Fluorescence imaging can support surgical decision-making, and various probes and imaging methods are applied in the clinic and in preclinical studies to improve precision cancer surgery.

Complete cancer resection and diagnosis

Complete tumour resection is often the main goal of cancer surgery. Fluorescence imaging can guide surgeons to remove otherwise undetectable cancer lesions to enable complete tumour resection.

Hepatobiliary and pancreatic cancer

Fluorescence-guided hepatic surgery[144], and, in particular, the use of ICG, is well established in the clinic. In 2021, the administration routes, dose, observation window and other properties of ICG reached an international consensus for hepatic surgery[3]. In addition, NIR-II fluorescence imaging is clinically applied for the detection of hepatic cancer[6], with an accuracy of 91.43%[6] for hepatic cancer detection. Fluorescence-guided surgery can also be applied to detect colorectal cancer liver metastases[145], allowing the resection of more metastatic lesions compared with the control group (3.03 versus 2.28) and leading to a significant reduction of the 1-year recurrence rate to 19% (versus 47% in the control group). However, cirrhosis remains a challenge for fluorescent hepatic imaging. Around 90% of hepatic cancer is estimated to concomitantly develop with cirrhosis as comorbidity[146,147]. ICG can be trapped in cirrhotic nodules causing false positives[3,6,148], similar to other nanoscale probes[37,149]. 'AND-gate' probes can address this challenge by requiring co-activation by multiple factors. Alternatively, cancer-specific small molecular probes could be applied[90,150]; however, hepatic cancer-specific fluorescent probes remain limited.

Cholangiocarcinoma (bile duct cancer) has a low 5-year survival rate (~7–20%), and treatment would greatly benefit from precision surgery[151,152]. Although cholangiocarcinoma cells do not take up ICG, lymphatic dissection could be achieved by fluorescence- guided surgery[3]. Intraoperative ICG injection into the liver can visualize lymph nodes for resection to allow accurate staging and to reduce the recurrence risk[153]. Similarly, pancreatic cancer treatment would benefit from accurate lymphatic dissection. For example, the EGFR-targeted fluorophores panitumumab-IRDye800 and cetuximabIRDye800 allow precise resection of pancreatic tumours and associated lymphatic metastases[37,154,155]. Clinical data show that pancreatic cancer can be specifically identified by these fluorophores, with a sensitivity of 90.3% and a specificity of 74.5%. The sensitivity of lymphatic metastasis imaging is lower (67.2%)[37], owing to the low perfusion efficiency of the probe in lymphatic flow. The probe SGM-101 targeting CEA (highly expressed in multiple types of cancer) can also guide pancreatic surgery for precise resections in the clinic (NCT02973672)[156].

Thoracic cancer

Pulmonary cancer surgery necessitates high precision to preserve pulmonary function[157–159]. Pulmonary nodules can be fluorescently imaged by injecting 1.0 mg kg^{-1} ICG (24 h prior surgery) through the peripheral vein[160,161]. A study involving 36 patients showed that ICG fluorescence can localize 9 lesions that were undetectable by preoperative imaging[162]. In patients receiving an intraoperative peripheral venous injection of ICG (~0.2–0.6 mg kg^{-1}), lesions were indicated by 'negative staining' (weak fluorescence in lesion areas, and strong fluorescence in surrounding healthy tissues)[163,164]. Alternatively, ICG can be inhaled to visualize pulmonary lesions[165]. Nebulized inhalation of ICG (0.25 mg kg^{-1}) can guide surgeons to localize small ground-glass opacity in patients with lung cancer, with a high negative fluorescence contrast, because nebulized ICG fills healthy pulmonary alveoli but not pulmonary lesions (probe filling defect)[5].

Molecularly targeted probes have also been explored for pulmonary cancer surgery. For example, the FDA approved the FRα-targeted OTL38 for clinical use in September 2021, following its first clinical application in 2017 (ref.[166]). OTL38 showed a sensitivity of 95.6% for pulmonary cancer detection in a study involving 50 patients (NCT02872701)[167]. In this trial, OTL38-based intraoperative imaging also improved surgical outcomes (such as finding additional pulmonary nodules unknown preoperatively, locating lesions that surgeons could not find and revealing positive margins that surgeons thought were negative) for 26% of 110 patients with pulmonary cancer[168].

Oesophageal cancer surgery also benefits from fluorescence imaging. A clinical trial (NCT04173676) with 84 patients demonstrated the feasibility of ICG fluorescence imaging to visualize lymph node drainage and guide tumour resection[169]. In addition, early-stage oesophageal cancer can be diagnosed by a dual-target visualization method[77]. By imaging the spatial expression of both EGFR and ErbB2, a sensitivity of 92% and a specificity of 89% were

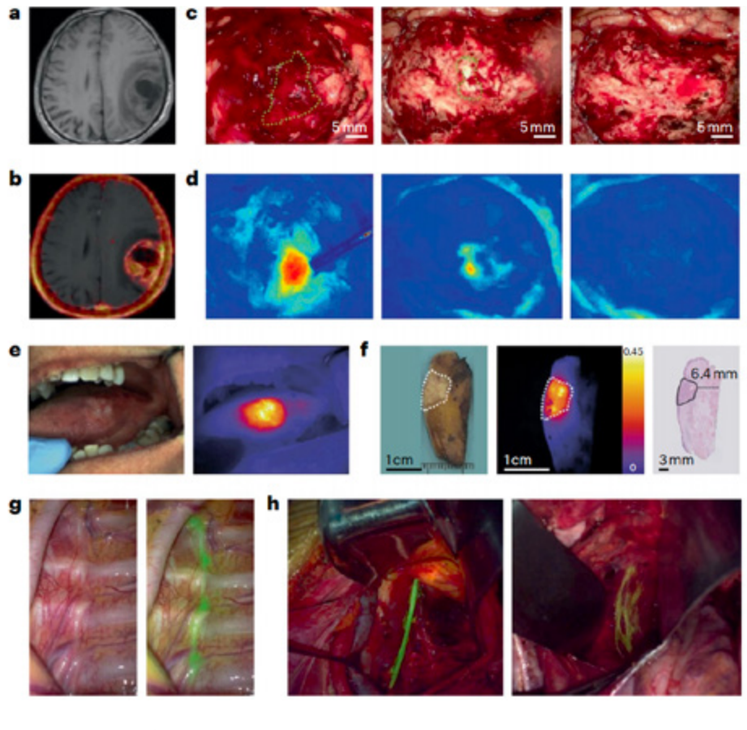


Fig.4 Intraoperative fluorescence imaging of cancer tissue and nerves. a, Preoperative axial T1-weighted magnetic resonance imaging (MRI) detects a left temporal and parietal glioblastoma. **b–d,** The glioblastoma-specific dual- modal probe 68Ga-IRDye800CW-BBN precisely visualizes the tumour margin in positron emission spectroscopy (PET) (panel b), and fluorescence imaging can guide tumour resection (panels c and d). **e,** The Onconano Medicine (ONM)-100 nanoprobe can precisely guide the resection of a squamous cell carcinoma in the tongue. **f,** The ex vivo fluorescence image of the resected specimen can guide the pathological examination. Molecular pathology assessment is thus intraoperatively achievable. **g,h,** Fluorescence imaging of thoracic sympathetic ganglions (panel g) and pelvic obturator and hypogastric nerves (panel h) can reduce iatrogenic injuries. Panels a–d reproduced with permission from ref. 72, Ivyspring International Publisher. Panels e,f adapted form ref. 51, Springer Nature Limited. Panel h adapted form ref. 190, Springer Nature Limited. Panel g image courtesy of Dr. Jian Zhou.

achieved in the detection of oesophageal cancer (NCT03589443).

Gastrointestinal cancer

Lymphadenectomy is required in gastric and colorectal cancer treatment, because lymph node resection can benefit prognosis. Injecting non-targeted probes (for example, ICG, MB and fluorescein) into the mucosa or serosa can visualize lymph nodes to aid in lymphadenectomy under fluorescence observation. In a double-armed randomized clinical trial with 266 patients, ICG NIR imaging was investigated for guiding laparoscopic D2 lymphadenectomy[15]. The results demonstrated that 50.5 ± 15.9 nodes could be retrieved using fluorescence imaging, whereas 42.0 ± 10.3 nodes were found by visual inspection. Although this approach has a sensitivity of 86.8%, the diagnostic value of fluorescence imaging for the detection of metastatic lymph nodes remains limited owing to the low specificity of 29.5%[170,171]. This randomized trial demonstrated the value of routine fluorescence imaging-guided lymphadenectomy for gastric cancer; however, gastric cancer-specific probes remain limited. HER2, VEGF and PDL1 may be feasible targets; however, the heterogeneity of gastric cancer needs to be considered. In addition, small-molecule probes may be suitable for lymphatic imaging.

Molecularly targeted fluorescence imaging has been used for precision colorectal cancer surgery since 2015 (ref. [172]). In addition, fluorescence imaging-guided cytoreductive surgery of colorectal cancer peritoneal metastases is being investigated in clinical trials. For example, the probe SGM-101 can visualize CEA distribution and guide resection of colorectal cancer, including metastases (NCT02973672)[38,173]. Moreover, ICG can be applied for colorectal lymphatic mapping (UMIN000038982)[174,175], enabling the localization of lymph nodes with high precision. Alternatively, targeted probes, such as SMG-101, could be explored.

Breast and gynaecologic cancer

Non-targeted probes, including ICG and MB, have long been applied in breast cancer surgery, albeit initially not for real-time fluorescence imaging. Fluorescence imaging has high sensitivity

Nat Rev Bioeng. 2023. 1(3): 161-179 Published online: 3 February 2023

to detect breast cancer margins and SLNs[8,102,134], in particular, if ICG and MB are simultaneously applied[176]. The combined spectral information can provide 88% precision in the detection of SLNs (NCT03619967)[176]. However, the lesion detection rate of these non-targeted probes may be reduced by preoperative chemotherapy[177]. Alternatively, molecularly targeted probes, such as Bevacizumab-IRDye800CW (targeting VEGF), may be more suitable[178].

Fluorescent imaging with ICG also allows lymph node mapping in cervical cancer, with a detection rate of 96%, compared with 46% of isosulfan blue staining[179]. OTL38, which is targeting FRα, has also been explored for ovarian cancer imaging[180], revealing 29% more occult malignant lesions, compared with non-image-guided surgery (NCT02317705).

Other cancers

Glioma is one of the most malignant cancers, and therefore various probes and imagingmethods are beingexplored forglioma resection. In particular, orally administered 5-ALA (20 mg $kg^{-1} \cdot m^2$) specifically accumulates in glioma, allowing the guidance of microscopic surgery by fluorescence imaging in the clinic (clinical trial reference number in Joint Chinese University of Hong Kong: 2017-314)[181]. Intravenously injected ICG also accumulates in glioma lesions, enabling 100% detection of glioblastoma by NIR-II imaging, and extending overall survival by 3.5 months (ChiCTR2000029402)[182]. By integrating deep convolutional neural networks, non-targeted ICG fluorescence images can further reveal pathological information (for example, Ki-67 expression)[143]. Multimodal molecularly targeted imaging further improves glioma resection; for example, the positron emission tomography (PET)–fluorescence probe ^{68}Ga-IRDye800CW-BBN (targeting the GRPR)[72] achieves a sensitivity of 93.9% and a specificity of 100% for 42 foci (Fig. 4a–d).

Various probes have been explored for head and neck cancer. For example, anti-EGFR–antibody–IRDye800CW conjugations[36,42,183,184] can be applied to image tumour margins and lymphatic metastases, and for ex vivo specimen analysis (NCT01987375 and NCT02415881). Oral, oropharyngeal and oesophageal epithelial cancers can be targeted by gargling of probes to image tumour margins with more than 95% sensitivity and specificity (NCT03085147)[75]. Alternatively, the pH-activatable probe ONM-100 (ref. [51]) can be intravenously administered. Once it reaches the acidic TME, the probe becomes fluorescent (Fig. 4e,f), allowing the detection of occult lesions (EudraCT 2017-003543-38).

Fluorescence imaging has also been applied for urinary cancer[185,186]. For example, ICG-based NIR-II fluorescence imaging allows the identification of tumour margins in nephron-sparing surgery[185]. Here, the lesion needing removal had cystic renal masses, which are ischaemic compared with the surrounding healthy tissue. Therefore, a NIR-II negative fluorescence strategy with a high contrast ratio (>4.8) was employed to delineate the surgical margin. To improve the resection rate of bladder cancer, the IRDye800-conjugated probe PLSWT7-DMI targeting overexpressed CD44v6 (ref. [186]) can be peritumourally administered. The probe accumulates in bladder lesions, allowing the identification of small satellite lesions in benign suspicious tissues, with more than 91.2% sensitivity and 90% specificity (ChiCTR-DDD-17012616).

Reducing iatrogenic injury

Many postoperative complications are related to iatrogenic injury. Fluorescence imaging can be applied to reduce the damaging of healthy tissues during surgery.

Image-guided nerve preservation

Nerve damage may severely affect surgical outcomes[187,188]. Nerves can be intraoperatively imaged using fluorescent probes; for example, intravenous injection of ICG (5 mg kg^{-1}) allows visualization of thoracic sympathetic ganglions and pelvic nerves[189]. Using this approach, obturator, genitofemoral and hypogastric nerves could be safely and effectively detected at a rate of 100%, 93.7% and 81%, respectively, in patients with cervical cancer during radical hysterectomy[190,191] (Fig. 4g,h), improving clinical outcomes. However, the mechanism of ICG uptake by nerves is not yet fully understood but should be identified to allow the development of nerve-specific fluorescent probes.

Preventing complications

Iatrogenic injury to healthy tissues, such as the common bile ducts, may result in severe complications, such as biliary fistula and chylothorax. Fluorescence visualization of healthy tissues by intraoperative injection of probes ('fluorescent stain') can prevent complications, for example, during colorectal anastomosis.

In hepatic surgery, biliary injury can be prevented by fluorescent imaging using intraoperatively injected ICG to visualize the biliary duct, even in patients with dense adhesions around the hepatoduodenal ligament[192], as demonstrated in clinical trials (NCT04942665 and NCT04946591). Similarly, the thoracic duct can be preserved in fluorescent imaging-guided thoracic surgery using ICG injected into the bilateral inguinal region[193]. High-sensitivity fluorescent imaging can also make fistula easily detectable, for example, to prevent postoperative chylothorax. Similarly, anastomotic leaks in colorectal surgery can be detected by fluorescent imaging. Here, accumulation of intraoperatively injected probes reflect the blood supply in anastomotic structures[17,194]. Ischaemic structures, which are typically related to a high risk of an anastomotic leak, present weak fluorescence[17]. In addition, fluorescent imaging is being explored in many other surgical procedures that require high precision, including cephalic and eye-sparing surgeries[195,196].

Outlook

Since ICG was approved by the FDA for medical practice in the 1950s (ref. [14]), fluorescence imaging-guided cancer surgery has been greatly improved, and various fluorescence imaging technologies and probes have been developed[5,6,15,106,189]. However, the development of specific tumour-targeted probes lags behind clinical demand, with only a few being investigated in phase 0 and I clinical trials (Fig. 1). Large-sample clinical trials would be required to demonstrate patient benefits, that is, significantly improved, recurrence-free survival.

Importantly, standards need to be established for the imaging hardware systems and imaging performance interpretation. Without standardization, each new fluorescent probe needs to be tested with a specific imaging system in phase II and III clinical trials to achieve regulatory approval. National or international standardization would allow the use of standardized imaging systems for new probes, making clinical trial data comparable[1,94,197], and reducing costs and time. To achieve standardization, high-fidelity fluorescence imaging (HiFFI) could be applied, that is, the accurate representation of fluorescent probe biodistribution

in tissues, independent of a particular imaging system and tissue conditions[197]. The implementation of HiFFI requires calibration and assessment of the different parameters affecting fluorescence imaging performance.

In addition, interdisciplinary teams are required at the early stage of probe development and translation. Many new complex fluorescent probes with tumour-targeting ability are designed at the preclinical stage. However, these probes often have biosafety concerns, lack of stability, cannot be produced at a large scale and/or do not meet clinical demand, making their clinical translation limited. Therefore, a multidisciplinary team, including biologists, chemists, engineers, pharmacists and clinicians, should be involved from the early stages of probe design[1,2,4,106].

Finally, the development of intraoperative fluorescence imaging technologies should be accelerated to enable the clinical translation of new probes. For example, highly sensitive optical sensors in NIR cameras can detect signals from nanomolar concentrations of fluorescence probes[121]. Further improvement of optical sensors, in combination with AI algorithms, may enable picomolar sensitivity, which will substantially reduce the required administration dose of probes. Fluorescence and MPI multimodality intraoperative imaging may address the limitation of imaging depth[107,132], and AI methods may allow intraoperative quantification and interpretation. These technologies will contribute to the standardization of fluorescence imaging-guided surgery, ultimately lowering the barrier for the clinical translation of new probes.

Acknowledgements

The authors thank Z. Wang, X. Zhang and K. M. von Deneen for their advisory help with this article. The authors received support from the Ministry of Science and Technology of China under Grant No. 2017YFA0205200, the National Natural Science Foundation of China under Grant Nos 62027901, 92159305, 81930053, 81227901 and 82272029, the Beijing Science Fund under Grant No. JQ22013 and the Excellent Member Project of Youth Innovation Promotion Association CAS under Grant No. 2016124.

Author contributions

J.T. contributed to the conception of the Review. All authors contributed to the literature research, and to the writing and editing of this manuscript.

Competing interests

The authors declare no competing interests.

References

1. Mieog, J. S. D. et al. Fundamentals and developments in fluorescence-guided cancer surgery. Nat. Rev. Clin. Oncol. 2022;19, 9–22.
2. Hernot, S., van Manen, L., Debie, P., Mieog, J. S. D. & Vahrmeijer, A. L. Latest developments in molecular tracers for fluorescence image-guided cancer surgery. Lancet Oncol. 20, 2019;e354–e367.
3. Wang, X. et al. Consensus guidelines for the use of fluorescence imaging in hepatobiliary surgery. Ann. Surg. 2021;274, 97–106.
4. Alander, J. T. et al. A review of indocyanine green fluorescent imaging in surgery. Int. J. Biomed. Imaging. 2012; 940585.
5. Huang, W. et al. Intraoperative fluorescence visualization in thoracoscopic surgery. Ann. Thorac. Surg. 2022;115(3), e79-e81.
6. Hu, Z. et al. First-in-human liver-tumour surgery guided by multispectral fluorescence imaging in the visible and near-infrared-I/II windows. Nat. Biomed. Eng. 2020;4, 259–271.
7. Cwalinski, T. et al. Methylene blue — current knowledge, fluorescent properties, and its future use. J. Clin. Med. 2020;9, 3538.
8. Zhang, C. et al. Improved generative adversarial networks using the total gradient loss for the resolution enhancement of fluorescence images. Biomed. Opt. Express. 2019;10, 4742–4756.
9. Stammes, M. A. et al. Modalities for image- and molecular-guided cancer surgery. Br. J. Surg. 2018;105, e69–e83.
10. Wang, H. et al. Indocyanine green-incorporating nanoparticles for cancer theranostics. Ther anostics. 2018;8, 1227–1242.
11. Crawford, T. et al. pHLIP ICG for delineation of tumors and blood flow during fluorescence-guided surgery. Sci. Rep. 2020;10, 18356.
12. Nishis, N. et al. Optimal dosing strategy for fluorescence-guided surgery with panitumumab-IRDye800CW in head and neck cancer. Mol. Imaging Biol. 2020;22, 156–164.
13. Moore, G. E. Fluorescein as an agent in the differentiation of normal and malignant tissues. Science. 1947;106, 130–131.
14. Porcu, E. P. et al. Indocyanine green delivery systems for tumour detection and treatments. Biotechnol. Adv. 2016;34, 768–789.
15. Chen, Q. Y. et al. Safety and efficacy of indocyanine green tracer-guided lymph node dissection during laparoscopic radical gastrectomy in patients with gastric cancer: a randomized clinical trial. JAMA Surg. 2020;155, 300–311.
16. Dip, F. et al. Randomized trial of near-infrared incisionless fluorescent cholangiography. Ann. Surg. 2019;270, 992–999.
17. De Nardi, P. et al. Intraoperative angiography with indocyanine green to assess anastomosis perfusion in patients undergoing laparoscopic colorectal resection: results of a multicenter randomized controlled trial. Surg. Endosc. 2020;34, 53–60.
18. Jørgensen, M. G., Hermann, A. P., Madsen, A. R., Christensen, S. & Sørensen, J. A. Indocyanine green lymphangiography is superior to clinical staging in breast cancer-related lymphedema. Sci. Rep. 2021;11, 21103.
19. Zhang, R. R. et al. Beyond the margins: real-time detection of cancer using targeted fluorophores. Nat. Rev. Clin. Oncol. 2017;14, 347–364.
20. Ginimuge, P. R. & Jyothi, S. D. Methylene blue: revisited. J. Anaesthesiol. Clin. Pharmacol. 2010;26, 517–520.
21. Verbeek, F. P. et al. Intraoperative near infrared fluorescence guided identification of the ureters using low dose methylene blue: a first in human experience. J. Urol. 2013;190, 574–579.
22. Hillary, S. L., Guillermet, S., Brown, N. J. & Balasubramanian, S. P. Use of methylene blue and near-infrared fluorescence in thyroid and parathyroid surgery. Langenbecks Arch. Surg. 2018;403, 111–118.
23. Handgraaf, H. J. M. et al. Intraoperative near-infrared fluorescence imaging of multiple pancreatic neuroendocrine tumors: a case report. Pancreas. 2018;47, 130–133.
24. Boughey, J. C. et al. Sentinel lymph node surgery after neoadjuvant chemotherapy in patients with node-positive breast cancer: the ACOSOG Z1071 (Alliance) clinical trial. Jama. 2013;310, 1455–1461.
25. Liu, J. et al. Percutaneous contrast-enhanced ultrasound for localization and diagnosis of sentinel lymph node in early breast cancer. Sci. Rep. 2019;9, 13545.
26. Cwalinski, T. et al. Methylene blue-current knowledge, fluorescent properties, and its future use. J. Clin. Med. 2020;9, 3538.
27. Héritier Barras, A. C., Walder, B. & Seeck, M. Serotonin syndrome following methylene blue infusion: a rare complication of antidepressant therapy. J. Neurol. Neurosurg. Psychiatry. 2010;81, 1412–1413.
28. Wang, L. M., Banu, M. A., Canoll, P. & Bruce, J. N. Rationale and clinical implications of fluorescein-guided supramarginal resection in newly diagnosed high-grade glioma. Front. Oncol. 2021;11, 666734.
29. Sun, Z. et al. Fluorescein-guided surgery for spinal gliomas: analysis of 220 consecutive cases. Int. Rev. Neurobiol. 2020;151, 139–154.
30. Acerbi, F. et al. Fluorescein-guided surgery for malignant gliomas: a review. Neurosurg. Rev. 2014;37, 547–557.
31. Hadjipanayis, C. G. & Stummer, W. 5-ALA and FDA approval for glioma surgery. J. Neurooncol. 2019;141, 479–486.
32. Mahmoudi, K. et al. 5-Aminolevulinic acid photodynamic therapy for the treatment of high-grade gliomas. J. Neurooncol. 2019;141, 595–607.
33. Stummer, W. et al. Fluorescence-guided surgery with 5-aminolevulinic acid for resection of malignant glioma: a randomised controlled multicentre phase III trial. Lancet. Oncol. 2006;7, 392–401.
34. Folli, S. et al. Immunophotodiagnosis of colon carcinomas in patients injected with fluoresceinated chimeric antibodies against carcinoembryonic antigen. Proc. Natl Acad. Sci. USA. 1992;89, 7973–7977.
35. Harlaar, N. J. et al. Molecular fluorescence-guided surgery of peritoneal carcinomatosis of colorectal origin: a single-centre feasibility study. Lancet Gastroenterol. Hepatol. 2016;1, 283–290.
36. Rosenthal, E. L. et al. Sensitivity and specificity of cetuximab-IRDye800CW to identify regional metastatic disease in head and neck cancer. Clin. Cancer Res. 2017;23, 4744–4752.
37. Lu, G. et al. Tumour-specific fluorescence-guided surgery for pancreatic cancer using panitumumab-IRDye800CW: a phase 1 single-centre, open-label, single-arm, dose-escalation study. Lancet Gastroenterol. Hepatol. 2020;5, 753–764.
38. Boogerd, L. S. F. et al. Safety and effectiveness of SGM-101, a fluorescent antibody targeting carcinoembryonic antigen, for intraoperative detection of colorectal cancer: a dose-escalation pilot study. Lancet Gastroenterol. Hepatol. 2018;3, 181–191.
39. Lauwerends, L. J. et al. Real-time fluorescence imaging in intraoperative decision making for cancer surgery. Lancet. Oncol. 2021;22, e186–e195.
40. Miller, S. E. et al. First-in-human intraoperative near-infrared fluorescence imaging of glioblastoma using cetuximab-IRDye800. J. Neurooncol. 2018;139, 135–143.
41. Rosenthal, E. L. et al. Safety and tumor specificity of cetuximab-IRDye800 for surgical navigation in head and neck cancer. Clin. Cancer Res. 2015;21, 3658–3666.
42. Gao, R. W. et al. Determination of tumor margins with surgical specimen mapping using near-infrared fluorescence. Cancer Res. 2018;78, 5144–5154.
43. Warram, J. M. et al. Antibody-based imaging strategies for cancer. Cancer Metastasis Rev. 2014;33, 809–822.
44. Goetz, M. et al. In vivo molecular imaging of colorectal cancer with confocal endomicroscopy by targeting epidermal growth factor receptor. Gastroenterology. 2010;138, 435–446.
de Valk, K. S. et al. First-in-human assessment of cRGD-ZW800-1, a zwitterionic, integrin-targeted, near-infrared fluorescent peptide in colon carcinoma. Clin. Cancer Res. 2020;26, 3990–3998.
46. Fidel, J. et al. Preclinical validation of the utility of BLZ-100 in providing fluorescence contrast for imaging spontaneous solid tumors. Cancer Res. 2015;75, 4283–4291.
47. Yamada, M. et al. A first-in-human study of BLZ-100 (tozuleristide) demonstrates tolerability and safety in skin cancer patients. Contemp. Clin. Trials Commun. 2021;23, 100830.
48. Barth, C. W. & Gibbs, S. L. Fluorescence image-guided surgery — a perspective on contrast agent development. Proc. SPIE Int. Soc. Opt. Eng. 2020;11222, 112220J.
49. van Dam, G. M. et al. Intraoperative tumor-specific fluorescence imaging in ovarian cancer by folate receptor-α targeting: first in-human results. Nat. Med. 2011;17, 1315–1319.
50. Hoogstins, C. E. et al. A novel tumor-specific agent for intraoperative near-infrared fluorescence imaging: a translational study in healthy volunteers and patients with ovarian cancer. Clin. Cancer Res. 2016;22, 2929–2938.
51. Voskuil, F. J. et al. Exploiting metabolic acidosis in solid cancers using a tumor-agnostic pH-activatable nanoprobe for fluorescence-guided surgery. Nat. Commun. 2020;11, 3257.
52. Zanoni, D. K. et al. Use of ultrasmall core-shell fluorescent silica nanoparticles for image-guided sentinel lymph node biopsy in head and neck melanoma: a nonrandomized clinical trial. JAMA Netw. 2021;4, e211936.
53. Hu, Z., Chen, W. H., Tian, J. & Cheng, Z. NIRF nanoprobes for cancer molecular imaging: approaching clinic. Trends Mol. Med. 2020;26, 469–482.
54. Zeng, W. et al. Ratiometric Imaging of MMP-2 activity facilitates tumor detection using activatable near-infrared fluorescent semiconducting polymer nanoparticles. Small. 2021;17, e2101924.
55. Blau, R. et al. Image-guided surgery using near-infrared Turn-ON fluorescent nanoprobes for precise detection of tumor margins. Theranostics 2018;8, 3437–3460.
56. Kamiya, M. et al. An enzymatically activated fluorescence probe for targeted tumor imaging. J. Am. Chem. Soc. 2007;129, 3918–3929.
57. Zhou, F. et al. γ-Glutamyl transpeptidase-activatable near-infrared nanoassembly for tumor fluorescence imaging-guided photothermal therapy. Theranostics. 2021;11, 7045–7056.
58. Kang, D., Cheung, S. T., Wong-Rolle, A. & Kim, J. Enamine N-oxides: synthesis and application to hypoxia-responsive prodrugs and imaging agents. ACS Cent. Sci. 2021;7, 631–640.
59. Chen, X. et al. Synergistic lysosomal activatable polymeric nanoprobe encapsulating pH sensitive imidazole derivative for tumor diagnosis. Small. 2018;14, 1703164.
60. Steinkamp, P. J. et al. A standardized framework for fluorescence-guided margin assessment for head and neck cancer using a tumor acidosis sensitive optical imaging agent. Mol. Imaging Biol. 2021;23, 809–817.
61. Guo, R. et al. GSH activated biotin-tagged near-infrared probe for efficient cancer imaging. Theranostics. 2019;9, 3515–3525.
62. Unkart, J. T. et al. Intraoperative tumor detection using a ratiometric activatable fluorescent peptide: a first-in-human phase 1 study. Ann. Surg. Oncol. 2017;24, 3167–3173.
63. Whitley, M. J. et al. A mouse-human phase 1 co-clinical trial of a protease-activated fluorescent probe for imaging cancer. Sci. Transl. Med. 2016;8, 320ra324.
64. Yim, J. J., Tholen, M., Klaassen, A., Sorger, J. & Bogyo, M. Optimization of a protease activated probe for optical surgical navigation. Mol. Pharm. 2018;15, 750–758.
65. Zhu, S., Tian, R., Antaris, A. L., Chen, X. & Dai, H. Near-infrared-II molecular dyes for cancer imaging and surgery. Adv. Mater. 2019;31, e1900321.
66. O'Connor, J. P. et al. Imaging biomarker roadmap for cancer studies. Nat. Rev. Clin. Oncol. 2017;14, 169–186.
67. van Leeuwen, F. W. B. et al. Trending: radioactive and fluorescent bimodal/hybrid tracers as multiplexing solutions for surgical guidance. J. Nucl. Med. 2020;61, 13–19.
68. Manca, G. et al. Novel experience in hybrid tracers: clinical evaluation of feasibility and efficacy in using ICG-99mTc nanotop for sentinel node procedure in breast cancer patients. Clin. Nucl. Med. 2021;46, e181–e187.
69. Verbeek, F. P. et al. Sentinel lymph node biopsy in vulvar cancer using combined radioactive and fluorescence guidance. Int. J. Gynecol. Cancer. 2015;25, 1086–1093.
70. Christensen, A. et al. Feasibility of real-time near-infrared fluorescence tracer imaging in sentinel node biopsy for oral cavity cancer patients. Ann. Surg. Oncol. 2016;23, 565–572.
71. Hekman, M. C. et al. Tumor-targeted dual-modality imaging to improve intraoperative visualization of clear cell renal cell carcinoma: a first in man study. Theranostics. 2018;8, 2161–2170.
72. Li, D. et al. First-in-human study of PET and optical dual-modality image-guided surgery in glioblastoma using (68)Ga-IRDye800CW-BBN. Theranostics. 2018;8, 2508–2520.
73. Derks, Y. H. W. et al. PSMA-targeting agents for radio- and fluorescence-guided prostate cancer surgery. Theranostics. 2019;9, 6824–6839.
74. Demétrio de Souza França, P. et al. A phase I study of a PARP1-targeted topical fluorophore for the detection of oral cancer. Eur. J. Nucl. Med. Mol. Imaging. 2021;48, 3618–3630.
75. Kossatz, S. et al. Validation of the use of a fluorescent PARP1 inhibitor for the detection of oral, oropharyngeal and oesophageal epithelial cancers. Nat. Biomed. Eng. 2020;4, 272–285.
76. de Souza França, P. D. et al. PARP1: a potential molecular marker to identify cancer during colposcopy procedures. J. Nucl. Med. 2021;62, 941–948.
77. Chen, J. et al. Multiplexed endoscopic imaging of Barrett's neoplasia using targeted fluorescent heptapeptides in a phase 1 proof-of-concept study. Gut. 2021;70, 1010–1013.
78. Pan, Y. et al. Endoscopic molecular imaging of human bladder cancer using a CD47 antibody. Sci. Transl. Med. 2014;6, 260ra148.
79. Buckle, T. et al. Translation of c-Met targeted image-guided surgery solutions in oral cavity cancer — initial proof of concept data. Cancers. 2021;13, 2674.
80. Onoyama, H. et al. Rapid and sensitive detection of early esophageal squamous cell carcinoma with fluorescence probe targeting dipeptidylpeptidase IV. Sci. Rep. 2016;6, 26399.
81. Mizushima, T. et al. Rapid detection of superficial head and neck squamous cell carcinoma by topically spraying fluorescent probe targeting dipeptidyl peptidase-IV. Head Neck. 2018;40, 1466–1475.
Walker, E. et al. Rapid visualization of nonmelanoma skin cancer. J. Am. Acad. Dermatol. 2017;76, 209–216.e9.
83. Walker, E. et al. A protease-activated fluorescent probe allows rapid visualization of keratinocyte carcinoma during excision. Cancer Res. 2020;80, 2045–2055.
84. Sensarn, S. et al. A clinical wide-field fluorescence endoscopic device for molecular imaging demonstrating cathepsin protease activity in colon cancer. Mol. Imaging Biol. 2016;18, 820–829.
85. Mitsunaga, M. et al. Fluorescence endoscopic detection of murine colitis-associated colon cancer by topically applied enzymatically rapid-activatable probe. Gut. 2013;62, 1179–1186.
86. Yang, R. Q. et al. Surgical navigation for malignancies guided by near-infrared-ii fluorescence imaging. Small Meth. 2021;5, e2001066.
87. Carr, J. A. et al. Shortwave infrared fluorescence imaging with the clinically approved near-infrared dye indocyanine green. Proc. Natl Acad. Sci. USA. 2018;115, 4465–4470.
88. Cosco, E. D. et al. Flavylium polymethine fluorophores for near- and shortwave infrared imaging. Angew. Chem. 2017;56, 13126–13129.
89. Bandi, V. G. et al. Targeted multicolor in vivo imaging over 1,000 nm enabled by nonamethine cyanines. Nat. Meth. 2022;19, 353–358.
90. Widen, J. C. et al. AND-gate contrast agents for enhanced fluorescence-guided surgery. Nat. Biomed. Eng. 2021;5, 264–277.
91. Zheng, X. et al. Successively activatable ultrasensitive probe for imaging tumour acidity and hypoxia. Nat. Biomed. Eng. 2017;1, 0057.
92. Cornelissen, B. et al. Translational molecular imaging in exocrine pancreatic cancer. Eur. J. Nucl. Med. Mol. Imaging 2018;45, 2442–2455.
93. Hadjipanayis, C. G., Widhalm, G. & Stummer, W. What is the surgical benefit of utilizing 5-aminolevulinic acid for fluorescence-guided surgery of malignant gliomas? Neurosurgery. 2015;77, 663–673.
94. Pogue, B. W. et al. Fluorescence-guided surgery and intervention — an AAPM emerging technology blue paper. Med. Phys. 2018;45, 2681–2688.
95. Billings, C., Langley, M., Warrington, G., Mashali, F. & Johnson, J. A. Magnetic particle imaging: current and future applications, magnetic nanoparticle synthesis methods and safety measures. Int. J. Mol. Sci. 2021;22, 7651.
96. Song, G. et al. Janus iron oxides @ semiconducting polymer nanoparticle tracer for cell tracking by magnetic particle imaging. Nano Lett. 2018;18, 182–189.
97. Wang, G. et al. Sensitive and specific detection of breast cancer lymph node metastasis through dual-modality magnetic particle imaging and fluorescence molecular imaging: a preclinical evaluation. Eur. J. Nucl. Med. Mol. Imaging. 2022;49, 2723–2734.
98. Choi, H. S. et al. Design considerations for tumour-targeted nanoparticles. Nat. Nanotechnol. 2010;5, 42–47.
99. Yang, J. et al. Gold/α-lactalbumin nanoprobes for the imaging and treatment of breast cancer. Nat. Biomed. Eng. 2020;4, 686–703.
100. Shen, D. et al. Selective imaging of solid tumours via the calcium-dependent high-affinity binding of a cyclic octapeptide to phosphorylated Annexin A2. Nat. Biomed. Eng. 2020;4, 298–313.
101. Ayo, A. & Laakkonen, P. Peptide-based strategies for targeted tumor treatment and imaging . Pharmaceutics. 2021;13, 481.
102. Zhang, Z. et al. Intraoperative fluorescence molecular imaging accelerates the coming of precision surgery in China. Eur. J. Nucl. Med. Mol. Imaging. 2022;49, 2531–2543.
Vahrmeijer, A. L., Hutteman, M., van der Vorst, J. R., van de Velde, C. J. & Frangioni, J. V. Image-guided cancer surgery using near-infrared fluorescence. Nat. Rev. Clin. Oncol. 2013;10, 507–518.
104. Singhal, S. The future of surgical oncology: image-guided cancer surgery. JAMA Surg. 2016;151, 184–185.
105. Hyun, H. et al. Structure-inherent targeting of near-infrared fluorophores for parathyroid and thyroid gland imaging. Nat. Med. 2015;21, 192–197.
106. Wang, K. et al. Optical molecular imaging frontiers in oncology: the pursuit of accuracy and sensitivity. Engineering 2015;1, 308–323.
107. KleinJan, G. H. et al. Toward (hybrid) navigation of a fluorescence camera in an open surgery setting. J. Nucl. Med. 2016;57, 1650–1653.
108. van Oosterom, M. N. et al. Extending the hybrid surgical guidance concept with freehand fluorescence tomography. IEEE Trans. Med. Imaging. 2020;39, 226–235.
109. Kitai, T., Inomoto, T., Miwa, M. & Shikayama, T. Fluorescence navigation with indocyanine green for detecting sentinel lymph nodes in breast cancer. Breast Cancer. 2005;12, 211–215.
110 van den Berg, N. S. et al. (Near-infrared) Fluorescence-guided surgery under ambient light conditions: a next step to embedment of the technology in clinical routine. Ann. Surg. Oncol. 2016;23, 2586–2595.
111. Elliott, J. T. et al. Review of fluorescence guided surgery visualization and overlay techniques. Biomed. Opt. Express. 2015;6, 3765–3782.
112. Glatz, J. et al. Concurrent video-rate color and near-infrared fluorescence laparoscopy. J. Biomed. Opt. 2013;18, 101302.
113. Fengler, J. Near-infrared fluorescence laparoscopy — technical description of PINPOINT® a novel and commercially available system. Colorectal Dis. 2015;17, 3–6.
114. Troyan, S. L. et al. The FLARE™ intraoperative near-infrared fluorescence imaging system: a first-in-human clinical trial in breast cancer sentinel lymph node mapping. Ann. Surg. Oncol. 2009;16, 2943–2952.
115. Ottermo, M. V. et al. The role of tactile feedback in laparoscopic surgery. Surg. Laparosc. Endosc. Percutan. Tech. 2006;16, 390–400.
116. Keating, J. et al. Near-infrared intraoperative molecular imaging can locate metastases to the lung. Ann. Thorac. Surg. 2017;103, 390–398.
117. Graves, C. E. & Duh, Q.-Y. Fluorescent technologies for intraoperative parathyroid identification. Ann. Thyroid. 2020;5, 26.
118. Behrooz, A. et al. Multispectral open-air intraoperative fluorescence imaging. Opt. Lett. 2017;42, 2964–2967.
119. He, K. et al. Comparison between the indocyanine green fluorescence and blue dye methods for sentinel lymph node biopsy using novel fluorescence image-guided resection equipment in different types of hospitals. Transl. Res. 2016;178, 74–80.
120. Doenst, T., Diab, M., Sponholz, C., Bauer, M. & Färber, G. The opportunities and limitations of minimally invasive cardiac surgery. Dtsch. Arztebl Int. 2017;114, 777–784.
121. DSouza, A., Lin, H., Henderson, E., Samkoe, K. & Pogue, B. Review of fluorescence guided surgery systems: identification of key performance capabilities beyond indocyanine green imaging. J. Biomed. Opt. 2016;21, 080901.
122. Mao, Y. et al. Development and application of the near-infrared and white-light thoracoscope system for minimally invasive lung cancer surgery. J. Biomed. Opt. 2017;22, 066002.
123. Daskalaki, D., Aguilera, F., Patton, K. & Giulianotti, P. C. Fluorescence in robotic surgery. J. Surg. Oncol. 2015;112, 250–256.
124. Tjalma, J. J. J. et al. Quantitative fluorescence endoscopy: an innovative endoscopy approach to evaluate neoadjuvant treatment response in locally advanced rectal cancer. Gut. 2020;69, 406–410.
125. Achterberg, F. B. et al. Clinical translation and implementation of optical imaging agents for precision image-guided cancer surgery. Eur. J. Nucl. Med. Mol. Imaging. 2021;48, 332–339.
126. Koga, H. et al. Comparison of 2K and 4K imaging systems for laparoscopic repair of choledochal cyst in children. J. Pediatr. Surg. 2022;57, 235–238.
127. Liu, Y. et al. First in-human intraoperative imaging of HCC using the fluorescence goggle system and transarterial delivery of near-infrared fluorescent imaging agent: a pilot study. Transl. Res. 2013;162, 324–331.

Nat Rev Bioeng. 2023. 1(3): 161-179 Published online: 3 February 2023

128. Shao, P. et al. Designing a wearable navigation system for image-guided cancer resection surgery. Ann. Biomed. Eng. 2014;42, 2228–2237.
129. Tonetti, J., Boudissa, M., Kerschbaumer, G. & Seurat, O. Role of 3D intraoperative imaging in orthopedic and trauma surgery. Orthop. Traumatol. Surg. Res. 2020;106, S19–S25.
130. Quang, T. T., Chen, W. F., Papay, F. A. & Liu, Y. Dynamic, real-time, fiducial-free surgical navigation with integrated multimodal optical imaging. IEEE Photonics J. 2021;13, 1–13.
131. Azargoshasb, S. et al. Advancing intraoperative magnetic tracing using 3D freehand magnetic particle imaging. Int. J. Comput. Assist. Radiol. Surg. 2022;17, 211–218.
132. Mason, E. E. et al. Concept for using magnetic particle imaging for intraoperative margin analysis in breast-conserving surgery. Sci. Rep. 2021;11, 13456.
133. de Jongh, S. J. et al. Back-table fluorescence-guided imaging for circumferential resection margin evaluation using bevacizumab-800CW in patients with locally advanced rectal cancer. J. Nucl. Med. 2020;61, 655–661.
134. Zhang, P. et al. Real-time navigation for laparoscopic hepatectomy using image fusion of preoperative 3D surgical plan and intraoperative indocyanine green fluorescence imaging. Surg. Endosc. 2020;34, 3449–3459.
135. Zhang, C., Wang, K. & Tian, J. Adaptive brightness fusion method for intraoperative near-infrared fluorescence and visible images. Biomed. Opt. Express 13, 1243–1260 (2022).
136. Quang, T., Zhou, M., Papay, F. & Liu, Y. 2018 IEEE Int. Symp. Signal Processing and Information Technology (ISSPIT) 2018;1–6.
137. Ma, Z., Wang, F., Wang, W., Zhong, Y. & Dai, H. Deep learning for in vivo near-infrared imaging. Proc. Natl Acad. Sci. USA. 2021;118, e2021446118.
138. Koch, M. et al. Video-rate optical flow corrected intraoperative functional fluorescence imaging. J. Biomed. Opt. 2014;19, 046012.
139. Feruglio, P. F. et al. Noise suppressed, multifocus image fusion for enhanced intraoperative navigation. J. Biophotonics. 2013;6, 363–370.
140. Madani, A. et al. Artificial intelligence for intraoperative guidance: using semantic segmentation to identify surgical anatomy during laparoscopic cholecystectomy. Ann. Surg. 2022;276, 363–369.
141. Shademan, A. et al. Supervised autonomous robotic soft tissue surgery. Sci. Transl. Med. 2016;8, 337ra364.
142. Cahill, R. A. et al. Artificial intelligence indocyanine green (ICG) perfusion for colorectal cancer intra-operative tissue classification. Br. J. Surg. 2020;108, 5–9.
143. Shen, B. et al. Real-time intraoperative glioma diagnosis using fluorescence imaging and deep convolutional neural networks. Eur. J. Nucl. Med. Mol. Imaging. 2021;48, 3482–3492.
144. Ishizawa, T. et al. Real-time identification of liver cancers by using indocyanine green fluorescent imaging. Cancer. 2009;115, 2491–2504.
145. He, K. S. et al. Efficacy of near-infrared fluorescence-guided hepatectomy for the detection of colorectal liver metastases: a randomized controlled trial. J. Am. Coll. Surg. 2022;234, 130–137.
146. Garrido, A. & Djouder, N. Cirrhosis: a questioned risk factor for hepatocellular carcinoma. Trends Cancer 2021;7, 29–36.
147. Kanwal, F. & Singal, A. G. Surveillance for hepatocellular carcinoma: current best practice and future direction. Gastroenterology. 2019;157, 54–64.
148. Marino, M. V., Podda, M., Fernandez, C. C., Ruiz, M. G. & Fleitas, M. G. The application of indocyanine green-fluorescence imaging during robotic-assisted liver resection for malignant tumors: a single-arm feasibility cohort study. HPB. 2020;22, 422–431.
149. Yu, W. Q., Liu, R., Zhou, Y. & Gao, H. L. Size-tunable strategies for a tumor targeted drug delivery system. ACS Cent. Sci. 2020;6, 100–116.
150. Tang, C., Du, Y., Liang, Q., Cheng, Z. & Tian, J. Development of a novel histone deacetylase-targeted near-infrared probe for hepatocellular carcinoma imaging and fluorescence image-guided surgery. Mol. Imaging Biol. 2020;22, 476–485.
151. Banales, J. M. et al. Cholangiocarcinoma 2020: the next horizon in mechanisms and management. Nat. Rev. Gastroenterol. Hepatol. 2020;17, 557–588.
152. Zhang, H., Yang, T., Wu, M. C. & Shen, F. Intrahepatic cholangiocarcinoma: epidemiology, risk factors, diagnosis and surgical management. Cancer Lett. 2016;379, 198–205.
153. Zhang, Y. et al. Clinical application of indocyanine green fluorescence imaging in laparoscopic lymph node dissection for intrahepatic cholangiocarcinoma: a pilot study (with video). Surgery. 2022;171, 1589–1595.
154. Tummers, W. S. et al. Intraoperative pancreatic cancer detection using tumor-specific multimodality molecular imaging. Ann. Surg. Oncol. 2018,25, 1880–1888.
155. Tummers, W. S. et al. Detection of visually occult metastatic lymph nodes using molecularly targeted fluorescent imaging during surgical resection of pancreatic cancer. HPB. 2019;21, 883–890.
156. Hoogstins, C. E. S. et al. Image-guided surgery in patients with pancreatic cancer: first results of a clinical trial using SGM-101, a novel carcinoembryonic antigen-targeting, near-infrared fluorescent agent. Ann. Surg. Oncol. 2018;25, 3350–3357.
157. Zhou, J., Yang, F., Jiang, G. C. & Wang, J. Applications of indocyanine green based near-infrared fluorescence imaging in thoracic surgery. J. Thorac. Dis. 8, S738–S743 (2016).
158. Newton, A. D., Predina, J. D., Nie, S. M., Low, P. S. & Singhal, S. Intraoperative fluorescence imaging in thoracic surgery. J. Surg. Oncol. 2018;118, 344–355.
159. Matsuura, Y., Ichinose, J., Nakao, M., Okumura, S. & Mun, M. Recent fluorescence imaging technology applications of indocyanine green in general thoracic surgery. Surg. Today. 2020;50, 1332–1342.
160. Kim, H. K. et al. Intraoperative pulmonary neoplasm identification using near-infrared fluorescence imaging. Eur. J. Cardiothorac. Surg. 2016;49, 1497–1502.
161. Okusanya, O. T. et al. Intraoperative near-infrared imaging can identify pulmonary nodules. Ann. Thorac. Surg. 2014;98, 1223–1230.
162. Mao, Y. M. et al. The identification of sub-centimetre nodules by near-infrared fluorescence thoracoscopic systems in pulmonary resection surgeries. Eur. J. Cardiothorac. Surg. 2017;52, 1190–1196.
163. Li, H. et al. Clinical application of near-infrared thoracoscope with indocyanine green in video-assisted thoracoscopic bullectomy. J. Thorac. Dis. 2016;8, 1841–1845.
164. Li, H., Zhou, J., Yang, F. & Wang, J. Identifying interlobar fissure in a Craig grade 4 fissureless patient by near-infrared thoracoscopy. J. Thorac. Dis. 2018;10, E52–E54.
165. Quan, Y. H. et al. Evaluation of intraoperative near-infrared fluorescence visualization of the lung tumor margin with indocyanine green inhalation. JAMA Surg. 2020;155, 732–740.
166. Predina, J. D., Newton, A., Connolly, C. & Singhal, S. Folate receptor-targeted molecular imaging improves identification of malignancy during pulmonary resection: a case report. J. Cardiothorac. Surg. 2017;12, 110.
167. Predina, J. D. et al. Intraoperative molecular imaging combined with positron emission tomography improves surgical management of peripheral malignant pulmonary nodules. Ann. Surg. 2017;266, 479–488.
168. Gangadharan, S. et al. Multiinstitutional phase 2 clinical trial of intraoperative molecular imaging of lung cancer. Ann. Thorac. Surg. 2021;112, 1150–1159.
169. Wang, X. J. et al. Near-infrared fluorescence imaging-guided lymphatic mapping in thoracic esophageal cancer surgery. Surg. Endosc. 2022;36, 3994–4003.
170. Huang, Z.-N. et al. Assessment of indocyanine green tracer-guided lymphadenectomy in laparoscopic gastrectomy after neoadjuvant chemotherapy for locally advanced gastric cancer: results from a multicenter analysis based on propensity matching. Gastric Cancer 2021;24, 1355–1364.
171. Zhong, Q. et al. Clinical implications of indocyanine green fluorescence imaging-guided laparoscopic lymphadenectomy for patients with gastric cancer: a cohort study from two randomized, controlled trials using individual patient data. Int. J. Surg. 2021;94, 106120.
172. Burggraaf, J. et al. Detection of colorectal polyps in humans using an intravenously administered fluorescent peptide targeted against c-Met. Nat. Med. 2015;21, 955–961.
173. Schaap, D. P. et al. Carcinoembryonic antigen-specific, fluorescent image-guided cytoreductive surgery with hyperthermic intraperitoneal chemotherapy for metastatic colorectal cancer. Br. J. Surg. 107, 2020;334–337.
174. Nishigori, N. et al. Visualization of lymph/blood flow in laparoscopic colorectal cancer surgery by ICG fluorescence imaging (Lap-IGFI). Ann. Surg. Oncol. 2016;23, 266–274.
175. Satoyoshi, T. et al. Timing of indocyanine green injection prior to laparoscopic colorectal surgery for tumor localization: a prospective case series. Surg. Endosc. 2021;35, 763–769.
176. Blair, S. et al. Hexachromatic bioinspired camera for image-guided cancer surgery. Sci. Transl. Med. 2021;13, eaaw7067.
177. Zhang, C. et al. Methylene blue-based near-infrared fluorescence imaging for breast cancer visualization in resected human tissues. Technol. Cancer Res. Treat. 2019;18, 1533033819894331.
178. Lamberts, L. E. et al. Tumor-specific uptake of fluorescent bevacizumab-IRDye800CW microdosing in patients with primary breast cancer: a phase I feasibility study. Clin. Cancer Res. 2017;23, 2730–2741.
179. Frumovitz, M. et al. Near-infrared fluorescence for detection of sentinel lymph nodes in women with cervical and uterine cancers (FILM): a randomised, phase 3, multicentre, non-inferiority trial. Lancet Oncol. 2018;19, 1394–1403.
180. Randall, L. M., Wenham, R. M., Low, P. S., Dowdy, S. C. & Tanyi, J. L. A phase II, multicenter, open-label trial of OTL38 injection for the intra-operative imaging of folate receptor-α positive ovarian cancer. Gynecol. Oncol. 2019;155, 63–68.
181. Chan, D. T. M., Sonia, H. Y. P. & Poon, W. S. 5-Aminolevulinic acid fluorescence guided resection of malignant glioma: Hong Kong experience. Asian J. Surg. 2018;41, 467–472.
182. Shi, X. et al. Near-infrared window II fluorescence image-guided surgery of high-grade gliomas prolongs the progression-free survival of patients. IEEE Trans. Biomed. Eng. 2022;69, 1889–1900.
183. Nishio, N. et al. Optical molecular imaging can differentiate metastatic from benign lymph nodes in head and neck cancer. Nat. Commun. 2019;10, 5044.
184. van Keulen, S. et al. The sentinel margin: intraoperative ex vivo specimen mapping using relative fluorescence intensity. Clin. Cancer Res. 2019;25, 4656–4662.
185. Cao, C. et al. Intraoperative near-infrared II window fluorescence imaging-assisted nephron-sparing surgery for complete resection of cystic renal masses. Clin. Transl. Med. 2021;11, e604.
186. Shang, W. et al. A clinical study of a CD44v6-targeted fluorescent agent for the detection of non-muscle invasive bladder cancer. Eur. J. Nucl. Med. Mol. Imaging. 2022;49(9):3033-3045.
187. 187.Walsh, E. M. et al. Fluorescence imaging of nerves during surgery. Ann. Surg. 2019;270, 69–76.
188. Wang, L. G. et al. Near-infrared nerve-binding fluorophores for buried nerve tissue imaging. Sci. Transl. Med. 2020;12, eaay0712.
189. He, K. S. et al. Near-infrared intraoperative imaging of thoracic sympathetic nerves: from preclinical study to clinical trial. Theranostics. 2018;8, 304–313.
190. He, K. et al. Intraoperative near-infrared fluorescence imaging can identify pelvic nerves in patients with cervical cancer in real time during radical hysterectomy. Eur. J. Nucl. Med. Mol. Imaging. 2022;49(8):2929-2937.
191. Pei, G. et al. The safety and feasibility of intraoperative near-infrared fluorescence imaging with indocyanine green in thoracoscopic sympathectomy for primary palmar hyperhidrosis. Thorac. Cancer. 2020;11, 943–949.
192. Wang, P. A. et al. Detection of the common bile duct in difficult bile duct exploration using indocyanine green fluorescence imaging: a case report. Photodiagnosis Photodyn. Ther. 2021;36, 102610.
193. Yang, F. et al. Near-infrared fluorescence-guided thoracoscopic surgical intervention for postoperative chylothorax. Interact. Cardiovasc. Thorac. Surg. 2018;26, 171–175.
194. Morales-Conde, S. et al. Fluorescence angiography with indocyanine green (ICG) to evaluate anastomosis in colorectal surgery: where does it have more value? Surg. Endosc. 2020;34, 3897–3907.
195. Ye, Z. P., Yang, X. Y., Li, W. S., Hou, B. & Guo, Y. Microsurgical resection of cervical spinal cord arteriovenous malformations: report of 6 cases. World Neurosurg. 2016;96, 362–369.
196. Maheshwari, A. & Finger, P. T. Cancers of the eye. Cancer Metastasis Rev. 2018;37, 677–690.
197. Koch, M., Symvoulidis, P. & Ntziachristos, V. Tackling standardization in fluorescence molecular imaging. Nat. Photonics. 2018;12, 505–515.
198. Linssen, M. D. et al. Roadmap for the development and clinical translation of optical tracers cetuximab-800CW and trastuzumab-800CW. J. Nucl. Med. 2019;60, 418–423.
199. Souto, E. B. et al. Nanopharmaceutics: part I — clinical trials legislation and good manufacturing practices (GMP) of nanotherapeutics in the EU. Pharmaceutics. 2020;12, 146.
200. Chapman, S. et al. Nanoparticles for cancer imaging: the good, the bad, and the promise. Nano Today. 2013;8, 454–460.
201. Pogue, B. W. & Rosenthal, E. L. Review of successful pathways for regulatory approvals in open-field fluorescence-guided surgery. J. Biomed. Opt. 2021;26, 030901.
202. Tummers, W. S. et al. Regulatory aspects of optical methods and exogenous targets for cancer detection. Cancer Res. 2017;77, 2197–2206.

Neurosurgery

Research Article

Near-Infrared Window II Fluorescence Image-Guided Surgery of High-Grade Gliomas Prolongs the Progression-Free Survival of Patients

Xiaojing Shi[3,4,*], Zhe Zhang[5,*], Zeyu Zhang[3,5], Caiguang Cao[3,4], Zhen Cheng[7] ✉, Zhenhua Hu[3,4] ✉, Jie Tian[1,3,4,5] ✉, Nan Ji[1,2,5] ✉

Abstract

Objective: This translational study aims to investigate the clinical benefits of indocyanine green (ICG) based near-infrared window II (NIR-II) fluorescence image-guided surgery (FGS) on high-grade glioma (HGG) patients.

Methods: Patients were randomly assigned to receive FGS or traditional white light image-guided surgery (WLS). The detection rate of NIR-II fluorescence was observed. Complete resection rate, progression-free survival (PFS), overall survival (OS), and neurological status were compared. Tissue samples were obtained from the FGS group, with the diagnosis based on the surgeons and the fluorescence recorded for comparison of diagnostic capability. Patients with WHO grade III gliomas or glioblastomas (GBM) were analyzed separately.

Results: 15 GBM and 4 WHO grade III glioma patients in the FGS group and 18 GBM and 4 WHO grade III glioma patients in the WLS group were enrolled. The detection rate of NIR-II fluorescence was 100% for GBM. The complete resection rate was significantly increased by the FGS for GBM (FGS, 100% [95% CI 73.41-100] vs. WLS, 50% [95% CI 29.03-70.97], *P*

= 0.0036). The PFS and OS of the FGS group were also significantly prolonged (Median PFS: FGS, 9.0 months vs. WLS, 7.0 months, $P < 0.0001$; Median OS: FGS, 19.0 months vs. WLS, 15.5 months, $P = 0.0002$). No recurrence was observed in WHO grade III glioma patients.

Conclusions: NIR-II FGS achieves a much better complete resection rate of GBM than conventional WLS, leading to greatly improved survival of GBM patients.

Significance: NIR-II FGS is a highly promising technique worthy of exploring more clinical applications.

Index Terms:

Near-infrared window II, Fluorescence image-guided surgery, Glioblastoma, Indocyanine green.

[1] Beijing Advanced Innovation Center for Big Data-Based Precision Medicine, School of Medicine, Beihang University, Beijing, China

[2] China National Clinical Research Center for Neurological Diseases, Beijing, China

[3] CAS Key Laboratory of Molecular Imaging, Beijing Key Laboratory of Molecular Imaging, The State Key Laboratory of Management and Control for Complex Systems, Institute of Automation, Chinese Academy of Sciences, China

[4] School of Artificial Intelligence, University of Chinese Academy of Sciences, China

[5] Department of Neurosurgery, Beijing Tiantan Hospital, Capital Medical University, China

[6] Engineering Research Center of Molecular and Neuro Imaging of Ministry of Education, School of Life Science and Technology, Xidian University, China

[7] Molecular Imaging Center, Shanghai Institute of Materia Medica, Chinese Academy of Sciences, Shanghai, China

* Xiaojing Shi and Zhe Zhang contributed equally to this work.

Introduction

Glioblastoma (GBM) occurs as the most common primary tumor in the central nervous system[1]. The 5-year overall survival rate of GBM patients is only ~5%[2, 3]. Maximal safe resection is recommended as a beneficial approach to improve the overall survival (OS) and the progression-free survival (PFS), benefiting the life quality of patients[4–6], which is strongly recommended for surgical decision by the European Society for Medical Oncology (ESMO) and National Comprehensive Cancer Network (NCCN) guideline of the central nervous system. However, maximal safe resection of GBM is hardly achieved because the GBM often infiltrates into the eloquent area. Besides, distinguishing the tumor from the non-tumor tissue in the resection margin even in the non-eloquent area is also difficult[7].

Several techniques including intraoperative ultrasound (iUS), intraoperative magnetic resonance imaging (iMRI), and neuro-navigation have been applied to assist neurosurgeons to achieve improved GBM resection during surgery[8]. Preoperative magnetic resonance imaging (MRI) based neuro-navigation can be affected by brain shift and deformation, reducing the accuracy of locating the tumor after craniotomy[9]. The iUS suffers limited resolution and is susceptible to interference from edema and bleeding during the resection, leading to poor judgment of the residual tumor. The iMRI is the only technique that improves the overall survival of glioma patients, but limitations such as inconvenience, time-consuming operation, and high cost restrict its' application in neurosurgery[10].

Therefore, a novel real-time imaging technique for precise intraoperative image-guided neurosurgery is urgently needed[11–16]. This demand has inspired the investigation of fluorescence image-guided surgery (FGS) techniques. For example, dyes emitting fluorescence in the visible wavelength (400-700 nm) such as 5-aminolevulinic acid (5-ALA) induced protoporphyrin IX (PpIX, λex = 407 nm, λem = 620 nm) and fluorescein sodium (FS, λex = 494 nm, λem = 512 nm) have been studied for real-time FGS, and they have improved the extent of resection (EOR) and PFS of high-grade glioma patients, including patients with GBM [17–20]. In 2006, a randomized controlled clinical trial demonstrated that 5-ALA based FGS has resulted in 65% of patients achieving complete resection of the tumor, while 36% of patients achieved complete resection in the white-light group[17]. 5-ALA based fluorescence imaging also has achieved a rather high positive-predictive value (PPV) in tumor detection, facilitating 5-ALA based FGS to be reliable to visualize the tumor[21]. As for FS, studies have proved that intraoperative bolus injection leads to its accumulation in areas with blood-brain barrier damage[22]. In a study of FS based FGS of high-grade gliomas implemented in 2018, 82.61% of the 46 patients involved achieved complete resection[20]. FS also has a higher sensitivity in identifying tumor tissues compared to 5-ALA[19]. However, the visible-light fluorescence has limitations such as poor tissue penetration and auto-fluorescence, which may decrease the contrast between the tumor and surrounding non-tumor tissue. Therefore, the near-infrared window I (NIR-I, 700-900 nm) fluorescence imaging has been investigated in gliomas resection surgery with FDA approved indocyanine green (ICG, λex = 760 nm, λem = 830 nm). Previous clinical studies have demonstrated that ICG passes the disrupted blood-brain barrier and accumulates in GBM[23], rendering it a promising optical probe for intraoperative imaging of GBM. Moreover, ICG injected at a higher dose and 24 hours ahead of imaging can achieve even higher sensitivity and negative-predictive value (NPV), which enables surgeons to find more residual tumors[24].

Recently, near-infrared window II (NIR-II, 1,000-1,700 nm) fluorescence imaging has been demonstrated to possess significant advantages in biological imaging compared with the conventional NIR-I fluorescence imaging in recent studies. Low autofluorescence of tissue in the NIR-II spectrum enables accurate in vivo detection of the fluorophore. Furthermore, the low tissue absorption and scattering property of NIR-II light provide a high contrast image of deeper tissue compared with fluorescence imaging in NIR-I and visible spectrum. The outstanding optical imaging properties of NIR-II fluorescence have led to outstanding performance of NIR-II imaging in broad of preclinical applications[25, 26]. Although numerous studies confirm that NIR-II out-performs NIR-I fluorescence imaging in pre-clinical studies using small animal models, research on the clinical application of NIR-II imaging is rare and in infancy, which is mainly attributed to the lack of clinical approved imaging instruments and molecular probes. More importantly, until now there is no report to investigate the clinical impact and treatment efficacy of NIR-II image-guided surgery. In recent years, ICG was reported to have fluorescence in the NIR-II region in addition to the emission peak in the NIR-I region. This facilitated a fast clinical translation of NIR-II fluorescence imaging[25]. The first clinical application of NIR-II fluorescence imaging was reported using ICG in a group of hepatocellular carcinoma patients and proved a better imaging performance of NIR-II compared with NIR-I[26].

Herein, we have developed and characterized a novel multispectral imaging system (visible/NIR-I/NIR-II) suitable for intraoperative brain tumor imaging. Then a randomized control clinical trial has been conducted to evaluate medical value and treatment efficacy of NIR-II image-guided surgery. More specifically, GBM patients were randomly assigned as FGS group or white light image-guided surgery (WLS) group. The outcome of the surgery such as detection rate, complete resection rate, PFS, OS, and neurological function of GBM patients have been analyzed. The medical value and benefits of NIR-II FGS have been clearly demonstrated by comparison with conventional surgery under white light which is the current standard clinical practice.

Materials and Methods

A. Construction of Intraoperative Brain Tumor Multispectral Imaging System

To perform NIR-II FGS of gliomas, a novel multispectral imaging system was developed, which can acquire color (400-700 nm), NIR-I (700-900 nm), and NIR-II (1,000-1,700 nm) images intraoperatively. The imaging system was composed of an imaging sub-system and a controlling sub-system. The imaging sub-system was used to achieve the color image and NIR-II/I fluorescence images, which consisted of a laser generation unit, a visible light imaging unit, a NIR-I imaging unit, and a NIR-II imaging unit. The NIR-II imaging unit contained a camera (NIRvana: 640, Teledyne Princeton Instruments, USA) using InGaAs imaging chip, a lens specially designed for shortwave-wavelength infrared imaging with a high performance (SWIRON 2.8/50, Schneider Kreuznach, Germany), and a long-pass filter (over 1000 nm, FEL1000 Longpass Filter, Thorlabs, USA). The NIR-I imaging unit included an electron-multiplying charge-coupled device (EMCCD, ProEM-HS: 1024BX3, Teledyne Princeton Instruments, USA), a lens (VHF 35M-MP SWIR, Spacecom, Japan), and a spectral filter (over 850 nm, FEL0850 Longpass Filter, Thorlabs, USA). A mobile phone (Huawei Enjoy 9, Huawei, China) was connected with the controlling unit to serve as the visible light imaging unit. The laser generation unit is composed of an 808 nm laser, a liquid-core optical fiber, and a collimator. The collimator converted the concentrated light beam into a dispersed and homogenize light spot. The power of the laser was set to be 50 mW/cm^2. The controlling sub-system which included a laser distance measurement unit, a controlling handle, and a computer was set to control the imaging subsystem to rotate so that images of every side of the tumor cavity were acquired.

A specialized program was realized using MATLAB (MATLAB R2018b, The MathWorks Inc., USA) to convert the fluorescence image from a grayscale image to a pseudocolor image. A threshold was assigned intraoperatively to indicate the signal intensity of tumors. Pixels with signal intensity below the threshold were displayed with no pseudo color to indicate normal tissue, while pixels with signal intensity above the threshold were assigned a color from the gradient region of yellow and blue to indicate tumor tissue. The color of pixels with higher signal intensity was closer to yellow, while the color of pixels with signal intensity closer to the threshold was closer to blue.

The multispectral imaging system was 160 cm in the length, and 60 cm in the width. The height of the imaging system was adjustable, ranging from 140 to 190 cm. This guaranteed the changeable imaging distance.

B. Patients' Characteristics

Patients matching the following criteria were enrolled: (1) patients aged 18-75 years with suspected newly diagnosed, untreated gliomas, who were eligible for surgical resection; (2) patients with KPS over 70; (3) patients with only one solid

IEEE Trans Biomed Eng. 2022. 69(6): 1889-1900 Published online: 24 November 2021

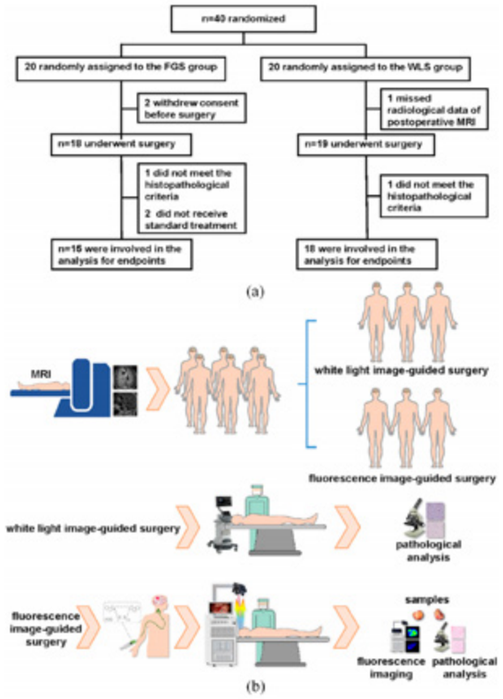


Fig.1 Clinical trial profile. The patient enrollment process (a), and the schematic diagram of the trial (b), were displayed above.

contrast-enhanced lesion on MRI before randomization, which is not located in the midline, basal ganglia, cerebellum, or brain stem of the brain; (4) patients with normal heart, bone marrow, liver, and kidney function, which are determined by laboratory tests before surgery (ie. hemoglobin >110g/L, platelet count >100×10^9, total bilirubin level < 1.5 × upper limit of normal (ULN), alanine aminotransferase/glutagory aminotransferase < 2.5 × ULN; creatinine < 1.5 × ULN); (5) patients who are compatible with follow-up; (6) women of child-bearing age receiving a pregnancy test within 7 days before initiation of treatment with negative results; (7) male and female patients with fertility agreeing to use effective contraceptive measures to ensure no pregnancy during the study period and within 3 months after discontinuation of treatment; (8) patients volunteered to sign the informed consent form; (9) patients have complete medical records for analysis. Exclusion criteria were as follows: (1) patients who are unable to sign the informed consent form; (2) patients with gliomas that are not suitable for resection; (3) patients allergic to ICG; (4) patients with any unstable systemic disease (including active infections, uncontrolled hypertension, unstable angina, angina pectoris within the last 3 months, congestive heart failure, occurred within 12 months of enrollment myocardial infarction, severe arrhythmia requiring medication, liver, kidney or metabolic disease); (5) patients who are infected with human immunodeficiency virus (HIV) or with active hepatitis; (6) patients who have participated in other clinical trials within the past 30 days; (7) patients with mental illness, cognitive impairment, who are unable to understand the experimental scheme and side effects and to complete the experimental arrangements and follow-up. The patients enrolled were randomly allocated to the FGS group or the WLS group.

Assuming that the complete resection rate of the FGS group and WLS group are 85% and 40% respectively, the sample size of each group was required to be 15 (α = 0.05, two-sided type, and power (1 – β) of 80%. Sample size ratio is 1:1). With a maximum of 30% incomplete follow-up or dropout expected, 20 patients were planned to be involved in each of the groups.

The protocol was authorized by the Ethics Committee of Beijing Tiantan Hospital, Capital Medical University. The clinical trial was registered in the Chinese Clinical Trial Registry (ChiCTR2000029402). From March 22 to August 23, 2019, 40 GBM patients were enrolled. All patients were given informed consent for their agreements. Patients were randomly allocated to the FGS group (n = 20) and the WLS group (n = 20). In the FGS group, 5 patients were excluded for withdrawing consent before surgery (n = 2), not meeting histopathological criteria after surgery (n = 1), and not receiving standard treatment (n = 2). In the WLS group, 2 patients were excluded for missing radiological data of postoperative MRI (n = 1) and not meeting the histopathological criteria after surgery (n = 1). In the end, 15 patients in the FGS group and 18 in the WLS group met the inclusion criteria of this trial (Fig. 1(a)). All the patients in both of the groups received Stupp standard treatment after surgery.

Eight patients with WHO grade III patients were also enrolled and analyzed separately.

C. Study Design

Patients all went through MRI examination before surgery. For the patients assigned to the FGS group, ICG (1mg/kg) was injected intravenously 48 hours before intraoperative fluorescence imaging. NIR-II/I fluorescence images of tumor was acquired intraoperatively and the NIR-II fluorescence images were shown to the surgeons to guide the tumor resection under the microscope. Tissue samples were obtained for ex vivo fluorescence imaging and histopathological analysis. For the patients in the WLS group, placebo was not employed. And the tumor was resected under the microscope in a conventional manner. The grade of each patient in both of the group was determined by pathological analysis of tumor tissue sample after surgery (Fig. 1(b)).

D. Intraoperative NIR-II/I Fluorescence Imaging of GBM and Surgery Under the Guidance of NIR-II Fluorescence Images

The intraoperative brain tumor imaging system was sterilely draped before utilization in the operating room. At the beginning of the surgery, the neuro-navigation based on preoperative MRI was applied only for determining the position of the incision. Upon opening of the dura and the exposure of the cortex, the imaging system was positioned near the operation bed and the working distance was adjusted to 50 cm. Color images were acquired under the light in the operating room. Then the light was turned off and NIR-II/I fluorescence images were acquired with the exposure time ranging from 500 to 2000 ms. The presence or absence of NIR-II/I fluorescence was recorded for each patient.

The detection rate of the fluorescence was calculated as follows: detection rate = number of patients with tumor fluorescence/ number of patients involved in the FGS group. For patients with the fluorescence of tumors, the resection extent was displayed by the NIR-II fluorescence images. The gross tumor was removed by the surgeons under the microscope referring to the NIR-II fluorescence images. After the surgeon was satisfied with the resection, color images and NIR-II/I fluorescence images were acquired again to prompt whether the tumor tissue was left. Tissue with residual NIR-II fluorescence signal was removed with the consideration of the neurological function reservation.

E. Ex Vivo NIR-II/I Fluorescence Imaging of Tissue Samples

Tissue samples with a side length of about 1 cm were obtained from the gross tumor and the tissues with residual NIR-II fluorescence. Color and NIR-II/I fluorescence images of the samples set on black cardboard were obtained using our imaging system in the operating room.

F. Diagnosis of Tissue Samples Based on the Fluorescence Images and Surgeons in the Operating Room

The samples were coded whether they were tumor tissue or normal tissue by three surgeons who were blind to the fluorescence images while still in the operating room. In the meantime, the existence or absence of NIR-II/I fluorescence in the fluorescence images of each sample was coded by another surgeon, with the existence of fluorescence marked as tumor and absence of fluorescence as non-tumor tissue. The diagnosis based on the surgeons and fluorescence was then compared with the histopathological diagnosis of the samples obtained after the surgery, which served as the gold standard.

G. Endpoints

The primary endpoint was the proportion of patients without residual tumors measured on post-operative MRI. The secondary endpoints were the PFS 6 months and neurological function 3 months after surgery.

To evaluate the proportion of patients without residual tumor, the complete resection rate was introduced and calculated as follows: complete resection rate = the number of patients with complete resection of tumor / the number of patients in each group. Complete resection was defined as enhancement on T1-enhanced MRI with a volume of less than 0.175 cm^2 measured from the postoperative MRI obtained within 72 hours after the surgery.

The patients were followed up every 3 months to assess disease progression. Progression was defined according to the Response Assessment in Neuro-Oncology (RANO) criteria. PFS at 3, 6, 9, and 12 months were calculated as the proportion of patients without progression at a certain time. For example, PFS at 6 months after surgery (6m-PFS) = number of patients that don't have progress at 6 months after surgery/number of patients involved. When comparing the PFS, the impact of age, sex, neurological function, EOR, IDH, 1p19q, and MGMT promoter methylation was eliminated through calibration.

To analyze the neurological function, patients were divided into three groups according to the level of GBM infiltration to the eloquent area. Tumors located in non-eloquent areas were defined as eloquent grade I. Eloquent grade II tumors included the tumors located near eloquent brain areas. Eloquent grade III tumors referred to those involving the eloquent brain areas. As the indexes of neurological function, general physical performance and neurologic status were evaluated by KPS and the NIHSS respectively. Preoperative (pre-op) evaluation was performed within 7 days before surgery, and postoperative (post-op) evaluation was completed within 72 hours after surgery (imm. post-op) and 3 months after surgery (3m. post-op).

H. Pre- and Post-Operative MRI

The preoperative MRI was performed within 7 days before surgery and postoperative MRI within 72 hours and every 3 months after surgery with Dimeglumine Gadopentetate Injection (0.1 mmol/kg, Beijing Beilu Pharmaceutical Co., Ltd., China) injected intravenously. All the MRI was performed using a 3.0T General Electric clinical scanner (Discovery MR750, General

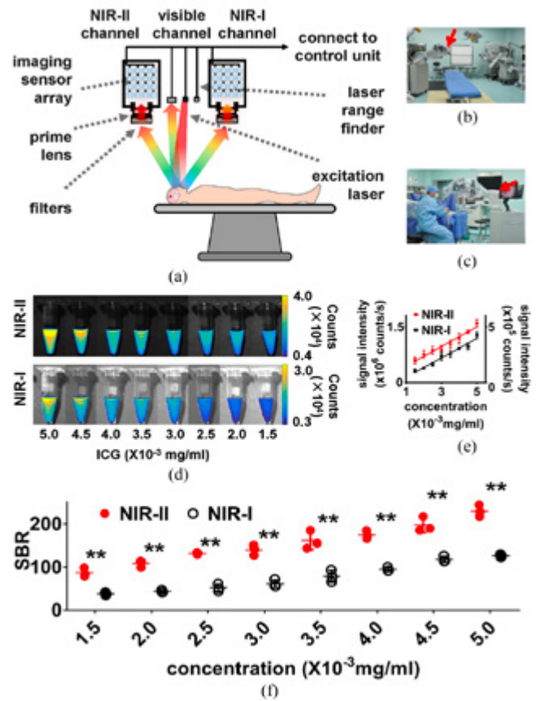


Fig.2 The description of the multispectral fluorescence imaging system. (a), The schematic diagram of the multispectral fluorescence imaging instrument. (b), and (c), the instrument (pointed out by the red arrow) placed in the operating room and used in NIR-II fluorescence image-guided surgery. (d), NIR-II/I fluorescence images of ICG dissolved in FBS of different concentrations. (e), the correlation function between the fluorescence intensity and the concentrations were Y = 0.26 × X + 0.18 for NIR-II and Y = 0.87 × X − 0.40 for NIR-I. (f), NIR-II fluorescence imaging has a significantly higher SBR than NIR-I. The minimum concentration of ICG in FBS that can be detected by the instrument was 64.5 fM (5 × 10−11mg/ml) for NIR-II and 3.22 fM (2.5 × 10−12mg/ml) for NIR-I.

Electric Company, USA) and each slice was 6 mm thick. Contrast-enhanced T1-weighted (T1W) sequences were used for volumetric analysis.

I. Histopathologic and Molecular Analysis

The histopathological grade of all the tissue samples was classified by three neuropathologists who were masked to the study based on the 2016 World Health Organization (WHO) Classification of Tumors of the Central Nervous System.

To evaluate the Ki-67 index of samples, immunohistochemistry staining was performed to the sample. Slices of tissue microarray sections were scanned using a digital whole slide scanner at 400× magnification (Aperio AT2, Leica, Germany). The expression of Ki-67 were analyzed using the Aperio ImageScope (12.3.0.5056, Leica, Germany). For each tissue section, counting of Ki-67 immunoreactive cells and nonreactive cells were performed on the whole section. The Ki-67 index = the number of Ki-67 positive cells / (the number of Ki-67 positive cells + the number of Ki-67 negative cells).

Molecular detection of IDH status, 1p19q codeletion, and MGMT promoter methylation were recorded according to Electronic Medical Record.

J. Image Analysis

The tumor volumes were calculated using MRIcron software (www.nitrc.org). The tumor was manually segmented on each slice of MRI, with the volume on each slice calculated by the software. The total tumor volume was the accumulation of volume on each slice. All tumor volumes were evaluated by three neuro-radiologists who were blinded to the patients' clinical information. The EOR = (preoperative tumor volume – postoperative tumor volume) / preoperative tumor volume ×100%.

The region of interest analysis using ImageJ (National Institute of Health, USA) was applied to quantitatively measure the NIR-II/I fluorescence intensity. The tumor-to-normal tissue ratio (TNR) of the in vivo fluorescence images and the signal-to-background ratio (SBR) of the ex vivo fluorescence images were calculated as follow: TNR = mean signal intensity of the tumor region / mean signal intensity of the normal tissue region; SBR = mean signal intensity of the tumor sample region / mean signal intensity of the blackboard region.

K. Statistical Analysis

The quantitative data included the TNR of intraoperative NIR-II/I fluorescence images and the SBR of fluorescence images of the tumor tissues and non-tumor tissues. Quantitative data were presented as mean ± s.d.. A two-sided Mann-Whitney U-test was employed for data comparisons between two groups. To evaluate the difference among the pre- and post-operative (imm. and 3m. post-op) NIHSS and KPS, Kruskal-Wallis tests, and Dunn's multiple comparisons were applied. Spearman's correlation analysis and Pearson's correlation analysis were applied to evaluate the correlations between the SBR and the WHO grade as well as the Ki-67 index of the samples respectively. Clinical characteristics, including sensitivity, specificity, NPV, PPV, and accuracy between two groups (NIR-II and surgeon; NIR-II and NIR-I), were compared using the Chi-square test and Fisher exact test. The log-rank test was performed to assess PFS based on prognostic factors between the two groups.

Results

A. The Intraoperative Brain Tumor Multispectral Imaging System

To perform NIR-II FGS for patients with gliomas, an intraoperative brain tumor multispectral imaging system was first constructed, which was capable of NIR-I, NIR-II, and color imaging, and was composed of two sub-systems for imaging and controlling (Fig. 2(a)). The key parameters of the system were determined and are listed in Table I. The system can be easily placed in the neurosurgical operating room (Fig. 2(b)) and conveniently used by neurosurgeons. For the FGS group, the neurosurgeons depended on the NIR-II fluorescence images to guide the resection (Fig. 2(c)).

B. Verification of the NIR-II/I Imaging System and Tumor Resection Method Under the Guidance of NIR-II Images Using Phantoms and Tumor-Bearing Mice

The imaging system was first verified by the phantom study. The NIR-II/I fluorescence intensity acquired by the system had a linear correlation with the ICG concentration (Fig. 2(d)), with correlation equations to be $Y = 0.26\times X + 0.18$ ($R^2 = 0.96$) for NIR-II and $Y = 0.87\times X - 0.40$ ($R^2 = 0.97$) for NIR-I (Fig. 2(e)). More importantly, NIR-II fluorescence imaging achieved much higher SBR compared with NIR-I. For ICG with a concentration of 1.5×10^{-3} mg/ml, SBR of 86.70 ± 5.78 for NIR-II vs. 37.75 ± 1.93 for NIR-I were obtained (Fig. 2(f)).

Phantom imaging study demonstrated that both NIR-I and NIR-II imaging can differentiate the four capillaries filled with ICG solution with no intralipid covered on them (Fig. S1A, row 1). When the capillaries were submerged 2 mm and 5 mm below the surface of the intralipid, the four capillaries were still distinguished by NIR-II/I imaging (Fig. S1(a), row 2, and 3). But when the capillaries were submerged 7 mm below the surface, it became difficult to distinguish the 2 capillaries with the distance of 5 mm using both NIR-II and NIR-I imaging, but the 2 capillaries with the distance of 10 mm were still distinguished on the fluorescent images (Fig. S1(a), row 4). When the capillaries were submerged 12 mm below the surface, the 2 capillaries with a distance of 10 mm were not distinguished (Fig. S1(a), row 5). The quantitative plot of intensity across a line of interest showed a higher contrast of NIR-II than NIR-I to distinguish the capillary from the background signal (Fig. S1(a), column 3, and 5).

Both NIR-II and I fluorescence imaging of orthotopic U87MG tumor-bearing mice showed that ICG can accumulate in the GBM with good contrast. The fluorescence of the tumor was visualized even without opening the scalp (Fig. S1(b), column 1), and the tumor became more obvious upon opening the skull (Fig. S1(b), column 2). Then the tumor was removed under the guidance of the NIR-II fluorescence images (Fig. S1(b), column 3, and 4). Quantitative data of the images showed that the TNR of both NIR-II and NIR-I dropped dramatically after the removal of the tumor (Fig. S1(c)).

C. Intraoperative NIR-II/I Fluorescence Imaging and Surgery Under the Guidance of NIR-II Fluorescence Images

For a participant with GBM, the preoperative T1-enhanced MRI exhibited enhancement in the left frontal-parietal lobe as

Table 1 Key Parameters for the Intraoperative Brain Tumor Multispectral Imaging System Constructed

Instrument features	Parameters
Imaging channels	NIR-II, NIR-I
Device type	NIRvana: 640, Teledyne Princeton Instruments (NIR-II) ProEM-HS: 1024BX3, Teledyne Princeton Instruments (NIR-I)
Chip image area (mm×mm)	12.80×10.24 13.30×13.30
Highest temporal resolution (ms)	45.45 (NIR-II) 33.33 (NIR-I)
Working distance (cm)	50
Surgical field of view (cm× cm)	10.66×8.53 17.07×17.07
Sensor resolution (imaging pixels)	640×512 1024×1024
Imaging resolution (μm)	62.5 (NIR-II) 92 (NIR-I)
Sensitivity (ICG, fM)	64.50 (NIR-II) 3.22 (NIR-I)
Optical filter	1000 nm long pass, FEL 1000, Thorlabs (NIR II) 850 nm long pass, FEL0850, Thorlabs (NIR-I)
Laser fiber	liquid core optical fiber
Beam expander	Customized, made of a spherical glass Beam divergence 18 mrad
Image windows	NIR-II; NIR I; Visible (Color); Overlay

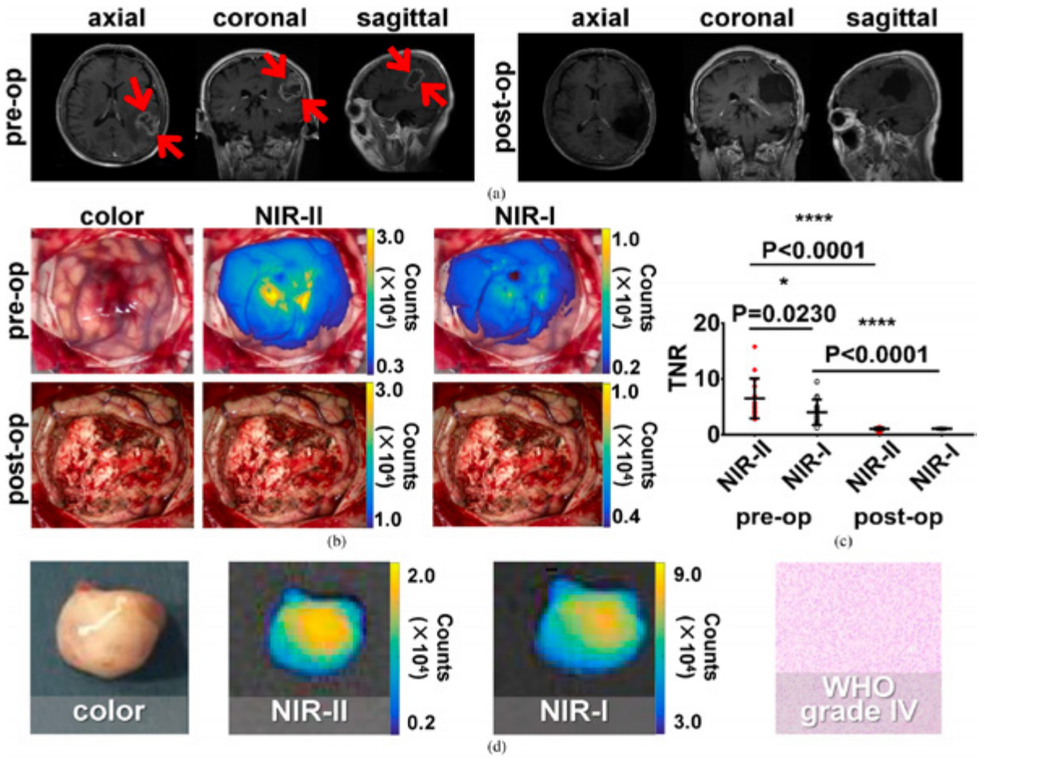


Fig.3 A typical patient with glioblastoma showing obvious tumor fluorescence intraoperatively. (a), the pre-operative T1-enhanced MRI demonstrated enhancement in left frontal-parietal lobe (left), and the post-operative T1-enhanced MRI displayed no residual enhancement (right). (b), the color and NIR-II or NIR-I fluorescence images were acquired upon the opening of the dura, and after all the tissue with NIR-II fluorescence signal was removed. (c), the TNR of NIR-II or NIR-I decreased sharply after resection. (d), the tissue sample obtained from the tumor (column 1) was imaged ex vivo after surgery and showed obvious NIR-II or NIR-I fluorescence (column 2 and 3). Post-operative histopathology images confirmed that the sample was tumor tissue (column 4).

pointed out by the red arrows (Fig. 3(a), left, labeled as pre-op). The postoperative MRI displayed no enhancement, which indicated total resection of the tumor (Fig. 3(a), right, labeled as post-op). After removing the bone flap and the dura, the color image and NIR-II/I fluorescence images were acquired above the cortex. The extent of resection can be displayed by the fluorescence images (Fig. 3(b), row 1, labeled as pre-op). The surgeons then removed the gross tumor under the assistance of a microscope referring to the NIR-II fluorescence image. After the surgeon declared that the tumor was totally resected, the NIR-II/I fluorescence images were acquired again, which displayed no residual NIR-II/I fluorescence (Fig. 3(b), row 2, labeled as post-op). Quantitative analysis showed that TNR of NIR-II were significantly higher than that of NIR-I (NIR-II 6.50 ± 3.45 vs. NIR-I 4.04 ± 2.20, P = 0.0230), which sharply dropped after the resection (NIR-II, before resection 6.50 ± 3.45 vs. after resection 1.05 ± 0.22, P < 0.0001; NIR-I, before resection 4.04 ± 2.20 vs. after resection 1.07 ± 0.13, P < 0.0001, Fig. 3(c)). Ex vivo images of tissue samples obtained from the tumor were acquired during the surgery (Fig. 3(d), column 1). The tissue samples displayed NIR-II/I fluorescence (Fig. 3(d), column 2 and 3), with further histopathological diagnosis demonstrated the samples to be tumor tissue (Fig. 3(d), column 4).

D. Ex Vivo Fluorescence Imaging and Diagnosis of the Samples

A total of 235 tissue samples were obtained from the 15 patients who underwent FGS, including 154 tumor tissue samples (65.53%) and 81 non-tumor tissue samples (34.47%) according to the histopathological diagnosis. Tumor tissue samples, classified into 3 grades (WHO grade II, III, and IV) according to the histopathology, displayed obvious NIR-II/I fluorescence (Fig. 4(b)–(d)), while non-tumor tissue samples displayed no obvious fluorescence (Fig. 4(a)). The SBR of NIR-II fluorescence imaging was significantly higher compared with NIR-I (P = 0.0070, Fig. 4(e)). With the analysis of the SBR of the tumor and non-tumor tissue, it is proved that the tumor had a significantly higher SBR than non-tumor tissue for both NIR-II and I (NIR-II P < 0.0001, NIR-I P < 0.0001, Fig. 4(f)). This indicated the feasibility of using SBR obtained from ex vivo tissue imaging as a diagnostic indi-

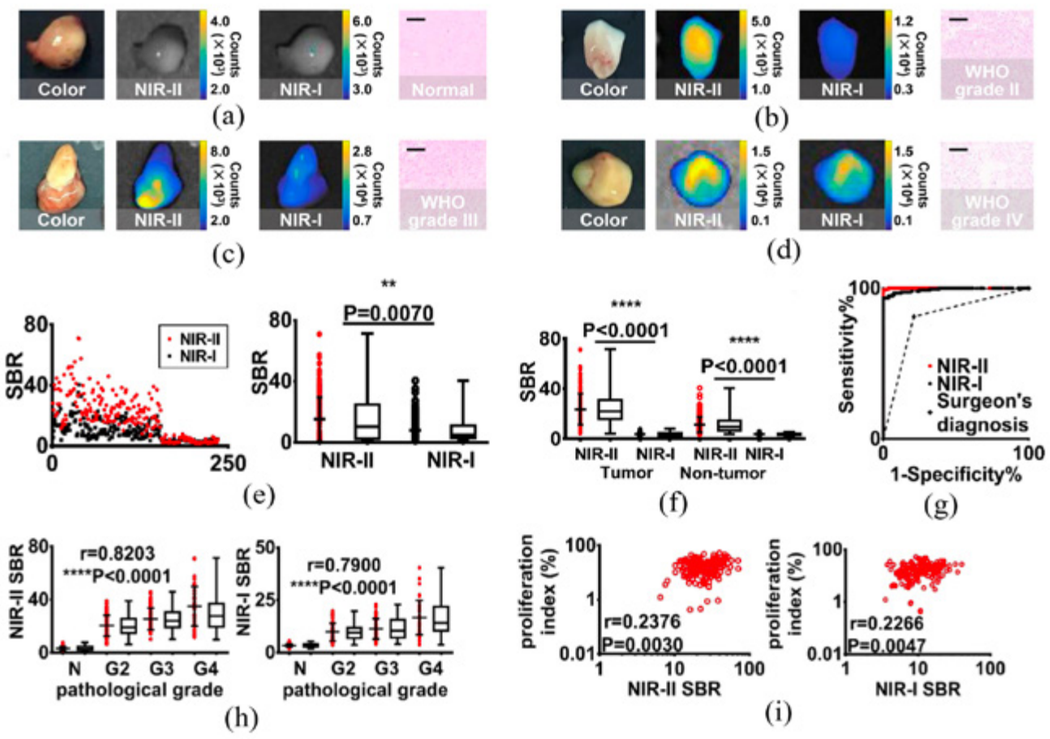


Fig.4 Fluorescence images of samples. (a), A non-tumor tissue showed no obvious fluorescence of NIR-II and NIR-I, while tumor tissues of WHO grade II (b), WHO grade III (c), and WHO grade IV (d) showed obvious fluorescence. The histopathology images were displayed at 400 times magnified, and the black scale chart represented 50 μm. (e), SBR of the NIR-II or NIR-I fluorescence images of the 235 samples were plotted (left) and compared (right). (f), significant differences were found between the SBR of tumor samples (n=154) and non-tumor samples (n=81) for both NIR-II (P < 0.0001) and NIR-I (P < 0.0001). (g), the ROC of NIR-II/I SBR and surgeon's diagnosis was plotted. (h), SBR of samples was correlated with varying WHO grades (NIR-II, r = 0.8203, P < 0.0001 vs. NIR-I, r = 0.7900, P < 0.0001). (i), scatter plot of log SBR vs. log proliferation index showed a correlation between them (NIR-II, r = 0.2376, P = 0.0030 vs. NIR-I, r = 0.2266, P = 0.0047).

IEEE Trans Biomed Eng. 2022. 69(6): 1889-1900 Published online: 24 November 2021

Table 2 Baseline Characteristics

Variables	FGS (n = 15)	WLS (n = 18)	P-value
Age (Mean, years)	51.73±11.24	53.83±14.73	0.6540
Sex (Male/Female)	7/8	12/6	0.6428
Pre-op KPS (Median, range)	90(70-90)	90(70-100)	0.8725
Pre-op NIHSS (Median, range)	1(1-2)	1(0-2)	0.4210
Pre-op TV (cm^3, Mean)	64.94±25.47	49.53±35.26	0.6295
IDH			1.0000
mutation	1	2	
wild-type	14	16	
1p/19q co-deletion	0	0	-
MGMT			0.7970
methylation	6	8	
unmethylation	9	10	
Eloquence			
Grade I/II/III	4/7/4	4/7/7	0.7347
detection rate (%)	100.00	-	-
complete resection rate (%)	100.00	50.00	0.0036
6m-PFS	100.00	66.67	0.0134
	NIR-II fluorescence diagnosis	**Surgeons' diagnosis**	***P*-value**
Sensitivity (%)	100.00	81.17	P < 0.0001
Specificity (%)	91.36	79.01	0.0449
PPV (%)	95.65	88.03	0.0182
NPV (%)	100.00	68.82	P < 0.0001
Accuracy (%)	97.02	80.51	P < 0.0001

FGS, fluorescence image-guided surgery; WLS, white light image-guided surgery; KPS, Karnofsky performance score; NIHSS, National Institutes of Health Stroke Scale; TV, tumor volume; PFS, progression-free survival; NPV, negative-predictive value; AUC, area under the curve.

Table 3 Characteristic Tests of Specimens

Variables	FGS (n = 15)	WLS (n = 18)	P-value
Age (Mean, years)	51.73±11.24	53.83±14.73	0.6540
Sex (Male/Female)	7/8	12/6	0.6428
Pre-op KPS (Median, range)	90(70-90)	90(70-100)	0.8725
Pre-op NIHSS (Median, range)	1(1-2)	1(0-2)	0.4210
Pre-op TV (cm^3, Mean)	64.94±25.47	49.53±35.26	0.6295
IDH			1.0000
mutation	1	2	
wild-type	14	16	
1p/19q co-deletion	0	0	-
MGMT			0.7970
methylation	6	8	
unmethylation	9	10	
Eloquence			
Grade I/II/III	4/7/4	4/7/7	0.7347
detection rate (%)	100.00	-	-
complete resection rate (%)	100.00	50.00	0.0036
6m-PFS	100.00	66.67	0.0134
	NIR-II fluorescence diagnosis	**Surgeons' diagnosis**	***P*-value**
Sensitivity (%)	100.00	81.17	P < 0.0001
Specificity (%)	91.36	79.01	0.0449
PPV (%)	95.65	88.03	0.0182
NPV (%)	100.00	68.82	P < 0.0001
Accuracy (%)	97.02	80.51	P < 0.0001

SBR, signal-to-background ratio; PPV, positive predictive value; NPV, negative predictive value; AUC, Area Under Curve.

cator to distinguish tumor from non-tumor tissue. Therefore, the receiver operating characteristic (ROC) curves were obtained to compare the diagnostic accuracy of NIR-II or NIR-I imaging and the surgeons' diagnosis. The area under curve (AUC) of the NIR-II or NIR-I imaging was significantly larger than that of surgeon's diagnosis (NIR-II 0.9997 [95% CI 0.9989 - 1.0000] vs. surgeons' diagnosis 0.8009 [95% CI 0.7384 - 0.8634], difference between groups 0.1988, P < 0.0001; NIR-I 0.9899 [95% CI 0.9813 - 0.9986] vs. surgeons' diagnosis 0.8009 [95% CI 0.7384 - 0.8634], difference between groups 0.1890, *P* < 0.0001, Fig. 4(g), Tables II and III). Compared with NIR-I fluorescence imaging, the AUC of NIR-II imaging was also significantly higher (NIR-II 0.9997 [95% CI 0.9989 - 1.0000] vs. NIR-I 0.9899 [95% CI 0.9813 - 0.9986], difference between groups 0.0098, *P* = 0.0204, Fig. 4(g)). This result suggested that NIR-II had the highest diagnostic capability, followed by NIR-I and surgeon's intraoperative diagnosis (Fig. 4(g)).

To further compare the diagnostic ability of NIR-II/I fluorescence imaging and surgeons' diagnosis, the indexes such as sensitivity, specificity, PPV, NPV, and diagnostic accuracy were calculated (Table III). The NIR-II had significantly higher sensitivity, specificity, PPV, NPV, and accuracy compared with surgeons' diagnoses (sensitivity, NIR-II: 100% [95% CI 97.07 - 100.00] vs. Surgeons: 81.17% [95% CI 74.22 - 86.60], difference between groups 18.83%, *P* < 0.0001; specificity, NIR-II: 91.36% [95% CI 82.96 - 96.01] vs. Surgeons: 79.01% [95% CI 68.84 - 86.56], difference between groups 12.35%, *P* = 0.0449; PPV, NIR-II: 95.65% [95% CI 91.13 - 98.04] vs. Surgeons: 88.03% [95% CI 81.57 - 92.48], difference between groups 7.62%, *P* = 0.0182; NPV, NIR-II: 100% [95% CI 94.09 - 100.00] vs. Surgeons, 68.82% [95% CI 58.79 - 77.36], difference between groups 31.18%, *P* < 0.0001; accuracy, NIR-II: 97.02 [95% CI 93.86 - 98.67] vs. Surgeons: 80.51% [95% CI 74.96 - 85.08], difference between groups 16.51%, *P* < 0.0001. Tables II and III). Besides, the diagnostic accuracy of the NIR-II fluorescence imaging was also significantly higher than that of NIR-I fluorescence imaging (Tables II and III).

Further investigation indicated a stronger correlation between SBR of NIR-II and the WHO grade of tissue samples compared with NIR-I (correlation coefficient: NIR-II 0.8203, *P* < 0.0001 vs. NIR-I 0.7900, *P* < 0.0001, Fig. 4(h)). The correlation between the SBR and proliferation index represented by the percentage of Ki-67 positive cells was also investigated (NIR-II, r = 0.2376, *P* = 0.0030 vs. NIR-I, r = 0.2266, *P* = 0.0047, Fig. 4(i)).

E. Detection Rate, Complete Resection Rate, PFS, and Neurological Function of GBM Patients

The detection rate of the NIR-II fluorescence imaging in this trial is 100%, with all the 15 glioblastoma patients showing obvious tumor fluorescence intraoperatively.

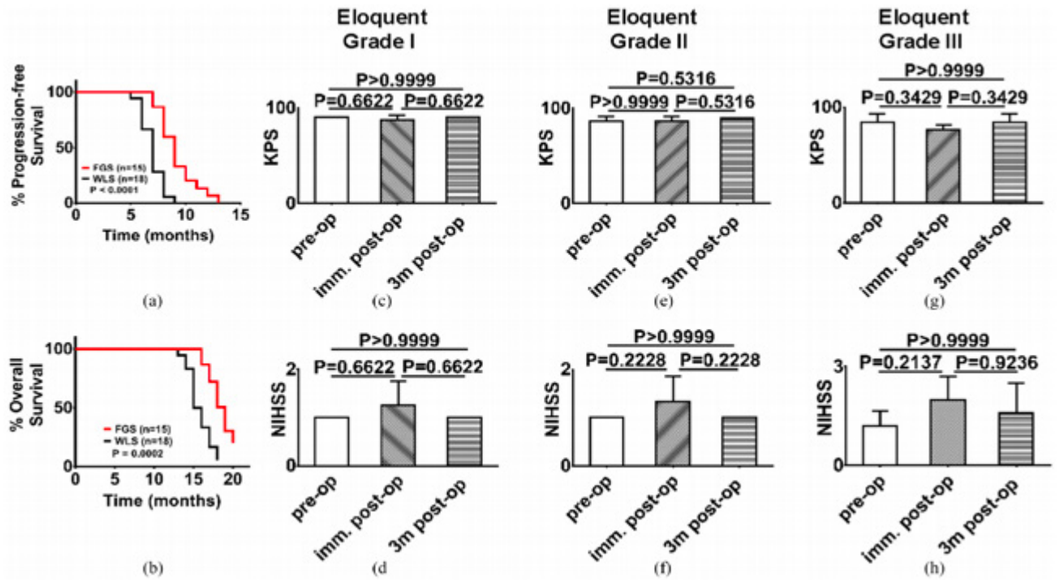


Fig.5 PFS, OS, and neurological function of patients. (a)–(b), PFS (a) and OS (b) of the FGS group was significantly prolonged compared with the WLS group (PFS, *P* < 0.0001; OS, *P* = 0.0002). (c)–(h), KPS (row 1) and NIHSS (row 2) of patients in the FGS group with eloquent grade I lesions (n = 4, column 1), patients with eloquent grade II lesions (n = 7, column 2) and patients with eloquent grade III lesions (n = 4, column 3).

Patients underwent FGS showed significantly higher tumor complete resection rate compared to those underwent routine white-light surgery (100% [13/13, 95% CI 73.41-100] vs. 50% [9/18, 95% CI 29.03-70.97], *P* = 0.0036, Table II). In the 15 patients who underwent FGS, two patients had residual fluorescence signal intraoperatively, with confirmation by the surgeon that the fluorescence signal infiltrated to the eloquent areas and complete resection could not be realized considering the protection of neurological function. Postoperative enhanced MRI confirmed that the 2 patients had residual tumor tissue. For the other 13 patients with total removal of fluorescent tissue, no residual tumor tissue was observed in postoperative MRI.

The PFS and OS of the FGS group were remarkably prolonged compared with the WLS group (PFS, *P* < 0.0001, Fig. 5(a); OS, *P* = 0.0002, Fig. 5(b)). Median PFS was 9.0 months for the FGS group and 7.0 months for the WLS group. Median OS of 19.0 months and 15.5 months were achieved by FGS and WLS groups. Importantly, PFS at 6 months for patients in FGS group was significantly higher than WLS group (100% [15/15, 95% CI 76.14-100.00] vs. 66.67% [12/18, 95% CI 43.57-83.90], *P* = 0.0134, Table II).

F. Detection Rate, Complete Resection Rate, PFS, and Neurological Function of WHO Grade III Glioma Patients

In addition to GBM patients, the performance of intraoperative NIR-II fluorescence imaging was also evaluated in patients with grade III gliomas. Eight patients were involved and randomly assigned to the WLS or FGS groups. Fluorescence of tumor was observed in 3 of the 4 patients in the FGS group, leading to a detection rate of 75%.

NIR-II FGS was performed on the 3 patients with the fluorescence of tumor, with a complete resection rate of 100% (3/3, 95% CI 38.25% to 100%) achieved. However, in 4 patients with grade III gliomas who underwent WLS, the complete resection rate was only 25% (1/4, 95% CI 3.41% to 71.09%). No recurrence was observed in patients from both of the groups.

G. Reservation of Neurological Function During Surgery Using NIR-II FGS

NIR-II FGS demonstrated the potential to protect neurological function. After the gross tumor was removed, the residual NIR-II fluorescence provided the surgeons with precise guidance of the residual tumor, which helped to discriminate the residual tumor from surrounding normal brain tissue, and avoided unnecessary resection. And the samples of tissues with residual fluorescent signal were diagnosed to be tumor tissues. The median Karnofsky Performance Scale (KPS) and National Institute of Health Stroke Scale (NIHSS) 3 months after surgery were 90 and 1, respectively, in both groups. No significant difference was observed in patients of the FGS group with different grades of eloquent area infiltration for both KPS and NIHSS (Fig. 5(c)–(h) and Table IV). The same result was observed in patients of the WLS group (Table IV).

Impressively, an important case with WHO grade III glioma showed that the intraoperative NIR-II fluorescence images helped to avoid paralysis. The pre-operative T1-enhanced MRI exhibited enhancement in the left parietal-frontal lobe (Fig. S2 (a), left, labeled as pre-op). The patient was diagnosed to have a high risk of paralysis of his right limbs after surgery. The post-operative T1-enhanced MRI displayed no enhancement, which showed total resection of the tumor (Fig. S2 (a), right, labeled as post-op). After opening the dura, the position of the tumor was visualized by the tumor fluorescence penetrating through the intact cortex (Fig. S2 (b), row 1, labeled as pre-op). Then the gross tumor was removed very carefully. After that, the color and NIR-II/I fluorescence images of the operation field were acquired, displaying the tissue with residual NIR-II fluorescent signal (Fig. S2 (b), row 2, labeled as residual). The tissue with residual NIR-II fluorescent signal was further removed until no NIR-II fluorescence was left (Fig. S2 (b), row 3, labeled as post-op). The in vivo TNRs of NIR-II were higher than those of NIR-I for both pre-op and residual (Fig. S2 (c)), which indicated that NIR-II fluorescence images displayed the residual fluorescent signal more obviously. The color and NIR-II/I fluorescent images of the sample from the gross tumor (Fig. S2 (d), row 1) and the tissue with residual fluorescence (Fig. S2 (d), row 2) also showed obvious ex vivo NIR-II and NIR-I fluorescent signal, with the histopathological diagnosis proved the sample to be WHO grade III and grade II, respectively. The motor function of the patient was successfully reserved by the guidance of NIR-II imaging (Supplementary movie).

Table 4 Comparison of Neurological Function for FGS and WLS Group

	KPS	pre-op	imm. post-op	3 m. post-op	*P* value
FGS	Grade I	90.00±0.00	87.50±4.33	90.00±0.00	0.3678
	Grade II	86.67±4.71	86.67±4.71	90.00±0.00	0.2969
	Grade III	84.00±8.00	76.00±4.90	84.00±8.00	0.1896
WLS	Grade I	92.50±4.33	87.50±4.33	92.50±4.33	0.2937
	Grade II	88.57±3.50	87.14±4.51	88.57±3.50	0.7451
	Grade III	82.86±7.00	74.28±4.95	77.14±4.52	0.0694
	NIHSS	pre-op	imm. post-op	3 m. post-op	*P* value
FGS	Grade I	1.00±0.00	1.25±0.43	1.00±0.00	0.3678
	Grade II	1.00±0.00	1.33±0.47	1.00±0.00	0.1194
	Grade III	1.20±0.40	2.00±0.63	1.60±0.80	0.1945
WLS	Grade I	0.75±0.83	0.75±0.83	0.75±0.83	1.0000
	Grade II	1.00±0.00	1.28+0.45	1.00±0.00	0.1218
	Grade III	0.85±0.35	2.00±0.53	2.00±0.53	0.0021

FGS, fluorescence image-guided surgery; WLS, white light image-guided surgery; KPS, Karnofsky performance score; NIHSS, National Institutes of Health Stroke Scale; pre-op, pre-operative measurement; imm. post-op, immediate post-operative measurement; 3 m. post-op, 3 months post-operative measurement.

Discussion

In this study, the imaging performance and treatment efficacy of NIR-II based FGS have been evaluated in human glioma resection surgery using our in-house developed multispectral imaging system and FDA approved ICG probe. The FGS has

been demonstrated to be a promising intraoperative real-time imaging technique for localizing GBM and residual tumors with high safety, high sensitivity, and real-time feedback. The properties of low photon scattering and absorption of tissue render the NIR-II fluorescence with a strong capability to detect tumors of larger depth. More importantly, our study clearly demonstrates that NIR-II based FGS achieves significant clinical benefits. The detection rate of the NIR-II FGS is 100% in patients with GBM. Moreover, compared with the WLS technique, the use of FGS lead to a dramatically improved complete resection rate (100% [95% CI 73.41-100] vs. 50% [95% CI 29.03-70.97], P = 0.0036) and significantly prolonged PFS and OS (PFS, P < 0.0001 and OS, P = 0.0002). The postoperative KPS and NIHSS measurements of the two groups also show no damage to the neurological function, indicating that the FGS is a safe technique and provides significant benefits to GBM patients.

It has been found that the complete resection rate of the FGS group is significantly higher than that of the WLS group in our study. Moreover, ICG based NIR-II FGS also performs better than 5-ALA, FS based FGS, and ICG based conventional NIR-I FGS in complete resection rate as reported previously[17, 20, 24]. In our study, the patients without residual fluorescence all achieve complete resection, demonstrating a complete resection rate of 100% (13/13). For the rest 2 patients without complete resection, residual tissue with fluorescence has been observed intraoperatively and reserved in order to conserve the neurological function of patients. Signal enhancement has also been observed in the postoperative enhanced MRI for these two patients. Whereas, complete resection rate of 50% (9/18) has been achieved in the WLS group, which is only half of the FGS group. Furthermore, the ICG based NIR-II FGS also out-performs 5-ALA and FS according to previous reports, as complete resection rate of ICG based NIR-I FGS reported in a study involving 15 patients with GBM is only 53.33% (8/15)[24] and that of 5-ALA and FS based FGS is 64.75% (90/139) and 82.60% (38/46) respectively[17, 20]. In a recently reported study of 5-ALA based FGS, only 3 out of 16 patients enrolled achieved complete resection, resulting in a complete resection rate to be 18.7%[28]. All of them are much lower than the complete resection rate (100%) of ICG based NIR-II FGS revealed in this study. The NIR-II fluorescence imaging technique can provide the surgeons with an accurate prompt of residual tumor, resulting in improved EOR and more complete resection. Previous studies suggest that improved EOR is beneficial to survival[7]. Therefore, ICG NIR-II imaging with a high complete resection rate of GBM greatly benefit the survival of patients.

Impressively, the PFS and OS has been prolonged in the NIR-II FGS group compared with the WLS group, and also with that of 5-ALA and FS based FGS reported previously. In our study, the median PFS of the FGS and WLS group was 9.0 months and 7.0 months, respectively. Median OS of 19.0 months and 15.5 months were achieved by FGS and WLS groups. However, median PFS and OS of 5.1 and 15.2 months in 139 patients for 5-ALA based fluorescence image-guided surgery were reported[17]. The median PFS and OS of FS based fluorescence image-guided surgery were 7 and 12 months[20]. In the most recent report of 5-ALA based fluorescence image-guided surgery, the mean PFS and OS were reported to be 5 ± 3 and 6.3 ± 4.6 months[28]. The 6m-PFS of the NIR-II FGS group is reported much higher than that of the WLS group (100% [95% CI 76.14-100.00] vs. 66.67% [95% CI 43.57-83.90], P = 0.0134), with a difference between the groups of 33.33%. Compared with 5-ALA based FGS reported, the NIR-II FGS has an even much higher 6m-PFS (100% vs. 41.0% and 46.2%)[17, 28]. For FS based FGS, 6m-PFS has been reported to be only 56.6%[20], which is 43.4% lower than that of the NIR-II FGS. Therefore, the PFS of the ICG based NIR-II FGS is prolonged compared with the previously reported 5-ALA and FS based FGS. It should be pointed out that the uncompleted total Stupp protocol in previous studies due to the medical condition when the trials were performed is unignorable when analyzing the survival of patients. Besides, although significant improvement of survival has already been achieved in our trial reported in the manuscript, the increase of 2 months and 3.5 months for PFS and OS is still less effective. The reasons are older age and IDH wild type of the patients enrolled in the trial. On the one hand, the mean ages of patients were 51.73±11.24 for the FGS group and 53.83±14.73 for the WLS group. As reported most recently, such an older age is a risk factor for shorter OS[29]. On the other hand, 14 of the 15 patients in the FGS group and 16 in the 18 patients in the WLS group were IDH wild type, which was reported to have shorter OS compared with IDH mutant type (IDH wild type, 1.2 years vs. IDH mutant type, 3.6 years)[30].

It is also worthy to note that in the previous study of ICG based NIR-I FGS, a dose of 5mg/kg has been administrated to the patients, with no significant acute toxicity observed[24]. In this study, the dose of ICG used in the FGS group is dramatically reduced to 1mg/kg, which is only twice the dose commonly used in clinical. Moreover, this dose is also much lower compared with the previous study reported (5mg/kg)[24]. No specific adverse event has been observed. The liver enzymes have been monitored before and after surgery, with no abnormal value observed. The best imaging time window has been explored in limited patients with such a low dose and finally set to be 48 h after injection. Although the NIR-II performs better and benefits more to the patients, our study also reveals a limitation of ICG based NIR-II fluorescence imaging for GBM. As ICG cannot specifically target GBM, the NIR-II fluorescence imaging based on ICG is also not specific for glioblastoma. The adjacent non-tumor tissue is possible to uptake ICG by diffusion or hyperplastic blood vessels, which causes the existence of false positives. It is reported that a fluorescent probe based on bombesin has shown high specificity for human glioma detection[31]. Thus, a targeted NIR-II probe will be prepared and explored in our future studies, which may further improve the clinical value of the NIR-II imaging technique for glioma detection and image-guided surgery.

Conclusion

In summary, our study demonstrates the feasibility of using NIR-II FGS in GBM resection. The ICG based NIR-II fluorescence can be observed in all the GBM patients involved in FGS. More importantly, with the guidance of NIR-II fluorescence images, the complete resection rate can be dramatically improved without damaging neurological functions. The NIR-II FGS technique can achieve a high 6m-PFS and greatly prolong the PFS and OS of the GBM patients. Moreover, ex vivo NIR-II fluorescence imaging outperforms NIR-I imaging and surgeons' diagnosis under white light in sample discrimination. It possesses high sensitivity and NPV and provides a convincing diagnosis of whether the tissue is a tumor. Overall, NIR-II FGS is a highly promising technique worthy of exploring more clinical applications.

IEEE Trans Biomed Eng. 2022. 69(6): 1889-1900 Published online: 24 November 2021

References

1. P. Diamandis and K. Aldape. World health organization 2016 classification of central nervous system tumors. Neurol. Clin. 2018; 36(3):439-447.
2. Q. T. Ostrom, et al. CBTRUS statistical report: Primary brain and other central nervous system tumors diagnosed in the United States in 2012–2016. Neuro-Oncology. 2019; 21(5):V1-V100.
3. B. M. Alexander and T. F. Cloughesy, Adult glioblastoma. J. Clin. Oncol. 2017; 35(21):2402-2409.
4. A. S. Jakola, et al., Comparison of a strategy favoring early surgical resection vs a strategy favoring watchful waiting in low-grade gliomas. JAMA. 2012; 308(18) :1881-1888.
5. K. L. Chaichana, et al., Recurrence and malignant degeneration after resection of adult hemispheric low-grade gliomas. J. Neurosurgery. 2010; 112(17):10-17.
6. N. Sanai and M. Berger. Surgical oncology for gliomas: The state of the art. Nature Rev. Clin. Oncol. 2018; 15(2) :112-125.
7. R. S. D'Amico, et al. Extent of resection in glioma–a review of the cutting edge. World Neurosurgery. 2017; 103: 538-549.
8. E. Belykh, et al. Intraoperative fluorescence imaging for personalized brain tumor resection: Current state and future directions. Front. Surg. 2016; 3:55.
9. D. W. Roberts, et al. Intraoperative brain shift and deformation: A quantitative analysis of cortical displacement in 28 cases. Neurosurgery. 1998; 43(4):749-758.
10. S. Hu et al. Real-time imaging of brain tumor for image-guided surgery. Adv. Healthcare Mater. 2018; 7(16).
11. C. Qin, et al. Recent advances in Cerenkov luminescence and tomography imaging. IEEE J. Sel. Topics Quantum Electron. 2011; 18(3):1084-1093.
12. 12.Z. Zhang, et al. Endoscopic Cerenkov luminescence imaging and image-guided tumor resection on hepatocellular carcinoma-bearing mouse models", Nanomedicine.2019; 17:62-70.
13. H. Guo, et al. A hybrid clustering algorithm for multiple-source resolving in bioluminescence tomography. J. Biophotonics. 2017; 11(4).
14. S. Zheng, et al. Radiopharmaceuticals and fluorescein sodium mediated triple-modality molecular imaging allows precise image-guided tumor surgery. Adv. Sci. 2019; 6(13).
15. M. Liu, et al. Cerenkov luminescence imaging on evaluation of early response to chemotherapy of drug-resistant gastric cancer. Nanomedicine. 2018; 14(1):205-213.
16. W. Si et al. Assessing performance of augmented reality-based neurosurgical training. Visual Comput. Ind. Biomed. Art. 2019; 2(1):1-10.
17. W. Stummer, et al. Fluorescence-guided surgery with 5-aminolevulinic acid for resection of malignant glioma: A randomised controlled multicentre phase III trial. Lancet Oncol. 2006; 7(5):392-401.
18. S. K. Kim, et al. Impact of fluorescence-guided surgery on the improvement of clinical outcomes in glioblastoma patients. Neuro-Oncology Pract. 2014; 1(3):81-85.
19. R. D. Valle, C. G. Hadjipanayis and W. Stummer. Established and emerging uses of 5-ALA in the brain: An overview. J. Neuro-Oncology. 2019; 141(3):487-494.
20. F. Acerbi, et al. Fluorescein-guided surgery for resection of high-grade gliomas: A multicentric prospective phase II study (FLUOGLIO). Clin. Cancer Res. 2018; 24(1):52-61.
21. B. Kiesel, et al. Systematic histopathological analysis of different 5-aminolevulinic acid–induced fluorescence levels in newly diagnosed glioblastomas. J. Neurosurgery. 2017; 129(2):341-353.
22. R. J. Diaz, et al. Study of the biodistribution of fluorescein in glioma-infiltrated mouse brain and histopathological correlation of intraoperative findings in high-grade gliomas resected under fluorescein fluorescence guidance. J. Neurosurgery, 2015; 122(6):1360-1369.
23. A. Ergin, et al. The feasibility of real-time in vivo optical detection of blood–brain barrier disruption with indocyanine green. J. Neuro-Oncology. 2012; 106(3): 551-560.
24. J. Y. K. Lee, et al. Intraoperative near-infrared optical imaging can localize gadolinium-enhancing gliomas during surgery. Neurosurgery. 2016; 79(6):856-871.
25. J. A. Carr, et al. Shortwave infrared fluorescence imaging with the clinically approved near-infrared dye indocyanine green. Proc. Nat. Acad. Sci. USA. 2018; 4465-4470.
26. Z. Hu, et al. First-in-human liver-tumour surgery guided by multispectral fluorescence imaging in the visible and near-infrared-I/II windows. Nature Biomed. Eng. 2020; 4(3):259-271.
27. C. W. Teng, et al. Applications of indocyanine green in brain tumor surgery: Review of clinical evidence and emerging technologies. Neurosurg Focus. 2021;50(1):E4.
28. G. A. Maragkos, et al. Fluorescence-guided high-grade glioma surgery more than four hours after 5-aminolevulinic acid administration. Front. Neurol. 2021; 12:644804.
29. N. Kudulaiti, et al. A nomogram for individualized prediction of overall survival in patients with newly diagnosed glioblastoma: A real-world retrospective cohort study. BMC Surg. 2021; 21(1):238.
30. A. M. Molinaro, et al. Association of maximal extent of resection of contrast-enhanced and non-contrast-enhanced tumor with survival within molecular subgroups of patients with newly diagnosed glioblastoma. JAMA Oncol.2020; 6(4):495-503.
31. D. Li et al. First-in-human study of PET and optical dual-modality image-guided surgery in glioblastoma using 68Ga-IRDye800CW-BBN. Theranostics. 2018; 8(9):2508–2520.

Neurosurgery

Research Article

Real-Time Intraoperative Glioma Diagnosis Using Fluorescence Imaging and Deep Convolutional Neural Networks

Biluo Shen[1,2,*], Zhe Zhang[3,4,*], Xiaojing Shi[1,2,*], Caiguang Cao[1,2], Zeyu Zhang[1,5], Zhenhua Hu[1,✉], Nan Ji[3,4,5,✉], and Jie Tian[1,2,5,6,✉]

Abstract

Purpose: Surgery is the predominant treatment modality of human glioma but suffers difficulty on clearly identifying tumor boundaries in clinic. Conventional practice involves neurosurgeon's visual evaluation and intraoperative histological examination of dissected tissues using frozen section, which is time-consuming and complex. The aim of this study was to develop fluorescent imaging coupled with artificial intelligence technique to quickly and accurately determine glioma in real-time during surgery.

Methods: Glioma patients (N = 23) were enrolled and injected with indocyanine green for fluorescence image–guided surgery.Tissue samples (N = 1874) were harvested from surgery of these patients, and the second near-infrared window (NIR-II, 1000–1700 nm) fluorescence images were obtained. Deep convolutional neural networks (CNNs) combined with NIR-II fluorescence imaging (named as FL-CNN) were explored to automatically provide pathological diagnosis of glioma in situ in real-time during patient surgery. The pathological examination results were used as the gold standard.

Results: The developed FL-CNN achieved the area under the curve (AUC) of 0.945. Comparing to neurosurgeons' judgment,with the same level of specificity >80%, FL-CNN achieved a much higher sensitivity (93.8% versus 82.0%, P < 0.001) with zero time overhead. Further experiments demonstrated that FL-CNN corrected >70% of the errors made by neurosurgeons. FL-CNN was also able to rapidly predict grade and Ki-67 level (AUC 0.810 and 0.625) of tumor specimens intraoperatively.

Eur J Nucl Med Mol Imaging. 2021. 48(11): 3482-3492 Published online: 27 April 2021

Conclusion: Our study demonstrates that deep CNNs are better at capturing important information from fluorescence images than surgeons' evaluation during patient surgery. FL-CNN is highly promising to provide pathological diagnosis intraoperatively and assist neurosurgeons to obtain maximum resection safely.

Trial registration: ChiCTR ChiCTR2000029402. Registered 29 January 2020, retrospectively registered

Keywords

Fluorescence imaging; Deep learning; Convolutional neural networks; Intraoperative pathology; Gliomas

[1] CAS Key Laboratory of Molecular Imaging, Beijing Key Laboratory of Molecular Imaging, The State Key Laboratory of Management and Control for Complex Systems, Institute of Automation, Chinese Academy of Sciences, 95 Zhongguancun East Road, Beijing, 100190 China

[2] School of Artificial Intelligence, University of Chinese Academy of Sciences, Beijing, China

[3] Department of Neurosurgery, Beijing Tiantan Hospital, Capital Medical University, No. 119 South Fourth Ring West Road, Fengtai District, Beijing, 100070 China

[4] China National Clinical Research Center for Neurological Diseases, Beijing, China

[5] Beijing Advanced Innovation Center for Big Data-Based Precision Medicine, School of Engineering Medicine, Beihang University, Beijing, China

[6] Engineering Research Center of Molecular and Neuro Imaging of Ministry of Education, School of Life Science and Technology, Xidian University, Xi'an, China

* Biluo Shen, Zhe Zhang, and Xiaojing Shi are co-first authors and have contributed equally to this work.

Introduction

Glioma accounts for 75% of malignant primary brain tumor in adults[1]. Among these brain tumor patients, more than half are glioblastoma which is the most lethal glioma and have a median overall survival of only 14.6 months[2]. Although advanced therapies have been developed for glioma patients, neurological surgery remains the major treatment modality that plays an important role in improving survival.

At present, microsurgery under white light is the common method used in neurosurgery clinic, but it is difficult for neurosurgeons to clearly identify glioma boundary, resulting in tumor residual and early recurrence. Therefore, it is crucial to make quick and accurate diagnosis of dissected tissues during surgery. Intraoperative pathological examination of frozen tissue sections using hematoxylin and eosin (H&E) staining is a conventional and reliable diagnostic approach. But it usually costs a long time (at least 20–30 min) and requires complicated procedures to obtain pathological results[3]. Moreover, it is not practical to freeze ten or hundreds of samples during the operation, which limits its applications for intraoperative real-time diagnosis of tumor especially for multiple tissue samples.

In the past few years, artificial intelligence techniques such as several deep convolutional neural networks (CNNs) have been developed for classification of medical images and show high performance[4–10]. In coupling with conventional radiological imaging techniques such as magnetic resonance imaging (MRI), deep CNNs have also been used in the management

and diagnosis of glioma to provide the grading [11] and genetic information[12], automate the pathological diagnosis[13, 14], and help determine prognosis and guide therapy[15]. However, all of these studies are mainly focused on preoperative planning and postoperative diagnosis and prediction.

Advances in fluorescence imaging[16–22] have brought real-time imaging-guided surgery to reality, which greatly increases complete resection rate in high-grade glioma. Indocyanine green (ICG) is a safe and economic near-infrared (NIR) fluorescence imaging agent that has been used in clinic to intraoperatively visualize glioma with high sensitivity and modest specificity[23]. We hypothesize that the application of CNNs to capture features from fluorescence imaging automatically has the potential to better provide accurate real-time visual information, and it helps neurosurgeons to distinguish tumor from non-tumor tissue during surgery.

Herein, a dataset of NIR fluorescence (FL) and white-light (WL) images from 1874 specimens obtained from surgery of glioma patients was constructed (Fig. 1a). Then deep CNNs combined with the second NIR window (NIR-II, 1000–1700 nm) fluorescence imaging of ICG (named as FL-CNN) were developed to distinguish tumor versus non-tumor for all brain specimens, diffuse lower-grade glioma (DLGG, WHO II-III) versus glioblastoma multiforme (GBM, WHO IV), and low level (<10%) versus high level (≥10%, see the "Materials and methods" section) of Ki-67 for tumor specimens (Fig. 1b). Experiments were conducted on this dataset to validate the performance of the proposed FL-CNN. Moreover, the performance of FL-CNN was compared with WL-CNN (CNNs that take WL images as input), as well as to the results obtained from three neurosurgeons who read FL and WL images independently, using the pathological examination results as the gold standard.

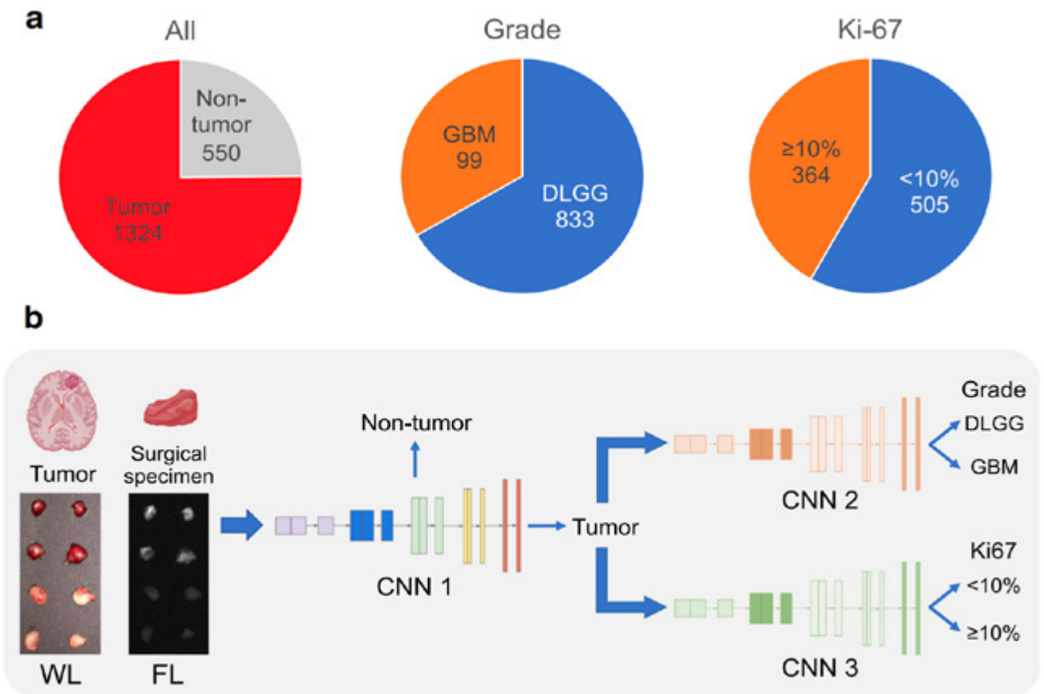


Fig.1 a Number of specimens per class with pathological examination results as the gold standard. Only tumor specimens had pathological results of tumor grade and Ki-67. b Specimens were resected by the guidance of NIR-II fluorescence imaging. Specimen images of WL and FL were obtained and fed into the CNNs for differentiation of tumor versus non-tumor. Images of tumor specimens were then fed into the CNNs for the classification of the grade and Ki-67 level. The prediction process by the models costed less than 1 s on CPU and can be faster on GPU; therefore, the time spent can be omitted.

Materials and methods

Study design

Our main research objective was to build CNNs (Fig. 1b, CNN 1, CNN 2, CNN 3) to distinguish tumor versus non-tumor for brain specimens, diffuse lower-grade glioma (DLGG) versus glioblastoma multiforme (GBM), and low level (<10%) versus high level (≥10%) of Ki-67 for tumor specimens based on their FL and WL images (FL-CNN and WL-CNN). A Ki-67 cutoff of 10% was chosen because it has been shown that few tumors with low proliferation rate were under the misclassification with it[24]. Therefore, we constructed a dataset consisting of WL and FL images from 1874 specimens from 23 patients with glioma. Of all specimens, using the pathological examination results as the gold standard, 1324 were tumor and 550 were non-tumor. Of all tumor specimens, 833 were DLGG and 99 were GBM, and 505 were with Ki-67 level <10% and 364 were ≥10% (Fig. 1a). The data for three tasks were randomly split into a training set (70%) and a test set (30%) in patient level. More specifically, every patient was first assigned to the training set or the test set, and then all specimens from the patient were assigned to the corresponding set. The specimens from a given patient appeared only in the training set or the test set, but not in the two sets at the same time. The number of specimens per class in the test sets is provided (Supplementary Fig. S1). Because we split at the patient level and the numbers of specimens in the patients were uneven, the proportion of specimens in the test set is not exactly 30%. After training on the training set, we then evaluated and compared the performance of FL-CNN, WL-CNN, and neurosurgeons for the classification of tumor versus non-tumor on the test set. We further validated our CNNs in new tasks in the diagnosis of glioma, including the classification of the grade and Ki-67 level of tumor specimens, which is impossible for neurosurgeons during surgery.

Study participants

Our dataset contained prospective, de-identified data from 23 patients enrolled from March 22, 2019, to April 22, 2020. Inclusion criteria included (1) male or female; (2) suspected as malignant glioma on preoperative contrast enhancement MRI; (3) voluntarily signed informed consent of surgical treatment and additional specimen beyond what was needed for routine clinical diagnosis; and (4) no contraindication of ICG. The study was approved by the Ethics Committee of Beijing Tiantan Hospital, Capital Medical University. All patients were given informed consent for their agreements. This study on patients with glioma was also explored in a clinical trial (ChiCTR2000029402) in China.

Imaging system

The imaging unit of the intraoperative brain tumor imaging system consisted of a laser generator sub-system and a NIR-II and color image combined imaging instrument. The NIR-II imaging sub-system was composed of a cooled InGaAs charge-coupled device (CCD, NIRvana: 640, Teledyne Princeton Instruments) camera, a high-performance lens corrected for shortwave-wavelength infrared (SWIR) wavelength range (SWIRON 2.8/50, Schneider Kreuznach), and a spectral filter (FEL1000 longpass filter, Thorlabs) assembled with the lens through an adapter. The detector in NIR-II camera was Peltier-cooled to minimize thermally generated noise. The laser generator sub-system consisted of a laser, an optical fiber, and a collimator. The output wavelength of the laser was 808 nm, which was applied as the excitation light for NIR-II fluorescence imaging. The collimator converted the gathered light beam from the end of the fiber into a dispersed light spot with relatively homogeneous energy in it. The power of the laser was set as 50 mW/cm^2. The NIR-II fluorescence image and the color image were acquired simultaneously. Besides the imaging unit, a controlling unit was also fitted in the system. This unit consisted of a laser distance–measuring instrument, a controlling handle, and a brunch of motors controlled by the handle. The motor enabled the imaging unit to rotate so that images of every side of the tumor cavity were acquired. The controlling unit was set for precise control of the working distance of the imaging unit and the reduction of touching the imaging unit, which might be above the operating field.

Surgical protocol

ICG was injected intravenously to patients, radiological diagnosis of glioma, at a dose of 1 mg/kg (Dandong, Yichuang Pharmaceutical Co., Ltd., China), 48 h before anesthesia starting. The dosage and injection time were chosen by other trials on a few patients. Then, the NIR-II fluorescence imaging instrument was used to guide glioma resection intraoperatively. The white-light and NIR-II fluorescence images were acquired in the operating room. All patients' tumor resections were performed by NJ who has more than 20 years' experience of surgical treatment of gliomas. Specimens were obtained from tumor margin during the surgery. More specifically, the tumor surface was uniformly divided into 8 parts from the view of cross-section, and around 10 samples were taken from each part of the tumor-margin areas, resulting in a total of around 80 samples per patient (Supplementary Fig. S2). The resection of surgical specimens was guided by fluorescence imaging, which reduced the chance of sampling error. H&E and histochemically stained sections of the samples were used for diagnosis and assessment of the Ki-67 index. Tumor specimens were confirmed to be with enough tumor cell load by histology.

Three neurosurgeons (ZXG, SYH, JSC) who have similar surgical experiences and qualifications were watching operation at the time and independently evaluated brain specimens with access to intraoperative information such as anatomical location, vascularity, and perfusion. Because CNNs take every sample as input and predict its pathological diagnosis, for a fair comparison, we designed that three neurosurgeons independently read all of the samples and provided their per-sample evaluation results. All of the metrics of the neurosurgeons (readers) were also calculated based on these per-sample results. For grading, all specimens were also independently classified by three neuropathologists (GLL, JMW, SYT), according to the current World Health Organization Classification of Central Nervous System. In the case of a discrepancy, the 3 observers simultaneously reviewed the slides in order to achieve a consensus, and the corresponding immunohistochemical staining would be performed if necessary. To count Ki67, immunostained slides of tissue microarray (TMA) sections were scanned using a Leica Aperio AT2 scanner (at ×400 magnification), and the images were analyzed using a Leica Aperio ImageScope v12.3.0.5056. The algorithm was chosen according to the positive cellular location of each antibody. Cytoplasmic v2 algorithm was chosen for antibody positivity in cytoplasm, and nuclear v9 algorithm for nuclear positivity. The data of specimens diagnosed as gliomas were used for analysis. It should be noticed that a patient usually has both tumor and non-tumor specimens, and these tumor specimens are usually of different grades and Ki-67 levels. Therefore, it was certainly incorrect to apply the pathological results of a whole tumor to all

samples from that tumor. All resected surgical specimens were sent for pathological examination. These pathological examination results of every specimen were used as the ground truth for model learning.

Hardware and software

All experiments were conducted on Google Colab GPU Runtime (T4/P100 GPUs). PyTorch[25] (version 1.0+) was used for data loading, model building, and training. The final statistical analysis was performed in R (version 3.6.1) and Python (3.7), using pROC[26] (version 1.15.3) and sklearn[27] (0.21.3) for calculating receiver operating characteristic (ROC) statistics, sensitivity, specificity, accuracy, PPV, NPV, and F_1 (F_1 score is the harmonic mean of the PPV and sensitivity and ranges from 0 to 1). Figures and Tables were generated using matplotlib[28] (version 3.1.2) and Apache ECharts (version 4.6.0).

Data preprocessing

Fluorescence images and white-light images of specimens were used as the only input of FL-CNN and WL-CNN. Fluorescence images produced by our fluorescence imaging system were not natural images like RGB color images or gray images and could not be used directly. The value of every pixel in the fluorescence image was the intensity of fluorescence signal, but not RGB value or gray value which ranged from 0 to 255. Therefore, pixel values of fluorescence images must be normalized nonlinearly to cope with traditional image processing pipeline. Tumor specimens produced strong fluorescence signal and non-tumor specimens produced weak fluorescence signal, so the normalized images of tumor specimens had larger pixel values and are brighter. It was noticed that these differences were only relative, but not absolute in the pixel values, because ambient light existed in the image and was likely to enhance the whole brightness. Randomly appeared white noises in the images might also influence these differences between tumor and non-tumor specimens. To solve these issues and make our CNNs more robust, heavy data augmentation was used to preprocess fluorescence images before CNN forwarding. Specifically, autocontrast and image denoising algorithms were applied firstly when needed to normalize the whole contrast of the image and remove noises. Then, random adjustment of brightness and contrast with a range of factor 1.0 was used to make CNNs more robust to absolute pixel value differences. Finally, the images were randomly flipped vertically, and patches were cropped from the images with a padding of 16. White-light images were natural RGB color images, so there was no need to do special preprocessing. Conventional data augmentation including random flip, rotate, and crop was used. The cropped patches from FL and WL images were sent to FL-CNN and WL-CNN, correspondingly. When testing, non-square images were zero-padded to meet the input requirements of CNNs.

Problem formulation

Classification of tumor versus non-tumor for all brain specimens, and DLGG versus GBM and Ki-67 level < 10% versus ≥10% for tumor specimens were all binary classification problem. Probabilities of the presence of positive classes (tumor, GBM and ≥ 10%) were predicted by CNN 1, CNN 2, and CNN 3, respectively. To solve class imbalance, two coefficients were introduced to reweight the different parts of losses. The sum of the weighted binary cross entropy (BCE) losses across all images was given by the following equations:

$$L_{\mathrm{BCE}}\left(y,\hat{y}\right) = -\sum_{i=1}^{m} \alpha_P y_i ln\left(\hat{y}_i\right) + \alpha_N (1-y_i)\ln\left(1-\hat{y}_i\right) \quad (1)$$

$$\alpha_P = \frac{|P|+|N|}{2|P|}, \alpha_N = \frac{|P|+|N|}{2|N|} \quad (2)$$

where y_i indicates the probability of the presence of a positive class that a model predicted given ith input image, and $\hat{y}i$ is the ith ground truth label. α_P and α_N are the balance coefficients of the positive and negative class, and | P | and | N | are the number of positive samples and negative samples for every task.

Model development

CNN 1, CNN 2, and CNN 3 were developed for the classification of tumor versus non-tumor, DLGG versus GBM and < 10% and ≥ 10%. For FL images and WL images, different models called FL-CNN and WL-CNN were developed. Specimen images were firstly fed into CNN 1 to classify whether they were tumor or non-tumor. Then, images of tumor specimens were fed into CNN 2 and CNN 3 in parallel to predict their grade and Ki-67 level, respectively.

To solve these three binary classification problems on FL and WL images and obtain accurate and fast models, transfer learning was employed based on EfficientNet-B0[29] which is one of state-of-the-art convolutional neural networks that achieves a good balance between performance and speed by carefully balancing network depth, width, and resolution. Compared with commonly used ResNets or Inception, EfficientNets can achieve the same level or better performance with an order of magnitude fewer parameters, which better meets the real-time requirements during the operation. The EfficientNet-B0 used here has only 5.3 M parameters and 0.39B FLOPS. For every task on FL or WL images, an EfficientNet-B0 was created and its parameters were initialized from the models pretrained on ImageNet. Then all layers except the last layer were used to extract features from images, and the last layer was replaced with a fully connected layer with a neuron for binary classification (tumor versus non-tumor, DLGG versus GBM, and < 10% versus ≥10%). The Xavier normal initializer[30] was used to initialize these fully connected layers. Dropout[31] was also applied before the last layer with a probability of 0.5 to avoid overfitting.

To better utilize the pretrained models and mitigate the issue of relatively few samples, there were 2 typical strategies for transfer learning to choose: (1) training a logistic regression classifier on the fixed feature extracted from the penultimate layer of the pretrained network, and (2) fine-tuning the entire pretrained network. The latter was found to be more effective for our problems. The optimization process used the Adam optimizer, with an initial learning rate of 0.001 and weight decay of 0.0001, using the weighted binary cross entropy loss function. The learning rate

was decayed with a cosine annealing[32] every iteration with linear warmup. Early stopping was not used because of the utilization of cosine annealing strategy.

Gradient-weighted class activation mapping

To gain insight into the representations learned by the CNN for classification, gradient-weighted class activation mapping (GCAM) was used for producing "visual explanations" for decisions, making the CNNs more transparent and explainable. FL and WL images of tumor and non-tumor specimens were randomly sampled, and their class-specific activation maps were presented, including colored GCAM, GCAM saliency, GCAM saliency × image, GCAM heatmap, and GCAM heatmap × image. Saliency × image/heatmap × image was generated by putting GCAM saliency/heatmap on the image, which made GCAM saliency/heatmap more recognizable. The last stage of the CNNs was used as the target layer and target classes were used to guide backpropagation and generate CAM.

Statistical analysis

The ROC analysis and AUC were calculated to assess model differences for WL images and FL images on three tasks. All confidence intervals at 95% were computed based on 1000 iterations of the bootstrap method. Sensitivity, specificity, PPV, NPV, and F_1 score of the FL-CNN for classification of tumor versus non-tumor were calculated at optimal decision thresholds with sensitivity >90%. Neurosurgeons' performance was calculated based on the read results of the specimens in the test set. F_1 score is complementary to the AUC and less sensitive than the AUC in cases of class imbalance. AUC, accuracy, sensitivity, specificity, and F_1 score of the CNNs for classification of the grade and Ki-67 level were calculated at optimal decision thresholds that the point of the ROC curve was closest to the perfect (1,0) coordinate. A detailed transformation of predicted probability into decision using decision thresholds for three tasks on FL and WL images was provided (Supplementary Fig. S3). P values for comparisons were computed using a standard permutation test using 10,000 random resampling of the data.

Results

Classification performance of tumor versus non-tumor

The performance of FL-CNN distinctly exceeded neurosurgeon's performance in the classification of tumor tissue versus non-tumor (Fig. 2a). FL-CNN achieved an AUC of 0.945 (95% confidence interval (CI) 0.925–0.960), which performed much better than that of neurosurgeons (reader (FL) vs. reader (WL): sensitivity (0.912 vs. 0.820); specificity (0.606 vs. 0.827)).

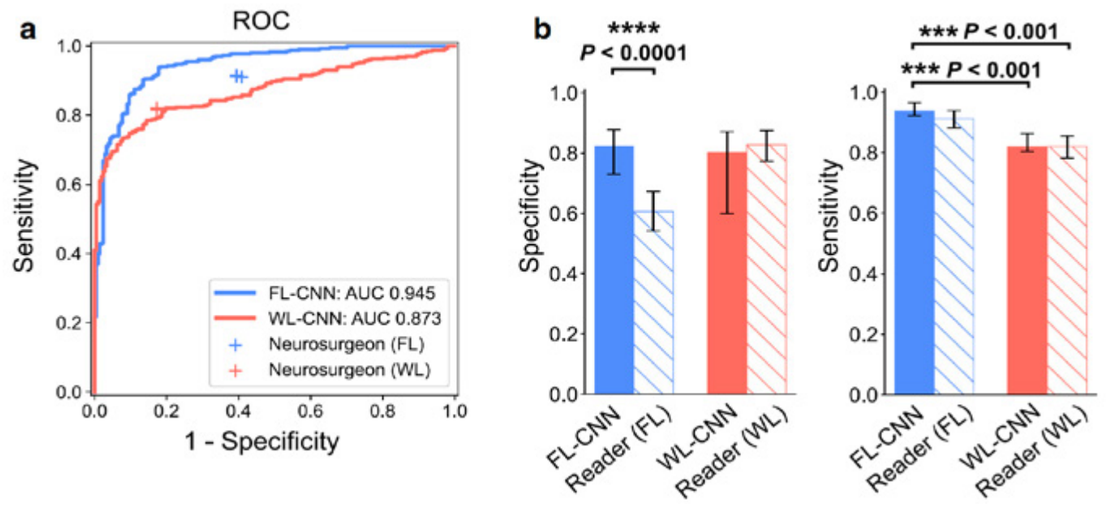


Fig.2 Diagnostic performance of the CNNs and neurosurgeons (readers). a, Receiver operating characteristic (ROC) curves calculated for the CNNs and neurosurgeons on FL and WL images for the classification of tumor tissue versus non-tumor. The lines represent the ROC achieved by the CNNs. Individual neurosurgeon performance is indicated by crosses. Results of FL and WL are colored blue and orange, respectively. **b,** Specificity and sensitivity of the CNNs and averaged individual neurosurgeons (readers) are plotted, using pathological examination results as the gold standard, and compared on FL and WL. The error bars represent the 95% confidence interval computed based on 1000 iterations of the bootstrap method. P values were computed using a two-sided permutation test with 10,000 random re- sampling of the data. All results were obtained on the test set (N = 608)

Table 1 Diagnostic performance of FL-CNN, WL-CNN and averaged individual neurosurgeons (reader) and the differences between FL-CNN and other three approaches, using pathological examination results as the gold standard

	Specificity	Sensitivity	PPV	NPV	F_1
FL-CNN	0.822	0.938	0.910	0.872	0.924
	(0.729, 0.877)	(0.922, 0.966)	(0.866, 0.936)	(0.835, 0.925)	(0.900, 0.940)
Reader (FL)	0.606	0.912	0.817	0.783	0.862
	(0.541, 0.672)	(0.881, 0.938)	(0.778, 0.848)	(0.711, 0.843)	(0.834, 0.883)
	+0.216*	+0.025	+0.094*	+0.090*	+0.062*
	(0.125, 0.303)	(−0.038, 0.088)	(0.059, 0.129)	(0.008, 0.171)	(0.019, 0.104)
	P< 0.0001	P=0.2106	P<0.0001	P=0.0159	P=0.0017
Reader (WL)	0.827	0.820	0.901	0.705	0.859
	(0.773, 0.875)	(0.782, 0.855)	(0.868, 0.929)	(0.645, 0.762)	(0.832, 0.884)
	−0.005	+0.118*	+0.009	+0.168*	+0.065*
	(−0.096, 0.087)	(0.053, 0.185)	(−0.031, 0.049)	(0.094, 0.239)	(0.017, 0.113)
	P=0.5216	P=0.0003	P=0.3231	P<0.0001	P=0.0042
WL-CNN	0.803	0.821	0.889	0.699	0.853
	(0.599, 0.872)	(0.804, 0.863)	(0.792, 0.926)	(0.644, 0.760)	(0.815, 0.878)
	+0.019	+0.118*	+0.021	+0.174*	+0.071*
	(−0.072, 0.111)	(0.050, 0.185)	(−0.019, 0.062)	(0.102, 0.247)	(0.022, 0.118)
	P=0.3636	P=0.0002	P=0.1544	P<0.0001	P=0.0016

*Denotes that there are significant differences between these two results (P < 0.05)

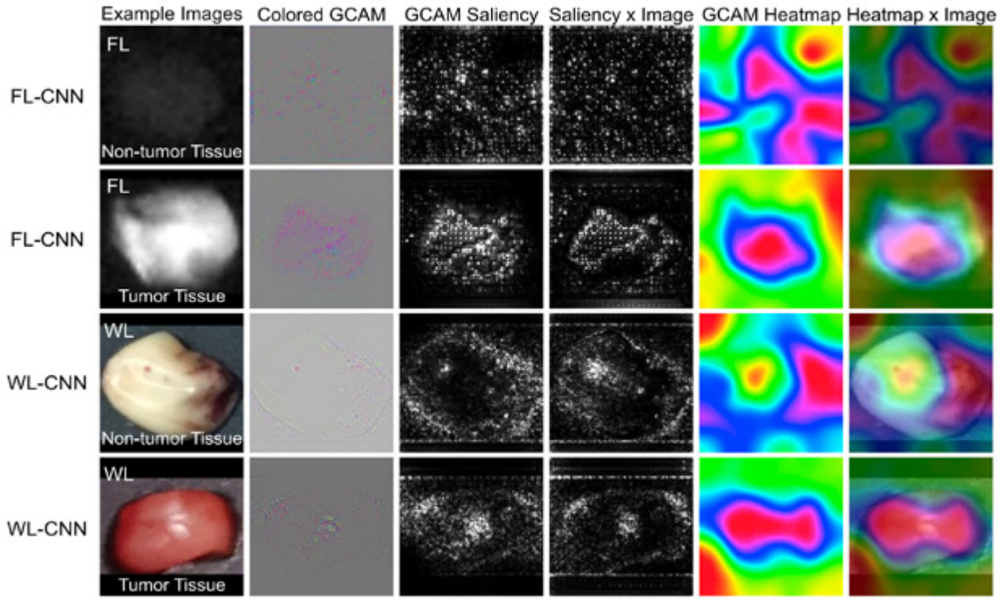


Fig.3 Gradient-weighted Class Activation Maps (GCAMs) visualize the learned feature representations for classification of tumor tissue versus non-tumor. FL/WL images of tumor/non-tumor tissues were randomly sampled. Colored GCAM, GCAM saliency, saliency × image, GCAM heatmap, and heatmap × image are shown. Saliency × image/heatmap × image was generated by putting GCAM saliency/heatmap on the image, which makes GCAM saliency/heatmap more recognizable. The target layer of GCAM was the last stage of the CNNs. Target classes were used to guide backpropagation and generate CAM. For preprocessing, non- square images were zero-padded to square, which led a black pad on the top/bottom or left/right.

Eur J Nucl Med Mol Imaging. 2021. 48(11): 3482-3492 Published online: 27 April 2021

Table 2 Performance of the proposed FL-CNN and WL-CNN on the classification of the grade and Ki-67 level of tumor specimens compared to the gold standard pathological examination results

		AUC	Accuracy	Sensitivity	Specificity	F_1
Grade	FL-CNN	0.810	0.875	0.606	0.909	0.519
		(0.712, 0.874)	(0.826, 0.905)	(0.429, 0.758)	(0.867, 0.939)	(0.374, 0.650)
	WL-CNN	0.688	0.696	0.545	0.715	0.286
		(0.600, 0.758)	(0.639, 0.747)	(0.379, 0.714)	(0.655, 0.768)	(0.188, 0.387)
		+0.127*	+0.179*	+0.061	+0.194*	+0.234*
		(0.016, 0.235)	(0.108, 0.250)	(−0.152, 0.273)	(0.122, 0.266)	(0.110, 0.360)
		P=0.0091	P<0.0001	P=0.2341	P<0.0001	P<0.0001
Ki-67	FL-CNN	0.625	0.611	0.778	0.433	0.673
		(0.560, 0.688)	(0.545, 0.649)	(0.388, 0.911)	(0.302, 0.748)	(0.502, 0.744)
	WL-CNN	0.689	0.679	0.844	0.504	0.731
		(0.620, 0.751)	(0.615, 0.729)	(0.740, 0.921)	(0.349, 0.595)	(0.656, 0.781)
		−0.063	−0.073*	−0.089	−0.056	−0.065*
		(−0.161, 0.034)	(−0.152, 0.007)	(−0.200, 0.022)	(−0.173, 0.063)	(−0.141, 0.007)
		P=0.1013	P=0.0440	P=0.0594	P=0.1839	P=0.0406

*Denotes that there are significant differences between these two results (P < 0.05)

Furthermore, there was a significant difference between the performance of FL-CNN and WL-CNN (AUC of 0.873, 95% CI 0.843–0.900, P<0.001). The results further demonstrated that FL-CNN not only significantly improved the specificity of diagnosis compared with neurosurgeons' judgment based on FL images (Fig. 2b left, P<0.0001) but also simultaneously achieved a higher sensitivity compared with neurosurgeons' judgment based on WL images or WL-CNN (Fig. 2b right, WL images: P<0.001; WL-CNN: P<0.001). It was also noticed that, compared with neurosurgeons' judgment on FL images, FL-CNN achieved significantly higher PPV (positive predictive value), NPV (negative predictive value), and F_1 score (Table 1, all P<0.05). While compared with neurosurgeons' judgment on WL images and WL-CNN, FL-CNN achieved significantly higher NPV and F_1 score (all P<0.01). From error analysis, it was found that FL-CNN corrected most of the errors made by neurosurgeons (Supplementary Fig. S4). Over 2/3 of the all specimens were classified correctly by both FL-CNN and neurosurgeons. For the errors made by neurosurgeons, more than 70% of them (90/121, 86/117, 85/116 for FL images, 82/108, 83/108, 85/110 for WL images) were corrected by FL-CNN.

Feature visualization by GCAM

Gradient-weighted Class Activation Mapping (GCAM) produced colored GCAM, GCAM saliency, and GCAM heatmap which revealed recognizable features learned by CNNs for the classification of tumor tissue versus non-tumor (Fig. 3). For example, for FL-CNN, fluorescence signal of the non-tumor tissue was weak; therefore colored GCAM, GCAM saliency, and GCAM heatmap were sparse (first row). On the contrary, strong fluorescence signal of the tumor tissue produced dense-colored GCAM, GCAM saliency, and GCAM heatmap (second row). As for WL-CNN, there were differences between colored GCAM, GCAM saliency, and GCAM heatmap. Specifically, for the non-tumor tissue, colored GCAM and GCAM saliency concentrated more on the contours, but the GCAM heatmap put attention on the abnormal part (rightmost) of the non-tumor tissue where is rich in blood vessels. While for the tumor tissue, colored GCAM and GCAM saliency focused more on the contours and the center, but the GCAM heatmap cared the whole specimen.

Classification performance of grade and Ki-67

It is well-known that neurosurgeons cannot obtain the grading and Ki-67 level information for the resected specimen during the operation. Importantly, here, we demonstrated that CNNs with strong learned features were generalizable to new tasks in the diagnosis of glioma, including the classification of the grade and Ki-67 level of tumor specimens (Fig. 4, Supplementary Fig. S5, and Table 2). FL-CNN and WL-CNN achieved AUC of 0.810 and 0.688 on the classification of grade (DLGG (grade II and grade III) vs. GBM (grade IV)), and 0.625 and 0.689 on the classification of Ki-67 level (< 10% vs. ≥ 10%), correspondingly. For the task of grade, FL-CNN achieved higher AUC, accuracy, sensitivity, specificity, and F_1 score than that of WL-CNN. There were significant differences between their AUC, accuracy, specificity, and F_1 score (all P<0.01). While for the task of Ki-67 level, WL-CNN performed better in all of AUC, accuracy, sensitivity, specificity, and F_1 score than that of FL-CNN. Among these metrics, WL-CNN achieved significantly higher accuracy (P = 0.0440)

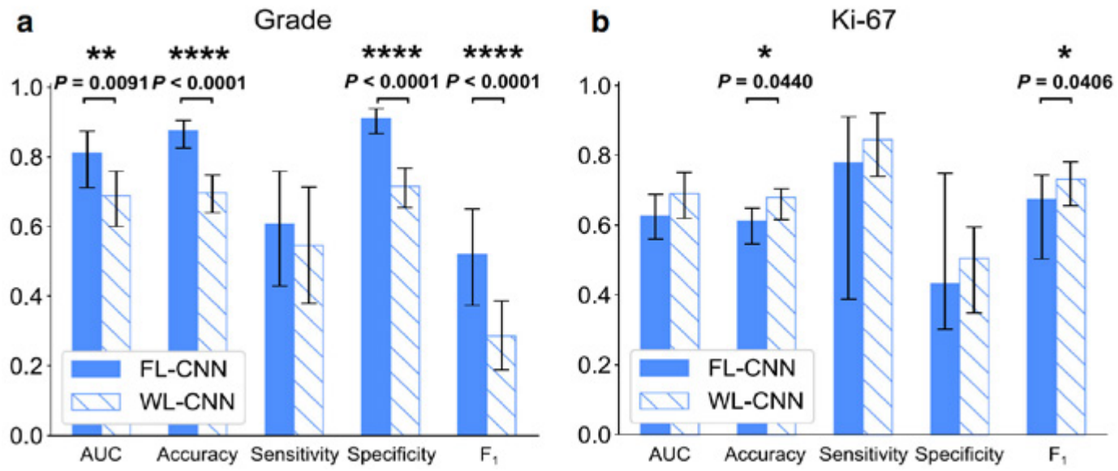


Fig.4 Performance of the CNNs for the classification of tumor grade and Ki- 67 level. a, Predicted grade of specimens are compared to the gold standard pathological examination results. AUC, accuracy, sensitivity, specificity, and F1 score of FL-CNN and WL-CNN are compared. **b,** Predicted Ki-67 level of specimens is compared to the gold standard pathology results. AUC, accuracy, sensitivity, specificity, and F1 score of FL-CNN and WL-CNN are compared. All error bars represent the 95% confidence interval computed based on 1000 iterations of the bootstrap method. N = 296 for grade and N = 262 for Ki-67

and F_1 score ($P = 0.0406$). It was also found that those wrongly classified non-tumor specimens by FL-CNN in error analysis were mostly classified as DLGG or < 10%. The trend that FL-CNN showed better overall performance on the classification of tumor versus non-tumor was in agreement with the results on the task of grade, but not the task of Ki-67 level. In summary, the results on the classification of the grade and Ki-67 level highlighted the CNNs' ability of learning and generalization.

Discussion

To the best of our knowledge, this study is the first demonstration of deep CNNs for predicting pathological diagnosis during fluorescence image–guided surgery. Previous works of deep learning on medicine are mainly concentrated on the fields of preoperative imaging and postoperative histopathology, aiming to automate analysis in an end-to-end way which saves time, resource, and labor. Unlike many of these works showing comparable performance to human experts, we have demonstrated that deep CNNs enable an approach to significantly improve accuracy of intraoperative diagnosis with zero time overhead, thus meeting the demand for fast and accurate tumor diagnosis during surgery.

Surgical resection is the main treatment regimen for glioma, which is associated with quality of life and survival[33]. With the updating operation concept for treatment, the maximum safe resection of glioma becomes highly important. Although more advanced imaging techniques have been applied intraoperatively, fast tumor diagnosis with high-throughput is still unavailable. To overcome this problem, FL-CNN has been developed and demonstrated to have the ability to efficiently distinguish tumor and non-tumor tissues during the neurosurgery. FL-CNN presents a high AUC of 0.945, sensitivity over 90%, and specificity over 80% on the classification of tumor versus non-tumor, which shows the potential to rapidly and precisely diagnose brain specimens and assist neurosurgeons to identify tumor boundary, thus protecting neurological functions during maximum tumor resection. Furthermore, our high-throughput method provides pathological diagnosis for even dozens or hundreds of specimens so that it can meet the demand of determining whether the tumor boundary requires further resection for neurosurgeons. In contrast to recent work using stimulated Raman histology and deep neural networks[3], we mainly focus on the specimen-level classification of tumor versus non-tumor and have conducted experiments on a larger dataset. Moreover, resection of surgical specimens in our method is guided by fluorescence imaging, which reduces the chances of sampling error. It is worth noting that our method using NIR-II fluorescence image not only guides tumor resection intraoperatively but also distinguishes tumor and non-tumor tissue especially in the boundary of the tumor.

The developed CNNs learn a non-linear mapping between fluorescence intensity distribution and pathological results, which is not like those defined a threshold for attributing a certain fluorescence level to be tumor or not. Therefore, they can differentiate tumor from non-tumor specimens better than neurosurgeons. Moreover, it can also provide effective information on grading and proliferation intraoperatively. These relatively objective evidences may assist surgeons in making individual resection decisions for each part of a tumor during operation, especially for these tumors which located in the functional area. If a specimen is suspected of being with high-grade and/or Ki67 level ≥10%, aggressive extent of resection should be taken into account for this site.

FL-CNN is established on NIR-II fluorescence imaging, which has a significant advantage over the first NIR window (NIR-I, 700–900 nm) in optical imaging characteristics, such as lower scattering and background signal[34], to produce a clear contrast between tumor and non-tumor tissue. Compared with clinically available 5-ALA fluorescence, NIR fluorescence typically has higher sensitivity and lower specificity (Supplementary Table S1). However, equipped with deep learning, our FL-CNN shows comparable specificity (0.822 vs. 0.811) than that of 5-ALA while keeping higher sensitivity (0.938 vs. 0.706). The experiment results have been confirmed by the gold standard of pathological examination, and the readers for diagnosis of specimens are with the same diagnostic experiences and qualification (Supplementary Table S2 and Supplementary Table S3), which ensures that the performance measurement of CNNs and neurosurgeons is precise, and the comparison between them is objective.

In the future, we plan to extend our CNNs to predict precise grading of tumors, in detail, from grade I to IV with a larger dataset. In addition, the proposed CNN-based approach also has the potential to predict significant genetic and molecular epidemiology of adult diffuse glioma, such as isocitrate dehydrogenase (IDH) mutation and 1p/19q chromosome co-deletion, which may provide more real-time intraoperative evidence for individual surgery strategies and early postoperative comprehensive treatment.

Code availability

The deep learning models are developed using standard libraries and scripts (PyTorch) available at https://pytorch.org/. The software used for basic image processing (OpenCV and PIL) is available at https://opencv.org/ and https://github.com/python-pillow/Pillow. Custom codes for the deployment of the algorithms are available for research purposes from the corresponding authors upon reasonable request.

Author contribution

JT, NJ, and ZH conceived the idea of the project. BS wrote the manuscript in addition to designing, performing, and analyzing all experiments. BS, ZZ, and XS performed the experiments. BS and CC wrote the code to achieve different tasks. XS, ZZ, and ZYZ collected the information on patients. CC and ZYZ assisted with data analysis. JT, NJ, and ZH designed, supervised, and analyzed all experiments, in addition to assisting with manuscript preparation. All authors read and approved the final manuscript.

Funding

This study was supported by the National Key Research and Development Program of China (2017YFA0205200), National Natural Science Foundation of China (NSFC) (62027901, 92059207, 81930048, 81930053, 81227901, 81801864), the Chinese Academy of Sciences (QYZDJ-SSW-JSC005), Beijing Natural Science Foundation (JQ19027), Capital Characteristic Clinical Application Project (Z181100001718196), the innovative research team of high-level local universities in Shanghai, and the Zhuhai High-level Health Personnel Team Project (Zhuhai HLHPTP201703).

Data availability

Data and materials are available for research purposes from the corresponding authors upon reasonable request.

Ethics approval

All procedures involving human participants were in accordance with the ethical standards of the institutional and/or national research committee and with the 1964 Helsinki declaration and its later amendments or comparable ethical standards.

Consent to participate

All patients were given informed consent for their agreements.

Conflict of interest

The authors declare no competing interests.

References

1. Lapointe S, Perry A, Butowski NA. Primary brain tumours in adults. Lancet. 2018;392:432–446.
2. Ostrom QT, Gittleman H, Liao P, Vecchione-Koval T, Wolinsky Y, Kruchko C, et al. CBTRUS statistical report: primary brain and other central nervous system tumors diagnosed in the United States in 2010–2014. Neuro-Oncol. 2017;19:v1–v88.
3. Hollon TC, Pandian B, Adapa AR, Urias E, Save AV, Khalsa SSS, et al. Near real-time intraoperative brain tumor diagnosis using stimulated Raman histology and deep neural networks. Nat Med. 2020;26:52–58.
4. Campanella G, Hanna MG, Geneslaw L, Miraflor A, Werneck Krauss Silva V, Busam KJ, et al. Clinical-grade computational pathology using weakly supervised deep learning on whole slide images. Nat Med. 2019;25:1301–1309.
5. Kather JN, Pearson AT, Halama N, Jäger D, Krause J, Loosen SH, et al. Deep learning can predict microsatellite instability directly from histology in gastrointestinal cancer. Nat Med. 2019;25:1054–1056.
6. Coudray N, Ocampo PS, Sakellaropoulos T, Narula N, Snuderl M, Fenyö D, et al. Classification and mutation prediction from non-small cell lung cancer histopathology images using deep learning. Nat Med. 2018;24:1559–1567.
7. Hannun AY, Rajpurkar P, Haghpanahi M, Tison GH, Bourn C, Turakhia MP, et al. Cardiologist-level arrhythmia detection and classification in ambulatory electrocardiograms using a deep neural network. Nat Med. 2019;25:65–69.
8. Lee H, Yune S, Mansouri M, Kim M, Tajmir SH, Guerrier CE, et al. An explainable deep-learning algorithm for the detection of acute intracranial haemorrhage from small datasets. Nat Biomed Eng. 2019;3:173–182.
9. Dong D, Tang L, Li ZY, Fang MJ, Gao JB, Shan XH, Ying XJ, Sun YS, Fu J, Wang XX, Li LM, Li ZH, Zhang DF, Zhang Y, Li ZM, Shan F, Bu ZD, Tian J, Ji JF. Development and validation of an individualized nomogram to identify occult peritoneal metastasis in patients with advanced gastric cancer. Ann Oncol. 2019;30(3):431–438.
10. Dong D, Fang MJ, Tang L, Shan XH, Gao JB, Giganti F, Wang RP, Chen X, Wang XX, Palumbo D, Fu J, Li WC, Li J, Zhong LZ, De Cobelli F, Ji JF, Liu ZY, Tian J. Deep learning radiomic nomogram can predict the number of lymph node metastasis in locally advanced gastric cancer: an international multicenter study. Ann Oncol. 2020;31(7):912–920.
11. Yang Y, Yan LF, Zhang X, Han Y, Nan HY, Hu YC, et al. Glioma grading on conventional MR images: a deep learning study with transfer learning. Front Neurosci. 2018;12:804. doi: 10.3389/fnins.2018.00804.
12. Li Z, Wang Y, Yu J, Guo Y, Cao W. Deep learning based radiomics (DLR) and its usage in noninvasive IDH1 prediction for low grade glioma. Sci Rep. 2017;7:5467.
13. Yonekura A, Kawanaka H, Prasath VBS, Aronow BJ, Takase H. Automatic disease stage classification of glioblastoma multiforme histopathological images using deep convolutional neural network. Biomed Eng Lett. 2018;8:321–327.
14. Ker J, Bai Y, Lee HY, Rao J, Wang L. Automated brain histology classification using machine learning. J Clin Neurosci. 2019;66:239–245.
15. Mobadersany P, Yousefi S, Amgad M, Gutman DA, Barnholtz-Sloan JS, Velázquez Vega JE, et al. Predicting cancer outcomes from histology and genomics using convolutional

networks. Proc Natl Acad Sci U S A. 2018;115:E2970–E29E9.
16. Hu Z, Fang C, Li B, Zhang Z, Cao C, Cai M, et al. First-in-human liver-tumour surgery guided by multispectral fluorescence imaging in the visible and near-infrared-I/II windows. Nat Biomed Eng. 2020;4:259–271 .
17. Qin C, Zhong J, Hu Z, Yang X, Tian J. Recent advances in Cerenkov luminescence and tomography imaging. IEEE J Sel Top Quantum Electron. 2011;18:1084–1093.
18. Hongbo G, Xiaowei H, Muhan L, Zeyu Z, Zhenhua H, Jie T. Weight multispectral reconstruction strategy for enhanced reconstruction accuracy and stability with Cerenkov luminescence tomography. IEEE Trans Med Imaging. 2017;36:1337–1346.
19. Hu Z, Zhao M, Qu Y, Zhang X, Zhang M, Liu M, et al. In vivo 3-dimensional radiopharmaceutical-excited fluorescence tomography. J Nucl Med. 2017;58:169–174.
20. Liu M, Zheng S, Zhang X, Guo H, Shi X, Kang X, et al. Cerenkov luminescence imaging on evaluation of early response to chemotherapy of drug-resistant gastric cancer. Nanomedicine. 2018;14:205–213.
21. Song T, Liu X, Qu Y, Liu H, Bao C, Leng C, Hu Z, Wang K, Tian J. A Novel Endoscopic Cerenkov Luminescence Imaging System for Intraoperative Surgical Navigation. Mol Imaging. 2015;14:443–9.
22. Hu Z, Chi C, Liu M, Guo H, Zhang Z, Zeng C, Ye J, Wang J, Tian J, Yang W, Xu W. Nanoparticle-mediated radiopharmaceutical-excited fluorescence molecular imaging allows precise image-guided tumor-removal surgery. Nanomedicine. 2017;13(4):1323–1331.
23. Lee JY, Thawani JP, Pierce J, Zeh R, Martinez-Lage M, Chanin M, et al. Intraoperative near-infrared optical imaging can localize gadolinium-enhancing gliomas during surgery. Neurosurgery. 2016;79:856–871.
24. Spyratos F, Ferrero-Poüs M, Trassard M, Hacène K, Phillips E, Tubiana-Hulin M, et al. Correlation between MIB-1 and other proliferation markers: clinical implications of the MIB-1 cutoff value. Cancer. 2002;94:2151–2159.
25. Paszke A, Gross S, Massa F, Lerer A, Bradbury J, Chanan G, et al. PyTorch: an imperative style, high-performance deep learning library. 31st Conference on Neural Information Processing Systems; 2017.
26. Robin X, Turck N, Hainard A, Tiberti N, Lisacek F, Sanchez JC, et al. pROC: an open-source package for R and S+ to analyze and compare ROC curves. BMC Bioinformatics. 2011;12:77.
27. Pedregosa F, Varoquaux G, Gramfort A, Michel V, Thirion B, Grisel O, et al. Scikit-learn: machine learning in Python. J Mach Learn Res. 2011;12:2825–2830.
28. Hunter JD. Matplotlib: a 2D graphics environment. Comput Sci Eng. 2007;9:90–95. doi: 10.1109/MCSE.2007.55.
29. Tan M, Le Q. EfficientNet: rethinking model scaling for convolutional neural networks. Proceedings of the 36th International Conference on Machine Learning; 2019. p. 6105–14.
30. Glorot X, Bengio Y. Understanding the difficulty of training deep feedforward neural networks. Proceedings of the 33th International Conference on Artificial Intelligence and Statistics; 2010. p. 249–56.
31. Srivastava N, Hinton GE, Krizhevsky A, Sutskever I, Salakhutdinov R. Dropout: a simple way to prevent neural networks from overfitting. J Mach Learn Res. 2014;15:1929–1958.
32. Loshchilov I, Hutter F. SGDR: stochastic gradient descent with warm restarts. International Conference on Learning Representations; 2017.
33. Laws ER, Parney IF, Huang W, Anderson F, Morris AM, Asher A, et al. Survival following surgery and prognostic factors for recently diagnosed malignant glioma: data from the Glioma Outcomes Project. J Neurosurg. 2003;99:467–473.
34. Carr JA, Franke D, Caram JR, Perkinson CF, Saif M, Askoxylakis V, et al. Shortwave infrared fluorescence imaging with the clinically approved near-infrared dye indocyanine green. Proc Natl Acad Sci U S A. 2018;115:4465–4470.

Neurosurgery

Research Article

First-in-Human Study of PET and Optical Dual-Modality Image-Guided Surgery in Glioblastoma Using ^{68}Ga-IRDye800CW-BBN

Deling Li,[1,3,4,*] Jingjing Zhang,[2,*] Chongwei Chi,[3,*] Xiong Xiao,[1,4] Junmei Wang,[5] Lixin Lang,[6] Iqbal Ali,[6] Gang Niu,[6] Liwei Zhang,[1,4] Jie Tian,[3] ✉ Nan Ji,[1,4] ✉ Zhaohui Zhu,[2] ✉ and Xiaoyuan Chen[6] ✉

Abstract

Purpose: Despite the use of fluorescence-guided surgery (FGS), maximum safe resection of glioblastoma multiforme (GBM) remains a major challenge. It has restricted surgeons between preoperative diagnosis and intraoperative treatment. Currently, an integrated approach combining preoperative assessment with intraoperative guidance would be a significant step in this direction.

Experimental design: We developed a novel ^{68}Ga-IRDye800CW-BBN PET/near-infrared fluorescence (NIRF) dual-modality imaging probe targeting gastrin-releasing peptide receptor (GRPR) in GBM. The preclinical in vivo tumor imaging and FGS were first evaluated using an orthotopic U87MG glioma xenograft model. Subsequently, the first-in-human prospective cohort study (NCT 02910804) of GBM patients were conducted with preoperative PET assessment and intraoperative FGS.

Results: The orthotopic tumors in mice could be precisely resected using the near-infrared intraoperative system. Translational cohort research in 14 GBM patients demonstrated an excellent correlation between preoperative positive PET uptake and intraoperative NIRF signal. The tumor fluorescence signals were significantly higher than those from adjacent brain tis-

sue in vivo and ex vivo ($p < 0.0001$). Compared with pathology, the sensitivity and specificity of fluorescence using 42 loci of fluorescence-guided sampling were 93.9% (95% CI 79.8%-99.3%) and 100% (95% CI 66.4%-100%), respectively. The tracer was safe and the extent of resection was satisfactory without newly developed neurologic deficits. Progression-free survival (PFS) at 6 months was 80% and two newly diagnosed patients achieved long PFS.

Conclusions: This initial study has demonstrated that the novel dual-modality imaging technique is feasible for integrated pre- and intraoperative targeted imaging via the same molecular receptor and improved intraoperative GBM visualization and maximum safe resection.

Keywords

Glioblastoma, Dual-modality imaging, Positron emission tomography (PET), Near-infrared fluorescence, Intraoperative imaging, Gastrin-releasing peptide receptor

[1] Department of Neurosurgery, Beijing Tiantan Hospital, Capital Medical University, Beijing, China

[2] Department of Nuclear Medicine, Peking Union Medical College Hospital, Chinese Academy of Medical Sciences and Peking Union Medical College, Beijing, China

[3] Key Laboratory of Molecular Imaging, Chinese Academy of Science, Beijing, China

[4] China National Clinical Research Center for Neurological Diseases (NCRC-ND), Beijing, China

[5] Department of Neuropathology, Beijing Neurosurgical Institute, Capital Medical University, Beijing, China

[6] Laboratory of Molecular Imaging and Nanomedicine (LOMIN), National Institute of Biomedical Imaging and Bioengineering (NIBIB), National Institutes of Health (NIH), Bethesda, Maryland, United States

* These authors contributed equally to this work.

Introduction

Maximum safe resection of magnetic resonance (MR) contrast-enhanced tumor is the current goal for the treatment of both newly-diagnosed [1] and recurrent [2] glioblastoma multiforme (GBM). It is extremely challenging to achieve this goal because of the aggressive and infiltrative growth, especially for GBM involving eloquent areas in the brain. Preoperative imaging assessment and intraoperative image-guided surgery are key for this aim.

Several trials confirmed that even in recurrent GBM patients, complete or maximum resection of enhancing part could be beneficial [2]. However, for recurrent GBM following surgery, radiotherapy, and chemotherapy, preoperative contrast-enhanced MRI alone cannot differentiate recurrence from radionecrosis. In this respect, positron emission tomography (PET) and MR spectroscopy (MRS) imaging have some added value [3]. Also, for newly-diagnosed GBM, biological tumor volume determined by ^{18}F-fluoroethyl-L-tyrosine (FET) PET imaging was an important prognostic biomarker and assisted in maximal PET-guided tumor resection [4].

Intraoperatively, the tumor margins are indistinguishable from the normal brain using a white-light microscope. Fluorescence-guided surgery (FGS) by 5-aminolevulinic acid (5-ALA) permits real-time intraoperative guidance for tumor visualization and benefits patient survival [5-13]. However, 5-ALA cannot be evaluated preoperatively for overall uptake, especially for the secondary GBM which might have lower grade tumor regions with low sensitivity to this agent [14]. Another clinically used optical probe, fluorescein sodium, is a nonspecific fluorophore that is extracellular and associated with breakdown of the BBB. At present, techniques for preoperative evaluation by PET and MRI and intraoperative image-guided surgery using the same molecular target in glioma patients are not available.

We hypothesized that intraoperative optical imaging of the tumor-specific molecular target positively labeled by preoperative PET would be of significant advantage for GBM surgery navigation. One of the molecular targets in GBM is the gastrin-releasing peptide receptor (GRPR), which has been shown to be overexpressed and play a role in the development of gliomas [15]. We previously developed ^{68}Ga-labeled bombesin (BBN) peptide derivative NOTA-Aca-BBN (7-14) (denoted as ^{68}Ga-BBN), which specifically targets GRPR in gliomas with a high tumor-to-background ratio [16]. In this study, we extended this concept by conjugating IRDye800CW, a near-infrared fluorophore [17-24], to form the ^{68}Ga-IRDye800CW-BBN PET/NIRF dual-modality imaging tracer (Fig. 1A). We assessed our hypothesis in a preclinical model and defined the optimal criteria for translation to the first-in-human study. We analyzed the accuracy of this technique for tumor detection by correlating intraoperative NIRF signal with the pathology of image-guided sampling and its effectiveness for improving the extent of resection of both newly diagnosed and recurrent GBM. Furthermore, we evaluated the safety and adverse effects of optical probe utilization.

Theranostics. 2018. 8(9): 2508–2520 Published online: 03 April 2018

Materials and Methods

Study design

A novel PET/NIRF dual-modality imaging probe, ^{68}Ga-IRDye800CW-BBN, was evaluated for its accuracy and safety in a preclinical orthotopic U87MG glioma xenograft model and in a small cohort of GBM patients. Patients with MRI imaging and/or pathological evidence of newly diagnosed or recurrent GBM were enrolled with a written informed consent during the period of April 2016 to October 2017 in Peking Union Medical College hospital and Beijing Tiantan Hospital. Exclusion criteria were mental illness; severe liver or kidney disease with serum creatinine > 3.0 mg/dl; any hepatic enzyme level 5 times or more than normal upper limit; severe allergy or hypersensitivity to IV radiographic contrast; claustrophobia to accept the PET/CT or PET/MRI scanning; pregnancy or breast feeding. The aim of this study was to explore the feasibility of the dual-modality imaging tracer and intraoperative NIRF navigation system for the surgical resection of gliomas while avoiding severe neurological deficits. We, therefore, did not strictly exclude the tumor location, such as the tumors adjacent to or even involving basal ganglia, thalamus or other eloquent areas. The surgeons were blinded to the neuropathology and the neuroradiologists and neuropathologists were blinded to intraoperative fluorescence. The trial was registered at ClinicalTrial.Com (NCT 02910804).

Molecular imaging probe synthesis

Waters 600 high-performance liquid chromatography (HPLC) system with a Waters 996 Photodiode Array Detector (PDA) using a preparative C_{18} HPLC column (PROTO 300 C_{18} 5 μm, 250 x 20 mm, Higgins Analytical, Inc.) was used for peptide purification. The peptides were analyzed using a Perkin-Elmer 200 series HPLC pump with a Waters 2487 UV detector and an analytical C_{18} HPLC column (Waters Symmetry C_{18} 5 μm, 150 x 3.9 mm). Mass spectra were obtained with a Waters LC-MS system (Waters, Milford, MA) that included an Acquity UPLC system coupled to a Waters Q-Tof Premier high-resolution mass spectrometer. All chemicals were purchased from Sigma-Aldrich (St. Louis, MO) unless otherwise stated in the procedure.

Preparation of NOTA-IRDye800CW-BBN

To a 20 mL glass vial containing 27.5 mg of BBN (7-14) in 2.6 mL of DMF 9.5 mg of Fmoc-lys(Boc)-OH, 25 μL of N,N-diiso-

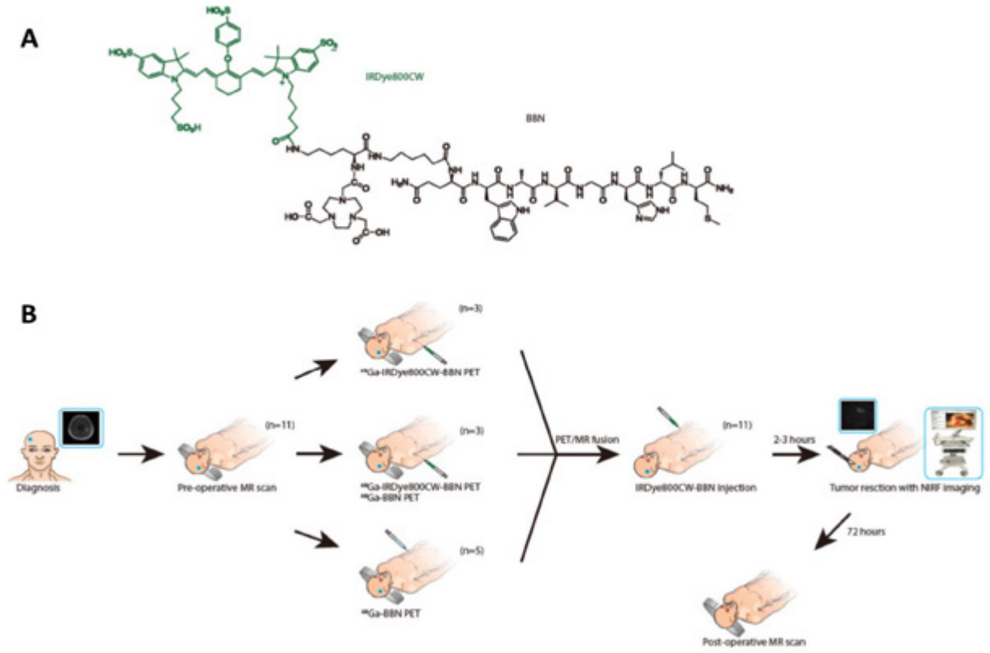


Fig.1 The chemical structure of IRDye800CW-BBN tracer and the scheme of this first-in-human study. (A) Chemical structure of IRDye800CW (green) with the BBN (black). (B) Enrollment and research scheme for the GBM patients.

propylethylamine (DIPEA) and 5 μL of diethyl cyanophosphonate (DECP) were added. The mixture was stirred at room temperature for 2 h and analyzed with LC-MS that showed formation of desired product Fmoc-lys(Boc)-BBN. Fmoc protecting group was removed by adding 0.6 mL of piperidine and stirred at room temperature for 1 h. HPLC purification and freeze-drying gave 18.5 mg lys(Boc)-BBN with 71% yield. LC-MS: $[MH]^+$ = 1279.5933 (m/z), calc: 1280.7063 ($C_{60}H_{96}N_{16}O_{13}S$).

Lys(Boc)-BBN (18.5 mg) was dissolved in 2 mL of DMSO, DIPEA (20 μL) and 2,2'-(7-(2-((2,5-dioxopyrrolidin-1-yl)oxy)-2-oxoethyl)-1,4,7-triazonane-1,4-diyl)diacetic acid (NOTA-NHS ester, CheMatech) (24.0 mg, 2 eq.) were added to the solution. The mixture was stirred at room temperature for 20 min and monitored with HPLC. After lys(Boc)-BBN was consumed and LC-MS showed desired product NOTA-lys(Boc)-BBN, DMSO was removed by freeze drying and Boc protecting group was removed by 0.1 mL TFA. The mixture was then purified with HPLC to give 6.5 mg NOTA-lys-BBN with (or at) 30.6% yield. LC-MS: $[MH]^+$ = 1464.6552 (m/z), calc: 1465.7864 ($C_{67}H_{107}N_{19}O_{16}S$).

To a 20 mL glass vial containing 6.5 mg NOTA-lys-BBN in 1 mL of DMSO 6.0 mg of IRdye800CW NHS ester (LI-COR, Lincoln, Nebraska) and 10 μL DIPEA were added. The mixture was stirred at room temperature for 1 h and purified with HPLC to give 2 mg of the desired product with 18.5% yield and >97% purity. LC-MS: $[(MHH)/2]^{++}$ = 1224.9103 (m/z), calc: 2450.0165 ($C_{113}H_{159}N_{21}O_{30}S_5$).

GBM model preclinical research

All animal experiments were approved by the Institutional Animal Care and Use Committee of Peking University. Five-week-old athymic female BALB/c nude mice, purchased from the Department of Experimental Animals, Peking University Health Science Center, were orthotopically transplanted with 1×10^6 U87MG cells in PBS into the brain. After 2 weeks, the mice were anesthetized with an injection of a mixture of ketamine, xylene, and sterile distilled water (0.2 mL) at a ratio of 7:3:4. Based on the results of the feasibility study, image-guided surgery was performed on a small animal operating table (Py2-501213, Harvard, USA) using our surgical navigation system for precise tumor detection after intravenous injection of 0.1 mg (0.1 mL) of IRDye800CW-BBN probe.

A total of 18 mice were placed under our imaging system. Three experienced surgeons removed the orthotopic tumor under NIR fluorescence guidance. All fluorescent tumor tissues were excised during surgery and frozen at -80 °C in optimum cutting temperature (OCT) compound (Leica, Germany) immediately after surgery. The tumors were cryosectioned (Leica CM1950, Leica) to yield sections of 4-μm thickness for hematoxylin and eosin (H&E) staining. The frozen OCT sections were fixed in acetone for 10 min.

PET imaging and image analysis

^{68}Ga-BBN was synthesized following a procedure reported previously [16,25]. IRDye800CW-BBN was synthesized under current good manufacturing practices (cGMP) by LI-COR company [25]. The radiolabeling of ^{68}Ga-IRDye800CW-BBN was performed in a sterile hot cell. ^{68}Ga was eluted from a ^{68}Ge/ ^{68}Ga generator (Eckert &Ziegler, Berlin, Germany) using 0.05 M HCl and mixed with 1.25 M NaOAc buffer to adjust the pH value to 4.0. The mixture was then directly transferred to a 1 mL plastic tube containing 40 μg of NOTA-IRDye800CW-BBN. After shaking, the mixture was incubated in a heating block at 100 °C for 10 min. Then the reaction mixture was cooled down, dissolved in sterile phosphate-buffered saline, and passed through 0.22 μm aseptic filtration membrane. Thin-layer liquid chromatography (BIOSCAN, USA) was used to test the radiochemical purity with CH3OH:NH4OAc (v/v 1:1) as the developing solution. The radiochemical purity of the product ^{68}Ga-IRDye800-BBN was over 95%.

Among the 14 patients, 4 patients received simultaneous PET/MR and the other 10 patients received PET/CT. ^{68}Ga-BBN PET/CT and ^{68}Ga-BBN PET/MR scanning was performed at 30 min after tracer administration. ^{68}Ga-IRDye800CW-BBN PET/CT and ^{68}Ga-IRDye800CW-BBN PET/MRI was performed at 30 min and 60 min after tracer administration. A single dose of 74-148 MBq ^{68}Ga-BBN or ^{68}Ga-IRDye800CW-BBN (1.85 MBq per kilogram of body weight) was injected intravenously. Brain PET was performed with 10-min PET acquisition covering the whole head of the patient. The images were transferred to a MMWP workstation (Siemens) for analysis.

For the 10 patients who underwent ^{68}Ga-BBN and/or ^{68}Ga-IRDye800CW-BBN PET/CT, PET images were co-registered to MR images with automatic image registration and manual positioning was performed as needed.

General biodistribution and temporal and intersubject stability were determined by visual analysis. Volumes of interest for normal brain tissues and the concerned lesions were drawn using 3-dimensional ellipsoid isocontouring, and the radioactivity concentrations and SUVs in these volumes of interest were obtained using the workstation software. The results were expressed as SUV_{mean} and SUV_{max}. MR and PET images were compared and then fused together to visualize the uptake area and the adjustment of the boundaries.

Clinical assessment and follow up

Before each time of tracer injection for preoperative PET imaging or intraoperative FGS, we obtained a 12-lead electrocardiogram (ECG) for patients, and the vital signs including blood pressure, heart rate, respiratory rate and blood oxygenation were monitored. Any discomforts were simultaneously recorded, such as nausea, vomiting, short breath, etc. The baseline parameters in blood (complete chemistries, complete metabolic panel and erythrocyte, white cell or platelet count) were obtained. For safety assessment, the same blood tests were repeatedly performed within 3 days after tracer usage. To rule out the pyrogenic effect, the patient temperature was recorded twice daily. If the temperature was over 38.5 °C, the number of postoperative day was recorded and the suspected reason for fever was assessed, including postoperative central nervous system infection (PCNSI), aseptic meningitis, pneumonia, urinary tract infection, etc. Cerebrospinal fluid analysis via lumber puncture was necessary for fever differential diagnosis. For assessing patients' neurologic deficits or neuropsychological effect correlating to tumor resection, preoperative symptoms and neurologic examination were recorded and newly developed postoperative neurologic deficits were recorded on the postoperative day one (POD1) and POD7. The patient survival was followed up by enhancing MRI every three months. The tumor progression and overall survival were based on RANO criteria [26]. The PFS-6 was defined as the proportion of patients with no progression 6 months after operation.

Theranostics. 2018. 8(9): 2508–2520 Published online: 03 April 2018

Intraoperative NIRF imaging

1.0 mg IRDye800CW-BBN of 1 mL saline was injected intravenously 2 h before anesthesia induction. FGS was performed using our intraoperative imaging system, as previously described[27-30]. Near-infrared (NIR) fluorescence images were acquired and displayed in real time. Based on our previous methods, we further updated our system to provide an improved optical path design, optimized handheld light source, and efficient image algorithms for best visualization. Relative fluorescent units (RFU) were measured for tumor and background, and signal-to-background ratio (SBR) was calculated by dividing in vivo tumor or ex vivo tissue RFU by respective RFU [18, 31].

If the tumor involved the cortex area, the handheld NIRF detector was used immediately after dura opening to visualize whether the positive fluorescence was obvious and determine the tumor borderline. The tumor was resected along the boundary (usually within the region of reactive gliosis) to decrease blood loss under the guidance of white-light microscope (M205FA, Leica, Germany). The tumor bed or cavity was then illuminated with NIRF detector. If fluorescence was present in safe area (likely not the direction of eloquent area), the tissue was further resected and the specimens from different loci were separately submitted to neuropathology. If safe, one biopsy form nonfluorescent area around tumor cavity was collected. However, for the patients with tumors involving eloquent areas, no obligatory tissue biopsy from nonfluorescent area was obtained. The RFU of ex vivo tissues were also measured.

These patients did not receive any other fluorescence-guided operation intraoperatively. Any other techniques, such as intraoperative ultrasound and MRI, were not utilized. If a navigation system was used, the simultaneous PET/MR was directly imported in the platform of Medtronic Navigation system STEALTHSTATION TREON Plus (No.1088309). If only PET/CT was performed, the enhanced MRI imaging and ^{68}Ga-BBN or ^{68}Ga-IRDye800CW-BBN PET/CT imaging were imported and fused in the same platform. The navigation system was only used for incision, bone flap, cortex incision region or cortical fistulization design and was not used while resecting the tumor or dissecting the residual tumor around the tumor cavity.

Image analysis

The preoperative contrast-enhanced MRI was performed within 1 week preoperatively. Early postoperative MRI was obtained within 72 h after operation. All MR scans were performed on a 3.0 T scanner with a head coil, and 0.1 mmol/kg body weight Magnevist was injected intravenously. Slice thickness was 5 mm. All MRI scans were evaluated centrally at the department of neuroradiology in Beijing Tiantan Hospital.

The volumes were calculated with manual segmentation of tumor outline using Picture Archiving and Communication Systems (PACS) system (Neusoft PACS Version 5.5) and the areas on each slice were added and the sum was multiplied by the thickness of each section [32]. The contrast-enhanced volume was defined as the area of high signal intensity on contrast-enhanced T_1-weighted (T1W) MRI.

The completeness of tumor resection was determined based on the contrast-enhanced volume less than 0.175 cm^3 [5]. The extent of resection was calculated as (preoperative contrast- enhanced volume-postoperative contrast enhanced volume)/ preoperative contrast enhanced volume *100%.

Pathological analysis

The samples were managed according to the protocol published previously[16]. The pathology was determined by three neuropathologists separately, and if any discrepancy, the consensus was reached by another higher-level pathologist. The criteria of pathology diagnosis are the 2016 World Health Organization Classification of Tumors of the Central Nervous System (CNS WHO) [33].

Statistical analysis

Statistical analysis was performed by using GraphPad Prism 6.0. Values were expressed as means ± SD. The sensitivity, specificity and other diagnostic parameters were defined [34]. The RFU and SBR were compared by using the Paired t test.

Results

Preclinical optical imaging of GBM animal model

We examined whether our probe could delineate clear margins of orthotopic brain tumors in situ and further refine tumor resection. As shown in Fig. 2, initial post-injection images revealed not only the bulk tumor but also highlighted the invasive and irregular tumor margins.

During the traditional surgery of the orthotopic tumors, the remnant tumor tissues could not be detected by the naked eye even by three experienced surgeons and it was difficult to avoid the dissection of healthy brain tissues. For mice experiment, we injected the IRDye800CW-BBN probe, orthotopic tumors could be completely resected using the near-infrared intraoperative system. During the entire operation, the orthotopic brain tumor margins were clearly visualized assisting the surgeons to perform the precise resection of tumors. If the fluorescence signal indicated the presence of remnant tumor tissues around the margins of the surgical cavity, additional surgery of the tumor margins could be performed and confirmed by pathology.

Overall characteristics of this cohort

Fourteen patients were enrolled in this cohort. There were 12 males and 2 females, and the median age was 47 years old. There were 8 newly diagnosed and 6 recurrent GBM. Among the 6 recurrent GBM patients, two patients had the first diagnosis of glioblastoma multiforme, while the other 4 had anaplastic astrocytoma. According to the classification by Sawaya and colleagues [35], 10 patients presented with grade III lesions (tumors in eloquent brain areas), 2 patients with grade II (near-eloquent brain areas) and 2 patients with grade I lesions. Median preoperative tumor volume was 55.49 cm^3 (range, 7.00-159.19 cm^3) based on contrast-enhanced T1W MRI.

Preoperative PET imaging and biodistribution

The biodistribution of radiotracer ^{68}Ga-BBN in healthy volunteers and glioma patients have previously been reported [16]. All 14 patients underwent preoperative PET. Three of the patients accepted PET scanning with both ^{68}Ga-BBN and ^{68}Ga-IRDye-800CW-BBN within one week for comparative analysis of the two

tracers. We observed similar biodistribution in normal brain tissues with the standardized uptake value SUV_{mean} of 0.10 ± 0.02. ^{68}Ga-BBN PET showed prominent tracer accumulation in the lesions. Quantitative analysis yielded SUV_{max} and SUV_{mean} values of 1.70 ± 0.39 and 1.08 ± 0.30, respectively, and tumor-to-background (T/B) ratios based on SUV_{max} and SUV_{mean} were 19.54 ± 4.20 and 12.12 ± 2.38, respectively. In ^{68}Ga-IRDye800CW-BBN PET, additional uptake of brain blood pool was observed at 30 and 60 min after injection, as well as a low background signal in the normal brain tissues with the SUV_{mean} of 0.08 ± 0.03. Similar tracer accumulation within the brain lesions was detected on ^{68}Ga-IRDye800CW-BBN PET scans compared with ^{68}Ga-BBN for the same patients (Fig. 3). Quantitative analysis yielded SUV_{max} and SUV_{mean} values on ^{68}Ga-IRDye800CW-BBN PET of 1.47 ± 0.26 and 1.01 ± 0.22, respectively, and T/B ratios based on SUV_{max} and SUV_{mean} were 19.61 ± 2.76 and 13.43 ± 1.27, respectively. Thus, no significant difference of radiotracer biodistribution in normal brain tissues and tumor lesions was found between ^{68}Ga-BBN and ^{68}Ga-IRDye800CW-BBN PET (P > 0.05).

The remaining 11 patients underwent ^{68}Ga-BBN PET (n = 7) or ^{68}Ga-IRDye800CW-BBN PET (n = 4). ^{68}Ga-BBN PET imaging showed positive results in 7 patients (4 newly diagnosed and 3 recurrent) with quantitative SUV_{max} values of 1.67 ± 0.39 and T/B ratios of 18.09 ± 3.5. ^{68}Ga-IRDye800CW-BBN PET showed tracer accumulation in the 4 patients (2 newly diagnosed and 2 recurrent) with quantitative SUV_{max} and T/B ratios of 1.01 ± 0.39 and 14.5 ± 4.3, 0.93 ± 0.25 and 20.0 ± 2.5 at 30 min and 60 min, respectively.

Intraoperative optical and postoperative imaging assessment

Among the 14 patients enrolled, tumors from 12 patients were in the cortex and white matter areas, whereas the other two were deeply seated in the thalamus and medial temporal and insula (Patients 4 and 5 in Table 1). In the case of 12 patients, the fluorescence was illuminated immediately after opening the dura. The boundary of normal cortex and the tumor could be readily outlined. However, in Patients 4 and 5 with deep-seated tumors, after initial cortical fistulization, the brain retractor was utilized for sufficient tumor exposure. In these two cases, the fluorescence signal was weaker (Fig. S1B) than in patients with tumors involving the cortex area and those who had a much larger cavity after surgical tumor debulking.

The intraoperative IRDye800CW-BBN FGS appeared to have clear advantages as illustrated by the example of Patient 3 displayed in Figure 4. When the dura was opened, the tumor fluorescence in the cortical area was obvious and was not affected by the superficial blood due to enough washout interval (Fig. 4B). After surgery, the residual tumor could not be differentiated from

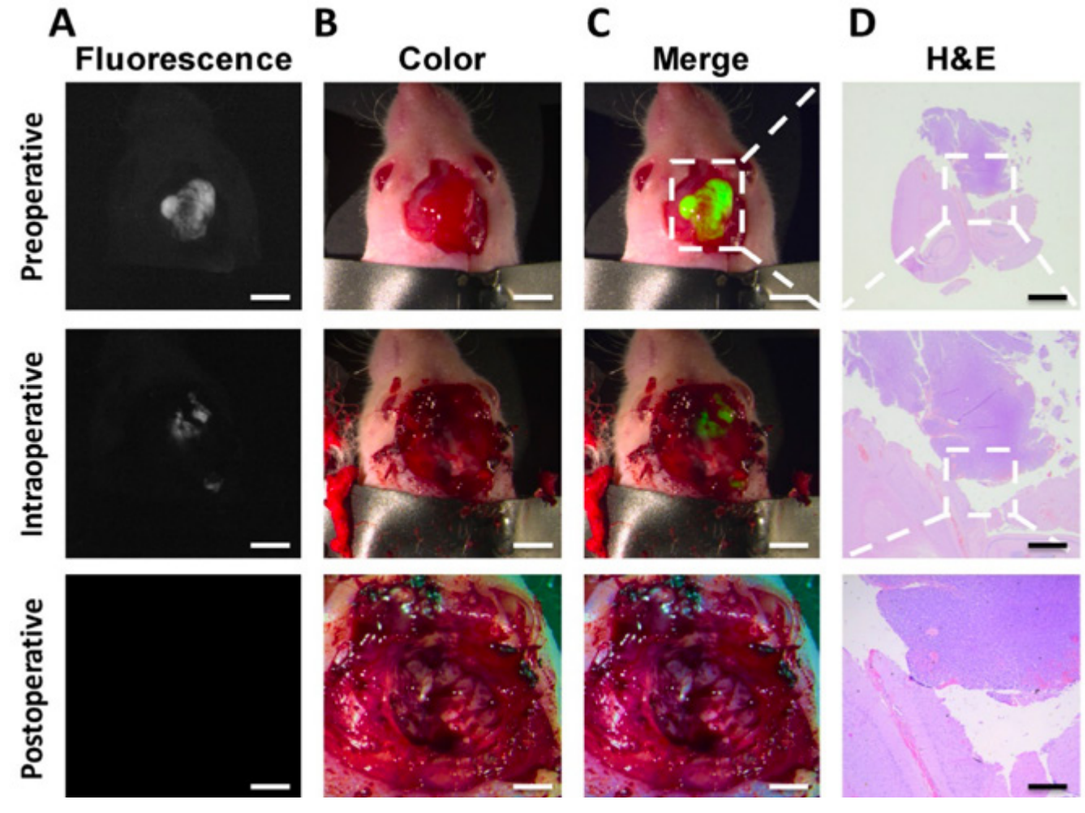


Fig.2 The intraoperative fluorescence-guided surgery of GBM. The fluorescence image confirmed tumor existence of the nude mice (A). color images were acquired to evaluate the residuals in a step-by-step manner (B). The fluorescence and color images showed that all the fluorescent tissues were removed from the mouse (C). The H&E images confirmed the results of tumor (D). Scale bars, preoperative row, 5 mm; intraoperative row, 5 mm; postoperative row, 3 mm. Scale bar, H&E column 2, 1, 0.2 mm, respectively for rows 1-3.

Table 1 Clinical characteristics, tumor location, clinical symptoms and fluorescence-guided surgery of this GBM cohort. The quantitative assessment of preoperative tumor volume in MRI and PET, extent of resection as well as the intraoperative fluorescence was recorded.

Patient No.	Gender (M/F)	Age	Tumor Location	Eloquence Grade	Recurrent tumor (Y/N)	Preoperative T1 post-Gd enhancement (cm^3)	Postoperative T1 post-Gd enhancement (cm^3)	% of resection	Complete resection (Y/N, <175 mm^3)	Visible fluorescence after resection (Y/N)	Fluorescence density & location (same with postoperative MRI enhancement? Y/N)	Preoperative symptoms	Postoperative status
1	M	48	Right Parietal/ Occipital	III	N	83.09	0.108	99.9	Y	Y	Minimal, deep cavity (Y)	Right-sided hemiparesis (IV)	Same
2	M	59	Left Parietal/ Occipital	III	N	16.90	0.145	99.1	Y	N	/	Intracranial hypertension; facial numbness	Right-sided hemiparesis (II), recovered 1 month postoperatively
3	M	55	Left Frontal/ Temporal /Parietal	III	N	71.57	0	100	Y	N	/	Right extreme numbness; fine motor control difficulty	Same
4	M	15	Thalamus / Midbrain	III	N	14.53	0.510	96.5	N	Y	Deep cavity (Y)	Intracranial hypertension; left vision difficulty; hearing loss	Improved
5	M	46	Left Temporal / Insula	II	N	8.51	0.800	90.6	N	Y	Deep cavity (Y)	Intracranial hypertension; Right-sided hemiparesis (II)	Improved
6	M	37	Left Frontal & Insula	III	N	29.67	0	100	Y	N	/	Intracranial hypertension	Improved
7	M	64	Left Temporal & Insula	III	N	87.76	0.152	98.3	Y	N	/	Intracranial hypertension; dysphonia	Improved
8	M	53	Right Temporal	I	N	7.00	0	100	Y	N	/	Secondary epilepsy	Improved
9	F	49	Left Frontal/ Parietal/Insula	III	Y	96.20	7.30	92.4	N	Y	Anterior cavity (Y)	Right-sided hemiparesis (III-IV); motor aphasia	Same
10	M	60	Right Frontal	I	Y	57.68	0.158	99.7	Y	N	/	Epilepsy	Improved
11	F	39	Right Frontal/ corpus callusum	III	Y	53.31	8.460	84.1	N	Y	Deep cavity & corpus callosum (Y)	Intracranial hypertension	Improved
12	M	31	Left Frontal	II	Y	24.55	1.793	92.7	N	Y	Deep cavity (Y)	Intracranial hypertension	Improved
13	M	28	Right Frontal/ Temporal	III	Y	57.86	14.649	74.7	N	Y	Anterior cavity (Y)	left-sided hemiparesis (I-II)	Same
14	M	42	Left Temporal / Occipital	III	Y	195.19	3.413	98.3	N	Y	Anterior cavity & splenium of corpus callosum (Y)	Headache; hemianopia; writing inability; memory deficiency	Headache; memory improved

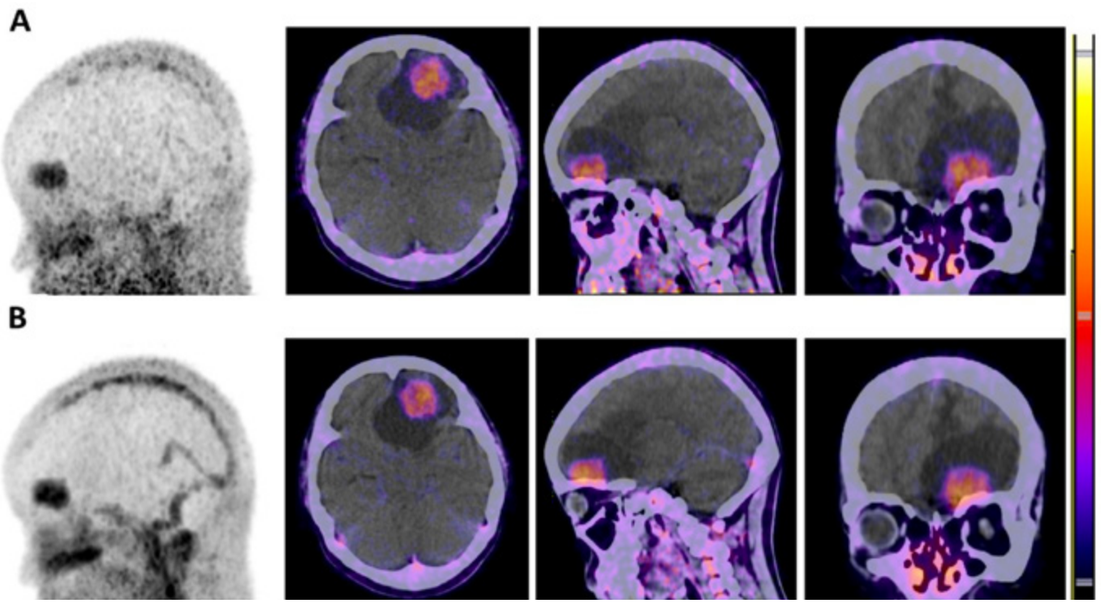


Fig.3 Similar uptakes of the 68Ga-NOTA-BBN and 68Ga-IRDye800-NOTA-BBN tracers in PET/CT for a newly-diagnosed GBM patient. (A) 68Ga-NOTA-BBN (7-14) PET MIP and PCT/CT images 30 min after 68Ga-NOTA-BBN infusion. (B) 68Ga-IRDye800-NOTA-BBN (7-14) PET MIP and PCT/CT images 60 min after 68Ga-IRDye800-NOTA-BBN administration.

the adjacent brain tissue by white light microscopy but clearly showed positive fluorescence in the deep tumor cavity by the dual-modality imaging (Fig. 4C). After all fluorescent areas were totally resected (Fig. 4D), the postoperative MRI did not show residual enhancement (Fig. 4E). The pathology and GRPR immunostaining analysis confirmed the accuracy of fluorescence-based sampling and GRPR specificity (Fig. 4G-J).

With the strictest criteria of less than 0.175 cm^3 as complete resection [5], 7 patients achieved complete resection. For newly diagnosed GBM, complete resection was achieved in 6 out of 8 patients except for Patients 4 and 5, who had deep-seated tumors located in the thalamus and medial temporal insula, respectively eloquence grade III and grade II. In recurrent GBM, complete resection was achieved in 1 out of 6 patients due to the extremely huge area of contrast enhancement and radionecrosis following surgical intervention, radiotherapy, and chemotherapy. However, if we considered complete resection as removal of more than 95% of the initially enhanced tumor volume [8], the probe helped achieve complete resection in 9 patients, especially 7 among 8 newly diagnosed GBM patients.

We compared the intraoperative fluorescence signals with the residual enhancement areas in postoperative MRIs (Table 1). If the visible fluorescence was left in tumor cavity to protect the involved eloquent areas, the postoperative MRI showed residual contrast-enhanced tumors in the same position except in Patient 1 with complete resection of tumor but minimal fluorescence in the deep tumor cavity. Examples of details of contrast enhanced MRI, both from the residual tumors in postoperative MRI and intraoperative fluorescence left in the cavity, are shown in Fig. S1 for Patient 4, Fig. S2 for Patient 5, Fig. S3 for Patient 9, Fig. S4 for Patient 11, Fig. S5 for Patient 12, and Fig. S6 for Patient 14. These figures showed that the intraoperative fluorescence was identical to the enhancement in the postoperative MRI, which were eloquent areas that had to be protected intraoperatively.

In vivo and *ex vivo* fluorescence and correlation with pathology

The optical probe was uptaken well by the tumor and washed out by the adjacent normal brain. The RFU of the tumors were significantly higher than those in the background *in vivo* (137.9 ± 67.3 vs. 41.6 ± 24.2, $p < 0.0001$) and *ex vivo* (142.2 ± 38.3 vs. 33.0 ± 12.7, $p < 0.0001$). The SBR of the *in vivo* and *ex vivo* tissue was not significantly different (Fig. 5).

A total of 31 fluorescent and 11 nonfluorescent *ex vivo* specimens were obtained intraoperatively. The details of their location, fluorescence signal, pathology, and WHO grading were shown in Table S2. Examples of two nonfluorescent tumor specimens from Patient 12 were displayed in Fig. S7B and Fig. S7C. These two specimens were false negatives, one of which was the tumor boundary tissue with scattered tumor cells in the brain tissue with a large amount of atypical gliosis; the

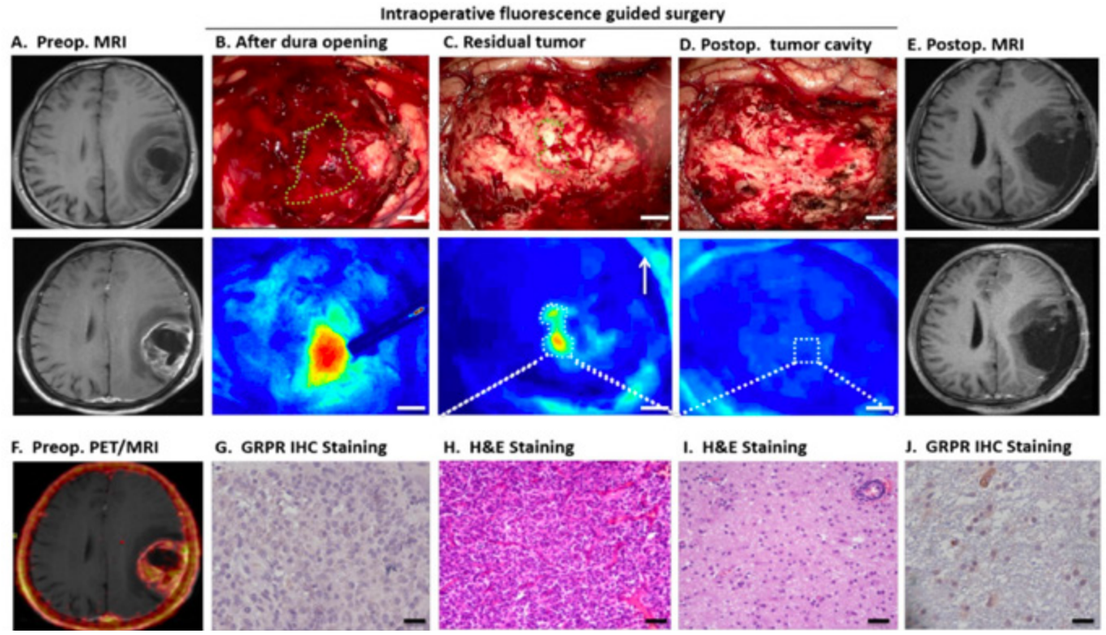


Fig.4 68Ga-IRDye800-BBN PET/NIRF dual-modality imaging guided GBM resection for patient 3. Axial T1-weighted (T1W) MRI showed a left temporal and parietal glioblastoma (eloquence III) in a 55-year-old man and obvious enhancement 30 min after intravenous injection of gadolinium (A). The fused 68Ga-BBN PET/MRI showed positive probe uptake with clear margin (F). After dura opening, the fluorescent tumor was obviously seen by the NIRF imaging system, and indicated with the green dashed line in the white-light imaging (B, Scale bar, 5mm.). Of note, the blood was not fluorescent and did not influence the tumor visualization. It was difficult to differentiate the residual tumor (indicated with green dashed line) and adjacent normal brain tissue by intraoperative white-light microscope (C); however, the residual tumor was fluorescent in the deep tumor cavity (C) and was confirmed by H&E staining (H, scale bar 50um) and had abundant GRPR positive cells (G, scale bar 20um). After resecting the residual fluorescent tumor, the cavity showed no fluorescence (D) and further small tissue foci along the cavity was confirmed as normal brain tissue by H&E staining (H) and only a few scattered GRPR positive cells can be found (J). The postoperative enhancing MRI demonstrated complete resection of enhanced region (E).

other was diagnosed as oligodendroglioma and astrocytoma with an aggressive growth pattern in the low-grade region of the tumor. These examples indicate that relatively smaller density of tumor cells or lower grade areas of the secondary GBM might be nonfluorescent.

The match between the NIRF signal and pathology was summarized in Table S3. The sensitivity was calculated to be 93.9% (31/33, 95% CI 79.8%-99.3%). The specificity was very strict with normal brain tissue and no evidence of any grade of tumor and was 100% (9/9, 95% CI 66.4%-100%). Therefore, the specimen-by-specimen analysis yielded a diagnostic accuracy of 95.2% (40/42). With stringent pathology criteria for all grades of glioma, the positive predictive value (PPV) and the negative predictive value (NPV) were 100% (95% CI 88.8%-100%) and 81.8% (95% CI 48.2%-97.7%), respectively. To quantify the fluorescence signal, the SBR of pathology demonstrated GBM ex vivo tissue was significantly higher than that of non GBM (4.91 ± 0.61 vs. 1.14 ± 0.19, p = 0.0003).

Safety and adverse effects

Patients' discomforts and other safety issues (liver and renal toxicity and pyrogenic effect) of IRDye800CW-BBN tracer after intraoperative utilizeation are presented in Table S1. No allergy or renal function damage was noticed. Hepatic enzymes, especially glutamic-pyruvic transaminase, were initially increased in most patients within the first week after surgery but subsequently normalized with no clinical significance. Five patients had fever within 4 to 7 days postoperatively. The PCNSI or aseptic meningitis were confirmed by the clinical manifestation and cerebrospinal fluid analysis. Among the 14 patients enrolled, 11 patients complained of transient nausea which usually disappeared within 15 minutes.

Patient survival

As shown in Table 2, all patients were followed up with the median period of 6.5 months (range 1.5-18.9 months). The

pathologic molecular profiling associated with patients' survival, including MGMT methylation status, TERT mutational status, IDH mutational status and 1p19q codeletion status, and postoperative therapy were also shown. Among the 5 newly diagnosed GBM patients with longer than 6 months follow-up, 4 patients achieved PFS-6, thus the PFS-6 was 80%. Of note, Patients 1 and 3 with complete resection and following treatment of standard Stupp protocol did not progress after 16.2 and 12.2 months since operation. Even for the recurrent GBM with complete resection in Patient 10, the tumor did not progress after 18.8 months.

Discussion

There is a critical need for a specific tumor visualization technique capable of distinguishing the tumor from normal brain intraoperatively that can assist surgeons to achieve gross total resection of the infiltrative GBM while benefiting patients by protecting neurological functions. In the past, a variety of anatomical imaging techniques have been utilized for guiding tumor resection, such as MRI-based neuronavigation, intraoperative ultrasound and MRI (iMRI), and metabolism-based intraoperative imaging, such as 5-ALA or fluorescein sodium-induced fluorescence imaging. These techniques improved gross total resection (from 69.1%-84.4%) and led to significant prolongation of PFS [5, 36-39]. However, there are limitations to each of these techniques. The navigation system cannot solve the intraoperative brain shift and is difficult to precisely resect the tissue based on the preoperative MRI navigation. In addition to being cost prohibitive, iMRI disrupts the flow of surgery adding at least one additional hour of operative time and cannot integrate with PET imaging intraoperatively. 5-ALA optical imaging has relatively low sensitivity and specificity particularly in heterogeneous tumors [14, 40, 41]. Furthermore, these techniques cannot evaluate the same specific tumor target pre- and intraoperatively.

In the present study, we developed a unique dual-modality PET/optical imaging probe which was based on our previously described ^{68}Ga-BBN PET tracer to specifically image the GRPR receptor expression in vivo on gliomas of different WHO grades [16]. This is the first translational study performed in GBM patients comparing the preoperative GRPR receptor biodistribution with the traditionnal gadolinium enhancement in MRI. This unique dual-modality imaging probe not only enabled preoperative assessment for resection accuracy but also allowed real-time optical navigation intraoperatively for achieving maximal safe resection.

We observed a strong correlation between the PET uptake, fluorescence, and GBM pathology, indicating that the tracer uptake was a result of specific GRPR binding. Several significant advantages of this probe in the first-in-human study were obvious. First, an extremely low dose of probe was sufficient for PET/optical imaging (40 μg per patient for preoperative PET and 1 mg per patient for intraoperative optical imaging vs. 20 mg/kg for oral 5-ALA and 5 mg/kg for intravenous fluorescein sodium). Second, the dual-modality probe could be used preoperatively and intraoperatively and was both safe and well-tolerated. And third, compared to the white light microscope identifying tumors based on superficial texture or color change, this near-infrared fluorescence-based technique was far more sensitive. This was especially helpful in detecting the residual foci with penetration depths of up to several millimeters after debulking most of the tumor and ensuring tumor resection within the tumor range and not damaging the adjacent normal brain. This cohort achieved 80% PFS-6 for newly-diagnosed GBM patients, higher than 46% in those of 5-ALA [42]. The PFS of the two patients with complete resection, more than 16.2 and 12.2 months, were longer than reported before (median PFS, 7 months [13] and 6.9 months [43]). Thus, this dual-modality imaging GRPR-specific probe could be utilized intraoperatively to visualize tumor margins without brain shift and might improve patient survival.

The trial of 5-ALA and fluorescein only enrolled newly diagnosed, untreated malignant glioma patients and excluded patients with tumors of the midline, basal ganglia, and other locations that did not allow complete resection [5, 13]. Our series of 14 GBM patients included 8 newly diagnosed and 6 recurrent GBM, among which 10 patients having tumors of eloquence grade III and 2 with eloquence grade II. In order to protect the neurofunctions, the tumors in some patients were not able to be resected completely. Another operation influencing factor was the preoperative tumor volume. The median volume based on enhancing T1 weighted MRI in this cohort was 55.49 cm^3, which was much larger than that in a phase II study of fluorescein-guided surgery (28.75 cm^3) [13]. Significantly, of the 8 newly diagnosed GBM, 6 patients achieved complete resection even with 5 tumors in eloquent brain areas as eloquence grade III. In the other 2 patients, complete resection was not possible as one tumor was in the thalamus involving midbrain and the other was in the temporal and insula lobe. Although the residual tumors exhibited positive fluorescence in resection cavity intraoperatively, complete resection was avoided to protect neurofunctions.

At this point, the optical imaging technique was not optimal for the deep-seated tumors (Patients 4 and 5) and, due to the light diffusion in deep tumor cavity, the SBR was not adequate during surgery. In future clinical trials, the correlation between the NIRF intensity and cellularity, proliferation index, and other molecular pathological characteristics will be analyzed to further optimize the dual-imaging probe. Although the technique appears to have significant potential for larger safe extent of resection and better prognosis, the limited number of patients with insufficient follow-up interval did not allow more definitive correlation of this technique with clinical outcomes. Future work will be designed in randomized clinical trials with more strict inclusion criteria, for example enrollment of only newly diagnosed patients with GBM eligible for total resection, to assess the effectiveness of this technique in improving patient survival.

In conclusion, this first-in-human study highlights an approach that uses the PET/NIRF dual-modality technique

Table 2 Patient follow-up data including postoperative therapy, the survival profile and associated pathology profiling.

Patient No.	Molecular pathology profiling	Complete resection (Y/N)	Follow-up duration (months)	Postoperative therapy	PFS for newly GBM (months)	OS for newly GBM (months)	OS for recurrent GBM (months)
1	MGMT(+),1p19q codeletion(-)	Y	16.2	RT + concomitant TMZ + TMZ (6)	16.2+	/	/
2	MGMT(+),TERTmutation(+), IDHmutation(-), 1p19q codeletion(-)	Y	9.2	TMZ (5)	3.9	9.2	/
3	MGMT(+),TERTmutation(-), IDHmutation(+), 1p19q codeletion(-)	Y	12.2	RT + concomitant TMZ + TMZ (10)	12.2+	/	/
4	MGMT(-),TERTmutation(-), IDHmutation(-), 1p19q codeletion(-)	N	8.1	TMZ (6)	7.4	8.1	/
5	MGMT(+),TERTmutation(+), IDHmutation(+), 1p19q codeletion(-)	N	6.4	RT + concomitant TMZ +TMZ (6)	6.4+	/	/
6	MGMT(-),TERTmutation(-), IDHmutation(-), 1p19q codeletion(+)	Y	2.0	RT + PCV chemotherapy	2.0+	/	/
7	MGMT(+),TERTmutation(+), IDHmutation(-)	Y	1.5	RT + concomitant TMZ	1.5+	/	/
8	MGMT(+),TERTmutation(+), IDHmutation(-)	Y	1.5	RT + concomitant TMZ	1.5+	/	/
9	MGMT(-),IDHmutation(-), 1p19q codeletion(-)	N	6.4	No	/	/	6.4
10	MGMT(-),IDHmutation(-), 1p19q codeletion(-)	Y	18.9	No	/	/	18.9+
11	MGMT(+),IDHmutation(+), 1p19q codeletion(-)	N	1.5	No	/	/	1.5
12	MGMT(+),IDHmutation(+), 1p19q codeletion(-)	N	6.5	TMZ (5)	/	/	6.5
13	MGMT(-),TERTmutation(+), IDHmutation(+), 1p19q codeletion(-)	N	10.6	TMZ + bevacizumab (5)	/	/	10.6
14	MGMT(+),TERTmutation(+), IDHmutation(-), 1p19q codeletion(-)	N	5.5	RT + concomitant TMZ + TMZ (6)	/	/	5.5

RT (radiotherapy), TMZ (temozolomide), PCV (procarbazine, lomustine, vincristine), PFS (Progression-free survival), OS (Overall survival).

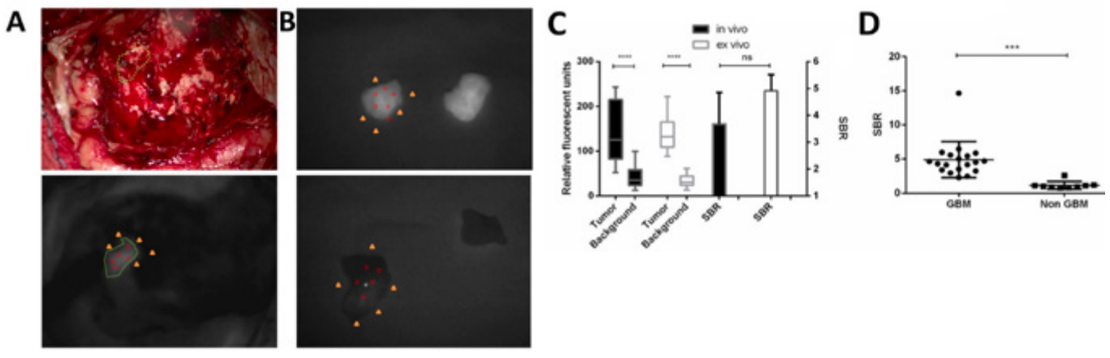


Fig.5 Quantification of fluorescence imaging for in vivo and ex vivo pathology demonstrated GBM or adjacent brain tissue. Relative fluorescent units (RFU) were acquired during intraoperative fluorescent imaging of residual tumor in vivo and NIRF region superimposed on white light (A). The ex vivo tissue of the fluorescent GBM tissue and adjacent brain tissue both demonstrated by pathology were shown in (B). Example of RFU calculation is shown. Five points are chosen in the fluorescent gross tumor (red circles) and another five points in the surrounding cortical or tumor cavity as background (yellow triangles), the mean RFU are calculated and the Signal-to-background ratio (SBR) is thus calculated. The RFU of the tumor were significantly higher (****$p < 0.0001$) than those in the background, in vivo and ex vivo. But the SBR of in vivo and ex vivo tissue was not different significantly (C). The SBR of pathology demonstrated GBM ex vivo tissue was significantly higher (*** $p < 0.001$) than that of non GBM. Data are RFU and SBR ± SD (D).

with ^{68}Ga-IRDye800CW-BBN in the preoperative assessment and FGS of GBM. This novel imaging probe has demonstrated its potential for maximum safe resection of difficult to access tumors without damaging the normal brain tissue.

Acknowledgments

We thank Kunshan He, Yamin Mao, Shixin Jiang, Yun Cui and Wenqiang Che for technical assistance. Funding: This work was supported in part by the Intramural Research Program of the National Institute of Biomedical Imaging and Bioengineering, National Institutes of Health. The work was also supported by National Key Technology Research and Development Program of the Ministry of Science and Technology of China (2014BAI04B01, 2017YFA0205200), the National Natural Science Foundation of China Projects (81502156) and Beijing Nova Program(xx2017017).

Author contributions

The project was initially conceptualized and the entire project was supervised by D.L., J.Z., Z.Z. and X.C. The preclinical study and NIRF navigation system were supervised by J.T. Clinical trial leads were Z.Z., L.Z. and N.J. and the operation were done by N.J. Image/data acquisition was performed by J.Z., D.L., C.C., X.X. and N.J. All authors participated in the interpretation of the reported experiments or results. D.L., J.Z. C.C. and I.A. wrote the manuscript, which was then further refined by Z.Z., N.J. and X.C. All other authors reviewed the final version of the manuscript.

Competing Interests

The authors have declared that no competing interest exists.

References

1. Marko NF, Weil RJ, Schroeder JL, Lang FF, Suki D, Sawaya RE. Extent of resection of glioblastoma revisited: personalized survival modeling facilitates more accurate survival prediction and supports a maximum-safe-resection approach to surgery. J Clin Oncol. 2014;32:774–82.
2. Suchorska B, Weller M, Tabatabai G, Senft C, Hau P, Sabel MC. et al. Complete resection of contrast-enhancing tumor volume is associated with improved survival in recurrent glioblastoma-results from the DIRECTOR trial. Neuro Oncol. 2016;18:549–56.
3. Shah AH, Snelling B, Bregy A, Patel PR, Tememe D, Bhatia R. et al. Discriminating radiation necrosis from tumor progression in gliomas: a systematic review what is the best imaging modality? J Neurooncol. 2013;112:141–52.
4. Suchorska B, Jansen NL, Linn J, Kretzschmar H, Janssen H, Eigenbrod S. et al. Biological tumor volume in 18FET-PET before radiochemotherapy correlates with survival in GBM. Neurology. 2015;84:710–9.
5. Stummer W, Pichlmeier U, Meinel T, Wiestler OD, Zanella F, Reulen HJ. Fluorescence-guided surgery with 5-aminolevulinic acid for resection of malignant glioma: a randomised controlled multicentre phase III trial. Lancet Oncol. 2006;7:392–401.
6. Hingtgen S, Figueiredo JL, Farrar C, Duebgen M, Martinez-Quintanilla J, Bhere D. et al. Real-time multi-modality imaging of glioblastoma tumor resection and recurrence. J Neurooncol. 2013;111:153–61.
7. Hadjipanayis CG, Widhalm G, Stummer W. What is the Surgical Benefit of Utilizing 5-Aminolevulinic Acid for Fluorescence-Guided Surgery of Malignant Gliomas? Neurosurgery. 2015;77:663–73.
8. Teixidor P, Arraez MA, Villalba G, Garcia R, Tardaguila M, Gonzalez JJ. et al. Safety and Efficacy of 5-Aminolevulinic Acid for High Grade Glioma in Usual Clinical Practice: A Prospective Cohort Study. PLoS One. 2016;11:e0149244.
9. Schebesch KM, Proescholdt M, Hohne J, Hohenberger C, Hansen E, Riemenschneider MJ. et al. Sodium fluorescein-guided resection under the YELLOW 560 nm surgical microscope filter in malignant brain tumor surgery-a feasibility study. Acta Neurochir (Wien) 2013;155:693–9.
10. Acerbi F, Cavallo C, Broggi M, Cordella R, Anghileri E, Eoli M. et al. Fluorescein-guided surgery for malignant gliomas: a review. Neurosurg Rev. 2014;37:547–57.
11. Rey-Dios R, Hattab EM, Cohen-Gadol AA. Use of intraoperative fluorescein sodium fluorescence to improve the accuracy of tissue diagnosis during stereotactic needle biopsy of high-grade gliomas. Acta Neurochir (Wien) 2014;156:1071–5. discussion 5.
12. Zhao S, Wu J, Wang C, Liu H, Dong X, Shi C. et al. Intraoperative fluorescence-guided resection of high-grade malignant gliomas using 5-aminolevulinic acid-induced porphyrins: a systematic review and meta-analysis of prospective studies. PLoS One. 2013;8:e63682.
13. Acerbi F, Broggi M, Schebesch KM, Hohne J, Cavallo C, De Laurentis C. et al. Fluorescein-Guided Surgery for Resection of High-Grade Gliomas: A Multicentric Prospective Phase II Study (FLUOGLIO) Clin Cancer Res. 2018;24:52–61.
14. Jaber M, Wolfer J, Ewelt C, Holling M, Hasselblatt M, Niederstadt T. et al. The Value of 5-Aminolevulinic Acid in Low-grade Gliomas and High-grade Gliomas Lacking Glioblastoma Imaging Features: An Analysis Based on Fluorescence, Magnetic Resonance Imaging, 18F-Fluoroethyl Tyrosine Positron Emission Tomography, and Tumor Molecular Factors. Neurosurgery. 2016;78:401–11. discussion 11.
15. Flores DG, Meurer L, Uberti AF, Macedo BR, Lenz G, Brunetto AL. et al. Gastrin-releasing peptide receptor content in human glioma and normal brain. Brain Res Bull. 2010;82:95–8.
16. Zhang J, Li D, Lang L, Zhu Z, Wang L, Wu P. et al. 68Ga-NOTA-Aca-BBN (7-14) PET/CT in Healthy Volunteers and Glioma Patients. J Nucl Med. 2016;57:9–14.
17. Cohen R, Vugts DJ, Stigter-van Walsum M, Visser GW, van Dongen GA. Inert coupling of IRDye800CW and zirconium-89 to monoclonal antibodies for single- or dual-mode fluorescence and PET imaging. Nat Protoc. 2013;8:1010–8.
18. Rosenthal EL, Warram JM, de Boer E, Chung TK, Korb ML, Brandwein-Gensler M. et al. Safety and Tumor Specificity of Cetuximab-IRDye800 for Surgical Navigation in Head and Neck Cancer. Clin Cancer Res. 2015;21:3658–66.
19. Zinn KR, Korb M, Samuel S, Warram JM, Dion D, Killingsworth C. et al. IND-directed safety and biodistribution study of intravenously injected cetuximab-IRDye800 in cynomolgus macaques. Molecular imaging and biology: MIB: the official publication of the Academy of Mol Imaging. 2015;17:49–57.
20. Center D-HM. A Microdose Evaluation Study of ABY-029 in Recurrent Glioma (ABY-029) https://clinicaltrialsgov/ct2/show/NCT02901925.
21. Rosenthal E. Phase I Panitumumab IRDye800 Optical Imaging Study. https://clinicaltrialsgov/ct2/show/NCT02415881.
22. van Dam GM. VEGF-targeted Fluorescent Tracer Imaging in Breast Cancer. http://clinicaltrialsgov/show/NCT01508572.
23. Lamberts LE, Koch M, de Jong JS, Adams ALL, Glatz J, Kranendonk MEG. et al. Tumor-Specific Uptake of Fluorescent Bevacizumab-IRDye800CW Microdosing in Patients with Primary Breast Cancer: A Phase I Feasibility Study. Clin Cancer Res. 2017;23:2730–41.
24. Rosenthal EL, Moore LS, Tipirneni K, de Boer E, Stevens TM, Hartman YE. et al. Sensitivity and Specificity of Cetuximab-IRDye800CW to Identify Regional Metastatic Disease in Head and Neck Cancer. Clin Cancer Res. 2017;23:4744–52.
25. Liu Z, Niu G, Wang F, Chen X. (68)Ga-labeled NOTA-RGD-BBN peptide for dual integrin and GRPR-targeted tumor imaging. Eur J Nucl Med Mol Imaging. 2009;36:1483–94.
26. Wen PY, Macdonald DR, Reardon DA, Cloughesy TF, Sorensen AG, Galanis E. et al. Updated response assessment criteria for high-grade gliomas: response assessment in neuro-oncology working group. J Clin Oncol. 2010;28:1963–72.
27. Chi C, Du Y, Ye J, Kou D, Qiu J, Wang J. et al. Intraoperative imaging-guided cancer surgery: from current fluorescence molecular imaging methods to future multi-modality imaging technology. Theranostics. 2014;4:1072–84.
28. Mao Y, Wang K, He K, Ye J, Yang F, Zhou J. et al. Development and application of the near-infrared and white-light thoracoscope system for minimally invasive lung cancer surgery. J Biomed Opt. 2017;22:66002.
29. He K, Chi C, Kou D, Huang W, Wu J, Wang Y. et al. Comparison between the indocyanine green fluorescence and blue dye methods for sentinel lymph node biopsy using novel fluorescence image-guided resection equipment in different types of hospitals. Transl Res. 2016;178:74–80.
30. Chi C, Zhang Q, Mao Y, Kou D, Qiu J, Ye J. et al. Increased precision of orthotopic and metastatic breast cancer surgery guided by matrix metalloproteinase-activatable near-infrared fluorescence probes. Sci Rep. 2015;5:14197.
31. Lee JYK, Cho SS, Zeh R, Pierce JT, Martinez-Lage M, Adappa ND, Folate receptor overexpression can be visualized in real time during pituitary adenoma endoscopic transsphenoidal surgery with near-infrared imaging. J Neurosurg; 2017. pp. 1–14.
32. Sorensen AG, Patel S, Harmath C, Bridges S, Synnott J, Sievers A. et al. Comparison of diameter and perimeter methods for tumor volume calculation. J Clin Oncol. 2001;19:551–7.
33. Louis DN, Perry A, Reifenberger G, von Deimling A, Figarella-Branger D, Cavenee WK. et al. The 2016 World Health Organization Classification of Tumors of the Central Nervous System: a summary. Acta Neuropathol. 2016;131:803–20.
34. Bossuyt PM, Reitsma JB, Bruns DE, Gatsonis CA, Glasziou PP, Irwig L. et al. STARD 2015: an updated list of essential items for reporting diagnostic accuracy studies. BMJ. 2015;351:h5527.
35. Sawaya R, Hammoud M, Schoppa D, Hess KR, Wu SZ, Shi WM. et al. Neurosurgical outcomes in a modern series of 400 craniotomies for treatment of parenchymal tumors. Neurosurgery. 1998;42:1044–55. discussion 55-6.
36. Mahboob S, McPhillips R, Qiu Z, Jiang Y, Meggs C, Schiavone G. et al. Intraoperative Ultrasound-Guided Resection of Gliomas: A Meta-Analysis and Review of the Literature. World Neurosurg. 2016;92:255–63.
37. Gessler F, Forster MT, Duetzmann S, Mittelbronn M, Hattingen E, Franz K. et al. Combination of Intraoperative Magnetic Resonance Imaging and Intraoperative Fluorescence to Enhance the Resection of Contrast Enhancing Gliomas. Neurosurgery. 2015;77:16–22. discussion.
38. Kuhnt D, Becker A, Ganslandt O, Bauer M, Buchfelder M, Nimsky C. Correlation of the extent of tumor volume resection and patient survival in surgery of glioblastoma multiforme with high-field intraoperative MRI guidance. Neuro Oncol. 2011;13:1339–48.
39. Senft C, Bink A, Franz K, Vatter H, Gasser T, Seifert V. Intraoperative MRI guidance and extent of resection in glioma surgery: a randomised, controlled trial. Lancet Oncol. 2011;12:997–1003.
40. Hauser SB, Kockro RA, Actor B, Sarnthein J, Bernays RL. Combining 5-Aminolevulinic Acid Fluorescence and Intraoperative Magnetic Resonance Imaging in Glioblastoma Surgery: A Histology-Based Evaluation. Neurosurgery. 2016;78:475–83.
41. Widhalm G, Wolfsberger S, Minchev G, Woehrer A, Krssak M, Czech T. et al. 5-Aminolevulinic acid is a promising marker for detection of anaplastic foci in diffusely infiltrating gliomas with nonsignificant contrast enhancement. Cancer. 2010;116:1545–52.
42. Stummer W, Tonn JC, Mehdorn HM, Nestler U, Franz K, Goetz C. et al. Counterbalancing risks and gains from extended resections in malignant glioma surgery: a supplemental analysis from the randomized 5-aminolevulinic acid glioma resection study. Clinical article. J Neurosurg. 2011;114:613–23.
43. Stupp R, Mason WP, van den Bent MJ, Weller M, Fisher B, Taphoorn MJ. et al. Radiotherapy plus concomitant and adjuvant temozolomide for glioblastoma. N Engl J Med. 2005;352:987–96.

Ophthalmology

Research Article

First-in-human Orbital Tumor Surgery Guided by Near-Infrared II Window Fluorescence Imaging: A Feasibility Study

Zeyu Zhang[1,2,*], Lishuang Guo[1,2,*], Lan Yao[3,*], Yueyue Li[3], Yan Hei[3], Qi Wang[3], Xiaoyi Wang[3], Rui Ma[3], Xinji Yang[3] ✉, Zhenhua Hu[4,5] ✉, Wei Wu[3] ✉

[1] School of Engineering Medicine Beijing Advanced Innovation Center for Big Data - Based Precision Medicine Beihang University Beijing China

[2] Key Laboratory of Big Data - Based Precision Medicine (Beihang University) Ministry of Industry and Information Technology Beijing China

[3] Senior Department of Ophthalmology 3rd Medical Center of Chinese PLA General Hospital Beijing China

[4] CAS Key Laboratory of Molecular Imaging, Beijing Key Laboratory of Molecular Imaging, and State Key Laboratory Management and Control for Complex Systems Institute of Automation Chinese Academy of Sciences Beijing China

[5] School of Artificial Intelligence University of Chinese Academy of Sciences Beijing China

* Zeyu Zhang, Lishuang Guo and Lan Yao contributed equally to this work.

Abstract

Precise resection of orbital tumors is a critically important but elusive issue. Fluorescence imaging in the near-infrared II window (NIR-II) holds the potential to provide the surgeons with real-time identification for orbital tumors. Here, for the first time, we evaluated the feasibility and clinical value of NIR-II fluorescence imaging in orbital tumor surgery. To establish the method of NIR-II fluorescence imaging for orbital tumors, we developed a NIR-II fluorescence imaging system and indocyanine green (ICG) served as the fluorescent contrast agent. Twenty-two patients diagnosed with orbital tumors and scheduled for standard-of-care surgery were enrolled in this study. Time-course NIR-II fluorescence imaging of two patients with superficial orbital tumors showed the optimum imaging time was 2 h post injection of ICG.

Fifteen patients were allocated for diagnostic test, which showed that both the in situ and ex vivo NIR-II fluorescence imaging showed better sensitivity and specificity than the surgeon judgment. In the feasibility trial of the remaining five patients, the surgeon encountered 34 suspicious regions and surgical decisions were changed nine times due to NIR-II fluorescence imaging. The resultant seven additional resections were justified by histopathology and the two conservative treatments did not result in recurrence. Based on these findings, we suggested that ICG-based NIR-II fluorescence imaging was feasible to guide precise resection of orbital tumors. A future randomized controlled trial with a larger cohort is encouraged to further verify the clinical value.

Keywords

Fluorescence imaging, ICG, NIR-II imaging, Orbital tumor

Introduction

Orbital tumors often substantially affect the appearance and visual function of patients, with surgical intervention serving as the primary treatment modality. Due to the close proximity of orbital tumors to critical anatomical structures, including optic nerves, extraocular muscles, and blood vessels, surgical management must prioritize the preservation of these vital tissues while also considering esthetic outcomes. Therefore, precise resection is of paramount importance in the management of orbital tumors.[1] Over the last 100 years, surgeons mainly rely on visualization and palpation to identify tumors during surgery. When the surgeons have difficulty in the identification of tumors, intraoperative frozen section analysis of selected tissue specimens is the gold standard to make a diagnosis.[2] However, frozen section analysis is time-consuming and can only examine a few samples, making the precise resection of orbital tumors still challenging.[3]

Several fluorescent probes were found to be capable of accumulating in the tumors, which made the tumors fluoresce under the excitation of an external light source. The intraoperative fluorescence imaging holds the potential to provide the surgeons with real-time identification for infinite tumor tissues.[4] In detail, the fluorescence imaging in the near-infrared I window (NIR-I, 700–900 nm) is most widely used in fluorescence-guided surgery due to the lower photon scattering and tissue autofluorescence.[5] Besides, the fluorescence probe indocyanine green (ICG) with NIR-I emission spectrum is the only US Food and Drug Administration (FDA)-approved NIR imaging fluorophore. To date, the ICG-based NIR-I fluorescence imaging has shown good diagnostic performance in the clinical trials of liver cancers,[6] pancreatic neoplasms,[7] colorectal cancer,[8] meningioma,[9] bone and soft tissue sarcomas.[10] However, it is unclear that whether intraoperative fluorescence imaging could guide the precise resection of orbital tumors characterized by open small-incision (<3 cm). Furthermore, for the sake of widespread clinical implementation of fluorescence guided surgery, the quality of fluorescence imaging needs further improvement and the clinical value needs further identification.[11]

Fortunately, the recent advent of fluorescence imaging in the second NIR window (NIR-II, 1000–1700 nm) provides an even higher signal-to-noise ratio and deeper tissue penetration than NIR-I imaging.[12, 13] Besides, by switching the NIR-I imaging system to NIR-II imaging equipment, the FDA-approved contrast agent ICG enables state-of-the-art NIR-II fluorescence imaging.[14] Previously, we have reported the first-in-human study of NIR-II fluorescence imaging for liver cancers using the home-built NIR-II equipment and clinically viable ICG.[15] The results show that intraoperative NIR-II imaging provides higher tumor-detection sensitivity, higher tumor-to-normal-liver-tissue signal ratio and higher tumor-detection rate compared with NIR-I imaging.[15] Encouraged by this, we hypothesized that ICG-based NIR-II fluorescence imaging could identify the orbital tumors. To explore the feasibility of applying this technology to guide precise resection of orbital tumors, we first established a method of NIR-II fluorescence imaging for orbital tumors based on a home-built fluorescence imaging system. Furthermore, we assessed the diagnostic accuracy of the NIR-II fluorescence imaging in the identification of orbital tumors. Finally, we preliminary evaluated its clinical value in the precise resection of orbital tumors.

Methods

Study design

This study combined a diagnostic test and feasibility trial and consisted of 3 parts (Figure S1). In part I, 2 patients with superficial orbital mass were enrolled to establish the method of NIR-II fluorescence imaging for orbital tumors. Part II was a prospective diagnostic test with 15 orbital tumor patients. In part III, a single-arm feasibility trial, five orbital tumor patients were enrolled to study the effect of NIR-II fluorescence imaging on intraoperative decision making.

The 22 patients were recruited from the senior department of ophthalmology in the 3rd medical center of Chinese PLA general hospital from November 2020 to December 2022 via convenience sampling. Patients aged 18 years or older were eligible if they were clinically diagnosed with orbital solid tumors by two experienced orbital doctors and scheduled for standard-of-care surgery. Exclusion criteria included: age <18 years, allergy to iodine or shellfish and unfitness for surgery. Besides the routine examinations, all patients underwent preoperative magnetic resonance imaging (MRI) of the eye with intravenous gadolinium. The characteristics of the study patients are listed in Table S1.

NIR-II fluorescence imaging system

The NIR-II fluorescence imaging system consisted of an open-field and closed-field imaging model. The open-field sub-system was composed of a liquid-cooling InGaAs charge-coupled camera (CCD, Cheetah 640, Xenics), which was integrated with a large depth-of-field lens (focal length 50 mm, maximum iris 1.8) and a 1100 nm longpass optical filter (FELH1100, Thorlabs). Notably, the CCD camera was mounted on a rotatable articulated arm for flexibly adjusting the imaging view. A hand-held 792 nm laser generator (output power 2.0 W, Changchun Leirui Optoelectronic Technology) was used to excite the fluorophores. For the closed-field sub-system, the CCD camera and laser generator were fixed on the top of the black box, which could occlude from ambient light. The key parameters of the NIR-II imaging system are listed in Table S2.

Preoperative time-course NIR-II fluorescence imaging for the superficial orbital mass

The patients with superficial orbital mass received intravenous infusion of 0.7 mg kg^{-1} body weight of ICG (Dandong Yichuang Pharmaceutical, China). At 15 min, 30 min, 1 h, 2 h, 3 h, 4 and 5 h post injection of ICG, fluorescence imaging was performed using the home-built NIR-II imaging instrument in the ward. The next day, the patients underwent standard-of-care surgery without intraoperative fluorescence imaging. Finally, the orbital mass was diagnosed by histopathology.

Intraoperative NIR-II fluorescence imaging for orbital tumors

We performed intraoperative NIR-II fluorescence imaging in patients with various gadolinium-enhancing orbital tumors. According to the results of time-course NIR-II fluorescence imaging, 0.7 mg kg^{-1} body weight of ICG (Dandong Yichuang Pharmaceutical, China) was intravenously injected 2 h before surgery. During the standard-of-care orbital surgery, in situ NIR-II fluorescence imaging of the main body of orbital tumors and regions of interest where the surgeon needed an auxiliary diagnosis were performed. Besides, after resection, the tumor bed was evaluated for residual fluorescence. All the resected samples were subjected to ex vivo imaging in the closed-field NIR-II fluorescence imaging system in the operating room. After the surgery, all the samples were assessed by histopathology.

Fluorescence analysis

For the pre-operative time-course NIR-II fluorescence imaging, tumor-to-normal tissue ratio (TNR) was quantitatively calculated by comparing the mean fluorescent intensity of the orbital mass with that of the surrounding normal tissue. For the in situ imaging, fluorescence positive was defined by three assessors (Z.Z., L.G. and W.W.) through the majority rule when showing an obvious hyperfluorescence compared with surrounding normal tissue. In contrast, fluorescence negative was defined as isofluorescent or hypofluorescent compared with surrounding normal tissue. For the ex vivo imaging, TNR was quantitatively calculated by comparing the mean fluorescent intensity of samples of interest with that of each patient's own normal tissue. The exploratory optimal TNR cutoff value of the ex vivo imaging was defined through the maximum Youden index. The fluorescence imaging assessors were available for clinical information but blinded to the histopathology results.

Histopathology assessment

Histopathology assessment served as the gold standard for the diagnosis of the resected samples. The samples were fixed in formalin, embedded in paraffin and serially sectioned at 5 μm thickness. The sections were then stained with hematoxylin and eosin (H&E) according to the standard procedure. Two experienced pathologists (Y.L. and Y.H.), who were available to the clinical information but blinded to the results of NIR-II fluorescence imaging, examined the slides and reached agreement for pathological diagnosis.

Statistical analysis

The judgments from the surgeon, in situ fluorescent imaging and ex vivo fluorescent imaging were compared with the histopathology results. To compare the diagnostic accuracy, we calculated sensitivities, specificities, the receiver-operating characteristic curves and the area under the curve (AUC) with 95% confidence intervals. The statistical analysis was performed by SPSS software (version 19).

Results

Preoperative time-course NIR-II fluorescence imaging in patients with superficial orbital masses

To determine the feasibility of NIR-II fluorescence imaging of orbital tumors and the optimum imaging time after the administration of ICG, we first enrolled 2 patients with superficial orbital mass (Figure S1, part I), who allowing noninvasive, real-time imaging. As early as 15 min post intravenous injection of 0.7 mg kg^{-1} body weight ICG, we found that the gadolinium-enhancing squamous cell carcinoma of conjunctiva, which was validated by the post-resection histopathology, was clearly fluorescing (Figure 1A,B). Furthermore, the NIR-II fluorescence signal persisted for at least 5 h (Figure 1C–H). Quantitative analysis showed that the fluorescence intensity was maintained at a high level from

Interdiscip Med. 2025. 3(1):e20240048 Published online: 9 January 2025

15 min to 2 h post injection, followed by a gradual decrease from 2 to 5 h (Figure 1I). Notably, the TNR of NIR-II fluorescence imaging peaked at 2 h post injection (Figure 1J). However, the gadolinium-enhancing orbital inflammatory mass proven by the post-resection histopathology was nonfluorescent (Figure S2). Besides, the epidermoid cyst that did not enhance with gadolinium was hypofluorescent (Figure S3). These results suggested that ICG-based NIR-II imaging could be used to localize gadolinium-enhancing tumors other than inflammatory or cystic lesions, which had great clinical implications for fluorescence imaging-guided tumor resection.

Intraoperative in situ NIR‐II fluorescence imaging of orbital tumors

Orbital tumors are often resected with an open small incision (<3 cm), which makes the tumors visible only through a limited angle. We therefore assembled an open-field NIR-II fluorescence imaging system allowing arbitrarily adjusting the angle of the laser emitter and fluorescence receiver to enhance the excitation and acquisition of fluorescent signals in orbital tumors (Figure 2A, Figure S4). Motivated by the fluorescent orbital tumor (squamous cell carcinoma of conjunctiva) and high TNR at 2 h post injection of ICG, we intravenously injected 0.7 mg kg^{-1} body weight ICG into the patients (n = 15) 2 h prior to surgery and found that intraoperative in situ NIR-II fluorescence imaging was affected by the exposure extent of tumors. When the tumor was underexposed (Figure 2B), the NIR-II fluorescence imaging was not clear (Figure 2B'). However, the tumor could be clearly visualized by NIR-II fluorescence imaging once it was adequately exposed (Figure 2C,C'). Besides, both the orbital malignant tumors (orbital hemangiopericytoma, orbital malignant peripheral nerve sheath tumor) and orbital benign tumors (orbital pleomorphic adenoma) were clearly fluorescing during the surgery (Figure 2D–G).

Next, we further assessed the diagnostic accuracy of in situ fluorescence imaging for orbital tumors (Figure S1, part II). The surgeon first made an initial judgment about whether the suspicious regions contained tumor tissues. Subsequently, the suspected regions were subjected to NIR-II fluorescence imaging and the tissues were qualitatively judged as fluorescence positive

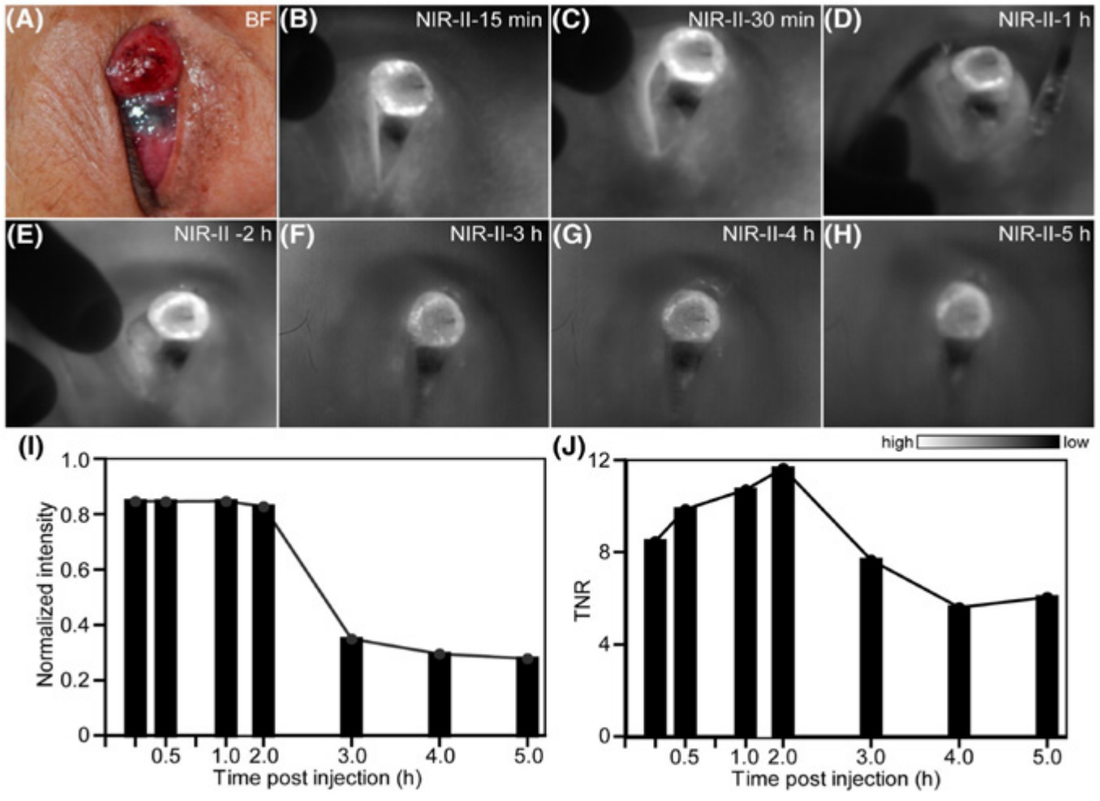


Fig.1 Time-course NIR-II fluorescence imaging of patients with squamous cell carcinoma of conjunctiva. **(A)** Bright field image of conjunctival squamous cell carcinoma. **(B–H)** Time course of NIR-II fluorescence images of conjunctival squamous cell carcinoma. **(I)** Normalized fluorescence intensity of conjunctival squamous cell carcinoma at different time points post injection of ICG. **(J)** Tumor-to-normal tissue ratio of conjunctival squamous cell carcinoma at different time points post injection of ICG. ICG, indocyanine green.

or negative by comparing their fluorescence intensity with that of the surrounding normal tissues. We encountered 22 suspicious regions, including tumor bed, para tumor tissue and so on, all of which were adequately exposed and underwent in situ NIR-II fluorescence imaging. In general, 14 suspicious regions were judged as fluorescence positive and 12 specimens were proved to contain tumors by histopathology (representative images in Figure 3A–D). Besides, 8 specimens were fluorescence negative and 5 specimens proved to be absent of tumor (representative images in Figure 3E–H). Compared with the surgeon's judgment, in situ NIR-II fluorescence imaging demonstrated higher sensitivity (80.0% vs. 66.7%), specificity (71.4% vs. 42.9%) and AUC (0.757 vs. 0.548) (Table 1).

Intraoperative ex vivo NIR‐II fluorescence imaging of orbital tumors

Due to the small operation field (incision <3 cm), the deep-seated tumors are difficult to acquire high-precision imaging results in situ. In this case, we developed ex vivo NIR-II fluorescence imaging to identify tumors. Considering the fluorescence imaging was vulnerable to ambient light and camera angle, we constructed a closed-field NIR-II fluorescence imaging system, which shielded the ambient light and fixed the camera angle (Figure 4A). Total 86 samples (26 primary tumor tissues, 44 suspicious para tumor tissues and 16 normal tissues) resected from the 15 patients were subjected to ex vivo NIR-II fluorescence imaging and pathological examination (Figure S1, part II). We found that all the primary tumors were clearly fluorescing (representative images in Figure 4B), while the normal tissues (orbital adipose tissue) were hypofluorescent (representative images in Figure 4C). The fluorescence of para tumor tissues that were suspected as tumors by the surgeon were heterogeneous (Figure 4D). We quantitatively analyzed the average fluorescence intensity and calculated TNR with normal tissues served as their own internal control. With pathological examination as the gold standard, the

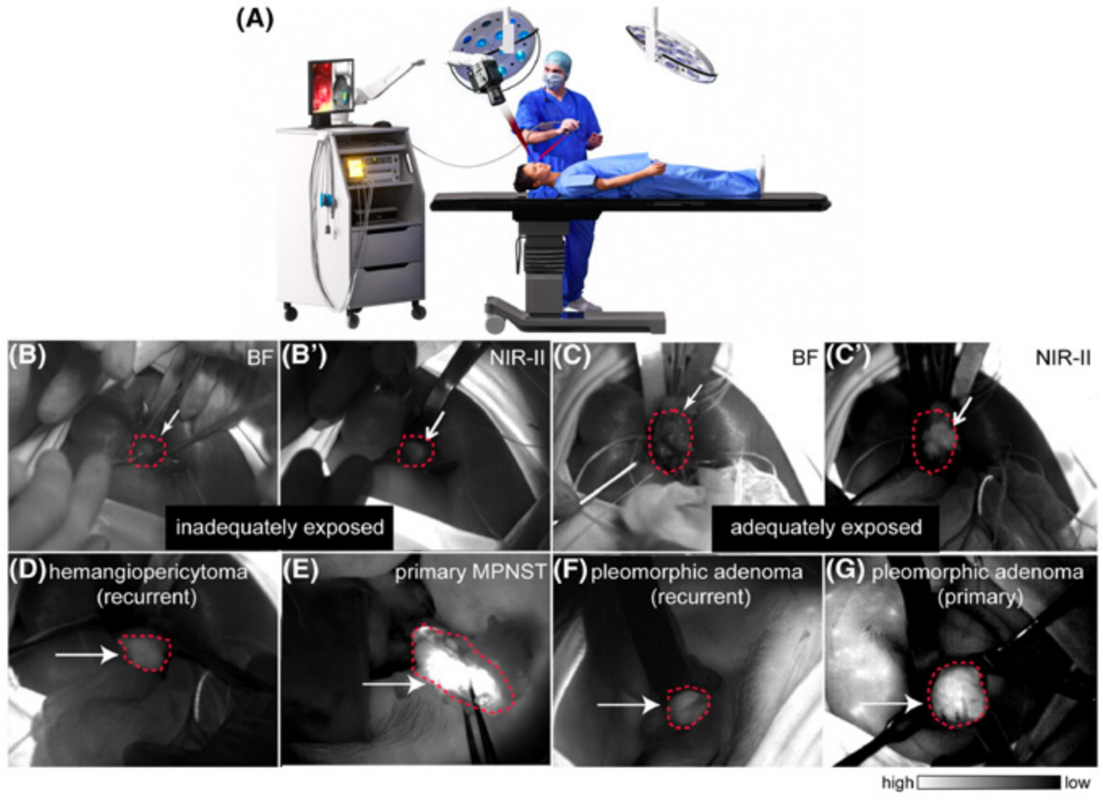


Fig.2 Intraoperative in situ NIR-II fluorescence imaging of patients with orbital tumors. (A) Application diagram of the intraoperative open-field NIR-II fluorescence imaging. **(B and B')** Bright field image and corresponding NIR-II fluorescence imaging of unfully-exposed orbital tumor (hemangiopericytoma). **(C and C')** BF image and corresponding NIR-II fluorescence imaging of fully-exposed orbital tumor, which was the same as the tumor in B and B'. Red dotted circles and arrows indicate the orbital tumors. **(D)** Intraoperative in situ NIR-II fluorescence imaging of the main body of recurrent orbital hemangiopericytoma. **(E)** Intraoperative in situ NIR-II fluorescence imaging of the main body of recurrent orbital malignant peripheral nerve sheath tumor. **(F, G)** Intraoperative in situ NIR-II fluorescence imaging of the main body of recurrent and primary orbital pleomorphic adenoma.

optimal TNR cutoff of 1.21 produced the highest sum of sensitivity (92.6%) and specificity (93.7%) based on the data of 86 samples. For the 44 suspicious para tumor tissues, the optimal TNR cutoff remained 1.21 with 85.7% sensitivity and 93.7% specificity. Compared with the surgeon and in situ imaging, ex vivo NIR‐II fluorescence imaging using a TNR cutoff of 1.21 showed the highest sensitivity (93.3%) and specificity (85.7%) for the same 22 samples (Table 1). The AUC of ex vivo NIR-II fluorescence imaging was also higher than that of the surgeon (0.895 vs. 0.548). Besides, ex vivo NIR-II imaging showed good correspondence between the fluorescence signal and tumor status on histopathology and higher TNR than NIR-I imaging (Figure S5). Notably, the ex vivo NIR-II fluorescence imaging and quantitative analysis could be finished in about 2 min, allowing real-time intraoperative identification of tumors.

Clinical value of intraoperative NIR-II fluorescence imaging for guiding precise resection of orbital tumors

To assess the clinical value of intraoperative NIR-II fluorescence imaging, we studied the effect of this imaging method on intraoperative decision making (Figure S1, part III). Firstly, according to visualization and palpation, the primary surgeon (X.Y.) made an initial judgment about whether the suspicious regions (such as wound bed or para tumor tissue) contained tumor tissues and whether they needed surgical resection. Then, intraoperative NIR-II fluorescence imaging was used to identify the suspicious regions. Finally, the primary surgeon (X.Y.) makes a final decision on whether to remove the tissue. We encountered 34 suspicious regions in five orbital tumor patients, all of which were adequately exposed and underwent in situ NIR-II fluorescence imaging. Notably, the in situ NIR-II fluorescence imaging changed surgical decisions in 9 suspicious regions from the 5 patients (26.5%): 7 additional resections and 2 conservative treatments (Table S3). Histopathology confirmed that all the 7 additionally resected tissues contained tumors, which was of great significance to reduce tumor recurrence and improve prognosis. Besides, the 5 patients did not experience recurrence during an average follow-up period of 31.6 months post-surgery.

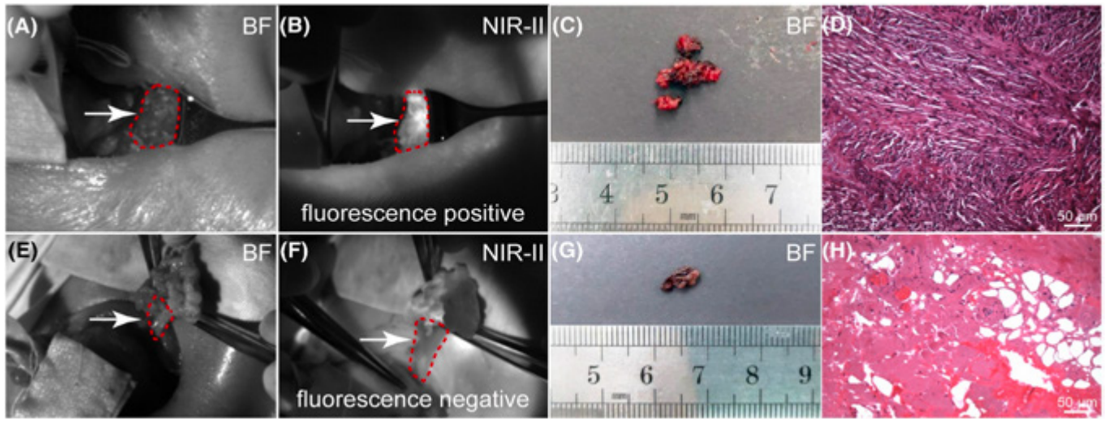


Fig.3 In situ NIR-II fluorescence imaging and pathological examination for suspicious lesions. (A, B) BF image and corresponding NIR-II fluorescence imaging of the tumor bed in the open field. Red dotted circles and arrows indicate the region of interest where the surgeon needed an auxiliary diagnosis. The area of interest was judged as fluorescence positive by the surgeon. **(C, D)** BF image and corresponding H&E staining of the resected sample as shown in A, B. Pathological examination showed that the sample contained neoplastic tissue. **(E, F)** BF image and corresponding NIR-II fluorescence imaging of the para tumor tissue in the open field. Red dotted circles and arrows indicate the region of interest where the surgeon needed an auxiliary diagnosis. The area of interest was judged as fluorescence negative by the surgeon. **(G, H)** BF image and corresponding H&E staining of the resected sample as shown in E, F. Histological examination showed that there was no neoplastic tissue in the sample. BF, bright field.

Table 1 Diagnostic accuracy of surgeons and NIR-II fluorescent imaging.

	Surgeon		In situ fluorescent imaging		Ex vivo fluorescent imaging	
	Positive	Negative	Positive	Negative	Positive	Negative
Histopathology positive	10	5	12	3	14	1
Histopathology negative	4	3	2	5	1	6
Sensitivity (CI[a])	66.7% (38.7%–87.0%)		80.0% (51.4%–94.7%)		93.3% (66.0%–99.7%)	
Specificity (CI)	42.8% (11.8%–79.7%)		71.4% (30.3%–94.9%)		85.7% (42.0%–99.2%)	
AUC (CI)	0.548 (0.282–0.813)		0.757 (0.525–0.989)		0.895 (0.724–1.000)	

[a]CI, confidence interval.

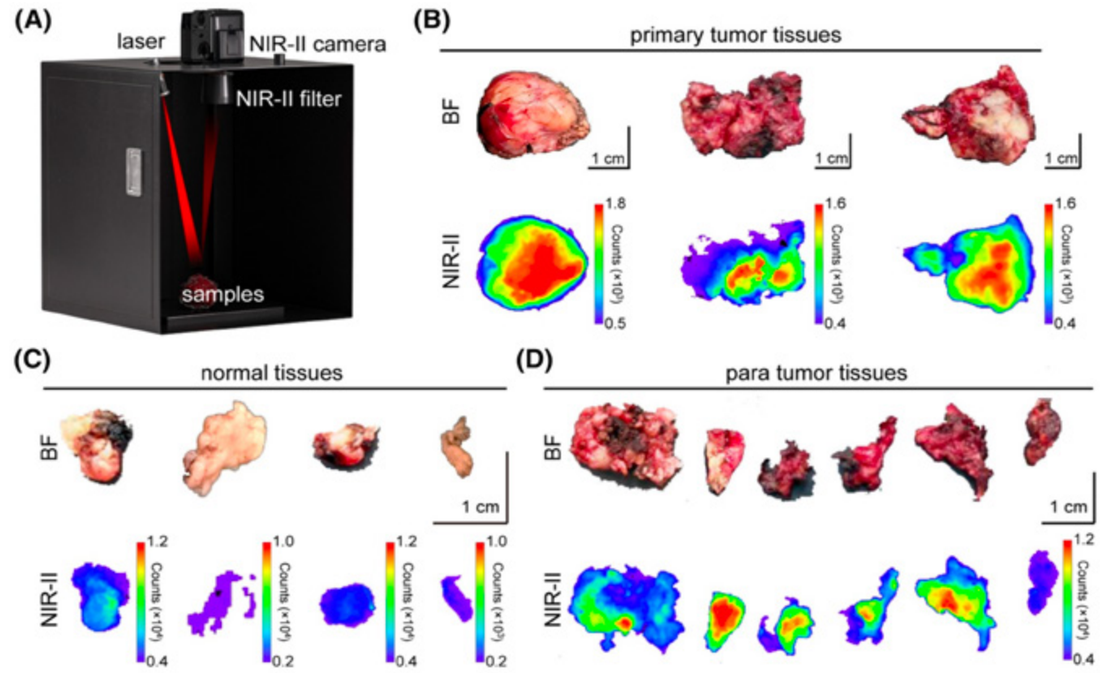


Fig.4 Closed-field ex vivo NIR-II fluorescence imaging. (A) Schematic diagram of the closed-field NIR-II fluorescence imaging. **(B–D)** Representative bright field images and corresponding NIR-II fluorescence imaging of primary tumor tissues, normal tissues and para tumor tissues.

Safety of NIR-II fluorescence imaging

Compared with the standard-of-care surgery, fluorescence-guided surgery requires extra ICG administration and irradiation with an infrared laser. In our study, injection of ICG did not induce any adverse drug events. We also did not find redness, swelling, painless of irradiation site, or vision loss as a result of the laser irradiation.

Discussion

Surgery of orbital tumors is characterized by small incisions, limited resectable tissue mass and complicated anatomy structures. The precise resection of orbital tumors has always been a challenge. As far as we know, this is the first-in-human study regarding the use of NIR-II fluorescence guidance for precision resection of orbital tumors.

It is well known that ICG, as a nonspecific probe, is capable to accumulate in many kinds of solid tumors via the enhanced permeability and retention (EPR) effect.[16] Besides, there was a direct correlation between the fluorescence intensity of ICG within the tumor and gadolinium-enhancement on the preoperative MRI.[17] Consistently, we also found that ICG-based NIR-II fluorescence imaging can localize gadolinium-enhancing orbital malignant and benign tumors. However, whether ICG could accumulate in non-neoplastic mass is rarely reported. There are only some clinic reports that choroidal granulomas (a kind of ocular inflammatory mass) are hypofluorescent on ICG angiography.[18, 19] In this work, we found that after systemic administration of ICG, the non-neoplastic masses (inflammatory and cyst masses) were nonfluorescent or hypofluorescent. Our study pro-

vided a strong support for the ICG-based fluorescence imaging to identify orbital tumors. However, due to the small sample size, more caution is needed when extrapolating our observations to draw a conclusion that non-neoplastic masses could not be visualized by ICG fluorescence.

Through dynamic imaging, we found that the TNR of NIR-II fluorescence imaging of the orbital tumor peaked at 2 h post intravenous injection of 0.7 mg kg^{-1} body weight ICG. Considering that the half-life time of ICG in blood is 2.5–3 min, we believed that ICG was quickly cleared from the orbital normal tissues. Consistently, Yokoyama and colleagues have also suggested that for head and neck cancers, the optimum surgical time in NIR fluorescent image-guided surgery is from 30 min to 2 h after the ICG injection due to the higher tumor visibility.[20]

High-quality in situ NIR-II fluorescence imaging of orbital tumors could be achieved only when the tumors are adequately exposed. In addition to fluorescence imaging itself, how to assess the fluorescence images is of great significance to real time guide surgical decisions. Considering the in situ open-field fluorescence imaging was susceptible to interference from ambient light, reflectance, and imaging angles, especially in the orbit with complex and heterogeneous topography, it was impractical to perform rigorous and objective imaging analysis.[21, 22] As a result, the fluorescence images were interpreted by three assessors by qualitatively comparing the fluorescence intensity of the region of interest to that of the adjacent normal tissue. Similarly, Liberale and colleagues also qualitatively assess the in situ fluorescence images in the ICG-based fluorescence navigation surgery for peritoneal carcinomatosis from colorectal cancer.[8] As a supplement to in situ fluorescence imaging, ex vivo NIR-II fluorescence imaging is especially suitable for real-time intraoperative identification of inadequately exposed lesions. We quantitatively calculated the TNR of ex vivo fluorescence images with each patient's own normal tissue served as control to minimize the variations in tumor physiology, tissue properties, timing and clearance.[23] Previous studies have shown that TNR is independent of ICG dose, tumor size and tumor histology.[7, 17] By statistical analysis, TNR 1.21 was set as the critical value for the objective identification of surgeon's suspicious samples, which showed a high sensitivity (92.6%) and specificity (93.7%). However, the TNR cutoff of 1.21 might be inapplicable to the other oncologic settings. Previously, we have developed ex vivo NIR-II fluorescence imaging coupled with artificial intelligence technique for real-time intraoperative identification of glioma, which achieves a high sensitivity (93.8%) and specificity (82.2%).[24] However, using artificial intelligence techniques demands extensive amounts of data, which is impractical for the clinically rare tumors. Notably, for the regions of interest where the surgeon needed auxiliary diagnosis, both the in situ and ex vivo NIR-II fluorescence imaging showed better diagnostic accuracy than the surgeon judgment through conventional methods, which suggested that ICG-based NIR-II fluorescence imaging had important clinical implications for the orbital tumor surgery.

Although ICG-based intraoperative fluorescence imaging has preliminarily proved its safety and efficacy, many clinical trials mainly focus on diagnosis performance and it is unclear whether patients benefit from this innovation.[25] More recently, Keereweer and colleagues suggested that the effect of fluorescence-guided surgery on intraoperative decision making is the most objective outcome measurement to assess the clinical value of this imaging method.[11] With the aid of in situ NIR-II fluorescence imaging, the surgeon changed nine intraoperative decisions and seven additional resections were justified by histopathology, which increased the probability of complete resections. Besides, the 2 conservative treatments did not result in recurrence. Although the proportion of changing surgical decisions resulting from NIR-II fluorescence imaging was only 26.5%, this approach held great promise for clinical application due to its safety and economy. Notably, the surgeon in our study was very experienced in orbital tumors surgery, which suggested that ICG-based intraoperative fluorescence imaging may provide greater assistance for newly trained orbital surgeons. As a result, there is reason to believe that the NIR-II fluorescence imaging could improve the oncological and functional outcomes. Consistently, in a landmark randomized controlled trial, fluorescence-guided surgery with 5-aminolevulinic acid has been proven to enable more complete resections of malignant glioma and improve progression-free survival.[26] More recently, Rosenthal and colleagues have reported that panitumumab-IRDye800CW based fluorescence imaging improved surgical decision making in 3 cases out of 14 patients (21.4%).22 Although molecular imaging improves the specificity, the development and clinical translation of cancer-specific fluorescence imaging contrasts is time-consuming and expensive.[16, 27]

Although our study provides a proof of concept of orbital tumor surgery guided by NIR-II fluorescence imaging, some important limitations should be addressed. Firstly, the limited sample size of 22 patients may constrain the generalizability of the findings. Secondly, subjective analysis of fluorescence imaging and convenience sampling could cause selection bias, information bias, and confounding bias. Another limitation was the lack of pre-specified TNR cut off to evaluate the fluorescence imaging results.

Taken together, our study showed that ICG-based NIR-II fluorescence imaging was feasible to guide precise resection of orbital tumors. We should develop an objective and real-time method for analyzing fluorescence imaging results in future studies. Furthermore, a larger sample size with random sampling is recommended to prove the clinical value of NIR-II fluorescence imaging in the precise resection of orbital tumors.

Funding information

Postdoctoral Science Foundation of China, Grant/Award Numbers: 2018M643859, 2021M690007: National Natural Science Foundation of China, Grant/Award Numbers: 62027901, 92059207, 8193053, 81227901, 8210236; Beiing Clinical Distinctive Diagnosis and Treatment Technology Research and Transformation Project, Grant/Award Number. 2210007422089; National Key Research and Development Program of China, Grant/Award Number: 2017YFA020520; Being Natural Science Foundation, Grant/Award Number: 1019027: CAS Youth Interdisciplinary Team, Grant/Award Number: JCTD-2021-08

Conflict of interest statement

The authors declare no conflict of interests.

Ethics statement

This study was performed according to the tenets of the Declaration of Helsinki, approved by the ethics committee of the 3rd Medical Center of Chinese PLA General Hospital (2020-004), and registered at the Chinese Clinical Trial Registry (ChiCTR2000039908). All participants were informed about the main study information (including the research objective, experimental procedures, potential adverse events, etc.), and gave written consent before data collection.

Consent for publication

We have got the consents for publication from the patients.

Acknowledgments

This work was supported by the Beijing Clinical Distinctive Diagnosis and Treatment Technology Research and Transformation Project (Z221100007422089), Postdoctoral Science Foundation of China (2018M643859, 2021M690007), National Key Research and Development Program of China (2017YFA0205200), National Natural Science Foundation of China (62027901, 92059207, 81930053, 81227901, 82102236), Beijing Natural Science Foundation (JQ19027), and CAS Youth Interdisciplinary Team (JCTD-2021-08).

References

1. N. Weizman, G. Horowitz, Z. Gil, D. M. Fliss, JAMA Otolaryngol. Head Neck Surg. 2013, 139, 841.
2. M. S. Alam, A. Tongbram, S. Krishnakumar, J. Biswas, B. Mukherjee, Indian J. Ophthalmol. 2019, 67, 1988.
3. S. Fakurnejad, G. Krishnan, S. van Keulen, N. Nishio, A. C. Birkeland, F. M. Baik, M. J. Kaplan, A. D. Colevas, N. S. van den Berg, E. L. Rosenthal, B. A. Martin, Front. Oncol. 2020, 9, 1476.
4. R. Liu, Y. Xu, K. Xu, Z. Dai, Aggregate 2021, 2, e23.
5. C. Wu, J. Gleysteen, N. T. Teraphongphom, Y. Li, E. Rosen thal, Int. J. Oral Sci. 2018, 10, 10.
6. T. Ishizawa, N. Fukushima, J. Shibahara, K. Masuda, S. Tamura, T. Aoki, K. Hasegawa, Y. Beck, M. Fukayama, N. Kokudo, Cancer 2009, 115, 2491.
7. A. D. Newton, J. D. Predina, M. H. Shin, L. G. Frenzel‐Sulyok, C. M. Vollmer, J. A. Drebin, S. Singhal, M. K. Lee, Ann. Surg. 2019, 270, 12.
8. G. Liberale, S. Vankerckhove, M. G. Caldon, B. Ahmed, M. Moreau, I. E. Nakadi, D. Larsimont, V. Donckier, P. Bourgeois, Ann. Surg. 2016, 264, 1110.
9. J. Y. K. Lee, J. T. Pierce, J. P. Thawani, R. Zeh, S. Nie, M. Martinez‐Lage, S. Singhal, J. Neurosurg. 2018, 128, 380.
10. F. Nicoli, D. B. Saleh, B. Baljer, C. D. Chan, T. Beckingsale, K. M. Ghosh, M. Ragbir, K. S. Rankin, Ann. Surg. 2021, 273, e63.
11. L. J. Lauwerends, P. B. A. A. van Driel, R. J. Baatenburg de Jong, J. A. U. Hardillo, S. Koljenovic, G. Puppels, L. Mezza notte, C. W. G. M. Löwik, E. L. Rosenthal, A. L. Vahrmeijer, S. Keereweer, Lancet Oncol. 2021, 22, e186.
12. G.Hong, A.L.Antaris, H. Dai, Nat. Biomed. Eng. 2017, 1, 0010.
13. G.Deng, S. Zhang, X. Peng, L. Liu, Y. Tan, P. Gong, B. Z. Tang, L. Cai, P. Zhang, Chem. Biomed. Imaging 2024. https://doi.org/ 10.1021/cbmi.4c00011
14. J. A. Carr, D. Franke, J. R. Caram, C. F. Perkinson, M. Saif, V. Askoxylakis, M.Datta, D.Fukumura, R.K.Jain, M.G.Bawendi, O. T. Bruns, Proc. Natl. Acad. Sci. USA 2018, 115, 4465.
15. Z. Hu, C. Fang, B. Li, Z. Zhang, C. Cao, M. Cai, S. Su, X. Sun, X. Shi, T. Zhou, Y. Zhang, C. Chi, P. He, X. Xia, Y. Chen, S. S. Gambhir, Z. Cheng, J. Tian, Nat. Biomed. Eng. 2020, 4, 259.
16. E. Rosenthal, J. Warram, K. Bland, K. Zinn, Ann. Surg. 2015, 261, 46.
17. J. Y. Lee, J. P. Thawani, J. Pierce, R. Zeh, M. Martinez‐Lage, M. Chanin, O. Venegas, S. Nims, K. Learned, J. Keating, S. Sin ghal, Neurosurgery 2016, 79, 856.
18. Y. S. Modi, A. Epstein, S. Bhaleeya, J. W. Harbour, T. Albini, J. Ophthal. Inflamm. Infect. 2013, 3, 58.
19. A. Invernizzi, C. Mapelli, F. Viola, M. Cigada, L. Cimino, R. Ratiglia, G. Staurenghi, A. Gupta, Retina 2015, 35, 525.
20. J. Yokoyama, M. Fujimaki, S. Ohba, T. Anzai, R. Yoshii, S. Ito, M. Kojima, K. Ikeda, Onco-Targets Ther. 2013, 6, 325.
21. S. van Keulen, N. Nishio, S. Fakurnejad, N. S. van den Berg, G. Lu, A. Birkeland, B. A. Martin, T. Forouzanfar, D. A. Colevas, E. L. Rosenthal, J. Am. Coll. Surg. 2019, 229, 560.
22. S. van Keulen, N. Nishio, S. Fakurnejad, A. Birkeland, B. A. Martin, G. Lu, Q. Zhou, S. U. Chirita, T. Forouzanfar, A. D. Colevas, N. S. van den Berg, E. L. Rosenthal, J. Nucl. Med. 2019, 60, 758.
23. W.S.Tummers, J. M. Warram, N. S. van den Berg, S. E. Miller, R. J. Swijnenburg, A. L. Vahrmeijer, E. L. Rosenthal, Thera nostics 2018, 8, 5336.
24. B. Shen, Z. Zhang, X. Shi, C. Cao, Z. Hu, N. Ji, J. Tian, Eur. J. Nucl. Med. Mol. Imaging 2021, 48, 3482.
25. F. Dip, L. Boni, M. Bouvet, T. Carus, M. Diana, J. Falco, G. C. Gurtner, T. Ishizawa, N. Kokudo, E. Lo Menzo, P. S. Low, J. Masia, D. Muehrcke, F. A. Papay, C. Pulitano, S. Schneider Koraith, D. Sherwinter, G. Spinoglio, L. Stassen, Y. Urano, A. Vahrmeijer, E. Vibert, J. Warram, S. D. Wexner, K. White, R. J. Rosenthal, Ann. Surg. 2022, 275, 685.
26. W. Stummer, U. Pichlmeier, T. Meinel, O. D. Wiestler, F. Zanella, H. J. Reulen, Lancet Oncol. 2006, 7, 392.
27. Y. Liao, Z. Peng, X. Liu, Y. Hu, J. Zhang, Interdiscip. Med. 2023, 1, e20230024.

Interdiscip Med. 2025. 3(1):e20240048 Published online: 9 January 2025

Stomatology

Research Article

Near-Infrared Fluorescence Imaging With an MET-Targeting Probe for Biopsy Site Selection in Patients with Oral Potentially Malignant Disorders

Jingbo Wang[1,*], Xuemin Shen[2,3,*], Qifan Ma[1,*], Lin Yang[1,4,*], Xiaoyu Zhou[5], Luting Wang[5], Junqi Cui[6], Chunye Zhang[6], Guojun Li[7], Neil Gross[7], Siyi Li[3,8], Ruimin Huang[9], Changyou Zhan[10], Zhen Cheng[5], Kun Wang[11], Jie Tian[11] ✉, Ying Yuan[1] ✉, and Xiaofeng Tao[1,13] ✉

Summary

Accurate detection of malignant transformation in oral potentially malignant disorders (OPMDs) is crucial for guiding effective treatment and improving patient management. This study evaluates the potential of MET-binding peptide-indocyanine green (cMBP-ICG), a mesenchymal-epithelial transition factor (MET)-targeted near-infrared fluorescence imaging (NIRFI) probe, for biopsy site selection in OPMDs. Preclinical results demonstrate the superior accuracy of NIRFI-assisted biopsy over conventional oral examination (COE)-based biopsy in detecting high-grade dysplasia (HGD) or squamous cell carcinoma (SCC) and reducing missed detection rates. In a clinical trial with 50 patients, NIRFI-assisted biopsy achieves significantly higher diagnostic accuracy compared to COE-based biopsy (91% vs. 72%, p = 0.0005). These findings underscore the importance of NIRFI in enhancing diagnostic precision, supporting early detection and enabling timely and accurate treatment interventions for patients with OPMDs. The clinical trial is registered under the registration number ChiCTR2300074454.

Cell Rep Med. 2025; 12:101978 Published online: 24 February 2025

[1] Department of Radiology, Shanghai Ninth People's Hospital, Shanghai Jiao Tong University School of Medicine, Shanghai 200011, China
[2] Department of Oral Mucosal Diseases, Shanghai Ninth People's Hospital, College of Stomatology, Shanghai Jiao Tong University School of Medicine, Shanghai 200011, China
[3] National Clinical Research Center for Oral Diseases, Shanghai Key Laboratory of Stomatology & Shanghai Research Institute of Stomatology, Shanghai 200011, China
[4] Department of Radiology, Fujian Branch of Shanghai Children's Medical Center, Fujian Children's Hospital, Fujian 350014, China
[5] State Key Laboratory of Drug Research, Molecular Imaging Center, Shanghai Institute of Materia Medica, Chinese Academy of Sciences, Shanghai 201203, China
[6] Department of Pathology, Shanghai Ninth People's Hospital, Shanghai Jiao Tong University School of Medicine, Shanghai 200011, China
[7] Department of Head and Neck Surgery, The University of Texas MD Anderson Cancer Center, Houston, TX 77030, USA
[8] Department of Oral & Maxillofacial-Head & Neck Oncology, Shanghai Ninth People's Hospital, College of Stomatology, Shanghai Jiao Tong University School of Medicine, Shanghai 200011, China
[9] Center for Drug Safety Evaluation and Research, Shanghai Institute of Materia Medica, Chinese Academy of Sciences, Shanghai 201203, China
[10] Department of Pharmacology, School of Basic Medical Sciences & Center of Medical Research and Innovation, Shanghai Pudong Hospital & State Key Laboratory of Molecular Engineering of Polymers, Fudan University, Shanghai 200433, China
[11] CAS Key Laboratory of Molecular Imaging, Beijing Key Laboratory of Molecular Imaging, The State Key Laboratory of Management and Control for Complex Systems, Institute of Automation, Chinese Academy of Sciences, Beijing 100190, China
* These authors contributed equally

Introduction

Oral potentially malignant disorders (OPMDs) are oral mucosal conditions with the potential to progress to oral squamous cell carcinoma (OSCC); the overall malignant transformation rate for OPMDs is 7.9%.[1] Presently, there is no effective method to prevent transformation of OPMDs to OSCC. Consequently, timely and accurate detection of malignant transformation of OPMDs is critical for improving prognosis. Notably, reported rates of early diagnosis of in situ OSCC are only 44%–55%.[2,3]

The method most employed for early detection of malignant transformation of OPMDs is conventional oral examination (COE)-based biopsy, which involves biopsy of suspected sites of disease under white light inspection and palpation. However, COE-based biopsy is highly subjective and relies heavily on the clinician's experience. Various auxiliary methods have been used to identify malignant progression of OPMDs, including vital staining, oral cytology, and light-based techniques, but none has demonstrated a significant improvement in diagnostic accuracy compared to COE-based examination.[4] Therefore, it is imperative to explore additional diagnostic adjuncts to enhance the early detection of OPMDs.

In recent years, optical techniques, such as near-infrared fluorescence imaging (NIRFI) following topical application of near-infrared fluorescence (NIRF) probes, have exhibited significant potential in diagnosing superficial solid tumors.[5,6] By applying probes targeting specific biomarkers to the mucosal surface and performing visual inspections using NIRFI, one can detect small mucosal lesions and achieve early cancer diagnosis, such as PARPi-FL for oral cancer detection[7] and IRdye800-antiCD44v6 for invasive bladder cancer detection.[8] Surface application of probes is rapid and noninvasive and particularly suitable for superficial lesions such as OPMDs.

Mesenchymal-epithelial transition factor (MET) plays a crucial role in tumorigenesis by activating the hepatocyte growth factor (HGF)/MET pathway, which triggers key signaling molecules such as protein kinase B (AKT) and mitogen-activated protein kinase.[9] This activation drives early tumor cell proliferation, survival, and invasion, marking the initial stages of cancer development.[10] Dysregulation of MET signaling is a significant factor in the

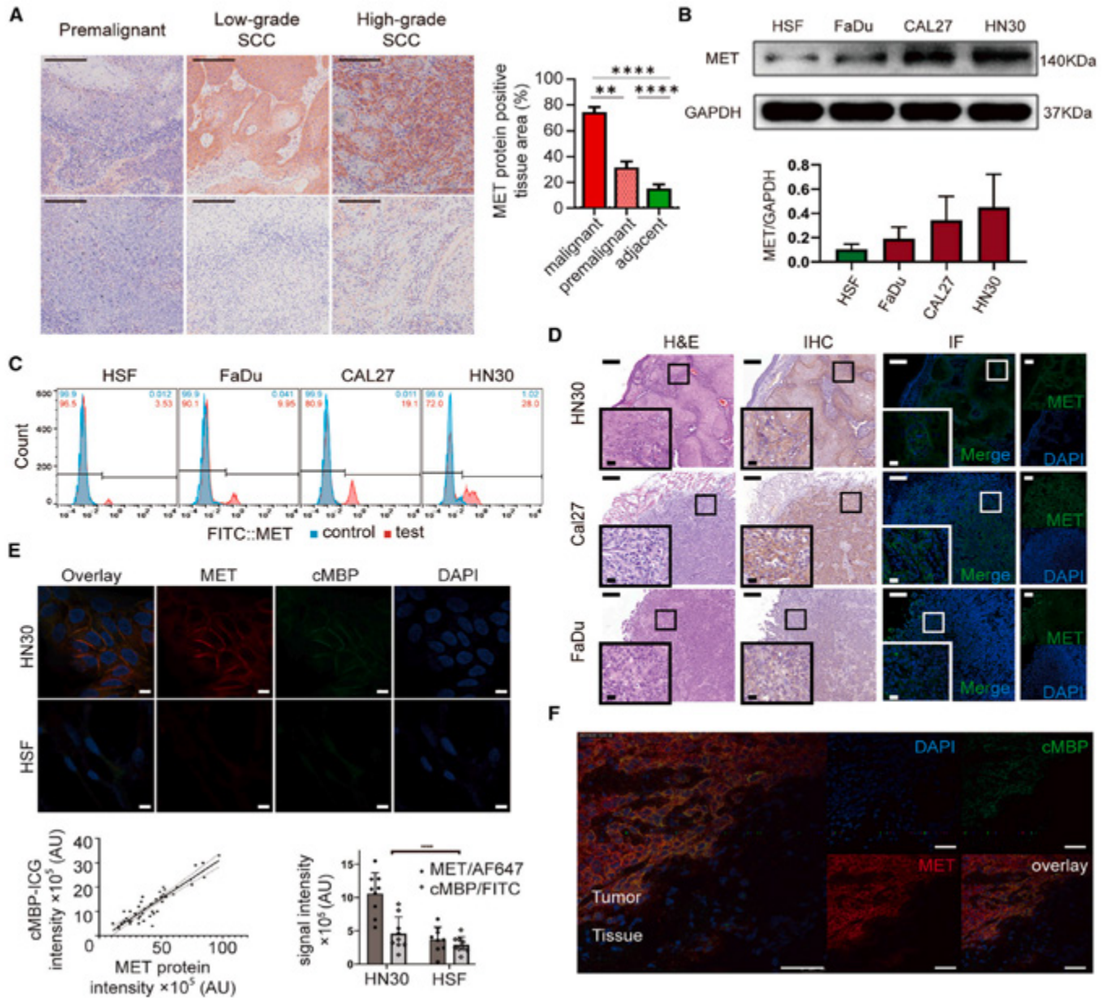


Fig.1 Verification of elevated MET expression in patient samples and orthotopic tumor tissues.
(A) Immunohistochemical detection of MET using an anti-MET antibody in various grades of OSCC (top row) and adjacent normal epithelial tissues (bottom row). Brown: MET-positive tissue. Blue: hematoxylin counterstain. Bar graph, mean (SD) proportion of tissue area positive for MET expression was 74.50% (9.8%) in malignant tissues, 31.67% (14.8%) in premalignant tissues, and 15.11% (9.6%) in adjacent normal epithelial tissues. Malignant vs. premalignant, $p < 0.0001$; malignant vs. adjacent, $p < 0.0001$; premalignant vs. adjacent, $p = 0.0027$. Scale bars, 250 μm. n (specimens) = 9 biological replicates. Data are represented as mean ± SEM, with error bars shown only above the mean, analyzed using unpaired Student's t test. **p < 0.01, ****p < 0.0001.
(B and C) (B) Western blot analysis of MET protein levels in cell lines FaDu, CAL27, and HN30 and control keratin epithelial cell line HSF (top). Bar graph quantification of MET expression (bottom). (C) Quantitative measurement of expression levels of FITC-conjugated MET in OSCC cell lines and control keratin epithelial cell line by flow cytometry. Data are represented as mean ± SEM, with error bars shown only above the mean. (B and C) n (HSF, CAL27, HN30, and FaDu) = 3 biological replicates.
(D) H&E staining (left), immunohistochemical detection (middle), and immunofluorescence (right) of MET expression in oral SCC orthotopic tumor tissues. Blue: DAPI-stained nuclei. Green: AF647-conjugated MET. The long horizontal scale bars correspond to 200 μm, while the short horizontal scale bars represent 20 μm. n (ex vivo sections) = 9 biological replicates.
(E) Localization of cMBP/FITC in HN30 and HSF cells via confocal imaging. Blue: DAPI-stained nuclei. Green: FITC-labeled cMBP. Red: AF647-conjugated anti-MET. Scale bars, 10 μm. Correlation in HN30 cells was evaluated with Pearson R-squared test. Pixel intensity of nine regions of interest from three cell slide pairs analyzed with ImageJ. n (cell slides) = 3 biological replicates. Data are represented as mean ± SEM, with error bars shown only above the mean, analyzed using unpaired Student's t test. ****p < 0.0001.
(F) After intravenous injection of cMBP-ICG into OSCC nude mouse model, tumor tissues were harvested, frozen sections were prepared, and the distribution of MET in the frozen sections was assessed via immunofluorescence staining. Blue: DAPI-stained nuclei. Green: cMBP-ICG. Red: AF647-conjugated anti-MET. Scale bars, 50 μm. n (negative control group, cMBP-ICG injection group, and ICG injection group) = 3 biological replicates.

Cell Rep Med. 2025; 12:101978 Published online: 24 February 2025

onset of tumorigenesis, making it a critical target for preventing cancer initiation.[11] Notably, MET is overexpressed and aberrantly activated in over 80% of OSCC cases, compared to less than 30% in normal epithelial tissues,[12] highlighting its potential as a biomarker for early detection.[13,14] Our previously synthesized peptide-based NIRF dye, MET-binding peptide-indocyanine green (cMBP-ICG), has been demonstrated to specifically target OSCC by binding to MET, which enables the early detection of MET overexpression in the initial stages of OSCC development.[15]

The aim of this project was to determine whether cMBP-ICG-based NIRFI could improve the accuracy of biopsy site selection in OPMDs compared to COE. We first validated the expression levels of MET in different pathological tissue types using paraffin-embedded sections from biopsy specimens and surgical resection specimens from patients with OPMDs and OSCC. We then confirmed the in vitro and in vivo tumor-targeting capability of cMBP-ICG using OSCC cell lines and an orthotopic mouse model of OSCC. Further, we evaluated the utility of NIRFI with cMBP-ICG in biopsy site selection for OPMDs using the 4-nitroquinoline 1-oxide (4-NQO) mouse model. Subsequently, we conducted an exploratory clinical trial of NIRFI with cMBP-ICG involving 50 subjects with OPMDs.

Results

Toxicity of cMBP-ICG

Statistical analysis revealed significant alterations in white blood cell count, lymphocyte and neutrophil proportions, and serum albumin and total cholesterol levels at 24 h and 14 days after cMBP-ICG administration and a significant alteration in hemoglobin level at 14 days. No significant differences were observed in the results of other routine blood and biochemical tests between before and after cMBP-ICG administration (Figure S1; Table S1)

MET expression in human tongue tumors and adjacent nonmalignant tissue

In all of the human tongue tumor specimens, immunohistochemical analysis showed that high levels of MET expression deci sively distinguished tumor from normal tissue (Figure 1A). The percentage of tissue that stained positive for MET varied from 9.2% to 25.6% in normal tissue, whereas it varied from 23.0% to 82.0% in in precancerous tissue and cancerous tissue. The mean (SD) MET-positive area was 15.11% (9.6%) in nonmalignant tissue, 31.67% (14.8%) ($p = 0.0027$ vs. nonmalignant) in premalignant tissue, and 74.50% (9.8%) ($p < 0.0001$ vs. nonmalignant, $p < 0.0001$ vs. premalignant) in malignant tissue. On receiver operating characteristic (ROC) curve analysis, the best cutoff for separating tumor and normal tissue was found to be a 27.5% MET-positive area, which resulted in an area under the curve (AUC) of 0.9588, a sensitivity of 0.867, and a specificity of 0.933.

MET expression in cell lines

We previously proved the binding affinity between cMBP and MET.[15,16] To select the best cell line to study NIRFI with cMBP-ICG, we measured MET expression in OSCC cell lines: FaDu, CAL27, and HN30, which have high MET expression. Western blotting showed higher expression of MET in OSCCs than in HSF cells, while the difference between OSCCs was not significant (Figure 1B). Quantitative measurement of the expression levels of fluorescein isothiocyanate (FITC)-labeled MET in cells and HSF cells by flow cytometry showed MET positivity rates of 3.53% in HSF, 9.95% in FaDu, 19.1% in CAL27, and 28.0% in HN30 cells (Figure 1C). Thus, HN30 cells were chosen to build xenograft models of human MET-positive OSCC. H&E staining, immunohistochemistry staining, and immunofluorescence of ex vivo sections of these cell lines' subcutaneous tumor tissues showed regions with obvious positive findings compared to the findings in healthy tongue tissues (Figure 1D).

Colocalization of MET and cMBP in oral tumor tissue specimens

MET antibody staining colocalized with FITC-labeled cMBP fluorescence (Rcoloc. = 0.9145, R2 = 0.8363; 95% confidence interval [CI] 0.84670.9531) (Figure 1E). cMBP not only displayed the quantity of MET present in a cell but also bound specifically to cells that express MET.

In vivo optical imaging after cMBP-ICG local injection in CDX

To check the targeting of cMBP-ICG in vivo, we injected cMBP-ICG into the edge of three mice tongues without neoplasms (negative control) and performed tumor imaging with a DPM-III-01 fluorescence stereoscope. In addition, six cell-derived xenografts (CAL27) were randomly divided into two groups. Group 1 (n = 3) was the cMBP-ICG intratumorally injection group, and group 2 (n = 3) was the ICG intratumorally injection group. Fluorescence imaging (Figure S2) demonstrated substantial cMBP-ICG and ICG aggregation in tongue regions damaged by cancer but no signal aggregation in tongues without tumors after cMBP-ICG injection. The mean tumor-to-background ratio (TBR) was 3.697 (1.568) in the cMBP-ICG group, 2.849 (0.798) in the ICG group, and 0.906 (0.267) in the negative control group. The TBRs differed significantly between the cell-derived xenograft groups and the negative control group (both $p < 0.0001$). In comparison, there was no difference in TBR between the cMBP-ICG group and the ICG group ($p = 0.4363$). Of note, under the condition of local injection, the difference in mean fluorescence intensity (MFI) between the cMBP-ICG group and the negative control group was similar to that between the ICG group and the negative control group (Figure S2A). This may be due to the short time between injection and imaging. A longer time may result in washout of nontarget small-molecular-weight probes, such as ICG, while target probes, such as cMBP-ICG, remain. Strong retention of the probe after local injection was confirmed by correlating the cMBP-ICG signal with H&E and immunohistochemical staining of tongue sections (Figure S2B). The results showed that cMBP-ICG was targeted to OSCC. Under the condition of a fluorescence microscope with a corresponding excitation/emission band, cMBP-ICG can be directly used for fluorescence imaging of frozen sections without additional staining steps. Fluorescence staining in frozen histological slices exhibited green fluorescence (cMBP-ICG) in tumor areas, and MET/AF647 confirmed that the cMBP-ICG-positive areas demonstrated overexpression of MET (Figure 1F).

Carcinogenesis and MET expression in 4-NQO-treated mice

In the analysis of carcinogenesis and MET expression in 4-NQO-treated mice (Figure 2A), pathological analysis of 15 slides from the 15 mice in the control group revealed no lesion, while 60 slides from the 15 mice in the test group revealed multiple lesions (Figure 2B), including 62 cases of low-grade dysplasia (LGD), 48 cases of high-grade dysplasia (HGD), 6 cases of carcinoma in situ (CIS), and 5 cases of invasive carcinoma (ICA) (Figure 2C). The distribution of these lesion types over time is illustrated in Figure 2D. The mean (SD) number of lesions per mouse was 1.00 (0.76) at 12 weeks, 1.87 (1.19) at 16 weeks, 2.33 (1.18) at 20 weeks, and 2.87 (1.36) at 24 weeks (Figure 2C). The number of lesions differed significantly between normal controls and those killed at 16 weeks, 20 weeks, and 24 weeks, as well as between the mice killed at 12 weeks and those killed at 24 weeks ($p < 0.0001$) and between the mice killed at 12 weeks and those killed at 20 weeks ($p < 0.01$). Comparisons between other groups did not show significant differences (Table S2).

Representative findings on immunohistochemistry to assess MET expression in different stages of OPMDs and OSCCs are shown in Figure 2E. The mean (SD) MET-positive proportion of the total lesion area ("MET-positive area") was 31.6% (12.3%) for LGD, 63.9% (18.5%) for HGD, 63.0% (13.7%) for CIS, and 80.0% (14.3%) for ICA (Figure 2F). Findings on pairwise comparisons among the different pathological types are summarized in Table S3. Relationships between time since 4-NQO treatment and MET-positive area, lesion diameter, and lesion type are summarized in Figure 2G.

The performance of MET-positive area as a classifier of dysplasia versus carcinoma and as a classifier of LGD versus HGD or OSCC was evaluated using ROC curves. For all slides, MET expression differentiated dysplasia from carcinoma with a specificity of 0.74, sensitivity of 0.82, and AUC of 0.82. MET expression differentiated LGD from HGD or later malignancy with a specificity of 0.83, sensitivity of 0.93, and AUC of 0.94 (Figure 2H).

Real-time NIRFI-assisted biopsy in the 4-NQO-induced OSCC mouse model

NIRFI in the 4-NQO-induced OSCC mouse model (Figures S3A and S3B) revealed greater fluorescence signal intensity in the neoplastic regions than in the adjacent uninvolved mucosa (Figure S3C). Ex vivo NIRFI demonstrated a mean (SD) TBR of 6.3 (2.7) for the HGD and SCC cases and 1.8 (1.3) for the normal epithelia and LGD cases ($p = 0.003$). Ex vivo NIRFI demonstrated an MFI of 17.4 (8.9) arbitrary units (a.u.) for the HGD and SCC cases and 3.5 (9.2) a.u. for the normal epithelia and LGD cases ($p = 0.0007$). NIRFI-assisted biopsy had greater accuracy than COE-based biopsy for detecting HGD or SCC (0.90 vs. 0.77; $p < 0.0001$) (Table 1).

In the 4-NQO-induced OSCC mouse model, the mean (SD) detection rate for HGD and OSCC was higher for NIRFI-assisted biopsy than for COE-based biopsy (0.66 [0.27] vs. 0.39 [0.25], $p = 0.002$), and the difference was particularly pronounced in the mice with biopsy at 24 weeks ($p < 0.0001$) (Table 2). The mean (SD) missed detection rate for HGD and OSCC was lower for NIRFI-assisted biopsy than for COE-based biopsy (0.01 [0.04] vs. 0.36 [0.2], $p < 0.0001$).

A multivariate logistic regression analysis indicated that, compared to COE-based biopsy, NIRFI-assisted biopsy was associated with a significantly lower HGD and carcinoma missed detection rate (OR = 0.024, $p < 0.001$) and significantly higher HGD and carcinoma (OR = 8.14, $p < 0.001$) and carcinoma (OR = 3.62, $p = 0.04$) detection rates (Table S4). Compared to the mice with biopsy at 20 weeks, the mice with biopsy at 24 weeks had significantly higher detection rates for HGD and carcinoma (OR = 1.36, $p = 0.01$) and carcinoma (OR = 1.38, $p = 0.04$). The ROC curves from the multivariate logistic regression analysis yielded an AUC of 0.80 for NIRFI-assisted biopsy ($p < 0.0001$), indicating high accuracy and statistical significance in the detection rates (Figure S4).

Clinical study of NIRFI-assisted biopsy for patients with OPMDs

Patient characteristics

From June through December 2023, 76 patients were assessed and 50 were enrolled and randomly assigned to the NIRFI-assisted biopsy group (25 patients; mean age 56.4 [SD 11.2] years; 11 men [44%]) or the COE-based biopsy group (25 patients; mean age 54.4 [SD 14.4] years; 9 men [36%]). Participant demographics and baseline characteristics were similar between the groups (Table S5). Age, biopsy type (COE-based vs. NIRFI-assisted), and baseline oral fluorescence signal intensity were similar between the pathologically positive (HGD or OSCC) and pathologically negative (normal epithelium or LGD) groups (Table S6).

Diagnostic accuracy

Each patient had two biopsy sites selected, one was based on COE and the other on the basis of NIRFI, for a total of 100 selected biopsy sites (Figure 3). In 46 of the 50 patients, the two biopsy sites were concordant.

Based on NIRFI, 65 biopsy sites were classified as negative (normal epithelium or LGD) and 35 were classified as positive (HGD or OSCC); based on COE, 50 biopsy sites were classified as negative and 50 were classified as positive. Final pathological results were negative for 64 biopsy sites and positive for 36 biopsy sites. Representative fluorescence images of patients are shown in Figure 4A. The MFI and TBR for all biopsy sites are presented in Figure 4B. The diagnostic performance of NIRFI-assisted biopsy and COE-based biopsy is presented in Table 3. Figure 4C presents two cases where the biopsy sites selected by NIRFI and COE did not align. NIRFI-assisted biopsy demonstrated higher accuracy, sensitivity, specificity, positive predictive value, and negative predictive value. ROC curves were generated for both groups (Figure 4D) and showed AUCs of 0.91 for the NIRFI-assisted biopsy group and 0.71 for the COE-based biopsy group.

Quantification of cMBP-ICG fluorescence

For the pathologically negative and pathologically positive groups, respectively, mean (SD) cMBP-ICG fluorescence values were as follows: pre-wash MFI, 72 (42) a.u. and 106 (48) a.u. ($p = 0.01$); after-wash MFI, 47 (48) a.u. and 70 (50) a.u. ($p = 0.12$); pre-wash TBR, 1.2 (0.56) and 1.7 (0.55 ($p = 0.002$); and after-wash TBR, 1.3 (1.1) and 2.9 (0.99 ($p < 0.0001$) (Figure 4E). ROC curves for distinguishing between pathologically negative and positive lesions using four different indicators are shown in Figure

Cell Rep Med. 2025; 12:101978 Published online: 24 February 2025

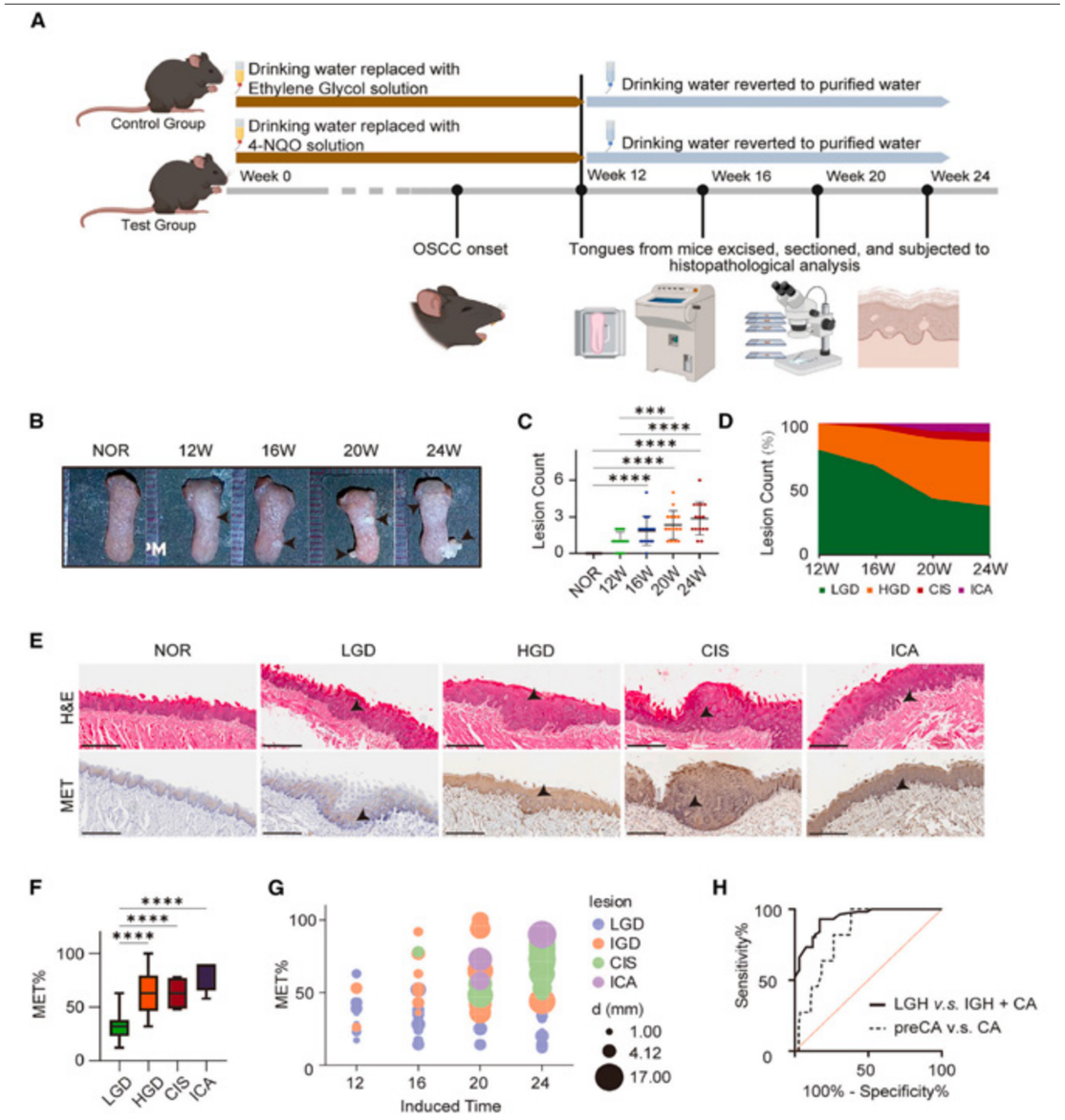


Fig.2 Lesion development and MET expression in the 4-NQO-induced OSCC mouse model.
(Aand B) (A) Overview of the experiments. Three mice from each group were killed at 0, 12, 16, 20, and 24 weeks. Tissue samples from the tongues of sacrificed mice were collected and subjected to histopathological examination after magnetic resonance imaging. (B) Typical presentations of tongue lesions in mouse model at different times after 4-NQO initiation. NOR, normal controls; W, weeks. (A and B) n (control) = 15, n (4-NQO-treated mice) = 15 biological replicates.
(C) Number of lesions of different pathological types at various times after 4-NQO initiation. Data are represented as mean ± SEM, analyzed using unpaired Student's t test. ***$p < 0.001$, ****$p < 0.0001$.
(D) Distribution of lesions of different pathological types at different times after 4-NQO initiation. W, weeks.
(E) H&E staining (top) and immunohistochemistry staining (bottom) of lesions of different pathological types. NOR, normal controls. Scale bars, 300 μm.
(F) Percentage of lesion area positive for MET for lesions of different pathological types. Data are represented as mean ± SEM, analyzed using unpaired Student's t test. ****$p < 0.0001$.
(G) Percentage of lesion area positive for MET, lesion diameter, and distribution of lesions of different pathological types at different times after initiation of 4-NQO.
(H) Receiver operating characteristic (ROC) curves evaluating the performance of MET-positive area as a classifier.
(C–H) n (lesions) = 121 biological replicates.

Table 1 Diagnostic performance of NIRFI-assisted biopsy and COE-based biopsy in mouse tongue lesions

	NIRFI-assisted biopsy			COE-based biopsy		
	20 weeks	24 weeks	Combined	20 weeks	24 weeks	Combined
Sensitivity	0.87	0.79	0.86	0.65	0.50	0.59
Specificity	0.82	0.89	0.93	0.82	0.89	0.89
PPV	0.69	0.83	0.89	0.63	0.75	0.79
NPV	0.93	0.86	0.91	0.84	0.72	0.76
Accuracy	0.84	0.85	0.90	0.77	0.73	0.77

COE, conventional oral examination; NIRFI, near-infrared fluorescence imaging; NPV, negative predictive value; PPV, positive predictive value. A positive test result is defined as a lesion with a pathological diagnosis of high-grade dysplasia (HGD) or squamous cell carcinoma (SCC). A negative test result is defined as a lesion with a pathological diagnosis of normal epithelial tissue or low-grade dysplasia (LGD).

4F. The AUC for pre-wash MFI was 0.55 with a cutoff value of 93.13 a.u. (sensitivity: 0.68, specificity: 0.66). The AUC for pre-wash TBR was 0.63 with a cutoff value of 1.23 a.u. (sensitivity: 0.95, specificity: 0.49). The AUC for after-wash MFI was 0.72 with a cutoff value of 38.43 (sensitivity: 0.74, specificity: 0.60). The AUC for after-wash TBR was 0.93 with a cutoff value of 1.59 (sensitivity: 1.00, specificity: 0.86). Using these four indicators to establish a logistic regression diagnostic model resulted in an overall AUC of 0.78 (sensitivity: 0.80, specificity: 0.75).

Safety

Following cMBP-ICG fluorescence imaging, no patient experienced anaphylaxis or local irritation or discomfort.

Discussion

In this study, we confirmed that MET-positive OSCC cells preferentially absorbed the peptide-based NIRF probe cMBP-ICG. We further confirmed that the targeted smear-based fluorescent probes can accurately determine the degree of epithelial dysplasia and identify suspicious OSCC lesions, regardless of specific diseases. This improves the early detection rate of early tumors. Therefore, this study provides a modular and flexible approach for different screening and exclusion goals of OSCC in various scenarios, potentially offering a convenient and safe new detection method to improve the early diagnosis rate of OSCC.

NIRFI has high sensitivity, uses non-ionizing radiation, and has simple operation and low cost, characteristics that make NIRFI particularly suitable for real-time clinical imaging. Handheld real-time NIRFI devices for head and neck cancer have gradually matured, and some of them have entered the stage of clinical trials.[17,18] NIRFI can detect tissue signals up to a depth of 5–6 mm. Given that OSCC arises from squamous cells on the surface of oral mucosa, NIRFI is optimal for early detection of OSCC lesions. Furthermore, incorporating a targeting element specific to tumor molecular markers can significantly enhance the diagnostic performance of NIRFI. MET-targeted NIRFI offers a practical, noninvasive tool for early detection of OSCC, well suited to outpatient settings and large-scale screening. Its molecular specificity allows for real-time biopsy, accurately marks high-risk lesions, minimizes the need for extensive biopsy sampling, and reduces patient discomfort. With its straightforward operation, NIRFI requires minimal clinical training and may help streamline diagnostic workflows. This technique's sensitivity to MET expression in OSCC may also provide a targeted approach that is both cost-effective and highly accessible, improving efficiency in cancer detection and intervention. Therefore, targeted NIRFI can assist in achieving clinical accuracy by providing "real-time illumination" of early suspicious OSCC nests at the millimeter level to guide clinical biopsy. This is a feasible approach for achieving early cancer intervention and improving prognosis.

The current experiment's merit lies in establishing a practical imaging protocol for OPMDs. Prior to this study, various methods were employed to enhance the precision of OPMD examination, including vital stains like toluidine blue, oral cytology (Oral CDx brush biopsy), light-based detection systems (e.g., ViziLite and VELscope), oral spectroscopy, and analyses of blood and saliva. Although these methods have their own advantages and disadvantages, the main drawback lies in the instability of the results and the alteration of the lesion morphology.[4,19,20] In contrast, the fluorescent examination used in this study offers unique benefits. For instance, in comparison to cytological examination, early identification and excision of high-risk oral leukoplakia can significantly decrease the likelihood of malignant transformation. Unlike with vital staining, with fluorescent staining, the morphology and color of the lesion itself remain unchanged. The different imaging outcomes of the lesion under two light sources can be separately observed through inspection with the naked eye and NIRFI display screen analysis.

Use of the 4-NQO-induced OSCC mouse model is another advantageous feature of this study. Previous studies that relied on biopsy sampling lacked data on false negatives and false positives due to a lack of pathological verification in areas judged to be negative by the sampling doctor.[21] In our current study, we employed an animal model to perform histopathological examination of 5-μm paraffin sections from the remaining tongue that was not sampled, enabling detection of any lesions missed by the two sampling methods and ensuring more comprehensive and reliable results.

Cell Rep Med. 2025; 12:101978 Published online: 24 February 2025

Table 2 Missed detection rates and detection rates of NIRFI-assisted biopsy and COE-based biopsy in mouse tongue OPMDs and carcinomas

Lesion type and time since start of 4-NQO	NIRFI-assisted biopsy	COE-based biopsy	*p* value
Missed detection rates			
HGD and carcinoma	–	–	–
– 20 weeks	0.02 ± 0.05	0.36 ± 0.20	0.001
24 weeks	0	0.37 ± 0.20	<0.0001
Combined	0.01 ± 0.04	0.36 ± 0.20	<0.0001
Carcinoma	–	–	–
– 20 weeks	0.20 ± 0.06	0.09 ± 0.10	0.19
24 weeks	0	0.02 ± 0.06	0.33
Combined	0.01 ± 0.04	0.05 ± 0.10	0.11
Detection rates			
HGD and carcinoma	–	–	–
– 20 weeks	0.48 ± 0.22	0.31 ± 0.10	0.21
24 weeks	0.85 ± 0.18	0.46 ± 0.10	<0.0001
Combined	0.66 ± 0.27	0.39 ± 0.25	0.002
Carcinoma	–	–	–
– 20 weeks	0.37 ± 0.26	0.39 ± 0.10	0.94
24 weeks	0.39 ± 0.17	0.40 ± 0.15	0.95
Combined	0.39 ± 0.19	0.40 ± 0.13	0.92

4-NQO, 4-nitroquinoline 1-oxide; COE, conventional oral examination; HGD, high-grade dysplasia; NIRFI, near-infrared fluorescence imaging; OPMDs, oral potentially malignant disorders. Values in table are mean ± SD unless otherwise indicated.

In our prospective randomized controlled trial using topical application of the targeted fluorescent imaging probe cMBP-ICG for identification of malignant transformation from OPMD to OSCC, we found that cMBP-ICG fluorescence achieved favorable accuracy. Until now, the early diagnosis of OSCC has mainly relied on the clinician's visual inspection to determine the necessity of a biopsy and select an appropriate biopsy site. Our study provided preliminary evidence that cMBP-ICG fluorescence imaging can significantly enhance the ability to differentiate between benign and malignant lesions, thereby improving the efficacy of biopsy procedures.

In this study, the classification of cases as pathologically negative or positive was based on the corresponding clinical intervention strategy. In patients with oral epithelial dysplasia, the rate of malignant transformation is approximately 12.1%.[22] A longitudinal study further revealed that the rates of malignant transformation for mild, moderate, and severe dysplasia were 8.1%, 16.1%, and 38.5%, respectively.[23] Therefore, in cases of mild dysplasia, clinicians typically adopt a follow-up approach, while in cases of moderate to severe epithelial dysplasia, surgical excision is performed[24] Thus, we defined pathologically negative as OPMD or mild dysplasia.

The process of malignant transformation of OPMDs is slow and insidious, initially manifesting only as cytological changes. The histopathological results obtained from biopsy are regarded as the criterion standard in managing OPMDs.[25] Therefore, it is crucial to optimize the timing and location of the biopsy. Precise assessment of lesions can prevent unnecessary invasive procedures, enhance the accuracy of biopsies, avert missed or delayed diagnoses, and ensure timely intervention for patients.

At present, none of the adjunctive tests, including vital staining, oral cytology, and light-based and combined tests, are adequate substitutes for biopsy and histological assessment.4 We attempted to use targeted fluorescence imaging to improve the specificity of fluorescent attachment and to minimize nonspecific attachment by gargling. In fluorescence imaging, we can obtain morphological information beyond what can be observed with the naked eye. The information arises from changes at the molecular level, which are related to the MET expressed by tumor cells. During the subjective process of identifying high-risk lesions using real-time cMBP-ICG fluorescence imaging, researchers integrated various characteristics, such as quantifying the disparity between suspicious sites and surrounding mucosa, assessing signal uniformity, and evaluating the smoothness of lines within high signal areas. Our study showed that NIRFI with cMBP-ICG achieved a diagnostic accuracy of 91% and a specificity of 93%, accurately identifying lesions as pathologically negative that had initially been diagnosed as positive, thus reducing the occurrence of false positives by three-quarters. These findings indicate that cMBP-ICG fluorescence imaging has higher accuracy than COE in identifying high-risk lesions and assists in the biopsy of OPMDs.

To ensure consistency across patients, we used hard palate fluorescence as a baseline reference to control individual variability in fluorescence signals due to differences in oral mucosa. However, the factors such as oral hygiene, mucosal texture, and MET expression levels may still impact signal variability, indicating the need for further refinement in standardization techniques to enhance the reliability and reproducibility of our imaging results.

Our analysis showed significant TBR variability between male and female patients (data not shown), with a higher fluorescence at lesion margins in males, which may potentially indicate a greater lesion dispersion. Such differences may align with reports of gender-based disparities in biomarkers influencing tumor behavior and imaging metrics.[26] These findings might highlight the importance of gender as a variable for improvement of diagnostic consistency.

Consequently, individual differences in oral status could influence the quantification of fluorescence results. This discrepancy may be attributed to interindividual variations in physical adsorption capacity of fluorescent agents and baseline MET expression among patients with diverse oral conditions. However, by comparing the MFI of the lesion site with that of the surrounding normal mucosa, it was possible to estimate the risk level of the lesions. Therefore, TBR may be more useful than MFI in distinguishing low-risk and high-risk lesions.

In addition, our randomized controlled trial was designed with particular attention to the difficulty in selecting biopsy sites due to the often-large-size OPMD lesions. We found that at least 50% of the patients in the trial had OPMDs exceeding an area of 1 square centimeter, posing challenges for clinicians in selecting appropriate biopsy sites. In the COE group, we observed a patient with initially negative biopsy histological results. However, within 3 months of follow-up, the wound exhibited erosion, and subsequent diagnosis revealed moderately differentiated SCC necessitating surgical intervention. Therefore, accurate selection of the most suitable biopsy site can permit timely diagnosis of patients who

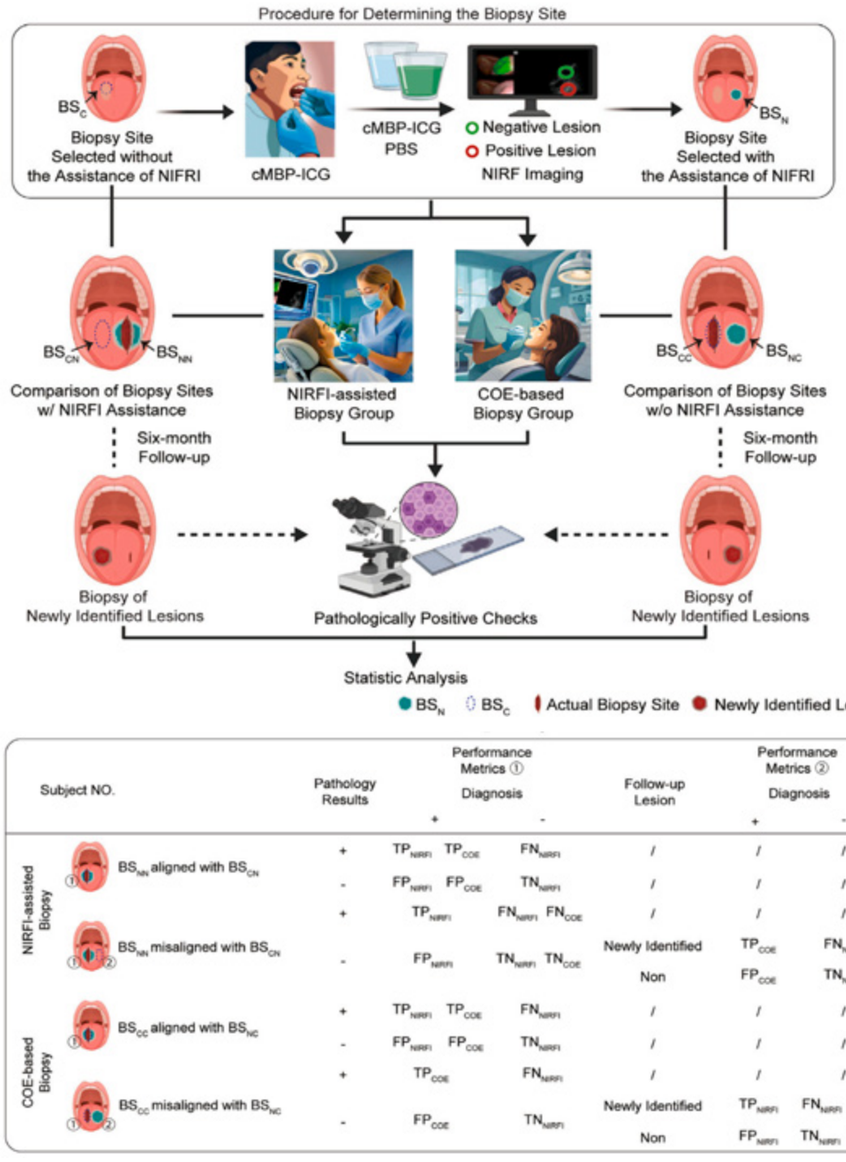


Fig.3 Design of the clinical trial.
Patients with OPMDs underwent visual inspection and NIRFI examination of the oral cavity prior to biopsy. First, an oral mucosal specialist independently selected the most appropriate biopsy site (BSC) based on visual inspection without reference to NIRFI, documented the biopsy site with photos, and assigned a clinical diagnosis. Next, an NIRFI operator selected the most appropriate biopsy site with NIRFI assistance (BSN), captured key frames, and marked the site directly on the images, which were then documented along with the clinical diagnosis. Subsequently, patients in the NIRFI-assisted biopsy group underwent biopsy at BSN, while subjects in the COE-based biopsy group underwent biopsy at BSC. Six months after biopsy, all patients were re-examined visually to check for new lesions, and any newly identified lesions were biopsied using the biopsy method used previously. All biopsy tissues were paraffin embedded and H&E stained and categorized as negative (normal epithelium, LGD) or positive (HGD, SCC). BSNN, NIRFI-assisted biopsy sites in the NIRFI-assisted biopsy group; BSCN, specialist-selected biopsy sites without NIRFI in the NIRFI-assisted biopsy group; BSCC, specialist-selected biopsy sites without NIRFI in the COE group; BSNC, NIRFI-assisted biopsy sites in the COE-based biopsy group; FN, false negative; FP, false positive; TN, true negative; TP, true positive. Subscript NIRFI indicates the NIRFI-assisted biopsy group, and subscript COE indicates the COE-based biopsy group.

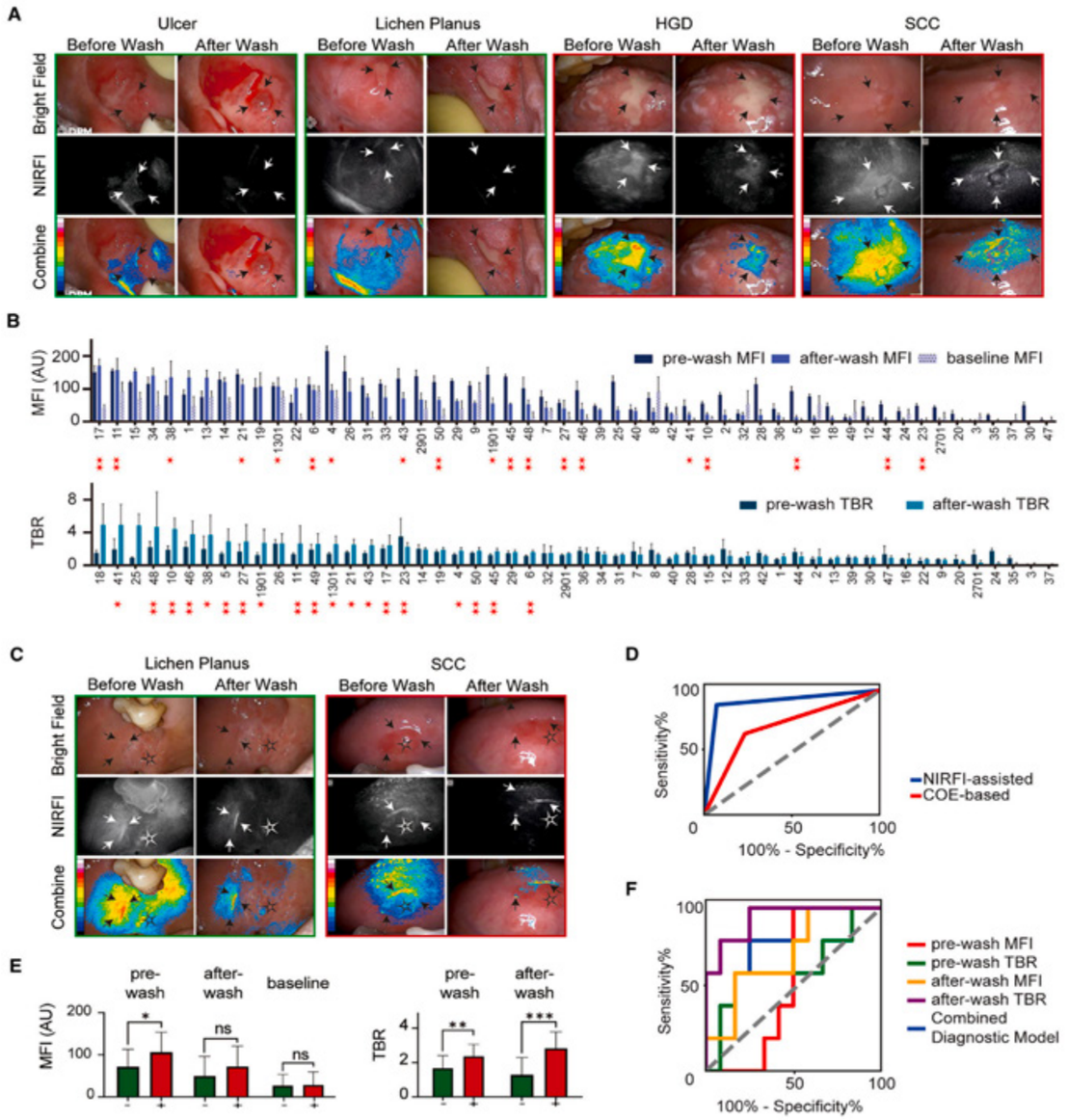


Fig.4 Clinical cMBP-ICG fluorescence imaging of OPMDsl.
(A) Representative bright-field images (top), black and white NIRFI images (middle), and combined pseudo-color fluorescence and bright-field images (bottom) of biopsy sites. The left two panels depict typical imaging findings for pathologically negative cases (ulcer and lichen planus), while the right two panels depict typical imaging findings for pathologically positive cases (HGD and SCC). Before the wash step, fluorescence signals were similar in all four panels due to physical attachment of cMBP-ICG. After the wash step, non-targeted cMBP-ICG is removed, and fluorescence signals are higher in pathologically positive cases than in pathologically negative cases.
(B) Pre-wash, after-wash, and baseline palate MFI and TBR for all cases, arranged in descending order of after-wash MFI (top row) and TBR (bottom row). No asterisk: pathologically negative. One asterisk: HGD. Two asterisks: SCC.
(C) Representative bright-field images (top), black and white NIRFI images (middle), and combined pseudo-color fluorescence and bright-field images (bottom) from

need intervention. We used the cMBP-ICG fluorescence imaging results as the basis for biopsy sampling in the experimental group and explored the value of fluorescence for biopsy guidance. The results indicate that cMBP-ICG fluorescence imaging has the potential to enhance diagnostic specificity, reduce surgeon errors in site selection, and improve biopsy accuracy and effectiveness. For general stomatology departments, fluorescence imaging may offer a greater enhancement in diagnostic efficiency.

Although our current study found that the 4-NQO-induced OSCC mouse model effectively simulated the carcinogenesis, it has certain limitation. The tumors predominantly formed on the dorsum of the tongue were different from the lateral locations typically seen in human patients,[27,28] which may impact translational relevance. While our clinical trial demonstrated the feasibility and diagnostic potential of MET-targeted NIRFI, the relatively small sample size limits the generalizability of these findings and restricts further subgroup analysis. Therefore, larger prospective and more diverse studies are needed to confirm our findings. Lastly, although no adverse events were noted, further evaluation of long-term safety with repeated probe applications remains needed to assess the potential influence by probe accumulation in tissues, immune responses of patient tolerance, and localized tissue mild inflammation effects.

In conclusion, this study developed a fluorescent dye, cMBP-ICG, and utilized a 4-NQO-induced mouse model of spontaneous OSCC to successfully replicate the progression of OPMDs to OSCC. By incorporating cMBP-ICG with a real-time NIRFI platform for biopsy assistance, the detection accuracy of early precancerous lesions was elevated from 77% to 90%. NIRFI-assisted biopsy outperformed COE-based biopsy in detecting HGD and exhibited a higher detection rate and a lower missed detection rate. In the preliminary exploratory clinical trial in patients with OPMDs, the most appropriate biopsy sites indicated by NIRFI matched the most appropriate biopsy sites indicated by COE, and NIRFI clearly delineated lesions. These results suggest that NIRFI with cMBP-ICG has the potential to offer a novel noninvasive real-time method to guide biopsy sampling. Ultimately, this approach may revolutionize current clinical diagnosis and treatment protocols for OPMDs, leading to an improved early detection rate of OSCC. Furthermore, theoretically, this approach may also be applicable to any other superficial tumor that follows its own progression process and involves critical biomarkers. To support the broader clinical adoption of MET-targeted NIRFI, future directions should focus on optimizing setup of requirements to enhance operator training and refine imaging standardization procedures.

Limitations of the study

The study has several limitations. Firstly, the 4-NQO-induced OSCC mouse model exhibits translational limitations, as tumors primarily form on the dorsum of the tongue, differing from the lateral sites commonly observed in human patients. Future studies could incorporate alternative models, such as orthotopic tumor implantation in lateral tongue sites, or advanced immunodeficient models like non-obese diabetic/severe combined immunodeficiency mice, to better mimic human OSCC. Secondly, the relatively small sample size of the clinical trial limits generalizability and restricts subgroup analyses. For instance, significant TBR variability was observed between male and female patients, with higher fluorescence at lesion margins in males, potentially indicating greater lesion dispersion. Such gender-based differences may impact diagnostic consistency and warrant further investigation. However, due to the limited dataset, further analyses could not be performed to confirm these observations, leaving this as a hypothesis rather than a definitive conclusion. Larger, multicenter studies are needed to validate these findings and explore how demographic factors and lesion characteristics influence diagnostic performance. Finally, the long-term safety of repeated probe applications remains uncertain. Potential risks, such as tissue accumulation, immune responses, and localized inflammation, require further investigation. Longitudinal studies and repeated-dose experiments are essential to ensure clinical safety and feasibility.

Table 3 Diagnostic performance of NIRFI-assisted biopsy and COE-based biopsy in patients with OPMDs

	NIRFI-assisted biopsy	COE-based biopsy	*p* value
Accuracy	0.91 (0.83, 0.95)	0.72 (0.62, 0.80)	0.0005
Sensitivity	0.88 (0.81, 0.93)	0.65 (0.55, 0.74)	0.0001
Specificity	0.93 (0.86, 0.96)	0.76 (0.68, 0.84)	0.002
PPV	0.90 (0.83, 0.95)	0.68 (0.59, 0.77)	0.0001
NPV	0.91 (0.84, 0.95)	0.74 (0.64, 0.82)	0.001

COE, conventional oral examination; NIRFI, non-infrared fluorescent imaging; NPV, negative predictive value; OPMDs, oral potentially malignant disorders; PPV, positive predictive value.
Values in parentheses are 95% CIs. A positive test result is defined as a lesion with a pathological diagnosis of high-grade dysplasia (HGD) or squamous cell carcinoma (SCC). A negative test result is defined as a lesion with a pathological diagnosis of normal epithelial tissue or low-grade dysplasia (LGD).

Resource availability

Lead contact

Requests for further information and resources should be directed to and will be fulfilled by the lead contact, Xiaofeng Tao (cjr.taoxiaofeng@vip.163.com).

cases with differing biopsy sites as determined by NIRFI and COE. Arrows: NIRFI-assisted biopsy sites. Stars: COE-based biopsy sites.
(D) Comparison of MFI and TBR between the pathologically negative (green) and pathologically positive (red) groups.
(E) ROC curves for NIRFI-assisted biopsy and COE-based biopsy in distinguishing pathologically negative and pathologically positive OPMDs. Data are represented as mean ± SEM, with error bars shown only above the mean, analyzed using unpaired Student's t test. *p < 0.05, **p < 0.01, ***p < 0.001; ns, not significant.
(F) Multivariable ROC curve analysis for different methods of distinguishing pathologically negative and pathologically positive OPMDs.
(A–F) n (participants) = 50 biological replicates. n (selected biopsy sites) = 100 technical replicates.(G) Percentage of lesion area positive for MET, lesion diameter, and distribution of lesions of different pathological types at different times after initiation of 4-NQO.
(H) Receiver operating characteristic (ROC) curves evaluating the performance of MET-positive area as a classifier.
(C–H) n (lesions) = 121 biological replicates.

Materials availability

There are restrictions to the availability of cMBP-ICG due to the lack of an external centralized repository for its distribution and our need to maintain the stock. We are glad to share cMBP-ICG with reasonable compensation by requester for its processing and shipping.

Data and code availability

•The datasets generated during this study are included in the manuscript and supplementary materials.

•No new code was created or used in this study.

•Any additional information required to reanalyze the data reported in this work paper is available from the lead contact upon request

Acknowledgments

We thank Professor Qifan Yan (East China University of Science and Technology) for advice on optical imaging techniques and Researcher Jingya Sun (Shanghai Institute of Materia Medica, Chinese Academy of Sciences) for guidance on preclinical experiments. We also appreciate the contributions of Jun Wu, Yuan Yuan, Yunjing Zhu, Rui Wang, Qi Fan, Gongxin Yang, and Jiliang Ren to the early stages of this research. This work was supported by the National Natural Science Foundation of China (grant nos. 82172049 and 82172051), the Clinical Research Program of Shanghai Ninth People's Hospital, Shanghai Jiao Tong University School of Medicine (grant no. JYLJ202205), the Shanghai Municipal Commission of Health and Family Planning (grant no. 172), the Medical-Engineering Cross-Research Fund (grant no. YG2024QNA23), and the Cross-disciplinary Research Fund of Shanghai Ninth People's Hospital (JYJC202304).

Declaration of interests

The authors have a related patent "Near-infrared fluorescence imaging agent targeting c-Met and its use" filed by X.T. et al., Shanghai Ninth People's Hospital, China, 2022 (patent number 202210118240.6).

Experimental model and study participant details

Animal models

Mice were purchased from the experimental animal center of Shanghai Ninth People's Hospital, Shanghai JiaoTong University. The animals were housed in a specific-pathogen-free facility under a 12-h light/12-h dark cycle. The temperature ranged from 24°C to 26°C, and the humidity ranged from 50% to 70%. Male mice were selected for this study to reflect the higher incidence of oral squamous cell carcinoma (OSCC) observed in males in epidemiological studies.29 The animal experiments were conducted at Shanghai Ninth People's Hospital and approved by the hospital's Ethics Office (approval number SH9H-2020-A620-1), and all procedures were carried out in accordance with NIH standards for laboratory animal care and use. To develop a mimic of subcutaneous human HNSCC tumors, 2 × 106 Cal27 cells in 100 μL of PBS were inoculated into the lower back of 4-week-old BALB/c-nu/nu mice. We conducted the experiments when tumors attained a volume of 100 mm3–150 mm3. For the orthotopic HNSCC model, 1.2 × 106 Cal27 cells in 20 μL of PBS were directly inoculated into the tongue of 4-week-old BALB/c-nu/nu mice. Mice were observed daily for tumor growth and weight loss. Images of the tumors were acquired every 2 to 3 weeks. To evaluate the feasibility of NIRFI with surface application of cMBP-ICG for detecting precancerous lesions and early OSCC, we used the 4-NQO-induced OSCC mouse model, which effectively mimics human oral carcinogenesis, dynamically progressing from normal mucosa to hyperplasia, dysplasia, and carcinoma. 4-NQO was dissolved in 2% mother liquor containing 1,2 propylene glycol and diluted to a concentration of 50 μg/mL with sterilized tap water. The solution was stored in a light-protected container and used as drinking water for model animals. Thirty 8-week-old male C57BL/6 mice were randomly assigned to the test group (N = 15) or the control group (N = 15). Mice in the test group received water containing 4-NQO for the initial 12 weeks and then received sterilized tap water. Mice in the control group received a solution of 10 g/mL ethylene glycol in water for the initial 12 weeks and then received sterilized tap water.

Cell lines and cell culture

The HNSCC cell lines FaDu (hypopharyngeal SCC; male, Shanghai Institute of Biochemistry and Cell Biology, Shanghai, China), Cal27 (tongue SCC; male, Shanghai Institute of Biochemistry and Cell Biology), WSU-HN30 (pharynx SCC; male, Yukacell, Shanghai, China) were grown in monolayers at 37°C with 5% CO2. The HSF cell line (keratin epithelial cell; Yukacell) was also used, though its gender is not specified in the available literature, and this limitation is acknowledged. All cell lines were authenticated using short tandem repeat (STR) profiling to confirm their identity. Mycoplasma contamination was tested using PCR-based mycoplasma detection assays, and all cell lines were confirmed to be mycoplasma-free before use. We inoculated the FaDu cells in MEM enriched with 10% (v/v) FBS and 1% PenStrep and the Cal27, WSU-HN30, and HSF cells in DMEM enriched with 10% (v/v) FBS and 1% PenStrep.

Human participants

To better understand the role of MET as a clinical signature for OSCC, we compared the expression patterns of MET between human oral cancer tissues and adjacent nonmalignant tissues in 9 tissue specimens (detailed information in Table S7) from surgical excisions performed at the Department of Pathology of Shanghai Ninth People's Hospital. The mean age of patients in this cohort was 57 years (range: 37–70 years), and the group consisted of 5 females and 4 males, all of East Asian descent. The specimens were from lesions histopathologically classified as premalignant lesion (3 specimens), low-grade cancer (3 specimens), and high-grade cancer (3 specimens). Premalignant lesions were defined as high-grade epithelial neoplasia and SCC in situ. Low-grade cancer was defined as lesions in which most of the tumor cells had a nonmalignant appearance and the cancer was well differentiated. High-grade cancer was defined as lesions in which the tumor cells had a very different appearance from that of nonmalignant tissue and were poorly differentiated.30 All tissue samples were formalin-fixed and paraffin-embedded (FFPE) for histopathological evaluation and immunohistochemistry. Using receiver operating characteristic curve analysis, we evaluated

MET's ability to discriminate between tumor and normal tissue. The use of human tissues was approved by the Institutional Review Board at Shanghai Ninth People's Hospital, and all the subjects granted informed consent (approval number SH9H-2020-T147-3). The clinical trial was conducted at Shanghai Ninth People's Hospital and was approved by the institutional review board of the Chinese Clinical Trial Registry (ChiCTR2300074454). Written informed consent was obtained from all patients. The clinical trial protocol is available in the supplemental information. Briefly, from June 2023 through December 2023, fifty patients (aged ≥ 18 years) diagnosed with OPMD25,31,32,33 were recruited (detailed information is in Table S8). The mean age of participants was 54 years (range: 25-76 years), with a female-to-male ratio of 2:1 (34 females, 16 males). All participants were of East Asian descent. All patients were randomly assigned to two groups (25 pergroup) using a computer-generated random number sequence to minimize selection bias.

Method details

Synthesis and characterization of cMBP-ICG

cMBP peptide was chosen as the targeting ligand on the basis of our previous work15,16 showing that cMBP has strong docking affinity to MET (KD = 3.96 × 10−7 M) and because cMBP has been shown to have potential use in tumor treatment34 and imaging.15,35 ICG was selected as the imaging probe because of its high signal-to-background ratio and biological safety.36

cMBP-ICG was synthesized by coupling sulfo-ICG-maleimide (Lumiprobe, Hunt Valley, MD, USA) with a custom MET-binding peptide (KSLSRHDHIHHHK).15 The reaction was conducted in the dark at room temperature and monitored by reverse-phase high-performance liquid chromatography (RP-HPLC). Free ICG dye was removed using RP-HPLC, and the purified cMBP-ICG was lyophilized by China Peptides Co. (Suzhou, China). For imaging studies, 5 μL of PBS was added to 70 ng of lyophilized cMBP-ICG. Detailed synthesis and purification steps are provided in the supplemental information.

In vivo toxicological evaluation of cMBP-ICG

For the toxicological evaluation of cMBP-ICG, we used five 8-week-old male C57BL/6 mice. A 2.5-mM cMBP-ICG solution was administered in place of drinking water for 24 h, after which normal drinking water was restarted. Blood samples were collected from the orbital venous plexus at baseline, 24 h after the start of cMBP-ICG administration, and 14 days after the start of cMBP-ICG administration, and a complete blood cell count (white blood cells, red blood cells, hemoglobin, hematocrit, mean corpuscular volume, mean corpuscular hemoglobin, mean corpuscular hemoglobin concentration, platelets) and blood biochemistry studies (alanine aminotransferase, aspartate aminotransferase, alkaline phosphatase, blood urea nitrogen, creatine, glucose, total protein, albumin) were performed.

Confocal and light microscopy imaging

Immunohistochemistry (IHC) and immunofluorescence (IF) were performed at the Shanghai Institute of Materia Medica (Chinese Academy of Sciences, China) with a confocal microscope (NOL-LSM 710, Carl Zeiss, Germany).

For IHC, paraffin-embedded, formalin-fixed 3-μm sections were deparaffinized with EZPrep buffer (Ventana Medical Systems, Tucson, AZ, USA); antigen retrieval was performed with CC1 buffer (Ventana Medical Systems); and sections were blocked for 30 min with Background Buster solution (Innovex, Richmond, CA). Sections were incubated with an anti-MET rabbit monoclonal antibody (ab51067; Abcam, Shanghai, China) that specifically binds both human and mouse MET for 5 h at a 1:300 dilution. For protein detection, a DAB detection kit (DAB-0031; MXB Biotechnologies, China) was used according to the manufacturer's instructions, and sections were counterstained with hematoxylin and coverslipped with Permount (Fisher Scientific, Pittsburgh, PA).

For IF, detection was also performed with the anti-MET rabbit monoclonal antibody (ab51067), followed by incubation with Alexa Fluor 488 secondary goat anti-rabbit antibody (#4412, Cell Signaling Technology, MA, USA) prepared according to the manufacturer's instructions. Sections were counterstained with 4′,6-diamidino-2-phenylindole (DAPI) for 10 min and coverslipped with Mowiol mounting medium (Sigma-Aldrich, St. Louis, MO). Incubating with the rabbit IgG instead of the primary antibody controlled for nonspecific binding of the secondary antibody.

Hematoxylin-eosin (H&E) staining of neighboring sections was done to assess the morphological properties of the tissues. Digitalization of the tumor sections was done with a NanoZoomer Digital Pathology scanner (NanoZoomer 2.0-RS, Hamamatsu Photonics) for quantification of the MET proteins. NanoZoomer Digital Pathology software (NDP.view2, version 2.9.29) was employed to assess at least 10 fields per section. In the IHC-stained tissues, we performed thresholding on the brown (MET) and blue (tissue) sites, and we computed the relative MET-positive area by dividing the brown area by the overall tissue area. The MET-positive area was computed via thresholding the red fluorescent area and dividing it by the overall tissue area, which was assessed on the basis of the intensity of blue fluorescence in all nuclei that were thresholded via DAPI staining. The determined intensities of fluorescence were averaged over all nuclei in every field of view, with intensity values between 0 and 255. Correlation of cMBP uptake and MET expression was determined by the inter- and intra-cellular co-localization of the targeted fluorescent probe with MET antigen in cell climbing slides or histological sections.

Western blotting

For western blotting analysis of MET protein expression, RIPA lysis buffer (Beyotime Biotechnology, Shanghai, China) was used to concentrate proteins from cell lines. Electrophoresis was performed with sodium dodecyl sulfate polyacrylamide gels (Beyotime Biotechnology) using 10 μg of purified protein in each cell line or human esophageal tissue. The separated proteins were transferred to microporous polyvinylidene difluoride membranes (Roche, USA) and then blocked using 5% bovine serum albumin (Scientific Phygene, Fuzhou, China). The membranes were then incubated in anti-MET rabbit monoclonal antibody (ab51067) or GAPDH monoclonal antibody (#5174, Cell Signaling Technology) at 4°C overnight. After washing and incubation with HRP-conjugated secondary antibodies (#98164, Cell Signaling Technology) at room temperature for 1 h,

Gension Enhanced ECL (solution A: solution B = 1:1) (Gension, Guangzhou, China) was used to detect protein bands, and they were imaged on a ChemiDocXRS + imaging system (Bio-Rad, USA). Semiquantitative assessment of MET along with GAPDH was done with ImageJ software (National Institutes of Health, USA).

Flow cytometry

For flow cytometry analysis of MET expression, adherently grown cells were detached using pancreatic enzyme (Sigma-Aldrich, St. Louis, MO, USA), and harvested cells were incubated with 300 μL of rabbit IgG isotype antibody (02–6102; Invitrogen) or rabbit monoclonal antibody to MET (ab216574) at 4°C for 30 min. Subsequently, cells were rinsed in PBS and incubated with Alexa Fluor 488 secondary goat anti-rabbit antibody (#4412) for 30 min. After rinsing, cells were resuspended in 400 μL of PBS. Fluorescence analysis was performed using a flow cytometer (CytoFLEX LX, Beckman Coulter, Inc., IN, USA) with a count of 1 × 104 living cells per sample. The flow cytometry data were analyzed with FlowJo software (FlowJo, version 10.9.0, Ashland, OR, USA).

NIRFI with cMBP-ICG to identify OSCC in CDXs

To test NIRFI with cMBP-ICG in mice with CDXs, we injected a solution of 5 μL of PBS and 70 ng of cMBP-ICG lyophilized powder into the mouse tongues and then performed fluorescence imaging. The mice were maintained under anesthesia with ketamine (0.1 mg/g body weight) during probe injection and imaging. A preclinical fluorescence laryngoscope imaging platform (DPM-III-01, Zhuhai Dipu Medical Technology Co., Ltd.) was used for real-time fluorescence imaging. Photos were acquired before and 30 min after injection of the probe. We used the same instrument settings in all the procedures involving imaging (exposure time of 30 ms, excitation power of 20%, gain of 3 dB). In addition, we maintained the distance between the laryngoscope and the tissue surface at approximately 10 mm. To acquire the photos, we slowly scanned the tumor area along with neighboring nonmalignant mucosa. In the course of this process, we utilized real-time white light imaging for visual guidance, as well as focusing. ImageJ software was used for image analysis. The tumor-to-background ratio (TBR) was defined as the fluorescence intensity of the tumor divided by the fluorescence intensity of the adjacent tissue. We harvested the whole tongues for ex vivo imaging. Following biodistribution assessment, we fixed the tumor tissues in 4% PFA along with optimal cutting temperature compound (SAKURA, USA) for IHC assessment accompanied by frozen-tissue immunofluorescence imaging.

Tumors and MET expression in the 4-NQO model

Three mice from each group—4-NQO-treated and control—were sacrificed at 0, 12, 16, 20, and 24 weeks, respectively. Tissue samples from the tongues of sacrificed mice were collected and subjected to histopathological analysis to determine tumor development time and stage and MET expression (Figure S5). The mice were monitored at 12, 16, 20, and 24 weeks using 9.4T magnetic resonance imaging (Biospec94/30USR, Bruck, Germany). In the imaging protocols, the parameters were set as follows: For the T1-RARE sequence, the echo time was 6.00 ms, and the repetition time was 800.00 ms. The flip angle was 180.00°. The pixel spacing was 0.075 mm × 0.075 mm, and the slice thickness was 0.50 cm. For the T2-TurboRARE sequence, the echo time was 33.35 ms, and the repetition time was 2,500.00 ms. The flip angle remained at 180.00°, with the same pixel spacing and slice thickness as for the T1-RARE sequence.

NIRFI to identify OPMD in the 4-NQO model

To test NIRFI with cMBP-ICG in the 4-NQO-induced OSCC model, we used forty 8-week-old male C57BL/6 mice A solution of 5 μL of PBS and 70 ng of cMBP-ICG lyophilized powder was prepared. Forceps were used to expose the tongue, and the cMBP-ICG solution was dripped onto the tongue for 1 min, ensuring complete exposure of the entire oral mucosa. After the mouse tongue was washed twice with PBS to eliminate any residual unbound compounds, the preclinical NIRFI platform described above under "NIRFI with cMBP-ICG to identify OSCC in CDXs" was utilized for real-time NIRFI. Photos were obtained using the same protocol as described.15 TBR was defined as the fluorescence intensity of the tumor divided by the fluorescence intensity of the adjacent tissue. During topical application of the cMBP-ICG solution and subsequent imaging, mice were maintained under anesthesia with ketamine at a dose of 0.1 mg per gram of body weight.

Twenty to 24 weeks after the start of 4-NQO induction, the abundance and distribution of tongue lesions in mice closely resembled those observed in human OPMDs.37 Consequently, real-time NIRFI-assisted biopsies were performed at 20 weeks and 24 weeks. The 40 mice were stratified on the basis of time since initiation of 4-NQO induction (20 weeks or 24 weeks) and were randomly allocated into two groups (1:1) using a tandem design as described previously.38 Mice in each group underwent two biopsies. In the NIRFI-assisted biopsy group, NIRFI-assisted biopsy was the first biopsy, and COE-based biopsy was the second biopsy. In the COE-based biopsy group, COE-based biopsy was the first biopsy, and NIRFI-assisted biopsy was the second biopsy.39 The criterion standard was findings on histopathological evaluation of H&E-stained, paraffin-embedded tissue sections. All biopsied lesions were graded by pathologists specializing in oral lesions who were blinded to group assignments. Lesions were classified as normal epithelial tissue, low-grade dysplasia (LGD), high-grade dysplasia (HGD), carcinoma in situ (CIS), or invasive carcinoma (ICA). All lesions within the remaining tongue tissues were meticulously annotated on slides by a pathologist with 20 years of expertise in oral and maxillofacial pathology. The numbers and pathological classifications of the biopsied lesions and the lesions within the remaining tongue tissues were documented for subsequent analysis.

Exploratory clinical trial

A single-center prospective randomized controlled trial of NIRFI-assisted biopsy versus COE-based biopsy was approved by the institutional review board of the Chinese Clinical Trial Registry (ChiCTR2300074454). The inclusion and exclusion criteria are detailed in Figure S6. Eligible patients were randomized 1:1 to the real-time NIRFI-assisted biopsy group or COE-based biopsy group using a computer-generated random sequence.

The oral conditions of all patients were thoroughly assessed

by an experienced oral mucosal specialist, who selected and documented what the specialist judged to be the most appropriate biopsy site and assigned a clinical diagnosis of LGD, HGD, or OSCC. Following this, all patients underwent NIRFI, during which the NIRFI operator selected and documented what the operator judged to be the most appropriate biopsy site and assigned a clinical diagnosis of LGD, HGD, or OSCC.15 Subsequently, patients in the NIRFI-assisted biopsy group underwent biopsy at the site selected by the NIRFI operator, while subjects in the COE-based biopsy group underwent biopsy at the site selected by the oral mucosal specialist without reference to NIRFI. The NIRFI procedure was detailed in our previous report.15 All patients were assessed by the same experienced oral mucosal specialist. After the NIRFI procedure, mucosal toxicity and patients' subjective experiences were recorded. Six months after biopsy, all patients were re-examined visually to check for new lesions, and any newly identified lesions were biopsied using the biopsy method used previously. All biopsy specimens were sectioned, embedded in paraffin, stained with H&E, subjected to histopathological analysis, and categorized as negative (normal epithelium, LGD) or positive (HGD, SCC). Patients, pathologists, and data analysts were blinded to the intervention.

Quantification and statistical analysis

For real-time NIRFI-assisted biopsy in mice, logistic mixed models were employed to analyze the detection rate and missed detection rate, considering treatment group (NIRFI-assisted biopsy vs. COE-based biopsy) and time since initiation of 4-NQO induction (20 weeks vs. 24 weeks). The detection rate was calculated as the number of lesions histologically confirmed as HGD, CIS, or ICA on the first biopsy divided by the total number of samples histologically confirmed as HGD, CIS, or ICA. The missed detection rate was defined as the number of lesions histologically confirmed as HGD, CIS, or ICA on the second biopsy divided by the total number of samples histologically confirmed as HGD, CIS, or ICA. The two-sided 95% confidence interval was computed for the treatment odds ratio (OR) between the test and control groups. An OR less than 1 for missed diagnosis rate indicates that NIRFI-assisted biopsy is superior to COE-based biopsy due to lower miss rates, while an OR greater than 1 for detection rate suggests that NIRFI-assisted biopsy is superior to COE-based biopsy due to higher detection rates. The chi-square test was used to determine the sensitivity of missed diagnosis rates and detection rates, while the Wilcoxon rank-sum test was used to analyze the mean number of neoplasms detected on the second biopsy and the mean number of neoplasms detected on the second biopsy with no lesion detected on the first biopsy.

For the clinical trial, the primary aim was to determine if NIRFI-assisted biopsy had higher accuracy in diagnosing HGD, the presence of which is a key factor in surgical decisions, and identified more malignant lesions than COE-based biopsy. The secondary aim was to develop a model using NIRFI for more accurate future diagnoses. The mean fluorescence intensity and TBR were computed for all lesions and subjected to a stratified analysis based on pathological findings to investigate the utility of these metrics in diagnostic classification. This exploratory clinical study also included a critical assessment of adverse effects of the cMBP-ICG solution, such as anaphylaxis (including mucosal edema), and whether the taste was acceptable. The detailed protocol for assessing the diagnostic performance of NIRFI-assisted biopsy and COE-based biopsy is illustrated in Figure 3 and described in the Clinical Trial Protocol in the supplemental information.

Statistical analyses were performed using GraphPad Prism version 9.5 and Python version 3.12.4 for advanced data processing and visualization. Data are presented as mean values with error bars representing standard deviations of biological replicates. Unpaired two-tailed Student's t-tests were used for two-group comparisons. One-way and two-way analysis of variance (ANOVA) was performed for multiple-group comparisons, followed by Tukey's post hoc test for pairwise comparisons where significant differences were detected. ROC curves were applied to evaluate the diagnostic performance of MET expression and fluorescence-based imaging related key variables, with AUC values used to quantify classification accuracy. Logistic regression analysis was applied to assess factors associated with missed detection rates and detection rates in NIRFI-assisted and COE-based biopsy groups. The results are presented as odds ratios (ORs) with 95% confidence intervals (CIs). A P-value < 0.05 was considered statistically significant. Significance levels are denoted in figures with asterisks (*p< 0.05, **p< 0.01, ***p< 0.001, ****p< 0.0001).

Additional resources

The clinical trial is registered under registration number ChiCTR2300074454. (https://www.chictr.org.cn/showproj.html?proj=200268).

References

1. Warnakulasuriya, S., Kujan, O., Aguirre-Urizar, J.M., Bagan, J.V., Gonza-lez-Moles, M.A., Kerr, A.R., Lodi, G., Mello, F.W., Monteiro, L., Ogden, G.R., et al. (2021). Oral potentially malignant disorders: A consensus report from an international seminar on nomenclature and classification, convened by the WHO Collaborating Centre for Oral Cancer. Oral Dis. 27, 1862–1880.
2. Seoane, J., Alvarez-Novoa, P., Gomez, I., Takkouche, B., Diz, P., Warna-kulasiruya, S., Seoane-Romero, J.M., and Varela-Centelles, P. (2016). Early oral cancer diagnosis: The Aarhus statement perspective. A systematic review and meta-analysis. Head Neck 38, E2182–E2189.
3. Nieminen, M., Aro, K., Ma¨ kitie, A., Harlin, V., Kainulainen, S., Jouhi, L., and Atula, T. (2021). Challenges in diagnosing head and neck cancer in primary health care. Ann. Med. 53, 26–33.
4. Walsh, T., Macey, R., Kerr, A.R., Lingen, M.W., Ogden, G.R., and Warna-kulasuriya, S. (2021). Diagnostic tests for oral cancer and potentially malignant disorders in patients presenting with clinically evident lesions. Cochrane Database Syst. Rev. 7, CD010276.
5. Zhang, Z., Du, Y., Shi, X., Wang, K., Qu, Q., Liang, Q., Ma, X., He, K., Chi, C., Tang, J., et al. (2024). NIR-II light in clinical oncology: opportunities and challenges. Nat. Rev. Clin. Oncol. 21, 449–467.
6. Hu, Z., Chen, W.-H., Tian, J., and Cheng, Z. (2020). NIRF Nanoprobes for Cancer Molecular Imaging: Approaching Clinic. Trends Mol. Med. 26, 469–482.
7. Deme´ trio De Souza Franc¸ a, P., Kossatz, S., Brand, C., Karassawa Zanoni, D., Roberts, S., Guru, N., Adilbay, D., Mauguen, A., Valero Mayor, C., Weber, W.A., et al. (2021). A phase I study of a PARP1-targeted topical fluorophore for the detection of oral cancer. Eur. J. Nucl. Med. Mol. Imag. 48, 3618–3630.
8. Shang, W., Peng, L., He,K., Guo, P.,Deng, H.,Liu, Y., Chen, Z., Tian, J., and Xu, W. (2022). A clinical study of a CD44v6-targeted fluorescent agent for the detection of non-muscle invasive bladder cancer. Eur. J. Nucl. Med. Mol. Imag. 49, 3033–3045.
9. Knowles, L.M., Stabile, L.P., Egloff, A.M., Rothstein, M.E., Thomas, S.M., Gubish, C.T., Lerner, E.C., Seethala, R.R., Suzuki, S., Quesnelle, K.M., et al. (2009). HGF and c-Met Participate in Paracrine Tumorigenic Pathways in Head and Neck Squamous Cell Cancer. Clin. Cancer Res. 15, 3740–3750.
10. Saintigny, P., William, W.N., Foy, J.-P., Papadimitrakopoulou, V., Lang, W., Zhang, L., Fan, Y.H., Feng, L., Kim, E.S., El-Naggar, A.K., et al. (2018). Met Receptor Tyrosine Kinase and Chemoprevention of Oral Cancer. J. Natl. Cancer Inst. 110, 250–257.
11. Lim, Y.C., Kang, H.J., and Moon, J.H. (2014). C-Met pathway promotes self-renewal and tumorigenecity of head and neck squamous cell carcinoma stem-like cell. Oral Oncol. 50, 633–639.
12. Seiwert, T.Y., Jagadeeswaran, R., Faoro, L., Janamanchi, V., Nallasura, V., El Dinali, M., Yala, S., Kanteti, R., Cohen, E.E.W., Lingen, M.W., et al. (2009). The MET receptor tyrosine kinase is a potential novel therapeutic target for head and neck squamous cell carcinoma. Cancer Res. 69, 3021–3031.
13. Liang, M., Yang, M., Wang, F., Wang, X., He, B., Mei, C., He, J., Lin, Y., Cao, Q., Li, D., and Shan, H. (2021). Near-infrared fluorescence-guided resection of micrometastases derived from esophageal squamous cell carcinoma using a c-Met-targeted probe in a preclinical xenograft model. J. Contr. Release 332, 171–183.
14. Wu, J., Liu, J., Lin, B., Lv, R., Yuan, Y., and Tao, X. (2021). Met-Targeted Dual-Modal MRI/NIR II Imaging for Specific Recognition of Head and Neck Squamous Cell Carcinoma. ACS Biomater. Sci. Eng. 7, 1640–1650.
15. Wang, J., Li, S., Wang, K., Zhu, L., Yang, L., Zhu, Y., Zhang, Z., Hu, L., Yuan, Y., Fan, Q., et al. (2023). A c-MET-Targeted Topical Fluorescent Probe cMBP-ICG Improves Oral Squamous Cell Carcinoma Detection in Humans. Ann. Surg Oncol. 30, 641–651.
16. Wu, Y., Fan, Q., Zeng, F., Zhu, J., Chen, J., Fan, D., Li, X., Duan, W., Guo, Q., Cao, Z., et al. (2018). Peptide-Functionalized Nanoinhibitor Restrains Brain Tumor Growth by Abrogating Mesenchymal-Epithelial Transition Factor (MET) Signaling. Nano Lett. 18, 5488–5498.
17. van Keulen, S., van den Berg, N.S., Nishio, N., Birkeland, A., Zhou, Q., Lu, G., Wang, H.-W., Middendorf, L., Forouzanfar, T., Martin, B.A., et al. (2019). Rapid, non-invasive fluorescence margin assessment: Optical specimen mapping in oral squamous cell carcinoma. Oral Oncol. 88, 58–65.
18. van Keulen, S., Nishio, N., Fakurnejad, S., van den Berg, N.S., Lu, G., Birkeland, A., Martin, B.A., Forouzanfar, T., Colevas, A.D., and Rosenthal, E.L. (2019). Intraoperative tumor assessment using real-time molecular imaging in head and neck cancer patients. J. Am. Coll. Surg. 229, 560–567.e1.
19. Chen, Y., Wang, S., and Zhang, F. (2023). Near-infrared luminescence high-contrast in vivo biomedical imaging. Nat. Rev. Bioeng. 1, 60–78.
20. Vogel, P., Ru€ckert, M.A., Friedrich, B., Tietze, R., Lyer, S., Kampf, T., Hennig, T., Do¨ lken, L., Alexiou, C., and Behr, V.C. (2022). Critical Offset Magnetic PArticle SpectroScopy for rapid and highly sensitive medical point-of-care diagnostics. Nat. Commun. 13, 7230.
21. Essat, M., Cooper, K., Bessey, A., Clowes, M., Chilcott, J.B., and Hunter, K.D. (2022). Diagnostic accuracy of conventional oral examination for detecting oral cavity cancer and potentially malignant disorders in patients with clinically evident oral lesions: Systematic review and meta-analysis. Head Neck 44, 998–1013.
22. Mehanna, H.M., Rattay, T., Smith, J., and McConkey, C.C. (2009). Treatment and follow-up of oral dysplasia - a systematic review and meta-analysis. Head Neck 31, 1600–1609.
23. Nevanpää, T.T. · Terävä, A.E., Laine, H.K., and Rautava, J. (2022). Malignant transformation of oral epithelial dysplasia in Southwest Finland. Sci. Rep. 12, 8261.
24. Edwards, P.C. (2014). The natural history of oral epithelial dysplasia: perspective on Dost et al. Oral Surg. Oral Med. Oral Pathol. Oral Radiol. 117, 263–266.
25. Speight, P.M., Khurram, S.A., and Kujan, O. (2018). Oral potentially malignant disorders: risk of progression to malignancy. Oral Surg. Oral Med. Oral Pathol. Oral Radiol. 125, 612–627.
26. Li, C.H., Haider, S., Shiah, Y.-J., Thai, K., and Boutros, P.C. (2018). Sex Differences in Cancer Driver Genes and Biomarkers. Cancer Res. 78, 5527–5537.
27. Connelly, S.T., and Schmidt, B.L. (2004). Evaluation of pain in patients with oral squamous cell carcinoma. J. Pain 5, 505–510.
28. Bhattacharya, A., Janal, M.N., Veeramachaneni, R., Dolgalev, I., Dubey-kovskaya, Z., Tu, N.H., Kim, H., Zhang, S., Wu, A.K., Hagiwara, M., et al. (2020). Oncogenes overexpressed in metastatic oral cancers from patients with pain: potential pain mediators released in exosomes. Sci. Rep. 10, 14724.
29. Klasen, C., Wuerdemann, N., Rothbart, P., Prinz, J., Eckel, H.N.C., Suchan, M., Kopp, C., Johannsen, J., Ziogas, M., Charpentier, A., et al. (2023). Sex-specific aspects in patients with oropharyngeal squamous cell carcinoma: a bicentric cohort study. BMC Cancer 23, 1054.
30. Yang, E.C., Tan, M.T., Schwarz, R.A., Richards-Kortum, R.R., Gillenwater, A.M., and Vigneswaran, N. (2018). Noninvasive diagnostic adjuncts for the evaluation of potentially premalignant oral epithelial lesions: current limitations and future directions. Oral Surg. Oral Med. Oral Pathol. Oral Radiol. 125, 670–681.
31. Abati, S., Bramati, C., Bondi, S., Lissoni, A., and Trimarchi, M. (2020). Oral Cancer and Precancer: A Narrative Review on the Relevance of Early Diagnosis. Int. J. Environ. Res. Publ. Health 17, 9160.
32. Villa, A., Villa, C., and Abati, S. (2011). Oral cancer and oral erythroplakia: an update and implication for clinicians. Aust. Dent. J. 56, 253–256.
33. Carrard, V.C., and van der Waal, I. (2018). A clinical diagnosis of oral leukoplakia; A guide for dentists. Med. Oral Patol. Oral Cir. Bucal 23, e59–e64.
34. Meng, X., Zhao, Y., Han, B., Zha, C., Zhang, Y., Li, Z., Wu, P., Qi, T., Jiang, C., Liu, Y., and Cai, J. (2020). Dual functionalized brain-targeting nanoinhibitors restrain temozolomide-resistant glioma via attenuating EGFR and MET signaling pathways. Nat. Commun. 11, 594.
35. Kim, E.-M., Park, E.-H., Cheong, S.-J., Lee, C.-M., Kim, D.W., Jeong, H. J., Lim, S.T., Sohn, M.-H., Kim, K., and Chung, J. (2009). Characterization, biodistribution and small-animal SPECT of I-125-labeled c-Met binding peptide in mice bearing c-Met receptor tyrosine kinase-positive tumor xenografts. Nucl. Med. Biol. 36, 371–378.
36. Wang, H., Li, X., Tse, B.W.-C., Yang, H., Thorling, C.A., Liu, Y., Touraud, M., Chouane, J.B., Liu, X., Roberts, M.S., and Liang, X. (2018). Indocya nine green-incorporating nanoparticles for cancer theranostics. Theranostics 8, 1227–1242.
37. Naik, K., Janal, M.N., Chen, J., Bandary, D., Brar, B., Zhang, S., Dolan, J.C., Schmidt, B.L., Albertson, D.G., and Bhattacharya, A. (2021). The Histopathology of Oral Cancer Pain in a Mouse Model and a Human Cohort. J. Dent. Res. 100, 194–200.
38. Wallace, M.B., Sharma, P., Bhandari, P., East, J., Antonelli, G., Lorenzetti, R., Vieth, M., Speranza, I., Spadaccini, M., Desai, M., et al. (2022). Impact of Artificial Intelligence on Miss Rate of Colorectal Neoplasia. Gastroenterology 163, 295–304.e5.
39. Chen, J., Jiang, Y., Chang, T.-S., Joshi, B., Zhou, J., Rubenstein, J.H., Wamsteker, E.J., Kwon, R.S., Appelman, H., Beer, D.G., et al. (2021). Multiplexed endoscopic imaging of Barrett's neoplasia using targeted fluorescent heptapeptides in a phase 1 proof-of-concept study. Gut 70, 1010–1013.

Cell Rep Med. 2025; 12:101978 Published online: 24 February 2025

Stomatology

Research Article

Multispectral Fluorescence Imaging of EGFR and PD-L1 for Precision Detection of Oral Squamous Cell Carcinoma: A Preclinical and Clinical Study

Nenghao Jin[1,2,3*], Yu An[4*], Yu Tian[1,5*], Zeyu Zhang[4*], Kunshan He[3,7], Chongwei Chi[3,6], Wei Mu[4] ✉, Jie Tian[3,4] ✉, and Yang Du[3,6] ✉

Abstract

Background: Early detection and treatment are effective methods for the management of oral squamous cell carcinoma (OSCC), which can be facilitated by the detection of tumor-specific OSCC biomarkers. The epidermal growth factor receptor (EGFR) and programmed death-ligand 1 (PD-L1) are important therapeutic targets for OSCC. Multispectral fluorescence molecular imaging (FMI) can facilitate the detection of tumor multitarget expression with high sensitivity and safety. Hence, we developed Nimotuzumab-ICG and Atezolizumab-Cy5.5 imaging probes, in combination with multispectral FMI, to sensitively and noninvasively identify EGFR and PD-L1 expression for the detection and comprehensive treatment of OSCC.

Methods: The expression of EGFR and PD-L1 was analyzed using bioinformatics data sources and specimens. Nimotuzumab-ICG and Atezolizumab-Cy5.5 imaging probes were developed and tested on preclinical OSCC cell line and orthotopic OSCC mouse model, fresh OSCC patients' biopsied samples, and further clinical mouthwash trials were conducted in OSCC patients.

Results: EGFR and PD-L1 were specifically expressed in human OSCC cell lines and tumor xenografts. Nimotuzumab-ICG and Atezolizumab-Cy5.5 imaging probes can specifically target to the tumor sites in an in situ human OSCC mouse model with good safety. The detection sensitivity and specificity of Nimotuzumab-ICG in patients were 96.4% and 100%, and 95.2% and 88.9% for Atezolizumab-Cy5.5.

Conclusions: EGFR and PD-L1 are highly expressed in OSCC, the combination of which is important for a precise prognosis of OSCC. EGFR and PD-L1 expression can be sensitively detected using the newly synthesized multispectral fluorescence imaging probes Nimotuzumab-ICG and Atezolizumab-Cy5.5, which can facilitate the sensitive and specific detection of OSCC and improve treatment outcomes.

Trial registration: Chinese Clinical Trial Registry, ChiCTR2100045738. Registered 23 April 2021, https://www.chictr.org.cn/bin/project/edit?pid=125220

Supplementary Information: The online version contains supplementary material available at 10.1186/s12916-024-03559-w.

Keywords

Oral squamous cell carcinoma (OSCC), Epidermal growth factor receptor (EGFR), Programmed death-ligand 1 (PD-L1), Multispectral fluorescence molecular imaging, Imaging probe

[1] Medical School of Chinese PLA, Beijing, 100853 China

[2] Department of Stomatology, The First Medical Centre, Chinese PLA General Hospital, Beijing, 100853 China

[3] CAS Key Laboratory of Molecular Imaging, Beijing Key Laboratory of Molecular Imaging, Institute of Automation, Chinese Academy of Sciences, Beijing, 100190 China

[4] Key Laboratory of Big Data-Based Precision Medicine (Beihang University), Ministry of Industry and Information Technology of the People' S Republic of China, School of Engineering Medicine, Beihang University, Beijing, 100191 China

[5] Department of Stomatology, Beijing Integrated Traditional Chinese and Western Medicine Hospital, Beijing, 100039 China

[6] University of Chinese Academy of Sciences, Beijing, 100080 China

[7] State Key Laboratory of Computer Science and Beijing Key Lab of Human-Computer Interaction, Institute of Software, Chinese Academy of Sciences, Beijing, 100190 China

* Nenghao Jin, Yu An, Yu Tian and Zeyu Zhang contributed equally to this work.

BMC Med. 2024. 22(1):342 Published online: 26 August 2024

Background

Oral malignancies account for 3–5% of all malignant tumors. Oral squamous cell carcinoma (OSCC) is a kind of oral malignant tumor with high malignant degree and poor prognosis. In 185 countries around the world, there are about 476,000 new cases of OSCC and about 226,000 deaths [1]. The overall mortality rate of oral and oropharyngeal cancers has increased by 0.5% per year over the past 10 years [2]. After comprehensive treatment, the 5-year survival rate remains at 50%, and the survival rate of patients with advanced disease decreases to 27% [3, 4]. The poor prognosis of patients with OSCC is partially due to a delayed diagnosis. Early screening and timely treatment can effectively prevent the progression of OSCC, thereby increasing the survival rate of patients [5, 6]. Currently, the diagnostic methods for OSCC mainly involve visual inspection and tactile examination of the oral cavity, head and neck lymph nodes, and traditional medical imaging such as computed tomography (CT) and magnetic resonance imaging (MRI) [7]. However, some OSCCs appear similar to oral ulcers or underlying oral malignant diseases (OPMDs) [8, 9], leading to misdiagnosis. The gold standard for a definitive OSCC diagnosis is pathological examination, which is invasive, time-consuming, and involves complicated procedures [10–12]. Hence, there is an urgent need for new ways to detect tumors noninvasively and sensitively.

Near-infrared fluorescence (NIRF) imaging, through the injection or application of fluorescent imaging probes, allows tumors to be fluorescently lightened in the corresponding diseased areas, providing precise guidance for discriminating healthy and tumor tissues safely [13]. The most common NIR dyes used for in vivo NIRF tumor imaging are indocyanine green (ICG), Cy5, Cy5.5, Cy7 and IRDye800CW [14]. ICG is the amphiphilic small-molecule NIRF dye approved by the food and drug administration (FDA) for the surgical treatment of head and neck tumors [15]. ICG was first used for NIRF imaging in 9 patients with head and neck squamous cell carcinoma (HNSCC) [16]. Bredell et al. detected cervical sentinel lymph nodes in the soft tissue after peritumoral injection of ICG in patients with oropharyngeal cancer [17]. However, free ICG and other NIR dyes are non-specific and cannot be used for tumor-targeted imaging. NIR dyes can be coupled with tumor-specific ligands such as antibodies, metabolic substrates, cell surface peptides, and growth factors to recognize tumor cells [18–21]. In HNC, Cetuximab-800CW was evaluated by fluorescence-guided imaging (FGI) for high sensitivity to tumor detection [22, 23]. Multispectral fluorescence imaging (FMI) mainly uses broad-spectrum light and can simultaneously detect multiple biomarkers expressed in tumors. Chen et al. demonstrated the feasibility of detecting multiple targets in human for the first time in Barrett's neoplasia study. Multispectral FMI can facilitate precise and early detection of tumors [24]. Compared with target-FMI with a single tracer, multispectral FMI can improve the sensitivity and specificity of tumor identification [25]. For localized, small-scale tumors, the extracellular matrix (ECM) may prevent the penetration of intravenously administered macromolecules, leading to missed diagnoses of small lesions [26]. The use of micro-dose fluorescent imaging probes to spray or smear the diseased area enables almost instant imaging [27]. For OSCC, the entire oral mucosa can be topically applied with targeted imaging probes, and suspected cancer lesions can be directly lightened and correspondingly detected [28–32].

The epidermal growth factor receptor (EGFR) and programmed death-ligand 1 (PD-L1) are two key important therapeutic targets for OSCC. Targeted therapy, represented by EGFR antibody drugs, and immunotherapy, represented by anti-PD-1/PD-L1 antibodies, have provided new strategies for the treatment of HNSCC. Cetuximab, an anti-EGFR monoclonal antibody (mAb), was the first FDA-approved molecular-targeted drug for the treatment of HNSCC [33] and has been approved as a first-line treatment for relapsed and/or metastatic HNSCC. Fluorescently labeled cetuximab can be utilized for targeted FMI of OSCC to evaluate the targeted recognition of anti-EGFR fluorescently labeled antibodies in and around the tumor after systemic administration [34]. de Wit JG et al. [23] reported that Cetuximab-800CW can be used for the detection of positive tumor margins through 66 OSCC tumors and can safely locate surgical margins during surgery. Nimotuzumab has a lower affinity than Cetuximab, and has less effect on the recognition and killing of normal tissue cells [35]. PD-L1 is a transmembrane receptor that, after binding to PD-L1/PD-L2, can prevent cellular immunity. PD-L1 antibody drugs can relieve this inhibition and enhance the cellular immune response against tumor cells by blocking the PD-1/PD-L1 signaling pathway [36]. The potential for imaging with Atezolizumab and its ability to predict responses to PD-L1 immunotherapy were initially assessed in a human study using zirconium-89-labeled Atezolizumab (anti-PD-L1) [37]. Many cancers, including OSCC, are molecularly heterogeneous, and the detection of multiple targets is needed for more accurate clinical diagnosis and guidance for personalized therapy.

Hence, the aims of this study is to validate EGFR and PD-L1 as specific biomarkers for OSCC and develop multispectral Nimotuzumab-ICG and Atezolizumab-Cy5.5 fluorescence imaging probes to quantify the dynamic expression of dual-target EGFR and PD-L1 from preclinical in vitro human OSCC cell lines, in vivo OSCC orthotopic mouse models, to clinical OSCC patient tumor specimens, and topical application as mouthwash in OSCC patients. The new imaging strategies, quick and sensitive detection methods, and experimental evidence for the sensitive detection of OSCC biomarkers provided in this study will help to provide guidance for the early detection of OSCC, targeted therapy and immunotherapy (Fig. 1).

Methods

Bioinformatics analysis

The data used to compare EGFR and PD-L1 expression in HNSCC and normal tissues are available in the gene expression profiling interactive analysis (GEPIA) database at http://gepia.cancer-pku.cn.

Clinical model prediction based on receiver operator characteristic (ROC) analysis

One hundred and twelve OSCC patients treated at the Chinese PLA General Hospital between December 2018 and December 2019 were retrospectively analyzed. The inclusion criteria were patients who underwent surgery for the first time at our hospital and were diagnosed with OSCC based on complete clinical and follow-up records. Exclusion criteria: (1) presence of other concomitant tumors; (2) presence of distant metastases; (3) history of preoperative antineoplastic therapy; (4) serious postoperative complications. The follow-up period was three years, and the patients were re-examined every three months. The time of recurrence, metastasis, or death was defined as the cutoff time. The follow-up period ended on December 1, 2022. Receiver operating characteristic (ROC) curve analysis was performed based on EGFR and PD-L1 expression. EGFR and PD-L1 expression was evaluated by two independent pathologists in our hospital who were blinded to the study design. EGFR expression was detected using immunohistochemistry (IHC). The negative, weak positive, moderate positive, strong positive staining were respectively defined as -, + , + + , + + + . PD-L1 expression was measured using PD-L1 IHC 22C3 pharmDx (Dako 22C3, Dako, Denmark) and ranged from 0 to 99% as determined using the Tumor Proportion Score (TPS).

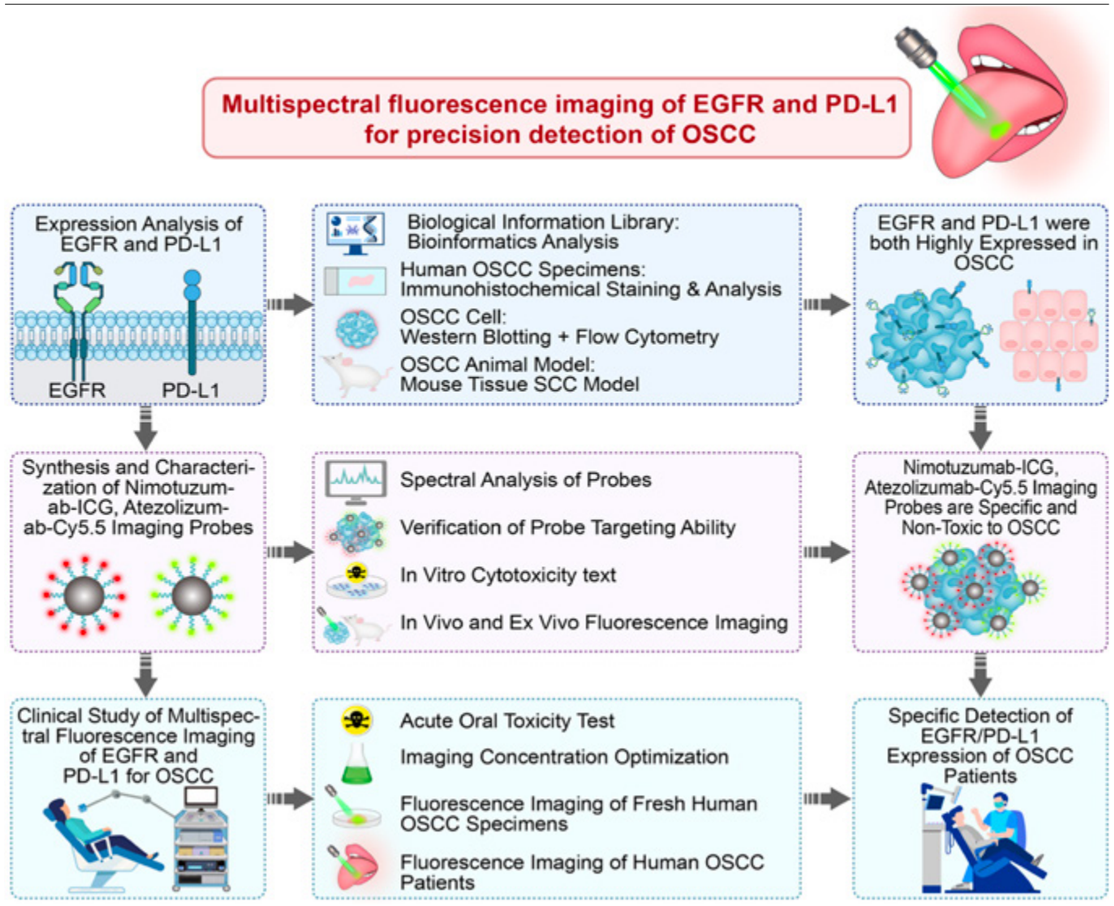


Fig.1 Study flowchart

EGFR and PD-L1 expression analysis via IHC of human OSCC

Analyses of EGFR and PD-L1 expression were conducted on biospecimens from the Department of Stomatology, First Medical

Center, Chinese PLA General Hospital. All biopsy specimens were diagnosed as OSCC by the Department of Pathology. The biospecimens were then embedded and sliced continuously. Tissue sections were incubated with bovine albumin (BSA, GC305010; Servicebio, Wuhan, China) for 30 min and Rabbit monoclonal antibody to EGFR (RRID: AB_869579; Abcam, Cambridge, UK) and Rabbit monoclonal antibody to PD-L1 (RRID: AB_2687878; Abcam, Cambridge, UK) at 4 °C overnight. The slides were then exposed to HRP peroxidase-labeled Goat Anti-Rabbit IgG (RRID: AB_2811189; Servicebio, Wuhan, China) and incubated for 1 h. Subsequently, the sections were stained with hematoxylin and eosin (H&E) for analysis. The expression levels of EGFR and PD-L1 were quantified using H-scores (0–300). Images were then captured using a scanner (Digital Sight DS-U3, Eclipse E100, Nikon, Japan), and H-scores were calculated by ImageJ Fiji (NIH, Bethesda, MD, USA).

Cell culture

Normal human oral keratinocytes (HOK) (ScienCell Research Laboratories Inc., USA) cells were cultured in Roswell Park Memorial Institute 1640 (RPMI-1640) medium (Thermo Fisher Scientific) containing 10% fetal bovine serum (FBS) (Thermo Fisher Scientific Australia Pty Ltd., Australia) and 1% penicillin–streptomycin (Macgene Biotechnology, China). Human OSCC CAL27 cells (RRID: CVCL_1107; ATCC, Manassas, VA, USA), CAL27-Fluc cells (RRID: CVCL_1107; Cobioer Biosciences Co., Ltd., China) and HSC3 cells ((RRID: CVCL_1288; ATCC, Manassas, VA, USA) were cultured in Dulbecco's modified Eagle's medium (DMEM) (Thermo Fisher Scientific (CHINA) Co., Ltd., China) containing 10% FBS and 1% penicillin–streptomycin. All cells were cultured in a Cell Culture Dish (Corning Inc., USA). All experiments were performed using mycoplasma-free cells. All human cell lines were authenticated using STR profiling within the last three years.

EGFR and PD-L1 expression analysis in different cells via western blotting and flow cytometry

HOK, CAL27, CAL27-Fluc and HSC3 cells were cultured and collected. Total protein was extracted from cells using precooled Pierce RIPA Buffer (Thermo Fisher Scientific, USA) and Halt Protease Inhibitor Cocktail (Thermo Fisher Scientific, USA), and western blotting was conducted utilizing Rabbit monoclonal antibody to EGFR (RRID: AB_869579) and PD-L1 monoclonal antibody (RRID: AB_2756526; Proteintech Group, Inc., USA), polyclonal rabbit β-actin antibody (Cell Signaling Technology, USA), and secondary antibody (1:10,000, Jackson ImmunoResearch, USA) were used for western blot. All four cell types (1 × 106) were incubated with FITC labeled Anti-EGFR antibody (RRID:AB_298005) and APC Anti-PD-L1 antibody (ab206967, Abcam, Cambridge, UK). After 30 min incubation, the cells were suspended in Phosphate-Buffered Saline (PBS) (Thermo Fisher Scientific Co., Ltd., China) and analyzed using flow cytometry (FACSCanto™ II; BD Biosciences, USA). FlowJo (version10.8.1) software was used for data analysis. The experiment was repeated three times, and the average of the results was taken.

Human OSCC orthotopic mouse model

All animal experiments were approved according to the guidelines of the Institutional Animal Care and Use Committee (Permit No: IA21-2203–24) of the Institute of Automation, Chinese Academy of Sciences. PBS (50 μL) containing 5 × 106 HSC3 or CAL27-Fluc cells were injected into the tongues of 6-week-old male BALB/c-nu/nu mice anesthetized with isoflurane (RWD Life Science, China). The feeding method is to give soft food or softened food with feed water. HSC3 and CAL27-Fluc tumor xenografts were harvested 7–10 days after inoculation; H&E staining was performed. Primary anti-EGFR antibody (RRID: AB_869579) and anti-PD-L1 antibody (RRID: AB_2687878) were used for immunohistochemical and immunofluorescence staining to analyze the expression of EGFR and PD-L1 in human OSCC tumor xenograft mouse models.

Synthesis of Nimotuzumab-ICG and Atezolizumab-Cy5.5

ICG-NHS-ester (330 nM, dissolved in 300 μL DMSO, Sigma-Aldrich) was added to humanized monoclonal EGFR antibody (5 mg, 33 nM, Nimotuzumab, Biotech Pharma, China) (dye/antibody ratio was 1:20) in conjugation buffer (5 mL, 0.1 M PBS), and the solution was reacted in the dark at 25 °C with continuous oscillation overnight. The mixture was concentrated to 0.8 mL using a centrifugal filter unit (3 kDa MWCO, Amicon) and purified three times via centrifugation at 8,500 rpm for 15 min. Similarly, Cy5.5-NHS-ester (330 nM, dissolved in 300 μL 0.1 M PBS, New Research Bioscience, China) was added to humanized monoclonal anti-PD-L1 antibody (Atezolizumab, Roche Registration GmbH, Switzerland) in conjugation buffer (5 mL, 0.1 M PBS), and the solution was reacted in the dark at 25 °C with continuous oscillation overnight. The mixture was concentrated and purified thrice using a centrifugal filter unit (3 kDa MWCO, Amicon). The conjugation efficiency was calculated.

In vitro cell viability experiments and spectroscopic analysis

Logarithmic growth-phase HOK, CAL27-Fluc, and HSC3 cells were seeded (5×10^3/well) in 96-well culture plates (Corning Inc., USA) overnight. Nimotuzumab-ICG, Atezolizumab-Cy5.5 and the mixture were added into the culture plates at different concentrations (2.5, 5, 10, 20, 40, 80, 160, and 320 μg/mL), respectively. After 24 h incubation, cells were washed thrice with PBS and cultured in 10% CCK-8 medium (CA1210; Solarbio Science and Technology Co., Ltd., China) for 30 min; the absorbance at 450 nm was determined using a spectrophotometric microplate reader (Synergy HT; BioTek, USA).

The spectra of excitation light and absorption light of Nimotuzumab-ICG and Atezolizumab-Cy5.5 were tested by fluorescence spectrophotometer (F-7000, Hitachi, Japan) (The scanning speed is 1200 nm/min, the spectral bandwidth is 10 nm, and the sampling interval is 0.2 nm) and near-infrared spectrophotometer (UV-3600 Plus, Shimadzu, Japan), respectively.

In Vivo and Ex vivo fluorescence molecular imaging (FMI) and safety evaluation

CAL27-Fluc OSCC tumor-bearing mice were injected with Nimotuzumab-ICG (0.2 mg) and Atezolizumab-Cy5.5 (0.2 mg), and their mixture via the caudal vein. The block group (normal mice) was intraperitoneally injected with Nimotuzumab (0.2 mg) and Atezolizumab (0.2 mg) 1 h before the intravenous injection of the imaging probes. FMI images were captured at different time points (pre-, 2, 6, 12, and 48 h) using an IVIS® Spectrum/CT (Caliper Life Sciences, USA), and the tumor to background ratio (TBR) was calculated using the region of interest (ROI) measurement tool with Fiji software.

After 24 h, the mice were sacrificed, and the serum were collected for detection of liver function indices, including alanine aminotransferase (ALT) and aspartate aminotransferase (AST) using an automatic blood biochemical auto analyzer (7600; Hitachi, Tokyo, Japan). The tongues, hearts, livers, spleens and kidneys were collected for ex vivo FMI by IVIS® SpectrumCT. H&E staining was performed on organs after ex vivo imaging. Resected fresh CAL27-Fluc tumor-bearing mouse tongue tumor specimens were analyzed using immunofluorescence (IF) staining for EGFR and PD-L1 expression.

Probe fluorescence imaging of fresh human specimens

First, 10 fresh OSCC specimens were pre-tested to determine the optimal incubation concentration of the probe, and then a formal fluorescence imaging experiment on 20 OSCC specimens was followed.. A total of 30 resected fresh human OSCC specimens were rinsed in 5% goat serum (SL038, Solarbio Science and Technology Co., Ltd., China) to remove debris and mixed and incubated with Nimotuzumab-ICG and Atezolizumab-Cy5.5 at 20 °C for 3 min. Subsequently, the specimens were washed with PBS 3 times. A homemade multispectral fluorescence imaging system (Key Lab of Molecular Imaging, CAS) was used to perform imaging experiments on the specimens. The device can achieve optical resolution of 50 μm, bandwidth of 5 nm, imaging field of 12.5 × 12.5 cm^2, 50 fps time resolution (adjustable according to actual conditions), real-time imaging of white light image, near-infrared dual imaging channels of 665 nm and 785 nm simultaneously. After imaging experiments, the specimens were fixed in 4% paraformaldehyde (P1110; Macgene Biotechnology) for subsequent H&E, EGFR, and PD-L1 IHC and IF staining.

Fluorescence imaging of OSCC in human patients

This study was approved by the Ethics Committee of the Chinese PLA General Hospital (No. S2021-097–01) and registered in the Chinese Clinical Trial Registry (Registration Number: ChiCTR2100045738). All human patients signed informed consent, and the patients gargled 5 mL of Nimotuzumab-ICG (0.4 mg/mL) and Atezolizumab-ICG (0.4 mg/mL) for approximately 30 s. Next, the patients gargled ultrapure water for 30 s three times, and the interval between Nimotuzumab-ICG and Atezolizumab-ICG imaging was 1 h. White-light and fluorescence images were obtained using a commercialized Digital Precision Medicine imaging device H2800 (DPM, Beijing, China). After surgical treatment, fresh specimens were obtained for the probe-spraying experiment, H&E staining, EGFR, PD-L1 IHC staining, and IF staining. EGFR and PD-L1 expression were defined as —, + , + + , + + + for negative, weak positive, medium positive, and strong positive expression.

Statistical analysis

The optimal cutoff values for the expression of EGFR and PD-L1 were determined from the ROC curves. Statistical analyses were performed using SPSS (version 21.0; IBM, Armonk, NY, USA) and GraphPad Prism software (version 9; GraphPad Software Inc., San Diego, CA, USA). Differences between paired data were tested using the Wilcoxon test. Statistical significance was set as *P < 0.05, ** P < 0.01, ***P < 0.001, **** P < 0.0001.

Results

Validation of EGFR and PD-L1 as specific OSCC biomarkers

According to the GEPIA dataset, the expression levels of EGFR and PD-L1 were significantly higher in HNSCC tumors than para tumor tissues (Fig. 2A). The EGFR and PD-L1 gene expression profiles across all HNSCC tumor samples (n = 519) and paired normal tissues (n = 44) were expressed as log2[transcripts per million (TPM) + 1]]. Patients with OSCC had high EGFR and PD-L1 expression. The expression of EGFR and PD-L1 is associated with the prognosis of patients with HNSCC. The correlation between EGFR expression and disease-free survival (DFS) and overall survival (OS) in 493 patients with HNSCC, and PD-L1 expression, DFS, and OS in 466 patients with HNSCC were analyzed using the GEPIA dataset. EGFR overexpression was significantly associated with OS (*P = 0.045), whereas high expression of PD-L1 was associated with shorter DFS (*P = 0.01) (Fig. 2B).

The statistical data for OSCC patients (n = 112) are shown in Supplementary Table 1. The areas under the curve corresponding to high expression of EGFR and PD-L1 were 0.791 and 0.641, respectively, but the corresponding curve area for the combined prediction is 0.836 (95% Confidence Interval (CI): 0.744 to 0.928), suggesting that the combination of EGFR and PD-L1 dual-targets is important for the precise prognosis of OSCC (Fig. 2C).

To confirm that EGFR and PD-L1 are specific biomarkers for OSCC, biospecimen slides from patients with OSCC (n = 59) were immunohistochemically stained with anti-EGFR and anti-PD-L1 antibodies. The demographics of patients with OSCC (n = 59) are shown in Additional file 1: Table S1. EGFR and PD-L1 expression levels were distinctly higher in OSCC tumors than in para tumor tissues (Fig. 2D). We clearly distinguished tumor tissues from normal tissues by immunohistochemical staining for EGFR and PD-L1. The EGFR H-Score and PD-L1 H-Score in OSCC and para tumor tissues were 141.2 vs. 67.19 and 116.2 vs. 69.66, respectively (**** P < 0.0001) (Fig. 2E).

Detection of EGFR and PD-L1 expression in in

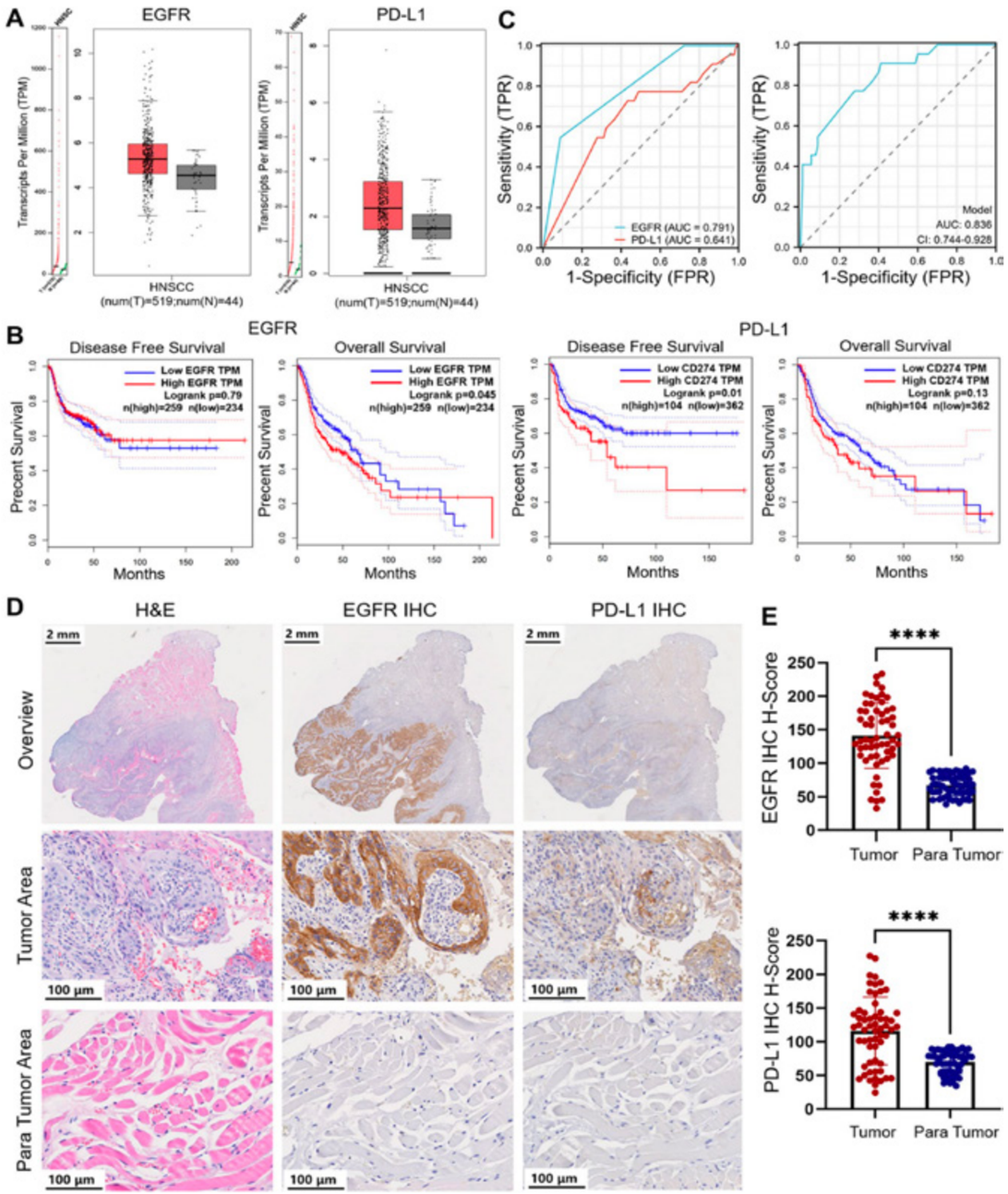


Fig.2 Expression and analysis of EGFR and PD-L1 in HNSCC in GEPIA database and OSCC patients. A Statistical analysis of EGFR and PD-L1 expression in HNSCC tumors and normal tissues obtained from the GEPIA database. Log2(TPM + 1) was used for the log-scale. HNSCC, Head and Neck Squamous Cell Carcinomas. **B** The correlation of EGFR and PD-L1 expression related to disease free survival (DFS) and overall survival (OS). **C** Receiver operating characteristic analysis of EGFR and PD-L1. FPR, False Positive Rate; TPR, True Positive Rate; AUC, Area Under Curve. **D** Representative EGFR and PD-L1 IHC and H&E histology obtained from OSCC biospecimens. Scale bar of overview, 2 mm. Scale bar of tumor and para tumor, 100 μm. **E** IHC H-scores of EGFR and PD-L1 expression in IHC samples (n = 59 patients). **** $p < 0.0001$

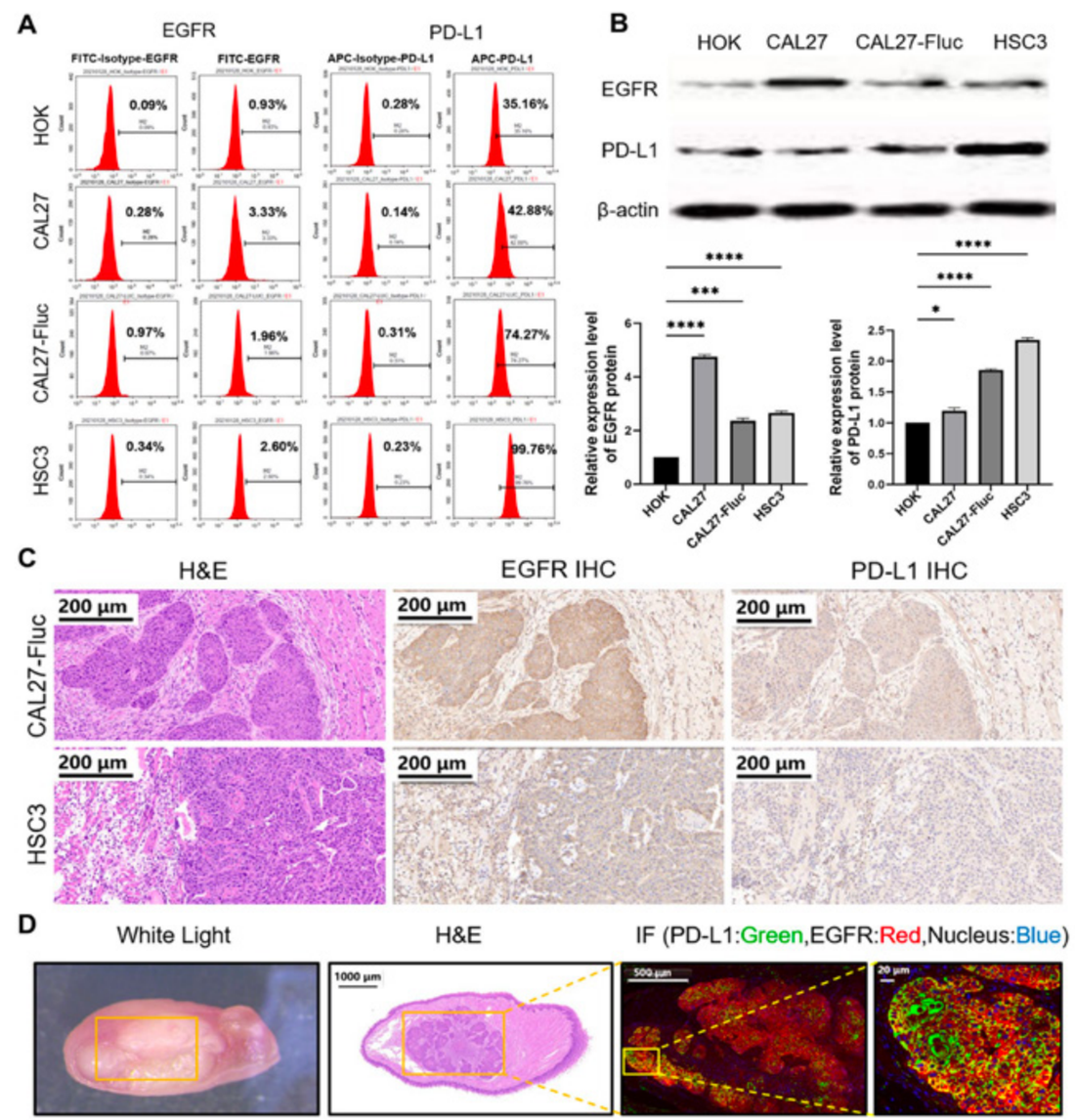


Fig.3 Detection of EGFR and PD-L1 Expression in in vitro OSCC cells and in vivo orthotopic OSCC tumor model. A FACS analysis of HOK, CAL27, CAL27-fLUC, and HSC3 cells for detection of EGFR and PD-L1 expression. **B** Western blotting analysis of EGFR and PD-L1 expression in HOK, CAL27, CAL27-fLUC, and HSC3 cell lines. *$P < 0.05$, ***$P < 0.001$, ****$P < 0.0001$. **C** H&E, EGFR and PD-L1 IHC staining of OSCC tumor xenograft. Scale bar, 200 μm. **D** White light, H&E, immunofluorescence staining (IF) obtained from CAL27-fLUC tumor xenografts. H&E Scale bar, 1,000 μm. Both PD-L1 and EGFR are over-expressed in the cell membrane and stained in green and red, respectively; the nucleus is stained in blue. Scale bar, 500 and 20 μm

Vitro OSCC cells and in vivo orthotopic OSCC tumor model

The expression of EGFR and PD-L1 was relatively higher in CAL27, CAL27-Fluc, and HSC3 cells than in HOK cells, used as control (Fig. 3A). EGFR and PD-L1 protein expression was significantly higher in CAL27 (~4.75-fold, **** $P<0.0001$, ~1.19-fold, * $P<0.05$), CAL27-Fluc (~2.36-fold, *** $P<0.001$, ~1.85-fold, **** $P<0.0001$), and HSC3 (~2.65-fold, **** $P<0.0001$, ~2.34-fold, **** $P<0.0001$) cells than in HOK cells (Fig. 3B). IHC staining showed that EGFR and PD-L1 were both highly expressed in the tumor area in both CAL27-Fluc and HSC3 mouse models (Fig. 3C). EGFR and PD-L1 double IF staining also confirmed their high expression in the CAL27-Fluc mouse tumor xenografts (Fig. 3D). In general, our experiments confirmed that EGFR and PD-L1 were expressed at relatively higher levels in OSCC tumor tissues than in normal tissues.

Characterization of Nimotuzumab-ICG and Atezolizumab-Cy5.5 imaging probes

Nimotuzumab and Atezolizumab were reacted with ICG-NHS and Cy5.5-NHS to yield Nimotuzumab-ICG and Atezolizumab-Cy5.5, respectively (Additional file 1: Fig. S1). The conjugation efficiency was 93.42% and 92.02%, respectively. Nimotuzumab-ICG had an excitation wavelength of 808 nm and absorption peak at 790 nm, which were partially offset from those of free ICG (Excitation: 815 nm), indicating that the dye was conjugated to Nimotuzumab. The spectral characterization of Atezolizumab-Cy5.5 also showed a shift from the excitation wavelength of free Cy5.5 (Excitation: 691 nm), indicating that the dye was linked to Atezolizumab, with excitation and absorption peak of Atezolizumab-Cy5.5 were 670 nm and 679 nm, respectively (Additional file 1: Fig. S2). The cell viability of different human OSCC cells was not influenced when the concentrations of Nimotuzumab-ICG and Atezolizumab-Cy5.5, were lower than 320 μg/mL. These results suggest that Nimotuzumab-ICG and Atezolizumab-Cy5.5 were relatively biocompatible and safe for further in vivo study (Additional file 1: Fig. S3).The in vivo toxicity of Nimotuzumab-ICG and Atezolizumab-Cy5.5 was evaluated in healthy male BALB/c-nu/nu mice; The mice were euthanized 24 h post-injection of PBS, Nimotuzumab-ICG, Atezolizumab-Cy5.5, and Nimotuzumab-ICG and Atezolizumab-Cy5.5 injection (4 mg/kg). Serum assessment showed that the ALT and AST levels were within the normal range in all four groups (Additional file 1: Fig. S4). In addition, no obvious histopathological changes were observed in the major organs (heart, liver, kidney, or spleen) (Additional File 1: Fig. S5). Nimotuzumab-ICG and Atezolizumab-Cy5.5 were further tested for in vivo transoral toxicity and proved to be safe (Additional file 1: Table S2). These results demonstrated that Nimotuzumab-ICG and Atezolizumab-Cy5.5 were well-developed and safe.

The in vivo biodistribution and tumor targeting of Nimotuzumab-ICG and Atezolizumab-Cy5.5

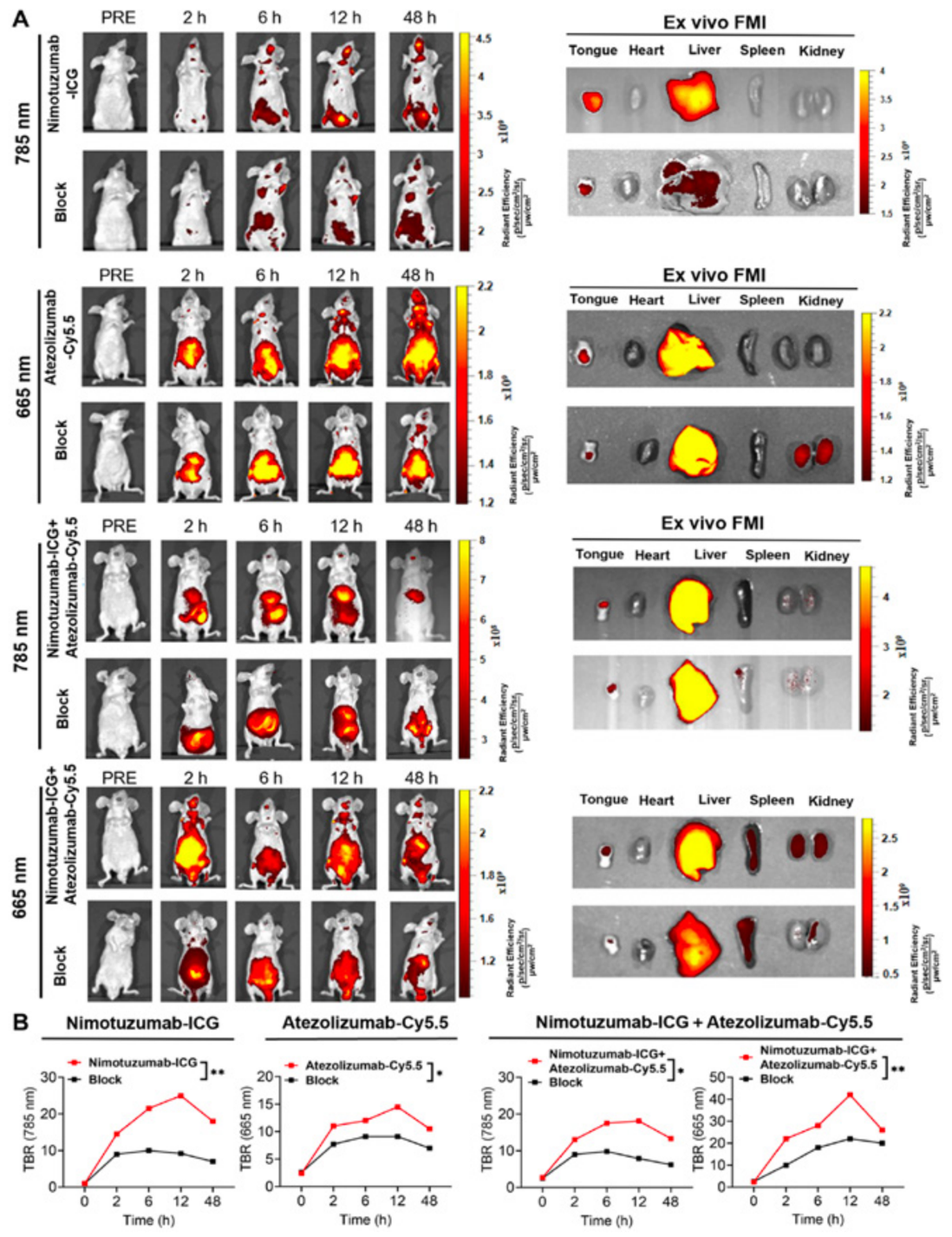
An orthotopic human CAL27-Fluc OSCC tumor mouse model was established and bioluminescence imaging (BLI) was performed to locate the OSCC tumor xenograft (Additional file 1: Fig. S6). CAL27-Fluc oral tumor-bearing mice were divided into different groups: Nimotuzumab-ICG, Atezolizumab-Cy5.5, Nimotuzumab-ICG + Atezolizumab-Cy5.5, and corresponding blocking groups. The fluorescence signals of ICG and Cy5.5 were detected at 785 nm and 665 nm, respectively (Fig. 4A). The fluorescence signal in the Nimotuzumab-ICG group was detected at 2 h post-injection, peaked at 12 h post-injection, gradually decreased, and remained detected 48 h post-injection. The fluorescence signal of the Atezolizumab-Cy5.5 group was detected at 2 h post-injection and peaked at 12 h post-injection. After the simultaneous injection of Nimotuzumab-ICG and Atezolizumab-Cy5.5, both fluorescence signals were detected at 2 h and peaked at 12 h post-injection. The FMI TBR of the target group was higher than that of the corresponding block group at the corresponding time points. The difference in the TBR was more significant at 12 h than other time points. (Fig. 4B). After 48 h of in vivo observation, the tumors and major organs were dissected for ex vivo FMI. The fluorescence signal of the tumor region in the targeted group was higher than that in the blocking group. The fluorescence signals of Nimotuzumab-ICG and Atezolizumab-Cy5.5 were stronger in the liver and certain signals in the kidney, indicating that the imaging probes were mainly metabolized through the liver and some through kidney. Animal study suggested that Nimotuzumab-ICG and Atezolizumab-Cy5.5 dual-targeting imaging probes possessed good OSCC tumor-targeting capability and safety, making them suitable for further clinical application and translation.

Identification of EGFR and PD-L1 expression on OSCC patients' fresh biopsied samples using Nimotuzumab-ICG and Atezolizumab-Cy5.5 imaging probes

For the identification of multitarget expression, a homemade multispectral fluorescence imaging system was developed and used to conduct imaging experiments on patient specimens, and white light and multispectral fluorescence images were obtained. Figure 5A shows the working model diagram and prototype of the multispectral fluorescence imaging system. Fresh OSCC specimens from 10 patients were topically treated with Nimotuzumab-ICG and Atezolizumab-Cy5.5 with different concentrations. The optimal incubation concentration of Nimotuzumab-ICG and Atezolizumab-Cy5.5 was found to be 0.4 mg/mL (Additional file 1: Fig. S7) for 3 min (Additional file 1: Fig. S8). The obvious fluorescence signals of Nimotuzumab-ICG and Atezolizumab-Cy5.5 from the OSCC tumor region could be specifically detected, while

(See figure on next page.)

Fig.4 Biodistribution of Nimotuzumab-ICG and Atezolizumab-Cy5.5 in an orthotopic OSCC mouse model. A In vivo FMI of an OSCC orthotopic mouse model injected with Nimotuzumab-ICG, Atezolizumab-Cy5.5, or a combination of both, respectively. The blocking group represents the pre-administration of corresponding antibody drugs Ex vivo FMI of the tongue with OSCC tumor and major organs 48 h post-injection. **B** TBR analysis of in vivo FMI signal intensity in different groups at different time points. The TBR was significantly different at 12 h postinjection. FMI, fluorescence molecular imaging; TBR, tumor to background ratio. *$P<0.05$, **$P<0.01$



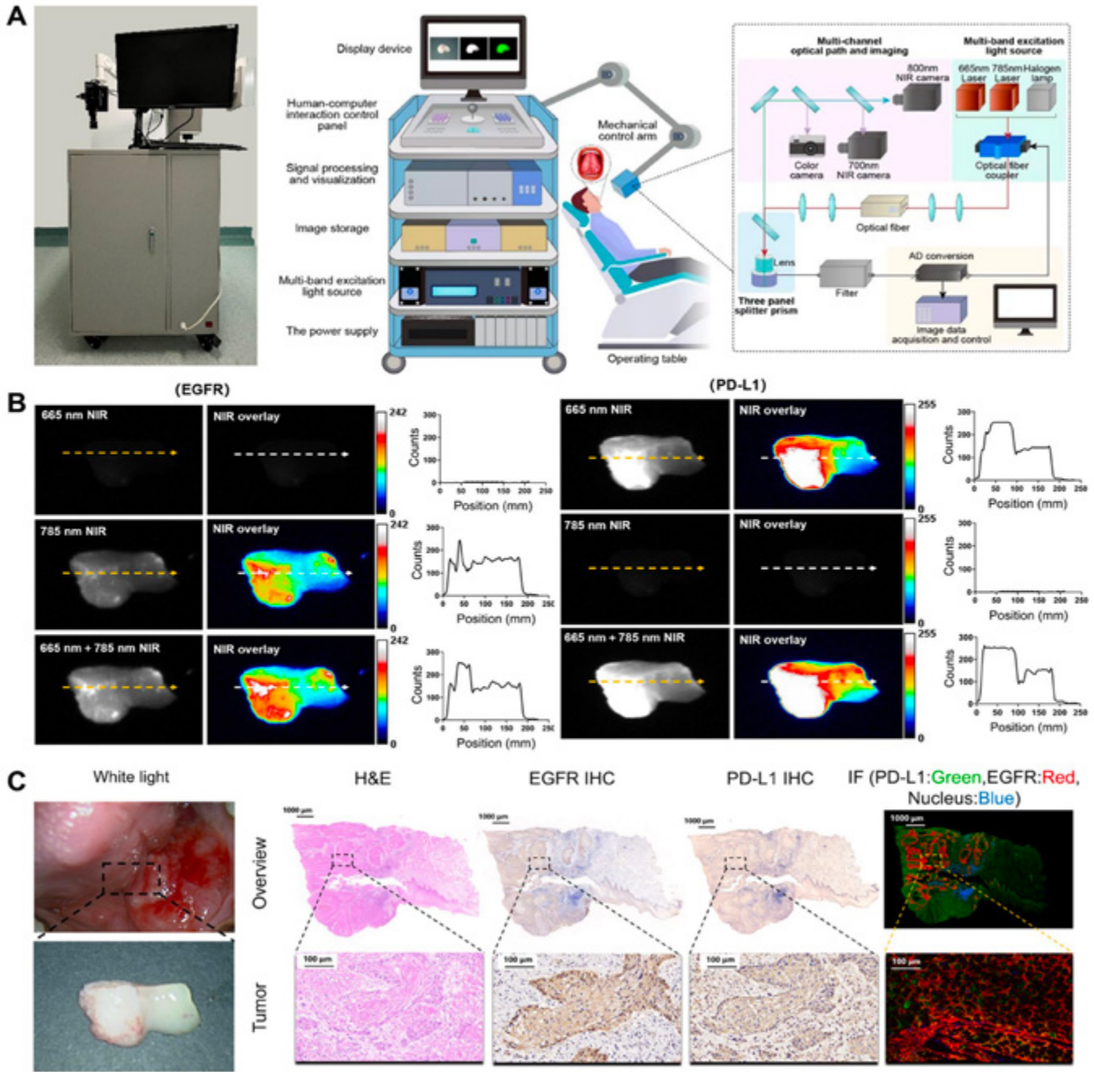


Fig.5 Nimotuzumab-ICG and Atezolizumab-Cy5.5 imaging probes were used to detect fresh OSCC biopsy samples. A The working model diagram and prototype of the home-made multispectral fluorescence imaging system. **B** Representative NIR and NIR overlay image of Nimotuzumab-ICG and Atezolizumab-Cy5.5 staining of fresh OSCC biospecimen from patients. Orange and white arrows correspond to the position and orientation of the cross-sectional fluorescence intensity profiles of the NIR and NIR overlay regions, respectively. Quantitative analysis showed that the fluorescence intensity in the tumor area and the para tumor area. NIR, Near-infrared. **C** White light, H&E, EGFR IHC, PD-L1 IHC, and IF staining of fresh biospecimen from OSCC patients. Scale bar, 1,000 μm and 100 μm

adjacent normal areas did not show fluorescence signals (Fig. 5B). Quantitative analysis showed that Nimotuzumab-ICG imaging discriminated between tumor and para tumor. Under 785 nm NIR, the TBR of the tumor was higher than para tumor (30.05±1.87 vs 20.27±2.35, ** $P<0.01$). In addition, under 665 nm+785 nm NIR, the TBR of tumors was higher than that of para tumor (27.59±1.33 vs 16.81±1.39, *** $P<0.001$). Similarly, Atezolizumab-Cy5.5 could clearly distinguish tumors from parathyroid tumors. Under 665 nm NIR and 665 nm+785 nm NIR, the TBR of tumor and para tumor were (23.18±2.52 vs 14.07±1.51, ** $P<0.01$) and (20.15±1.55 vs 11.32±1.02, ** $P<0.01$), respectively. This observation was further confirmed by H&E, EGFR, and PD-L1 immunohistochemical and immunofluorescence staining of patient's specimens. The expression levels of EGFR and PD-L1 in OSCC tumor tissues were also observed based on the fluorescence intensity produced by excitation light irradiation at 665 nm and 785 nm. The higher the fluorescence intensity, the higher were the biomarker expression levels (Fig. 5C). Therefore, we further performed multiplexed fluorescence imaging of EGFR and PD-L1 in 30 fresh OSCC patients' specimens. FMI results, immunohistochemical staining, and immunofluorescence staining showed that the sensitivity and specificity of Nimotuzumab-ICG were 96.4% (95%CI: 79.8%~99.8%) (27/28) and 100% (95%CI: 19.8%~100%) (2/2), respectively. The sensitivity and specificity of Atezolizumab-Cy5.5 were 95.2% (95%CI: 74.1%~99.7%) (20/21) and 88.9% (95%CI: 50.7%~99.4%) (8/9), respectively. The high imaging sensitivity and specificity of the imaging probes with high safety indicate the feasibility of topical application in human patients with OSCC in situ.

Fluorescence imaging of Nimotuzumab-ICG and Atezolizumab-ICG in OSCC patients in situ

Nimotuzumab-ICG and Atezolizumab-ICG were topically applied as mouthwashes to 8 OSCC patients with OSCC. The fluorescence imaging of EGFR and PD-L1 dual targets was mainly performed using the Digital Precision Medicine imaging device H2800 (DPM, Beijing, China), which possesses an endoscopic detector that can be applied to patients' mouths. Quantitative analysis after gargling with Nimotuzumab-ICG (0.4 mg/ml) showed that EGFR expression was specifically highly expressed in tumor tissues but not in normal mucosa tissues (Fig. 6A, top, 23.9±1.17 vs 3.01±0.24, **** $P<0.0001$). After surgical treatment, tissue specimens were subjected to ex vivo fluorescence imaging, H&E staining, and immunohistochemical staining. Quantitative analysis showed that the TBR in the tumor was higher than that in the para tumor (Fig. 6A, bottom, 48.02±4.65 vs 19.27±1.973, *** $P<0.001$). Similarly, after gargling with Atezolizumab-ICG (0.4 mg/ml), quantitative analysis showed that the TBR in the tumor was higher than that in the para tumor in both in situ and ex vivo experiments. The TBR of the tumor and para tumor were 23.4±2.19 vs 5.34±0.61, (*** $P<0.001$) and 27.47±2.43 vs 17.06±1.52 (** $P<0.01$), respectively (Fig. 6B). The fluorescence imaging data of 8 cases of OSCC are summarized in Additional file 1: Table S3. The ex vivo FMI, HE, and IHC data were almost consistent with in vivo FMI observations, showing that specific tumor areas can be fluorescently illuminated by the targeted imaging probes.

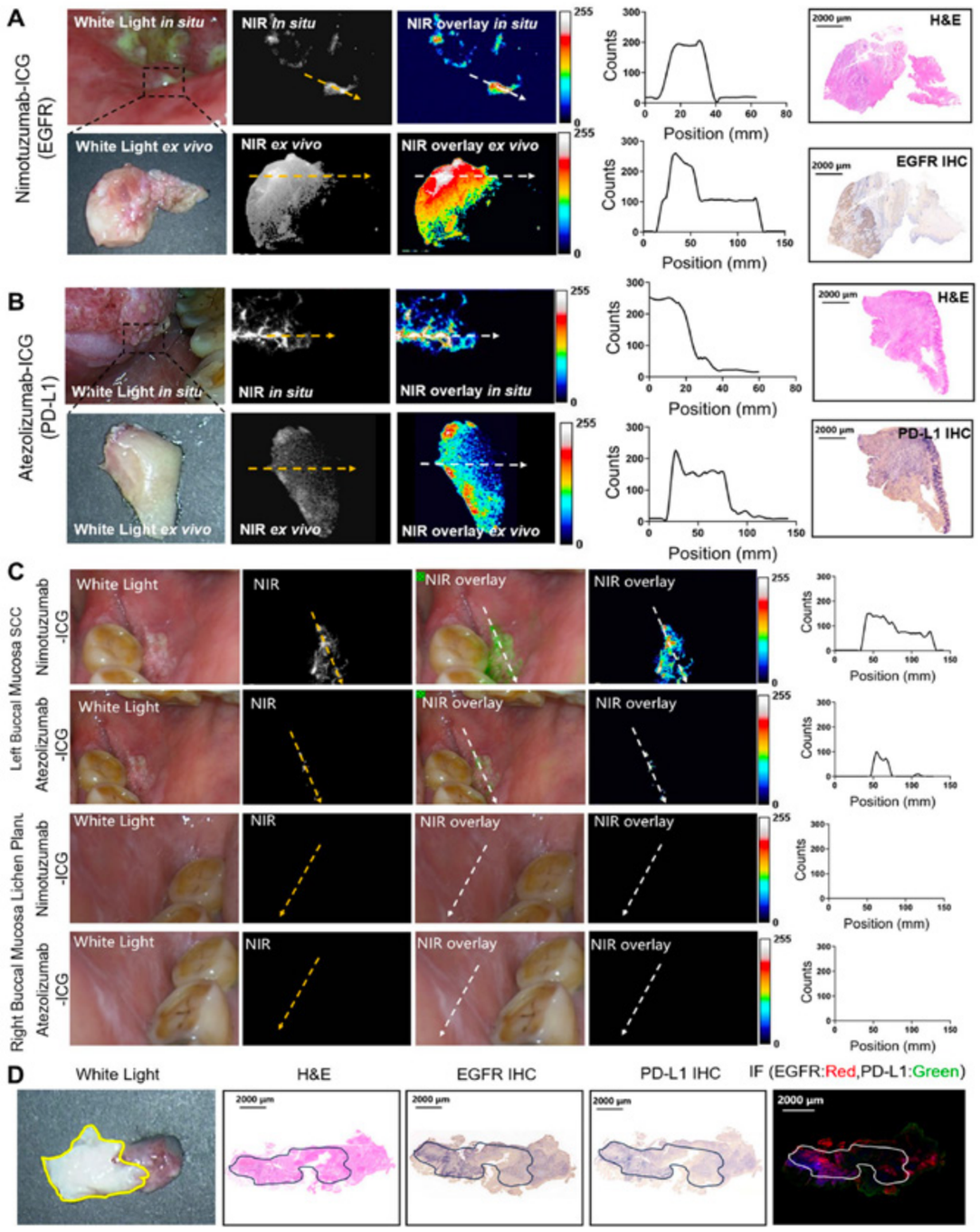
Interestingly, a patient had buccal mucosal SCC on the left side and buccal mucosal lichen planus on the right side of the mouth. After gargling with Nimotuzumab-ICG and Atezolizumab-ICG imaging probes, fluorescence signal was observed in the left buccal mucosa, whereas no trace of fluorescence signal was observed in the right buccal mucosa (Fig. 6C). The data validated the specificity of the Nimotuzumab-ICG and Atezolizumab-ICG probes for the detection of OSCC. These in vivo observations were further verified via subsequent IHC and IF experiments (Fig. 6D).

Discussion

Sensitive detection of tumor-specific biomarkers can facilitate the early and accurate detection of OSCC and provide guidance for precision therapy. At present, a number of studies have demonstrated the feasibility of OSCC fluorescence guided localization and guidance of surgical margin resection. Early diagnosis of OSCC was achieved through oral spray fluorescence recognition imaging [29,30]. EGFR and PD-L1 are key targets in OSCC. Herein, we developed Nimotuzumab-ICG and Atezolizumab-Cy5.5 imaging probes combined with multispectral FMI to facilitate the noninvasive detection of EGFR and PD-L1 with high sensitivity, specificity and safety. We further translated our dual-target imaging strategy from preclinical OSCC bearing animal studies to clinical patients with OSCC, which showed great potential for the comprehensive management of OSCC for early detection and image-guided therapy, including targeted therapy, surgery, and immunotherapy.

EGFR and PD-L1 are important therapeutic targets in OSCC. EGFR, a transmembrane glycoprotein, is highly expressed in 90% of HNSCC cases and is a strong prognostic indicator of head and neck cancer [38,39]. Maurizi et al. found that EGFR levels are associated with the risk of recurrence and death [40]. PD-L1 is also highly expressed on the surface of HNSCC [41]. The expression of PD-L1 in various solid tumors, such as esophageal, gastric, and thyroid cancers, is associated with poor prognosis [42,43]. Bioinformatics analysis from GEPIA Datasets and immunohistochemical staining of 59 human OSCC biological specimens from the Chinese PLA General Hospital showed that EGFR and PD-L1 were highly expressed in OSCC. The dataset obtained based on GEPIA also verified that high EGFR expression in HNSCC was correlated with OS. Overexpression of PD-L1 in HNSCC is associated with DFS, not OS, which is consistent with previous findings [44]. However, whether the expression of EGFR or PD-L1 in HNSCC is correlated with OS or DFS may be subjected to differences due to the sample numbers and follow-up time. Based on a 3-year retrospective analysis of 112 patients with OSCC treated at the Chinese PLA General Hospital, a ROC curve was used to predict the clinical model. The combination analysis of EGFR and PD-L1 expression in predicting the 3-year OS of patients with OSCC can improve the prediction accuracy. Therefore, both EGFR and PD-L1 can not only be used as prognostic markers for OSCC but also as potential markers for guiding antitumor therapy.

Multiplexed FMI technology provides good opportunities for noninvasive and multitarget detection with high sensitivity and safety. A variety of malignant tumors, including OSCC, have tumor molecular heterogeneity [45], The multispectral fluorescence probes make up for the situation that the imaging of a single mode



or the recognition of a single target makes the ability of tumor characterization and boundary analysis relatively challenging. And multispectral is more powerful than single spectrum in defining tumor heterogenous properties and boundary analysis [24]. And thus the detection of multitargets is most likely to improve both the sensitivity and specificity of tumor recognition and for accurate clinical diagnosis and guidance of treatment. The fluorescence-labeled anti-EGFR antibody Cetuximab-IRDye800CW has been used to locate tumors and surrounding tissues in advanced HNSCC [34]. Intravenous injection of Cetuximab-IRDye800 in patients with HNSCC achieved high sensitivity and specificity and successfully distinguished tumors from normal tissues in FMI-guided surgical studies [46,47]. As a humanized monoclonal antibody, Nimotuzumab has a high affinity and can bind to the extracellular domain of EGFR and inhibit EGF binding [48] Nimotuzumab has been approved in several countries for the treatment of HNSCC [49] and glioma [50] based on clinical trials of various malignancies [51]. Nimotuzumab has the advantage of low toxicity compared with Cetuximab [35]. Therefore, in this study, we developed a novel EGFR targeting Nimotuzumab-ICG fluorescence imaging probe. In OSCC tumor tissues with high EGFR expression, Nimotuzumab-ICG showed a higher fluorescence imaging signal and better image contrast than images of tumors with low or no EGFR expression. Moreover, we developed an Atezolizumab-Cy5.5 fluorescence imaging probe targeting the PD-L1 molecule, which can realize noninvasive and dynamic imaging of PD-L1 expression and provide guidance for safe immunotherapy. Targeted molecular imaging of PD-L1 is an effective method for dynamic and noninvasive evaluation of PD-L1 expression; however, the main administration method is the intravenous route [37,52–54]. In this study, we administered imaging probes through topically administration [27–32], which can achieve almost instant imaging of EGFR and PD-L1 by spraying the target area with micro-doses of fluorescent imaging probes and detecting suspected cancer lesions. Multispectral FMI imaging of Nimotuzumab-ICG and Atezolizumab-Cy5.5 is a new non-invasive, sensitive and specific way to identify tumors. Ultimately, we will be able to offer more precise and personalized treatments.

To further promote clinical translation, we applied our imaging probes as mouthwashes to 8 OSCC patients. Since the homemade multispectral fluorescence imaging system is still in the prototype stage, it cannot be used in the surgery room. Hence, we utilized the commercialized Digital Precision Medicine imaging device H2800, though this system has only one channel for detecting ICG fluorescence signal. Hence, we developed Nimotuzumab-ICG and Atezolizumab-ICG imaging probes and applied them consecutively to OSCC patients through a mouthwash. Our imaging method is quick sensitive and specific in detecting EGFR and PD-L1 expression in patients with OSCC, which was further validated by post-surgical histology and immunohistochemistry. Moreover, our imaging strategy can discriminate tumor lesions from other oral diseases, such as buccal mucosa lichen planus. For the future clinical application of homemade multispectral fluorescence imaging system can not only provide early identification and diagnosis of OSCC, but also provide guidance for clinical surgical boundary recognition and anti-tumor targeted therapy and immunotherapy. In addition, it is still necessary to further optimize the imaging algorithm and autofocus algorithm, eliminate the image distortion caused by oral haze, and continuously improve the image recognition ability.

Conclusions

We developed a multispectral FMI imaging strategy that demonstrated the feasibility of concurrently detecting multiple tumor biomarkers and the potential for the early detection of tumors that are molecularly heterogeneous. We synthesized the multispectral fluorescence imaging probes Nimotuzumab-ICG and Atezolizumab-Cy5.5 with OSCC targeted imaging performance and good biosafety. Make up for the situation that the imaging method of a single mode or the recognition of a single target makes the ability of tumor characterization and boundary analysis relatively Challenging. Combined with the homemade multispectral fluorescence imaging system, the EGFR and PD-L1 expression can be identified and quantified from preclinical OSCC tumor-bearing mouse models to clinical OSCC patients, which facilitates early cancer detection and provide guidance for anti-tumor targeted therapy, image-guided surgery, and immunotherapy of OSCC. We demonstrated a proof-of-concept for detecting multiple targets concurrently in patients with OSCC neoplasia, which is promising for a wide range of clinical applications, including early screening and surveillance, biopsy guidance, quick staining of fresh biopsies, in vivo diagnosis, and intraoperative margin delineation.

Acknowledgements

The authors thank Weisheng Wen, Jingqiu Bu, Lei Zhang, Peng Chen, Qing Xi, Huawei Liu, Yipeng Ren, Lin Feng, Fei Chen, Lejun Xing, Bo Wei and Ye Tao for the support during the fresh OSCC patients' biospecimens collection, Rui Wu for manuscript proofreading.

Abbreviations

OSCC	Oral squamous cell carcinoma
EGFR	Epidermal growth factor receptor
PD-L1	Programmed death-ligand 1
FMI	Fluorescence molecular imaging

See figure on the last page

Fig.6 Fluorescence imaging of Nimotuzumab-ICG and Atezolizumab-ICG in OSCC human patients. A White light, NIR, and NIR overlay images were obtained by oral gargling experiment of Nimotuzumab-ICG on OSCC patients in clinical application. A dotted white line was drawn from tumor area to para tumor tissue to calculate the counts of fluoresce signal. The expression of EGFR was further imaged with Nimotuzumab-ICG in fresh biopsied specimens of OSCC patients, and verified using IHC and H&E staining. Scale bar, 2000 μm. **B** White light, NIR, and NIR overlay images were obtained by oral gargling experiment of Atezolizumab-ICG on OSCC patients for clinical application. The expression of PD-L1 was imaged with Atezolizumab-ICG in fresh biopsied specimens of OSCC patients, and verified using IHC. Scale bar, 2000 μm. **C** Nimotuzumab-ICG and Atezolizumab-ICG were used in the oral gargling experiment, and white light, NIR, and overlayed NIR images of both the left (with OSCC area) and right (with lichen planus) buccal mucosa were obtained. The fluorescence intensity was measured, calculated, and verified via pathology. **D** H&E, EGFR IHC, PD-L1 IHC, and IF staining were performed on fresh OSCC specimens on the patient's left buccal mucosa. The yellow line indicated the gross tumor range in fresh surgical specimens. The black line shows the tumor areas in H&E staining and IHC staining, while the white line shows the tumor areas in IF staining. Scale bar, 2,000 μm.

CT	Computed Tomography
MRI	Magnetic Resonance Imaging
NIRF	Near-infrared fluorescence
ICG	Indocyanine green
HNSCC	Head and Neck squamous cell carcinoma
ROC	Receiver operator characteristic
IHC	Immunohistochemistry
H&E	Hematoxylin and eosin
ROI	Region of interest
TBR	Tumor to background ratio

Authors' contributions

NH J drafted the manuscript. NH J and Y T performed the experiments, collected OSCC tissue specimen. Y A developed a home-made multispectral fluorescence imaging system. NH J, ZY Z and KS H analyzed the data. CW C performed part of the experiments. W M, J T and Y D designed the study and revised the manuscript. All authors read and approved the final manuscript.

Funding

This work was supported by the National Natural Science Foundation of China (82272111, 92159303, 62027901), the National Key R&D Program of China (Grant number 2023YFC3402800), and Beijing Natural Science Foundation under Grant (L232097).

Availability of data and materials

The datasets used and analyzed during our study are available from the corresponding author on reasonable request.

Ethics approval and consent to participate

Our study was approved by the Ethics Committee of Chinese PLA General Hospital (No. S2021-097–01). All participants provided written informed consent. The animal experiments were approved by the guidelines of the Institutional Animal Care and Use Committee (Permit No: IA21-2203–24) at the Institute of Automation, Chinese Academy of Sciences, and the experiments were conducted in conformity with approved guidelines. Author confirm that all the experiments on the use of human tissue samples confirm that all experiment were performed in accordance with the Declaration of Helsinki's guidelines and regulations. The study was approved and the participants gave their informed consent.

Consent for publication

Not applicable.

Competing interests

The authors declare that they have no competing interests.

References

1. Sung H, Ferlay J, Siegel RL, Laversanne M, Soerjomataram I, Jemal A, et al. Global cancer statistics 2020: GLOBOCAN estimates of incidence and mortality worldwide for 36 cancers in 185 countries. CA Cancer J Clin. 2021;71(3):209–49.
2. Siegel RL, Miller KD, Fuchs HE, Jemal A. Cancer statistics, 2022. CA Cancer J Clin. 2022;72:7–33.
3. Gyawali B, Shimokata T, Honda K, Ando Y. Chemotherapy in locally advanced head and neck squamous cell carcinoma. Cancer Treat Rev. 2016;44:10–6.
4. Sadreddini S, Baradaran B, Aghebati-Maleki A, Sadreddini S, Shanehbandi D, Fotouhi A, et al. Immune checkpoint blockade opens a new way to cancer immunotherapy. J Cell Physiol. 2019;234:8541–9.
5. Madhura MG, Rao RS, Patil S, Fageeh HN, Alhazmi A, Awan KH. Advanced diagnostic aids for oral cancer. Dis Mon. 2020;66: 101034.
6. Silverman S Jr, Kerr AR, Epstein JB. Oral and pharyngeal cancer control and early detection. J Cancer Educ. 2010;25:279–81.
7. Bhatia N, Lalla Y, Vu AN, Farah CS. Advances in optical adjunctive AIDs for visualisation and detection of oral malignant and potentially malignant lesions. Int J Dent. 2013;2013:194029.
8. Glen P, Botha E. Early detection and prevention of head and neck cancers. Br Dent J. 2022;233:726–30.
9. Wang Y, Zhang X, Wang S, Li Z, Hu X, Yang X, et al. Identification of metabolism-associated biomarkers for early and precise diagnosis of oral squamous cell carcinoma. Biomolecules. 2022;12:400.
10. Steigen SE, Søland TM, Nginamau ES, Laurvik H, Costea DE, Johannessen AC, et al. Grading of oral squamous cell carcinomas-Intra and interrater agreeability: Simpler is better? J Oral Pathol Med. 2020;49:630–5.
11. Wick MR. The hematoxylin and eosin stain in anatomic pathology-An often-neglected focus of quality assurance in the laboratory. Semin Diagn Pathol. 2019;36:303–11.
12. Lajolo C, Gioco G, Rupe C, Patini R, Rizzo I, Romeo U, et al. Patient perception after oral biopsies: an observational outpatient study. Clin Oral Investig. 2021;25:5687–97.
13. Keereweer S, Kerrebijn JD, van Driel PB, Xie B, Kaijzel EL, Snoeks TJ, et al. Optical image-guided surgery–where do we stand? Mol Imaging Biol. 2011;13:199–207.
14. Koller M, Qiu SQ, Linssen MD, Jansen L, Kelder W, de Vries J, et al. Implementation and benchmarking of a novel analytical framework to clinically evaluate tumor-specific fluorescent tracers. Nat Commun. 2018;9(1):3739.
15. Nagaya T, Nakamura YA, Choyke PL, Kobayashi H. Fluorescence-Guided Surgery. Front. Oncol. 2017;7:314.
16. Yokoyama J, Fujimaki M, Ohba S, Anzai T, Yoshii R, Ito S, et al. A feasibility study of NIR fluorescent image-guided surgery in head and neck cancer based on the assessment of optimum surgical time as revealed through dynamic imaging. Onco Targets Ther. 2013;6:325–30.
17. Bredell MG. Sentinel lymph node mapping by indocyanin green fluorescence imaging in oropharyngeal cancer - preliminary experience. Head Neck Oncol. 2010;2:31.
18. Xu M, Rettig MP, Sudlow G, Wang B, Akers WJ, Cao D, et al. Preclinical evaluation of Mab CC188 for ovarian cancer imaging. Int J Cancer. 2012;131:1351–9.
19. Andreev OA, Dupuy AD, Segala M, Sandugu S, Serra DA, Chichester CO, et al. Mechanism and uses of a membrane peptide that targets tumors and other acidic tissues in vivo. Proc Natl Acad Sci USA. 2007;104:7893–8.
20. Yang JA, Kong WH, Sung DK, Kim H, Kim TH, Lee KC, et al. Hyaluronic acid-tumor necrosis factor-related apoptosis-inducing ligand conjugate for targeted treatment of liver fibrosis. Acta Biomater. 2015;12:174–82.
21. Keereweer S, Mol IM, Kerrebijn JD, Van Driel PB, Xie B, de BaatenburgJong RJ, et al. Targeting integrins and enhanced permeability and retention (EPR) effect for optical imaging of oral cancer. J Surg Oncol. 2012;105:714–8.
22. Voskuil FJ, de Jongh SJ, Hooghiemstra WTR, Linssen MD, Steinkamp PJ, de Visscher SAHJ, et al. Fluorescence-guided imaging for resection margin evaluation in head and neck cancer patients using cetuximab-800CW: a quantitative dose-escalation study. Theranostics. 2020;10(9):3994–4005.
23. de Wit JG, Vonk J, Voskuil FJ, de Visscher SAHJ, Schepman KP, Hooghiemstra WTR, et al. EGFR-targeted fluorescence molecular imaging for intraoperative margin assessment in oral cancer patients: a phase II trial. Nat Commun. 2023;14(1):4952.
24. Chen J, Jiang Y, Chang TS, Joshi B, Zhou J, Rubenstein JH, et al. Multiplexed endoscopic imaging of Barrett's neoplasia using targeted fluorescent heptapeptides in a phase 1 proof-of-concept study. Gut. 2021;70:1010–3.
25. Hu Z, Fang C, Li B, Zhang Z, Cao C, Cai M, et al. First-in-human liver-tumour surgery guided by multispectral fluorescence imaging in the visible and near-infrared-I/II windows. Nat Biomed Eng. 2020;4(3):259–71.
26. Netti PA, Berk DA, Swartz MA, Grodzinsky AJ, Jain RK. Role of extracellular matrix assembly in interstitial transport in solid tumors. Cancer Res. 2000;60:2497–503.
27. Rosenthal EL, Warram JM, de Boer E, Basilion JP, Biel MA, Bogyo M, et al. Successful translation of fluorescence navigation during oncologic surgery: a consensus report. J Nucl Med. 2016;57:144–50.
28. Lu G, Fakurnejad S, Martin BA, Van Den Berg NS, Van Keulen S, Nishio N, et al. Predicting therapeutic antibody delivery human head and neck cancers. Clin Cancer Res. 2020;26:2582–94.
29. Kossatz S, Pirovano G, De DemétrioSouza França P, Strome AL, Sunny SP, Zanoni DK, et al. Validation of the use of a fluorescent PARP1 inhibitor for the detection of oral, oropharyngeal and oesophageal epithelial cancers. Nat Biomed Eng. 2020;4:272–85.
30. de DemétrioSouza França P, Kossatz S, Brand C, KarassawaZanoni D, Roberts S, Guru N, et al. A phase I study of a PARP1-targeted topical fluorophore for the detection of oral cancer. Eur J Nucl Med Mol Imaging. 2021;48:3618-3630.26.
31. Wang J, Li S, Wang K, Zhu L, Yang L, Zhu Y, et al. A c-MET-targeted topical fluorescent pRObe cMBP-ICG improves oral squamous cell carcinoma detection in humans. Ann Surg Oncol. 2023;30:641–51.
32. Buckle T, van Alphen M, van Oosterom MN, van Beurden F, Heimburger N, van der Wal JE, et al. Translation of c-met targeted image-guided surgery solutions in oral cavity cancer-initial proof of concept data. Cancers (Basel). 2021;13:2674.
33. Vermorken JB, Specenier P. Optimal treatment for recurrent/metastatic head and neck cancer. Ann Oncol. 2010;21(Suppl 7):252–61. 10.1093/annonc/mdq453 [PubMed] [CrossRef] [Google Scholar]
34. de Boer E, Warram JM, Tucker MD, Hartman YE, Moore LS, de Jong JS, et al. In Vivo Fluorescence Immunohistochemistry: Localization of Fluorescently Labeled Cetuximab in Squamous Cell Carcinomas. Sci Rep. 2015;5:10169.
35. Allan DG. Nimotuzumab: evidence of clinical benefit without rash. Oncologist. 2005;10:760–1.
36. Mahoney KM, Rennert PD, Freeman GJ. Combination cancer immunotherapy and new immunomodulatory targets. Nat Rev Drug Discov. 2015;14:561–84.
37. Bensch F, van der Veen EL, Lub-de Hooge MN, Jorritsma-Smit A, Boellaard R, Kok IC, et al. 89Zr-atezolizumab imaging as a non-invasive approach to assess clinical response to PD-L1 blockade in cancer. Nat Med. 2018;24:1852–8.
38. Zanotti L, Paderno A, Piazza C, Pagan E, Bignotti E, Romani C, et al. Epidermal growth factor receptor detection in serum and saliva as a diagnostic and prognostic tool in oral cancer. Laryngoscope. 2017;127:E408–14.
39. Nicholson RI, Gee JM, Harper ME. EGFR and cancer prognosis. Eur J Cancer. 2001;37(Suppl 4):S9-15.
40. Maurizi M, Almadori G, Ferrandina G, Distefano M, Romanini ME, Cadoni G, et al. Prognostic significance of epidermal growth factor receptor in laryngeal squamous cell carcinoma. Br J Cancer. 1996;74:1253–7.
41. Wang X, Teng F, Kong L, Yu J. PD-L1 expression in human cancers and its association with clinical outcomes. Onco Targets Ther. 2016;9:5023–39.
42. Wu P, Wu D, Li L, Chai Y, Huang J. PD-L1 and survival in solid tumors: a meta-analysis. PLoS One. 2015;10:e0131403.
43. Chowdhury S, Veyhl J, Jessa F, Polyakova O, Alenzi A, MacMillan C, et al. Programmed death-ligand 1 overexpression is a prognostic marker for aggressive papillary thyroid cancer and its variants. Oncotarget. 2016;7:32318–28.
44. Ukpo OC, Thorstad WL, Lewis JS Jr. B7–H1 expression model for immune evasion in human papilloma virus-related oropharyngeal squamous cell carcinoma. Head Neck Pathol. 2013;7:113–21.
45. Turajlic S, Sottoriva A, Graham T, Swanton C. Resolving genetic heterogeneity in cancer. Nat Rev Genet. 2019;20(7):404–16.
46. Rosenthal EL, Warram JM, de Boer E, Chung TK, Korb ML, Brandwein-Gensler M, et al. Safety and tumor specificity of cetuximab-IRDye800 for surgical navigation in head and neck cancer. Clin Cancer Res. 2015;21:3658–66.
47. Warram JM, de Boer E, van Dam GM, Moore LS, Bevans SL, Walsh EM, et al. Fluorescence imaging to localize head and neck squamous cell carcinoma for enhanced pathological assessment. J Pathol Clin Res. 2016;2:104–12.
48. Mateo C, Moreno E, Amour K, Lombardero J, Harris W, Pérez R. Humanization of a mouse monoclonal antibody that blocks the epidermal growth factor receptor: recovery of antagonistic activity. Immunotechnology. 1997;3:71–81.
49. Crombet T, Osorio M, Cruz T, Roca C, del Castillo R, Mon R, et al. Use of the humanized anti-epidermal growth factor receptor monoclonal antibody h-R3 in combination with radiotherapy in the treatment of locally advanced head and neck cancer patients. J Clin Oncol. 2004;22:1646–54.
50. Ramos TC, Figueredo J, Catala M, González S, Selva JC, Cruz TM, et al. Treatment of high-grade glioma patients with the humanized anti-epidermal growth factor receptor (EGFR) antibody h-R3: report from a phase I/II trial. Cancer Biol Ther. 2006;5:375–9.
51. Bayés M, Rabasseda X, Prous JR. Gateways to clinical trials. Methods Find Exp Clin Pharmacol. 2007;29:697–735.
52. Peng Z, Lu C, Shi G, Yin L, Liang X, Song G, et al. Sensitive and quantitative in vivo analysis of PD-L1 using magnetic particle imaging and imaging-guided immunotherapy. Eur J Nucl Med Mol Imaging. 2023;50:1291–305.
53. An Y, Bian C, Yan D, Wang H, Wang Y, Du Y, et al. A Fast and Automated FMT/XCT Reconstruction Strategy Based on Standardized Imaging Space. IEEE Trans Med Imaging. 2022;41:657–66.
54. Du Y, Jin Y, Sun W, Fang J, Zheng J, Tian J. Advances in molecular imaging of immune checkpoint targets in malignancies: current and future prospect. Eur Radiol. 2019;29:4294–302.

BMC Med. 2024. 22(1):342 Published online: 26 August 2024

Stomatology

Research Article

A c-MET-Targeted Topical Fluorescent Probe cMBP-ICG Improves Oral Squamous Cell Carcinoma Detection in Humans

Jingbo Wang [1], Siyi Li [2], Kun Wang [3], Ling Zhu [1], Lin Yang [1], Yunjing Zhu [1], Zhen Zhang [2], Longwei Hu [2], Yuan Yuan [1], Qi Fan [1], Jiliang Ren [1], Gongxin Yang [1], Weilong Ding [1], Xiaoyu Zhou [4], Junqi Cui [5], Chunye Zhang [5], Ying Yuan [6], Ruimin Huang [7] ✉, Jie Tian [8] ✉, Xiaofeng Tao [9] ✉

Abstract

Introduction: The postoperative survival of oral squamous cell carcinoma (SCC) relies on precise detection and complete resection of original tumors. The mucosal extension of the tumor is evaluated visually during surgery, but small and flat foci are difficult to detect. Real-time fluorescence imaging may improve detection of tumor margins.

Materials and methods: In the current study, a peptide-based near-infrared (NIR) fluorescence dye, c-MET-binding peptide-indocyanine green (cMBP-ICG), which specifically targets tumor via c-MET binding, was synthetized. A prospective pilot clinical trial then was conducted with oral SCC patients and intraoperatively to assess the feasibility of cMBP-ICG used to detect tumors margins. Fluorescence was histologically correlated to determine sensitivity and specificity.

Results: The immunohistochemistry (IHC) results demonstrated increased c-Met expression in oral SCC compared with normal mucosa. Tumor-to-background ratios ranged from 2.71 ± 0.7 to 3.11 ± 1.2 in different concentration groups. From 10 patients with oral SCC, 60 specimens were collected from tumor margins. The sensitivity and specificity of discriminative value derived from cMBP-ICG application in humans were respectively 100% and 75%.

Conclusions: Topical application of cMBP-ICG is feasible and safe for optimizing intraoperative visualization and tumor margin detection in oral SCC patients, which could clinically increase the probability of complete resections and improve oncologic outcomes.

[1] Department of Radiology, Ninth People's Hospital, School of Medicine, Shanghai Jiao Tong University, Shanghai, China.
[2] Department of Oral and Maxillofacial-Head and Neck Oncology, Ninth People's Hospital, School of Medicine, Shanghai Jiao Tong University, Shanghai, China.
[3] CAS Key Laboratory of Molecular Imaging, Beijing Key Laboratory of Molecular Imaging, The State Key Laboratory of Management and Control for Complex Systems, Institute of Automation, Chinese Academy of Sciences, Beijing, China.
[4] Molecular Imaging Center, Shanghai Institute of Materia Medica, Chinese Academy of Sciences, Shanghai, China.
[5] Department of Pathology, Ninth People's Hospital, School of Medicine, Shanghai Jiao Tong University, Shanghai, China.
[6] Department of Radiology, Ninth People's Hospital, School of Medicine, Shanghai Jiao Tong University, Shanghai, China.
[7] Molecular Imaging Center, Shanghai Institute of Materia Medica, Chinese Academy of Sciences, Shanghai, China.
[8] CAS Key Laboratory of Molecular Imaging, Beijing Key Laboratory of Molecular Imaging, The State Key Laboratory of Management and Control for Complex Systems, Institute of Automation, Chinese Academy of Sciences, Beijing, China.
[9] Department of Radiology, Ninth People's Hospital, School of Medicine, Shanghai Jiao Tong University, Shanghai, China.

Ann Surg Oncol. 2023. 30(1): 641-651 Published online: 02 October 2022

Introduction

Approximately 95% of all head and neck cancers are squamous cell carcinoma (SCC), the most common of which is oral SCC (excluding non-melanoma cutaneous cancers).[1] Oral SCCs are primarily treated surgically with adequate resection margins to ensure complete resection and to minimize functional impairment related to the procedure. The mucosal extension of the tumor usually is evaluated by visual inspection.[2,3] However, translation of information from preoperative imaging into the actual situation in the patient during surgery is challenging, and macroscopic evaluation of a tumor in the oral cavity by palpation during surgery is difficult and inaccurate. Moreover, the precursor lesions, such as oral leukoplakia and submucous fibrosis, can subsequently progress to cancers,[4] whereas the ability to detect malignant transformation early is limited, and preoperative biopsies may suffer from sample error.[5] Therefore, it is necessary to develop supplementary methods for precise detection of early malignancy and delineation of mucosal extension of the tumor.

The merging of targeted probes with clinical user-friendly imaging technologies provides a powerful and easy tool for the early and precise detection of cancer.[6–8] Near-infrared (NIR) fluorescence-guided surgery is a promising technique for superficial head and neck lesions using tumor-targeting fluorescent agents (e.g., panitumumab-IRDye800CW, cetuximab-IRDye800CW).[9,10] For local small-distance metastases, extracellular matrix (ECM) may prevent the penetration of intravenously administered macromolecular agents and cause a higher miss rate for small lesions[11] due to the different mean fluorescence intensity (MFI) and tumor background ratio (TBR). Instead, mouth-washing topical administration of the targeted probe could be an alternative approach, which could cover the entire oral mucosa and directly screen out suspicious cancer foci without restriction from other tissues.[12] Meanwhile, the interval between probe administration and imaging would be significantly reduced to minutes and least affected by individual difference.[13,14]

As a c-MET-targeting peptide, c-MET-binding peptide (cMBP) has been developed for tumor imaging and gene delivery.[15–17] Therefore, instead of intravenous delivery of NIR fluorescence dye, we propose that topically applied, NIR fluorescently labeled, simply synthesized homing-peptide-based, oral SCC-targeting contrast agent, c-MET-binding peptide-indocyanine green (cMBP-ICG), can be preferable for superficial, invasive, and heterogenous tumors such as oral SCC.

This study aimed to determine the safety and feasibility of cMBP-ICG topical application of real-time NIR fluorescence imaging for oral SCC. To study the validity of this method, we conducted a clinical trial for pre- and intraoperative detection of

primary tumor and tumor spread.

Methods

Synthesis and Characterization of cMBP-ICG

The NIR fluorescent dye, Sulfo-ICG-Maleimide (Adipogen Corporation, San Diego, CA, USA), was conjugated to a custom-synthesized peptide (KSLSRHDHIHHHK) and purified by ChinaPeptides Co. (Suzhou, China) (Fig. S1).

Clinical Study Design and Participants

An exploratory, open-label, single-arm, single-center, two-group, parallel dose-escalation was held to assess the feasibility of cMBP-ICG for detecting tumor margins and cancer foci. This trial was undertaken with Asian patients and approved by the institutional review board of the Chinese Clinical Trial Registry (ChiCTR2200058058). Written informed consent was obtained from all the patients.

Between October 2021 and February 2022, the study enrolled 10 patients with clinically suspicious, biopsy- proven, primary or recd and neck SCC (details shown in Table S1), who were scheduled to undergo standard-of-care surgery with curative intent at Shanghai Ninth Peoples' Hospital. All the enrolled patients were 18 years old or older, with a life expectancy longer than 12 weeks. The exclusion criteria for this study and the entire flowchart are shown in Fig. S2.

All the enrolled patients underwent preoperative imaging (CT and/or MRI). The tumor-node-metastasis (TNM) stage was determined in accordance with the American Joint Committee on Cancer (AJCC) eighth edition criteria. According to the time of admission, enrolled patients were classified into two groups. Different concentrations of cMBP-ICG were used for fluorescence imaging in the different groups.

In Vivo and Ex Vivo Clinical Imaging Procedures

Lyophilized powder of cMBP-ICG (1.0 mg, 3.6×10^{-4} mmol) was dissolved in ultrapure water (145.7 or 72.8 mL) to a concentration of 2.5 or 5.0 μM. In order of enrollment, the first five cases used a 5.0-μM concentration for gargling or ex vivo specimen surface smearing, and the next five cases used a 2.5-μM concentration. For preoperative in vivo cMBP-ICG application, the patients gargled 25 mL of cMBP-ICG solution for 30 s, then spit it out (twice). Next, the patients gargled 30 mL of ultrapure water for 30 s and spit it out (twice).

For imaging investigations, videos were acquired before topical application, after topical application pre-wash, and after topical application post-wash using a fluorescence laryngoscope. The camera lens was aimed at the region of interest (ROI) and manually focused. The same instrument settings were used for all the imaging procedures (exposure time, 30 ms; excitation power, 20%; gain, 3 dB, at 60 frames per second). The distance between the lens and surface of the ROI was kept at about 10 mm.[6] The videos were acquired by slow scanning of the tumor area and surrounding normal mucosa (non-tumor region).

The patients then underwent surgery the next day. For intraoperative ex vivo back-table fluorescence-guided imaging (FGI), the resected tumor specimens were collected directly after excision, and the fresh (non-fixed) samples were incubated with cMBP-ICG at either of the aforementioned concentrations. Then, the samples were rinsed for 1 min with phosphate-buffered saline (PBS) to clear unbound cMBP-ICG (twice), followed by direct NIR fluorescence imaging. Because the fluorescent probe is coated on the surface of resected tumor specimens, the fluorescence images cannot be compared directly with the cross-section. Small tissues from the tumor margin were cut from specimens labeled as high-fluorescence (suspicious of cancer) or low-fluorescence intensity, respectively. The surgeon with 20 years of experience performing maxillofacial surgery, who was blinded to the imaging results, predicted the malignant possibility of specimens according to their visual features and tactile textures. The detection was compared with fluorescence imaging findings, with reference to histopathologic results.

Histopathologic Processing and Adverse Events Report

Histopathologic processing of the surgical specimens was performed by a board-certified head and neck pathologist. Intraoperatively, frozen-section staining was routinely performed using hematoxylin and eosin (H&E) with real-time guidance from NIR fluorescence imaging. The remaining tumor tissue was embedded in paraffin, and 5-μm-thick sections were obtained. Two neighboring sections were stained with H&E and immunohistochemistry (IHC) for c-MET. A board-certified pathologist masked to NIR fluorescence results evaluated the H&E slides microscopically and outlined the tumor areas. In the analysis of ex vivo tissue, the pathology diagnosis was used as the gold standard for tumor detection.

Adverse events were reported on the basis of federal regulations and the National Cancer Institute Common Terminology Criteria for Adverse Events (v5.0). The workflow of the clinical trial is shown in Fig. 1.

Image and Statistical Analysis

For the image analysis, ImageJ software (1.53q, NIH, Bethesda, USA) was used. The tumor-to-background ratio (TBR) was determined as the ratio of fluorescence intensity of tumor ROI (FI_{tumor}) and fluorescence intensity of tumor- adjacent tissue ROI ($FI_{adjacent\ tissue}$). For in vivo imaging, fluorescence intensities of six ROIs were selected from the gross oral SCC tumor area, and six other ROIs were selected from the surrounding non-tumorous tissues. Whenever possible, the ROIs were equally spaced and spread across each area in the surgical field. The mean fluorescence intensity (MFI) was defined as the total fluorescence signal divided by the total number of pixels within the ROI. An overall MFI was calculated using the MFIs from the ROIs. Ex vivo imaging was used to determine the sensitivity and specificity of cMBP-ICG for surgical specimens. A receiver operating characteristic (ROC) analysis was performed on data from the small tissue cut from specimens' surfaces. The pathologist assessed whether the tumor was present in the tissue using a binary (yes/no) approach according to H&E stains of paraffin sections.

Descriptive statistics, including the MFI and TBR, are presented as mean ± standard deviation. The MFI and TBR of the 10 in vivo lesions and ex vivo specimens from all the patients were compared using the unpaired t test (two-tailed). We calculated the predictive values of the fluorescence signal of the fresh tissues against the H&E result. A *P* value lower than 0.05 was considered statistically significant. Statistics and figures were generated using GraphPad Prism (GraphPad, version 8.0, San Diego, CA, USA) and the R language (R Foundation, Vienna, Austria) pROC package (version 1.18.0) and the yardstick package (version 0.0.9).

Results

cMBP-ICG Targets c-MET for Optical Imaging of Human Oral SCC

All 10 patients completed ex vivo fluorescence imaging, and 8 patients completed preoperative in vivo fluorescence imaging. In vivo imaging was not performed for patient 5 or patient 8 due to limitation of mouth opening. Patient 9 was a non-tumor patient, so the MFI for patient 9 was not included in the TBR statistics.

Both preoperative in vivo and intraoperative ex vivo imaging showed the pronounced fluorescence signal in the tumor area compared with the surrounding uninvolved mucosa for both coating concentrations. As the concentration doubled, the mean fluorescence intensity of both the tumor and the background increased. The preoperative imaging showed that the TBR of primary tumors was 4.12 ± 0.7 in the 5.0-μM group and 4.08 ± 2.0 in the 2.5-μM group. The mean fluorescence intensities (MFIs) of primary tumors and adjacent tissue were respectively 65.09 ± 21.8 a.u. and 18.23 ± 8.3 a.u. in the 5.0-μM group and 36.65 ± 30.9 a.u. versus 10.21 ± 10.6 a.u. in the 2.5-μM group.

The intraoperative imaging showed that the TBR of primary tumors was 2.71 ± 0.7 in the 5.0-μM group and 3.11 ± 1.2 in the 2.5-μM group. The MFIs of primary tumors and adjacent tissue were respectively 47.35 ± 9.0 a.u. and 21.14 ± 8.2 a.u. in the 5-μM group and 32.45 ± 34.2 a.u. versus 13.38 ± 15.2 a.u. in the 2.5-μM group (Fig. 2A).

Tissue samples from nine patients were available for c-MET expression analysis via IHC (excluding 1 non-tumor patient). Based on the pathologic assessment, c-MET IHC staining was analyzed and quantified in tumor, mucosal epithelium, and deep margin (i.e., healthy muscle tissue). The mean ratio of the c-MET area (marked by diaminobenzidine, DAB) over the total tumor tissue area was 57.3% ± 17.8%, which was significantly higher than in normal mucosal epithelium (8.4% ± 3.6%) or in the deep muscular margin (4.1% ± 2.2%), indicating high c-MET expression in the tumor (Fig. 2B; $p < 0.0001$ in both compared groups). The patients' TBR, MFI, and DAB/tissue area were summarized in Fig. S3.

To determine the specificity and sensitivity of cMBP- ICG for

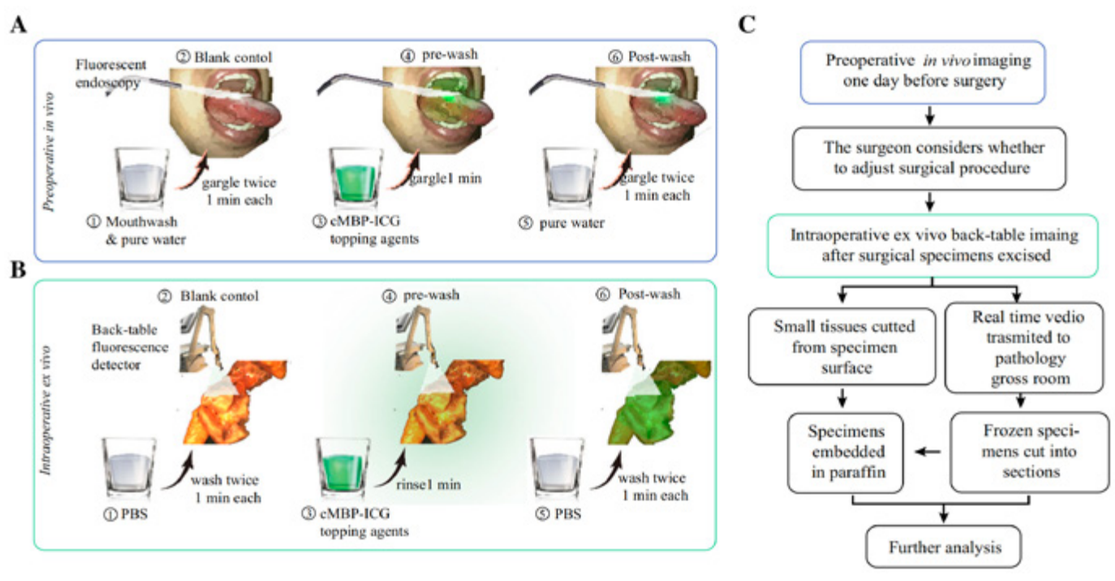


Fig.1 Workflow of fluorescence imaging-based head and neck squamous cell carcinoma (SCC) delineation.(A) After careful mouth-washing (step 1), patients (n = 10) with clinically suspicious or biopsy-proven head and neck SCC were examined using a Digital Precision Medicine imaging device H2000 (DPM, Beijing, China) with an endoscopic camera and an ICG-optimized Light Emitting Diode (LED)-filter system. The tumor area and the surrounding margins were imaged as a blank control (step 2). After gargling, a solution of cMBP-ICG (step 3) at different concentrations (2.5 IM or 5 IM, each dose n = 5) for 1 min, a pre-wash imaging procedure was performed (step 4). The patients then gargled ultrapure water for 1 min as a clearing solution (step 5), followed by cMBP-ICG administration of post-wash imaging (step 6). (B) Immediately after resection, tissue specimens, including margin samples, were imaged ex vivo in a vertical near-infrared imaging device Z2000 (DPM) following the same protocol described earlier. (C) Preoperative images were taken into consideration during the surgical procedure plan. Intraoperative back-table videos were transmitted in real time to the pathology gross room as frozen section's references. Small tissues were cut from specimens' high and low fluorescence intensity surfaces, respectively, for further analysis. cMBP-ICG, c-MET- binding peptide-indocyanine green

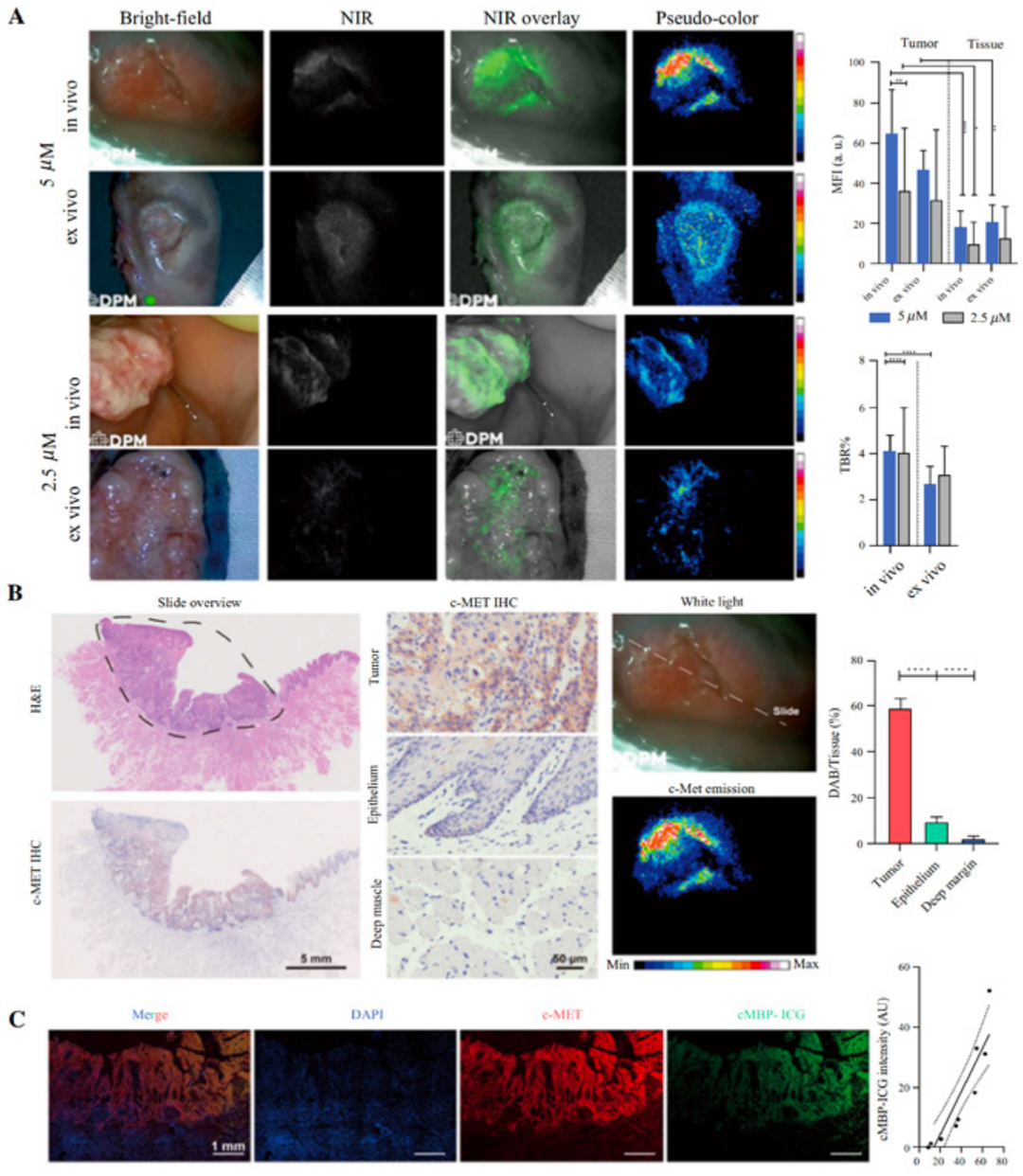


Fig.2 Analysis of cMBP-ICG dosage selection in vivo and ex vivo after fluorescence imaging, and correlation between c-MET expression and cMBP-ICG signal intensity. (A) Snapshots of two patients from different dosage groups. The MFI and TBR of each group and each application procedure (in vivo/ex vivo) were calculated following the same process. (*$p < 0.05$, **$p < 0.01$, ***$p < 0.001$, ****$p < 0.0001$. Data are presented as mean ± SEM.) (B) Representative c-MET immunohistochemistry images and hematoxylin and eosin images from a paraffin-embedded tumor section of a patient (slide overview) showing an area of head and neck squamous cell carcinoma (SCC) (black circle). Preoperative in vivo cMBP-ICG imaging of the patient showing the slide location in the whole tumor.(C) Immunofluorescence of the paraffin-embedded tumor shown in panel B. cMBP-ICG, c-MET- binding peptide-indocyanine green; MFI, mean fluorescence intensity; TBR, tumor-to-background ratio; SEM, standard error of the mean.

Ann Surg Oncol. 2023. 30(1): 641-651 Published online: 02 October 2022

Table 1 Sensitivity and specificity of fluorescence for tumor surface samples

Samples	Group 1	Group 2	Both groups	Surgeons
Concentration (μM)	5	2.5		
Sensitivity (%)	100	46	71	60
Specificity (%)	75	88	83	95
PPV	80	79	83	93
NPV	100	61	73	71
AUC	0.88	0.65	0.78	NA
95 % CI	0.88–1	0.53–0.833	0.68–0.88	NA

PPV Positive predictive value, *NPV* Negative predictive value, *AUC* Area under the curve, *CI* Confidence interval

neoplastic tissue, the MFI data from 60 tumor margin specimens were used to create an ROC curve. The area under the curve (AUC), the average positive predictive value (PPV), and the negative predictive value (NPV) are shown in Table 1.

Adjacent paraffin-embedded tumor sections were stained with c-MET/AF488, cMBP-ICG, and DAPI. Immunofluorescence (IF) images showed co-localization of c-MET/AF488 and cMBP-ICG with nearly identical tissue shapes. The correlation test showed that cMBP-ICG localization was significantly associated with c-MET localization ($R^2 = 0.8319$; $p < 0.01$; Fig. 2C).

cMBP-ICG Enables the Screening of Small Cancer Foci

In one patient, a suspicious region was detected 2 mm above the primary gum cancer area during preoperative in vivo NIR fluorescence imaging. The attending surgeon expanded the surgical removal area accordingly. This suspicious micro-lesion also was visualized in intraoperative ex vivo NIR fluorescence imaging. An intraoperative frozen section was sliced with guidance from the ex vivo NIR fluorescence imaging, ensuring that the suspicious lesion was present in the frozen section. The pathology results verified this suspicious lesion as severe dysplasia of the epithelium, which had a high probability of cancerization (Fig. 3A). A two dimensional (2D) fluorescence intensity histogram showed the signal enhancement in the tumor area and the suspicious region (Fig. 3B).

The attending surgeon suspected a gum leukoplakia in a patient to be a local metastasis considering its anatomic proximity to the primary tongue tumor. However, the NIR fluorescence intensity of this area in preoperative in vivo imaging was not higher than that of the adjacent normal tissue. This finding did not affect the operation plan. Still, the NIR fluorescence intensity of this area in the excised specimen was not higher than in the adjacent normal tissue. The pathologic analysis of frozen section of this area showed normal mucosa (Fig. 3C). A 2D fluorescence intensity histogram showed the signal enhancement only in the tumor area (Fig. 3D).

cMBP-ICG Shows Potential for Rapid Biopsy and Tumor Grading

The biopsy for one patient showed that one lesion of buccal mucosa was tumor negative. The attending physician speculated that it was a tumor and needed to be removed. High intensity of both in vivo and ex vivo NIR fluorescence suggested partial cancerization (Fig. 4A). Postoperative pathology results confirmed that the expression of c-MET in the high-fluorescence signal area was high, and that local small cancer foci were present in this area (Fig. 4B). A 2D fluorescence intensity histogram showed the signal enhancement in the high c-Met expression area (Fig. 4C).

The 10 cases in this study included intraepithelial neoplasia (n = 1) (Fig. 5A), well-differentiated oral SCC (n = 2), moderately well-differentiated oral SCC (low grade) (n = 6) (Fig. 5B), and moderately differentiated oral SCC (intermediate grade) (n = 1) (Fig. 5C). The MFI and TBR of the moderately well-differentiated oral SCC and the moderately differentiated ORAL SCC were analyzed by unpaired *t* test (Fig. S4). There were significant differences in all the outcomes.

The topical usage of cMBP-ICG at a relatively high concentration did not result in any grade 1 or higher adverse events for the patients with oral SCC.

Discussion

The detection of mucosal extension and skip lesion is essential for patients with oral SCC for complete resection and minimized functional impairment. Lugol's iodine staining is a traditional method for imaging and screening of cancer, primarily in esophageal cancer and cervical cancer. Although this

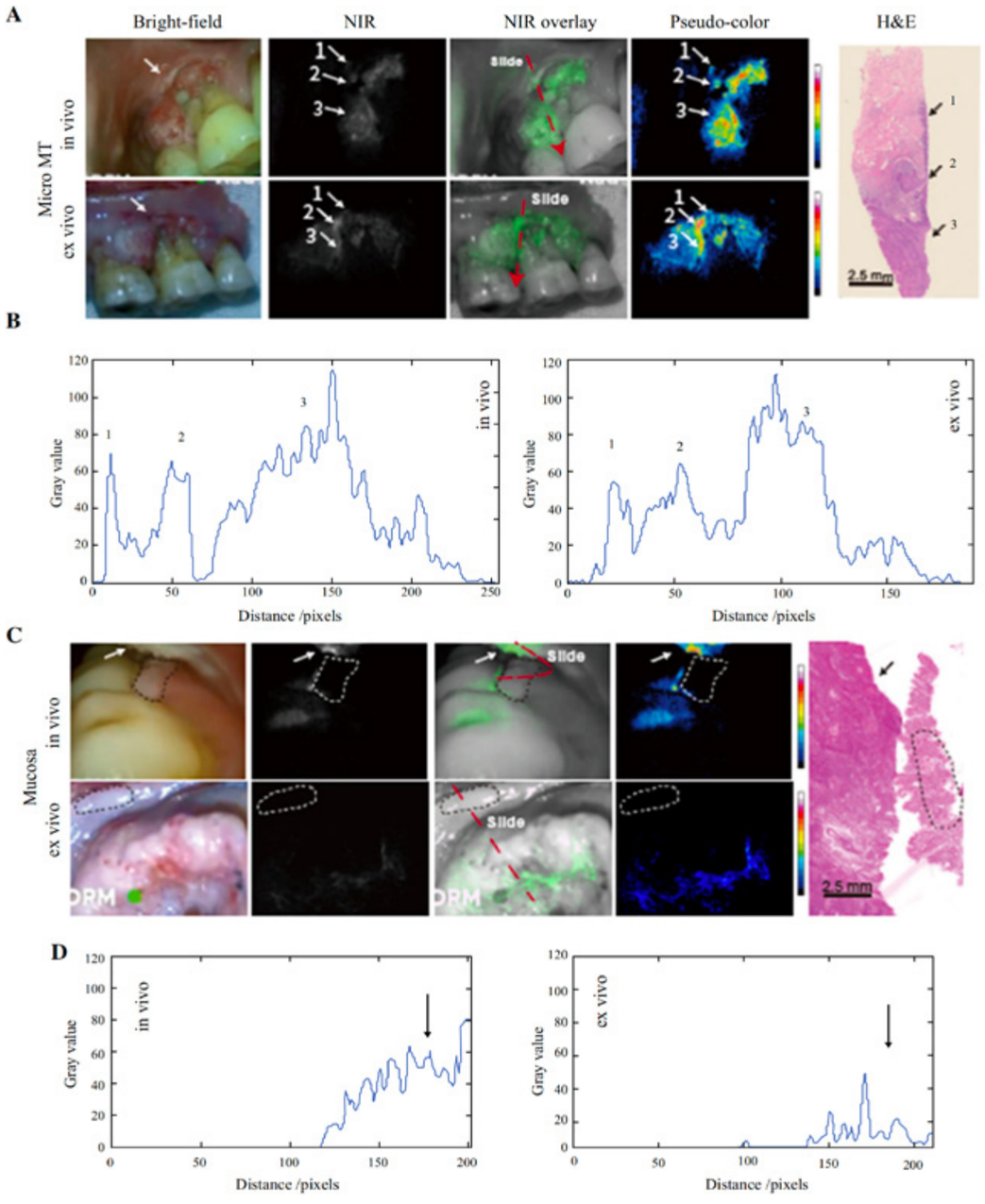


Fig.3 A Suspicious lesions discovered and C a nontumor lesion screened out during preoperative imaging procedure. Frozen sections were cut according to the real-time videos. The section locations (red dashed line) were ensured to meet the region of interest. (A) Severe dysplasia (arrows 1 and 2) detected 2 mm above the primary gum cancer area (arrow 3). (B) Two-dimensional (2D) fluorescence- intensity histogram illustrating the signal enhancement in the tumor area and the suspicious region. (C) A gum leukoplakia (dashed circle) adjacent to primary tongue cancer (arrow) that proved to be normal mucosa pathologically. (D) A 2D fluorescence-intensity histogram illustrating the signal enhancement in the tumor area. NIR, near infrared; H&E, hematoxylin and eosin.

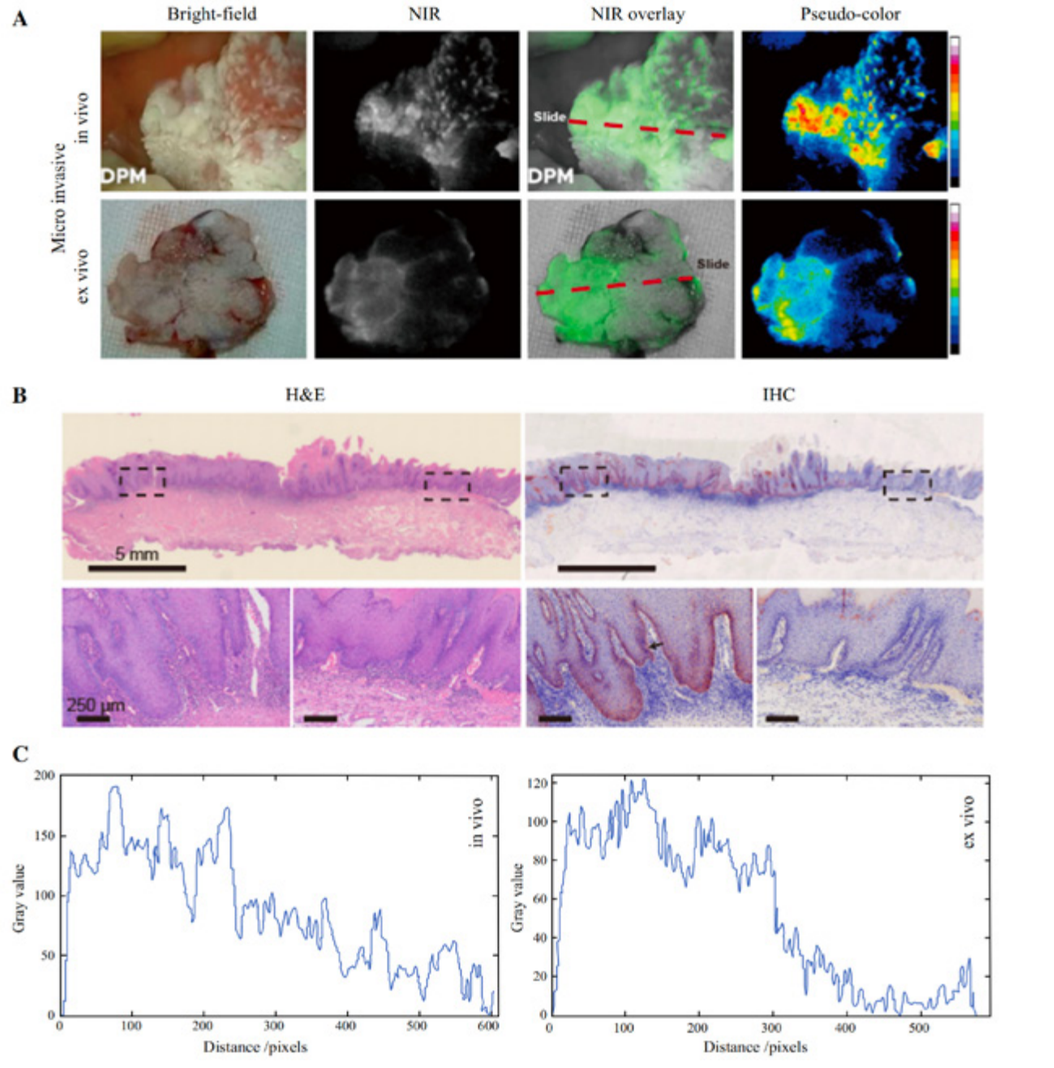


Fig.4 Heavily keratinized mucosa with small cancer foci in one patient. (A) Snapshots from preoperative (upper row) and intraoperative (lower row) imaging. (B) Hematoxylin and eosin (H&E) and immunohistochemistry (IHC) of the frozen sections. The lower row demonstrates enlarged views of the two areas framed in black in the upper row. The section locations (red dashed line in panel A) were ensured to meet the region of interest.(C) Two- dimensional (2D) fluorescence-intensity histogram illustrating the signal enhancement in the high c-Met expression area.

technique is sensitive, its specificity is relatively low, and it is time-consuming. Lugol stain also leads to esophageal spasms and sometimes pain in Lugol chromoendoscopy, which might be more insufferable for oral cancer patients. Moreover, it is unavailable for non- keratinized mucosa detection and not related to pathologic grading of oral SCC.[18,19]

For superficial oral lesions using tumor-targeting fluorescent agents, NIR fluorescence-guided surgery is a promising alternative. The advantages of NIR ligands include greater penetration depth and lower autofluorescence than fluorophores emitting in the visible-wavelength range.[7,8,20,21] As reported previously, more than 60–80% of oral SCCs have shown c-Met protein overexpression.[22–24] Therefore, c-Met could serve as a promising biomarker for diagnosis and imaging of oral SCC.

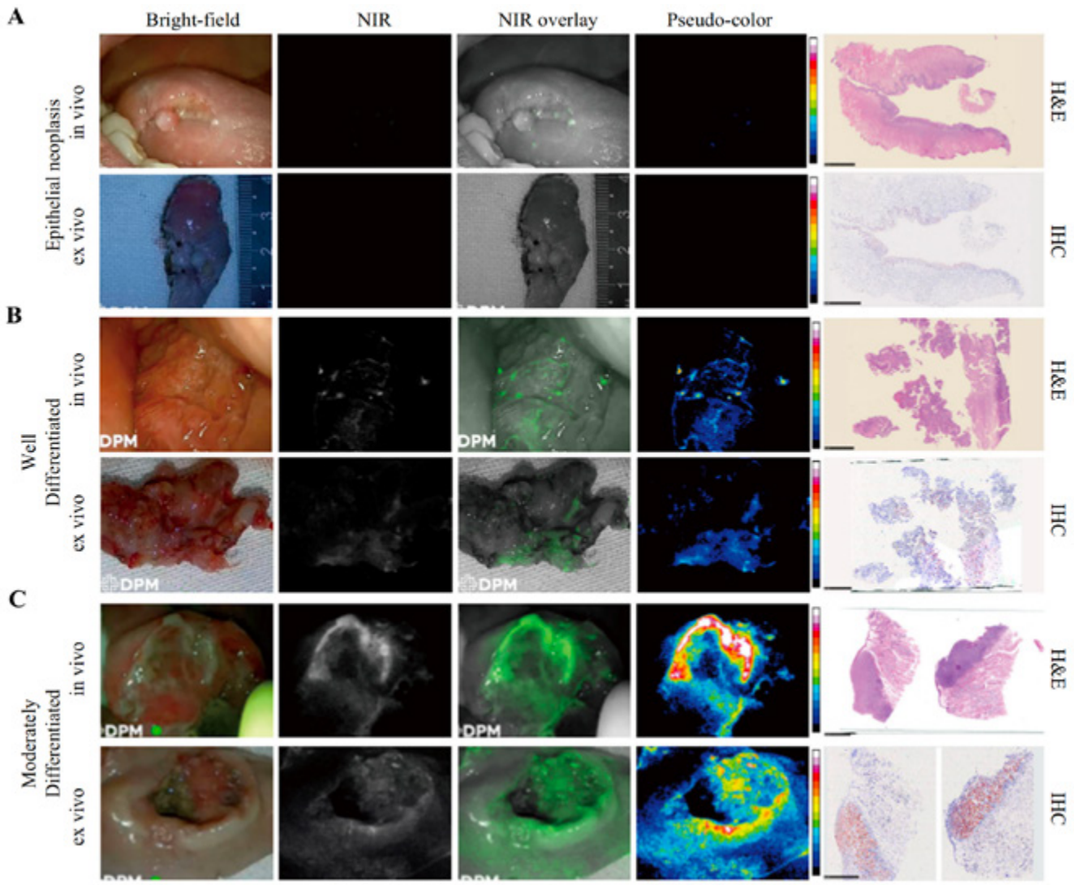


Fig.5 Comparison of epithelial neoplasia and two grades of head and neck squamous cell carcinoma (SCC). A Epithelial neoplasia showing low fluorescence intensity (FI) in both in vivo and ex vivo imaging. The frozen section shows low c-MET expression of this lesion. B Highly differentiated head and neck SCC showing slightly increased FI compared with panel A. The frozen section shows about 25% of the c-MET expression area fraction. C Moderately differentiated head and neck SCC showing high FI in in vivo and ex vivo imaging. The frozen section shows about 90% of the c-MET expression area fraction.

Based on our previous work,[16] cMBP peptide was selected as the targeting ligand because of its high docking affinity to c-Met and known application in tumor therapy[25] and imaging.[26,27] This homing peptide may offer many properties including high tumor penetration, low immunogenicity, and cheap synthesis.[28] Indocyanine green was chosen as the imaging agent due to its biomedical safeness and high signal-to-background ratio.[29]

In this study, a coating concentration of 5.0-μM displayed better imaging contrast in a dark room during preoperative in vivo experiment. In contrast, under intra-operative ex vivo conditions, surgical lighting background in the operation theater caused higher background noise to sensors of the camera, and the concentration of 2.5-μM ensured a higher TBR. Regarding visual perception of real- time fluorescence imaging, the tumor area could be visualized more clearly in 5.0-μM group. High TBR from the 2.5-μM group beneficated from low background noise, but it did not effectively help to discriminate tumor regions. Therefore, MFI may be a more suitable index to referee tumor fluorescence imaging effectiveness. The ROC results in this study demonstrated that the 5.0-μM group had a higher AUC. The PPV and NPV also were higher in the 5.0-μM group, agreeing with the visual effect.

Due to the ‘‘areal cancerization’’ feature of oral SCC,[4] microscopic cancer foci or premalignant lesions may discretely occur around the primary cancer area. This characteristic is a key

underlying cause for the high relapse rate of oral SCC. We believe that the first patient (Fig. 3A, whose occult lesion was detected by fluorescence imaging) benefited from the approach used in this study. Our NIR fluorescence imaging method was proven capable of identifying and locating such small cancerous foci or precancerous lesions. The attending surgeon can revise surgical procedure accordingly to suppress the probability of cancer relapse.

Oral SCC can invade various mucosa spaces through mucosa folds and tunnels.

For the second patient (Fig. 3B), the suspicious leukoplakia was located in an area highly suggestive of a metastasis. Conservatively, surgeons are inclined to excise such lesions. However, oral environments of patients with oral cancer usually are unhealthy, exhibiting mucocutaneous striatal abnormalities without pathologic significance. Excessive excision may unnecessarily impair the physiologic function. Near-infrared fluorescence imaging may assist the conventional technique in differentiating cancer foci for long-term follow-up of mucosal lesions and in preventing overtreatment.

Biopsy is not very effective in detecting early-stage carcinoma *in situ* given that the cancerized area may be too small and the biopsy puncture area may not cover the cancerized area. The aberrant activation and overexpression of c-MET is a very early event in the development of squamous cell carcinoma.[30] In the current study, topical application of c-MET-targeting fluorescence dye was superior in detecting the early-stage cancer. Expression of C-MET varied with the severity of epithelial dysplasia. Specifically, the level of c-MET expression descended from carcinoma in situ via highly atypical hyperplasia to normal mucosa. For the patient mentioned in the third RESULTS section, the observed NIR fluorescence intensity agreed well with this trend, reflecting c-MET expression. Therefore, topical application of cMBP-ICG can be used to guide biopsy sampling and may shift the detection of oral SCC to an earlier time point.

This study had many strengths. First, topically applied real-time imaging agents are well-suited for the study of head and neck cancer.[14] Given that oral SCC develops from the mucosal epithelium in the oral cavity, pharynx, and larynx[31] and is present on the oral and oropharyngeal surfaces, gargling may be an excellent choice for noninvasive and convenient prompt investigation. Namely, the mouth-washing topical application of the targeting imaging agents may be an optimal approach given that mouthwash covers the entire oral mucosa and directly screens out suspicious small cancer foci without restriction from the other tissues.

Second, the topical application significantly reduced the imaging time of the NIR fluorescence probes (within minutes).[13,14,32] The fast renal clearance of peptide-based targeting agents,[28] is not seen as a drawback, but rather as a benefit from the perspective of medication safety.

The relatively small sample size limited this research. The tumor tissues resided sub-surface. NIR fluorescence imaging was conducted at surfaces of ROI, while imaging information of cross-section of tumor tissues was not obtained. Relevant study regarding in-depth imaging is ongoing. The NIR imaging obtained in this study cannot be compared with that obtained via intravenous injection. More studies on surface application of NIR contrast agents may address the biases of single-center clinical trials.

Conclusion

In conclusion, the topical application of cMBP-ICG showed good biosafety and specificity for oral SCC. Although the current clinical trial was a pilot study, it suggested the remarkable potential of cMBP-ICG for delineating tumor margins, showing concealed minor tumor foci and micro metastasis and indexing oral SCC differentiation grades. Also, as a quick, convenient, and economical method for detecting oral SCC, c-MBP-ICG could be potentially used in the near future for long-term follow-up evaluation of leukoplakia, guidance of biopsy and surgical procedure, and postoperative evaluation of oral SCC patients.

Acknowledgment

Jingbo Wang, Siyi Li, and Kun Wang contributed equally to this work. This study was supported by funds from the National Natural Science Foundation of China (Nos. 91859202, 82172049, 91859106 and 82172001).

Disclosures

The authors declare that they have no conflict of interest.

References

1. Chi AC, Day TA, Neville BW. Oral cavity and oropharyngeal squamous cell carcinoma: an update. CA Cancer J Clin. 2015;65:401–21.
2. Leemans CR, Braakhuis BJ, Brakenhoff RH. The molecular biology of head and neck cancer. Nat Rev Cancer. 2011;11:9–22.
3. Hinni ML, Ferlito A, Brandwein-Gensler MS, Takes RP, Silver CE, Westra WH, et al. Surgical margins in head and neck cancer: a contemporary review. Head Neck. 2013;35:1362–70.
4. Leemans CR, Snijders PJ, Brakenhoff RH. The molecular land- scape of head and neck cancer. Nat Rev Cancer. 2018;18:269.
5. Liang M, Yang M, Wang F, Wang X, He B, Mei C, et al. Near- infrared fluorescence-guided resection of micrometastases derived from esophageal squamous cell carcinoma using a c-Met- targeted probe in a preclinical xenograft model. J Control Release. 2021;332:171–83.
6. Newton AD, Predina JD, Shin MH, Frenzel-Sulyok LG, Vollmer CM, Drebin JA, et al. Intraoperative near-infrared imaging can identify neoplasms and aid in real-time margin assessment during pancreatic resection. Ann Surg. 2019;270:12–20.
7. Nishio N, van den Berg NS, van Keulen S, Martin BA, Fakurnejad S, Teraphongphom N, et al. Optical molecular imaging can differentiate metastatic from benign lymph nodes in head and neck cancer. Nat Commun. 2019;10:1–10.
8. De Boer E, Harlaar NJ, Taruttis A, Nagengast WB, Rosenthal EL, Ntziachristos V, Van Dam GM. Optical innovations in surgery. Br J Surg. 2015;102:e56-72.
9. Rosenthal EL, Warram JM, De Boer E, Chung TK, Korb ML, Brandwein-Gensler M, et al. Safety and tumor specificity of cetuximab-IRDye800 for surgical navigation in head and neck cancer. Clin Cancer Res. 2015;21:3658–66.
10. Nishio N, Van Den Berg NS, Van Keulen S, Martin BA, Fakurnejad S, Zhou Q, et al. Optimal dosing strategy for fluorescence-guided surgery with panitumumab-IRDye800CW in head and neck cancer. Mol Imaging Biol. 2020;22:156–64.
11. Lu G, Fakurnejad S, Martin BA, Van Den Berg NS, Van Keulen S, Nishio N, et al. Predicting therapeutic antibody delivery into human head and neck cancers. Clin Cancer Res. 2020;26:2582–94.
12. Netti PA, Berk DA, Swartz MA, Grodzinsky AJ, Jain RK. Role of extracellular matrix assembly in interstitial transport in solid tumors. Cancer Res. 2000;60:2497–503.
13. Kossatz S, Pirovano G, Deme´trio De Souza Franc¸a P, Strome AL, Sunny SP, Zanoni DK, et al. Validation of the use of a fluorescent PARP1 inhibitor for the detection of oral, oropharyngeal and oesophageal epithelial cancers. Nat Biomed Eng. 2020;4:272–85.
14. Deme´trio De Souza Franc¸a P, Kossatz S, Brand C, Karassawa, Zanoni D, Roberts S, Guru N, et al. A phase I study of a PARP1- targeted topical fluorophore for the detection of oral cancer. Eur J Nucl Med Mol Imaging. 2021;48:3618–30.
15. Wu Y, Fan Q, Zeng F, Zhu J, Chen J, Fan D, et al. Peptide- functionalized nanoinhibitor restrains brain tumor growth by abrogating mesenchymal-epithelial transition factor (MET) sig- naling. Nano Lett. 2018;18:5488–98.
16. Wu J, Yuan Y, Tao X-F. Targeted molecular imaging of head and neck squamous cell carcinoma: a window into precision medi- cine. Chin Med J Engl. 2020;133:1325–36.
17. Xu H, Stabile LP, Gubish CT, Gooding WE, Grandis JR, Sieg- fried JM. Dual blockade of EGFR and c-Met abrogates redundant signaling and proliferation in head and neck carcinoma cells. Clin Cancer Res. 2011;17:4425–38.
18. Gruner M, Denis A, Masliah C, Amil M, Metivier-Cesbron E, Luet D, et al. Narrow-band imaging versus Lugol chromoendoscopy for esophageal squamous cell cancer screening in normal endoscopic practice: randomized controlled trial. Endoscopy. 2021;53:674–82.

19. Petruzzi M, Lucchese A, Baldoni E, Grassi FR, Serpico R. Use of Lugol's iodine in oral cancer diagnosis: an overview. Oral Oncol. 2010;46:811–3.
20. Gao RW, Teraphongphom NT, Van Den Berg NS, Martin BA, Oberhelman NJ, Divi V, et al. Determination of tumor margins with surgical specimen mapping using near-infrared fluorescence. Cancer Res. 2018;78:5144–54.
21. Zhu B, Godavarty A. Near-infrared fluorescence-enhanced optical tomography. BioMed Res Int. 2016;2016:1–10.
22. Chen Y-S, Wang J-T, Chang Y-F, Liu B-Y, Wang Y-P, Sun A, Chiang C-P. Expression of hepatocyte growth factor and c-Met protein is significantly associated with the progression of oral squamous cell carcinoma in Taiwan. J Oral Pathol Med. 2004;33:209–17.
23. Freudlsperger C. Prognostic value of c-Met expression in oral squamous cell carcinoma. Exp Therapeut Med. 2009;1:69–72.
24. Sun Z, Liu Q, Ye D, Ye K, Yang Z, Li D. Role of c-Met in the progression of human oral squamous cell carcinoma and its potential as a therapeutic target. Oncol Rep. 2017;39:209–16.
25. Meng X, Zhao Y, Han B, Zha C, Zhang Y, Li Z, et al. Dual functionalized brain-targeting nanoinhibitors restrain temozolomide-resistant glioma via attenuating EGFR and MET signaling pathways. Nat Commun. 2020;11:594.
26. Lin B, Wu J, Wang Y, Sun S, Yuan Y, Tao X, Lv R. Peptide functionalized upconversion/NIR II luminescent nanoparticles for targeted imaging and therapy of oral squamous cell carcinoma. Biomater Sci. 2021;9:1000–7.
27. Kim E-M, Park E-H, Cheong S-J, Lee C-M, Kim DW, Jeong H-J, et al. Characterization, biodistribution, and small-animal SPECT of I-125-labeled c-Met binding peptide in mice bearing c-Met receptor tyrosine kinase-positive tumor xenografts. Nucl Med Biol. 2009;36:371–8.
28. Cooper BM, Iegre J, O'Donovan DH, O¨ lwega¨rd Halvarsson M, Spring DR. Peptides as a platform for targeted therapeutics for cancer: peptide–drug conjugates (PDCs). Chem Soc Rev. 2021;50:1480–94.
29. Wang H, Li X, Tse BW-C, Yang H, Thorling CA, Liu Y, et al. Indocyanine green-incorporating nanoparticles for cancer theranostics. Theranostics. 2018;8:1227–42.
30. Yuspa SH, VanHook AM. Science-signaling podcast for 21 June 2016: MET and skin cancer. Sci Signal. 2016;9:c14.
31. Argiris A, Karamouzis MV, Raben D, Ferris RL. Head and neck cancer. Lancet. 2008;371:1695–709.
32. Kossatz S, Brand C, Gutiontov S, Liu JTC, Lee NY, Go¨nen M, et al. Detection and delineation of oral cancer with a PARP1- targeted optical imaging agent. Sci Rep. 2016;6:21371.

Thoracic Surgery

Research Article

Efficacy of Near-Infrared Fluorescence Video-Assisted Thoracoscopic Surgery for Small Pulmonary Nodule Resection with Indocyanine Green

Kun Wang[1,2,*], Weiyuan Huang[1,*], Xianshan Chen[3,*], Gao Li[3], Na Li[4], Xiuming Huang[3], Xuqiang Liao[3], Jiali Song[1], Qianyu Yang[1], Kunshan He[5], Yu An[5], Xin Feng[2], Zeyu Zhang[5], Chongwei Chi[2], Jie Tian[1,5] ✉, Fengxia Chen[3] ✉, and Feng Chen[1] ✉

Abstract

Background: Small pulmonary nodules (<3 cm) can sometimes be unrecognizable and nonpalpable in video-assisted thoracoscopic surgery (VATS). Near-infrared fluorescence (NIF) VATS after indocyanine green (ICG) inhalation may effectively guide surgeons to locate the nodules.

Objective: This study aimed to investigate the safety, feasibility, and efficacy of ICG inhalation-based NIF imaging for guiding small pulmonary nodule resections.

Methods: Between February and May 2021, the first-stage, non-randomized trial enrolled 21 patients with different nodule depth, ICG inhalation doses, post-inhalation surgery times, and nodule types at a tertiary referral hospital. Between May 2021 and May 2022, the second-stage randomized trial enrolled 56 patients, who were randomly assigned to the fluorescence VATS (FLVATS) or the white-light VATS (WLVATS) group. The ratio of effective guidance and the time consumption for nodule localization were compared.

Results: The first-stage trial proved this new method is safe and feasible, and established a standardized protocol with optimized nodule depth (≤1 cm), ICG dose (0.20–0.25 mg/ kg), and

surgery window (50–90 min after ICG inhalation). In the second-stage trial, the FLVATS achieved 87.1% helpful nodule localization guidance, which was significantly higher than the WLVATS (59.1%, $p < 0.05$). The mean nodule locating time (standard deviation) was 1.8 [0.9] and 3.3 [2.3] min, respectively. Surgeons adopting FLVATS were significantly faster ($p < 0.01$), especially when locating small ground-glass opacities (1.3 [0.6] min vs. 7.0 [3.5] min, $p < 0.05$). Five of 31 nodules (16.1%) were only detectable by FLVATS, whereas both white light and palpation failed.
Conclusions: This new method is safe and feasible for small pulmonary nodule resection. It significantly improves nodule localization rates with less time consumption, and hence is highly worthy for clinical promotion.
Clinical Trial Registration: Chinese Clinical Trial Registry Identifier: ChiCTR2100047326

[1] Department of Radiology, Hainan General Hospital (Hainan Affiliated Hospital of Hainan Medical University), Haikou, Hainan Province, China.
[2] CAS Key Laboratory and Beijing Key Laboratory of Molecular Imaging, Institute of Automation, Chinese Academy of Sciences, Beijing, China.
[3] Department of Thoracic Surgery, Hainan General Hospital (Hainan Affiliated Hospital of Hainan Medical University), Haikou, Hainan Province, China.
[4] Department of Anesthesiology, Hainan General Hospital (Affiliated Hainan Hospital of Hainan Medical University), Haikou, Hainan, China.
[5] Beijing Advanced Innovation Center for Big Data-Based Precision Medicine, School of Medicine and Engineering, Beihang University, Beijing, China
*Kun Wang, Weiyuan Huang, and Xianshan Chen contributed equally to this work and should be considered co-first authors.

Introduction

Lung cancer is by far the leading cause of cancer death worldwide.[1] Millions of people have incidental pulmonary nodules identified in computed tomography (CT) scans every year, and many of them undergo surgical resections.[2] Video-assisted thoracoscopic surgery (VATS) is commonly applied for removing suspicious nodules;[3,4] however, it is challenging to localize small pulmonary nodules during the surgery, especially for those having ground-glass opacity (GGO) or semi-solid characteristics, which may be unrecognizable and nonpalpable, causing prolonged operation time or even unexpected change of the original surgical plan.[5,6] To minimize such risk, electromagnetic navigation bronchoscope of indocyanine green (ICG),[7] percutaneous injection of ICG,[8,9] methylene blue,[10,11] radiotracers,[12,13] or ethiodized oil,[14,15] as well as the insertion of metallic coils[16,17] and hook wires,[18,19] were proposed to achieve intraoperative localization of nodules, but they have various limitations, such as extra invasive action before operation, long-time radiation exposure, and diffused dye or dislodged markers misleading the location.[20] More importantly, these approaches only reveal the general location of the nodule,

but not the precise margins for resection.[20]

Recently, Quan et al. reported the intraoperative near-infrared fluorescence (NIF) visualization of the lung tumor margin with ICG inhalation in mouse and rabbit models, as well as ex vivo human lung specimens.[21] The inhaled ICG was distributed into the alveoli of healthy lung tissue, but rarely into the tumor with destroyed alveoli, which generate a negative contrast of NIF between the tumor and surrounding healthy tissues. This study proved that with the low dose (0.25 mg/kg) of ICG inhalation, NIF imaging achieved a clear visualization of the lung tumor margin in rabbit models, and the margin was verified by pathology. However, whether or not this method is safe and effective for patients with suspected malignant pulmonary nodules still remains questionable in real clinical VATS. We therefore conducted two-stage clinical trials to assess the safety, feasibility, and efficacy of ICG inhalation-based intraoperative NIF imaging for guiding small pulmonary nodule resection during VATS. The first stage was a prospectively controlled trial, which aimed to verify the safety and feasibility of ICG inhalation, as well as optimizing and standardizing the experimental protocols and conditions, and the second stage was a parallel-design, open-label, randomized trial that aimed to evaluate the actual clinical efficacy and benefits of NIF VATS over conventional white-light VATS in small pulmonary nodule resections.

Methods

Summary of the Study Design

The study received approval from the Institutional Review Board for Medical Ethics (IRB, grant no. 021-54) of the Hainan General Hospital (Hainan Affiliated Hospital of Hainan Medical University). The hospital performs more than 1000 VATS annually for pulmonary nodule resections. Written informed consent was obtained from all patients before their participation. The clinical trial was registered at the Chinese Clinical Trial Registry (ChiCTR2100047326).

Because this is the first clinical study of ICG inhalation-based NIF-guided VATS for small pulmonary nodule resections, a first-stage preliminary trial was conducted to investigate the safety, feasibility, optimal dose, optimal surgical time window, suitable nodule depth, and other relevant operation factors. Twenty-one patients with small pulmonary nodules suspicious for malignancy were eligibly enrolled from February to May 2021. Patients were aged 18–80 years and had (1) a pulmonary nodule <3 cm in diameter detected on CT scan; (2) <2 cm depth from the nodule edge to the nearest pleural surface on CT scan; and (3) suitable conditions to undergo VATS. Exclusion criteria were (1) allergic to ICG; (2) history of asthma or atelectasis; (3) history of chest surgery; (4) history of chemotherapy or radiotherapy for lung cancer, including neoadjuvant chemotherapy, concurrent chemotherapy, and adjuvant chemotherapy; and (5) unsuitable for surgery, such as clear indication of distantmetastasis or severe dysfunction of major organs.

After the surgical protocol was optimized and standardized based on the first-stage trial data, we initiated the second-stage parallel-design randomized clinical trial to evaluate its efficacy. From May 2021 to May 2022, 56 eligible patients were enrolled and randomly assigned to either the fluorescence VATS group (FLVATS, n = 30) or the whitelight VATS group (WLVATS, n = 26) using a coin toss. The random allocation was performed by a radiologist. Surgeons and patients were blinded to the assignment until the start of surgery. By learning from the first-stage practice, the nodule depth was changed from <2 cm to ≤1 cm for inclusion. Having pleural adhesion was added to the exclusion criteria to avoid the significant contamination of the NIF visual field caused by adhesion lysis. The remaining inclusion and exclusion criteria remained unchanged. The patient flow through the first- and second-stage trial is illustrated in Fig. 1.

Surgery Protocol

In the first-stage trial, patients autonomously inhaled ICG (Yichuang Pharmaceutical Limited Liability Company, Dandong, China) at a dose of 0.13–0.26 mg/kg by using a nebulizer with a 4–6 mL/min oxygen flow rate. This was conducted before anesthesia, in a sitting or semi-reclining position in the ward (electronic supplementary material [ESM] eFig. 1). Due to the individual difference in respiration, it took approximately 15–40 min for the entire ICG inhalation. Patients were then transferred to the operating room and surgery was started at a range of 15–125 min after ICG inhalation. In the second-stage trial, for the FLVATS group, the dose of ICG inhalation was fixed at a range of 0.20–0.25 mg/kg, and surgery was started 50–90 min after ICG administration. The remaining protocols remained unchanged. The detailed protocol is available in the ESM.

General anesthesia was carried out, with a double-lumen endobronchial tube inserted for lung isolation and single- lung ventilation.[22] Two-port VATS is the standard procedure at our hospital.[22,23] The detailed setting and surgery procedure is described in the ESM (eMethods). Wedge, segmental lobectomy, or lobectomy resection are performed according to the nodule location, size, and preliminary diagnosis obtained from the rapid intraoperative frozen sections.[2,24]

In the FLVATS group, the entire procedure was performed using a commercially available NIF thoracoscopic imaging system (DPM-III-01, Zhuhai Dipu Medical Technology Co., Ltd, Zhuhai, China) through the observation port.[25–28] This system offered real-time, three-window observation, including the white-light (color), fluorescence (monochrome), and overlap (pseudo-color) window. In the WLVATS group, the procedure was performed using an Olympus thoracoscopic imaging system (OTV-S400, Model: UHI-4) through the observation port.

Outcome Measurements

In the second-stage trial, the primary endpoint was the ratio of effective help for nodule localization and the time consumed for locating the nodule right after inserting the thoracoscope, while the secondary endpoints were the total number of intraoperative decision changes due to the guidance of NIF imaging. Therefore, we measured several intraoperative evaluation indexes, including the number of 'helpful/unhelpful' guidances in locating nodules using NIF imaging, white-light imaging, and palpation, as well as the number of intraoperative decision changes (if a nodule can only be detected by NIF imaging, it counted as a change in intraoperative decision),[29] the nodule locating time (time consumed for locating the nodule right after inserting

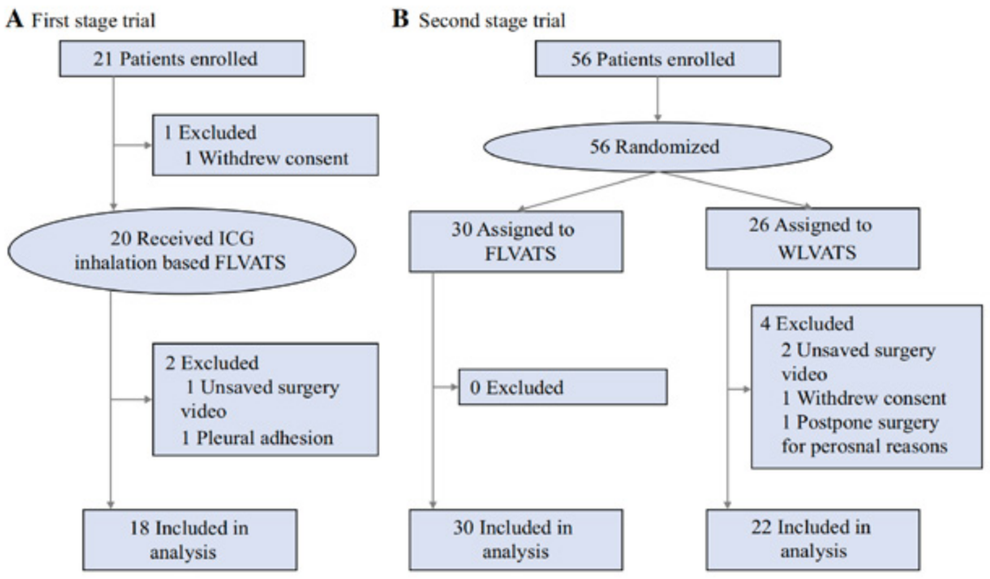


Fig.1 Study flowchart of two-stage clinical trials. a First- stage nonrandomized controlled trial; b second-stage parallel- design randomized trial. *ICG* indocyanine green, *FLVATS* fluorescence video-assisted thoracoscopic surgery, *WLVATS* white-light video-assisted thoracoscopic surgery

the thoracoscope), the in vivo and ex vivo nodule signal-to-background ratio (SBR), the amount of blood loss, and the entire surgery time. The SBR was measured by the bundled software of the NIF thoracoscopic imaging system. The detailed measurement procedure is described in the ESM (ESM eMethods and eFig. 2). We also recorded the postoperative evaluation indexes, including postoperative drainage, hospitalization days, and postoperative complications.

Sample Size and Statistical Analysis

In this study, the ratio of effective help for nodule localization was considered to be the main effectiveness evaluation index. The first-stage trial showed that the ratio of effective help using NIF imaging for patients with nodule depth ≤1 cm was 81.3%, and 45% for white-light imaging. We estimated that a minimum of 21 patients should be enrolled in each group to achieve a statistical significance (α= 0.05, β = 0.3, power = 70%). Given an expected withdrawal rate of 20%, each group should enroll at least 25 patients, for a total of 50 patients in the second-stage trial. Analyses were performed using GraphPad Prism version 9.0.4 (Home-GraphPad). Data were summarized using descriptive statis- tics, including mean and standard deviation (SD) for continuous variables, and numbers and ratios (%) for categorical variables. To compare the two groups, we conducted the two-sample *t*-test (normal distribution) or Mann–Whitney U test (non-normal distribution) for continuous variables, and Chi-square test for discrete variables. A *p*-value <0.05 was considered to be statistically significant.

Results

Patient Characteristics

A total of 21 patients enrolled in the first-stage clinical trial received ICG inhalation-based FLVATS. Three patients were excluded (one who withdrew consent, one with unsaved surgical video, and one with pleural adhesion caused by blood contamination) [Fig. 1a]. Eighteen patients (4 men and 14 women, mean [SD] age 58.5 [8.47] years) were included for analysis and for standardizing the second- stage clinical trial protocols (Table 1 and ESM eTable 1).

In the second-stage trial, 56 patients were randomized to either the FLVATS (n = 30) or WLVATS (n = 26) group. After surgery, no patients were excluded from the FLVATS group, but four patients were excluded from the WLVATS group (two with unsaved surgical video, one who withdrew consent, and one who postponed the surgery for personal reasons) [Fig. 1b]. Finally, 52 patients were included for comparisons. The mean [SD] age was 54.3 [10.7] years in the FLVATS group (12 men and 18 women) and 56.9 [11.1] years in the WLVATS group (15 men and 7 women) [Table 1]. The patient baseline characteristics were all balanced ($p < 0.05$).

Safety and Feasibility of the First-Stage Trial

In the first-stage trial, ICG inhalation-based FLVATS was performed to visualize 20 nodules in 18 patients, intraoperatively. No ICG-related intra- and postoperative complications were found for all patients, which proved the safety of this procedure.

We divided all nodules into helpful and unhelpful cases. In a helpful case, there was a clear negative contrast of NIF signals between the nodule and its surrounding lung tissue (Fig. 2a) and its SBR was always between 0 and 1. In an unhelpful case without effective visual guidance (Fig. 2b), the SBR was considered to be

Table 1 Patient demographics and nodule characteristics

Characteristic	*N* (%)			
	First-stage trial	Second-stage trial		
	FLVATS [*n* = 18]	FLVATS [*n* = 30]	WLVATS [*n* = 22]	*p*-Value
Age, years [mean (SD)]	58.5 (8.5)	54.3 (10.7)	56.9 (11.1)	0.309
BMI, kg/mm^2 [mean (SD)]	22.53 (2.35)	21.88 (2.79)	23.12 (2.71)	0.115
Sex				
Male	4 (22.2)	12 (40.0)	15 (68.2)	0.055
Female	14 (77.8)	18 (60.0)	7 (31.8)	
Smoker	1 (5.6)	5 (16.7)	7 (31.8)	NA
Size of nodule, cm^3 [mean (SD)]	2.00 (1.90)	5.95 (5.89)	5.87 (5.48)	0.962
Depth of nodule, cm [mean (SD)]	0.52 (0.64)	0.31 (0.39)	0.29 (0.35)	0.860
CT-detected nodules and types	20	31	22	
Solid	9 (45.0)	22 (71.0)	15 (68.2)	0.616
GGO	8 (40.0)	3 (9.7)	4 (18.2)	
Mixed	3 (15.0)	6 (19.3)	3 (13.6)	
Nodule location				
RUL	10 (50.0)	9 (29.0)	5 (22.7)	0.876
RML	0 (0.0)	1 (3.2)	0 (0.0)	
RLL	1 (5.0)	6 (19.4)	5 (22.7)	
LUL	6 (30.0)	11 (35.5)	8 (36.4)	
LLL	3 (15.0)	4 (12.9)	4 (18.2)	
Dose of ICG, mg/kg [mean (SD)]	0.23 (0.03)	0.24 (0.01)	NA	NA
Duration of inhalation, min [mean (SD)]	23.0 (6.8)	13.7 (5.3)	NA	NA
Surgery time after inhalation, min [mean (SD)]	59.6 (25.3)	62.4 (10.8)	NA	NA
Surgical procedure				
Wedge	12	14	11	0.854
Segmental lobectomy	0	2	3	
Lobectomy	6	14	8	
Final pathology				
Adenocarcinoma in situ/microinvasive adenocarcinoma	6 (30.0)	3 (9.7)	2 (9.1)	0.385
Invasive adenocarcinoma	12 (60.0)	21 (67.7)	12 (54.5)	
Benign	2 (10.0)	7 (22.6)	8 (36.4)	

SD standard deviation, *GGO* ground-glass opacity, *LLL* left lower lobe, *LUL* left upper lobe, *RLL* right lower lobe, *RML* right middle lobe, *RUL* right upper lobe, *NA* not applicable, *FLVATS* fuorescence video-assisted thoracoscopic surgery, *WLVATS* white-light video-assisted thoracoscopic surgery, *CT* computed tomography, *ICG* indocyanine green

Ann Surg Oncol. 2023. 30(9): 5912-5922 Published online: 30 June 2023

1. A similar concept was also applied to the white-light VATS and palpation (ESM eTable 1). In total, 13 of 20 nodules were helpful cases, and in one (patient no. 12), was only detected by NIF imaging; however, both white-light imaging and palpation failed to find the nodule (ESM eTable 1). For this particular case, FLVATS actually changed the intraoperative decision making; without its help, the surgical procedure would need to change from wedge resection to segmental lobectomy or lobectomy.

We evaluated four factors that might affect the performance of FLVATS, i.e. the nodule depth (Fig. 2c), ICG dose (Fig. 2d), surgery time (the time interval between the end of ICG inhalation and the beginning of surgery) [Fig. 2e], and nodule type (solid vs. GGO and mixed GGO) [Fig. 2f]. When comparing one factor, patients were selected to ensure that the other three factors were all balanced on both sides. The results showed that in vivo SBRs were better (closer to 0) for nodule depth ≤1 cm, dose >0.2 mg/kg, and surgery time >50 min, as well as GGO and mixed nodule types; however, only nodule depth showed a significant difference ($p < 0.05$) between two sides of the 1 cm threshold. Similar results were found for ex vivo SBR comparisons (ESM eFig. 3). Based on these findings, we improved and standardized the protocol of the second-stage trial. A nodule depth ≤1 cm was added to the inclusion criteria. For the FLVATS group, the ICG dose was fixed at a range of 0.20–0.25 mg/kg, and surgery promptly started at 50–90 min after ICG inhalation.

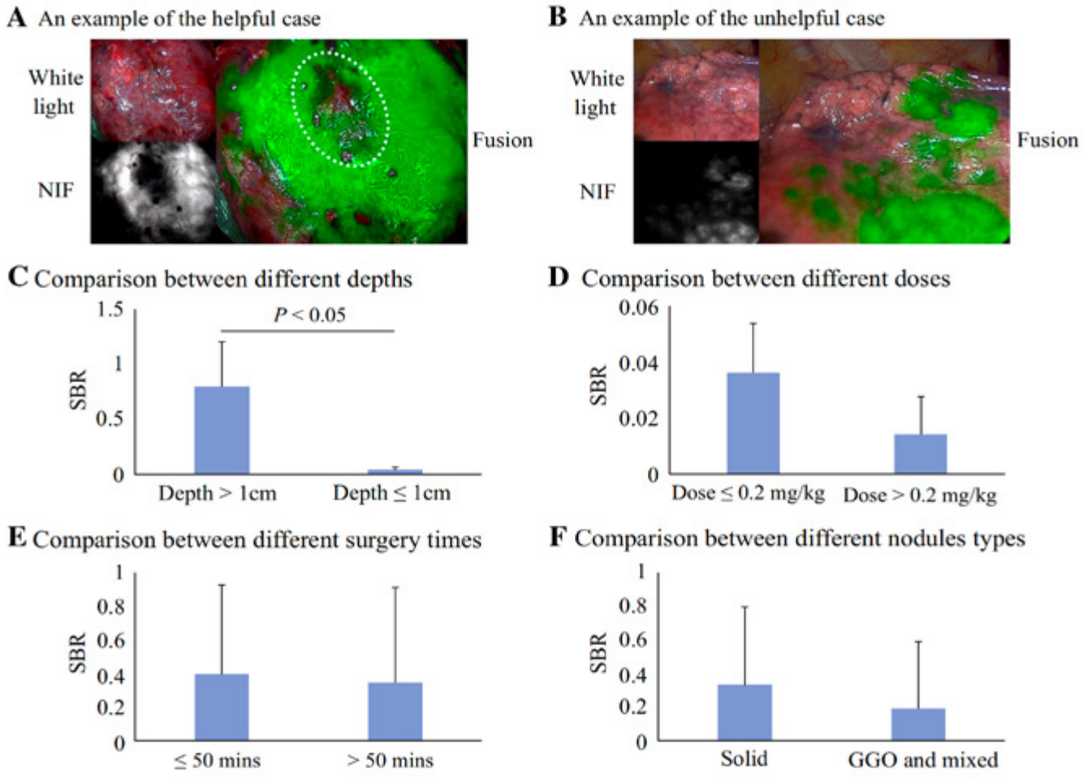


Fig.2 Representative images of intraoperative fluorescence visualization and evaluation of possible factors affecting its performance in vivo. (A) In the helpful case, the negative NIF contrast showed a clear nodule margin (within the white ellipse). (B) In the unhelpful case, NIF did not offer an effective visual guidance for surgeons. (C) Comparing SBRs between nodules with different depths inside the lung, which were measured in preoperative CT images. (D) Comparison of SBRs between patients who inhaled different doses of ICG. (E) Comparison of SBRs between different time intervals from the end of ICG inhalation to the beginning of surgery. (F) Comparison of SBRs between different nodule types in CT scans. *NIF* near-infrared fluorescence, *CT* computed tomography, *SBR* signal-to-background ratio, *GGO* ground-glass opacity, *ICG* indocyanine green

Ann Surg Oncol. 2023. 30(9): 5912-5922 Published online: 30 June 2023

Surgical Benefits of the Second-Stage Trial

In the second-stage trial, 31 nodules were resected in the FLVATS group and 27 (87.1%) of them were helpful cases with NIF guidance (ESM eTable 2). The four unhelpful nodules were all successfully detected by white light or palpation, or both. In comparison, white-light imaging only effectively helped surgeons to locate 13 (59.1%) of 22 nodules in the WLVATS group. Among the remaining nine nodules, six were located by palpation only and three were not detected by either method (ESM eTable 3; patient nos. 9, 20, and 22), including two GGOs and one mixed GGO. The effectiveness of intraoperative nodule localization was significantly different between FLVATS and WLVATS ($p = 0.019$) [Table 2].

ICG inhalation-based NIF imaging also significantly reduced the time consumed in locating nodules ($p = 0.002$) [Table 2]. The mean [SD] time needed to find the nodule right after inserting the thoracoscope was 1.8 [0.9] min in FLVATS, which was almost half of the mean time in WLVATS (3.3 [2.3] min). Furthermore, the mean [SD] nodule-locating time was 1.8 [1.0] min and 1.3 [0.6] min for solid and GGO nodules in FLVATS, respectively, which were significantly less than the corresponding time in WLVATS (solid: 2.6 [1.4] min, $p = 0.037$; GGO: 7.0 [3.5] min, $p = 0.041$). This revealed that ICG inhalation- based NIF imaging particularly benefited patients with small GGOs in their surgeries, with <20% time consumption for nodule localization. For mixed GGOs, FLVATS also used less time in locating nodules (2.2 [0.8] min) than WLVATS (2.5 [0.7] min) but the difference was not significant.

Among the 27 helpful cases in FLVATS, 10 nodules were not identifiable by white-light imaging but were detectable by palpation (ESM eTable 2); one example is shown in Fig. 3a and Video 1 (a palpable nodule with the benefit of ICG shown). Another five nodules were only detectable in NIF imaging (patient nos. 5, 12, 13, 22, and 23), but neither white light nor palpation could effectively localize these nodules. Two examples are shown in Fig. 3b and Video 2 (a non-palpable nodule with the benefit of ICG shown). Therefore, those five patients received extra critical benefits, as intraoperative decision making was effectively changed by NIF imaging guidance. This retained the possibility for surgeons to perform more accurate resections with less surgical trauma to the lung, rather than passively choosing extended operation procedures.

Table 2 Surgery performance comparison between FLVATS and WLVATS

Variable	Mean (SD)		
	FLVATS [$n = 30$]	WLVATS [$n = 22$]	p-Value
Removed nodules	31	22	
Helpful by imaging [n (%)]	27 (87.1)	13 (59.1)	**0.0192**
Unhelpful by imaging [n (%)]	4 (12.9)	9 (40.9)	
Unhelpful by WL imaging and palpation [n (%)]	5 (16.1)	3 (13.6)	0.807
No. of decision changes (%)	5 (16.1)	NA	
Nodule-locating time, min	1.8 (0.9)	3.3 (2.3)	**0.002**
Solid	1.8 (1.0)	2.6 (1.4)	**0.037**
GGO	1.3 (0.6)	7.0 (3.5)	**0.041**
Mixed	2.2 (0.8)	3.0 (1.0)	0.199
Surgery time, min	40.7 (32.8)	34.2 (22.3)	0.438
Solid	38.9 (34.2)	25.9 (14.1)	0.174
GGO	53.3 (28.5)	53.8 (38.6)	0.988
Mixed	41.3 (33.37)	60.67(2.5)	0.365
Blood loss, mL	39.3 (22.3)	34.1 (18.2)	0.881
Drainage, mL	455.0 (307.5)	398.2 (267.0)	0.508
Hospitalization, days	10.0 (3.4)	10.1 (4.2)	0.923

Bold values indicate statistical signifcance (p-value < 0.05)
SD standard deviation, *WL* white light, *GGO* ground-glass opacity, *NA* not applicable, *FLVATS* fuorescence video-assisted thoracoscopic surgery, *WLVATS* white-light video-assisted thoracoscopic surgery

Fluorescence Video-Assisted Thoracoscopic Surgery (FLVATS) in Different Nodule Types

Four pulmonary nodules were not captured *in vivo* by NIF imaging in the second-stage trial, and they were all solid nodules (ESM eTable 2); however, *ex vivo* NIF imaging still provided helpful visualizations for three of the nodules. Therefore, even if the FLVATS did not localize small nodules *in vivo*, it may still provide a quick and valuable bedside confirmation for surgeons on excised specimens.

Surprisingly, all GGOs (n = 3) and mixed GGOs (n = 6) were helpful cases in the FLVATS group. For all 31 resected nodules, the mean [SD] SBR of solid, GGO, and mixed GGO was 0.23 [0.38], 0.19 [0.13], and 0.03 [0.02] *in vivo*, as well as 0.13 [0.24], 0.14 [0.18], and 0.21 [0.39] *ex vivo*, respectively (ESM eFigs. 4a, b). There were no significant differences in SBRs between the different nodule types *in vivo* and *ex vivo*, with the exception of SBRs between *in vivo* GGO and mixed GGO (p = 0.018).

The mean [SD] SBR of malignant (n = 24) and benign (n = 7) nodules was 0.23 [0.36] and 0.03 [0.02] *in vivo*, and 0.18 [0.29] and 0.02 [0.01] *ex vivo*, respectively (ESM eFigs. 4c, d). Again, there were no significant differences in SBRs between different pathological types *in vivo* and *ex vivo*.

FLVATS in Smokers

ICG inhalation-based NIF imaging showed different visual effects between heavy smokers and non-smokers. There were a lot of black deposits spreading all over the lung in smokers, which disturbed the nodule localization in both white-light and fluorescence imaging (ESM eFig. 5). The nebulized ICG was not able to diffuse into those deposits, causing an unexpected

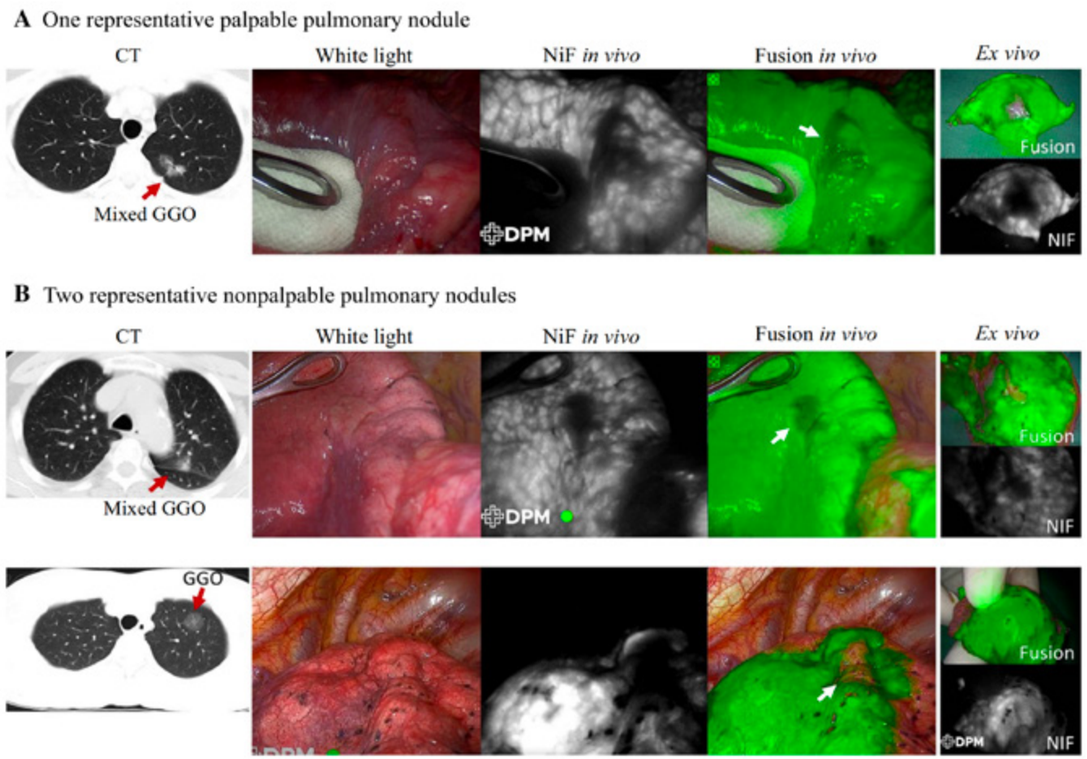


Fig.3 Intraoperative NIF imaging localized palpable and nonpalpable pulmonary nodules. a Representative images of a patient with a suspicious pulmonary nodule in CT scans (mixed GGO, red arrow). The nodule is unrecognizable in white-light images but is palpable and identifiable in NIF images, both in vivo (white arrow) and ex vivo. b Representative images of two patients with mixed GGO and GGO nodules indicated by CT scans (red arrows), respectively. Neither white-light imaging nor palpation could localize them, but NIF imaging showed clear margins (white arrows). NIF near-infrared fluorescence, CT computed tomography, GGO ground-glass opacity

negative contrast of fluorescence signals. However, the NIF imaging still provided helpful visual guidance for surgeons to find the nodule (ESM Fig. 5, the white arrow in the fusion image) because the nodule margin morphology was very different from those black deposits, although the contour of the nodule margin was not visualized as clearly as non-smokers. As a result, four of the five smokers were helpful cases in the FLVATS group.

Surgical Outcomes

No significant differences between the FLVATS and WLVATS groups were observed regarding the overall operative time (40.7 min vs. 34.2 min), intraoperative blood loss (39.3 mL vs. 34.1 mL), postoperative drainage (455.0 mL vs. 398.2 mL), and hospitalization days (10.0 vs. 10.1 days) [Table 2]. No complications related to ICG inhalation and NIF imaging were observed during the operations and hospitalizations for all enrolled 30 patients in the FLVATS group.

Discussion

Comparing with the study performed by Quan et al.[21] that only used animals and human lung specimens, our study is the first clinical application of ICG inhalation-based intra-operative NIF imaging for guiding pulmonary nodule resetions. The two

Ann Surg Oncol. 2023. 30(9): 5912-5922 Published online: 30 June 2023

clinical trials conducted by us systematically revealed the safety, feasibility, efficacy, and limitations of this strategy, which has not been reported in any other clinical studies.

The first-stage clinical trial proved the safety and feasibility of ICG inhalation. We did not find any ICG-related complications in all enrolled patients during their operations and following hospitalizations. This was likely due to the low dose of ICG. Only 0.20–0.25 mg/kg was needed, which is consistent with the study by Quan et al.[21] In comparison, the intravenous injection of ICG normally requires 1.0–5.0 mg/kg in various types of clinical applications,[30–37] which is 4- to 25-fold higher than inhalation and causes unnecessary accumulation of ICG in other organs besides the lung.

Even though the surgical procedure was not optimized in this trial, NIF imaging still effectively helped surgeons to locate 13 of 20 nodules, suggesting a good feasibility of this strategy. More importantly, this trial established a standardized protocol of using ICG inhalation and FLVATS. The optimized nodule depth, ICG dose, and surgical time were determined, and the method was proven to be feasible for all types of suspicious nodules detected in CT images. The standardized protocol may serve as a valuable reference for other groups adopting this method in pulmonary nodule resection. Surprisingly, patients with pleural adhesion are not suitable for this procedure because the operation of adhesion lysis will lead to significant contamination for NIF imaging.

The second-stage clinical trial proved the effectiveness of this method. With the help of extra NIF visualization from FLVATS, the pulmonary nodule detection rate was significantly improved by 28.0% compared with the conventional WLVATS. Moreover, 5 of 31 (16.1%) removed nodules were only detectable by FLVATS, in which both WLVATS and palpation were unhelpful. Several other clinical studies reported similar results, showing that 23–63% of pulmonary nodules were not detectable in surgeries.[29,38,39] This finding demonstrated a strong evidence proving that ICG inhalation and NIF imaging really offered irreplaceable benefits for intraoperative decision making in small pulmonary nodule resections.

FLVATS did not only help surgeons to locate small nodules with a significantly higher success rate but also, on average, reduced time consumption for seeking these small nodules by 45.5%. This improvement was particularly noticeable for small GGOs. It is commonly known that a small GGO is one of the most challenging scenarios in pulmonary nodule resections.[40] Because small GGOs usually have a similar appearance and tactile sensation with surrounding healthy tissues, surgeons have to spend more time locating them, and the intraoperative undetectable risk is high.[41] Our results showed that for locating small GGOs, surgeons, on average, spent 7.0 min in the WLVATS group, but two of the GGOs were still unidentifiable after spending more time trying to locate them, resulting in a change in the surgical plan from wedge resection to segmental lobectomy in these two cases. By contrast, in the FLVATS group, all small GGOs were successfully located, at an average time of only 1.3 min. We also observed that surgeons spent a similar amount of time locating solid, GGO, and mixed GGO nodules under FLVATS guidance.

In addition to the significantly higher nodule localization rate and speed, ICG inhalation and FLVATS are also very convenient to use. Preoperatively, they do not need any invasive injection or implantation of contrast agents[33,42,43] or physical markers,[44,45] and thus no radiation exposure is involved. Intraoperatively, the NIF thoracoscopic imaging system is very similar to conventional thoracoscopic systems. The general procedure of VATS remains unchanged and surgeons only need to learn some of the basic operations of the fluorescence thoracoscopy, such as switch NIF on/off, change display windows, use different pseudo color displays, etc. Therefore, all surgeons quickly adapted to this new method, suggesting that it has low learning cost and is easy to use in clinics. These advantages are likely to benefit junior surgeons with less experience of VATS, and speed up their training curves, which may eventually help to meet the challenge of growing global demand for cancer surgery and the related workforce.[46]

This method showed several limitations. The imaging depth of NIF is still the Achilles' heel;[21] thus, the method is not suitable for small nodules with more than 1 cm depth in CT images. Patients with pleural adhesion or who are allergic to ICG are not applicable either. Unfortunately, ICG is an untargeted contrast agent, and our study indicated that it was not able to distinguish benign and malignant nodules (Figs. 4c, d). To address this problem, targeted intraoperative molecular imaging using new fluorescent tracers might be a better option,[47] but it still takes years for these new drugs to get approval from regulation authorities in different countries.

This study also has limitations. First, we did not cover all possible pathological types of pulmonary nodules. Whether the effectiveness of ICG inhalation-based NIF imaging remains the same for squamous cell carcinoma, large cell carcinoma, other rare types of non-small cell lung cancer, and small cell lung cancer is still in doubt. However, we believe the method is likely to be feasible for all of these cancer types, precisely because ICG is not a molecular-specific agent, and malignant nodules, regardless of their pathological types, would destroy lung alveoli, eventually causing the negative fluorescence contrast of inhaled ICG.

Second, although NIF imaging showed well-defined nodule margins in most cases intraoperatively, pathological evidences were still absent from drawing a definitive conclusion of nodule margin visualization accuracy. This was because the fluorescence microscope system in our hospital did not have the near-infrared imaging ability, and it was not possible to verify the ICG distribution on rapid frozen sections. We further found that inhaled ICG was severely vanished in paraffin sections, making the pathological imaging within near-infrared spectrum days after surgeries unreliable. Therefore, the pathological examination protocol needs to be further optimized to verify the nodule margin visualization accuracy in future clinical trials.

Third, in the second-stage clinical trial, four nodules were not successfully visualized by NIF imaging and they were all solid nodules (ESM eTable 2). It is difficult to give a clear explanation based on these four cases right now. Moreover, the SBR between solid nodules and GGOs showed no significant difference (ESM eFig. 4), which is likely due to the small population of GGO patients (n = 3). Therefore, further clinical investigations with larger populations and multicenter comparisons are still needed to verify which type of patients are not eligible for this method.

Conclusions

To our knowledge, this study presents the first clinical use of ICG inhalation-based intraoperative NIF imaging for guiding pulmonary nodule resections. Our two consecutive trials demonstrated that this method is safe and feasible and can guide surgeons to achieve a higher nodule detection rate with much less time consumption compared with conventional surgical methods, especially for patients with small GGOs. The method can positively change intraoperative decision making for unrecognizable and nonpalpable small nodules. It is easy to use with little learning costs, and we suggest that it should be widely applied in future pulmonary nodule surgeries.

Author Contributions

JT, FXC, and FC had full access to all of the data in the study and take responsibility for the integrity of the data and the accuracy of the data analysis. Concept and design: KW, WYH, JT, FXC, FC. Acquisition, analysis, or interpretation data: KW, WYH, XSC, GL, NL, XMH, XQL, JLS, QYY, KSH, FC. Drafting of the manuscript: KW, WYH. Critical revision of the manuscript for important intellectual content: KW, WYH. Statistical analysis: KW, WYH. Obtained funding: KW, JT. Administrative, technical, or mate- rial support: KW, WYH, KSH, FXC, FC. Supervision: JT, FXC, FC.

Funding

This work was supported by the Ministry of Science and Technology of China under grant no. 2017YFA0205200; the National Natural Science Foundation of China under grant nos. 62027901, 81227901, 81930053, and 92159305; and the Excellent Member Project of Youth Innovation Promotion Association CAS (membership 2016124), and was supported by Hainan Province Clinical Medical Center.

Disclosures

Kun Wang, Weiyuan Huang, Xianshan Chen, Gao Li, Na Li, Xiuming Huang, Xuqiang Liao, Jiali Song, Qianyu Yang, Kunshan He, Yu An, Xin Feng, Zeyu Zhang, Chongwei Chi, Jie Tian, Fengxia Chen, and Feng Chen declare no conflicts of interest.

References

1. Sung H, Ferlay J, Siegel RL, et al. Global cancer statistics 2020: GLOBOCAN estimates of incidence and mortality worldwide for 36 cancers in 185 countries. CA Cancer J Clin. 2021; 71(3): 209–49.
2. Mazzone PJ, Lam L. Evaluating the patient with a pulmonary nodule: a review. JAMA. 2022; 327(3): 264–73.
3. McDermott S, Fintelmann FJ, Bierhals AJ, et al. Image-guided preoperative localization of pulmonary nodules for video-assisted and robotically assisted surgery. Radiographics. 2019; 39(5): 1264–79.
4. Hallet J, Rousseau M, Gupta V, et al. Long-term functional outcomes among older adults undergoing video-assisted versus open surgery for lung cancer: a population-based cohort study. Ann Surg. 2022; 277(6):e1348-e1354.
5. Refai M, Andolfi M, Barbisan F, et al. Computed tomography-guided microcoil placement for localizing small pulmonary nodules before uniportal video-assisted thoracoscopic resection. Radiol Med. 2020; 125(1): 24–30.
6. MacMahon H, Naidich DP, Goo JM, et al. Guidelines for management of incidental pulmonary nodules detected on CT images: from the Fleischner Society 2017. Radiology. 2017; 284(1): 228–43.
7. Abbas A, Kadakia S, Ambur V, Muro K, Kaiser L. Intraoperative electromagnetic navigational bronchoscopic localization of small, deep, or subsolid pulmonary nodules. J Thorac Cardiovasc Surg. 2017; 153(6): 1581–90.
8. Abbas A, Kadakia S, Ambur V, Muro K, Kaiser L. Intraoperative electromagnetic navigational bronchoscopic localization of small, deep, or subsolid pulmonary nodules. J Thorac Cardiovasc Surg. 2017; 153(6): 1581–90.
9. Rho J, Lee JW, Quan YH, et al. Fluorescent and iodized emulsion for preoperative localization of pulmonary nodules. Ann Surg. 2021; 273(5): 989–96.
10. Thistlethwaite PA, Gower JR, Hernandez M, Zhang Y, Picel AC, Roberts AC. Needle localization of small pulmonary nodules: Lessons learned. J Thorac Cardiovasc Surg. 2018; 155(5): 2140–7.
11. Martinez Criado Y, Perez Bertolez S, Cabello Laureano R, de Agustin Asensio JC. [CT-guided methylene blue labelling to locate a pulmonary nodule before thoracoscopic resection]. Cir Esp. Feb 2014; 92(2): 139-41.
12. Doo KW, Yong HS, Kim HK, Kim S, Kang EY, Choi YH. Needlescopic resection of small and superficial pulmonary nodule after computed tomographic fluoroscopy-guided dual localization with radiotracer and hookwire. Ann Surg Oncol. 2015; 22(1): 331–7.
13. Starnes SL, Wolujewicz M, Guitron J, Williams V, Scheler J, Ristagno R. Radiotracer localization of nonpalpable pulmonary nodules: a single-center experience. J Thorac Cardiovasc Surg. 2018; 156(5): 1986–92.
14. Park CH, Hur J, Lee SM, et al. Lipiodol localization for ground-glass opacity minimal surgery: rationale and design of the LOGIS trial. Contemp Clin Trials. 2015; 43: 194–9.
15. Choi BG, Kim HH, Kim BS, Kim KT, Shinn KS, Moon SW. Pulmonary nodules: CT-guided contrast material localization for thoracoscopic resection. Radiology. 1998; 208(2): 399–401. .
16. Powell TI, Jangra D, Clifton JC, et al. Peripheral lung nodules: fluoroscopically guided video-assisted thoracoscopic resection after computed tomography-guided localization using platinum microcoils. Ann Surg. 2004; 240(3): 481–8.
17. Bommart S, Bourdin A, Marin G, et al. Impact of preoperative marking coils on surgical and pathologic management of impalpable lung nodules. Ann Thorac Surg. 2014; 97(2): 414–8. .
18. Kang DY, Kim HK, Kim YK, Yong HS, Kang EY, Choi YH. Needlescopy-assisted resection of pulmonary nodule after dual localisation. Eur Respir J. 2011 ;37(1): 13–7.
19. Xu X, Yao Y, Shen Y, Zhang P, Zhou J. Clinical analysis of percutaneous computed tomography-guided hook wire localization of 168 small pulmonary nodules. Ann Thorac Surg. 2015; 100(5): 1861–7. .
20. Ji H, Wang X, Wang P, et al. Lanthanide-based metal-organic frameworks solidified by gelatin-methacryloyl hydrogels for improving the accuracy of localization and excision of small pulmonary nodules. J Nanobiotechnology. 2022; 0(1): 60.
21. Quan YH, Oh CH, Jung D, et al. Evaluation of intraoperative near-infrared fluorescence visualization of the lung tumor margin with indocyanine green inhalation. JAMA Surg. 2020; 155(8): 732–40.
22. Dimitrovska NT, Bao F, Yuan P, Hu S, Chu X, Li W. Learning curve for two-port video-assisted thoracoscopic surgery lung segmentectomy. Interact Cardiovasc Thorac Surg. 2022; 34(3): 402–7.
23. Huang C, Sun Y, Wu Q, et al. Simultaneous bilateral pulmonary resection via single-utility port VATS for multiple pulmonary nodules: a single-center experience of 16 cases. Thorac Cancer. 2021; 12(4): 525–33.
24. Bai C, Choi CM, Chu CM, et al. Evaluation of pulmonary nodules: clinical practice consensus guidelines for Asia. Chest. 2016; 150(4): 877–93.
25. He K, Hong X, Chi C, et al. Efficacy of near-infrared fluorescence-guided hepatectomy for the detection of colorectal liver metastases: a randomized controlled trial. J Am Coll Surg. 2022; 234(2): 130–7.
26. Huang W, Wang K, Chen F, et al. Intraoperative fluorescence visualization in thoracoscopic surgery. Ann Thorac Surg. 2023; 115(3): e79–81.
27. Wang K, Du Y, Zhang Z, et al. Fluorescence image-guided tumour surgery. Nature Reviews Bioengineering. 2023; 1(3): 161–79.
28. He K, Hong X, Chi C, et al. A new method of near-infrared fluorescence image-guided hepatectomy for patients with hepatolithiasis: a randomized controlled trial. Surg Endosc. 2020; 34(11): 4975–82.
29. He K, Hong X, Chi C, et al. A new method of near-infrared fluorescence image-guided hepatectomy for patients with hepatolithiasis: a randomized controlled trial. Surg Endosc. 2020; 34(11): 4975–82.
30. Mao Y, Chi C, Yang F, et al. The identification of sub-centimetre nodules by near-infrared fluorescence thoracoscopic systems in pulmonary resection surgeries. Eur J Cardiothorac Surg. 2017; 52(6): 1190–6.
31. Kasai Y, Tarumi S, Chang SS, et al. Clinical trial of new methods for identifying lung intersegmental borders using infrared thoracoscopy with indocyanine green: comparative analysis of 2- and 1-wavelength methods. Eur J Cardiothorac Surg. 2013; 44(6): 1103–7.
32. Lee JYK, Pierce JT, Thawani JP, et al. Near-infrared fluorescent image-guided surgery for intracranial meningioma. J Neurosurg. 2018; 128(2): 380–90.
33. He K, Zhou J, Yang F, et al. Near-infrared intraoperative imaging of thoracic sympathetic nerves: from preclinical study to clinical trial. Theranostics. 2018; 8(2): 304–13.
34. Predina JD, Newton AD, Keating J, et al. Intraoperative molecular imaging combined with positron emission tomography improves surgical management of peripheral malignant pulmonary nodules. Ann Surg. 2017; 266(3): 479–88.
35. Predina JD, Keating J, Patel N, Nims S, Singhal S. Clinical implications of positive margins following non-small cell lung cancer surgery. J Surg Oncol. Mar2016; 113(3): 264–9.
36. Keating JJ, Kennedy GT, Singhal S. Identification of a subcentimeter pulmonary adenocarcinoma using intraoperative near-infrared imaging during video-assisted thoracoscopic surgery. J Thorac Cardiovasc Surg. Mar2015; 149(3): e51–3.
37. Mao Y, Wang K, He K, et al. Development and application of the near-infrared and white-light thoracoscope system for minimally invasive lung cancer surgery. J Biomed Opt. 2017; 22(6): 66002.
38. 38.Cerfolio RJ, Bryant AS. Is palpation of the nonresected pulmonary lobe(s) required for patients with non-small cell lung cancer? A prospective study. J Thorac Cardiovasc Surg. 2008; 135(2): 261–8.
39. Hsu PK, Chuang LC, Wu YC. Electromagnetic navigation-guided preoperative localization of small malignant pulmonary tumors. Ann Thorac Surg. 2020; 109(5): 1566–73.
40. Luo T, Chen Q, Zeng J, Cai L, Huang X. Peripheral pure ground-glass opacity: segmentectomy versus wedge resection. J Cardiothorac Surg. 2021; 16(1): 260.
41. Sepesi B, Walsh GL. Surgical therapy of ground-glass opacities. Semin Diagn Pathol. 2014; 31(4): 289–92.
42. Kleedehn M, Kim DH, Lee FT, et al. Preoperative pulmonary nodule localization: a comparison of methylene blue and hookwire techniques. AJR Am J Roentgenol. 2016; 207(6): 1334–9.
43. Zhang B, Peng M, Yu F, et al. A novel technique for preoperative localization of pulmonary nodules using a mixture of tissue adhesive and iohexol under computed tomography guidance: a 140 patient single-center study. Thorac Cancer. 2021; 12(6): 854–63.
44. Rodrigues JCL, Pierre AF, Hanneman K, et al. CT-guided microcoil pulmonary nodule localization prior to video-assisted thoracoscopic surgery: diagnostic utility and recurrence-free survival. Radiology. 2019; 291(1): 214–22.
45. Lee MO, Jin SY, Lee SK, Hwang S, Kim TG, Song YG. Video-assisted thoracoscopic surgical wedge resection using multiplanar computed tomography reconstruction-fluoroscopy after CT guided microcoil localization. Thorac Cancer. 2021; 12(11): 1721–5.
46. Perera SK, Jacob S, Wilson BE, et al. Global demand for cancer surgery and an estimate of the optimal surgical and anaesthesia workforce between 2018 and 2040: a population-based modelling study. Lancet Oncol. 2021; 22(2): 182–9.
47. Kennedy GT, Azari FS, Bernstein E, et al. Targeted intraoperative molecular imaging for localizing nonpalpable tumors and quantifying resection margin distances. JAMA Surg. 2021; 156(11): 1043–50.

Ann Surg Oncol. 2023. 30(9): 5912-5922 Published online: 30 June 2023

Thoracic Surgery

Research Article

Near-Infrared Intraoperative Imaging of Thoracic Sympathetic Nerves: From Preclinical Study to Clinical Trial

Kunshan He,[1,2,4,*] Jian Zhou,[1,*] Fan Yang,[1,*] Chongwei Chi,[2,3] Hao Li,[1] Yamin Mao,[2,3] Bengang Hui,[1] Kun Wang,[2,3]✉ Jie Tian,[2,3,4,5]✉ and Jun Wang[1]✉

Abstract

The sympathetic nervous system controls and regulates the activities of the heart and other organs. Sympathetic nervous system dysfunction leads to disease. Therefore, intraoperative real-time imaging of thoracic sympathetic nerves (ITSN) would be of great clinical significance for diagnosis and therapy. The aim of this experimental study was to evaluate the feasibility and validity of intraoperative ITSN using indocyanine green (ICG).

Methods: ITSN using ICG was performed on 10 rabbits to determine its feasibility. Animals were allocated to two groups. The rabbits in one group received the same dose of ICG, but were observed at different times. The rabbits in the other group were administered different doses of ICG, but were observed at the same time. Signal to background ratio (SBR) was measured in regions of interest in all rabbits. Furthermore, fifteen consecutive patients with pulmonary nodules were intravenously injected with ICG 24 h preoperatively and underwent near-infrared (NIR) fluorescence imaging (FI) thoracoscopic surgeries between July 2015 and June 2016. A novel self-developed NIR and white-light dual-channel thoracoscope system was used. SBRs of thoracic sympathetic nerves were calculated in all patients.

Results: In the preclinical study, we were able to precisely recognize each rabbit's second (T2) to fifth (T5) thoracic ganglia on both sides of the spine using ITSN with ICG. In addition, we explored the relationship between SBR and the injection time of ICG and that between SBR and the dose of ICG. Using the novel dual-channel thoracoscope system, we were able to locate the ganglia from the stellate ganglion (SG) to the sixth thoracic ganglion (T6), as well as the chains between these ganglia in all patients with a high SBR value of 3.26 (standard deviation: 0.57). The pathological results confirmed our findings.

Conclusion: We were able to use ICG FI to distinguish thoracic sympathetic nerves during NIR thoracoscopic surgery. The technique may replace the rib-oriented method as standard practice for mapping the thoracic sympathetic nerves.

Keywords

Near-infrared, Intraoperative fluorescence imaging, Thoracoscopic surgery, Sympathetic nerves, Indocyanine green.

[1] Department of Thoracic Surgery, Peking University People's Hospital, No.11, Xi Zhi Men South Avenue, Beijing100190, China;

[2] CAS Key Laboratory of Molecular Imaging, Institute of Automation, Chinese Academy of Sciences, Beijing 100190, China;

[3] Beijing Key Laboratory of Molecular Imaging, Beijing 100190, China;

[4] University of Chinese Academy of Sciences, Beijing 100039, China.

[5] CAS Center for Excellence in Brain Science and Intelligence Technology, Institute of Automation, Chinese Academy of Sciences, Beijing, China.

* These authors contributed equally to this manuscript

Introduction

The sympathetic nervous system regulates the balance in many homeostatic mechanisms, such as gut motility and pupil diameter, and is responsible for priming the body for action, particularly in dangerous situations. Moreover, sympathetic system stimulation causes vasoconstriction of most blood vessels. So thoracic sympathetic nerves, as important parts of sympathetic system, are involved in the treatment of multiple diseases. Currently, endoscopic thoracic sympathectomy is indicated mainly for primary hyperhidrosis, especially that of the palm [1], axilla, and the face [2,3]. Despite the development of modern pharmacological and endovascular treatments, sympathetic surgery still plays a critical role in the treatment of specific cardiac conditions, such as angina [4], long QT syndrome [5], and ventricular tachycardia [6]. In addition, thoracic sympathetic ablation is indicated for a few painful conditions and ischemia, such as pancreatic pain [7], complex regional pain syndrome [8], Raynaud's phenomenon [9], and digital ischemia [10,11]. Therefore, accurate intraoperative recognition of the thoracic sympathetic nerves is critical for the treatment of related diseases and for the development of new therapies.

Although the slender white-colored sympathetic chain often can be seen underneath the parietal pleura paralleling the vertebral column and above the heads of the ribs, its size and width are variable. In addition, its cephalad-caudal course may be meandering or straight. So far, no ganglion has clearly been visualized [12]. Although there are several anatomic landmarks that surgeons use as guides to identify the thoracic sympathetic chain or ganglion during surgery, the International Society on Sympathetic Surgery and the Society of Thoracic Surgeons recommend using a rib-oriented nomenclature [2]. In general, each thoracic ganglion lies in the intercostal space between its corresponding ribs and is referred to based on the anatomical structure. Therefore, surgeons indirectly and roughly determine the locations of the ganglia by counting the ribs at the time of surgery. However, this method has some limitations. Some studies have confirmed that anatomic variations often cause changes in the corresponding spatial locations between thoracic ganglia and the ribs. For example, Street et al. found in their series that 6.25% of ganglions were located below their associated intercostal spaces rather than within their corresponding intercostal space. In addition, the stellate ganglion (SG), which was formed by the inferior cervical ganglion and the first thoracic ganglion (T1), was present in only 70% of specimens [13]. Chung et al. have reported that the SG and

Theranostics. 2018. 8(2): 304–313 Published online: 1 January 2018

the second thoracic ganglion (T2) are fused in 9.1% of patients [14]. Failure in the accurate identification of thoracic ganglia may result in operation failure and severe complications [2, 15].

Fluorescence imaging (FI) is a novel intraoperative imaging modality used to help guide the surgeon in the detection of benign and/or malignant tissues [16], and has been used for the detection and treatment of multiple diseases, such as ovarian cancer using specific FI [17], head and neck cancer [18] and peritoneal carcinomatosis from colorectal cancer [19,20] using non-specific FI. However, only a few FI studies of nerves in the clinical have been reported. Wagner et al. identified the contralateral periocardiophrenic neurovascular bundle by fluorescing the pericardiophrenic vessels during robotic thymectomy [21]. Chen et al. recognized facial nerve by highlighting the vessels inside the vasa nervorum during mastoidectomy [22]. Our team first reported that thoracic ganglia can be directly visualized during thoracoscopic indocyanine green (ICG) fluorescence guided surgery (ICG-FGS) in a case report [23,24]. Notably, ICG has been authorized by the Food and Drug Administration (FDA) for determining cardiac output, hepatic function and liver blood flow, and for ophthalmic angiography.

In this study, we firstly evaluated the feasibility of intraoperative real-time imaging of thoracic sympathetic nerves (ITSN) with ICG and explored the relationship between the signal to background ratio (SBR) and the injection time of ICG and that between SBR and the dose of ICG using a rabbit model. Because sympathetic nerves were subtle and difficult to detect, a fluorescence microscope system was developed. Then, to study the validity of this method, we carried out a clinical trial with our self-developed near-infrared (NIR) and white-light dual-channel thoracoscope system in Peking University People's Hospital.

Materials and Methods

Fluorescence Microscope System

We developed a modified fluorescence microscope system (Fig. 1A) in-house. Briefly, a traditional stereomicroscope (Leica M205 FA, Germany) was coupled with a color camera and an NIR scientific complementary metal-oxide-semiconductor (SCMOS) camera (pco.edge 5.5 m). An NIR laser source (center wavelength: 785 nm, maximum power: 800 mW) was combined with an optical filter module installed in the stereomicroscope through a uniform fiber, so that a specified wavelength of light was transmitted onto the imaging target. The emission light radiated by the excited fluorophore was first filtered by the filter module and then captured by the NIR camera. Similarly, the color camera

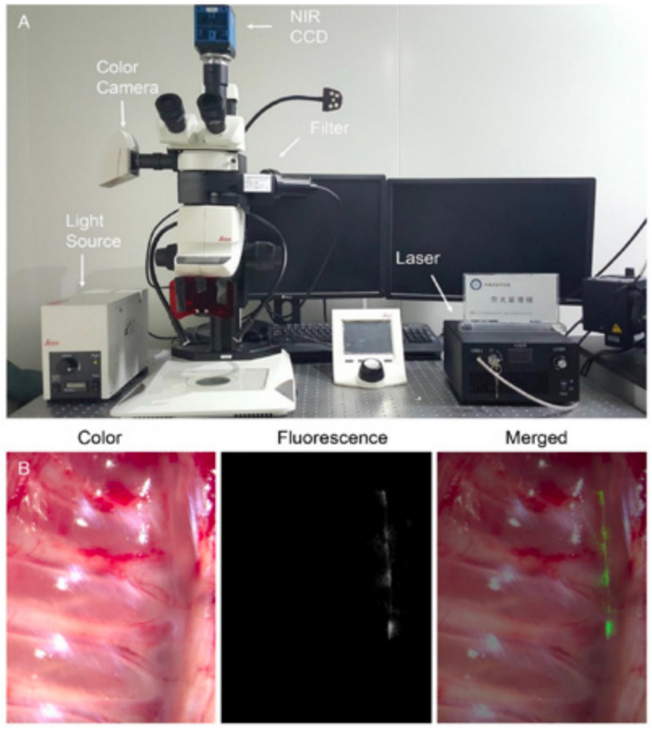


Fig.1 (A) Photograph of the modified fluorescence microscope system. (B) Ex vivo imaging of the rabbit's thoracic sympathetic nerve, including color, fluorescence, and merged images. NIR CCD: near-infrared charge-coupled device.

captured visible images illumined by the light emitting diode. This system was able to produce a strong and noise-free fluorescence image against the background and a bright and high-resolution visible image.

Fluorescence Endoscopic Imaging System

The NIR (800-900 nm) and white-light (400-650 nm) dual-channel thoracoscope system was developed by the Key Laboratory of Molecular Imaging of the Chinese Academy of Sciences on the basis of our previous studies [25-29]. A picture of the novel system is presented in Fig. 3A. Briefly, the system consisted of four modules: the light-source module, the detector module, the control module, and the display module. The spatial resolution of the system was 35 μm and the minimal detectable ICG concentration was 0.01 μM.

In addition to the ergonomic improvements compared to our previous system [27], the novel system used a custom prism with a 30° viewing angle. The use of this prism not only made probing the thoracic sympathetic nerve more convenient, but also resulted in a large aperture and a wide field. Due to the presence of high levels of noise and the weak fluorescence signal during this experiment, we designed a new image enhancement algorithm to improve the qualities of the color and fluorescence images. This system also had improved quantitative analysis functionality, which enabled us to perform the quantitative statistical analysis of the fluorescence intensity and the calculation of SBR in real-time. The quantification techniques of fluorescence intensity signal included fluorescence signal extraction based on fuzzy C-mean clustering and level-set algorithms, fluorescence intensity distribution analysis, the radiometric calculation of fluorescence image and other conventional image analysis methods.

Animals

Four male and six female Japanese white rabbits (weight: 1.75-2.4 kg, average: 2.15 kg) were purchased from Beijing Vital River Laboratory Animal Technology Co., Ltd. (China). The Institutional Animal Care and Use Committee of Peking University People's Hospital approved this animal study. To obtain the relationship between SBR and the injection time of ICG and that between SBR and the dose of ICG, we allocated the ten rabbits to two group. One group was the dose group and the other group was the timing group.

Patients

The subjects comprised 15 eligible patients who were scheduled for video-assisted thoracoscopic surgery at Peking University People's Hospital between July 2015 and June 2016. The characteristics of the patients are shown in Table 1. The inclusion criteria were as follows: age between 18 and 75, pulmonary nodules scheduled for thoracoscopy or thoracotomy, preoperatively normal liver function, no ICG or iodine allergies, negative findings on an ICG skin test, volunteering to participate in this study, and providing signed informed consent. The exclusion criteria were preoperative liver dysfunction, ICG or iodine allergies, positive results on an ICG skin test, other well-controlled comorbidities, and being deemed unsuitable for enrolment by the clinicians.

Before surgery, all patients were diagnosed with pulmonary nodules using high-resolution computed tomography with 1 mm slice thickness. All patients provided signed informed consent. The Peking University People's Hospital Institutional Review Board authorized this study (2015PHB157-01). The Clinical Trials number for the study is NCT02611245.

Administration of Contrast Agents

ICG (25 mg vials) was purchased from Tianyi Pharmaceutical Co., Ltd. (Liaoning, China). First, the rabbits in the timing group were injected with 10 mg/kg ICG in sterile water for injection (SWI) 24, 22, 20, 18, and 16 h preoperatively through the marginal ear vein. After calculating the SBR for each time point, the rabbits in the dose group were then injected with 7, 8.5, 10, 11.5, and 13 mg/kg of ICG in SWI 20 h preoperatively.

For patients' safety reasons, we referred to several studies [30-34] in tumor identification for pulmonary nodules and brain tumors and then chose the ICG concentration of 5 mg/kg. Three patients were respectively injected 5 mg/kg ICG 16, 20 and 24 h preoperatively. Through observation, we determined 5 mg/kg and 24 h preoperatively was the best combination. Then 15 patients were intravenously injected with 5 mg/kg of ICG 24 h preoperatively. No adverse reactions or allergic reactions were observed in any of the subjects.

Preclinical Imaging Procedure

After routine injection of ICG preoperatively, the rabbits were injected with 6 mg/kg of 0.7% sodium pentobarbital solution in the marginal ear vein. Upon disappearance of the corneal reflex, the

Table 1 Characteristics of the 15 patients who participated in this study

Study no.	Age	Sex	BMI	History of allergy	Tumor size (cm)	Tumor location	Pathology
1	52	M	25.76	NO	1*0.5	RUL	ADE
2	33	F	20.07	NO	1.2*0.7	LLL	CRC
3	74	F	25.01	NO	0.7*0.6	LUL	ADE
4	44	F	23.44	NO	0.6*0.5	RUL	AIS
5	30	M	19.69	NO	2*1	RML	CHO
6	63	M	26.99	NO	2.5*2	RML	CCRCC
7	65	F	19.53	NO	1.5*1	RLL	AIS
8	43	F	23.62	YES	5*4	RLL	ADE
9	61	F	23.44	NO	3*2	LUL	HCC
10	57	F	20.03	NO	0.6*0.4	RUL	ADE
11	52	M	25.59	NO	4*3	LML	HCC
12	61	F	26.37	NO	2.5*2	RLL	ADE
13	52	M	22.68	NO	5*4	RLL	ADE
14	50	F	22.32	NO	5*3	LLL	ADE
15	67	F	20.83	NO	3.2*2.2	RUL	ADE

ADE: adenocarcinoma; AIS: adenocarcinoma in situ; CCRCC: clear cell renal cell carcinoma; CHO: chondrosarcoma; CRC: colorectal cancer; F: female; HCC: hepatocellular carcinoma; LLL: left lower lobe; LML: left middle lobe; LUL: left upper lobe; M: male; RLL: right lower lobe; RML: right middle lobe; RUL: right upper lobe

rabbits were executed by injection of 50 mL of air through veins. A median thoracotomy was performed. The lung, heart, and aorta were then dissected and removed. The sympathetic nerves on either side of the spine were exposed. Lastly, the spine was cut from the thoracic apex to the diaphragm, and the ribs were cut 3 cm from the spine. The entire chest wall with contact parietal pleura was removed. Then the specimens were washed using physiological saline solution.

The dissected specimens were placed on the microscope table. After adjustments of the appropriate imaging distance and field of vision, a color image was captured. We then switched the microscope to NIR mode, turned off all of the laboratory light sources, and obtained a fluorescence image. Finally, under the guidance of fluorescence signal, we carefully removed the ICG-stained thoracic sympathetic ganglia and the chains on both sides of the spine.

Clinical Imaging Procedure

After the scheduled injection of ICG, the patients were placed in a lateral position and underwent double-catheter trachea insertion under general anesthesia. After routine disinfection, the thoracoscope was inserted at the seventh rib. Before the lung excision operation, the lung was pulled to the front and the posterior mediastinum was revealed. The sympathetic nerves were then explored from top to bottom. We determined and recorded the positions and fluorescence intensities of SG through T6 and the chains in between. Patient No. 11 was diagnosed with pulmonary nodules and posterior mediastinal tumor. After the lung nodules were removed, the mediastinal tumor and T3 were resected together, as they were too close to each other to separate. All excised specimens were then sent to the pathology department.

Histopathologic Assessment

All of the dissected specimens were fixed in 10% phosphate-buffered formalin for 24 h. Paraffin-embedded tissues were consecutively sliced at 5 μm intervals. First, the pathologist analyzed the unstained sections. The sections were then stained with hematoxylin-eosin (H&E) and examined according to the standard pathology protocol. This is because H&E staining may compromise the observation of the ICG fluorescence signal. Areas of the section with fluorescence signals merged with staining of the neurocyte were identified. In addition, we used tyrosine hydroxylase (TH) antibodies (Rabbit polyclonal anti-TH antibody, ab112, Abcam) to identify sympathetic ganglion cells and confirmed our findings [35].

Statistical Analysis

SBR of thoracic sympathetic nerves were calculated by the method as follows: Firstly, we used ImageJ (Image processing Software, National Institutes of Health, USA) to delineate ganglions or chains as a region of interest (ROI) and calculated the mean brightness value of ROI (V_{Signal}). Meanwhile, the surrounding background region was highlighted and the mean brightness value of this region ($V_{Backgroud}$) was also measured. SBR values for each thoracic sympathetic ganglion or chain were calculated six times to reduce errors by dividing V_{Signal} by $V_{Backgroud}$. The Kruskal-Wallis test was used to compare multiple independent samples. To maintain consistency in our calculations, we selected the bilateral second to fifth thoracic sympathetic ganglia (T2, T3, T4, and T5) and used their average value to denote each rabbit's SBR. We adopted this approach because the area and intensity of the NIR laser source were limited. Data analysis and graphing were performed using OriginPro 2016 (OriginLab Corporation, USA). P-values < 0.050 were considered statistically significant.

Results

Preclinical Study Results

The microscopic examinations enabled us to identify each rabbit's T2 to T5 ganglia (8 in total) on both sides of the spine. All of the sympathetic ganglia and the chains between them were identified using our FI method on the surface of the specimens. The areas with high SBR values in the fluorescence images matched the thoracic nerves as seen in the color images perfectly (Fig. 1B) and confirmed our findings. Shorter time intervals between the ICG injection and the operation led to stronger fluorescence signals in the rabbits in the timing group. However, the SBR for the rabbit injected with ICG 20 h preoperatively was the highest in the group ($p < 0.001$, Fig. 2A). In the dose group, larger doses of ICG led to stronger fluorescence signals. However, the SBR for the rabbit injected with 10 mg/kg of ICG was the highest in the group ($p < 0.001$, Fig. 2B). In the process of statistical analysis, n values of the number of samples are all equal to six.

Fluorescence microscopy confirmed the presence of fluorescence in the specimens (Fig. 2C), which were resected under the guidance of the fluorescence signal. We found large numbers of neurocytes in the areas with strong fluorescence signals (Fig. 2D). However, there were a few nerve cells in areas with weak fluorescence signals. We used pathological examination to verify our findings.

Clinical Trial Results

We used ITSN with ICG to successfully identify the thoracic sympathetic ganglia SG to T6 (12 in total) and the chains in between in each patient (Figs. 3B-D). The mean SBR value for all ganglia was 3.26 (standard deviation: 0.57), which was sufficiently high to assist the surgeons in identifying the ganglia during surgery. Moreover, the strong fluorescence signal lasted for longer than five hours. The calculated SBR values for SG through T6 for all subjects are shown in Fig. 4A. The SBR value for SG was the lowest ($p < 0.001$) and those for T2 to T6 were not significantly different from each other ($p > 0.050$). In the process of data statistics, n values of the number of samples are all equal to 30.

Fluorescence microscopy enabled us to find a strong fluorescence signal in the paraffin section from the thoracic sympathetic nerve specimen from patient No. 11 (Fig. 4B-D). The fluorescence was mainly distributed in areas with large numbers of nerve cells. H&E staining of the section confirmed our findings (Fig. 4E).

Discussion

Here we investigated the feasibility and validity of intraoperative ITSN with ICG in both a preclinical study and a clinical trial. We were able to identify T2 to T5 on both sides of the spine in

Theranostics. 2018. 8(2): 304–313 Published online: 1 January 2018

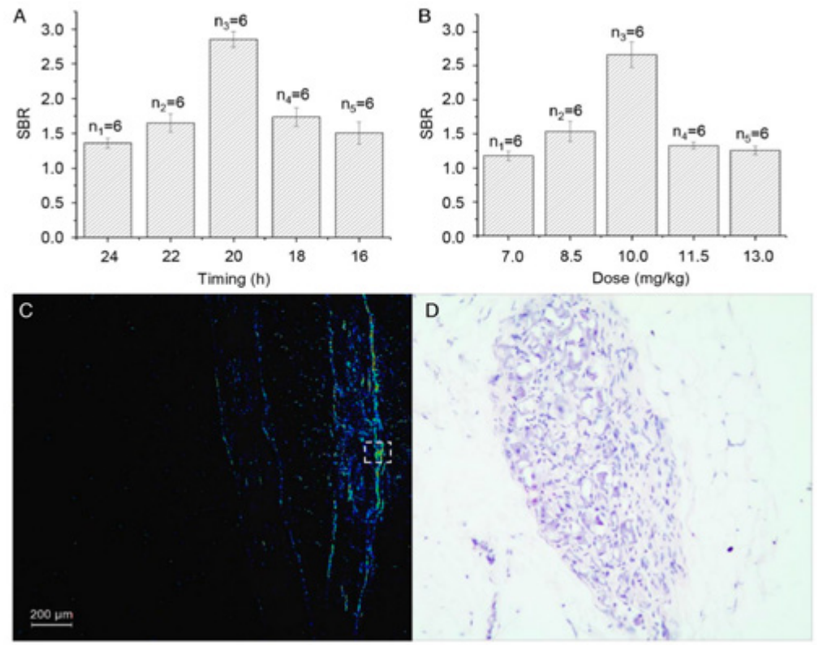


Fig.2 (A) The relationship between SBR and the injection time in each rabbit in the timing group. (B) The relationship between SBR and the dose of ICG in each rabbit in the dose group. (C) Representative fluorescence image of a paraffin section of a rabbit's thoracic sympathetic nerves. (D) H&E-stained cross-section of the area marked by the dotted box in Fig. Fig.2C.2C. SBR: signal to background ratio.

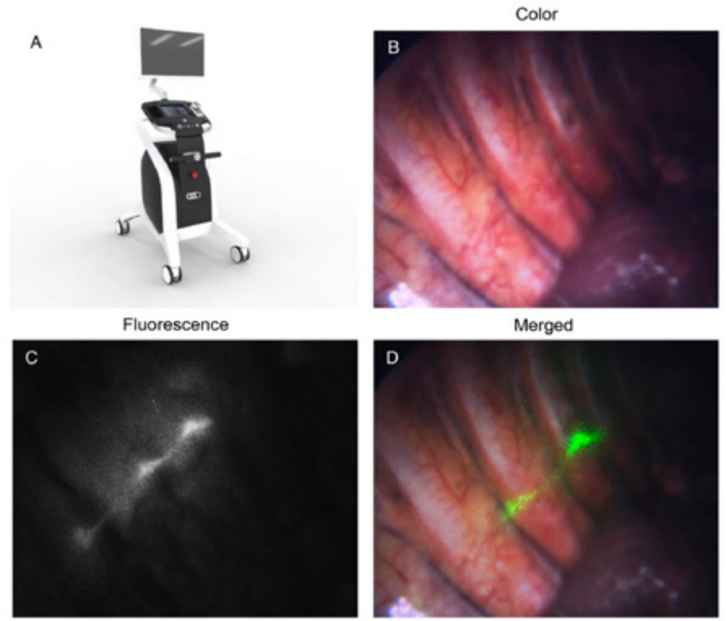


Fig.3 (A) A picture of the dual-channel thoracoscope system. (B-D) In vivo thoracic sympathetic nerve images of a patient, including color, fluorescence, and merged images.

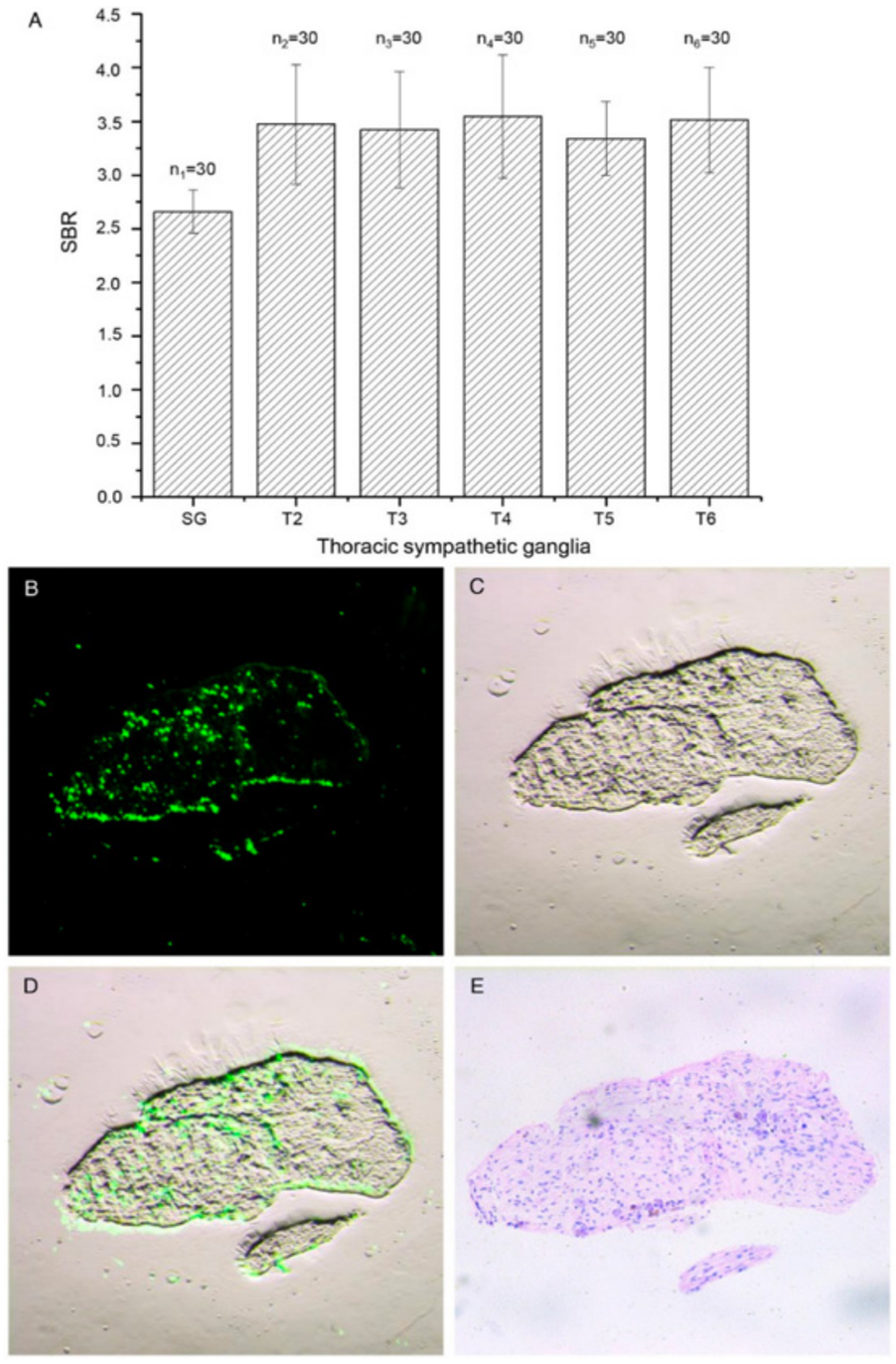


Fig.4 (A) The SBR values for SG to T6 for all patients. (B-D) Fluorescence, color and merged images of a paraffin section of the thoracic sympathetic nerve specimen from patient No. 11. (E) H&E-stained section of the area shown in Fig. Fig.4C.4C. SBR: signal to background ratio.

each rabbit and obtained the relationship between SBR and the injection time of ICG and that between SBR and the dose of ICG in the preclinical study. The false-negative rate was 0% (0/10 rabbits). We used the method described here to successfully identify the thoracic sympathetic ganglia SG through T6 (12 in total) and the chains in between in each patient in the clinical study. High SBR values in ITSN with ICG highly depend on the ICG dose, imaging timing, and the sensitivity of the imaging system. Therefore, we developed a modified fluorescence microscope system and an NIR and white-light dual-channel thoracoscope system especially optimized for NIR light collection efficiency. The combination of intraoperative ITSN with ICG and the novel thoracoscope system displayed enormous potential in clinical application.

The novel method described here has several advantages when compared to traditional approaches. First, the high-SBR and intraoperative real-time imaging contributes to the objective and accurate identification of thoracic sympathetic nerves during surgery. Second, NIR light can penetrate much deeper into blood and tissue than visible light. In addition, autofluorescence is very weak in this spectral range. Lastly, this method is minimally invasive and does not interfere with the conventional surgical procedure. Moreover, no adverse reactions or allergic reactions occurred in this study.

ICG is a water-soluble compound with a molecular weight of 755 Da and has been clinically approved for longer than 60 years by the FDA. When injected into the human vein, it binds intensely to high-density lipoprotein and low-density lipoprotein [36]. Its half-life is 150-180 s. According to the National Cancer Institute, ICG is excreted from the circulation exclusively by the liver into bile. At first, ICG was mainly used to determine cardiac output and hepatic function. In 2009, Ishizawa et al. reported the presence of illuminated liver tumors using ICG [37]. These tumors emitted light that peaked at around 830 nm when excited with NIR light. Nowadays, ICG FI plays an important role in sentinel lymph node detection [38, 39], lymphedema diagnosis and management [40], tumor identification [41] and organ perfusion assessment [42]. In this study, we for the first time used ICG FI to identify the thoracic sympathetic nerves.

Based on the properties of ICG and our preliminary studies, we believe that the high-SBR fluorescence signal from the thoracic sympathetic nerves may result from the specific structure of these nerves. There is a layer of connective tissue membrane containing blood vessels, nerves, and fat cells on the sympathetic ganglion surface. This later may lead to enhanced permeability and retention (EPR) of ICG, similar to certain types of cancer tissue [43, 44]. This phenomenon is more marked in humans than in rabbits, perhaps due to the larger sizes of the sympathetic nerves. Notably, the SBR value for the SG is lower than that for T2 through T6. This is because there is a fat pad in the hemithorax vertex that often covers the SG.

The EPR effect, firstly reported by Maeda et al., is a property that protein-bound molecules and other nano-sized materials passively accumulate in tumors after systemic administration [45]. Ideally, nerve-specific contrast agents should be adopted during nerve-sparing FI surgery. Nowadays, Whitney et al. are utilizing NIR fluorescent peptides that bind to nerve sheaths to develop nerve-specific agents on rat model [46]. And Gibbs-Strauss et al. are developing nerve-specific agents based on small, hydrophobic molecules that bind to the myelin of neurons on animal model [47]. However, no clinical trial has ever been reported on nerve-specific contrast agents.

Structurally, thoracic sympathetic nerves are important parts of the sympathetic nervous system and have both white and gray matter rami communicates [48]. Functionally, thoracic sympathetic nerves provide sympathetic innervation to the internal organs of the chest. Intraoperative real-time ITSN is conducive to the preservation of the nerves during certain surgeries, such as mediastinal tumor surgery, which is equally crucial to achieving optimal prognosis [16]. In addition, ITSN is critical for the accurate ablation or resection of ganglia and chains and in the diagnosis and treatment of related diseases. Moreover, this technique has huge potential for the development of novel therapeutic modalities. In our future work, we will further optimize the dose of ICG and the sensitivity of our imaging system, and attempt to use this method to visualize other nerves.

Conclusion

In this study, we successfully identified thoracic sympathetic nerves using ITSN with ICG in both preclinical and clinical studies. Moreover, the relationship between SBR and the injection time of ICG and that between SBR and the dose of ICG were explored, and a novel NIR and white-light dual-channel thoracoscope system was developed. Pathological studies confirmed our findings. This new method may replace the rib-oriented method as standard practice for the identification of the thoracic sympathetic nerves.

Abbreviations

FDA: Food and Drug Administration
FI: fluorescence imaging
H&E: hematoxylin-eosin
ICG: indocyanine green
ITSN: imaging of thoracic sympathetic nerves
NIR: near-infrared
ROI: region of interest
SBR: signal to background ratio
SG: stellate ganglion
SWI: sterile water for injection

Acknowledgments

This work was supported by the National Key Research and Development Program of China under Grant No. 2017YFA0205200 and 2016YFC0103702, the National Natural Science Foundation of China under Grant No. 81227901, 81527805, 61231004, 61501462 and 61671449, the International Innovation Team of CAS under Grant No. 20140491524, Beijing Municipal Science & Technology Commission No. Z161100002616022 and Peking University People's Hospital Research and Development Foundation (No. RDC2015-33).

All authors have read the journal's authorship agreement and the article has been reviewed by and approved by all named authors. Moreover, we thank Yun Wang and Fei Yang of Peking University People's Hospital for the help of pathological staining and analysis.

The clinical trial was registered using the name "NIR fluorescence imaging technique in thoracic surgery with ICG". The Clinical Trial number is NCT02084784.

Competing Interests

The authors have declared that no competing interest exists.

References

1. Hashmonai M, Licht PB, Schick CH, Bishof G, Cameron AEP, Connery CP. et al. Late results of endoscopic thoracic sympathectomy for hyperhidrosis and facial blushing (Br J Surg 2011; 98: 1719-1724) Brit J Surg. 2012;99:1719–24.
2. Cerfolio RJ, De Campos JR, Bryant AS, Connery CP, Miller DL, Decamp MM. et al. The Society of Thoracic Surgeons expert consensus for the surgical treatment of hyperhidrosis. Ann Thorac Surg. 2011;91:1642.
3. Nicholas R, Quddus A, Baker DM. Treatment of Primary Craniofacial Hyperhidrosis: A Systematic Review. Am J Clin Dermatol. 2015;16:361–70.
4. Abbate A, Hamza M, Cassano AD, Melchior R, Roberts C, Grizzard J. et al. Sympathectomy as a treatment for refractory coronary artery spasm. Int J Cardiol. 2012;161:7–9.
5. Schwartz PJ, Ackerman MJ. The long QT syndrome: a transatlantic clinical approach to diagnosis and therapy. Eur Heart J. 2013;34:3109–16.
6. Vaseghi M, Gima J, Kanaan C, Ajijola OA, Marmureanu A, Mahajan A. et al. Cardiac sympathetic denervation in patients with refractory ventricular arrhythmias or electrical storm: intermediate and long-term follow-up. Heart Rhythm the Official Journal of the Heart Rhythm Society. 2014;11:360.
7. Issa Y, Ahmed AU, Bouwense SA, van Santvoort HC, Van GH. Preoperative opioid use and the outcome of thoracoscopic splanchnicectomy in chronic pancreatitis: a systematic review. Surgical Endoscopy. 2014;28:405–12.
8. Agarwal-Kozlowski K, Lorke DE, Habermann CR, Schulte aEJ, Beck H. Interventional management of intractable sympathetically mediated pain by computed tomography-guided catheter implantation for block and neuroablation of the thoracic sympathetic chain: technical approach and review of 322 procedures. Anaesthesia. 2011;66:699–708.
9. Landry GJ. Current medical and surgical management of Raynaud's syndrome. J Vasc Surg. 2013;57:1710–6.
10. Coveliers HME, Hoexum F, Nederhoed JH, Wisselink W, Rauwerda JA. Thoracic sympathectomy for digital ischemia: A summary of evidence. J Vasc Surg. 2011;54:273–7.
11. Hoexum F, Coveliers HM, Lu JJ, Jongkind V, Yeung K, Wisselink W. Thoracic sympathectomy for upper extremity ischemia. Minerva Cardioangiol; 2016. p. 64.
12. Krasna MJ, Flowers J, Morvick R. Thoracoscopic sympathectomy. Surg Laparosc Endosc. 2010;20:323–30.
13. 13. Street E, Ashrafi M, Greaves N, Gouldsborough I, Baguneid M. Anatomical variation of rami communicantes in the upper thoracic sympathetic chain: A human cadaveric study. Ann Vasc Surg. 2016;34:243–9.
14. Chung IH, Oh CS, Koh KS, Kim HJ, Paik HC, Lee DY. Anatomic variations of the T2 nerve root (including the nerve of Kuntz) and their implications for sympathectomy. Journal of Thoracic & Cardiovascular Surgery. 2002;123:498–501.
15. Hashmonai M, Cameron AEP, Licht PB, Hensman C, Schick CH. Thoracic sympathectomy: a review of current indications. Surgical Endoscopy. 2016;30:1255–69.
16. Nguyen QT, Tsien RY. Fluorescence-guided surgery with live molecular navigation—a new cutting edge. Nature reviews Cancer. 2013;13:653.
17. van Dam GM, Themelis G, Crane LM, Harlaar NJ, Pleijhuis RG, Kelder W. et al. Intraoperative tumor-specific fluorescence imaging in ovarian cancer by folate receptor-α targeting: first in-human results. Nat Med. 2011;17:1315.
18. Moore LS, Rosenthal EL, Chung TK, De BE, Patel N, Prince AC, Characterizing the utilities and limitations of repurposing an open-field optical imaging device for fluorescence-guided surgery in head and neck cancer patients. J Nucl Med; 2016; 58.
19. Filippello A, Porcheron J, Klein JP, Cottier M, Barabino G. Affinity of Indocyanine Green in the Detection of Colorectal Peritoneal Carcinomatosis: The Role of Enhanced Permeability and Retention Effect. Surg Innov; 2016. p. 24.
20. Liberale G, Vankerckhove S, Caldon MG, Ahmed B, Moreau M, El Nakadi I. et al. Fluorescence imaging after indocyanine green injection for detection of peritoneal metastases in patients undergoing cytoreductive surgery for peritoneal carcinomatosis from colorectal cancer: a pilot study. Ann Surg. 2016;264:1110–5.
21. Wagner OJ, Louie BE, Vallières E, Aye RW, Farivar AS. Near-infrared fluorescence imaging can help identify the contralateral phrenic nerve during robotic thymectomy. Ann Thorac Surg. 2012;94:622–5.
22. Chen SC, Wang MC, Wang WH, Lee CC, Yang TF, Lin CF. et al. Fluorescence-assisted visualization of facial nerve during mastoidectomy: A novel technique for preventing iatrogenic facial paralysis. Auris Nasus Larynx. 2014;42:113–8.
23. Weng W, Liu Y, Zhou J, Li H, Yang F, Jiang G. et al. Thoracoscopic Indocyanine Green Near-Infrared Fluorescence for Thoracic Sympathetic Ganglions. Ann Thorac Surg. 2016;101:2394.
24. Zhou J, Yang F, Jiang G, Wang J. Applications of indocyanine green based near-infrared fluorescence imaging in thoracic surgery. J Thorac Dis. 2016;8:S738.
25. Leng CC, Tian J. Mathematical method in optical molecular imaging. Science China Information Sciences. 2015;58:31101–031101.
26. Chi C, Du Y, Ye J, Kou D, Qiu J, Wang J. et al. Intraoperative imaging-guided cancer surgery: from current fluorescence molecular imaging methods to future multi-modality imaging technology. Theranostics. 2014;4:1072–84.
27. Mao Y, Wang K, He K, Ye J, Yang F, Zhou J. et al. Development and application of the near-infrared and white-light thoracoscope system for minimally invasive lung cancer surgery. Journal of Biomedical Optics. 2017;22:66002.
28. Wang K, Chi C, Hu Z, Liu M, Hui H, Shang W. et al. Optical Molecular Imaging Frontiers in 0ncology: The Pursuit of Accuracy and Sensitivity. Engineering. 2015;1:309–23.
29. He K, Chi C, Kou D, Huang W, Wu J, Wang Y. et al. Comparison between the indocyanine green fluorescence and blue dye methods for sentinel lymph node biopsy using novel fluorescence image-guided resection equipment in different types of hospitals. Transl Res. 2016;178:74.
30. Judy RP, Keating JJ, Dejesus EM, Jiang JX, Okusanya OT, Nie S. et al. Quantification of tumor fluorescence during intraoperative optical cancer imaging. Sci Rep-Uk. 2015;5:16208.
31. Lee JY, Pierce JT, Thawani JP, Zeh R, Nie S, Martinezlage M, Near-infrared fluorescent image-guided surgery for intracranial meningioma. J Neurosurg; 2017. p. 1.
32. Lee JY, Thawani JP, Pierce J, Zeh R, Martinez-Lage M, Chanin M. et al. Intraoperative Near-Infrared Optical Imaging Can Localize Gadolinium-Enhancing Gliomas During Surgery. Neur osurgery. 2016;79:856.
33. Okusanya OT, Holt D, Heitjan D, Deshpande C, Venegas O, Jiang J. et al. Intraoperative near-infrared imaging can identify pulmonary nodules. Ann Thorac Surg. 2014;98:1223–30.
34. Zeh R, Sheikh S, Xia L, Pierce J, Newton A, Predina J. et al. The second window ICG technique demonstrates a broad plateau period for near infrared fluorescence tumor contrast in glioblastoma. Plos One. 2017;12:e0182034.
35. Seki A, Green HR, Lee TD, Hong L, Tan J, Vinters HV. et al. Sympathetic nerve fibers in human cervical and thoracic vagus nerves. Heart Rhythm. 2014;11:1411–7.
36. Yoneya S, Saito T, Komatsu Y, Koyama I, Takahashi K, Duvollyoung J. Binding properties of indocyanine green in human blood. Invest Ophth Vis Sci. 1998;39:1286.
37. Ishizawa T, Fukushima N, Shibahara J, Masuda K, Tamura S, Aoki T. et al. Real-time identification of liver cancers by using indocyanine green fluorescent imaging. Cancer. 2009; 115:2491.
38. Nguyen DP, Huber PM, Metzger TA, Genitsch V, Schudel HH, Thalmann GN. A Specific Mapping Study Using Fluorescence Sentinel Lymph Node Detection in Patients with Intermediate- and High-risk Prostate Cancer Undergoing Extended Pelvic Lymph Node Dissection. Eur Urol. 2016;70:734–7.
39. Ahmed M, Purushotham AD, Douek M. Novel techniques for sentinel lymph node biopsy in breast cancer: a systematic review. Lancet Oncology. 2014;15:351–62.
40. Takashi Sakurai MD, Mariko Endo MD, Ken Shimizu MD, Nobunari Yoshimizu MD, Kenichirou Nakajima MD, Pharmacist KN. et al. Axillary reverse mapping using fluorescence imaging is useful for identifying the risk group of postoperative lymphedema in breast cancer patients undergoing sentinel node biopsies. J Surg Oncol. 2014;109:612.
41. Vorst JRVD, Schaafsma BE, Hutteman M, Verbeek FPR, Liefers GJ, Hartgrink HH. et al. Near-Infrared Fluorescence-Guided Resection of Colorectal Liver Metastases. Cancer. 2013;119:3411.
42. Degett TH, Andersen HS, Gögenur I. Indocyanine green fluorescence angiography for intraoperative assessment of gastrointestinal anastomotic perfusion: a systematic review of clinical trials. Langenbeck Arch Surg. 2016;401:1–9.
43. Keating J, Newton A, Venegas O, Nims S, Zeh R, Predina J. et al. Near-Infrared Intraoperative Molecular Imaging Can Locate Metastases to the Lung. Ann Thorac Surg. 2016;103:390–8.
44. Jiang JX, Keating JJ, Jesus EM, Judy RP, Madajewski B, Venegas O. et al. Optimization of the enhanced permeability and retention effect for near-infrared imaging of solid tumors with indocyanine green. Am J Nucl Med Mol Imaging. 2015;5:390–400.
45. Matsumura Y, Maeda H. A New Concept for Macromolecular Therapeutics in Cancer Chemotherapy: Mechanism of Tumoritropic Accumulation of Proteins and the Antitumor Agent Smancs. Cancer research. 1986;46:6387.
46. Whitney MA, Crisp JL, Nguyen LT, Friedman B, Gross LA, Steinbach P. et al. Fluorescent peptides highlight peripheral nerves during surgery in mice. Nat Biotechnol. 2011;29:352.
47. Gibbsstrauss SL, Nasr KA, Fish KM, Khullar O, Ashitate Y, Siclovan TM. et al. Nerve-highlighting fluorescent contrast agents for image-guided surgery. Mol Imaging. 2011;10:91–101.
48. Krasna MJ. Thoracoscopic sympathectomy. Thorac Surg Clin. 2010;20:323.

Eur J Cardiothorac Surg. 2017. 52(6): 1190-1196 Published online: 27 July 2017

Thoracic Surgery

Research Article

The Identification of Sub-Centimetre Nodules by Near-Infrared Fluorescence Thoracoscopic Systems in Pulmonary Resection Surgeries

Yamin Mao[1,2,3,*], Chongwei Chi[1,2,3,*], Fan Yang[4,*], Jian Zhou[4,*], Kunshan He[1,2,3], Hao Lid[4], Xiuyuan Chen[4] , Jinzuo Ye[1,2,3], Jun Wang[4] and Jie Tian[1,2,3]

Abstract

Objectives: Current surgical procedures lack high-sensitivity intraoperative imaging guidance, leading to undetected micro tumours. In vivo near-infrared (NIR) fluorescence imaging provides a powerful tool for identifying small nodules. The aim of this study was to examine our experience of using 2 different NIR devices in pulmonary resection surgery.

Methods: From August 2015 to October 2016, 36 patients with lung nodules underwent NIR fluorescence imaging thoracoscopic surgery. Two NIR devices: a D-Light P system and a SUPEREYE system were used. Patients were administered an injection of indocyanine green (ICG) through the peripheral vein 24 h preoperatively. During surgery, traditional white-light thoracoscopic exploration was performed first, followed by ICG-fluorescent-guided exploration. All detected nodules were resected and examined by a pathologist.

Results: Of the 36 patients, 76 nodules were resected. ICG-fluorescent imaging identified 68 nodules during in vivo exploration. The mean signal-to-background ratio of lung nodules in NIR exploration was 3.29 ± 1.81. The application of NIR devices led to the detection of 9 additional nodules that were missed using traditional detection methods (1 mm computed tomography scan and white-light thoracoscopic exploration) in 7 patients (19.4%). Four of the 9 nodules were confirmed as malignant or atypical adenomatous hyperplasia (44.4%). The other 5 nodules

were confirmed as false-positive nodules. The sensitivities and positive predictive values of the ICG-fluorescent imaging for lung tumours were 88.7% and 92.6%, respectively.

Conclusions: This study demonstrated the feasibility and safety of using ICG-fluorescent imaging for multiple lung nodules identification in video-assisted thoracoscopic surgery pulmonary resection.

Clinical trial: gov number NCT02611245.

Key words

Lung cancer, Video-assisted thoracoscopic surgery, Cancer imaging, NIR fluorescence imaging, ICG

[1] CAS Key Laboratory of Molecular Imaging, Institute of Automation, Chinese Academy of Sciences, Beijing, China

[2] School of Computer and Control Engineering, University of Chinese Academy of Sciences, Beijing, China

[3] Beijing Key Laboratory of Molecular Imaging, Chinese Academy of Sciences, Beijing, China

[4] Department of Thoracic Surgery, Peking University People's Hospital, Beijing, China

Introduction

Lung cancer is the most common cancer type and the leading cause of cancer death in China[1]. Up to 15% of lung cancer patients develop synchronous or metachronous nodules[2, 3]. Meanwhile, when dealing with pulmonary metastasis tumours of other malignancies, the detection of all nodules is also challenging. Failure to remove all of the micro lesions during surgery might be one of the causes of recurrence. With the widespread use of video-assisted thoracoscopic surgery (VATS), manual palpation of pulmonary nodules is restricted; surgeons have to rely on visual inspection. However, white-light imaging as the primary intraoperative imaging method lacks the contrast between tumours and normal tissue[4]. For the current clinical imaging methods, superficially multiple micro lesions with a diameter of <5 mm are particularly difficult to detect[5]. Thus, patients with lung nodules need a new imaging technology to better identify small lung lesions and guide surgery in real time[6].

Fluorescence image-guided surgery is a highly sensitive and specific imaging method that has the potential to identify imperceptible lesions[7–9]. Currently, the most widely used NIR fluorescence dye is indocyanine green (ICG) (excitation: 778 nm and emission: 830 nm), which was approved by the Food and Drug Administration (FDA). The ICG is a very safe imaging agent that has few allergic reactions (approximately 0.003%) and is applied in various tumour detection because of its passive accumulation[10]. Several groups have proved the feasibility and benefits of near-infrared (NIR) fluorescence image-guided surgery in tumour nodules detection[11–16]. van Dam et al. showed that the use of fluorescence imaging technology detected significantly additional tumour nodules in ovarian cancer surgery[17]. Liberale et al. showed that NIR image-guided surgery discovered a higher number of subclinical lesions than conventional inspection for peritoneal carcinomatosis[18]. Moreover, Okusanya et al. performed open surgeries of lung cancer and successfully confirmed that ICG could remain in tumours 24 h after intravenous injection by enhanced permeability and retention (EPR) effect. They detected 5 additional non-palpable nodules guided by NIR fluorescence imaging[19]. Compared with open surgery, the treatment of lung cancer with VATS showed an urgent demand for fluorescence imaging guidance due to less manual palpation and more undiscovered additional nodules[20, 21]. However, research in this field has been restricted due to the lack of high-sensitivity fluorescence thoracoscopic systems. To satisfy this need, we developed a novel ultrasensitive fluorescence thoracoscopic system (SUPEREYE) that offers high-fluorescence collection efficiency and accurate registration. High sensitivity of imaging systems collects weak signals of small tumours. Furthermore, easy, robust and quick image registration can provide real-time white-light and fluorescence imaging guidance in lung cancer surgery.

The purpose of this study was to analyse our experience with 2 different NIR devices: the SUPEREYE system by Key Laboratory of Molecular Imaging, Chinese Academy of Science and the D-Light P system by Karl Storz Company, in pulmonary resection surgeries. We found that ICG-fluorescent imaging has the potential to detect small subclinical lung nodules. In this pilot study, we recruited 36 patients and reported the results of tumour imaging in NIR fluorescence image-guided lung cancer thoracoscopic surgery.

Eur J Cardiothorac Surg. 2017. 52(6): 1190-1196 Published online: 27 July 2017

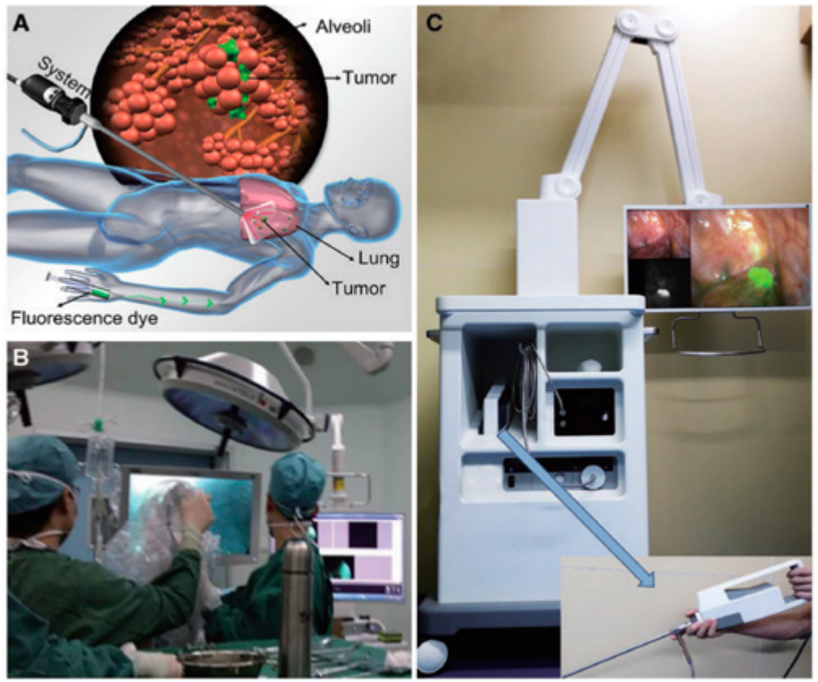


Fig.1 The design and clinical application of the SUPEREYE. (A) Schematic illustrations of our fluorescence thoracoscopic system used for lung cancer surgery. Patients were firstly injected with fluorescence dyes for labelling imaging region. NIR excited light and white light simultaneously illuminated the imaging region through the thoracoscope. Then our system provided the optical guidance about the spatial localization of tumours. (B) The SUPEREYE was applied in video-assisted thoracoscopic surgery lung cancer surgery. (C) The SUPEREYE.

Materials and Methods

Fluorescence thoracoscopic system

The SUPEREYE is a fluorescence thoracoscopic system developed for image-guided minimally invasive surgery. This system contains a colour imaging channel (400–650 nm) and a NIR fluorescence imaging channel (excitation: 785 ± 5 nm; emission: 840 ± 10 nm). Fluorescence imaging was designed especially for collecting the wavelength of ICG. We designed the system based on 3 aspects: (i) Image acquisition: a NIR light-optimum rigid clinical thoracoscope (HOPKINS II 26003BGA, Karl Storz, Tuttlingen, Germany) was used as system lens. The light collected from the lens is transmitted into a customized camera (Microview, Beijing, China). The camera contains 1 light splitter and 2 high-sensitivity and high-resolution camera chips for simultaneous colour and NIR fluorescence imaging. (ii) Illumination design: one 785-nm NIR excitation light source (MW-SGX-785, Changchun Lei Shi Optoelectronic Technology Co. Ltd, Changchun, Jilin, China) and one visible light source (XENON NOVA 300, Karl Storz) were coupled by a custom-made multimode bifurcated fibre bundle (Banglei Optoelectronic Technology Co. Ltd, Zhongshan, Guangdong, China) with small light coupling loss. (iii) Software development: the collected fluorescence and colour images can be accurately, quickly and robustly registered into merged images. The software simultaneously displays colour, fluorescence and merged images at a video rate. The spatial resolution of the system is 35 µm, and the sensitivity for ICG detection is 0.01 µm. We also used another commercial fluorescence thoracoscopic system to explore the feasibility of lung tumours detection: the D-Light P system (Karl Storz). This system sensitivity is 0.1 µm but currently it cannot simultaneously display colour and fluorescence images.

Patients

This study enrolled 36 patients (19 males and 17 females) who were scheduled for VATS pulmonary resection surgery in Peking University People's Hospital. The hospital's Institutional Review Board approved this study (2015PHB157-01), and all patients signed the informed consents. We also registered this clinical trial at ClinicalTrials.gov (NCT02611245). All patients had one or more pulmonary nodules diagnosed by chest high-resolution computed tomography (CT) with 0.1 cm slice thickness.

Patients who had ICG allergy were excluded.

Imaging procedure

Intraoperative lung cancer thoracoscopic surgery was guided by traditional white-light imaging and ICG-fluorescent imaging. Figure 1 illustrates the NIR fluorescence imaging-guided lung cancer surgery. Patients were administered ICG (Yichuang Pharmaceutical Limited Liability Company, Dandong, China) at a dose of 5 mg/kg according to patients' weight through a peripheral vein 24 h preoperatively[22]. The fluorescence thoracoscopic system was prepared and covered with a sterilized set. In the first step, surgeons located tumours according to a traditional standard operating procedure, which combined preoperative CT data and white-light thoracoscopy. In the next step, the detected lung nodules were subsequently investigated by the fluorescence thoracoscopic system. The colour, fluorescence and merged images of the nodules were simultaneously displayed and recorded at video rate. Meanwhile, we grossly examined the lung for extra subclinical tumour nodules detection in this procedure. All identified nodules were removed and marked for biopsies. The specimens were reviewed by 2 experienced pathologists (Kunkun Sun and Danhua Shen).

Analysis of fluorescence data

Fluorescence intensity of lung lesions was quantitatively analysed according to the recorded videos. The calculation method was as follows: we used an image processing software (ImageJ, National Institutes of Health, Bethesda, MD, USA) to delineate lung nodule as a region of interest (ROI), and then the software calculated the mean brightness value of ROI (B_{ROI}) within a range of 0–255. The background brightness ($B_{Background}$) was measured by calculating the mean brightness value of surrounding tissues. The signal-to-background ratio (SBR) was calculated by dividing the B_{ROI} by the $B_{Background}$. Each nodule was evaluated 3 times to reduce errors.

Statistical analysis

To compare the fluorescence intensity differences obtained while using the 2 fluorescence imaging systems (SUPEREYE and D-Light P), we performed Student's t-tests. The analysis was performed using Prism software version 4.0 (San Diego, CA, USA). Two-sample, one-way Student's t-tests were used to determine significant differences in the hypothesis that the SBR of SUPEREYE was higher than the SBR of D-Light P. If the P-value was <0.05, the SBR differences were considered to be valid.

Results

Characteristics of lung nodules

From August 2015 to October 2016, we enrolled 36 patients (age 56 ± 14 years) in this study. In total, 76 nodules (size 1.4 ± 1.2 cm) were detected by combining traditional methods with ICG-fluorescent imaging. From the 36 patients, 11 patients were diagnosed with metastasis from other cancers and 25 patients with non-small-cell lung cancer (NSCLC) (Table 1). We performed wedge resection in 14 patients, segmentectomy in 7 patients, lobectomy in 14 patients and pneumonectomy in 1 patient.

The ICG-fluorescent imaging method successfully identified 68 of the 76 nodules in vivo. The other 8 nodules that were located 1.3 cm or more beneath the pleural surface could not be detected. After excision and direct exposure of these nodules, all 76 nodules were fluorescent. Histology of these nodules showed that 71 pulmonary nodules were malignant and 5 nodules were false positive (hyperplasia and inflammation). The characteristics of the nodules are listed in Table 1. The mean SBR of the nodules was 3.29 ± 1.81 (range: 1.43–11.9). The 2 NIR devices could high-sensitivity detect lung nodules in pulmonary resection surgery (Fig. 2). We found that ICG-fluorescent imaging had a great imaging effect for squamous cell carcinoma (SBR: 4.08 ± 0.88) and pulmonary metastasis of hepatocellular carcinoma (HCC) (SBR: 6.09 ± 2.4). The mean SBR of adenocarcinoma nodules was 2.91. However, in some adenocarcinoma nodules, the SBR was as low as 1.43 and the contrast between the nodules and the surrounding tissues was less obvious.

The sensitivities and positive predictive values of ICG-fluorescent imaging for lung tumours were thus 88.7% (63 fluorescing lesions of the 71 malignant nodules) and 92.6% (63 cancers of the 68 fluorescing lesions), respectively.

Table 1 Individual data for patients (n = 36)

Characteristics	Value
Age (year)	56 ± 14
Gender (patients)	Men = 19; Woman = 17
Tumour size (cm)	1.4 ± 1.2
SBR [range]	
Tumour size >1 cm	3.46 (1.43–11.90)
Tumour size ≤1 cm	3.14 (1.47–7.67)
Tumour location (nodules)	
RUL	16
RML	12
RLL	28
LUL	11
LLL	9
Pathology (nodules)	SBR [range]
Adenocarcinoma (30)	2.91 (1.43–7.13)
SCC (4)	4.08 (2.75–5.12)
Breast (2)	3.29 (3.21–3.38)
HCC (11)	6.09 (3.97–11.9)
Colorectal cancer (11)	3.03 (1.87–5.16)
Osteosarcoma (10)	2.13 (1.90–2.52)
AAH (2)	2.66 (2.47–2.85)
Hyperplasia (5)	1.98 (1.53–3.6)
Inflammation (1)	3.57
System (nodules)	SBR [range]
SUPEREYE (19)	3.83 (2.25–7.13)
D-Light P (57)	3.11 (1.43–11.9)

SBR: signal-to-background ratio; RUL: right upper lobe; RML: right middle lobe; RLL: right lower lobe; LUL: left upper lobe; LLL: left lower lobe; SCC: squamous cell carcinoma; HCC: hepatocellular carcinoma; AIS: adenocarcinoma in situ; AAH: atypical adenomatous hyperplasia.

Eur J Cardiothorac Surg. 2017. 52(6): 1190-1196 Published online: 27 July 2017

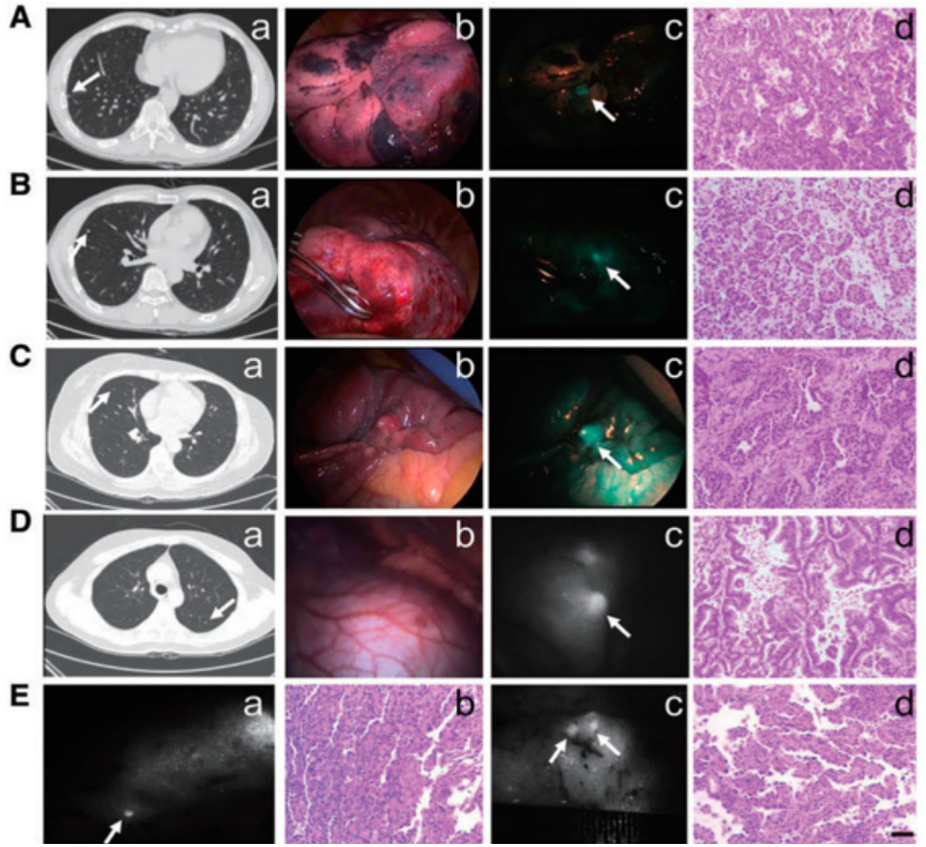


Fig.2 In vivo sub-centimetre pulmonary tumours imaging with near-infrared fluorescence thoracoscopic systems. (a–d) of (A–D): Computed tomography, colour, fluorescence and haematoxylin and eosin staining images of pulmonary tumours (white arrow). (A) Adenocarcinoma, tumour size: 0.5 cm; (B) pulmonary metastases of hepatocellular carcinoma, tumour size: 0.5 cm; (C) pulmonary metastases of breast cancer, tumour size: 1 cm; (D) pulmonary metastases of colorectal cancer, tumour size: 1 cm. (E) Additional pulmonary nodules only detected by indocyanine green-fluorescent imaging; (a) and (c) are representative fluorescence images of additional nodules (white arrow) (tumour size: 0.1 cm, 0.2 cm, 0.2 cm); (b) and (d) are the corresponding haematoxylin and eosin staining images showing that (a) is atypical adenomatous hyperplasia and (c) is adenocarcinoma in situ. Scale bar: 50 mm.

Indocyanine green-fluorescent imaging can identify sub-centimetre lung nodules

Although preoperative imaging provided information on the location of small nodules, it remains a challenge to localize sub-centimetre pulmonary nodules by VATS. To examine our experience of using ICG-fluorescent imaging to detect micro nodules, 2 NIR devices were used during surgery. For lung nodules with a size ≤1 cm, the fluorescence signals were clearly demarcated from the surrounding normal tissues with a mean SBR of 3.14 ± 1.59. ICG-fluorescent images collected either by our self-developed system (SBR: 3.83 ± 1.24) or by a commercial fluorescence thoracoscopic system (SBR: 3.11 ± 1.94) showed a significant tumour-to-surrounding tissue contrast compared with the traditional white-light imaging (Fig. 3).

Indocyanine green-fluorescent imaging can identify additional pulmonary nodules

Among the 76 nodules, 9 additional small lung nodules were detected only by the ICG-fluorescent imaging method in 7 of the 36 patients (19.4%). For the 9 nodules, 6 nodules were detected in different lobes than the primary tumours. The characteristics of these nodules are shown in Table 2. These 9 lesions comprised

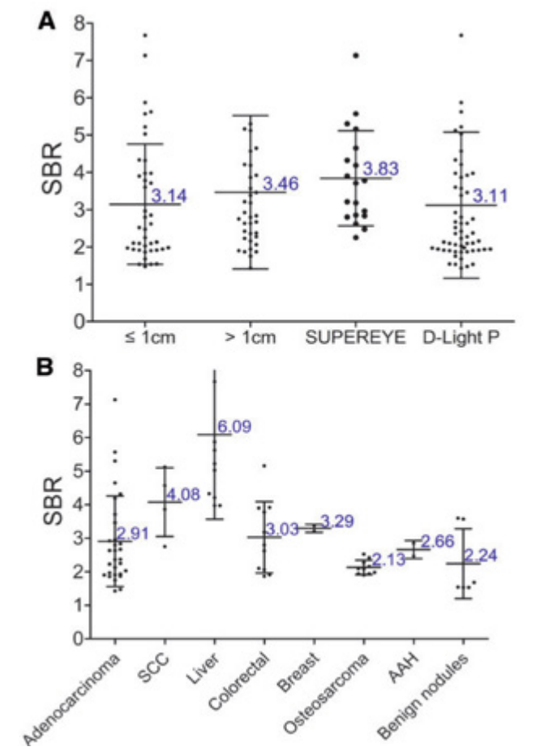
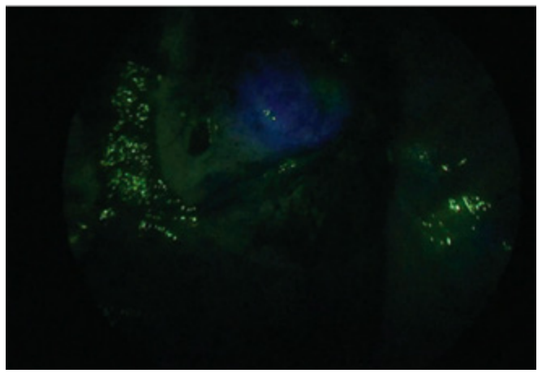


Fig.3 Fluorescence data of pulmonary nodules. (A) The SBR of tumour size ≤1 cm and >1 cm, and SBR of fluorescence images collected by our system (SUPEREYE) and by the commercial system (D-Light P). (B) SBR of different pulmonary nodules types. SBR: signal-to-background ratio.



Video 1 The video of pulmonary nodules with 2 NIR devices. The video displays real-time intraoperative fluorescence imaging of pulmonary adenocarcinoma, squamous cell carcinoma, metastasis of osteosarcoma, metastasis of colorectal cancer, metastasis of hepatocellular carcinoma, metastasis of breast cancer, and additional detected nodules.

2 adenocarcinoma in situ, 2 atypical adenomatous hyperplasia, and 5 false-positive nodules (hyperplasia and inflammation). The representative frames of additional small nodules and the corresponding histopathological results are shown in Fig. 2E (white arrow). They were missed by traditional white-light thoracoscopic exploration and CT images. In contrast, ICG-fluorescent imaging showed the 3 additional synchronous nodules with high SBR (2.85±0.11, 2.47±0.14 and 2.25±0.18). The tumour size were ≤0.2 cm. Histology results of these nodules were atypical adenomatous hyperplasia and adenocarcinoma in situ (Fig. 2E).

Discussion

In the treatment of malignant lung nodules, the efficacy of surgical resection remains limited by the lack of real-time high-sensitivity intraoperative imaging methods. Furthermore, incomplete resection results in postoperative recurrence of the malignancy. Therefore, the development of new high-sensitivity imaging methods, such as ICG-fluorescent imaging, shows great potential to detect additional subclinical nodules.

ICG is not a tumour-specific fluorescence dye, such as ligand-specific binding to tumour cell receptor, it accumulates in certain types of tumours because of the EPR effect[23–25]. The EPR effect is a passively accumulating effect due to the permeability effect of the nascent porous tumour blood vessels and the retention effect of dysfunctional tumour lymphatic system, which allows ICG to accumulate in tumour tissues. To obtain an optimal tumour-to-lung contrast, we have performed several pre-experiments of injection dose and time of ICG. The results demonstrated that the optimum dose was 5 mg/kg and that the best injection time was 24 h preoperatively. In combination with ICG, fluorescence imaging provided high-contrast tumour images and increased additional tumour detection rate. Okusanya et al. first demonstrated ICG could be applied for lung nodules imaging and verified ICG-fluorescent imaging guided open surgery could detect additional pulmonary nodules. However, in the treatment of lung cancer by VATS, only a few research studies have explored the application of ICG-fluorescent imaging[26], but the sensitivity and specificity of ICG-fluorescent image-guided lung cancer thoracoscopic surgery have not been studied.

More early stage lung cancer patients chose VATS as a superior alternative to open surgery due to minimal trauma, less bleeding and faster recovery, while the fluorescence thoracoscopic system applied in VATS was faced with a big challenge[27]. The poor NIR-light transmission and small apertures of the traditional white-light thoracoscope resulted in a massive light loss and low tumour-to-tissue contrast. Thus, many researchers have devoted themselves to developing high-sensitivity NIR fluorescence thoracoscopic systems. Venugopal et al. simultaneously optimized NIR fluorescence and colour imaging using a custom endoscope and a 2-charge-coupled device (CCD) camera[28]. Glatz et al. used a more sensitive electron-multiplying charge-coupled device camera to improve the NIR wavelength collection efficiencies[29]. In our case, we designed a fluorescence thoracoscopic system specially for ICG imaging. Its sensitivity for ICG imaging is about 10 times higher than that of the published fluorescence thoracoscopic system[28]. And we also used a commercial fluorescence imaging system (D-Light P) in this study.

The goal of our study was to validate our experience of using 2 different NIR devices, enabling high-sensitivity identification of

sub-centimetre pulmonary nodules in VATS lung cancer surgery. For sub-centimetre lung nodules, the commercial D-Light P system showed a significant tumour-to-surrounding tissue contrast (SBR: 2.91±1.62) compared with traditional white-light imaging. We found that ICG-fluorescent imaging had a higher SBR in squamous cell carcinoma and pulmonary metastasis of HCC than other lung tumours. The possible reason is that squamous cell carcinoma is an epithelial tumour that has both an exceptionally high endocytic rate and deficient tight junctions that lead to more ICG accumulating in cells. Furthermore, the HCC tumour cells expressed the membrane transporters' organic anion transporting polypeptide 1B3 and sodium–taurocholate co-transporting polypeptide, which mediates the cellular uptake of ICG[30]. A more detailed study would need to be performed to validate the relation between SBR and histopathology. Furthermore, our self-developed SUPEREYE system has a higher SBR of 3.69±1.37 than D-Light P ($P<0.05$). For the detected 76 nodules, the sensitivities and positive predictive values of the ICG-fluorescent imaging were 88.7% and 92.6%. Eight pulmonary nodules embedded deeply in the lung were undetected by ICG-fluorescent imaging, and the maximized detection depth of ICG-fluorescent method was 1.3 cm. Future studies on fluorescence thoracoscopic systems should focus on developing deep tissue imaging with new imaging technologies, such as a second NIR imaging method (wavelength: 1100–1400 nm).

Furthermore, we detected 4 additional positive nodules that were not revealed during standard surgical exploration. If these extra subclinical nodules were not resected, recurrence or metastasis of lung tumours might result in poor prognosis. Meanwhile, the extra resections were safe without obvious/prolong air leak. However, we also detected 5 additional false-positive nodules with the ICG-fluorescent imaging method. The histopathology results of these false-positive nodules were hyperplasia or inflammation. ICG as a non-specific fluorescence dye was diffused into tissues with hyperpermeable vascular structures by EPR effect, such as hyperplasia or inflammation. To reduce the false-positive results, surgeons could use alternative indications (inspection and palpation of nodules) to judge whether the fluorescence area should be removed or not. Targeted NIR probes that specifically bind lung tumour tissues have the potential to decrease false-positive nodules. Therefore, further studies will need to develop novel NIR targeting agents for increasing positive predictive values.

Currently, it is difficult to distinguish small multiple nodules from surrounding tissues via intraoperative white-light thoracoscopy, however, the ICG-fluorescent imaging method is good for sub-centimetre tumour detection. Therefore, by combining ICG-fluorescent imaging with preoperative CT data, the surgical exploration in pulmonary resections reveals the nodules located deeply in the lung and easily identifies sub-centimetre nodules. As a result, exploration time might be saved and the tumour detection rate might be improved. The next obvious step for us is to design a random, double-blind and multiple study to compare ICG-fluorescent imaging combining CT method with the traditional white-light imaging combining CT method for the detection of pulmonary nodules.

Table 2 Characteristics of the nodules identified only by ICG-fluorescent imaging

Patient no.	Cancer location	SBR	Histopathology	Tumour size (cm)
3	LUL	2.25±0.18	AIS	0.1
6	RLL	2.85±0.11	AAH	0.2
6	RLL	2.47±0.14	AAH	0.2
13	RUL	1.68±0.03	Hyperplasia	0.3
13	RLL	1.53±0.05	Hyperplasia	0.2
18	RLL	1.96±0.08	AIS	0.1
25	LLL	3.57±0.13	Inflammation	1.5
32	RLL	3.60±0.03	Hyperplasia	0.3
34	RUL	1.53±0.09	Hyperplasia	0.5

AIS: adenocarcinoma in situ; AAH: atypical adenomatous hyperplasia; ICG: indocyanine green.

Conclusion

In conclusion, we believe we have validated that ICG-fluorescent imaging with 2 NIR devices enables high-sensitivity visualization of sub-centimetre pulmonary nodules. In addition, we showed that ICG-fluorescent imaging also has the potential to detect additional positive lesions. The identification of these nodules might reduce tumour recurrence, which has a remarkable clinical potential for application in lung cancer.

Acknowledgements

We thank Lixue Zhang for his help with the clinical experiments, Kunkun Sun and Danhua Shen for the pathological analysis and Yu An and Shixin Jiang for the helpful discussions.

Funding

This work was supported by the National Natural Science Foundation of China [81227901, 81527805, 81501594, 61231004, 61501462, 61671449], the National Key Research Program [2017YFA0205200], the National Key Project of the Ministry of Science and Technology of China [2106YFC0103702], the Scientific Research and Equipment Development Project of Chinese Academy of Sciences [YZ201457] and the Key Research Program of the Chinese Academy of Sciences [KGZD-EW-T03].

Conflict of interest

None declared.

References

1. Chen W, Zheng R, Baade PD, Zhang S, Zeng H, Bray F et al. Cancer statistics in China, 2015. CA Cancer J Clin 2016;66:115.
2. Aliperti LA, Predina JD, Vachani A, Singhal S. Local and systemic recurrence is the Achilles heel of cancer surgery. Ann Surg Oncol 2010;18:603–7.
3. van Rens MT, Schramel FM, Elbers JR, Lammers JW. The clinical value of lung imaging fluorescence endoscopy for detecting synchronous lung cancer. Lung Cancer 2001;32:13–8.
4. Glatz J, Garcia-Allende PB, Becker V, Koch M, Meining A, Ntziachristos V. Near-infrared fluorescence cholangiopancreatoscopy: initial clinical feasibility results. Gastrointest Endosc 2014;79:664–8.
5. Keating JJ, Kennedy GT, Singhal S. Identification of a subcentimeter pulmonary adenocarcinoma using intraoperative near-infrared imaging during video-assisted thoracoscopic surgery. J Thorac Cardiovasc Surg 2015;149:e51–3.
6. Liu B, Feng Y, Zhang J, Li H, Li X, Jia H et al. Imaging of bronchioloalveolar carcinoma in the mice with the αvβ3integrin-targeted tracer 99m Tc-RGD-4CK. Transl Res 2013;162:174–80.

7. Chi C, Du Y, Ye J, Kou D, Qiu J, Wang J et al. intraoperative imaging-guided cancer surgery: from current fluorescence molecular imaging methods to future multi-modality imaging technology. Theranostics 2014;4:1072–84.
8. Vahrmeijer AL, Hutteman M, van der Vorst JR, van de Velde CJ, Frangioni JV. Image-guided cancer surgery using near-infrared fluorescence. Nat Rev Clin Oncol 2013;10:507–18.
9. Keereweer S, Van Driel PB, Snoeks TJ, Kerrebijn JD, Baatenburg de Jong RJ, Vahrmeijer AL et al. Optical image-guided cancer surgery: challenges and limitations. Clin Cancer Res 2013;19:3745–54.
10. Schaafsma BE, Mieog JS, Hutteman M, van der Vorst JR, Kuppen PJ, Lowik CW et al. The clinical use of indocyanine green as a near-infrared fluorescent contrast agent for image-guided oncologic surgery. J Surg Oncol 2011; 104:323–32.
11. Wang K, Chi C, Hu Z, Liu M, Hui H, Shang W et al. Optical molecular imaging frontiers in oncology: the pursuit of accuracy and sensitivity. Engineering 2015;1:309–23.
12. Zeng C, Shang W, Wang K, Chi C, Jia X, Cheng F et al. Intraoperative identification of liver cancer microfoci using a targeted near-infrared fluorescent probe for imaging-guided surgery. Sci Rep 2016;6:21959.
13. Fang C, Wang K, Zeng C, Chi C, Shang W, Ye J et al. Illuminating necrosis: from mechanistic exploration to preclinical application using fluorescence molecular imaging with indocyanine green. Sci Rep 2016;6:21013.
14. Gabon Q, Sayag D, Texier I, Navarro F, Boisgard R, Virieux-Watrelot D et al. Evaluation of intraoperative fluorescence imaging-guided surgery in cancer-bearing dogs: a prospective proof-of-concept phase II study in 9 cases. Transl Res 2016;170:73–88.
15. He K, Chi C, Kou D, Huang W, Wu J, Wang Y et al. Comparison between the indocyanine green fluorescence and blue dye methods for sentinel lymph node biopsy using novel fluorescence image-guided resection equipment in different types of hospitals. Transl Res 2016;178:74–80.
16. Kim HK, Quan YH, Choi BH, Park JH, Han KN, Choi Y et al. Intraoperative pulmonary neoplasm identification using near-infrared fluorescence imaging. Eur J Cardiothorac Surg 2016;49:1497–502.
17. van Dam GM, Themelis G, Crane LMA, Harlaar NJ, Pleijhuis RG, Kelder W et al. Intraoperative tumor-specific fluorescence imaging in ovarian cancer by folate receptor-alpha targeting: first in-human results. Nat Med 2011;17:1315–9.
18. Liberale G, Vankerckhove S, Caldon MG, Ahmed B, Moreau M, Nakadi IE et al. Fluorescence imaging after indocyanine green injection for detection of peritoneal metastases in patients undergoing cytoreductive surgery for peritoneal carcinomatosis from colorectal cancer: a pilot study. Ann Surg 2016; 264:1110–5.
19. Okusanya OT, DeJesus EM, Jiang JX, Judy RP, Venegas OG, Deshpande CG et al. Intraoperative molecular imaging can identify lung adenocarcinomas during pulmonary resection. J Thorac Cardiovasc Surg 2015;150:28–35 e1.
20. Liu Z, Miller SJ, Joshi BP, Wang TD. In vivo targeting of colonic dysplasia on fluorescence endoscopy with near-infrared octapeptide. Gut 2013;62:395–403.
21. Lerner SP, Goh A. Novel endoscopic diagnosis for bladder cancer. Cancer 2015;121:169–78.
22. Okusanya OT, Holt D, Heitjan D, Deshpande C, Venegas O, Jiang J et al. Intraoperative near-infrared imaging can identify pulmonary nodules. Ann Thorac Surg 2014;98:1223–30.
23. Ishizawa T, Masuda K, Urano Y, Kawaguchi Y, Satou S, Kaneko J et al. Mechanistic background and clinical applications of indocyanine green fluorescence imaging of hepatocellular carcinoma. Ann Surg Oncol 2014;21:440–8.
24. Satou S, Ishizawa T, Masuda K, Kaneko J, Aoki T, Sakamoto Y et al. Indocyanine green fluorescent imaging for detecting extrahepatic metastasis of hepatocellular carcinoma. J Gastroenterol 2013;48:1136–43.
25. Tummers QR, Hoogstins CE, Peters AA, de Kroon CD, Trimbos JB, Cj VDV et al. The value of intraoperative near-infrared fluorescence imaging based on enhanced permeability and retention of indocyanine green: feasibility and false-positives in ovarian cancer. PLoS One 2014;10:3435–40.
26. Keating J, Newton A, Venegas O, Nims S, Zeh R, Predina J et al. Near-infrared intraoperative molecular imaging can locate metastases to the lung. Ann Thorac Surg 2016;103:390–8.
27. Yang CFJ, Meyerhoff RR, Mayne NR, Singhapricha T, Toomey CB, Speicher PJ et al. Long-term survival following open versus thoracoscopic lobectomy after preoperative chemotherapy for non-small cell lung cancer. Eur J Cardiothorac Surg 2016;49:1615–23.
28. Venugopal V, Park M, Ashitate Y, Neacsu F, Kettenring F, Frangioni JV et al. Design and characterization of an optimized simultaneous color and near-infrared fluorescence rigid endoscopic imaging system. J Biomed Opt 2013;18:126018.
29. Glatz J, Varga J, Garcia-Allende PB, Koch M, Greten FR, Ntziachristos V. Concurrent video-rate color and near-infrared fluorescence laparoscopy. J Biomed Opt 2013;18:101302.
30. Onda N, Kimura M, Yoshida T, Shibutani M. Preferential tumor cellular uptake and retention of indocyanine green for in vivo tumor imaging. Int J Cancer 2016;139:673.

Breast Surgery

Research Article

Comparison Between the Indocyanine Green Fluorescence and Blue Dye Methods for Sentinel Lymph Node Biopsy Using Novel Fluorescence Image-Guided Resection Equipment in Different Types of Hospitals

Kunshan He[1,*], Chongwei Chi[1,5,*], Deqiang Kou[2,*], Wenhe Huang[3], Jundong Wu[3], Yabing Wang[4], Lifang He[3], Jinzuo Ye[1], Yamin Mao[1], Guojun Zhang[3] ✉, Jiandong Wang[2] ✉ and Jie Tian[1,5] ✉

Abstract

Sentinel lymph node biopsy (SLNB) has become a standard of care to detect axillary lymph metastasis in early-stage breast cancer patients with clinically negative axillary lymph nodes (ALNs). Current SLNB detection modalities comprising a blue dye, a radioactive tracer, or a combination of both have advantages as well as disadvantages. Thus, near-infrared (NIR) fluorescence imaging using indocyanine green (ICG) has recently been regarded as a novel method that has generated interest for SLNB around the world. However, the lack of appropriate fluorescence imaging systems has hindered further research and wide application of this method. Therefore, we developed novel fluorescence image-guided resection equipment (FIRE) to detect sentinel lymph nodes (SLNs). Moreover, to compare the ICG fluorescence imaging method with the blue dye method and to explore the universal feasibility of the former, a different type of hospital study was conducted. Ninety-nine eligible patients participated in the

study at three different types of hospitals. After subcutaneous ICG allergy testing, all the patients were subcutaneously injected with methylene blue (MB) and ICG into the subareolar area. Consequently, 276 SLNs (range 1–7) were identified in 98 subjects (detection rate: 99%) by using the ICG fluorescence imaging method. In contrast, the blue dye method only identified 202 SLNs (range 1–7) in 91 subjects (detection rate: 91.92%). Besides, the results of the fluorescence imaging method were similar in the three hospitals. Our findings indicate the universal feasibility of the ICG fluorescence imaging method for SLNB using the FIRE in early breast cancer detection.

Key Words

Near-infrared fluorescence; Fluorescence image-guided resection equipment; Breast cancer; Sentinel lymph node biopsy; Indocyanine green; Methylene blue

[1] Key Laboratory of Molecular Imaging of Chinese Academy of Sciences, Institute of Automation, Chinese Academy of Sciences, Beijing, 100190, China;

[2] Department of General Surgery, General Hospital of People's Liberation Army, Beijing 100853, China;

[3] The Breast Center, Cancer Hospital, Shantou University Medical College, Shantou, 515000, China;

[4] Department of Thyroid and Breast Surgery, Yijishan Hospital, Wannna Medical College, Wuhu, 241001, China.

[5] Key Laboratory of Molecular Imaging of Beijing, Beijing, 100190, China;

* These authors contributed equally to this work and should be considered as co-first authors.

Introduction

Traditionally, axillary lymph node dissection (ALND) has been frequently used to stage the axilla and to guide relevant treatment options during early breast cancer surgery (BCS). However, ALND may cause many side effects such as axillary subcutaneous effusion, upper limb lymphedema, and limitation of upper limb mobility and function and can thus seriously affect the quality of life of the patients[1-3]. In 2005 in the American Society of Clinical Oncology (ASCO) meeting, surgeons were recommended to use sentinel lymph node biopsy (SLNB) for most clinical axillary lymph node (ALN) negative breast cancer patients with axillary staging in order to alleviate the patients' pain and to improve treatment outcomes. In 2010, the National Comprehensive Cancer Network (NCCN) guidelines suggested that breast cancer patients clinically negative for ALN I, II should receive SLNB rather than ALND. Thus, SLNB now plays an important role in early breast cancer surgery[4-6].

Currently, SLNB can be performed using a blue dye, a radionuclide tracer, or a combination of both[7-9]. The combination method is generally regarded as the best practice for SLNB[10]. However, each of these methods has some shortcomings. For example, the detection rate using the blue dye is relatively low at about 65%–93%[11]. Moreover, the subcutaneous injection of blue dyes may cause tissue necrosis in patients receiving breast-conserving therapy and may thus affect the cosmetic results[12]. An important limitation of the radionuclide tracer method is that it is not extensively accessible due to the lack of nuclear medicine in many hospitals. These limitations have increased international research on near-infrared (NIR) fluorescence imaging methods for cancer therapy[13-16]. Many intraoperative fluorescence imaging navigation systems[17-20] have been developed. However, only a few have an adjustable field of view and can simultaneously display color, fluorescence, and merged images of tissues. To meet these challenges and to provide better surgical conditions, we developed novel fluorescence image-guided resection equipment (FIRE) for SLNB.

Indocyanine green (ICG) was used as the NIR florescent contrast agent, because ICG is the only NIR florescent agent authorized by both American and Chinese Food and Drug Administrations (FDAs) for clinical usage. Generally, ICG is used as a fluorescent indicator for ophthalmic angiography, cardiac output identification, and determination of liver blood flow[21-23]. The use of ICG in the NIR fluorescence imaging method for SLNB has the following advantages: high signal-to-background ratio (SBR), non-physical contact with patients, transcutaneous lymphatic vessel visualization, and real-time intraoperative imaging. Therefore, the NIR fluorescence imaging method is suitable for intraoperative SLNB.

To verify the universal feasibility of our ICG fluorescence imaging method for SLNB in early-stage breast cancer patients, a comparative trial between the NIR fluorescence imaging method and the blue dye method using methylene blue (MB) was conducted in three different types of hospitals. Further, we adopted the same standard operating procedure in the three hospitals: Chinese PLA General Hospital Breast Disease Center (general), Yijishan Hospital of Wannan Medical College (district), and Cancer Hospital of Shantou University Medical College (specialized).

Abbreviations: ALN = axillary lymph node; ALND = axillary lymph node dissection; ASCO = American Society of Clinical Oncology; BCS = breast cancer surgery; BMI = Body Mass Index; FDA = Food and Drug Administration; FIRE = fluorescence image-guided resection equipment; HE = Hematoxylin-Eosin; ICG = indocyanine green; IRB = Institutional Review Board; LED = light-emitting diode; MB = methylene blue; NCCN = National Comprehensive Cancer Network; NIR = near-infrared; SBR = signal-to-background ratio; SLN = sentinel lymph node; SLNB = sentinel lymph node biopsy.

Transl Res. 2016. 178: 74-80 Published online: 11 July 2016

Materials and Methods

Fluorescence imaging system

The FIRE was developed by the Key Laboratory of Molecular Imaging of Chinese Academy of Sciences based on our previous studies[24-26]. The general design and intraoperative application of the system, which comprised four sections—the light source section, detector section, controller section, and display section—are illustrated in Figure 1. The light source section was mainly composed of a visible light source (KL2500LCD, SCHOTT, Germany) and a NIR light source (center wavelength 760 nm, maximum power 200 mW).

The NIR light source consisting of 67 light-emitting diode (LED) bulbs was used to excite ICG and the visible light source illuminated the surgical field. The detector section mainly contained a color camera (Pilot piA1400-17gc, Basler, Germany), NIR camera (ProEM 1024B eXcelon3, Princeton Instrument, USA), beam splitter (25 mm NIR, 47012, Edmund Optics, USA), and an F mount lens (Nikon Nikkor 24-120 mm, f/4G ED VR). The beam splitter installed on the front end of the lens wad used to split the light into two beams (for color and fluorescence). The NIR fluorescence and visible light images were then captured separately by the two cameras. The controller section mainly included an application program, which was written by us for image acquisition, registration, fusion, enhancement, and reconstruction. Finally, the display section was composed of two high-definition monitors. Real-time intraoperative fluorescence, color, and merged images were displayed on the screen at a rate of 20 frames per second. The field of view of this system ranged from 25 cm × 25 cm to 60 cm × 60 cm at a work distance of 60 cm. The resolution was about 10 lp/mm and the sensitivity was approximately 0.03125 mg/ml ex vivo. Data storage could be completed automatically.

Patients

Ninety-nine eligible female patients (age 31–72 years, median age 52 years), who were diagnosed for T1–3 primary breast cancer with clinically negative lymph node, participated in this multicenter study between January 2014 and September 2015. The characteristics of the study subjects are summarized in Table 1. The average age of the patients was 51 years and the average



Fig.1 General design and intraoperative application of the FIRE. (A) The structure of the FIRE. (B) The FIRE was used during surgery at the Chinese PLA General Hospital Breast Center.

Table 1 Characteristics of the study subjects (n = 99)

Characteristics	Value	Percentage
Age		
30–40	14	14.14
41–50	35	35.35
51–60	28	28.28
61–70	21	21.21
71–80	1	1.01
BMI		
⩾18.5,<22	27	27.27
⩾22,<25	35	35.35
⩾25,<30	30	30.30
⩾30	7	7.07
Menstruation		
Ordinary	62	62.63
Disorderly	37	37.37
History of Allergy		
Yes	5	5.05
No	94	94.95
Family Medical History		0.00
Yes	4	4.04
No	95	95.96
Tumor Size		
Tis	3	3.03
T1	38	38.38
T2	47	47.47
T3	3	3.03
Tx	8	8.08
Type of Surgery		
MRM+SLNB	75	75.76
BCS+ALND+SLNB	2	2.02
BCS+SLNB	15	15.15
MRM+ALND+SLNB	7	7.07

Abbreviations: BMI, body mass index; ALN, axillary lymph node; ALND, axillary lymph node dissection; SLNB, sentinel lymph node biopsy; MRM, modified radical mastectomy; BCS, breast conserving surgery.

Body Mass Index (BMI) was 24.2 kg/m^2 (range 18.7–38.8). The inclusion criteria were female sex, preoperative diagnosis of clinical breast cancer, tumor diameter ≤ 3 cm, negativity for axillary lymph node, and absence of distant metastasis. The exclusion criteria included previous neoadjuvant chemotherapy or radiotherapy of the mammary area, previous surgery of the axillary area, ALN metastasis, inflammatory breast cancer, and pregnancy. This study was approved by the Institutional Review Board (IRB) of the three hospitals. Every patient provided written informed consent before the surgery. SLNB was performed by experienced surgeons in accordance with the same standard operating procedure. This experiment strictly followed the Helsinki Declaration and Chinese relative clinical trial norms, laws, and regulations. The Clinical Trails number was NCT02084784.

Administration of contrast agents

MB was purchased from Jichuan Pharmaceutical LLC, Jiangsu, China. ICG (25-mg vials) was bought from Yichuang Pharmaceutical LLC, Dandong, China. After anesthesia administration, 1 ml of 1% MB was subcutaneously injected in the 6, 9, and 12 o'clock directions of the breast near the areola. Immediately after 1–5 minutes of massage and sterilization of the injection sites, 1 ml of 0.5% ICG was subcutaneously injected in the same directions. The area was then again massaged and sterilized.

Imaging Procedure

After routine injection of MB and ICG, the FIRE was used to perform fluorescence imaging at ~60 cm distance from the surgical field. Particularly, the operating astral lamp was turned down and the visible light source of the FIRE was used to illuminate the surgical field. Before incision, percutaneous lymphatic drainage and potential SLNs were observed. Real-time color and fluorescence tissue images were simultaneously displayed on the upper screen. Meanwhile, the two kinds of images were merged into pseudo-colored (green) images displayed on the lower screen. After careful observation, the points of disappearance of the lymphatic pools and lymphatic vessels were marked. Notably, the special design of the FIRE enabled the surgeons to regulate the imaging angle and imaging field of view as required. Based on the SBR calculated using the ImageJ software, the fluorescence of a lymph node was determined. In this study, the SBR threshold value was defined at 1.2. After the standard MB guided SLNB procedure was completed, ICG stained SLNs and palpated SLNs were also carefully removed in the incised region. The excised SLNs were then separately examined and classified into the following categories: simultaneously identified by ICG and MB (ICG+/MB+), only identified by ICG (ICG+/MB-), only identified by MB (ICG-/MB+), and merely identified by palpation (ICG-/MB-).

Histopathologic analysis

All the intraoperative dissected specimens were examined by pathologists following the standard pathological procedure with Hematoxylin-Eosin (HE) staining.

Statistical analysis

SPSS (Statistical Product and Service Solutions) was employed for the data analysis. First, the SBR of the lymph nodes identified using ICG was calculated using ImageJ. The number of SLNs identified using MB and those identified using ICG were compared. Second, the detection rate of ICG, which was defined by the percentage of patients carrying SLNs identified by this method, and that of MB were separately calculated and compared. To prove the validity of the differences, Student's t-tests were conducted. A P-value <0.05 was considered to indicate statistical significance.

Results

Because the operation of the FIRE was easy and the equipment was robust and reliable, ICG fluorescence imaging was successfully completed and did not interfere with routine surgical procedures. The surgeons mastered the operation process with a short learning curve (about 10 cases). In addition, the display effect of the FIRE was fluent, and the equipment provided high-resolution and high-fidelity images. The process of ICG fluorescence image-guided SLNB using FIRE is illustrated in Figure 2. Before incision, percutaneous fluorescence identification of the lymphatic drainage and potential nodes was performed, and the SBR was high enough to guide the surgeons to locate the SLNs (Figure 2, A-C). Using the FIRE, minimal incision and precise resection were realized during the operation (Figure 2, D-F). The images of the excised SLN further confirmed the accuracy of this method (Figure 2, G-I).

A total of 194 SLNs were identified using ICG+/MB+ in 90 of the 99 patients. By calculation, 276 SLNs were identified in 98 of the subjects (detection rate 99%) using the ICG fluorescence imaging method. In contrast, only 202 SLNs were identified in 91 of the subjects (detection rate 91.92%) using the blue dye method, indicating that the number of SLNs detected by the former was more than that of the latter and the detection rate of the former was higher (P = 0.0094). Moreover, five palpated SLNs (ICG-/MB-) were all pathologically confirmed as lymph nodes, but the histopathology indicated that they were all tumor negative. Therefore, we believe that they were probably never SLNs in the first place. Of note, 35 patients were diagnosed with tumor-positive SLNs, all of which were identified using ICG (false negative rate: 0%), while only 32 were detected using MB (false negative rate: 8.57%).

In addition, the SLNs identified using ICG or MB were separately classified according to the age of the patients, BMI of the patients, and type of hospital (Table 3). A preliminary analysis showed that the efficiency of SLN detection was independent

Table 2 SLN detection using ICG and/or MB

Characteristics	Patients (n = 99)	Percentage	SLNs (n = 289)	Percentage
ICG+/MB+	90	90.91	194	67.13
ICG+/MB-	8	8.08	82	28.37
ICG-/MB+	1	1.01	8	2.77
ICG-/MB-	0	0	5	1.73

Abbreviations: SLN, sentinel lymph node; ICG, indocyanine green; MB, methylene blue.

Table 3 Classification of the identified SLNs by ICG or MB

Characteristics	Patients (ICG)	Percentage	Patients (MB)	Percentage
Age				
⩽40	14	100 (14/14)	13	92.86(13/14)
⩾41, ⩽50	35	100(35/35)	34	97.14(34/35)
⩾51, ⩽60	28	100(28/28)	25	89.29(25/28)
⩾61	21	95.45(21/22)	19	86.36(19/22)
BMI				
⩾18.5, <22	27	100(27/27)	25	92.59(25/27)
⩾22, <25	35	100(35/35)	33	94.29(33/35)
⩾25, <30	29	96.67 (29/30)	27	90.00(27/30)
⩾30	7	100(7/7)	6	85.71(6/7)
HOSPITAL				
General	38	97.44(38/39)	37	94.87(37/39)
District	30	100(30/30)	25	83.33(25/30)
Specialized	30	100(30/30)	29	96.67(29/30)

Abbreviations: SLN, sentinel lymph node; BMI, body mass index.

Transl Res. 2016. 178: 74-80 Published online: 11 July 2016

of these factors, indicating that the NIR fluorescence imaging method for SLN detection was a robust one. However, whether SLN identification using the blue dye method correlates with these factors needs to be investigated in future studies. Moreover, no adverse reactions were observed during this multicenter experiment. In conclusion, the ICG fluorescence imaging method using the FIRE was not inferior to the blue dye method, which was also confirmed by histopathological analyses.

Discussion

In this study, the universal feasibility of using the ICG fluorescence imaging method for SLNB in early-stage breast cancer patients was investigated. The combination of the FIRE and the NIR fluorescence imaging method showed a huge potential for clinical application. The particular design of the FIRE could simultaneously provide real-time intraoperative color, fluorescent, and merged images. Moreover, the field of vision was adjustable and data storage was automatic. In addition, this method did not interfere with routine operations and the surgeons managed to quickly learn the operation of this method, suggesting that the clinical application of the FIRE was very convenient.

The NIR fluorescence imaging method has several advantages over conventional methods. First, the high sensitivity and real-time imaging helps surgeons realize accurate intraoperative SLNB and minimal incision. Second, the higher tissue penetration of ICG compared to that of blue dyes allowed observations of the percutaneous lymphatic drainage and potential SLNs before incision. Finally, the minor side effects and robust performance make the wide application of this method feasible.

Based on our preliminary analysis, we believe that the high detection rate of the fluorescence imaging method may be the result of the higher optical sensitivity of ICG compared to that of MB and the low false negative rate of this method for SLNB can avoid the unnecessary need for ALND in patients with clinically negative SLNs[27]. Besides, obesity and age probably hinder the identification of SLNs[28]. However, SLNB can be stably achieved using fluorescence imaging possibly because of the higher tissue penetration of the fluorescent dye compared to that of blue dyes. Although the conditions in the different hospitals differed from one another, the ease with which the operation of the FIRE could be learnt and the common operating procedure contributed to realizing an optimal and steady detection of SLNs.

Based on our findings, we believe that the NIR fluorescence imaging method could be an alternative for SLNB to reduce patients' pain and to improve treatment outcomes in early breast cancer. In our future studies, we will conduct more research on the factors influencing the efficiency of the NIR fluorescence imaging method for SLNB, possibly by comparing breast peri-tumoral tracer injections and peri-areolar tracer injections, which are deemed to be equal in some studies[29, 30]. To further study the effectiveness of the NIR fluorescence imaging method, we will compare it with the standard radiocolloid and blue dye method and try to combine the technology of Google glass[31] with the FIRE to develop a novel wireless wearable device that can facilitate voice control and real-time display on the screen of the glass.

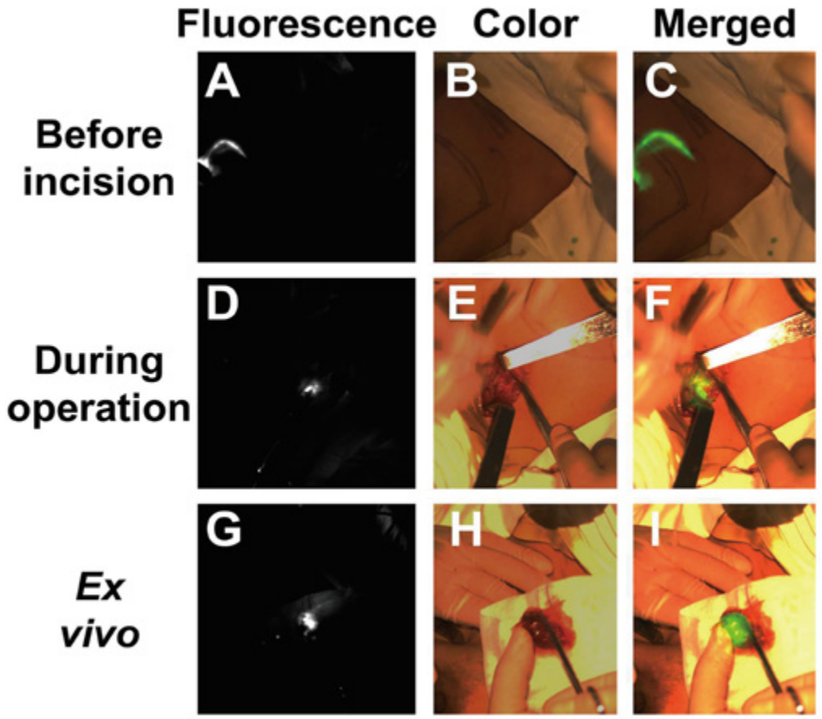


Fig.2 NIR fluorescence image-guided SLNB using the FIRE. (A-C) Percutaneous fluorescent identification of the lymphatic drainage before incision. (D-F) Precisely fluorescent image-guided SLN resection during surgery. (H-I) Images of the resected SLN ex vivo.

Conclusions

In this multicenter experiment, we compared the ICG fluorescence imaging method using the FIRE with the blue dye method using MB to evaluate the clinical feasibility of the former. The results showed that a high SLN identification rate and minimal incision could be similarly achieved in different hospitals with the assistance of the FIRE. Our results also indicate this method to be not inferior to the blue dye method.

Acknowledgements

Conflicts of Interest: All authors have read and understood the journal's policy on disclosure of potential conflicts of interest. There are no conflicts of interest to declare. This paper is supported by the National Natural Science Foundation of China under Grant Nos. 81227901, 81527805, 61231004, 61501462 and International Innovation Team, CAS, No. 20140491524.

All authors have read the journal's authorship agreement and the article has been reviewed by and approved by all named authors.

The Clinical Trails was registered with the name of Application of Surgical Navigation System in Sentinel Lymph Node of Breast Cancer Research with No. NCT02084784.

References

1. Ram R, Singh J, Mccaig E. Sentinel Node Biopsy Alone versus Completion Axillary Node Dissection in Node Positive Breast Cancer: Systematic Review and Meta-Analysis. Int J Cancer 2014;2014:513780-.
2. De Gournay E, Guyomard A, Coutant C, et al. Impact of sentinel node biopsy on long-term quality of life in breast cancer patients. Brit J Cancer 2013;109:2783-91.
3. Verbelen H, Gebruers N, Eeckhout FM, et al. Shoulder and arm morbidity in sentinel node-negative breast cancer patients: a systematic review. Breast Cancer Res Tr 2014;144:21-31.
4. Zavagno G, De Salvo GL, Scalco G, et al. A randomized clinical trial on sentinel lymph node biopsy versus axillary lymph node dissection in breast cancer: results of the Sentinella/GIVOM trial. Ann Surg 2008;247:207-13.
5. Krag D, Anderson S, Julian T. Comparison of sentinel lymph node resection to conventional axillary dissection in clinically node negative breast cancer patients: primary outcome results of NSABP B032 trial. Lancet Oncol 2010;11:927-33.
6. Krag DN, Anderson SJ, Julian TB, et al. Sentinel-lymph-node resection compared with conventional axillary-lymph-node dissection in clinically node-negative patients with breast cancer: overall survival findings from the NSABP B-32 randomised phase 3 trial. Lancet Oncol 2010;11:927-33.
7. Benson JR. An alternative to initial axillary-lymph-node dissection. Lancet Oncol 2010;11:908–9.
8. Straver ME, Meijnen P, Tienhoven Gv, et al. Sentinel Node Identification Rate and Nodal Involvement in the EORTC 10981-22023 AMAROS Trial. Ann Surg Oncol 2010;17:1854-61.
9. Mansel R E, MacNeill F, Horgan K, et al. Results of a national training programme in sentinel lymph node biopsy for breast cancer. Brit J Surg 2013;100:654–61.
10. van der Vorst JR, Schaafsma BE, Verbeek FPR, et al. Randomized Comparison of Near-infrared Fluorescence Imaging Using Indocyanine Green and 99 m Technetium With or Without Patent Blue for the Sentinel Lymph Node Procedure in Breast Cancer Patients. Ann Surg Oncol 2012;19:4104-11.
11. Morrow M, Rademaker A W, Bethke K P, et al. Learning sentinel node biopsy: results of a prospective randomized trial of two techniques. Surgery 1999;126:714-20; discussion 20-2.
12. Sarmela T, Huston TL, Simmons RM. A comparison of the adverse reactions associated with isosulfan blue versus methylene blue dye in sentinel lymph node biopsy for breast cancer. Am J Surg 2005;189:236–9.
13. Pitsinis V, Wishart G, Solomos M, et al. Indocyanine green fluorescence mapping for sentinel lymph node biopsy in early breast cancer. Surg Oncol 2015;41:S17.
14. Toh U, Iwakuma N, Mishima M, et al. Navigation surgery for intraoperative sentinel lymph node detection using Indocyanine green (ICG) fluorescence real-time imaging in breast cancer. Breast Cancer Res Tr 2015;153:337-44.
15. Akers WJ, Edwards WB, Kim C, et al. Multimodal sentinel lymph node mapping with single-photon emission computed tomography (SPECT)/computed tomography (CT) and photoacoustic tomography. Transl Res 2012;159:175-81.
16. Cabon Q, Sayag D, Texier I, et al. Evaluation of intraoperative fluorescence imaging–guided surgery in cancer-bearing dogs: a prospective proof-of-concept phase II study in 9 cases. Transl Res 2015;170:73-88.
17. Troyan SL, Kianzad V, Gibbs-Strauss SL, et al. The FLARE™ intraoperative near-infrared fluorescence imaging system: a first-in-human clinical trial in breast cancer sentinel lymph node mapping. Ann Surg Oncol 2009;16:2943-52.
18. Hirche C, Engel H, Kolios L, et al. An experimental study to evaluate the fluobeam 800 imaging system for fluorescence-guided lymphatic imaging and sentinel node biopsy. Surg Innov 2013;20:516-23.
19. Cahill RA, Anderson M, Wang LM, et al. Near-infrared (NIR) laparoscopy for intraoperative lymphatic road-mapping and sentinel node identification during definitive surgical resection of early-stage colorectal neoplasia. Surg Endosc 2012;26:197-204.
20. Liu Y, Zhao Y-M, Akers W, et al. First in-human intraoperative imaging of HCC using the fluorescence goggle system and transarterial delivery of near-infrared fluorescent imaging agent: a pilot study. Transl Res 2013;162:324-31.
21. Gotoh K, Yamada T, Ishikawa O, et al. A novel image□guided surgery of hepatocellular carcinoma by indocyanine green fluorescence imaging navigation. J Surg Oncol 2009;100:75-9.
22. Ishizawa T, Fukushima N, Shibahara J, et al. Real□time identification of liver cancers by using indocyanine green fluorescent imaging. Cancer 2009;115:2491-504.
23. Schaafsma BE, Mieog JSD, Hutteman M, et al. The clinical use of indocyanine green as a near- infrared fluorescent contrast agent for image-guided oncologic surgery. J Surg Oncol 2011;104:323-32.
24. Chi C, Ye J, Ding H, et al. Use of indocyanine green for detecting the sentinel lymph node in breast cancer patients: from preclinical evaluation to clinical validation. Plos One 2013;8:e83927.
25. Chi C, Du Y, Ye J, et al. Intraoperative Imaging-Guided Cancer Surgery: From Current Fluorescence Molecular Imaging Methods to Future Multi-Modality Imaging Technology. Theranostics 2014;4:1072-84.
26. Leng CC, Tian J. Mathematical method in optical molecular imaging. Sci China Inform Sci 2015;58.
27. Sugie T, Kassim KA, Takeuchi M, et al. A novel method for sentinel lymph node biopsy by indocyanine green fluorescence technique in breast cancer. Cancers 2010;2:713-20.
28. Cox CE, Dupont E, Whitehead GF, et al. Age and body mass index may increase the chance of failure in sentinel lymph node biopsy for women with breast cancer. Breast J 2002;8:88-91.
29. Mieog JSD, Troyan SL, Hutteman M, et al. Toward Optimization of Imaging System and Lymphatic Tracer for Near-Infrared Fluorescent Sentinel Lymph Node Mapping in Breast Cancer. Ann Surg Oncol 2011;18:2483-91.
30. Polom K, Murawa D, Nowaczyk P, et al. Breast cancer sentinel lymph node mapping using near infrared guided indocyanine green and indocyanine green–human serum albumin in comparison with gamma emitting radioactive colloid tracer. Eur J Surg Onc 2012;38:137-42.
31. Muensterer OJ, Lacher M, Zoeller C, et al. Google Glass in pediatric surgery: An exploratory study. Int J Surg 2014;12:281-9.

Hepatobiliary Surgery

Research Letter

NIR-II Fluorescence Image-Guided Surgery Prolongs the Relapse-Free Survival of Hepatocellular Carcinoma Patients

Zeyu Zhang [1,2,*], Cheng Fang [3,*], Kunshan He [2,*], Song Su [3], Chongwei Chi [2], Xiaojing Shi [2], Bo Li [3] ✉, Zhen Cheng [4] ✉, Zhenhua Hu [2] ✉, Jie Tian [1,2] ✉

[1] Key Laboratory of Big Data-Based Precision Medicine of Ministry of Industry and Information Technology, School of Engineering Medicine, Beihang University, Beijing, China.

[2] Department of General Surgery (Hepatobiliary Surgery), The Affiliated Hospital of Southwest Medical University, Luzhou, China.

[3] CAS Key Laboratory of Molecular Imaging, Beijing Key Laboratory of Molecular Imaging, Chinese Academy of Sciences, Beijing, China.

[4] Molecular Imaging Center, Shanghai Institute of Materia Medica, Chinese Academy of Sciences, Shanghai, People's Republic of China.

* These authors contributed equally to this work.

Introduction

Surgery plays a key role in the treatment of hepatocellular carcinoma (HCC), but radical dissection has long been a challenge.[1,2] A series of clinical studies have shown the great potential of fluorescence molecular imaging (FMI) to improve surgical efficacy, by visualizing occult lesions with a superior sensitivity in comparison to direct visual inspection and palpation.[3,4]

Recently, FMI in the second near-infrared window (900–1880 nm, NIR-II) has shown promising performance, providing enhanced sensitivity and improved depth for intra- operative cancer detection.[5,6] In 2020, our team reported the first-in-human study utilizing NIR-II FMI (with ICG) to guide HCC surgery. The data demonstrated that this novel technique was capable of visualizing occult HCC lesions (minimum size <3 mm in diameter) in ultrasonography, CT, MRI and NIR-I FMI (wavelength 700 – 900 nm); the surgical margin was better delineated, leading to improved surgical decision making.[6,7]

In this study, we evaluate whether NIR-II FMI can result in beneficial survival outcome for HCC patients, based on a five-year follow-up.

HPB(Oxford). 2024. 26(7.): 963-966 Published online: 5 June 2024

Methods

In total 53 HCC patients who received open surgery were enrolled from September 2017 until October 2018. These patients were allocated into two groups: NIR and non-NIR group. NIR group consisted of 21 patients who received NIR-II FMI for guidance. 32 patients in the non-NIR group, had surgeries carried out by visual inspection and palpation.

Overall survival (OS) was measured from the date of surgery until death of any causes. Relapse-free survival (RFS) referred to the duration from the date of surgery to the date of the first relapse. Kaplan– Meier curves were applied to reflect OS rates and RFS rates of the two groups.

The significance between Kaplan– Meier curves was calculated by Gehan–Breslow–Wilcoxon test. Two-sided Welch's t-test measured the significance between patient characteristics. P value < 0.05 was considered statistically significant.

Results

Characteristics of all the involved patients are summarized in Table 1, and more details are shown in the supplementary materials. The group of patients who underwent NIR-II guided surgery (n = 21) had an average age of 50.8 ± 9.9 (ranging from 29 to 67), while the non-NIR group (n = 32) had an average age of 53.1 ± 12.2 (ranging from 23 to 74). Two patients (9.5%) in the NIR group and six (18.8%) in the non-NIR group were female. Every enrolled subject had liver performance graded A according to the Child-Pugh classification. The preoperative serum AFP concentrations were divided into four ranks to reflect the malignant degrees of patients. Between the two groups, no statistical significance was observed for age, gender ratio or AFP.

From the postoperative follow-up data, the NIR group showed better RFS compared to the non-NIR group. 2 patients (9.5%) in the NIR group and 11 (34.4%) in the non-NIR group had relapse within 1 year after surgery. 3 years after surgery, the relapse rate increased to 38.1% in the NIR group and 68.8% in the non-NIR group. From the 5-Year follow-up data, relapse was reported in 11 patients (52.4%) of the NIR group, and in 25 patients (78.1%) of the non-NIR group. Consequently, lower relapse rates led to improved RFS in the NIR group, as illustrated in Kaplan–Meier curves as well (Fig. 1).

Notably, the patients with a high serum AFP concentration exhibited greater probability of relapse. Out of all the 53 patients, 13 had AFP levels exceeding 400 ng/ml (7 in the NIR group and 6 in the non-NIR group), and 11 of them encountered relapse during the follow-up period. In the NIR group, relapse occurred in 5 of the 7 (71.4%) AFP >400 patients after an average time of 24.4 months (range 12~38) from surgery. In the non-NIR group, all the 6 patients (100%) with high AFP level experienced relapse, and the average period was 20.2 months (range 5~61). In each group, the relapse rates for high AFP patients exceeded the cohort level by approximately 20 percent.

The OS, however, showed no statistical difference between the two groups (71.4% vs 56.3%, P = 0.131, Fig. 1d), which may be affected by different treatments for relapse. Of the 11 relapsed patients in the NIR group, 8 received targeted therapy and 5 died; 2 received interventional therapy and 1 died; the remaining 1 received radiofrequency ablation and was still alive. In the non-NIR group, in total 26 patients had disease relapse. 25 were found within 5 years post-surgery, and 1 was diagnosed in the 61st month. 3 of them received reoperation and 2 were still alive. 14 received targeted therapy and 9 died. 5 received interventional therapy (3 died) and 4 received radiofrequency ablation (2 died).

Table 1 Patient characteristics and the comparison

Variable	NIR group (n = 21)	Non-NIR group (n = 32)	Significance
Age			
Mean ± SD	50.8 ± 9.9	53.1 ± 12.2	$P = 0.467$
Range	[29, 67]	[23, 74]	
Gender			
Male: Female	19 : 2	26 : 6	$P = 0.341$
Child-pugh	A for all	A for all	–
Serum AFP			
> 25 ng/ml	11/21 (52.38%)	11/32 (34.38%)	$P = 0.207$
> 200 ng/ml	8/21 (38.10%)	9/32 (28.13%)	$P = 0.466$
> 400 ng/ml	7/21 (33.33%)	6/32 (18.75%)	$P = 0.257$
> 1000 ng/ml	5/21 (23.81%)	4/32 (12.50%)	$P = 0.321$
Surgical procedure	Open surgery, guided by multi-spectral NIR fluorescence imaging	Open surgery, based on visual inspection and palpation	–
Relapse			
1-Year	2/21 (9.52%)	11/32 (34.38%)	$^{*}P = 0.039$
3-Year	8/21 (38.10%)	22/32 (68.75%)	$^{**}P = 0.006$
5-Year	11/21 (52.38%)	25/32 (78.13%)	$^{**}P = 0.008$

The significances on relapse data were measured with Gehan– Breslow–Wilcoxon test. The asterisks represent significant differences, * for P ≤ 0.05 and ** for P ≤ 0.01.

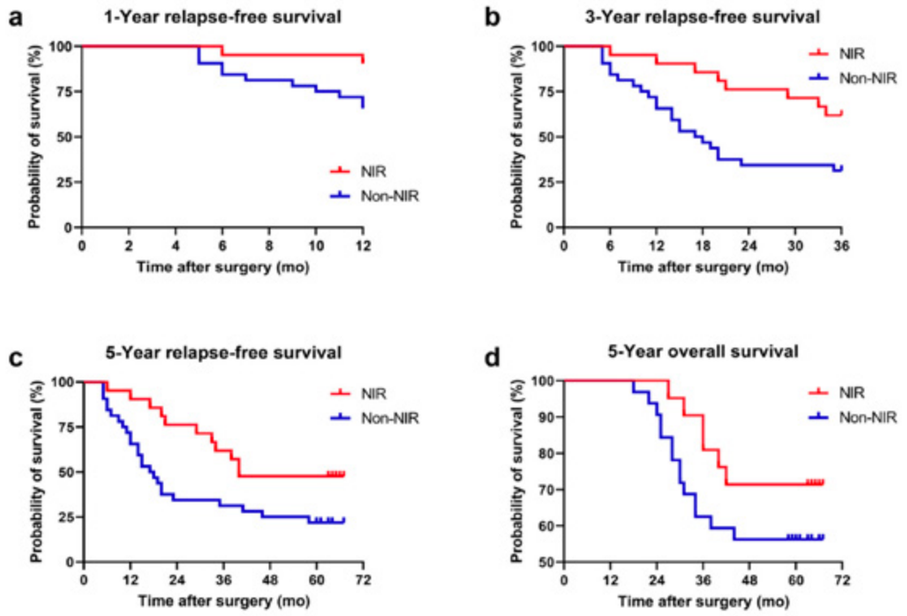


Fig.1 Kaplan–Meier curves exhibited that the NIR group had better RFS and OS than non-NIR group (blue). a 1-Year RFS comparison (*P = 0.039), b 3-Year RFS comparison (**P = 0.006), c 5-Year RFS comparison (**P = 0.008), d 5-Year OS comparison (P = 0.131). The significances were analyzed with Gehan-Breslow-Wilcoxon test.

NIR-II FMI guided surgery. RFS between NIR and non-NIR group is 90.5% vs 65.5% for 1-Year (*P = 0.039), 61.9% vs 31.2% for 3-Year (**P = 0.006), and 47.6% vs 21.9% for 5-Year (**P = 0.008), respectively.

The 5-Year OS comparison was not statistically significant (P = 0.131), although a 15.2% rise was observed in the NIR group. This result is most likely due to the inconsistencies in relapse treatments. While novel treatments are continually being introduced for HCC, a consensus on the optimal approach has not yet been reached. Therefore, RFS might be better than OS to evaluate surgical effects.

High level of AFP may cause greater risk of HCC relapse. For all 13 subjects with 400+ AFP, relapse occurred in 84.6% of them. Fluorescence imaging and other intraoperative techniques are therefore recommended for high AFP patients to reduce the risk of relapse.

In conclusion, by performing NIR-II fluorescence image-guided surgery for HCC, the relapse-free survival could be significantly improved, compared to the traditional hepatectomy group (using direct visual inspection and palpation). Although the cohort size may still be limited, these results may encourage the clinical translation of NIR-II FMI in various surgeries with expanded population.

Funding

This study was funded by the National Natural Science Foundation of China (NSFC) (62027901, 92059207, 81930053, 92359301, U23A20487, 81227901), the Chinese Academy of Sciences (QYZDJ-SSW-JSC005), Beijing Natural Science Foundation (7214266, JQ19027), CAS Youth Interdisciplinary Team (JCTD-2021-08), Strategic Priority Research Program of the Chinese Academy of Sciences (XDA16021200), the Double-A-Class Program for Youth Development (ZG216S2335), the Innovative Research Team of High-level Local Universities in Shanghai.

Ethics approval statement

The study has been approved by the Medical Ethics Review Committee of the Affiliated Hospital of Southwest Medical University.

Patient consent statement

All the patients involved in this study have sign the informed consent.

Clinical trial registration

The shown data were a part of the study registered in the Chinese Clinical Trial Registry (No. ChiCTR1900022453).

HPB(Oxford). 2024. 26(7.): 963-966 Published online: 5 June 2024

Data availability statement

Data will be made available upon reasonable request.

Declaration of generative AI in scientific writing

The authors declare that they have not used generative artificial intelligence (AI) and AI-assisted technologies in the writing process.

Conflicts of interest

None to declare.

References

1. Wang X, Teh CSC, Ishizawa T, Aoki T, Cavallucci D, Lee SY et al. Consensus guidelines for the use of fluorescence imaging in hepatobiliary surgery Ann Surg. 2021 Jul; 274:97-106
2. Zhu W, Zeng X, Hu H, Xiang N, Zeng N, Wen S et al. Perioperative and disease-free survival outcomes after hepatectomy for centrally located hepatocellular carcinoma guided by augmented reality and indocyanine green fluorescence imaging: a single-center experience J Am Coll Surg. 2023 Feb 1; 236:328-337
3. Lauwerends LJ, van Driel PBAA, Baatenburg de Jong RJ, Hardillo JAU, Koljenovic S, Puppels G et al. Real-time fluorescence imaging in intraoperative decision making for cancer surgery Lancet Oncol. 2021 May; 22:e186-e195
4. Wang K, Du Y, Zhang Z, He K, Cheng Z, Yin L et al. Fluorescence image-guided tumour surgery Nat Rev Bioeng. 2023 Mar; 1:161-179
5. Zhang Z, Fang C, Zhang Y, Su S, Li B, Liu G et al. NIR-II nano fluorescence image guided hepatic carcinoma resection on cirrhotic patient Photodiagnosis Photodyn Ther. 2022 Aug 30; 40, 103098
6. Hu Z, Fang C, Li B, Zhang Z, Cao C, Cai M et al. First-in-human liver-tumour surgery guided by multispectral fluorescence imaging in the visible and near-infrared-I/II windows Nat Biomed Eng. 2020 Mar; 4:259-271
7. Choi HS, Kim HK. Multispectral image-guided surgery in patients Nat Biomed Eng. 2020 Mar; 4:245-246

Hepatobiliary Surgery

Research Article

Efficacy of Near-Infrared Fluorescence-Guided Hepatectomy for the Detection of Colorectal Liver Metastases: A Randomized Controlled Trial

Kunshan He [1,2,3,4,*], Xiaopeng Hong [1,*], Chongwei Chi [1,5,*], Chaonong Cai [1], Yu An [1,2,3], Peiping Li [1], Xialei Liu [1], Hong Shan [1], Jie Tian [1, 2, 3, 5], Jian Li [1]

Abstract

Background: The application of indocyanine green fluorescence–guided hepatectomy for liver metastases from colorectal cancer is in the preliminary stage of clinical practice; thus, its efficacy needs to be determined. This study compared the number of intrahepatic colorectal liver metastases detected intraoperatively and postoperative recovery data between patients who underwent traditional hepatectomy (nonindocyanine green group) and traditional hepatectomy plus intraoperative indocyanine green fluorescence imaging (indocyanine green group).

Study design: Between January 2018 and March 2020, patients with potentially resectable colorectal liver metastases were randomly assigned to the nonindocyanine green or indocyanine green group. The number of intrahepatic colorectal liver metastases identified intraoperatively and based on postoperative recovery data were compared between both groups.

Results: Overall, we recruited 80 patients, among whom 72 eligible patients were randomly assigned. After allocation, 64 patients, comprising 32 in each group, underwent the allocated intervention and follow-up. Compared with the nonindocyanine green group, the mean number of intrahepatic colorectal liver metastases identified intraoperatively in the indocyanine green group was significantly greater (mean [standard deviation], 3.03 [1.58] vs 2.28 [1.35]; p = 0.045), the postoperative hospital stay was shorter (p = 0.012) and the 1-year recurrence rate was also lower (p = 0.017). Postoperative complications and 90-day mortality were comparable, with no statistical differences.

Conclusions: Indocyanine green fluorescence imaging significantly increases the number of intrahepatic colorectal liver metastases identified and reduces postoperative hospital stay and 1-year recurrence rate without increasing hepatectomy-related complications and mortality rates.

[1] The Fifth Affiliated Hospital, Sun Yat-sen University, Zhuhai, China.

[2] Beijing Advanced Innovation Center for Big Data-Based Precision Medicine, School of Medicine and Engineering, Beihang University, Beijing, China.

[3] Key Laboratory of Big Data-Based Precision Medicine, Beihang University, Ministry of Industry and Information Technology, Beijing, China.

[4] State Key Laboratory of Computer Science and Beijing Key Lab of Human-Computer Interaction, Institute of Software, Chinese Academy of Sciences, Beijing, China.

[5] CAS Key Laboratory of Molecular Imaging, the State Key Laboratory of Management and Control for Complex Systems, Institute of Automation, Chinese Academy of Sciences, Beijing, China.

* Drs He, Hong, and Chi contributed equally to this work.

Introduction

Globally, the incidence of colorectal cancer (CRC) ranks third and the mortality rate ranks fourth among other cancers.[1] The liver is the main target organ for hematogenous metastasis of CRC.[2] Approximately 20% to 25% of patients have colorectal liver metastases (CRLMs) when CRC is diagnosed, and up to 50% of patients will develop CRLMs within 3 years after being diagnosed with primary CRC.[3,4] The median survival time for untreated patients with liver metastases is only 6.9 months, and the 5-year survival rate for patients with unresectable CRLMs is <5%.[5] For patients whose primary tumors and liver metastases can be radically resected, the median survival time is 35 months, and the 5-year survival rate is 30% to 57%.[6,7] Some patients whose initial liver metastases cannot be eradicated can be converted to resectable states after comprehensive treatment.[8] Therefore, international mainstream CRC treatment guidelines, such as European Society for Medical Oncology, recommend radical surgery as the only potential cure for patients with CRLMs.[9,10]

Complete resection of liver metastases remains the best treatment modality for CRLMs; thus, eligible patients should receive surgical treatment at an appropriate time.[11] Despite improvements in surgical strategies and chemotherapy regimens, up to 65% to 80% of patients will experience a relapse after resecting CRLMs, with most recurrences appearing within 12 months.[12,13] A reasonable explanation for this phenomenon is that some metastases are likely to be missed at the time of liver resection.[14]

This is a challenging problem because the location and size of small metastatic lesions are variable and difficult to predict. Routinely recommended imaging modalities, such as CT, play important roles in the screening, diagnosis, and grading of CRLMs.[15,16] However, they are not sensitive to subcentimeter nodules and are rarely used intraoperatively. Intraoperative ultrasound (IOUS) is currently regarded as the gold standard for detecting liver metastases in open, laparoscopic, or robotic operations because it offers real-time visualization and high overall diagnostic accuracy.[17,18] However, IOUS also has several drawbacks because it can easily miss lesions <3 mm, its accuracy relies on subjective experience, and there is a “blind area” within 1 cm from the surface, which is particularly problematic because small CRLMs are mainly located on the liver’s surface.[19]

Because of less autofluorescence, optical scattering influence, and increased penetration depth,[20] near-in-frared (NIR) fluorescence imaging (NIR-FI) has been used in various settings such as lymph node dissection,[21] cancer detection,[22] and nerve-sparing procedures.[23] The application of NIR-FI in hepatectomy for CRLMs is in the preliminary stage. To the best of our knowledge, most studies had small sample sizes or were retrospective studies evaluating tumor detection efficacy[24] and survival benefit.[14] Van and colleagues[25] conducted a single-arm study on 40 patients and demonstrated that additional small and superficial CRLMs were

detected in 5 patients using NIR-FI, which were otherwise missed using conventional methods.

Therefore, prospective randomized controlled trials are warranted to evaluate the efficacy of NIR fluorescence-guided hepatectomy in patients with CRLMs. The primary aim of this study was to compare the number of intrahepatic CRLMs detected intraoperatively and based on postoperative recovery data between both indocyanine green (ICG) and non-ICG groups.

Methods

The ethics committee of the Fifth Affiliated Hospital of Sun Yat-sen University approved this study. Before the operation, all study participants provided written informed consent. The clinical trial number was ChiCTR2000039635, and the principles of the Declaration of Helsinki were strictly observed and implemented.

Patients

Eighty patients were enrolled from January 2018 until March 2020. The inclusion criteria were as follows: CRLMs diagnosed based on imaging and pathologic examination findings; completely resectable liver metastases with remaining liver volume were ≥30%; American Society of Anesthesiologists' grade 1 or 2; no serious cardiopulmonary or neurologic disease; performance status 0 to 1; aged 18 to 75 years; and provided written informed consent. The exclusion criteria included glomerular filtration rate <55 mL/min; pregnancy; breastfeeding; allergic to iodine, shellfish, or ICG.

Subjects who met the inclusion criteria were randomly and evenly assigned to the ICG and non-ICG groups. After allocation, patients with unresectable tumors, peritoneal metastasis, or other treatment options or those who withdrew consent were excluded. For synchronous metastases patients whose primary tumor had not been resected, the primary colorectal tumor and CRLMs were simultaneously removed during a single operation.

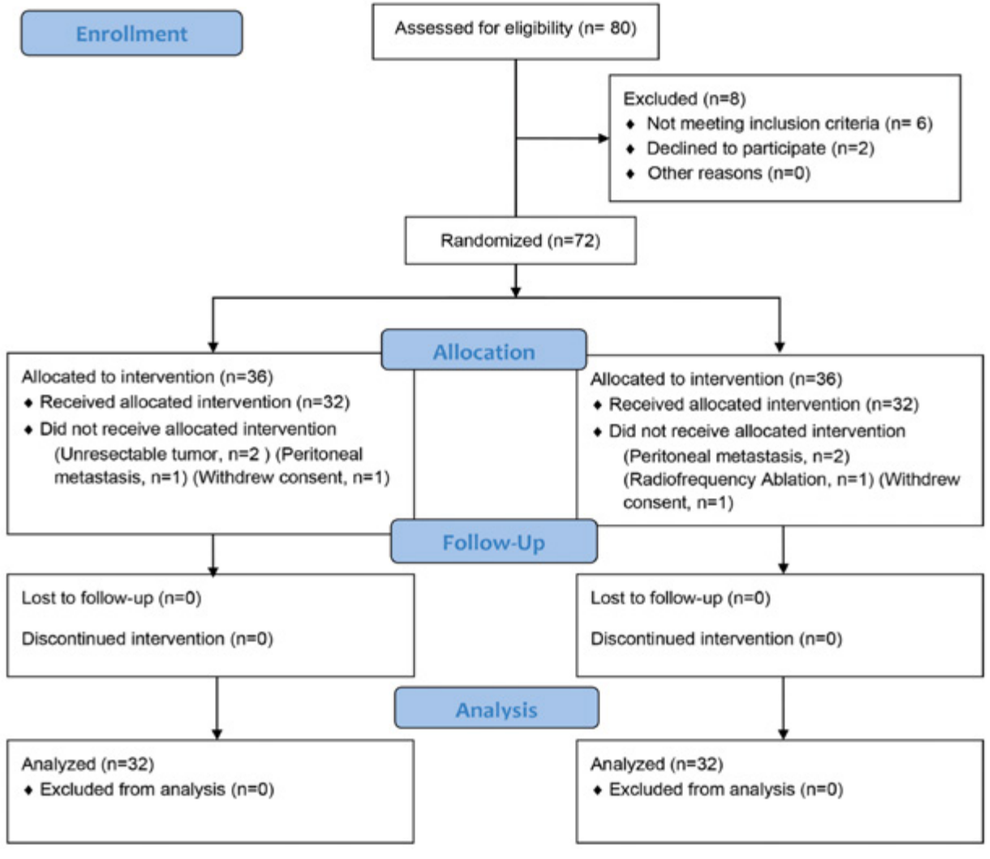


Fig.1 Consolidated Standards of Reporting Trials diagram of enrollment and allocation.

Randomization and ICG administration

After assessing for eligibility, 72 patients were randomly assigned with a 1:1 allocation ratio according to the method of block randomization using SPSS version 20.0 software before the operation (Fig. 1). Two patients in each group abandoned the allocated intervention and finally received chemotherapy because of peritoneal metastasis detected during the operation. The operation was performed by 2 teams of experienced surgeons using a standard protocol. Although operating surgeons were familiar with the group assignments, the postoperative nursing staff were masked to the group allocations.

After the ICG allergy test, each patient received an intravenous dose of 0.5 mg/kg ICG 24 hours before the operation in the ICG group. No adverse or allergic reactions associated with ICG use occurred during the perioperative period. A self-developed imaging system (DPM-III-01, Zhuhai Dipu Medical Technology Co., Ltd.) was used based on our previous studies.[26,27] The DPM-III-01 system could display NIR images, white-light images, or overlaid images, or all 3 images together according to the surgeon's needs.

Imaging procedure

In the ICG and non-ICG groups, after patients were placed under general anesthesia, the operation was initiated by performing visual exploration and IOUS based on preoperative imaging data of CT or MRI to locate suspicious lesions. Palpation was only performed during direct laparotomy or laparoscopic conversion to laparotomy. Additionally, NIR-FI was used to inspect the liver surface in the ICG group. Electrocautery and ultrasonic reamer were used to delimit the boundary of the detected lesions and perform limited resection. In the ICG group, the boundary was determined by the lateral margin of fluorescence signal. For patients with multiple lesions concentrated in the hemiliver or a certain liver segment, we performed hemihepatectomy or segmentectomy. After resecting the identified metastasis, the tumor margin was carefully examined for any remaining tumor using direct visual inspection. Additionally, the boundary of deep-located lesions was identified using NIR-FI after exposure or excision, and the resection planes were re-evaluated to ensure the radical resection in the ICG group.

Fluorescence microscopy

Through direct visual inspection and NIR-FI, we obtained biopsies from the transition zone between metastatic lesions and surrounding normal liver parenchyma from excised specimens, then embedded in paraffin and sectioned at 4 μm. Fluorescence microscope imaging was performed using an Olympus Bx53 mounted with the 130W U-HGLGPS guide coupling lighting system (Olympus, Tokyo, Japan). The sections were then stained with hematoxylin and eosin. White-light images from conventional microscopy were subsequently merged with fluorescence microscopic images.

Statistical analysis

The mean number of CRLMs detected intraoperatively per patient from the control groups of 2 previous studies was 2.25.[24,25] The current analysis was based on an α value of 0.05, a power of 80%, and a margin δ of 15%, indicating that each group needed to include at least 30 patients. Given the expected dropout rate of 20%, at least 36 patients needed to be enrolled in each group, totaling 72 participants. We used the mean number of CRLMs detected intraoperatively of each patient as the primary endpoint, and the patient's postoperative recovery was set as a secondary study endpoint. The signal-to-background ratio (SBR) of the fluorescent rim to the peripheral liver parenchyma was calculated using a previously described method.[28] Clinical characteristics between the groups were compared using an unpaired t-test for parametric continuous data, which are expressed as mean (standard deviation [SD]). Nonparametric continuous data were analyzed using the Mann-Whitney U test, which are expressed as medians with ranges. Categorical variables were compared using Pearson's chi-square test or Fisher's exact test, which are presented as frequencies. P value <0.05 was considered statistically different and 95% confidence intervals (CIs) were provided when appropriate.

Results

Finally, 64 patients received the allocated intervention and were eventually followed up. The ICG and non-ICG groups included 32 patients each (Fig. 1).

The baseline characteristics of the patients are summarized in Table 1. There were no significant differences between the ICG and non-ICG groups with respect to age, sex, neoadjuvant chemotherapy, location of primary tumor (colon or rectum), type of surgery (laparotomy, laparoscopy, or conversion to laparotomy), surgical procedure (limited resection vs hemihepatectomy or segmentectomy), number of CRLMs on CT/MRI (mean [SD] 2.00 [1.39] vs 2.03 [1.47]), largest hepatic tumor size >5 cm, preoperative CEA levels >200 ng/mL, synchronous or metachronous metastases, and comorbidities.

Primary endpoint

In the ICG group, preoperative diagnosis revealed 64 lesions; intraoperative visual exploration, IOUS, and palpation (if applicable) plus NIR-FI detected 104 lesions; and postoperative pathology confirmed 97 positive lesions. Among the 73 lesions detected using NIR-FI (Fig. 2A), 67 were pathologically confirmed to be positive, and their mean SBR was 4.49 (0.74); 6 nodules were confirmed to be negative based on histopathologic examination, their mean SBR was 4.11 (0.93), and there was no statistical difference between these SBR values (p = 0.817). In 8 patients, 20 small CRLMs were found using fluorescence only (Fig. 2B), and their diameters were significantly smaller than those of additional CRLMs identified using visual exploration, IOUS, or palpation (mean [SD] 3.95 [1.64] vs 9.30 [6.08] mm; p = 0.000). The average depth (distance from the liver surface) of the positive lesions detected using NIR-FI was significantly smaller than that of the positive lesions not detected using NIR-FI (mean [SD] 1.56 [2.35] vs 16.79 [8.78] mm; p=0.000). Although such deep-located CRLMs could not be detected using NIR-FI when the liver surface was explored, after tumor exposure, NIR-FI could be used

Table 1 Demographic and Clinical Characteristics of the Patients in the 2 Groups

Variable	ICG group (n = 32)	Non-ICG group (n = 32)	OR (95% CI)	p Value*
Age, y, mean	58.59 (11.29)	58.94 (10.47)	1.003 (0.958–1.050)	0.900†
Sex ratio, M:F	17:15	21:11	0.594 (0.217–11.625)	0.309
Chemotherapy before operation, n			0.401 (0.145–11.112)	0.076
Yes	22	15		
No	10	17		
Location of primary tumor, n			0.873 (0.314–12.426)	0.794
Colon	21	20		
Rectum	11	12		
Type of operation, n			Not available	0.159‡
Laparotomy	11	11		
Laparoscopy	19	14		
Conversion to laparotomy, n	2	7		
Operative procedure, n			0.644 (0.1–4.142)	1.000‡
Limited resection	30	29		
Hemihepatectomy or segmentectomy	2	3		
No. of CRLM on CT/MRI, mean (SD)	2.00 (1.39)	2.03 (1.47)	1.016 (0.717–11.439)	0.931†
Largest hepatic tumor >5 cm, n			1.615 (0.409–16.377)	0.491‡
Yes	4	6		
No	28	26		
Preoperative CEA >200 ng/mL, n			0.484 (0.042–15.621)	1.000‡
Yes	2	1		
No	30	31		
Synchronous metastases, n			2.444 (0.817–17.308)	0.106
Yes	19	25		
No	13	7		
Comorbidity, n				
COPD	1	1	1 (0.06–116.713)	1.000‡
DVT or PE	0	0	Not available	Not available
CVE	4	9	2.739 (0.746–110.056)	0.120‡
DM	2	3	1.552 (0.241–19.974)	1.000‡

*Chi-square test
†Student's t-test
‡Fisher's exact test
CRLM, colorectal liver metastases; CVE, cardiovascular events; DM, diabetes mellitus; DVT, deep venous thrombosis; ICG, indocyanine green; OR, odds ratio; PE, pulmonary embolism.

to guide the resected margin or determine the completeness of tumor resection in the excised specimen (Fig. 2C). Fluorescence signal was observed in normal hepatic tissues that were directly surrounding the CRLMs and were mainly located in the cytoplasm of the hepatocytes (Fig. 2D).

In the non-ICG group, preoperative diagnosis revealed 65 lesions; intraoperative visual exploration, IOUS, and palpation (when applicable) without NIR-FI detected 75 lesions; and postoperative pathology confirmed 73 positive lesions. The mean number of intrahepatic CRLMs identified intraoperatively per patient was significantly greater in the ICG group than in the non-ICG group (mean [SD] 3.03 [1.58] vs 2.28 [1.35]; p = 0.045). In both groups, no additional lesions were found only on postoperative pathology.

Secondary endpoint

Operative and short-term outcomes of patients in the 2 groups are shown in Table 2. There were no differences between the 2 groups with respect to the duration of surgery (odds ratio [OR] 1.003, 95% CI 0.958 to 1.050;p = 0.089), blood loss (100 [10 to 1300] vs 200 [20 to 2700] ml; p = 0.124), transfusion

J Am Coll Surg. 2022. 234:130–137 Published online: 1 February 2022

requirement (OR [odds ratio] 1.000, 95% CI 0.227 to 4.4; p = 1.000), reoperation requirement (OR 1.000, 95% CI 0.060 to 16.713; p= 1.000), 90-day mortality (0 vs 1; p = 1.000), and grade III or IV postoperative complications (OR 2.143, 95% CI 0.364 to 12.628; p = 0.672). The duration of postoperative hospital stay (7.5 [3–21] vs 10.5 [5–45] days; p = 0.012) and 1-year recurrence rate (OR 0.262, 95% CI 0.071 to 0.762; p = 0.017) were shorter and lower, respectively, in the ICG group than in the non-ICG group.

Among the 6 relapsed cases in the ICG group, one had superficial recurrence, and the remaining five had multiple superficial and deep metastases. Of the 15 relapsed cases in the non-ICG group, five had recurrences in the superficial area, including one recurrence in the surgical area, and the others had multiple superficial and deep metastases.

Discussion

This prospective randomized controlled trial aimed to determine the efficacy of ICG fluorescence-guided hepatectomy for patients with CRLMs. The findings demonstrated that NIR-FI was a safe and effective complement to existing methods, including visual exploration, IOUS, and palpation for the resection of CRLMs. Therefore, integrating NIR-FI into existing routine surgical procedures should be considered.

The liver is the most common site of distant metastasis of CRC.[29] Surgical resection is the cornerstone for treating liver metastasis of CRC.[30] It includes synchronous removal of the primary tumor and liver metastases during a single operation or metachronous resection in which the primary tumor is removed first, and liver metastasis resection is performed after a period of nutritional support and chemotherapy.[31] Despite recent improvements in diagnosis and management, most patients with CRLMs experience intrahepatic recurrence after curative hepatic resection.[32] A possible reason is that some small nodules were overlooked during preoperative diagnosis and intraoperative exploration using existing established methods.[14] Moreover, even if some CRLMs are detected before surgery, it is difficult to locate them during surgery because of their deep location or liver damage after chemotherapy.[33] Thus, novel intraoperative imaging techniques to better distinguish CRLMs from normal liver parenchyma are urgently required. To our knowledge, this is the first prospective randomized controlled trial to demonstrate a significant difference in the mean number of intrahepatic CRLMs

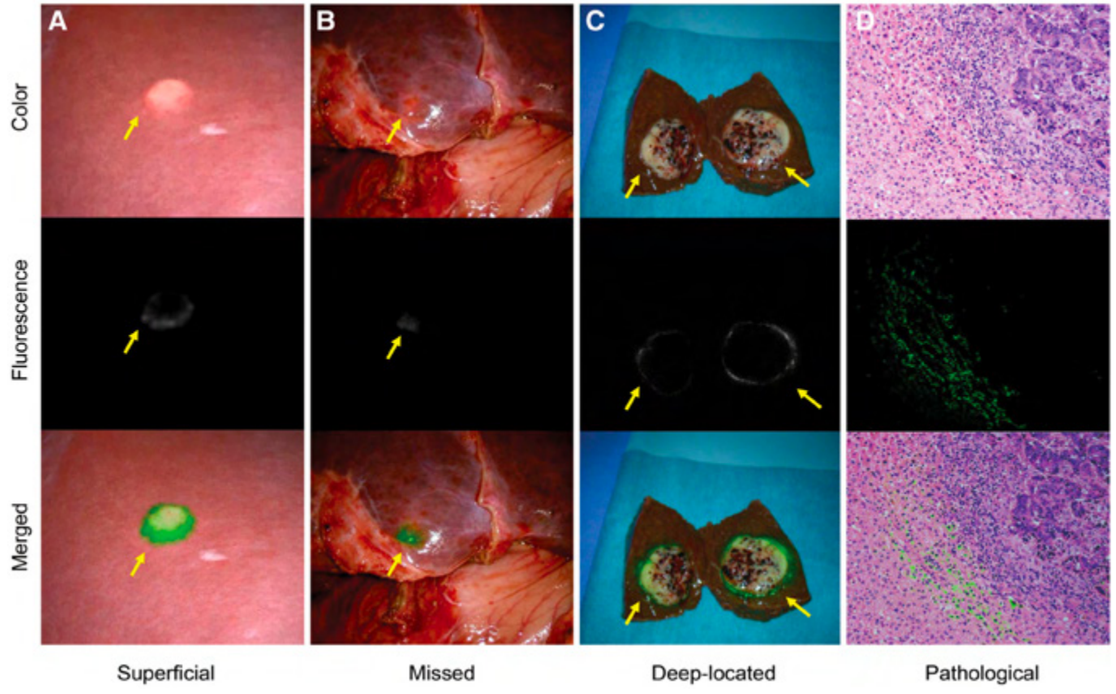


Fig.2 (A) Superficial lesion detected using conventional methods and near-infrared fluorescence imaging (NIR-FI). (B) Lesion missed using traditional methods but detected using NIR-FI. (C) Deep-located lesion detected using traditional methods and identified using NIR-FI only after exposure or excision. (D) Microscopic pathology. Arrowheads indicate colorectal liver metastases.

Table 2 Surgical and Short-Term Outcome of the Patients in the 2 Groups

Variables	ICG group (n = 32)	Non-ICG group (n = 32)	OR (95% CI)	p Value*
Duration of operation, min, mean (SD)	143.81 (74.53)	175.97 (74.50)	1.003 (0.958–1.050)	0.089†
Blood loss, mL, median (range)	100 (10–1300)	200 (20–2700)	Not available	0.124‡
Transfusion requirement, n	4	4	1 (0.227–4.4)	1.000§
No. of tumors, mean (SD)	3.03 (1.58)	2.28 (1.35)	0.750 (0.017–1.483)	0.045†
Postoperative hospital stay, d, median (range)	7.5 (3–21)	10.5 (5–45)	Not available	0.012‡
Reoperation, n	1	1	1 (0.06–16.713)	1.000§
90-day mortality, n	0	1	Not available	1.000§
Postoperative complication grade III or IV, n	2	4	2.143 (0.364–12.628)	0.672§
Recurrence in 1 y, n	6	15	0.262 (0.071–0.762)	0.017

*Chi-square test
†Student's *t*-test
‡Mann-Whitney U test
§Fisher's exact test
ICG, indocyanine green; OR, odds ratio

identified intraoperatively per patient with or without NIR-FI.

NIR-FI is an emerging optical imaging modality that has been used in recent years to provide surgeons with real-time guidance during surgery. It has the advantages of high resolution, high SBR, and large penetration depth, which has the potential to improve perioperative surgical treatment.[20] ICG is currently the most commonly used NIR fluorescent contrast agent and has been approved for clinical use since 1959. It is cheap, safe, and has a very low side effect rate.[34,35] NIR-FI with ICG has many clinical applications in hepatopancreatobiliary surgery, particularly for cholangiography, liver mapping, and tumor visualization.[36] Our study confirmed that this method could significantly identify many more smaller liver metastases of CRC, and these lesions showed rim-type fluorescence. Regarding this phenomenon, we used microscopy to observe the deformation of hepatocytes around the tumor, which occurred because of compression by the tumor, and this led to ICG retention. Additional subcapsular metastases that were only detected using NIR-FI were found in 25% (8/32) of patients in the ICG group. If these lesions had been missed, they would have caused a relapse soon after the operation, which would seriously influence the effect of surgical treatments or require another operation. However, 8% (6/73) of the nodules were found to be false-positive with the confirmation by histologic assessment. We did not find any bile duct proliferation, regenerative nodules, or atypical hyperplastic nodules in the resected tissues, which could explain the false-positive situation. This might account for the uptake and retention of the ICG associated with the impaired liver function. We also found that patients in the ICG group had shorter postoperative hospital stays, which could be related to the lower number of patients whose operations were converted to laparotomy. However, there were no statistical differences in the number of conversions to laparotomy between the 2 groups. This was likely due to the small sample size of the present study; therefore, further exploration and verification are required.

Conclusions

Because the CRLMs detected using NIR-FI were all superficial, with a maximum depth of 9 mm, we believe that this method should be used in combination with IOUS to take complete advantage of each method: IOUS can detect deep-located lesions with high sensitivity and NIR-FI can detect superficial tumors with high resolution and can provide real-time video navigation of the entire surgical process. Whether to achieve complete tumor resection with adequate margins is generally considered to be one of the most important predictors of recurrence and survival. In most cases, because of the inherent aggressiveness and invasiveness of tumors, the tumor boundary may be irregular or adjacent to blood vessels and functional nerves; thus, intraoperative decision making is very challenging and requires a trade-off between complete tumor resection and functional preservation. Based on our experience, NIR-FI is a good method to judge the tumor boundary not only before the resection, but also during and after the resection. In this study, the 1-year recurrence rate was significantly lower in the ICG group than in the non-ICG group, and this proves the usefulness of NIR-FI.

This study had some limitations, including the small sample size, short follow-up time, and possible biases because the surgeons were not blinded to the group assignments. In addition, because ICG does not have the ability to target CRLMs, it may lead to false positives. We plan to synthesize NIR probes that target CRC by coupling ICG with bevacizumab and to conduct multiple large-sample clinical trials or use visible and NIR-I/II instruments for multispectral imaging effective hepatectomy in patients with CRLMs.

Author Contributions

Study conception and design: He, Hong, Chi, J Li
Acquisition of data: Cai, P Li, Liu
Analysis and interpretation of data: He, Hong, Chi, An
Drafting of manuscript: He, Hong, Chi
Critical revision: Shan, Tian, J Li

Acknowledgment

The authors would like to acknowledge the instrumental and technical support of Multimodal Biomedical Imaging Experimental Platform, Institute of Automation, Chinese Academy of Sciences.

References

1. Arnold M, Sierra MS, Laversanne M, et al. Global patterns and trends in colorectal cancer incidence and mortality. Gut. 2017;66:683–691.
2. Siegel RL, Miller KD, Jemal A. Cancer statistics, 2020. CA Cancer J Clin. 2020;70:7–30.
3. Giannis D, Sideris G, Kakos CD, et al. The role of liver transplantation for colorectal liver metastases: A systematic review and pooled analysis. Transplant Rev (Orlando). 2020;34:100570.
4. Qin S, Liu GJ, Huang M, et al. The local efficacy and influencing factors of ultrasound-guided percutaneous microwave ablation in colorectal liver metastases: a review of a 4-year experience at a single center. Int J Hyperthermia. 2019;36:36–43.
5. Stewart CL, Warner S, Ito K, et al. Cytoreduction for colorectal metastases: liver, lung, peritoneum, lymph nodes, bone, brain. When does it palliate, prolong survival, and potentially cure? Curr Probl Surg. 2018;55:330–379.
6. Norén A, Sandström P, Gunnarsdottir K, et al. Identification of inequalities in the selection of liver surgery for colorectal liver metastases in Sweden. Scand J Surg. 2018;107:294–301.
7. Margonis GA, Sergentanis TN, Ntanasis-Stathopoulos I, et al. Impact of surgical margin width on recurrence and overall survival following R0 hepatic resection of colorectal metastases: a systematic review and meta-analysis. Ann Surg. 2018;267:1047–1055.
8. Larsen FO, Jensen BV, Nørgaard HH, et al. Intrahepatic oxaliplatin and systemic 5-FU +/- cetuximab in chemo-naïve patients with liver metastases from colorectal cancer. Oncology. 2019;96:299–308.
9. Creasy JM, Sadot E, Koerkamp BG, et al. Actual 10-year survival after hepatic resection of colorectal liver metastases: what factors preclude cure? Surgery. 2018;163:1238–1244.
10. De Falco V, Napolitano S, Roselló S, et al. How we treat metastatic colorectal cancer. ESMO Open. 2020;4[Suppl 2]:e000813.
11. Vallance AE, van der Meulen J, Kuryba A, et al. The timing of liver resection in patients with colorectal cancer and synchronous liver metastases: a population-based study of current practice and survival. Colorectal Dis. 2018;20:486–495.
12. Chiba N, Abe Y, Koganezawa I, et al. Efficacy of the Milan criteria as a prognostic factor in patients with colorectal liver metastases. Langenbecks Arch Surg. 2021;406:1129–1138.
13. Wong LH, Sutton TL, Walker BS, et al. Surgical and oncologic outcomes following repeat hepatic resection of colorectal liver metastasis: who benefits? Am J Surg. 2021;221:1114–1118.
14. Handgraaf HJM, Boogerd LSF, Höppener DJ, et al. Long-term follow-up after near-infrared fluorescence-guided resection of colorectal liver metastases: A retrospective multicenter analysis. Eur J Surg Oncol. 2017;43:1463–1471.
15. Xu J, Fan J, Qin X, et al.; China CRLM Guideline Group. Chinese guidelines for the diagnosis and comprehensive treatment of colorectal liver metastases (version 2018). J Cancer Res Clin Oncol. 2019;145:725–736.
16. Ren L, Zhu D, Benson AB 3rd, et al.; SINCE (Shanghai International Consensus Expert Group on Colorectal Liver Metastases) Group. Shanghai international consensus on diagnosis and comprehensive treatment of colorectal liver metastases (version 2019). Eur J Surg Oncol. 2020;46:955–966.
17. Coco D, Leanza S. Routine intraoperative ultrasound for the detection of liver metastases during resection of primary colorectal cancer - a systematic review. Maedica (Bucur). 2020;15:250–252.
18. van der Steen K, Bosscha K, Lips DJ. The value of laparoscopic intraoperative ultrasound of the liver by the surgeon. Ann Laparosc Endosc Surg. 2021;6:17.
19. Gossedge G, Vallance A, Jayne D. Diverse applications for near infra-red intraoperative imaging. Colorectal Dis. 2015;17[Suppl 3]:7–11.
20. Lauwerends LJ, van Driel PBAA, Baatenburg de Jong RJ, et al. Real-time fluorescence imaging in intraoperative decision making for cancer surgery. Lancet Oncol. 2021;22:e186–e195.
21. Chen QY, Xie JW, Zhong Q, et al. Safety and efficacy of indocyanine green tracer-guided lymph node dissection during laparoscopic radical gastrectomy in patients with gastric cancer: a randomized clinical trial. JAMA Surg. 2020;155:300–311.
22. Zhang RR, Schroeder AB, Grudzinski JJ, et al. Beyond the margins: real-time detection of cancer using targeted fluorophores. Nat Rev Clin Oncol. 2017;14:347–364.
23. He K, Zhou J, Yang F, et al. Near-infrared intraoperative imaging of thoracic sympathetic nerves: from preclinical study to clinical trial. Theranostics. 2018;8:304–313.
24. Peloso A, Franchi E, Canepa MC, et al. Combined use of intraoperative ultrasound and indocyanine green fluorescence imaging to detect liver metastases from colorectal cancer. HPB (Oxford). 2013;15:928–934.
25. van der Vorst JR, Schaafsma BE, Hutteman M, et al. Near-infrared fluorescence-guided resection of colorectal liver metastases. Cancer. 2013;119:3411–3418.
26. Hu Z, Fang C, Li B, et al. First-in-human liver-tumour surgery guided by multispectral fluorescence imaging in the visible and near-infrared-I/II windows. Nat Biomed Eng. 2020;4:259–271.
27. He K, Hong X, Chi C, et al. A new method of near-infrared fluorescence image-guided hepatectomy for patients with hepatolithiasis: a randomized controlled trial. Surg Endosc. 2020;34:4975–4982.
28. He K, Chi C, Li D, et al. Resection and survival data from a clinical trial of glioblastoma multiforme-specific IRDye800-BBN fluorescence-guided surgery. Bioeng Transl Med. 2021;6:e10182.
29. Kabir T, Syn N, Goh BKP. Current status of laparoscopic liver resection for the management of colorectal liver metastases. J Gastrointest Oncol. 2020;11:526–539.
30. Bredt LC, Rachid AF. Predictors of recurrence after a first hepatectomy for colorectal cancer liver metastases: a retrospective analysis. World J Surg Oncol. 2014;12:391.
31. Nitsche U, Weber C, Kaufmann B, et al. Simultaneous versus staged resection of colorectal cancer liver metastasis: a retrospective single-center study. J Surg Res. 2020;255:346–354.
32.Bogdanovic A, Despotovic J, Galun D, et al. Prognostic significance of CDH1, FN1 and VIM for early recurrence in patients with colorectal liver metastasis after liver resection. Cancer Manag Res. 2021;13:163–171.
33. Desolneux G, Isambert M, Mathoulin-Pelissier S, et al. Contrast-enhanced intra-operative ultrasound as a clinical decision making tool during surgery for colorectal liver metastases: the ULIIS study. Eur J Surg Oncol. 2019;45:1212–1218.
34. Onda N, Kimura M, Yoshida T, et al. Preferential tumor cellular uptake and retention of indocyanine green for in vivo tumor imaging. Int J Cancer. 2016;139:673–682.
35. Wang C, Tong F, Cao Y, et al. Long-term follow-up results of fluorescence and blue dye guided sentinel lymph node biopsy in early breast cancer. Breast Cancer Res Treat. 2021;188:361–368.
36. Majlesara A, Golriz M, Hafezi M, et al. Indocyanine green fluorescence imaging in hepatobiliary surgery. Photodiagnosis Photodyn Ther. 2017;17:208–215.

Hepatobiliary Surgery

Research Article

First-in-Human Liver-Tumour Surgery Guided by Multispectral Fluorescence Imaging in the Visible and Near-Infrared-I/II Windows

Zhenhua Hu[1,2,*], Cheng Fang[3,*], Bo Li[3,*], Zeyu Zhang[1,4,*], Caiguang Cao[1,2], Meishan Cai[1,2], Song Su[3], Xingwang Sun[3], Xiaojing Shi[1,2], Cong Li[1,2], Tiejun Zhou[3], Yuanxue Zhang[3], Chongwei Chi[1], Pan He[3], Xianming Xia[3], Yue Chen[3], Sanjiv Sam Gambhir[5] ✉, Zhen Cheng[5,#] and Jie Tian[1,2,4,6] ✉

Abstract

The second near-infrared wavelength window (NIR-II, 1,000–1,700 nm) enables fluorescence imaging of tissue with enhanced contrast at depths of millimetres and at micrometre-scale resolution. However, the lack of clinically viable NIR-II equipment has hindered the clinical translation of NIR-II imaging. Here, we describe an optical-imaging instrument that integrates a visible multispectral imaging system with the detection of NIR-II and NIR-I (700–900 nm in wavelength) fluorescence (by using the dye indocyanine green) for aiding the fluorescence-guided surgical resection of primary and metastatic liver tumours in 23 patients. We found that, compared with NIR-I imaging, intraoperative NIR-II imaging provided a higher tumour-detection sensitivity (100% versus 90.6%; with 95% confidence intervals of 89.1%–100% and 75.0%–98.0%, respectively), a higher tumour-to-normal-liver-tissue signal ratio (5.33 versus 1.45) and an enhanced tumour-detection rate (56.41% versus 46.15%). We infer that combining the NIR-I/II spectral windows and suitable fluorescence probes might improve image-guided surgery in the clinic.

[1] CAS Key Laboratory of Molecular Imaging, Beijing Key Laboratory of Molecular Imaging, The State Key Laboratory of Management and Control for Complex Systems, Institute of Automation, Chinese Academy of Sciences, Beijing, China.
[2] University of Chinese Academy of Sciences, Beijing, China.

Nat Biomed Eng. 2020. 4(3): 259-271 Published online: 23 December 2019

[3] Department of Hepatobiliary Surgery, Pathology and Nuclear Medicine, The Affiliated Hospital of Southwest Medical University, Luzhou, China.
[4] Engineering Research Center of Molecular and Neuro Imaging of Ministry of Education, School of Life Science and Technology, Xidian University, Xi'an, China.
[5] Molecular Imaging Program at Stanford, Bio-X Program, and Department of Radiology, Canary Center at Stanford for Cancer Early Detection, Stanford University, Stanford, CA, USA.
[6] Beijing Advanced Innovation Center for Big Data-Based Precision Medicine, School of Medicine, Beihang University, Beijing, China.
* These authors contributed equally: Zhenhua Hu, Cheng Fang, Bo Li, Zeyu Zhang.

Introduction

Fluorescence imaging in the near-infrared window I (NIR-I, 700–900 nm) has shown many benefits, in particular, high spatial and temporal resolution[1–7], not offered by other imaging modalities. It has gained recognition as a powerful technique and is expected to have an important role in a variety of clinical scenarios, for example, in fluorescence image-guided surgery and diagnostic imaging[8–12]. Besides several conventional small-molecule NIR dyes such as methylene blue, fluorescein sodium and indocyanine green (ICG), which were approved by the Food and Drug Administration for routine clinical use, many molecularly targeted fluorescent probes have been developed and are under active clinical evaluation, such as the folate receptor α-targeted fluorescent probe folate–FITC[13], the c-MET-targeted optical probe GE-137[14] and the epidermal growth factor receptor-targeted probe Cetuximab-IRDye800CW[15]. NIR-I fluorescence imaging is thus a promising approach for clinical applications.

Although NIR-I imaging performs better than imaging at visible wavelengths, recent advances in optical-imaging research have shown that imaging quality can be improved in living subjects by detecting in the second NIR window (NIR-II, 1,000–1,700 nm). This is mainly attributed to diminished tissue autofluorescence, reduced photon scattering and low levels of photon absorption at longer wavelengths[16,17]. Outstanding gains in performance when using the NIR-II window include light detection across centimetres of tissue, micrometre resolution at depths of millimetres and high target-to-background contrast, all achievable in real time.

However, NIR-II imaging has not been tested in a clinical environment, mainly because of a lack of suitable imaging instruments and optical probes. Although a variety of NIR-II optical probes, including nanoparticles, organic polymers and small-molecule dyes have been developed[18–29], these have not been tested in clinic. Recently, the conventional NIR-I dyes ICG and IRDye800CW have been found to show tail fluorescence in the NIR-II window[30], and clinically used ICG has been further proved to be suitable for NIR-II imaging with high performance in small-animal models[31,32]. These findings pave the way for the clinical translation of NIR-II imaging.

Motivated by these advances, we present the development of an integrated visible and NIR-I/II multispectral imaging instrument, and characterize its imaging performance at different infrared windows in phantom and animal studies. We also report the first-in-human study of visible, NIR-I and NIR-II multispectral imaging in 23 patients with liver cancer, injected with ICG, and compare the imaging performance of the NIR-I window with that of the NIR-II window in each patient, to evaluate the potential of intraoperative NIR-II fluorescence imaging and NIR-II image-guided surgery in the clinic (Fig. 1).

Results

Integrated visible and NIR-I/II multispectral imaging instrument for clinical use.

To translate the NIR-II imaging approach into the clinic, and understand its advantages and limitations over NIR-I imaging, we constructed an integrated visible and NIR-I/ II multispectral imaging instrument, covering the light spectrum range of 400–1,700 nm. This optical-imaging instrument consists of two sets of laser excitation equipment and three subsystems: NIR-II imaging, NIR-I imaging and visible light imaging for acquir- ing NIR-II fluorescence, NIR-I fluorescence and tissue anatomical information, respectively (Fig. 1b). The specific parameters of this instrument are listed in Supplementary Table 1. The multispectral instrument was easily placed in the surgical room for clinical use (Fig. 1c). Using the multispectral instrument, NIR-II and NIR-I imaging were performed in the operating room with illumination on and off, respectively (Supplementary Fig. 2a, NIR-II imaging; Supplementary Fig. 2b, NIR-I imaging).

NIR-I/II imaging of phantoms and tumour mice, and image-guided tumour resection.

To further study the performance of the developed imaging instrument, phantoms and tumour-bearing mice were used, and image-guided tumour resection in animal models was performed. In the phantom imaging study, both the NIR-II and NIR-I fluorescence signal intensities linearly correlated with the increasing concentration of ICG in fetal bovine serum (FBS) (Supplementary

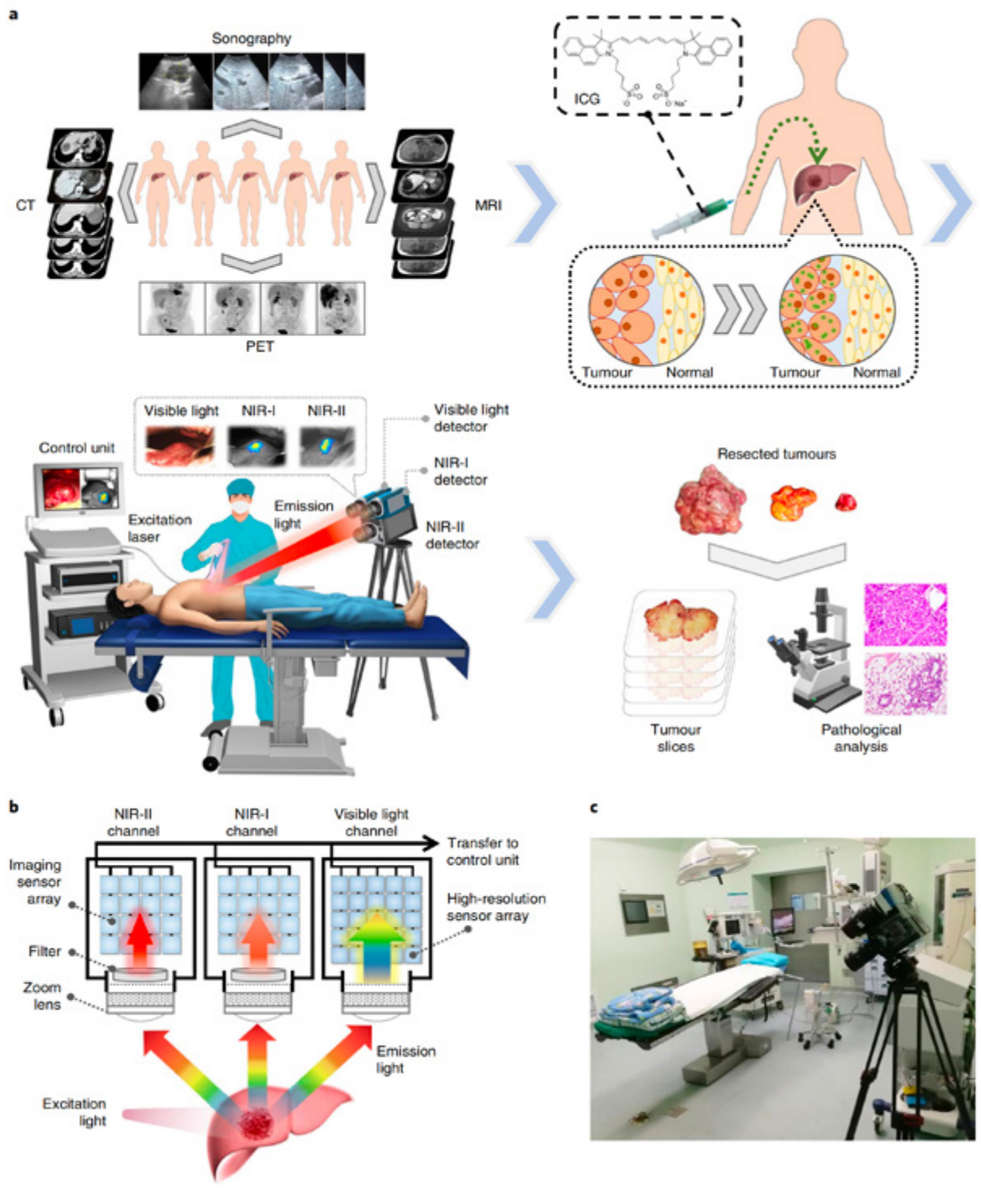


Fig.1 Description of the study plan and the visible and NIR-I/II multispectral imaging instrument for clinical applications. a, Patients with liver cancer were enroled in the study, and then received preoperative imaging examinations, including enhanced CT, MRI, ultrasonography and PET. Before surgery, the patients were injected with ICG intravenously at a dose of 0.5 mg kg−1 body weight as a routine preoperative liver function test. One to seven days later, on the day of surgery, the patients received a laparotomy. The liver surface was examined by the integrated NIR-I/II and visible multispectral imaging instrument and visible and NIR-I/II images were obtained. Tumours were resected by the guidance of ultrasonography and NIR-I imaging. During the resection, NIR-II images were also acquired. After the operation, visible and NIR-I/II images of the resected specimens were obtained. Pathological examination of the resected tissues was conducted. **b,** Schematic of the integrated visible and NIR-I/II multispectral imaging instrument. **c,** The customized visible and NIR-I/II multispectral imaging instrument placed in the operating room.

Nat Biomed Eng. 2020. 4(3): 259-271 Published online: 23 December 2019

Information and Supplementary Fig. 1a,b). Specifically, the correlation between NIR-I imaging intensity and ICG concentration was found to be $Y = 0.73 \times X + 0.69$ ($R^2 = 0.94$) for ICG in FBS (Supplementary Fig. 1b, left). Similarly, the correlation between NIR-II imaging intensity and ICG concentration was found to be $Y = 0.45 \times X + 0.19$ ($R^2 = 0.96$) for ICG in FBS (Supplementary Fig. 1b, right). Further quantitative analysis of the signal-to-background ratio (SBR) indicated that NIR-II imaging with ICG in FBS had a greater SBR, followed by NIR-I imaging with ICG in FBS (Supplementary Fig. 1c). For 4.5×10^{-3} mg ml^{-1} ICG, the SBR for NIR-II imaging and NIR-I imaging was 35.56 ± 0.26 and 16.85 ± 0.27, respectively. The minimum detectable concentration of ICG by the instrument was 77.4 fM for NIR-II imaging and 6.45 fM for NIR-I imaging, indicating the high sensitivity of the multispectral imaging instrument.

Moreover, both NIR-I and NIR-II imaging clearly differentiated three phantoms (prepared with ICG dissolved in FBS in capillary glass tubes) (Fig. 2a, first row). When these samples were covered by chicken breast tissue with a thickness of 2.0 mm, the phantoms remained clearly imaged and discriminated (Fig. 2a, second row). However, when 5.0 mm of chicken breast tissue was used, NIR-I imaging failed to distinguish the three phantoms, whereas NIR-II imaging was still capable of differentiating the three sources (Fig. 2a, third row), demonstrating the higher optical resolution of NIR-II over NIR-I. Lastly, both NIR-I and NIR-II detected signals from the phantoms, but NIR-I imaging failed to differentiate them, and NIR-II imaging was still capable of differentiating the three sources when 8 mm of chicken breast tissue was used as a cover (Fig. 2a, fourth row). Further quantitative analysis showed that the fluorescence signal intensity and SBRs obtained from NIR-I and NIR-II decreased with increasing depth of the phantoms (Fig. 2b,c). But regardless of the phantom depth, the SBRs of NIR-II were always significantly higher than those of NIR-I ($P < 0.01$) (Fig. 2c), indicating that better imaging quality was achieved by NIR-II over NIR-I using the multispectral imaging instrument.

NIR-I and NIR-II imaging of subcutaneous HepG2 tumour-bearing mice (n = 3 biologically independent animals per group) with tail-vein-injected ICG were further performed at 24 h post-injection. Both NIR-I and NIR-II imaging showed that ICG accumulated in the tumour and liver with good contrast (Fig. 2d). Tumours were then removed in both groups of mice under the guidance of fluorescence imaging. Quantitative analysis showed that both the NIR-I and NIR-II signal from the tumour region and tumour-to-normal-tissue ratio (TNR) markedly dropped after the resection (Fig. 2e,f). Quantitative analysis indicated that preoperative NIR-II imaging showed a significantly higher TNR than that of NIR-I (2.25 ± 0.06 versus 1.48 ± 0.04, $P < 0.001$), whereas postoperative NIR-II imaging showed a similar TNR to that of NIR-I (1.01 ± 0.02 versus 1.05 ± 0.04, $P = 0.24$) (Fig. 2f). Moreover, the SBR for liver (defined as the liver-signal-to-skin ratio) obtained from preoperative and postoperative NIR-II imaging were also significantly higher than those obtained from the corresponding NIR-I imaging ($P < 0.01$).

Intraoperative NIR-I/II imaging of patients with primary hepatocellular carcinoma, intrahepatic metastasis or extrahepatic metastasis.

Patients with liver cancer (n = 23) were enroled in the group (details of patient characteristics are listed in Supplementary Table 2), and they received preoperative imaging examinations, including enhanced computed tomography (CT), magnetic resonance imaging (MRI), ultrasonography and positron emission tomography (PET). Before surgery, the patients were injected with ICG intravenously at a dose of 0.5 mg kg^{-1} body weight as a routine preoperative liver function test. One to seven days later, on the day of surgery, the patients received a laparotomy. The liver surface was examined by the multispectral imaging instrument and visible, NIR-I and NIR-II images were obtained. Tumours were surgically resected by the guidance of intraoperative in vivo ultrasonography and NIR-I imaging, while in vivo NIR-II imaging was performed as a contrast. The resected tumours were also imaged with intraoperative ex vivo visible, NIR-I and NIR-II imaging.

The effects on image quality from environmental light were briefly tested. For a typical patient with liver cancer, the tumour could be identified in the visible light image using the multispectral instrument, as indicated by the white arrows in Supplementary Fig. 2c. We found that NIR-II imaging was barely affected by the illumination of operating room (Supplementary Fig. 2d). In contrast, NIR-I fluorescence was strongly disturbed and unable to be differentiated under room illumination (Supplementary Fig. 2e). In another patient, visible and NIR-II images of the liver surface were efficiently acquired with room illumination on (Supplementary Fig. 2f,g), whereas illumination off was necessary to acquire clear NIR-I tumour images (Supplementary Fig. 2h). Hence, in the following experiments, NIR-I imaging was always performed with room illumination off in this study.

For a typical patient with hepatocellular carcinoma (HCC), pre- operative enhanced CT showed a tumour located in liver segments VII and VIII (Couinaud segmentation) (Fig. 3a). The liver surface was visualized by visible light imaging (Fig. 3b). A nodule of liver cancer was successfully detected by an intense NIR-II and NIR-I fluorescence signal using intraoperative NIR-II and NIR-I imaging (Fig. 3c,d and Supplementary Fig. 8b,c). For a typical patient with intrahepatic metastasis, enhanced CT images showed two meta- static lesions in the liver (as one representative lesion, indicated by the red arrow in Fig. 3e). The multispectral instrument also detected the two intrahepatic metastases (Fig. 3f–h and Supplementary Fig. 8d-f) and visualized them, individually. For a typical patient with extrahepatic metastasis, both preoperative CT and PET imaging indicated primary liver cancer in liver segments II and III, but failed to detect the extrahepatic metastasis (Fig. 3i,j). After laparotomy, intraoperative NIR-II and NIR-I imaging revealed the metastatic lesion in the omentum (Fig. 3k–m and Supplementary Fig. 8g-i) and the peritoneum (data not shown). These results demonstrated that the combination of intraoperative NIR-II and NIR-I fluorescence imaging detected extrahepatic metastases overlooked by preoperative modalities, and that this finding changed the patient's staging and treatment options.

In these three representative examples, the white arrows correspond to the location and direction of cross-sectional fluorescence intensity profiles for both the NIR-II and NIR-I regions. The quantitative analysis results also showed that the NIR-II imaging discriminated a nodule of liver cancer more effectively compared with NIR-I (Fig. 3n). All the TNRs of NIR-II were much higher than those of NIR-I (primary HCC, 2.10 versus 1.07; intrahepatic metastasis, 2.83 versus 1.02 and 2.50 versus 1.01; extrahepatic metastasis, 1.19 versus 1.07). Further histopathological examination using hematoxylin and eosin (H&E) staining demonstrated that the dissected tumours were well-differentiated HCC (Fig. 3o, top), moderately differentiated HCC (Fig. 3o, middle) and moderately

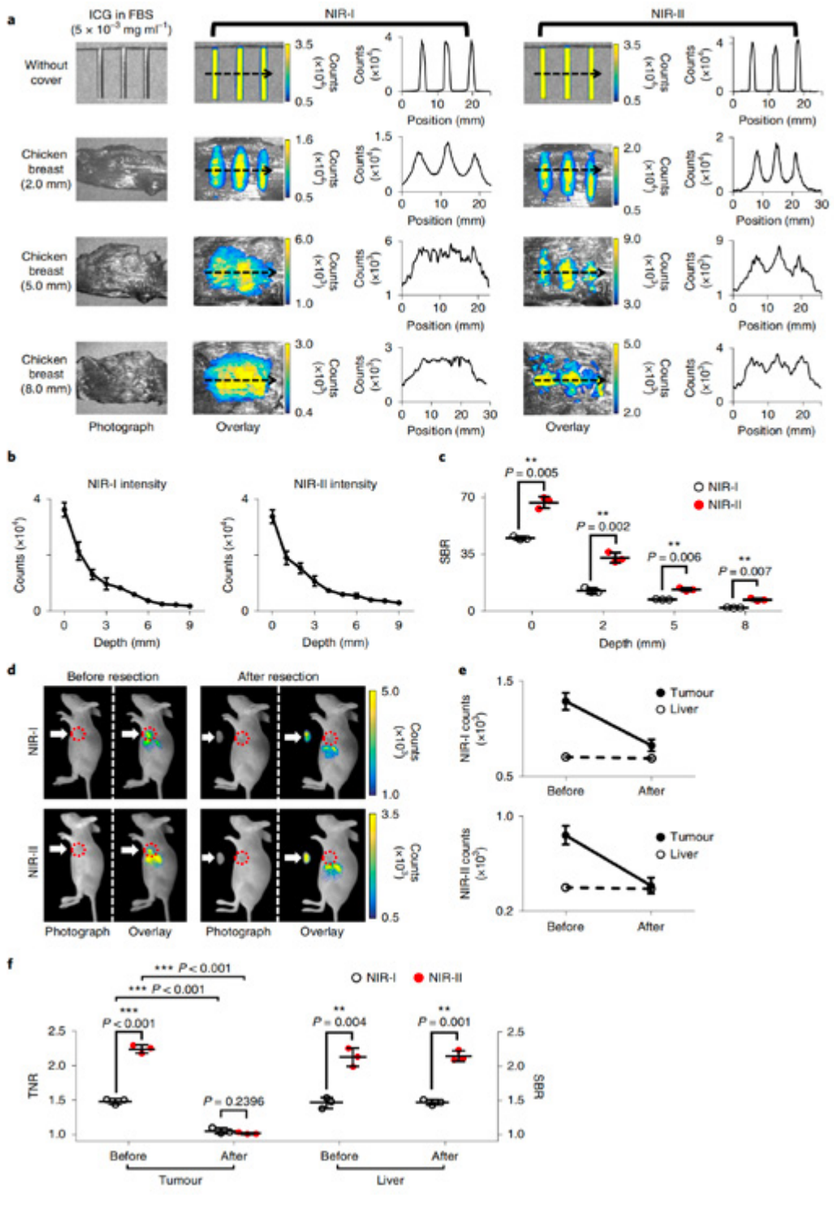


Fig.2 Comparison of the penetration and resolution of NIR-II and NIR-I imaging and the NIR-I/II image-guided tumour resection of subcutaneous HepG2 tumour-bearing mice. a, Visible light images and NIR-I/II images of the capillary glass tubes containing ICG dissolved in FBS. Arrows correspond to the location and direction of cross-sectional fluorescence intensity profiles for both the NIR-I and NIR-II regions. The capillary glass tubes were covered by chicken breast tissue with various thickness (1.0, 2.0, 3.0, 4.0, 5.0, 6.0, 7.0, 8.0 and 9.0 mm). **b,** The NIR-I/II fluorescence signal intensity decreased with increasing depth of the capillary glass tubes. **c,** There was a significant difference between the SBR of NIR-II and NIR-I imaging at various depths (P < 0.01). Significance was calculated by a two-sided Welch's t-test. **P < 0.01. **d,** The detection of the subcutaneous HepG2 tumour and image-guided resection by NIR-I/II imaging (first row and second row, resection guided by NIR-I and II imaging, respectively.). **e,** The NIR-I/II signal in the tumour position dropped dramatically after resection. **f,** Quantitative analysis indicated that preoperative NIR-II imaging showed a significantly higher TNR than that of NIR-I (2.25 ± 0.06 versus 1.48 ± 0.04, P < 0.001), whereas postoperative NIR-II imaging showed a slightly lower TNR than that of NIR-I but with no significant difference (1.01 ± 0.02 versus 1.05 ± 0.04, P = 0.2396). Significance was calculated by a two-sided Welch's t-test. **P < 0.01; ***P < 0.001. Data in b, c, e and f are mean ± s.d.

Nat Biomed Eng. 2020. 4(3): 259-271 Published online: 23 December 2019

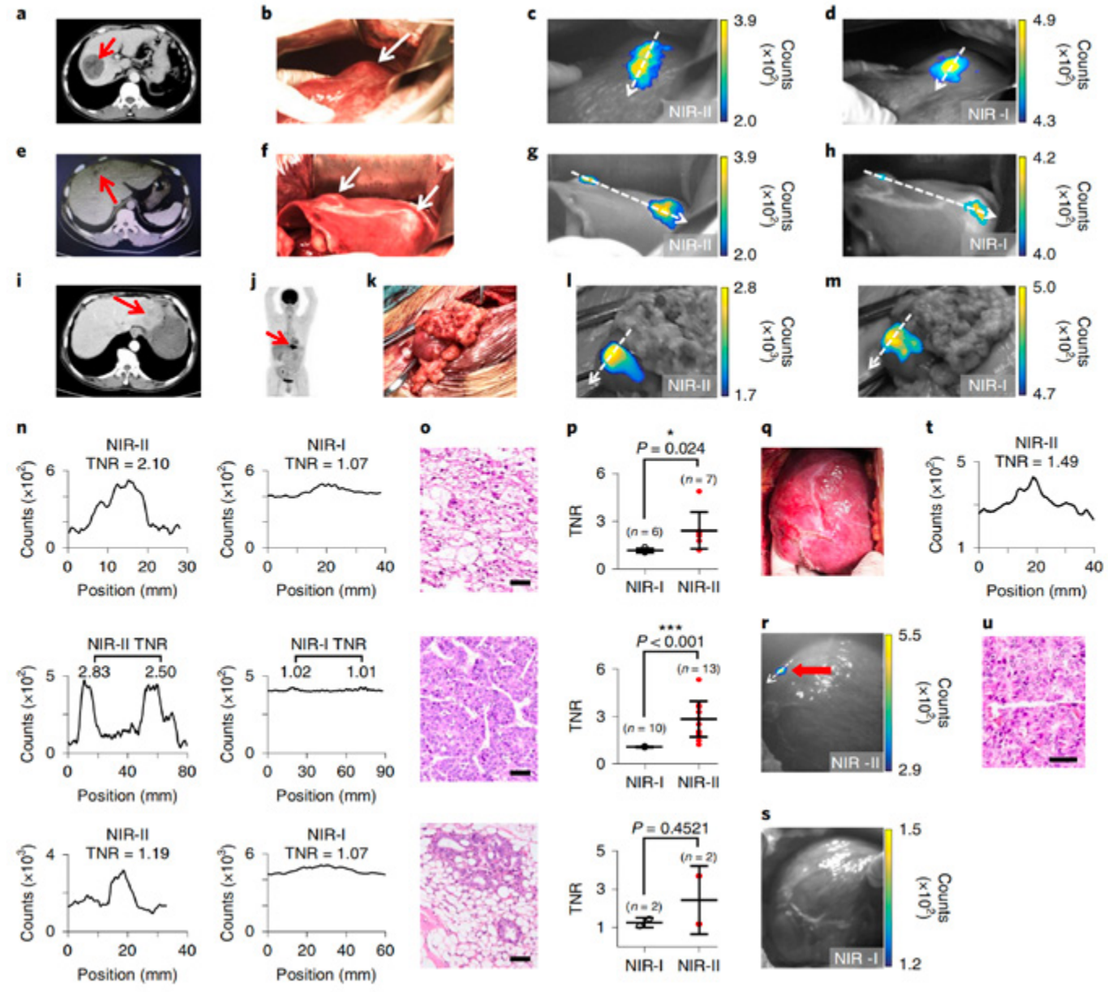


Fig.3 Intraoperative NIR-II/I imaging of patients with primary HCC, intrahepatic metastasis or extrahepatic metastasis. A total of 1,057 intraoperative fluorescence images, including 490 NIR-I images and 567 NIR-II images, were obtained. Additional results are included in Supplementary Figs. 2–8. **a,** For a typical patient with HCC, preoperative enhanced CT showed a tumour located in liver segments VII and VIII. **b,** The liver surface was visualized by visible light imaging with illumination from sunlight lamps in the surgery room. **c,d,** A nodule of liver cancer was successfully detected as intense NIR-II (c) and NIR-I (d) fluorescence signals using intraoperative NIR-II and NIR-I imaging. **e,** For a typical patient with intrahepatic metastasis, enhanced CT images showed two metastatic lesions in the liver (as one representative lesion indicated by the red arrow). **f–h,** The multispectral instrument detected two intrahepatic metastases, showing them separately, using visible light imaging (f), and intraoperative NIR-II (g) and NIR-I (h) imaging. **i–m,** For a typical patient with extrahepatic metastasis, preoperative CT (i) and PET (j) images clearly showed primary liver cancer in liver segments II and III and there was no extrahepatic metastasis. However, after the laparotomy, intraoperative NIR-II (l) and NIR-I (m) imaging found the metastatic lesion in the omentum (k). **n,** White arrows correspond to the location and the direction of cross-sectional fluorescence intensity profiles for both the NIR-II and NIR-I regions. The quantitative analysis results also showed that the NIR-II imaging discriminated a nodule of liver cancer more effectively compared with NIR-I. **o,** The H&E results showed that the tumours were well-differentiated HCC (top), moderately differentiated HCC (middle) and ICC (bottom). Scale bar, 50 μm. **p,** For all the patients with primary HCC (n = 11), NIR-II imaging achieved a significantly higher TNR over NIR-I imaging (P = 0.024, top). For all the patients with intrahepatic metastasis (n = 9), intraoperative NIR-II imaging showed a significantly higher TNR over NIR-I imaging (P < 0.001, middle). Lastly, it was found that the TNRs of NIR-II imaging obtained from two patients with extrahepatic metastasis were higher than those of NIR-I (bottom). Each point in the figure represents the result from one patient. Data are mean ± s.d. Significance was calculated by a two-sided Welch's t-test. *P < 0.05; ***P < 0.001. **q,** For a typical patient with HCC, the liver surface was visualized by visible light imaging. **r,** A small intrahepatic metastasis in the right liver was successfully detected by NIR-II imaging, as shown by the red arrow. **s,** However, NIR-I imaging failed to detect the lesion. **t,** The TNR of NIR-II was 1.49. **u,** Histopathological examination using H&E staining showed that the dissected lesion was moderately differentiated HCC. Scale bar, 50 μm.

differentiated cholangiocellular carcinoma (ICC) (Fig. 3o, bottom).

In this study, for all the patients with solitary HCC (n = 11), intraoperative NIR-II imaging detected seven HCC nodules, including two well-differentiated HCCs and five moderately differentiated HCCs. Intraoperative NIR-I imaging detected six HCC nodules, including two well-differentiated HCCs and four moderately differentiated HCCs. NIR-II imaging achieved a much higher TNR over NIR-I imaging (Fig. 3p, top; 2.43 ± 1.16 versus 1.17 ± 0.13, P = 0.024). For all the patients with intrahepatic metastasis (n = 9), intraoperative NIR-II imaging detected nine primary HCCs and four intrahepatic metastases, whereas NIR-I imaging detected seven primary HCCs and three intrahepatic metastases. Intraoperative NIR-II imaging also showed a much higher TNR over NIR-I imaging for these patients (Fig. 3p, middle; 2.83 ± 1.13 versus 1.07 ± 0.04, P < 0.001). Lastly, it was found that the TNRs of NIR-II imaging obtained from two patients with extrahepatic metastasis were higher than those of NIR-I (Fig. 3p, bottom).

We also found that NIR-II imaging was able to visualize some tumour lesions that were missed by NIR-I imaging. For example, the liver surface was visualized by visible light imaging in a patient with HCC (Fig. 3q). A small intrahepatic metastasis in the right liver was successfully detected by NIR-II imaging, as shown by the red arrow in Fig. 3r. However, NIR-I imaging failed to detect the lesion (Fig. 3s). The TNR of NIR-II was 1.49 (Fig. 3t). Histopathological examination using H&E staining showed that the dissected lesion was moderately differentiated HCC (Fig. 3u).

Intraoperative fluorescence image-guided tumour resection.

Tumour lesions recognized by surgeons first received visible light imaging by the multispectral imaging instrument (Fig. 4a). NIR-II fluorescence also identified the location of the tumour (Fig. 4b). The NIR-I fluorescence distribution pattern was consistent with that of the NIR-II image (Fig. 4c). Guided by ultrasonography and the visible light image, the tumour was resected and thought to be completely removed on the basis of the experience of the surgeons (Fig. 4d). Intraoperative ultrasonography also verified that there was no residual tumour (Fig. 4j). However, NIR-II and NIR-I imaging still detected fluorescence from the remaining tissue (Fig. 4e,f). Then, on the basis of the NIR-I images, further resection was per- formed. After this second resection, visual inspection indicated that there was no residual tumour (Fig. 4g), and optical imaging showed no NIR-II or NIR-I fluorescence in the remaining tissue either (Fig. 4h,i). The abovementioned two resected tissues were imaged and are shown in Fig. 4k,l, respectively. Quantitative analysis indicated that both the NIR-I and NIR-II signals from the tumour region had no obvious change after the first resection but hugely dropped after the second resection (Fig. 4m). For the first resection, the TNR of NIR-II imaging was also higher than that of NIR-I, and there was no difference for the TNR of NIR-II and NIR-I after the second resection (Fig. 4n). H&E staining showed that the two resected tumour tissues were both HCC (Fig. 4o). The results indicated that both intraoperative NIR-I and NIR-II imaging detected residual HCC, which were undetected by visual inspection and intraoperative ultrasonography.

NIR-II imaging also demonstrated the capability to delineate lesions that were missed by NIR-I imaging in the image-guided resection procedure. For a typical patient with HCC, guided by ultrasonography and the visible light image, the tumour was resected and considered to be completely removed on the basis of the experience of the surgeons (Fig. 4p). However, NIR-II imaging detected a residual fluorescent lesion (Fig. 4q) and NIR-I imaging failed to reveal any signals (Fig. 4r). This fluorescent lesion was con- firmed as abnormal by surgeons and then resected. Postoperative histopathological examination proved that the resected abnormal tissue was HCC (Fig. 4s).

NIR-I/II imaging of the resected specimens.

A typical primary HCC was resected and then clearly delineated ex vivo from intra- operative visible light, NIR-II and NIR-I images (Supplementary Fig. 3a–c). For a representative intrahepatic metastasis, the resected tumour specimen was sliced and imaged intraoperatively with the multispectral imaging instrument (Supplementary Fig. 3d–i). NIR-II and NIR-I imaging identified three extra lesions that were undetected by preoperative CT, as indicated by white and red arrows in Supplementary Fig. 3e–i. For an extrahepatic metastasis, on the basis of the NIR-I image, the metastatic lesion was resected (Supplementary Fig. 3j), and NIR-II and NIR-I fluorescence was observed from the resected tumour specimen (Supplementary Fig. 3k,l). The quantitative analysis showed that the NIR-II imaging discriminated lesions more effectively compared with NIR-I (Supplementary Fig. 3m–o). All the TNRs of NIR-II were much higher than those of NIR-I (primary HCC, 1.37 versus 1.04; intrahepatic metastasis, 2.63 versus 1.11 and 2.00 versus 1.24; extrahepatic metastasis, 5.73 versus 1.15). The H&E results demonstrated that the primary tumour was well-differentiated HCC (Supplementary Fig. 3p). For the intrahepatic metastases, one was found to be focal nodular hyperplasia (Supplementary Fig. 3q, number 1) and the other

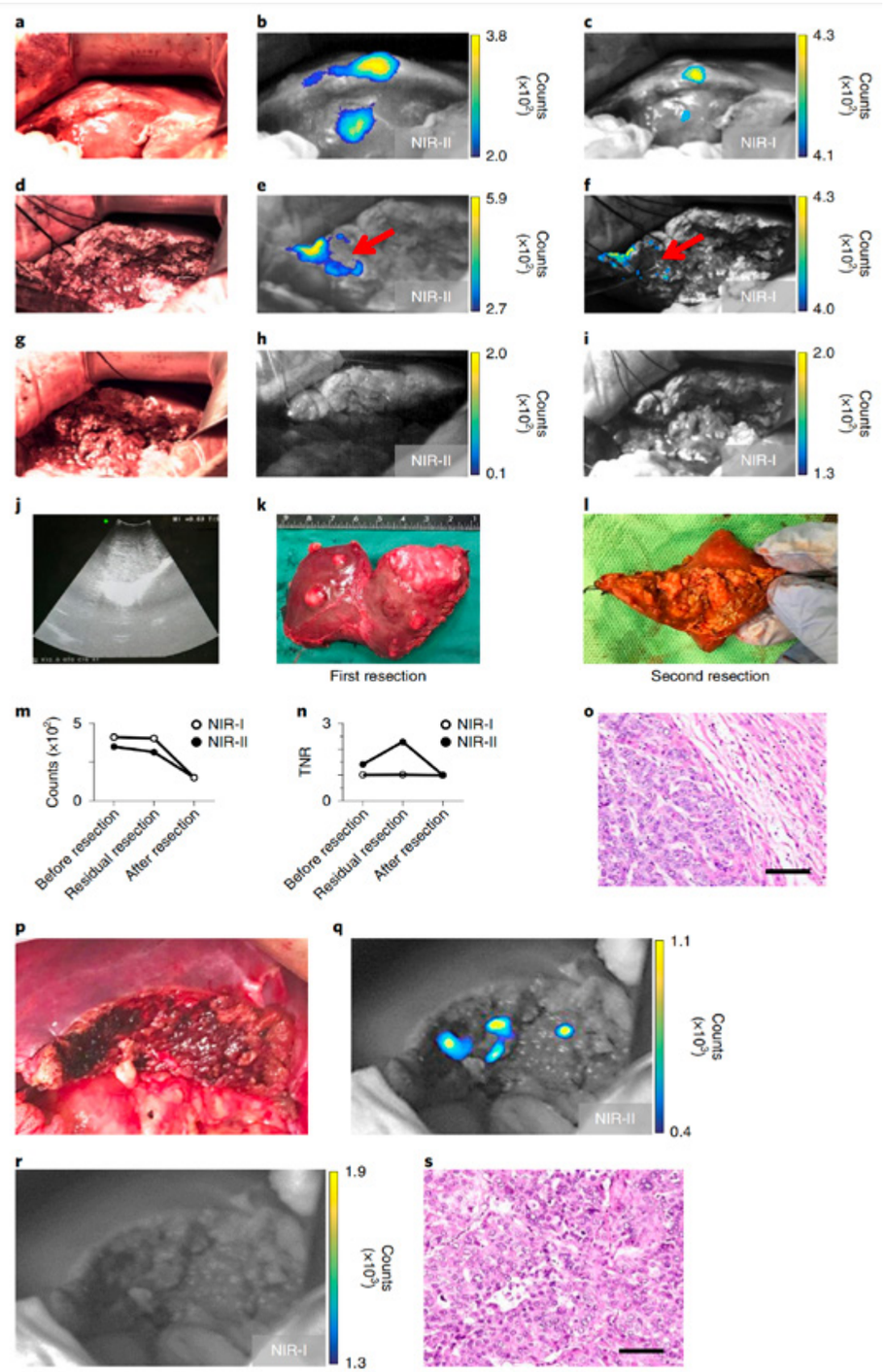


Fig.4 Intraoperative NIR-I/II fluorescence image-guided tumour resection. a, For a typical NIR-I image-guided surgery study, the visible image first showed a lesion in the liver tissue. **b,** NIR-II fluorescence also identified the location of the tumour. **c,** The NIR-I fluorescence distribution pattern was consistent with that of the NIR-II imaging. **d,** Guided by ultrasonography and the visible light image, the tumour was resected and thought to be completely removed on the basis of the experience of the surgeons. j, Intraoperative ultrasonography also verified there was no residual tumour. **e,f,** However, NIR-II (e) and NIR-I (f) imaging still detected fluorescence in the residual tissue (indicated by red arrows). Then, on the basis of the NIR-I image, further resection was performed. **g,** After this second resection, visual inspection indicated there was no residual tumour. **h,i,** Further, there was no NIR-II (h) or NIR-I (i) fluorescence signal in the residual tissue. **k,l,** The first (k) and second (l) resected tissues. **m,** Quantitative analysis indicated that both the NIR-I and NIR-II signals from the tumour region had no obvious change after the first resection, but hugely dropped after the second resection. **n,** For the first resection, the TNR of NIR-II imaging was also higher than that of NIR-I, and there was no difference for the TNR of NIR-II and NIR-I after the second resection. **o,** The two resected tumour tissues were shown to be HCC. Scale bar, 50 μm. **p,** For a typical patient with HCC, guided by ultrasonography and the visible light image, the tumour was resected and thought to be completely removed on the basis of the experience of the surgeons. **q,** NIR-II imaging detected fluorescence signals in the remaining tissue sections. **r,** NIR-I imaging did not reveal any signals. **s,** The fluorescent residual tissues were further resected and received histopathological examination to verify that the tissues were HCC. Representative H&E staining image showed that the resected lesion was HCC. Scale bar, 50 μm.

Nat Biomed Eng. 2020. 4(3): 259-271 Published online: 23 December 2019

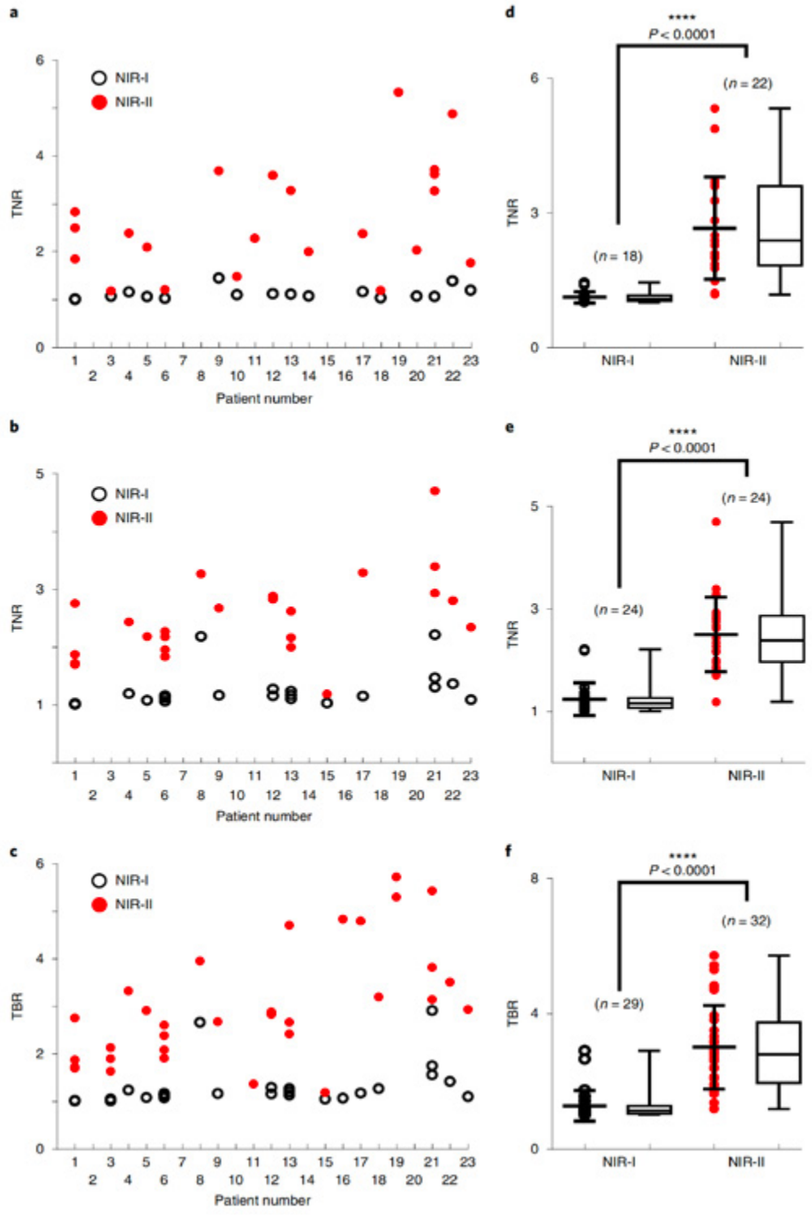


Fig.5 Comparison of TNR or TBR for NIR-II and NIR-I imaging. a, Quantitative analysis of the TNR of NIR-II and NIR-I imaging in the in vivo experiment. **b,** Quantification analysis of the TNR of NIR-II and NIR-I imaging in the ex vivo experiment. **c,** Quantitative analysis of the TBR of NIR-II and NIR-I imaging in the ex vivo experiment. Quantitative analysis of all patients clearly showed that the TNR or TBR for NIR-II imaging was much larger than that for NIR-I imaging both in the in vivo and ex vivo experiments. NIR-II, red solid circle; NIR-I, black hollow circle. **d,** In the in vivo experiment, there was a significant correlation difference between the TNR of NIR-II and NIR-I ($P < 0.0001$). The TNR of the NIR-II imaging results was obviously higher than that of the NIR-I results. **e,** In the ex vivo experiments, the TNR of NIR-II imaging was significantly higher than that of NIR-I imaging ($P < 0.0001$). **f,** In the ex vivo experiments, the TBR of NIR-II imaging was superior compared with NIR-I imaging ($P < 0.0001$). Data in d–f are mean ± s.d. Data range, median and quartiles are shown as box plots in d–f. Significance was calculated by a two-sided Welch's *t*-test. ****$P < 0.0001$.

two were shown to be HCC (Supplementary Fig. 3r,s, num- bers 2 and 3). The extrahepatic metastasis was shown to be HCC (Supplementary Fig. 3t).

For a typical patient with HCC (Fig. 3a–d), intraoperative NIR-II and NIR-I imaging detected the lesion (Fig. 3c,d). The intraoperative ultrasonography was used for demonstrating the position, depth and size of the tumour (Supplementary Fig. 4a). The resected fluorescent tissue (Supplementary Fig. 4b) was transversely incised into two parts along the maximum tumour diameter (Supplementary Fig. 4c). NIR-II and NIR-I fluorescence imaging was performed on the tumour specimen and no fluorescence was acquired in the normal liver tissues (Supplementary Fig. 4d, visible image; Supplementary Fig. 4e, NIR-II; Supplementary Fig. 4f, NIR-I). The quantitative analysis results showed that the NIR-II imaging discriminated lesions more effectively compared with NIR-I (Supplementary Fig. 4g,h).

For another typical patient with HCC (Supplementary Fig. 4i), intraoperative fluorescence imaging did not detect any lesions; however, the intraoperative ultrasonography detected a tumour at a depth of 20 mm (Supplementary Fig. 4j). The tumour was resected (Supplementary Fig. 4k). The specimen was transversely incised to expose the maximum tumour section, and was further sliced into pieces of approximately 10 mm thickness (Supplementary Fig. 4l). Every section received fluorescence imaging to detect all the tumour lesions. The NIR-II and NIR-I imaging results showed the cirrhotic nodule had no NIR-II or NIR-I fluorescence, while the tumour tissues were fluorescent (Supplementary Fig. 4m, visible image; Supplementary Fig. 4n, NIR-II; Supplementary Fig. 4o, NIR-I). The H&E results con- firmed that the tissue with the strongest optical signal (Supplementary Fig. 4m, arrow 1) was solid-type HCC (Supplementary Fig. 4p), the tissue with relatively weak fluorescence (Supplementary Fig. 4m, arrow 2) was glandular-type HCC (Supplementary Fig. 4q) and the non-fluorescent tissue (Supplementary Fig. 4m, arrow 3) was a cirrhotic nodule (Supplementary Fig. 4r). The quantitative analysis demonstrated again that NIR-II imaging had a stronger performance than NIR-I imaging in tumour identification (Supplementary Fig. 4s,t).

Comparison of imaging contrast ratio between NIR-I and NIR-II imaging.

The fluorescence intensity of tumour, normal liver tissue and ex vivo imaging background were plotted (Supplementary Fig. 9). The quantified data are listed in Supplementary Table 3. Tumour tissue, normal tissue or background could be differentiated by NIR-I or NIR-II fluorescence intensity. Notably, the differences between tumour signals and normal-tissue signals or background in NIR-II imaging were much more pronounced than those from NIR-I imaging, explaining why NIR-II imaging had improved performance in identifying lesions compared with NIR-I.

Quantitative analysis of all patients clearly showed that the TNR or tumour-to-background ratio (TBR) of NIR-II imaging was much higher than that of NIR-I imaging both in the in vivo and ex vivo imaging studies (Fig. 5a–c). The TNRs and TBRs of the NIR-I/II imaging studies are listed in Supplementary Table 6. In the in vivo imaging study, the mean TNR of NIR-II imaging was 2.66 ± 1.14, which was almost 2.4-fold higher than that of NIR-I (1.12 ± 0.12). The maximum TNR of in vivo NIR-II imaging and TBR of ex vivo NIR-II imaging were 5.33 and 5.72, respectively. However, the maximum TNR of in vivo NIR-I imaging and TBR of ex vivo

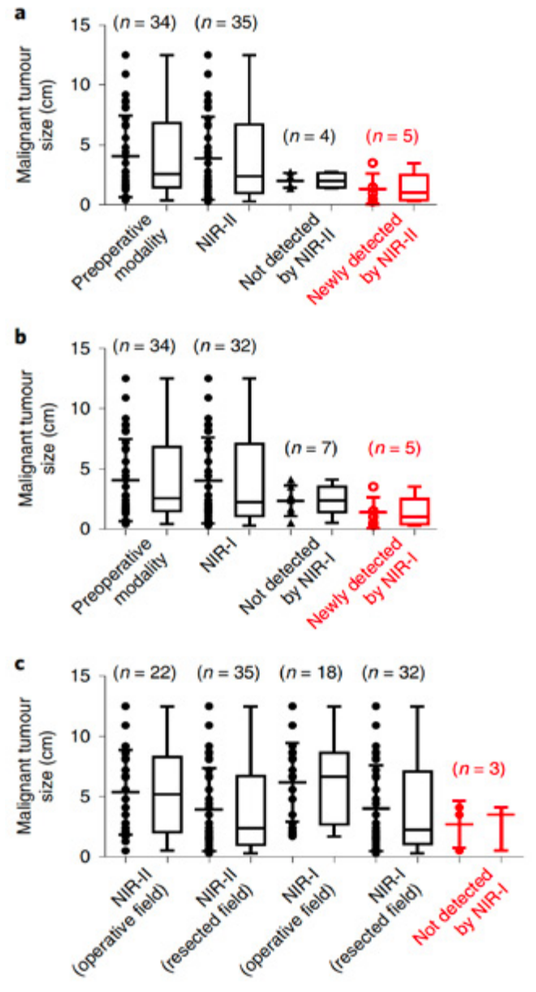


Fig.6 Comparison of tumour-detection ability of NIR-I/II imaging. a, Preoperative imaging modalities identified 34 lesions. A total 35 lesions were found by NIR-II imaging. NIR-II imaging identified 30 of 34 preoperatively diagnosed lesions. There were 4 of these 34 lesions that were not detected by NIR-II imaging. However, other than preoperatively diagnosed lesions, NIR-II fluorescence imaging visualized six new lesions. Five lesions were malignant and one was benign. **b,** NIR-I imaging detected a total of 32 lesions. NIR-I imaging identified 27 of 34 preoperatively diagnosed lesions. There were seven lesions that were not detected by NIR-I imaging. Besides the preoperatively diagnosed lesions, NIR-I fluorescence imaging also visualized six new lesions (five malignant lesions and one benign lesion). **c,** A total of 35 tumours were found by NIR-II imaging, including the in vivo intraoperative imaging and the ex vivo resected specimen imaging. Intraoperative NIR-II imaging visualized 22 lesions. The other 13 lesions were found in the sectioned specimens by NIR-II imaging. NIR-I imaging detected a total of 32 tumours: 18 tumours were detected in the intraoperative imaging and 14 tumours were detected in the resected specimen imaging. The 32 lesions detected by NIR-I imaging were all detected by NIR-II imaging. It is worth noting that NIR-II imaging found three extra tumours that could not be found by NIR-I imaging. Data range, median and quartiles are shown as box plots in a–c.

Table 1 Diagnostic results of NIR-II and NIR-I imaging

		Gold standard Positive	Gold standard Negative	CI	Sensitivity (%)	Specificity (%)	PPV	NPV	Accuracy
NIR-II	Positive	32	3	95%	100	88.46	91.43	100	91.43
	Negative	0	23		89.1-100	69.85-97.55	76.9-98.2	85.18-100	76.9-98.2
NIR-I	Positive	29	3	95%	90.63	88.46	90.63	88.46	82.86
	Negative	3	23		75.0-98.0	69.85-97.55	75.0-98.0	69.85-97.55	66.4-93.4

PPV, positive predictive value; NPV, negative predictive value.

NIR-I imaging were only 1.45 and 2.92, respectively. For both in vivo and ex vivo imaging studies, there was a significant improvement of the imaging contrast ratio in NIR-II compared with NIR-I (Fig. 5d–f; $P < 0.0001$ for in vivo and ex vivo). The distribution of the TNR/ TBR for NIR-II imaging was found to be mainly in the range of 2–4, much higher than that for NIR-I, which was mainly in the range of 1–2 (Fig. 5d–f).

Comparison of malignant tumour-detection ability of NIR-I and NIR-II imaging.

Overall, 23 patients had a total of 39 lesions including the primary tumour and metastases. Preoperative imaging modalities identified 34 malignant lesions. NIR-II imaging detected 35 malignant lesions and NIR-I identified 32 malignant lesions. The results are listed in Supplementary Table 7. NIR-II imaging identified 30 of 34 preoperatively diagnosed malignant lesions, including 20 lesions visualized by intraoperative in vivo NIR-II fluorescence imaging and the other 10 found in the sectioned specimens by intraoperative ex vivo NIR-II imaging. There were four lesions not detected by NIR-II imaging. However, other than preoperatively diagnosed lesions, NIR-II fluorescence imaging visualized five additional malignant lesions, including two detected by intraoperative in vivo NIR-II imaging and three found in NIR-II imaging of specimens (Fig. 6a).

NIR-I imaging identified 27 of 34 preoperatively diagnosed malignant lesions, including 17 lesions visualized by intraoperative in vivo NIR-I fluorescence imaging and the other 10 found by intraoperative ex vivo NIR-I imaging. There were seven lesions not detected by NIR-I imaging. However, other than preoperatively diagnosed lesions, NIR-I fluorescence imaging also visualized five additional malignant lesions, including one detected by intraoperative in vivo NIR-I imaging, and four found by ex vivo NIR-I imaging on specimens (Fig. 6b).

The six lesions newly detected by NIR-II or NIR-I imaging included three HCCs (three were moderately differentiated), two ICCs and one benign lesion (Supplementary Table 4). The benign lesion was later diagnosed as a focal nodular hyperplasia by histopathological analysis. Except one ICC, the diameter of the newly detected lesions was below 15 mm.

For the 35 tumours found by intraoperative NIR-II imaging, 22 tumours were visualized by in vivo imaging, and the other 13 tumours were found in the sectioned specimens by ex vivo imaging (Fig. 6c). Intraoperative NIR-I imaging detected 32 tumours in total: 18 tumours were detected in vivo and 14 tumours were detected in the resected specimen imaging. All of the 32 lesions detected by NIR-I imaging were also detected by NIR-II imaging. It is worth noting that NIR-II imaging found three extra tumours that were not detectable by NIR-I imaging.

The malignant tumour-detection rate of intraoperative in vivo NIR-II and NIR-I fluorescence imaging was calculated to be 56.41% (22/39, 95% confidence interval (CI) 39.6%–72.2%) and 46.15% (18/39, 95% CI 30.1%–62.8%), respectively. The detection rate was 100% (32/32, 95% CI 89.1%–100%) and 90.63% (29/32, 95% CI 75.0%–98.0%) for ex vivo NIR-II and NIR-I fluorescence imaging, respectively (Supplementary Table 5). Moreover, the detection sensitivity of NIR-II imaging was 100% (32/32, 95% CI 89.1%–100%) and its positive predictive value was 91.43% (32/35, 95% CI 76.9%– 98.2%), while the sensitivity of NIR-I imaging was 90.63% (29/32, 95% CI 75.0%–98.0%) and its positive predictive value was 90.63% (29/32, 95% CI 75.0%–98.0%) (Table 1). Lastly, the accuracy of tumour detection of NIR-II and NIR-I imaging was calculated to be 91.43% (32/35, 95% CI 76.9%–98.2%) and 82.86% (29/35, 95% CI 66.4%–93.4%), respectively.

Discussion

Fluorescence detection in the NIR-II window provides many advantages over the more conventional NIR-I imaging, including improved imaging depth sensitivity, higher spatial resolution and imaging contrast in small-animal models[15,16], and thus represents a promising field of study. Considering the interest in pursuing clinical NIR-I imaging, demonstrated by recent literature on the topic, and the potential utility that the NIR-I spectral window has for disease diagnosis and image-guided surgery[8–12], it is both crucial and urgent to determine whether NIR-II imaging provides similar benefits in clinical scenarios, and to evaluate its performance compared with NIR-I imaging. We have thus developed an integrated visible and NIR-II/I multispectral imaging instrument and performed the first-in-human study testing NIR-II imaging in a group of patients with liver cancer. The results will help to understand the potential role of NIR-II imaging in patient diagnosis and management, and to determine the advantages and limitations of both NIR windows in human applications.

The optical-imaging instrument covers the whole spectrum of visible, NIR-I and NIR-II light, providing the capability to image

Nat Biomed Eng. 2020. 4(3): 259-271 Published online: 23 December 2019

diseased tissue using a wide range of optical probes detectable in the NIR-I/II windows, and to directly compare the imaging performance of NIR-II and NIR-I in the same patients. An experiment carried out on a phantom containing ICG samples showed that the detection sensitivity of the multispectral instrument is 77.4 fM for NIR-II imaging and 6.45 fM for NIR-I imaging, suggesting that the instrument can detect targets with very low concentrations of contrast agent. It should also be noted that the higher sensitivity in vitro observed for ICG in the NIR-I over the NIR-II window is mainly attributed to the peak fluorescence emission intensity displayed by ICG in the NIR-I window, than in the tail-end of its emission in the NIR-II window.

Moreover, the phantom study shows that the optical resolution of NIR-II imaging is higher than that of NIR-I imaging. NIR-II imaging can distinguish three light sources underneath 8.0 mm of chicken breast tissue, whereas NIR-I imaging failed at this depth (Fig. 2a). Better imaging quality is also achieved using NIR-II imaging, compared with NIR-I, in small-animal models (Fig. 2d–f), mainly attributed to reduced tissue autofluorescence, reduced photon scattering and the low levels of photon absorption at longer wavelengths[15,16]. These results highlight the improved imaging performance of NIR-II over NIR-I, which are also consistent with previous findings[26,29–31].

Both in vivo and ex vivo intraoperative tumour imaging in patients clearly demonstrate that NIR-II imaging shows better image quality than NIR-I (Figs. 3 and 4). The TNRs or TBRs of NIR-II fluorescence imaging are significantly higher than that of NIR-I fluorescence imaging. During intraoperative in vivo imaging, the TNR of NIR-II imaging reached as high as 5.33, whereas the maximum TNR for NIR-I imaging was only 1.45 (Fig. 5). In the ex vivo imaging study, the TBR of NIR-II imaging was 5.72, almost twice the TBR of NIR-I imaging (only 2.92). Consistent with the high imaging contrast obtained for intraoperative NIR-II imaging, it also shows a higher malignant tumour-detection rate than that of NIR-I (in vivo imaging: 56.41% versus 46.15%; ex vivo imaging of resected specimens: 100% versus 90.63%) (Supplementary Table 5). This result is in line with the rate of HCC detection using intraoperative NIR-I fluorescence imaging (52–100%) or postoperative NIR-I imaging of resected tissue (100%) reported in the literature[33–36]. Moreover, the tumour-detection sensitivity of NIR-II and NIR-I imaging has been found to be 100% and 90.63%, and its positive predictive value is 91.43% and 90.63%, respectively (Table 1). Thus, NIR-II imaging shows a higher tumour-detection sensitivity and positive predictive value than that of NIR-I. All of these comparisons strongly suggest that NIR-II imaging is a better technique than NIR-I in clinical intraoperative liver-cancer imaging and image-guided surgery. A further advantage of using NIR-II imaging is its compliance with operating-room illumination, compared with NIR-I imaging that requires the lights to be switched off. This feature of NIR-II imaging provides convenience and feasibility for clinical applications. The advantages of complementing NIR-II and NIR-I for ICG detection during image-guided surgery of liver cancer are unclear. Further investigations of whether both windows can be combined to improve tumour imaging and treatment by using two or multiple probes specifically optimized for NIR-II and NIR-I imaging will be needed. The integrated imaging system developed in this study provides a solid foundation for this research direction.

Compared with the current preoperative imaging modalities (ultrasonography, MRI, CT) and intraoperative imaging techniques (ultrasonography), our studies show that intraoperative ICG-based NIR-I/II fluorescence imaging can detect the tumour lesions with no obvious imaging characteristics (Supplementary Table 7, Figs. 3 and 4, and Supplementary Fig. 3). After laparotomy, intraoperative NIR-I/II fluorescence imaging was able to detect the lesions missed by preoperative imaging modalities, which can substantially promote the accuracy of patient staging and management (Fig. 3). During surgery, NIR-I/II imaging can also identify residual lesions that are difficult to be recognized by surgeons or intraoperative ultrasonography (Fig. 4). Moreover, our imaging study revealed that ICG distributed quite uniformly in well-differentiated or moderately differentiated tumours, but partial-type and rim-type distributions were found in the poorly differentiated HCCs (Supplementary Fig. 5), which is consistent with previously reported findings[37].

However, using ICG for NIR-I/II fluorescence imaging has some limitations. In this study, ICG was selected for liver-cancer NIR-II imaging in patients because of its established use in the clinic. However, ICG is a non-targeted probe with suboptimal emission characteristics for NIR-II detection. It cannot distinguish malignant tumours from benign ones, and its accumulation in other tissues may lead to false positives (Table 1). It is expected that the performance of NIR-II imaging can be further improved with targeted probes that are purpose designed. Several IRDye-800CW-based probes are able to generate NIR-II fluorescence, although they are currently applied to NIR-I imaging. These dyes could be conjugated with tumour-targeted biomolecules (such as monoclonal antibodies or peptides) and used for NIR-II tumour imaging with the NIR-I/ II multispectral imaging system. Targeted fluorescent probes for NIR-II imaging could thus broaden the use of the multispectral imaging system for the detection of cancer and other diseases.

In summary, we have developed and applied an integrated visible and NIR-I/II multispectral imaging instrument with high detection sensitivity and resolution for the intraoperative NIR-II imaging of patients with cancer. Our study shows that NIR-II imaging has advantages over traditional NIR-I imaging in clinical scenarios, and thus highlights the promising clinical potential of intraoperative NIR-II fluorescence imaging and NIR-II image-guided surgery.

Methods

Study design

The goals of this study were to: (1) develop an integrated visible and NIR-I/II multispectral imaging instrument and technique for intraoperative fluorescence imaging and image-guided cancer surgery of patients; and (2) compare the NIR-II fluorescence imaging of the patients with NIR-I fluorescence imaging. We optimized the performance of the multispectral instrument, including the working distance, surgical field of view, imaging resolution, sensitivity and so on. Then, we demonstrated the feasibility of using the instrument to image HepG2 tumours and guide the tumour resection on mice. This pilot study of NIR-I/NIR-II imaging in patients with liver cancer has also been explored in a clinical trial (ChiCTR1900022453) in China.

Development of integrated visible and NIR-I/ II multispectral imaging instrument and image processing program

The optical-imaging instrument consists of two sets of laser

excitation equipment and the combined NIR-I/II and visible light imaging instrument. The NIR-II imaging subsystem is composed of a high-sensitivity InGaAs charge-coupled device (NIRvana 640, Teledyne Princeton Instruments) camera and lens (EF 24–70 mm F/2.8L II USM, Canon), connecting through an adapter that integrates an optical filter (1,000 nm LP, FEL1000, Thorlabs). The NIR-I imaging subsystem is composed of a high- sensitivity complementary metal–oxide–semiconductor (CMOS, PCO.edge 5.5m, PCO AG) and lens (EF 24–70 mm F/2.8L II USM, Canon). The lens and a filter (832 ± 18.5 nm BP, FF01-832/37, Semrock) are coupled with the CMOS camera using an adapter. Similarly, the visible imaging subsystem is made of a high-resolution colour-light CMOS camera (PCO.edge 5.5c, PCO AG) and a lens (EF 24–70 mm F/2.8L II USM, Canon). The excitation equipment includes the laser, optical fibre and beam expander. When the multispectral imaging instrument was operating, a 785 nm and 808 nm laser (output power 2.0 W, MW-GX-785 and MW-GX-808, Changchun Leirui Optoelectronic Technology) were employed as the excitation source for NIR-I and NIR-II imaging, respectively. The three subsystems operate independently from each other, to reduce the potential mutual interference and provide desirable performance in each spectrum range. A thermoelectric (Peltier) cooling method was adopted for all the subsystems, which conducted with high compatibility and little disturbance. Images of NIR-I, NIR-II and visible light were acquired in a parallel manner. The detailed information related to optics is presented in Supplementary Table 1.

A program was specially designed based on MATLAB (MathWorks) to pseudo-colour the fluorescence images intraoperatively. In this program, original images were firstly de-noised through median filtering (neighbourhood size 9 × 9). Then, fluorescence images were converted into pseudo-coloured according to pixel counts. High-intensity areas were shown with yellow, while blue represented low intensity. Moreover, a visualization threshold indicating signal intensity of normal tissues was intraoperatively assigned on the basis of surgeon diagnosis. Pixel counts above this threshold were pseudo-coloured, while the below part was identified as normal tissue signal and turned into transparent. The threshold could be adjusted for satisfying demands in different surgeries.

After acquisition of fluorescence and visible light images (NIR-II with LightField 6, Teledyne Princeton Instruments; NIR-I and visible light with Camware 4, PCO AG), the developed MATLAB program was immediately employed to generate pseudo-coloured results that presented the fluorescence intensity distribution. The generated pseudo-coloured results were overlaid on the white-light tissue images. Then, the surgeons were able to readily recognize the location of tumours and determine resection areas.

Phantom imaging study

To compare the penetration depth and resolution of NIR-I/II imaging, chicken breast tissues with various thicknesses were used to cover the capillary glass tubes (n = 3 per group) containing ICG (25 mg per kit, Dandong Yichuang Pharmaceutical, this product was approved for clinical use by China Food and Drug Administration) dissolved in FBS. The thicknesses used were: 1.0, 2.0, 3.0, 4.0, 5.0, 6.0, 7.0, 8.0 and 9.0 mm. Then, NIR-I/II fluorescence images were acquired. The relationships between the depth of the sources and the signal intensities or SBR were investigated.

In vivo mice imaging study

To study the feasibility of the multispectral imaging instrument for detecting and guiding resection of tumours, subcutaneous HepG2 carcinoma mouse models were established by the tumour-block transplant method. The HepG2 cell line and female athymic nude mice (n = 6 biologically independent animals, 4–6 weeks old, weight 17–25 g) were obtained from the Department of Experimental Animals (Academy of Military Medical Sciences). To establish mouse models, HepG2 tumour obtained from an orthotropic mouse model was split into several small blocks, and each block was approximately 2 mm^3. With isoflurane (RWD Life Science) anaesthetization, the mice received skin incision in the left front flank. Then a HepG2 block was implanted subcutaneously through the incision to each mouse, followed by incision closure. Povidone-iodine was used to disinfect during tumour model establishment. When tumours reached 7 mm in diameter around 20 d later, the HepG2 tumour-bearing mice (n = 3 biologically independent animals per group) were subjected to in vivo imaging studies. First, the mice were injected with ICG (0.1 mg ml^{-1}, 0.1 ml, diluted with sterile water for injection) through the tail vein, and at 24 h, the mice received NIR-II and NIR-I imaging for tumour detection and then NIR-II and NIR-I fluorescence image-guided tumour resection. A 500 ms exposure time was used for NIR-II imaging, while 300 ms exposure was used to acquire NIR-I images. The excitation laser power was 30–35 mW cm^{-2}. The excised tumour tissue was subjected to histopathological examination. All animal studies were approved by the Institutional Animal Care and Use Committee, Chinese Academy of Sciences. All procedures were carried out strictly in accordance with the appropriate institutional guidelines for animal research.

Patient characteristics

Patients were recruited from the Affiliated Hospital of Southwest Medical University in China between October 2017 and July 2018. Twenty-three patients with liver cancer were considered eligible for the study. Preoperative imaging modalities including CT, MRI, ultrasonography and PET were used to diagnose liver cancer (detailed information is provided in the Supplementary Information). Other inclusion criteria included an age of 18 years or older and written informed consent. Exclusion criteria were patient experience of claustrophobia, pregnancy or lactation. This study was approved by the Medical Ethics Review Committee of the Affiliated Hospital of Southwest Medical University and was registered at Chictr.org.cn. Baseline characteristics of all patients are shown in Supplementary Table 2. Surgical procedures were determined according to the American Joint Committee on Cancer (AJCC) liver-cancer resection standard and an ICG 15 min retention rate.

NIR-I/II imaging studies of patients

ICG (2.5 mg ml^{-1}, diluted with sterile water for injection) with a dose of 0.5 mg kg^{-1} body weight was injected intravenously within 1–7 d (mean 3.74 and median 4) before the surgery. In the operating room, after the laparotomy, the visual inspection, manual palpation and intraoperative ultrasonography (Pro Focus 2202, BK Medical) were first performed to examine whether there were any other metastatic tumours in the abdominal cavity. Liver tissues within 5 cm distance from the preoperatively detected lesion first received intraoperative ultrasonography. Then, the right hepatic lobe, left hepatic lobe, caudal hepatic lobe, hepatoduodenal ligament and other abdominal organs were scanned in sequence by intraoperative ultrasonography. In the right lobe, hepatic segments of S5, S8, S6 and S7 were successively scanned. In the left lobe, hepatic segments were scanned in the sequence S4, S2 and S3. Hepatic segment S1 was scanned in the caudal hepatic lobe. Any abnormal lesions detected by intraoperative ultrasonography were recorded. Subsequently, intraoperative in vivo NIR-I and NIR-II fluorescence imaging were used to examine the liver surface using the multispectral imaging instrument. An exposure time of 500 ms was set for NIR-II imaging, 300 ms for NIR-I imaging and 50 ms for visible imaging. The laser power for excitation was 30–50 mW cm^{-2} during NIR-I/II imaging. Illumination for visible imaging was provided by 28 W sunlight lamps installed on the ceiling of the surgery room.

For tumours detected by intraoperative in vivo NIR-I/II imaging, intraoperative ultrasonography was combined to confirm its depth, size and characteristics. The tumour was removed by the guidance of NIR-I fluorescence images. After resection, in vivo NIR-I and NIR-II fluorescence imaging were employed to determine whether there were residual lesions in the patient. The TNR was calculated as a parameter for the in vivo imaging study. The malignant tumour-detection rate was calculated, which was defined as the ratio of the malignant tumour number detected by ICG fluorescence imaging, including from both operative and resected fields, to the number of malignant tumours verified and detected by H&E examination.

Patient safety was assessed and graded according to the Common Terminology Criteria for Adverse Events (AE, version 5.0)[38] by monitoring vital signs and performing routine blood tests. Within the first 24 h after ICG injection, the research team kept in phone contact with each patient, monitoring for potential AE responses. We noted and analysed any possible side effects during the week following intraoperative NIR-I/II imaging.

NIR-I/II imaging studies in resected specimens

After tumour resection, the resected specimens were transversely incised along the maximum tumour diameter on the basis of surgeon diagnosis. Then, the specimens were further sliced into several pieces with a thickness of approximately 10 mm. Each of the tissue sections received intraoperative ex vivo NIR-I/II imaging, to detect all the tumour lesions. Lastly, tumour lesions underwent routine histopathological examination procedures. NIR-I/II fluorescence images were compared with the gold-standard H&E stained images. The TNR was also calculated as a parameter to the resected tissue along with normal liver tissue, and the TBR was used for the tumour specimen without normal liver tissue. Fluorescence from black paper, placed underneath the resected tissue, was used as the background.

Statistical analysis

To investigate the relationship between the NIR-II and NIR-I imaging, a two-sided Welch's *t*-test was employed to compare the quantitative data between two independent samples. Quantitative results are expressed as mean ± s.d.).

Reporting Summary

Further information on research design is available in the Nature Research Reporting Summary linked to this article.

Acknowledgements

This study was supported by the National Key Research and Development Program of China (2017YFA0205200, 2016YFC0102600), National Natural Science Foundation of China (NSFC) (81930053, 61622117, 81671759, 81227901), the Chinese Academy of Sciences (GJJSTD20170004), Beijing Natural Science Foundation (JQ19027), Beijing Nova Program (Z181100006218046), the Scientific Instrument Developing Project of the Chinese Academy of Sciences (YZ201672), the innovative research team of high-level local universities in Shanghai, and the Zhuhai High-level Health Personnel Team Project (Zhuhai HLHPTP201703). We acknowledge the instrumental and technical support of the multi-modal biomedical imaging experimental platform, Institute of Automation, Chinese Academy of Sciences.

Author contributions

J.T., Z.C. and Z.H. conceived the idea of the project. Z.H. wrote the manuscript in addition to designing, performing and analysing all experiments. Z.H., C.F., B.L. and Z.Z. performed the experiments. S.S., P.H. and X.X. collected the information on patients with liver cancer. X. Sun., T.Z. and Y.Z. assisted with histology. Y.C. assisted with PET/ CT imaging. C. Cao., M.C., X. Shi., C.L. and C. Chi. assisted with data analysis. Z.C. and S.S.G. assisted with experimental design, manuscript preparation and data/image analysis. J.T. designed, supervised and analysed all experiments, in addition to assisting with manuscript preparation.

Competing interests

The authors declare no competing interests.

References

1. James, M. L. & Gambhir, S. S. A molecular imaging primer: modalities, imaging agents, and applications. Physiol. Rev. 2012; 92: 897–965.
2. Vahrmeijer, A. L., Hutteman, M., van der Vorst, J. R., van de Velde, C. J. & Frangioni, J. V. Image-guided cancer surgery using near-infrared fluorescence. Nat. Rev. Clin. Oncol. 2013; 10: 507–518.
3. Vinegoni, C. et al. Indocyanine green enables near-infrared fluorescence imaging of lipid-rich, inflamed atherosclerotic plaques. Sci. Transl. Med. 2011; 3: 84ra45.
4. Choi, H. S. et al. Targeted zwitterionic near-infrared fluorophores for improved optical imaging. Nat. Biotechnol. 2013; 31: 148–153.
5. Tichauer, K. M. et al. Microscopic lymph node tumor burden quantified by macroscopic dual-tracer molecular imaging. Nat. Med. 2014; 20: 1348–1353.
6. Pan, Y. et al. Endoscopic molecular imaging of human bladder cancer using a CD47 antibody. Sci. Transl. Med. 2014; 6: 260ra148.
7. Miller, J. et al. Perfusion-based fluorescence imaging method delineates diverse organs and identifies multifocal tumors using generic near-infrared molecular probes. J. Biophoton. 2018; 11: e201700232.
8. van Manen, L. et al. A practical guide for the use of indocyanine green and methylene blue in fluorescence-guided abdominal surgery. J. Surg. Oncol. 2018; 118: 283–300.
9. Tipirneni, K. E. et al. Oncologic procedures amenable to fluorescence-guided surgery. Ann. Surg. 2017; 266：36–47.
10. Hutteman, M. et al. Randomized, double-blind comparison of indocyanine green with or without albumin premixing for near-infrared fluorescence imaging of sentinel lymph nodes in breast cancer patients. Breast Cancer Res. Treat. 2011; 127: 163–170.
11. Gurtner, G. C. et al. Intraoperative laser angiography using the SPY system: review of the literature and recommendations for use. Ann. Surg. Innov. Res. 2013; 7: 1.
12. Koller, M. et al. Implementation and benchmarking of a novel analytical framework to clinically evaluate tumor-specific fluorescent tracers. Nat. Commun. 2018; 9: 3739.
13. Van Dam, G. M. et al. Intraoperative tumor-specific fluorescence imaging in ovarian cancer by folate receptor-α targeting: first in-human results. Nat. Med. 2011; 17: 1315–1319.
14. Burggraaf, J. et al. Detection of colorectal polyps in humans using an intravenously administered fluorescent peptide targeted against c-Met. Nat. Med. 2015; 21: 955–961.
15. Rosenthal, E. L. et al. Sensitivity and specificity of cetuximab-IRDye800CW to identify regional metastatic disease in head and neck cancer. Clin. Cancer Res. 2017; 23: 4744–

4752.
16. He, S., Song, J., Qu, J. & Cheng, Z. Crucial breakthrough of second near-infrared biological window fluorophores: design and synthesis toward multimodal imaging and theranostics. Chem. Soc. Rev. 2018; 47: 4258–4278.
17. Hong, G., Antaris, A. L. & Dai, H. Near-infrared fluorophores for biomedical imaging. Nat. Biomed. Eng. 2017; 1: 0010.
18. Dang, X. et al. Layer-by-layer assembled fluorescent probes in the second near-infrared window for systemic delivery and detection of ovarian cancer. Proc. Natl Acad. Sci. USA. 2016; 113:5179–5184.
19. Hong, G. et al. Multifunctional in vivo vascular imaging using near-infrared II fluorescence. Nat. Med. 2012; 18: 1841–1846.
20. Robinson, J. T. et al. In vivo fluorescence imaging in the second near-infrared window with long circulating carbon nanotubes capable of ultrahigh tumor uptake. J. Am. Chem. Soc. 2012; 134: 10664–10669.
21. Hong, G. et al. Near-infrared II fluorescence for imaging hindlimb vessel regeneration with dynamic tissue perfusion measurement. Circ. Cardiovasc. Imaging. 2014; 7: 517–525.
22. Sun, Y. et al. Novel benzo-bis(1,2,5-thiadiazole) fluorophores for in vivo NIR-II imaging of cancer. Chem. Sci. 2016; 7: 6203–6207.
23. Zhang, X. D. et al. Traumatic brain injury imaging in the second near-infrared window with a molecular fluorophore. Adv. Mater. 2016; 28: 6872–6879.
24. Wang, R., Zhou, L., Wang, W., Li, X. & Zhang, F. In vivo gastrointestinal drug-release monitoring through second near-infrared window fluorescent bioimaging with orally delivered microcarriers. Nat. Commun. 8, 14702 (2017).
25. Cheng, K. et al. Synthesis, characterization, and biomedical applications of a targeted dual-modal near-infrared-II fluorescence and photoacoustic imaging nanoprobe. ACS Nano. 2017; 11: 12276–12291.
26. Wan, H. et al. A bright organic NIR-II nanofluorophore for three-dimensional imaging into biological tissues. Nat. Commun. 2018; 9: 1171.
27. Antaris, A. L. et al. A small-molecule dye for NIR-II imaging. Nat. Mater. 2016;15: 235–242.
28. Sun, Y. et al. Novel bright-emission small-molecule NIR-II fluorophores for in vivo tumor imaging and image-guided surgery. Chem. Sci. 2017; 8: 489–3493.
29. Sun, Y. et al. Novel dual-function near-infrared II fluorescence and PET probe for tumor delineation and image-guided surgery. Chem. Sci. 2018; 9: 2092–2097.
30. Antaris, A. L. et al. A high quantum yield molecule-protein complex fluorophore for near-infrared II imaging. Nat. Commun. 2017; 8: 15269.
31. Carr, J. A. et al. Shortwave infrared fluorescence imaging with the clinically approved near-infrared dye indocyanine green. Proc. Natl Acad. Sci. USA. 2018; 115: 4465–4470.
32. Starosolski, Z. et al. Indocyanine green fluorescence in second near-infrared (NIR-II) window. PLoS ONE. 2017; 12: e0187563.
33. Gotoh, K. et al. A novel image-guided surgery of hepatocellular carcinoma by indocyanine green fluorescence imaging navigation. J. Surg. Oncol. 2009; 100: 75–79.
34. Ishizawa, T. et al. Real-time identification of liver cancers by using indocyanine green fluorescent imaging. Cancer. 2009; 115: 2491–2504.
35. Morita, Y. et al. Detection of hepatocellular carcinomas with near-infrared fluorescence imaging using indocyanine green: its usefulness and limitation. Int. J. Clin. Oncol. 2013; 18: 232–241.
36. Ishizawa, T. et al. Mechanistic background and clinical applications of indocyanine green fluorescence imaging of hepatocellular carcinoma. Ann. Surg. Oncol. 2014; 21: 440–448.
37. Shimada, S., Ohtsubo, S., Ogasawara, K. & Kusano, M. Macro- and microscopic findings of ICG fluorescence in liver tumors. World J. Surg. Oncol. 2015; 13: 198.
38. Common Terminology Criteria for Adverse Events (CTCAE) Version 5.0 (US Department of Health and Human Services. 2017.
39. Hu, Z. et al. Dataset for first-in-human liver tumour surgery guided by multispectral fluorescence imaging in the visible and near-infrared-I/II windows. figshare. 2019.

Eur J Nucl Med Mol Imaging. 2022. 49(8): 2929–2937 Published online: 1 March 2022

Gynecology

Research Article

Intraoperative Near-Infrared Fluorescence Imaging Can Identify Pelvic Nerves in Patients with Cervical Cancer in Real Time During Radical Hysterectomy

Kunshan He[1,2,3,4,*], Pengfei Li[5,*], Zeyu Zhang[1,2,*], Jiaqi Liu[5,*], Pan Liu[5], Shipeng Gong[5], Chongwei Chi[3] ✉, Ping Liu[5] ✉, Chunlin Chen[5] ✉ and Jie Tian[1,2,3] ✉

Abstract

Purpose: Radical hysterectomy combined with pelvic lymphadenectomy is the standard treatment for early-stage cervical cancer, but unrecognized pelvic nerves are vulnerable to irreversible damage during surgery. This early clinical trial investigated the feasibility and safety of intraoperative near-infrared (NIR) fluorescence imaging (NIR-FI) with indocyanine green (ICG) for identifying pelvic nerves during radical hysterectomy for cervical cancer.

Methods: Sixty-six adults with cervical cancer were enrolled in this prospective, open-label, single-arm, single-center clinical trial. NIR-FI was performed in vivo to identify genitofemoral (GN), obturator (ON), and hypogastric (HN) nerves intraoperatively. The primary endpoint was the presence of fluorescence in pelvic nerves. Secondary endpoints were the ICG distribution in a nerve specimen and potential underlying causes of fluorescence emission in pelvic nerves.

Results: In total, 63 patients were analyzed. The ON was visualized bilaterally in 100% (63/63) of patients, with a mean fluorescence signal-to-background ratio (SBR) of 5.3±2.1. The GN was identified bilaterally in 93.7% (59/63) of patients and unilaterally in the remaining 4 patients, with a mean SBR of 4.1±1.9. The HN was identified bilaterally in 81.0% (51/63) of patients and unilaterally in 7.9% (5/63) of patients, with a mean SBR of 3.5±1.3. ICG fluorescence was detected in frozen sections of a nerve specimen, and was mainly distributed in axons. No ICG-related complications were observed.

Conclusion: This early clinical trial demonstrated the feasibility and safety of NIR-FI to visualize pelvic nerves intraoperatively. Thus, NIR-FI may help surgeons adjust surgical decision-making, avoid nerve damage, and improve surgical outcomes.
Trial registration: ClinicalTrials.gov NCT04224467

Keywords
Near-infrared fluorescence imaging, Indocyanine green, Pelvic nerves, Radical hysterectomy, Cervical cancer

[1] Beijing Advanced Innovation Center for Big Data-Based Precision Medicine, School of Engineering Medicine, Beihang University, Beijing, 100191 China
[2] Key Laboratory of Big Data-Based Precision Medicine (Beihang University), Ministry of Industry and Information Technology, Beijing, 100191 China
[3] CAS Key Laboratory of Molecular Imaging, The State Key Laboratory of Management and Control for Complex Systems, Institute of Automation, Chinese Academy of Sciences, Beijing, 100190 China
[4] State Key Laboratory of Computer Science and Beijing Key Lab of Human-Computer Interaction, Institute of Software, Chinese Academy of Sciences, Beijing, China
[5] Department of Obstetrics and Gynecology, Nanfang Hospital, Southern Medical University, Guangzhou, China
* Kunshan He, Pengfei Li, Zeyu Zhang and Jiaqi Liu contributed equally to this work.

Introduction

Cervical cancer is the fourth most common cancer in women worldwide[1]. The 5-year survival rate of stage III or IV cervical cancer is less than 30%, and its incidence tends to occur in younger ages in recent years[2]. Radical hysterectomy combined with pelvic lymphadenectomy is one of the most effective treatments for cervical cancer[3]. However, as the pelvic nerves are difficult to recognize and are vulnerable, the surgical outcome is limited by irreversible neural damage[4].

Unfortunately, damage to the pelvic nerves can result in severe motor, sensory, and autonomic dysfunction. As reported previously, the incidence of genitofemoral nerve (GN) damage is 3.5%, and causes paresthesia in the groin and perineum[5]. The incidence of obturator nerve (ON) injury is 1%, which may reduce thigh adduction and induce slight abnormal sensations in the inner thigh skin[6]. Furthermore, 30–80% of patients undergoing traditional radical hysterectomy have bladder, rectal, or sexual dysfunction, mainly caused by pelvic autonomic nerve injury[4]. Intraoperative nerve visualization is considered crucial to reducing pelvic nerve damage[7]. Clinically, the identification of pelvic nerves mainly depends on visual inspection, which relies heavily on the surgeon's experience[8]. Methods such as nerve stimulation have been employed to identify nerves; however, the procedure is complex and the effect is limited. Consequently, there has been a growing desire to develop novel nerve visualization methods[9, 10].

Currently, emerging near-infrared (NIR) fluorescence imaging (NIR-FI) is playing an increasingly important role in surgery[11, 12]. Because of its increased penetration depth, lower autofluorescence, and higher sensitivity, NIR-FI has been applied in tumor detection, lymphangiography, and vascular perfusion assessment[13–16]. Clinical observations have also revealed its potential to image nerves intraoperatively. Using widely employed fluorophore indocyanine green (ICG), we previously reported the feasibility of intraoperative NIR-FI for distinguishing thoracic sympathetic nerves in 15 patients with lung cancer[17].

Based on these findings, we hypothesized that intraoperative NIR-FI with ICG could be a new method for real-time identification of pelvic nerves during surgery. This early clinical trial investigated the feasibility and safety of intraoperative NIR-FI for identifying pelvic nerves during radical hysterectomy in patients with cervical cancer.

Methods

Study design

This prospective, open-label, single-arm clinical trial was approved by the Medical Ethics Committee of Nanfang Hospital of Southern Medical University (Ethics no. NFEC-2019-146), and registered at ClinicalTrials.gov (NCT04224467). The primary objective of this early clinical trial was to investigate the feasibility and safety of NIR-FI with ICG for identifying the pelvic nerves. Secondary endpoints were the distribution of ICG in a nerve specimen and potential underlying causes of fluorescence emission in pelvic nerves. Sixty-six patients with cervical cancer were enrolled and provided written informed consent before inclusion between February 2020 and June 2021. The inclusion criteria were as follows: cervical cancer with preoperative FIGO staging IB1-IIA2 (FIGO 2018 staging system), age >18 years, and scheduled for radical hysterectomy combined with pelvic lymphadenectomy. The exclusion criteria were as follows: a history of pelvic surgery, radiotherapy, or chemotherapy; pregnancy; and considered unsuitable for enrollment by clinicians.

Contrast agent

ICG (25 mg per vial) was purchased from Dandong Yichuang Pharmaceutical Co. Ltd., China. ICG has been approved for clinical use for more than 60 years, with good safety and fluorescence performance (peak absorption/emission, 800/830 nm)[18]. Each vial of ICG was dissolved in its own 10 ml injectable water as the stock solution. After an allergy test, intravenous infusion of ICG (5 mg/kg) diluted in 500 ml saline was administered 24 h prior to surgery based on our previous study of thoracic sympathetic nerves NIR-FI[17].

Fluorescence imaging

NIR-FI with ICG in vivo was performed using a DPM-I system (Zhuhai Dipu Medical Technology Co., Ltd.) developed for open surgery, in accordance with our previous studies[19, 20]. In brief, DPM-I consists of a hybrid light source generating two wavelength-isolated lights: 1200 lm of 420–700 nm light and 35 mW/cm^2 of 785 nm light. The fluorescence and color images were simultaneously acquired using custom optics and software at a work distance of 15–30 cm. Color images, fluorescence images, or merged images, or all three images together can be displayed as needed, with a resolution of 1280×1024. The depth of the imaging object from the surface should be within 10 mm. During pelvic lymphadenectomy, when the external iliac lymph nodes were removed, NIR-FI was used to visualize the GN on the lateral side of the external iliac artery and the surface of the psoas muscle. Similarly, the ON was visualized in the obturator space when the obturator lymph node was resected. During the radical hysterectomy, when the vaginal and lateral rectal spaces were opened, and the ureteral mesentery was exposed, the hypogastric nerve (HN) was visualized by fluorescence.

Histopathologic analysis

In one patient, the HN was accidentally cut off during exposure to the mesoureter. With the patient's consent, the nerve was used for histopathological analysis. Frozen transverse and longitudinal sections of the nerve (thickness, 10 mm) were prepared in a standard fashion and stored at −20°C for pathological analysis. Anti-myelin basic protein (MBP) antibody (1:200; ABN912, Sigma, St. Louis, MO, USA) was used to label the myelin sheath, rabbit anti-NF 200 antibody (1:800; N4142, Sigma, St. Louis, MO, USA) was used to label axons, and DAPI (1:5,000; Sigma, St. Louis, MO, USA) was used for nuclear staining. Fluorescence microscopy was performed using a laser confocal microscope (LSM980, Zeiss, Germany).

Cell tests

Human umbilical vein endothelial cells (HUVECs), vascular smooth muscle cells (VSMCs), and hepatic cells (HL-7702) were purchased from the cell bank of the Chinese Academy of Sciences (Shanghai, China) and cultured in DMEM medium containing 10% fetal bovine serum (FBS) and 1% penicillin-streptomycin solution (Gibco) in a humidified incubator (5% CO_2 at 37°C). Neurons and Schwann cells were obtained by primary cell culture, as described by Wen et al.[21].

ICG transport test

The uptake and secretion of ICG were compared between neurons, Schwann cells, HUVECs, VSMCs, and hepatic cells. Briefly, the cells in 12-well plates (counted as 2×10^5 cells/well) were incubated with 0.5 mg/ml ICG-containing medium. After incubation for 5 min, the cells were washed four times with 1 ml of phosphate buffered saline (PBS) and subsequently lysed with 300 µl of 1% Triton-X100 in PBS. Concentrations of ICG uptake were measured with a spectrophotometer (Varioskan Flash, Thermo Fisher Scientific) at 805 nm, using a standard curve. For the ICG secretion test, after incubation with ICG (0.5 mg/ml) for 5 min, the cells were washed four times with 1 ml of PBS; the medium was then replaced with DMEM containing 10% FBS and 1% penicillin-streptomycin solution. After incubation for 12 h, intracellular residual ICG concentrations were measured as described above.

Statistical analysis

The specific fluorescence of each identified pelvic nerve in vivo was analyzed based on intraoperatively recorded images. For each case, the fluorescence signal-to-background ratio (SBR) of the pelvic nerves relative to adjacent tissues was calculated three times to reduce deviation. First, regions of interest (ROIs) were delineated over the fluorescent pelvic nerves and surrounding tissue using ImageJ software (National Institutes of Health, USA). For each ROI, the mean fluorescence intensity was expressed within a range of 0–255, allowing the calculation of the SBR.

All statistical analyses were performed using SPSS 23.0 statistical software (Statistical Product and Service Solutions, Chicago, USA). Categorical variables are expressed as whole numbers and percentages, and were compared using the chi-square test. Continuous variables are expressed as mean ± standard deviation. One-way analysis of variance was used to compare SBRs among nerves. Multiple linear regression was used to estimate the impact of clinicopathological characteristics on the SBR of the ON, GN, and HN, including age, height, weight, preoperative FIGO stage, histology, differentiation, stromal invasion, lymphovascular space invasion (LVSI), parametrial tumor involvement, and lymphatic metastasis. P-values of 0.05 or less were considered statistically significant.

Results

Patient characteristics

Sixty-six consecutive patients were initially enrolled in this study. However, two patients temporarily refused intravenous ICG therapy before the surgery. Additionally, one patient

was intraoperatively diagnosed with suspected lymph node metastasis, which was confirmed by frozen pathology after lymph node biopsy; systematic pelvic lymphadenectomy and radical hysterectomy were not performed. Thus, 63 patients were analyzed. Their clinicopathologic characteristics are shown in Table 1. No ICG-related adverse events occurred in any patient.

Table 1 The clinicopathologic characteristics of patients (n=63)

Characteristics	Value	Percentage
Age (years)	49.41±10.317	
Histologic type		
Squamous cell	51	80.95
Adenocarcinoma	9	14.29
Adenosquamous	3	4.76
Cervical conization		
No	53	84.13
Yes	10	15.87
Preoperative FIGO stage		
IB1	24	38.10
IB2	13	20.63
IB3	4	6.35
IIA1	16	25.40
IIA2	6	9.52
Final FIGO stage		
IB1	18	28.57
IB2	8	12.70
IB3	3	4.76
IIA1	14	22.22
IIA2	3	4.76
IIB	2	3.17
IIC1P	15	23.81
Stromal invasion		
Superficial	22	34.92
Deep	41	65.08
Lymphovascular space invasion		
Negative	49	77.78
Positive	14	22.22
Parametrium		
Negative	61	96.83
Positive	2	3.17
Surgical margin		
Negative	61	96.83
Positive	2	3.17
Pelvic lymph nodes metastasis		
Negative	48	76.19
Positive	15	23.81

FIGO, International Federation of Gynecology and Obstetrics

Pelvic nerve NIR-FI

Using DPM-I with ICG, the ON was successfully identified bilaterally (Fig. 1a–c) in all patients, and the mean SBR of the ON was 5.3±2.1 (Table 2). The GN (Fig. 1d–f) was identified bilaterally in 93.7% (59/63) of patients and unilaterally in the remaining 4 patients. The mean SBR of the GN was 4.1±1.9. The HN (Fig. 1g–i) was identified bilaterally in 81.0% (51/63) of patients and unilaterally in 7.9% (5/63) of patients; the HN was not identified in 11.1% (7/63) of patients. The mean SBR of the HN was 3.5±1.3. The above three SBR values are high enough to assist surgeons in identifying the corresponding nerves during surgery, and there was no statistical difference among them (p=0.13). Moreover, a strong fluorescent signal lasted until the end of the operation in all cases, and no obvious intensity changes were observed during the entire operation. The longest observed fluorescence duration was 245 min.

On multiple linear regression, the SBR of the OB, ON, and HN was not related to the preoperative FIGO stage, age, weight, height, histology, differentiation, stromal invasion, LVSI, surgical margin invasion, parametrial tumor involvement, or lymph node metastasis (all p>0.05).

Pathologic findings

Fluorescent microscopy confirmed the presence of ICG fluorescent signal in the HN specimen, with fluorescence signals mainly in the cytoplasm rather than in the nucleus (Fig. 2a–d). Confocal laser scanning microscopy (CLSM) images revealed that the red ICG fluorescence overlapped with the green fluorescence of axons labeled with anti-NF 200 antibody (Fig. 2e–f), but showed little overlap with myelin sheath labeled by anti-MBP antibody (Fig. 2g–h). In other words, the ICG fluorescent signal was mainly distributed in the axons of the nerve specimen.

Cell test findings

After incubation with an ICG-containing medium for 5 min, ICG fluorescent signals were detected in all cells on CLSM images. Figure 3a–d shows that ICG can be absorbed by neuronal cells. The internalized ICG of neurons, Schwann cells, HUVECs, VSMCs, and HL-7702 cells was 1.46±0.15, 1.43±0.17, 1.48±0.23, 1.45±0.18, and 1.39±0.24 μg/10^6 cells, respectively. The internalized ICG did not significantly differ among cell types (p=0.97), as shown in Fig. 3e. In the ICG secretion test, after incubation with ICG (0.5 mg/ml) for 5 min and DMEM medium for 12 h, the residual ICG in neuronal cells was 0.61±0.31 μg/10^6 cells, which was significantly higher than that in other cell types (p=0.003), as shown in Fig. 3f.

Discussion

Here, we investigated the feasibility and safety of intraoperative NIR-FI using the DPM-I system with ICG to identify the pelvic nerves in a prospective trial. To the best of our knowledge, this is the first clinical trial of intraoperative NIR-FI with ICG for identifying the pelvic nerves during radical hysterectomy for cervical cancer. The bilateral identification rates of the ON, GN, and HN were 100% (63/63), 93.7% (59/63), and 81.0% (51/63), respectively. Pathological results and cell tests confirmed our

Eur J Nucl Med Mol Imaging. 2022. 49(8): 2929–2937 Published online: 1 March 2022

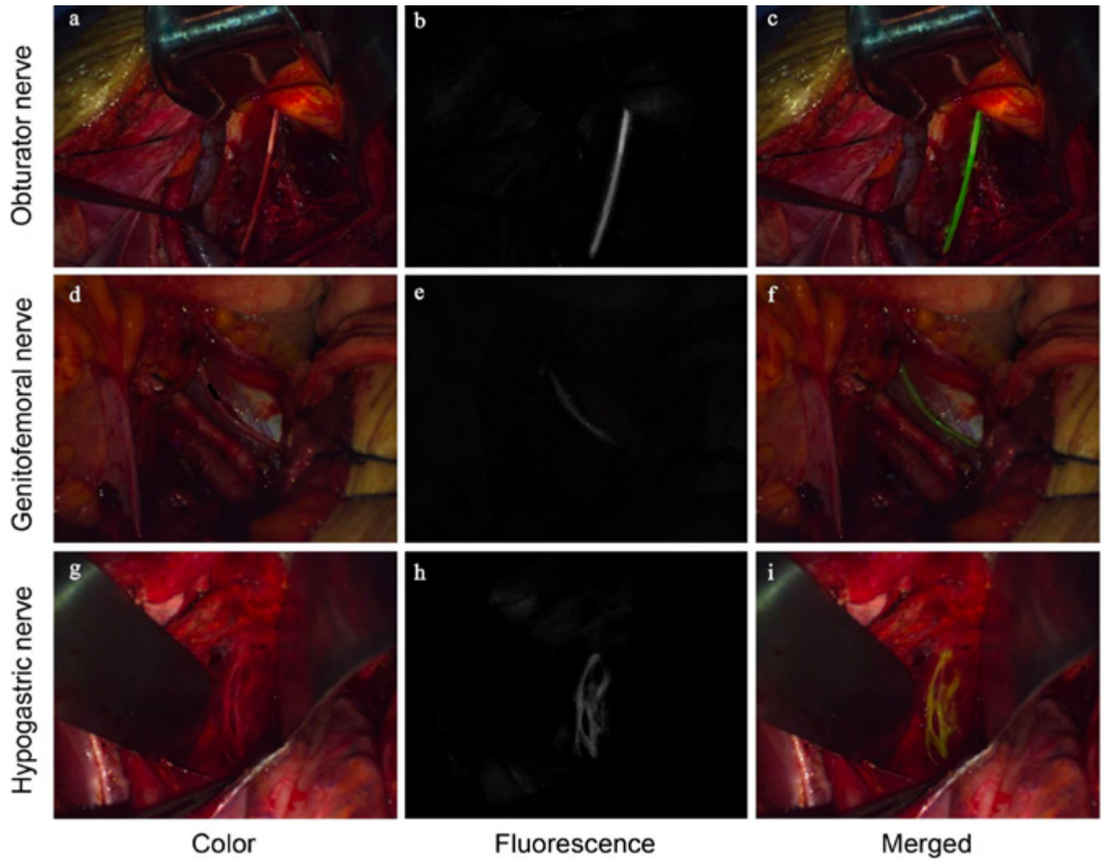


Fig.1 Representative images of the **a–c** obturator, **d–f** genitofemoral, and **e–h** hypogastric nerves

Table 2 The mean signal-to-background ratio of pelvic nerves

Pelvic nerves	SBR	*P* value
Obturator nerve	5.3±2.1	
Genitofemoral nerve	4.1±1.9	0.13
Hypogastric nerve	3.5±1.3	

findings, suggesting that this may be a new method for identifying pelvic nerves that may significantly reduce functional damage and improve surgical outcomes.

Although a cure is the main goal of surgery, the protection of important structures, such as nerves, is also critical to achieving the best patient prognosis[22, 23]. Iatrogenic nerve injury is one of the most frightening complications in surgical procedures, as well as a major source of morbidity in all surgical specialties[24]. In patients with cervical cancer undergoing radical hysterectomy combined with pelvic lymphadenectomy, extensive removal of the peri-cervix ligaments (uterosacral, main, and bladder-cervical ligaments, and paravaginal tissue) and para-aortic fibrous connective tissue is commonly applied[23]. Therefore, the pelvic nerves, including the ON, GN, and HN, are vulnerable to damage, which may cause bladder, anorectal, and sexual dysfunction[6, 25]. More seriously, approximately 50% of patients with these symptoms will suffer for life.

Because most nerves are relatively thin and located under the surrounding tissues, it is difficult for even experienced surgeons to identify them with the naked eye during surgery[26]. Furthermore, previous radiotherapy or surgery may lead to fibrotic tissue deposition and atypical surgical anatomical planes, rendering nerve recognition more challenging[24]. Currently, in some surgical procedures, surgeons use optical coherence tomography, Raman spectroscopy, or confocal laser endomicroscopy to help identify nerves. However, these methods lack widefield imaging capabilities. Intraoperative ultrasound has also shown potential in superficial nerve visualization, but its low resolution and lack of specificity hinder its clinical application. Electromyography, which

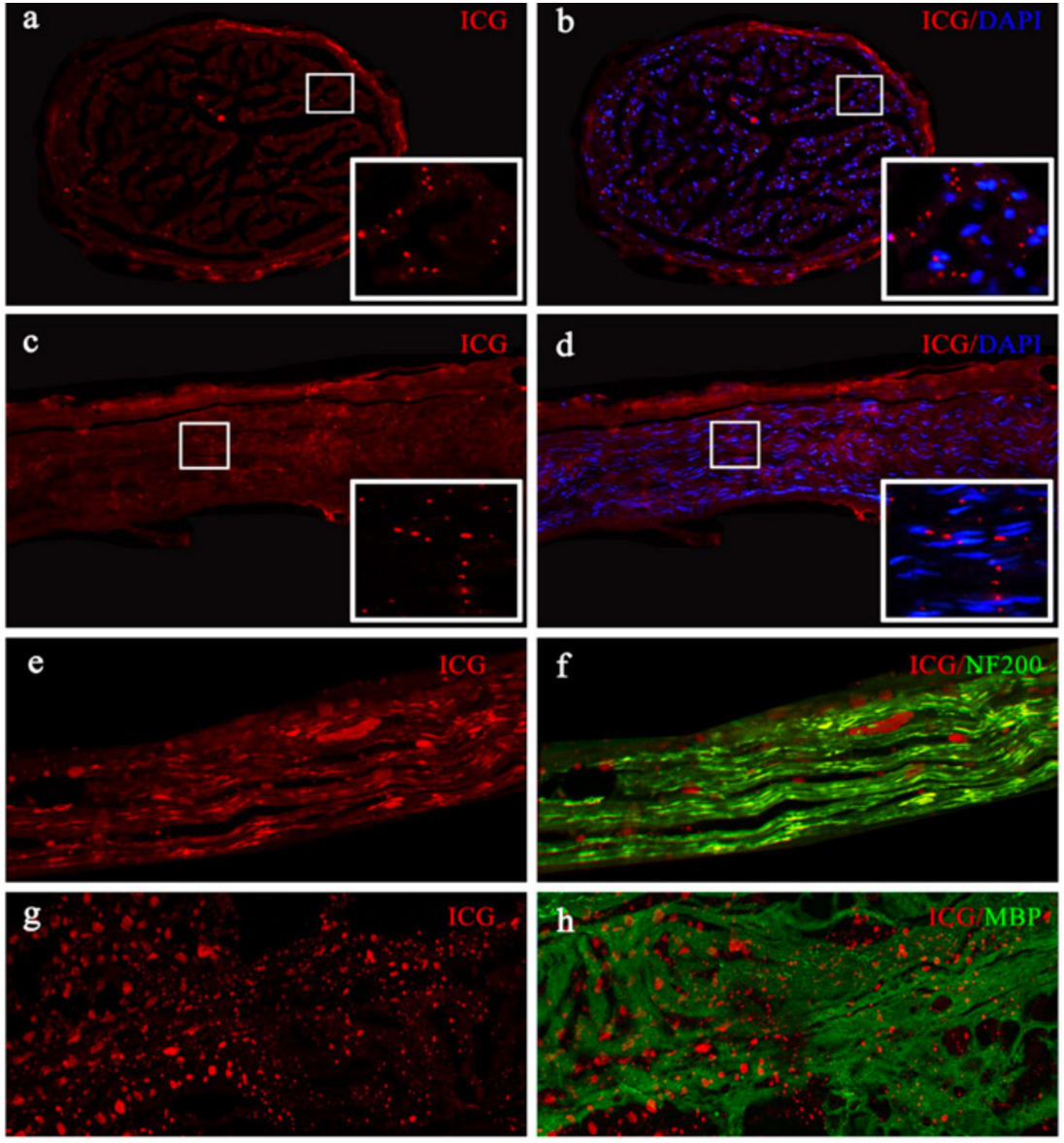


Fig.2 Fluorescent microscopy confirmed that ICG was mainly distributed in the axon of the hypogastric nerve. a–b, The transverse and **c–d,** longitudinal sections of the hypogastric nerve; **e–f,** ICG fluorescent signal distributed in axons labeled with anti-NF 200 antibody; and **g–h,** less ICG fluorescence signal in myelin sheath labeled with anti-MBP antibody

involves placing electrodes in the muscle innervated by the nerve of interest, is currently the most commonly used technique for intraoperative peripheral nerve identification. However, due to its many restrictions and time-consuming and labor-intensive use, it is rarely used in cervical cancer surgery at present. In summary, there is an urgent need to develop a new method for identifying nerves during surgery, with the goal of preventing accidental injury.

Fluorescence-guided surgery has shown great potential in pre-clinical research and clinical applications for identifying lesions

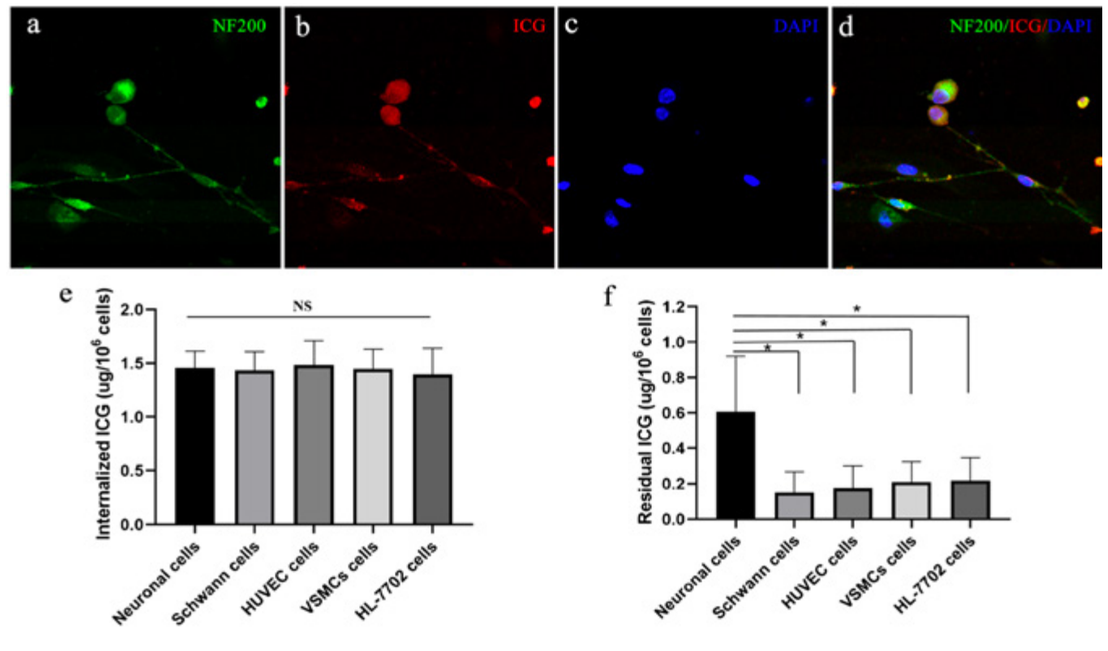


Fig.3 ICG uptake and secretion cell test. a–d, ICG can be taken up by neuronal cells. **e,** The internalized ICG of different cells is similar after 5 min of incubation with an ICG-containing medium. **f,** Neuronal cells secreted ICG significantly slower than other cells after incubation with 0.5 mg/ml ICG for 5 min and DMEM medium for 12h

and important functional tissues (such as nerves). In particular, fluorophores in NIR spectroscopy have aroused great interest from researchers. In this spectrum, tissue autofluorescence, photon absorption, and scattering fall to local minima, thereby achieving millimeter-level resolution and centimeter-level penetration depth. Non-specific fluorophores can highlight nerves through diffusion, active reuptake at synapses, or accumulate in adjective tissues. For example, Samarasena et al. used NeuroTrace to visualize enteric nerves located in the gastric mucosa in an animal model[27]. In contrast, targeted fluorophores improve the SBR by binding to specific moieties or proteins in nerves. Hingorani et al. synthesized FAM-HNP401 and measured the nerve-to-muscle contrast after its topical or systemic administration in pre-clinical trials[28]. However, the research and exploration of nerve NIR-FI are still in their infancy; especially, its application in clinical surgery for gynaecologic tumors is very rare.

In the present study, we found that NIR-FI with ICG could effectively identify the ON, GN, and HN. Although the HN was not identified in seven patients, this early clinical trial showed that the pelvic nerve NIR-FI results did not significantly correlate with the patient's age, height, weight, preoperative FIGO stage, histology, differentiation, stromal invasion, LVSI, parametrial tumor involvement, or lymph node metastasis. The lower identification rate for the HN may be related to the size of the nerve, as it is thinner than the ON and GN. Furthermore, in the cell tests, the uptake of ICG by neuronal cells was similar to that of other cells. However, neuron cells excrete ICG more slowly, leading to concentration differences within a certain period of time, which may be related to the axonal transport of ICG in neurons; this may be the cause of fluorescence emission in pelvic nerves under NIR-FI. Therefore, the ICG injection dose, timing, and sensitivity of NIR-FI devices are closely related to the imaging results.

We acknowledge that there are several limitations to this study. First, this was an early clinical trial, and its main purpose was to investigate the feasibility and safety of NIR-FI for identifying pelvic nerves. Therefore, it was designed as a single-arm study. We did not conduct a randomized controlled trial to compare nerve identification and injury rates between NIR-FI-guided surgery and traditional surgery. Second, we analyzed the NIR-FI of only the HN, not all pelvic autonomic nerves, such as the superior hypogastric plexus, pelvic splanchnic nerves, and inferior hypogastric plexus. Because the HN is easy to locate, it is suitable as an objective and reliable index of imaging results. Third, the follow-up time was too short to evaluate the relationship between the results of pelvic nerve NIR-FI and the patient's prognosis. Finally, ICG is not a nerve-targeted contrast agent. The development of new nerve-targeted contrast agents may provide better imaging results.

In conclusion, these results indicate that intraoperative NIR-FI using ICG can effectively and safely identify pelvic nerves in patients with cervical cancer in real time. The NIR-FI of nerves has the potential to reduce functional impairment and help surgeons adjust decision-making. This research lays the foundation for further clinical pelvic nerve NIR-FI trials, including the use of specific fluorophores, if available.

Author contribution

KH, PL, ZZ, and CC contributed to the concept and initial design. CC and JT obtained funding. All authors were involved in data acquisition and the study design. KH, PL, ZZ, CC, and JL performed the statistical analyses. PL and SG provided administrative, technical, or material support. PL, CC, and JT supervised. KH, PL, ZZ, and JL drafted the manuscript. All authors critically revised the manuscript for important intellectual content. All authors read and approved the final manuscript. CC and JT had full access to all the data in the study and took responsibility for the integrity of the data and the accuracy of the data analysis.

Funding

This work was supported by grants from the Ministry of Science and Technology of China (2017YFA0205200, 2019YFC0120800); National Natural Science Foundation of China (62027901, 81227901, 81930053, 82001984, 82102236, 82101701); Chinese Academy of Sciences (QYZDJ-SSW-JSC005); Beijing Municipal Science & Technology Commission (Z201100006820017, Z19111000110000); Project of High-Level Talents Team Introduction in Zhuhai City (HLHPTP201703); Basic and Applied Basic Research Fund of Guangdong Province (2019A1515110337 and 2021A1515010813); Guangdong Medical Science and Technology Research Fund Project (A2020077), and Nanfang Hospital President Fund (2019C005).

Data availability

The datasets generated during and/or analyzed during the current study are not publicly available due to the use of patient data but are available from the corresponding author on reasonable request.

Ethics approval

This study was approved by the Medical Ethics Committee of Nanfang Hospital of Southern Medical University (Ethics no. NFEC-2019-146), and registered at ClinicalTrials.gov (NCT04224467).

Conflict of interest

The authors declare no competing interests.

Informed consent

Informed consent was obtained from all participants included in the study.

References

1. Sung H, Ferlay J, Siegel RL, Laversanne M, Soerjomataram I, Jemal A, et al. Global cancer statistics 2020: GLOBOCAN estimates of incidence and mortality worldwide for 36 cancers in 185 countries. CA Cancer J Clin. 2021;71:209–249.
2. Berek JS, Kehoe ST, Kumar L, Friedlander M. Cancer of the ovary, fallopian tube, and peritoneum. Int J Gynecol Obstet. 2018;143(Suppl 2):59–78.
3. Koh WJ, Abu-Rustum NR, Bean S, Bradley K, Campos SM, Cho KR, et al. Cervical cancer, Version 3.2019, NCCN Clinical Practice Guidelines in Oncology. J Natl Compr Cancer Netw. 2019;17:64–84.
4. van Gent MDJM, Romijn LM, van Santen KE, Trimbos JBMZ, de Kroon CD. Nerve-sparing radical hysterectomy versus conventional radical hysterectomy in early-stage cervical cancer. A systematic review and meta-analysis of survival and quality of life. Maturitas. 2016;94:30–38.
5. Moawad GN, Wu C, Klebanoff JS, Urbina P, Alkatout I. Pelvic neuroanatomy: an overview of commonly encountered pelvic nerves in gynecologic surgery. J Minim Invasive Gynecol. 2021;28:178.
6. Wang XQ, Chen CL, Liu P, Li WL, Wang LL, Liu YL. The morbidity of sexual dysfunction of 125 Chinese women following different types of radical hysterectomy for gynaecological malignancies. Arch Gynecol Obstet. 2018;297:459–466.
7. Walsh EM, Cole D, Tipirneni KE, Bland KI, Udayakumar N, Kasten BB, et al. Fluorescence imaging of nerves during surgery. Ann Surg. 2019;270:69–76.
8. Diaz-Feijoo B, Bradbury M, Perez-Benavente A, Franco-Camps S, Gil-Moreno A. Nerve-sparing technique during laparoscopic radical hysterectomy: critical steps. J Minim Invasive Gynecol. 2018;25:1144–1145.
9. Lauwerends LJ. van Driel PBAA, Jong RJBd, Hardillo JAU, Koljenovic S, Puppels G, et al. Real-time fluorescence imaging in intraoperative decision making for cancer surgery. Lancet Oncol. 2021;22:E186–EE95.
10. You HJ, Shang WT, Min XD, Weinreb J, Li QB, Leapman M, et al. Sight and switch off: nerve density visualization for interventions targeting nerves in prostate cancer. Sci Adv. 2020;6:eaax6040.
11. Mieog JSD, Achterberg FB, Zlitni A, Hutteman M, Burggraaf J, Swijnenburg RJ, et al. Fundamentals and developments in fluorescence-guided cancer surgery. Nat Rev Clin Oncol. 2022;19:9–22.
12. Lee JYK, Cho SS, Stummer W, Tanyi JL, Vahrmeijer AL, Rosenthal E, et al. Review of clinical trials in intraoperative molecular imaging during cancer surgery. J Biomed Opt. 2019;24:1–8.
13. Chen QY, Xie JW, Zhong Q, Wang JB, Lin JX, Lu J, et al. Safety and efficacy of indocyanine green tracer-guided lymph node dissection during laparoscopic radical gastrectomy in patients with gastric cancer a randomized clinical trial. Jama Surg. 2020;155:300–311.
14. Dousse D, Vibert E, Nicolas Q, Terasawa M, Cano L, Allard MA, et al. Indocyanine green fluorescence imaging to predict graft survival after orthotopic liver transplantation: a pilot study. Liver Transpl. 2020;26:1263–1274.
15. He KS, Hong XP, Chi CW, Cai CN, Wang K, Li PP, et al. A new method of near-infrared fluorescence image-guided hepatectomy for patients with hepatolithiasis: a randomized controlled trial. Surg Endosc. 2020;34:4975–4982.
16. Shang WT, Peng L, He KS, Guo PY, Deng H, Liu Y, et al. A clinical study of a CD44v6-targeted fluorescent agent for the detection of non-muscle invasive bladder cancer. Eur J Nucl Med Mol Imaging. 2022 .
17. He KS, Zhou J, Yang F, Chi CW, Li H, Mao YM, et al. Near-infrared intraoperative imaging of thoracic sympathetic nerves: from preclinical study to clinical trial. Theranostics. 2018;8:304–313.
18. Wang CB, Tong FZ, Cao YM, Liu P, Zhou B, Liu HJ, et al. Long-term follow-up results of fluorescence and blue dye guided sentinel lymph node biopsy in early breast cancer. Breast Cancer Res Treatment. 2021;188:361–368.
19. He KS, Chi CW, Li DL, Zhang JJ, Niu G, Lv FQ, et al. Resection and survival data from a clinical trial of glioblastoma multiforme-specificIRDye800-BBNfluorescence-guided surgery. Bioeng Transl Med. 2021;6:e10182.
20. An Y, Wang K, Tian J. Recent methodology advances in fluorescence molecular tomography. Vis Comput Ind Biomed Art. 2018;1:1–11.
21. Wen JK, Qian CH, Pan MJ, Wang XH, Li YY, Lu YM, et al. Lentivirus-mediated RNA interference targeting RhoA slacks the migration, proliferation, and myelin formation of schwann cells. Mol Neurobiol. 2017;54:1229–1239.
22. Nguyen QT, Tsien RY. Fluorescence-guided surgery with live molecular navigation - a new cutting edge. Nat Rev Cancer. 2013;13:653–662.
23. Shi RX, Wei WW, Jiang PC. Laparoscopic nerve-sparing radical hysterectomy for cervical carcinoma emphasis on nerve content in removed cardinal ligaments. Int J Gynecol Cancer. 2016;26:192–198.
24. Wang LG, Barth CW, Kitts CH, Mebrat MD, Montaño AR, House BJ, et al. Near-infrared nerve-binding fluorophores for buried nerve tissue imaging. Sci Transl Med. 2020;12:eaay0712.
25. Muallem MZ, Diab Y, Sehouli J, Fujii S. Nerve-sparing radical hysterectomy: steps to standardize surgical technique. Int J Gynecol Cancer. 2019;29:1203–1208.
26. Glasgow HL, Whitney MA, Gross LA, Friedman B, Adams SR, Crisp JL, et al. Laminin targeting of a peripheral nerve-highlighting peptide enables degenerated nerve visualization. P Natl Acad Sci USA. 2016;113:12774–12779.
27. Samarasena JB, Ahluwalia A, Shinoura S, Choi KD, Lee JG, Chang KJ, et al. In vivo imaging of porcine gastric enteric nervous system using confocal laser endomicroscopy &molecular neuronal probe. J Gastroenterol Hepatol. 2016;31:802–807.
28. Hingorani DV, Whitney MA, Friedman B, Kwon JK, Crisp JL, Xiong Q, et al. Nerve-targeted probes for fluorescence-guided intraoperative imaging. Theranostics. 2018;8:4226–4237.

Gynecology

Image of the Month

Visualisation of Pelvic Autonomic Nerves Using NIR-II Fluorescence Imaging

Qiaojun Qu[1,2,*], Huilong Nie[3,*], Shuang Hou[3,*], Feng Wang[3], Kunshan He[2], Panxia Deng[3], Shangqiu Chen[3], Zeyu Zhang[2], Chongwei Chi[2], Zhenhua Hu[2,4] ✉, Hong Shan[5] ✉, Jie Tian[1,2] ✉

[1] College of Medical Imaging, Shanxi Medical University, Taiyuan, China

[2] CAS Key Laboratory of Molecular Imaging, Beijing Key Laboratory of Molecular Imaging, Institute of Automation, Chinese Academy of Sciences, Beijing, China

[3] Department of Gynaecology, The Fifth Affiliated Hospital of Sun Yat-Sen University, Zhuhai, China

[4] School of Artificial Intelligence, University of Chinese Academy of Sciences, Beijing, China

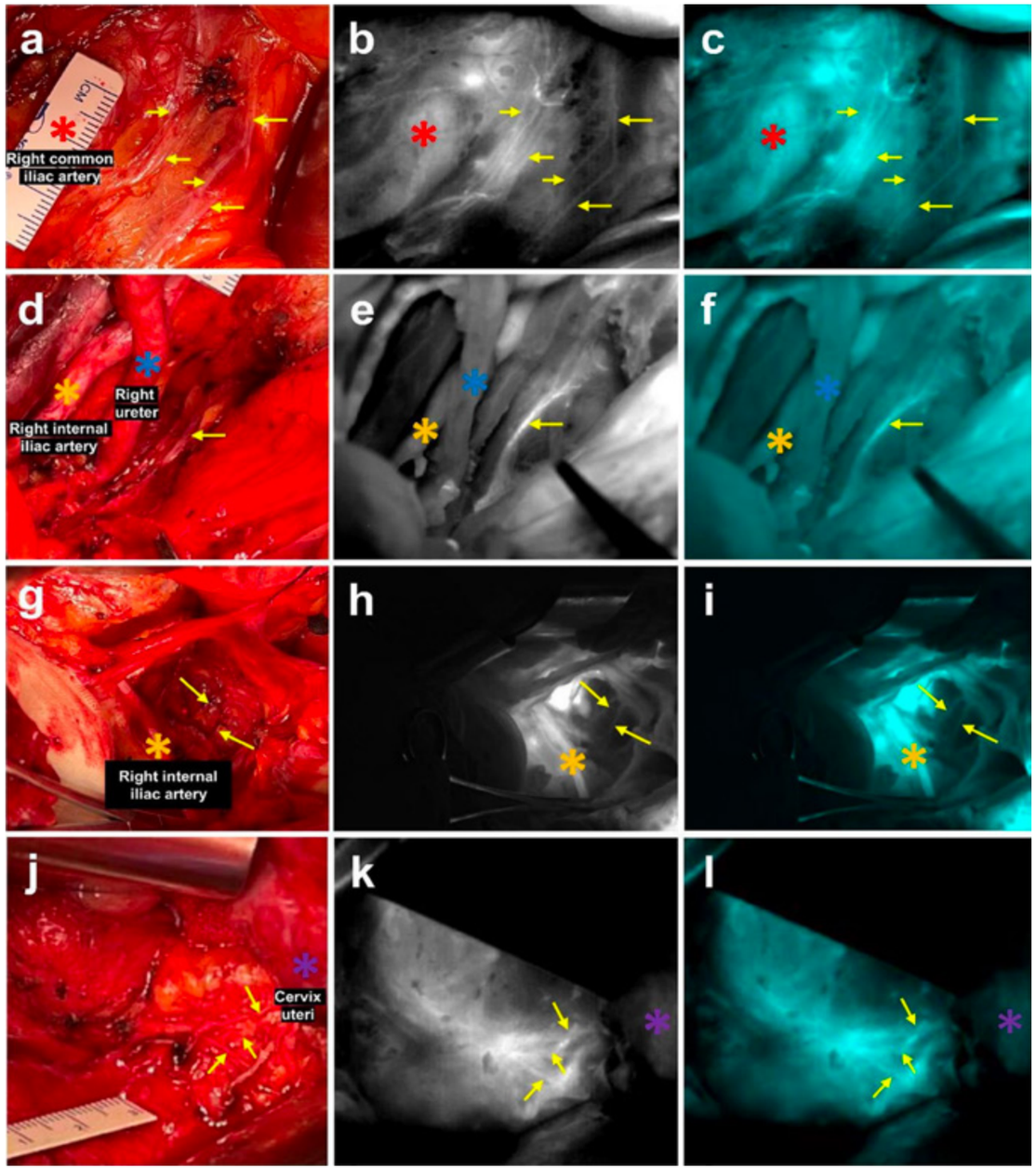
[5] Center for Interventional Medicine, The Fifth Affiliated Hospital of Sun Yat-Sen University, Zhuhai, China

* Qiaojun Qu, Huilong Nie, and Shuang Hou contributed equally to this work.

Intraoperative preservation of the pelvic autonomic nerves is critical in avoiding postoperative bladder dysfunction among cervical cancer patients[1–3]. However, it is difficult to visualise the small pelvic autonomic nerves. The second near-infrared (NIR-II, 1000–1700 nm) fluorescence imaging has properties of higher spatial resolution and imaging contrast[4–8]. This study determined the significance of a NIR-II fluorescence imaging test in identifying the small pelvic autonomic nerves.

A 51-year-old woman, diagnosed with cervical cancer, consented to being included in a clinical trial (NCT05087264). The patient underwent a radical hysterectomy with pelvic lymphadenectomy. Preoperatively, indocyanine green ([ICG], 5 mg/kg) was intravenously injected for 24 h, and it emitted a tail fluorescence in the NIR-II spectrum[4, 9]. Intraoperatively, NIR-II fluorescence imaging was performed to explore the imaging effects of the small nerves. The superior hypogastric plexus (b, c, arrow), hypogastric nerves (e, f, arrow), pelvic splanchnic nerves (h, i, arrow), and inferior hypogastric plexus-bladder branch (k, l, arrow) were highlighted by NIR-II imaging. They had a signal-to-background ratio of 1.8, 2.0, 1.5, and 1.4, respectively. These pelvic autonomic nerves were difficult to identify grossly during surgery because they were approximately 1 mm thick. Images a, d, g, and j were captured using a mobile phone, while the other images were obtained from the NIR-II fluorescence camera.

This study presented the clinical visualisation of small pelvic autonomic nerves using the NIR-II fluorescence imaging technique with ICG. An ongoing prospective study is being conducted to further assess the effectiveness and impact of this novel technique.



Funding

This work was supported by the National Key Research and Development Program of China (2017YFA0205200), National Natural Science Foundation of China (NSFC) (62027901, 81930053, 92059207, 81227901, 82102236, 82001984), Beijing Natural Science Foundation (JQ19027), CAS Youth Interdisciplinary Team (JCTD- 2021-08), Strategic Priority Research Program of the Chinese Academy of Sciences (XDA16021200), Zhuhai High-level Health Personnel Team Project (Zhuhai HLHPTP201703), Beijing Municipal Science & Technology Commission (Z19111000110000, Z201100006820017), and China Postdoctoral Science Foundation (2021M690007).

Ethics approval

This study was approved by the Committee of the Fifth Affiliated Hospital of Sun Yat-sen University.

Consent to participate

Written informed consent was obtained from the patient.

Consent for publication

The authors affirmed that the research participants provided informed consent for the publication of the images shown in Figure.

Competing interests

The authors declare no competing interests.

References

1. Muallem MZ, Diab Y, Sehouli J, Fujii S. Nerve-sparing radical hysterectomy: steps to standardize surgical technique. Int J Gynecol Cancer. 2019;29:1203–08.
2. Rob L, Halaska M, Robova H. Nerve-sparing and individually tailored surgery for cervical cancer. Lancet Oncol. 2010;11:292–301.
3. Kanao H, Fujiwara K, Ebisawa K, Hada T, Ota Y, Andou M. Various types of total laparoscopic nerve-sparing radical hysterectomies and their effects on bladder function. J Gynecol Oncol. 2014;25:198–205.
4. Hu Z, Fang C, Li B, Zhang Z, Cao C, Cai M, et al. First-in-human liver-tumour surgery guided by multispectral fluorescence imaging in the visible and near-infrared-I/II windows. Nat Biomed Eng. 2020;4:259–71.
5. Chang B, Li D, Ren Y, Qu C, Shi X, Liu R, et al. A phosphorescent probe for in vivo imaging in the second near-infrared window. Nat Biomed Eng. 2022;6:629–39.
6. Cao C, Jin Z, Shi X, Zhang Z, Xiao A, Yang J, et al. First clinical investigation of near-infrared window IIa/IIb fluorescence imaging for precise surgical resection of gliomas. IEEE Trans Biomed Eng. 2022.
7. Shi X, Zhang Z, Zhang Z, Cao C, Cheng Z, Hu Z, et al. Near-infrared window II fluorescence image-guided surgery of high-grade gliomas prolongs the progression-free survival of patients. IEEE Trans Biomed Eng. 2022;69:1889–900.
8. Cao C, Deng S, Wang B, Shi X, Ge L, Qiu M, et al. Intraoperative near-infrared II window fluorescence imaging-assisted nephron-sparing surgery for complete resection of cystic renal masses. Clin Transl Med. 2021;11:e604.
9. Carr JA, Franke D, Caram JR, Perkinson CF, Saif M, Askoxylakis V, et al. Shortwave infrared fluorescence imaging with the clinically approved near-infrared dye indocyanine green. Proc Natl Acad Sci USA. 2018;115:4465–70.

Urology

Research Article

A Clinical Study of a CD44v6-Targeted Fluorescent Agent for the Detection of Non-Muscle Invasive Bladder Cancer

Wenting Shang[1,*], Li Peng[2,3,*], Kunshan He[1,4,*], Pengyu Guo[2,3,*], Han Deng[1], Yu Liu[4], Ziyin Chen[2,3], Jie Tian[1,4] ✉, Wanhai Xu[2,3] ✉

Abstract

Background: Bladder cancer is the fifth most common malignancy in humans. Cystoscopy under white light imaging is the gold standard for bladder cancer diagnosis, but some tumors are difficult to visualize and can be overlooked, resulting in high recurrence rates. We previously developed a phage display-derived peptide-based near-infrared imaging probe, PLSWT7-DMI, which binds specifically to bladder cancer cells and is nontoxic to animals. Here, we report a clinical research of this probe for near-infrared fluorescence endoscopic detection of bladder cancer.

Results: The purity, efficacy, safety, and nontoxicity of PLSWT7-DMI were confirmed prior to its clinical application. Twenty-two patients diagnosed with suspected non-muscle invasive bladder cancer were enrolled in the present study. Following intravesical administration of the probe, the entire mucosa was imaged under white and near-infrared imaging using an in-house developed endoscope that could switch between these two modes. The illuminated lesions under near-infrared light were biopsied and sent for histopathological examination. We observed a 5.1-fold increase in the fluorescence intensity in the tumor samples compared to normal tissue, and the probe demonstrated a sensitivity and specificity of 91.2% and 90%, respectively. Common diagnostic challenges, such as small satellite tumors, carcinoma in situ, and benign suspicious mucosa, were visualized and could be distinguished from cancer. Furthermore, no adverse effects were observed in humans. These first-in-human results indicate that PLSWT7-DMI-based near-infrared fluorescence endoscopy is a safe and effective approach for the improved detection of bladder cancer, and may enable thorough resection to prevent recurrence.

Keywords
Bladder cancer; Near-infrared imaging; Peptide; Diagnosis; Endoscopy

[1] CAS Key Laboratory of Molecular Imaging, Beijing Key Laboratory of Molecular Imaging, the State Key Laboratory of Management and Control for Complex Systems, Institute of Automation, Chinese Academy of Sciences, Beijing 100190, China
[2] Urology Surgery Department, The Fourth Hospital of Harbin Medical University, Harbin, Heilongjiang 150001, People's Republic of China
[3] NHC Key Laboratory of Molecular Probes and Targeted Diagnosis and Therapy, Yiyuan Street #37, Nangang District, Harbin, Heilongjiang 150001, People's Republic of China
[4] Beijing Advanced Innovation Center for Big Data-Based Precision Medicine, School of Medicine and Engineering, Beihang University, Zhongguancun East Road #95, Haidian Dist., Beijing 100191, China
* Wenting Shang, Li Peng, Kunshan He, and Pengyu Guo are the parallel first authors.

Eur J Nucl Med Mol Imaging. 2022. 49(9): 3033-3045 Published online: 21 February 2022

Introduction

Bladder cancer (BC) is the fifth most common human malignancy, with an incidence of 81.2 per 100,000 individuals[1]. At initial presentation, approximately 70% of patients present with non-muscle invasive bladder cancer (NMIBC), in which the tumor is superficial (stage carcinoma in situ [CIS]), or limited to the mucosa (Ta) and submucosa (T1), and up to 90% of NMIBC cases are urothelial neoplasms[2, 3]. Urothelial neoplasms are polymorphic in nature and can appear as solitary or multiple, flat, or exophytic, at any site on the surface of the bladder urothelium[4]. Bladder cancer usually has a good prognosis, particularly with early detection at stage Ta or T1. Although white light endoscopy, which is recommended by cancer prevention guidelines, is an easily accessible and non-invasive method to detect BC, up to 30% of tumors can be missed, particularly small satellite tumors and flat CISs[5]. These missed residuals lead to a high recurrence rate of 70%, and relapsed tumors may progress to infiltrative cancer[6], which has a significant impact on patient morbidity and quality of life. In addition, BC can incur high treatment expenses and is a burden on medical care systems. Therefore, improving the detection of BC, particularly those tumors that are often overlooked by current methods, would improve the prognosis of patients with NMIBC.

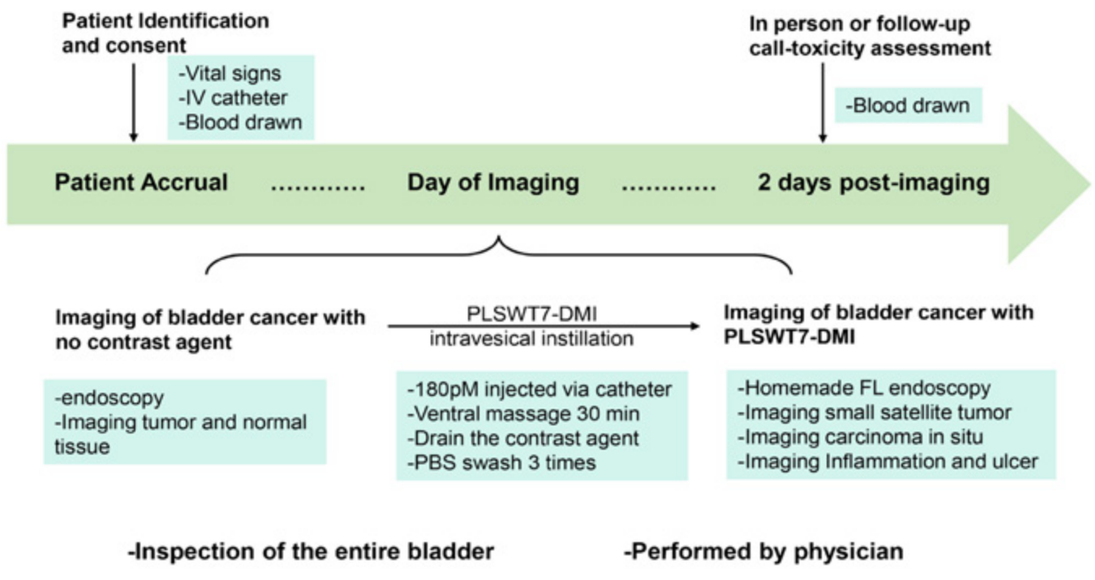
There are several barriers to overcome in the accurate diagnosis of NMIBC, including patient factors, physician factors, and the limitations of currently available diagnostic tests. Cancer prevention guidelines recommend imaging with white light (WL) endoscopy, which is the most commonly used diagnostic method for NMIBC detection, but this method can still lead to misdiagnosis and missed diagnosis[7–9]. The main cause of missed diagnosis is that the lesions cannot be seen under WL, particularly in the case of multifocal flat cancers[10, 11]. A missed diagnosis can also affect the accurate detection and complete resection of tumors, resulting in recurrent or advanced carcinoma[10, 12]. The presence of inflammatory diseases can lead to misdiagnosis[13–15]. Under WL cystoscopy, it is difficult to distinguish between inflammatory lesions and cancer, as well as benign and malignant lesions, which often leads to misdiagnosis [16]. Although clinicians can make a reliable diagnosis by biopsy, the need for invasive biopsy is a barrier to quick detection of bladder cancer. Additionally, it is impractical to perform a biopsy assessment of every lesion. Therefore, it is necessary to develop new detection methods to improve the diagnosis of NMIBC.

Recently, new imaging technologies have been developed to enhance tumor identification. Endoscopic methods, such as narrow-band imaging[17] and blue light cystoscopy [18], were developed to enhance cancer identification and guide endoscopic resection[19]. However, these methods are limited by high false-positive rates due to their low specificity[20]. Microscopic imaging techniques, including confocal laser endomicroscopy[21] and optical coherence tomography[22], can provide information on tissue

microarchitecture and cellular morphology but are not practical for surveying the entire bladder due to their narrow field of view. Near-infrared (NIR) fluorescence imaging with targeted probes has emerged as a promising technique for precise imaging[23]. NIR fluorescent probes consist of NIR fluorophore and a targeting agent[24]. NIR fluorophore emits light beyond the visible light spectrum and is not interfered with by endogenous substances, thus improving the accuracy of NIR imaging. We previously developed a NIR-based cancer-specific agent[25] that had promising efficacy in preliminary tests. The targeting agent was developed based on molecular changes that are specific to cancer, thus providing high specificity and sensitivity. In the present study, we demonstrate the potential of a NIR-based imaging strategy for improving NMIBC detection using targeted contrast agents. Recently, NIR imaging appeared to improve the detection of BC. Compared with commonly used tracer such as fluorescein[26], rhodamine [27], Cy3[28], Alexa dye[29], and 5-aminolaevulinic acid (ALA)[30], NIR tracer has higher penetration depth, stronger fluorescence intensity, and better light stability. The NIR tracer specifically binds to the tumor site and then highlights the malignant lesions from normal mucosa tissue. Zhe Feng et al. report an excretable IR-820 for in vivo NIR-II fluorescence cerebrovascular imaging for BC[31]. Jiaguo Huang et al. displayed a macromolecular reporter (CyP1) for near-infrared fluorescence imaging of bladder cancer[32]. Most of the works were animal research.

CD44 is a multifunctional transmembrane glycoprotein that is highly expressed in BC and is involved in cell adhesion, cell migration, tumor progression, and metastasis[33]. CD44v6, a CD44 isoform containing the CD44v6 exon, is also highly expressed in BC[34]. CD44v6 is required for the interaction between c-Met receptor tyrosine kinase and hepatocyte growth factor (HGF), which plays critical roles in tumor[35]. CD44v6 was expressed in a variety of tumors, such as head and neck cancer, and prostate cancer. CD44v6 is a marker of poor prognosis in patients with BC[36]. In addition, CD44v6 is closely related to the degree of malignancy and the stage of BC. Hesham S. Ata et al. report that CD44s and CD44v6 are in diagnosis and prognosis of human bladder cancer. It has very good therapeutic effect[37]. Therefore, targeting CD44v6 has tremendous potential for early BC diagnosis[38]. In a previous study, we identified a CD44v6-specific peptide, PLSWT (CSDRIMRGC), and labeled it with a NIR fluorophore, IRDye800CW, to synthesize the BC-specific NIR imaging probe PLSWT7-DMI[25]. As a tool for non-invasive in vivo identification of BC, the specificity of the probe has been con- firmed in BC cells, tumor-bearing mice, and ex vivo human bladders. The ex vivo results revealed that CD44v6-targeted NIR imaging can pinpoint multifocal lesions. PLSWT7-DMI has a high sensitivity and specificity[25]. Specific peptides and NIR fluorescence provide a biological basis for enhanced contrast and can achieve desirable tumor-to-background ratios (TBR) for in vivo detection.

Preclinical evaluation of PLSWT7-DMI has strongly supported its feasibility for clinical translation. In the present study, we report our initial findings with NIR fluorescence-guided endoscopy using the imaging probe PLSWT7-DMI (Chinese Clinical Trials Database registration number: ChiCTR-DDD-17012616). The purity, efficacy, safety, and nontoxicity of the agent were confirmed before clinical application. We performed a first-in-human clinical study using this probe, and demonstrated that it can bind specifically to BC tissue for visualization by NIR fluorescence endoscopy, thus improving the detection of easily over- looked BC lesions Scheme 1.



Scheme 1 Schematic overview of the PLSWT7-DMI clinical trial. 22 patients with BC confrmed by biopsy consented to the clinical study

Eur J Nucl Med Mol Imaging. 2022. 49(9): 3033-3045 Published online: 21 February 2022

Materials and methods

Study design

In a previous study[25], we synthesized a phage display-derived peptide-based probe (PLSWT7-DMI) and demonstrated its specificity for BC cells in vitro and in a mouse model. In the present study, we first applied the probe to ex vivo bladder specimens from eight patients to confirm its binding specificity. The PLSWT7-DMI probe was then intravesically administered to patients diagnosed with NMIBC (n = 22). This study was approved by the ethics committee of the Fourth Hospital of Harbin Medical University, China (YXLLSC-2017–09) and was registered in the Chinese Clinical Trials Database (ChiCTR-DDD-17012616). Informed consent was obtained from each patient prior to participation. The study was performed under the guidelines of the Declaration of Helsinki.

Imaging of the entire bladder was performed using our in-house developed dual WL and NIR endoscopy imaging system. The number of lesions detected by WL or NIR imaging was compared. Illuminated lesions under NIR imaging and suspected lesions under WL imaging were biopsied and sent for pathological examination to explore the correlation between the appearance of fluorescent signals and cancer lesions. In total, 108 biopsies were analyzed and used for sensitivity and specificity calculations. All biopsies were reviewed by a single pathologist who was blinded to the imaging results.

Cell culture

The human BC cell lines EJ and RT112, and the human normal urothelial cell line SV-HUC-1, were obtained from the Cell Culture Center at the Institute of Basic Medical Science (Chinese Academy of Medical Sciences) in 2016. The cell lines were checked and authenticated within 6 months using STR analysis (Biowing, Shanghai, China). The cells were grown at 37 °C and 5% CO_2 in a humidified atmosphere. Cells were maintained in Dulbecco's modified Eagle's medium (DMEM; Invitrogen Life Technology, Carlsbad, CA, USA) supplemented with 10% FBS.

Synthesis of fluorescently labeled peptides

BC-specific peptide selection and probe synthesis were performed as previously described (17). The C-terminus of CSDRIMRGC was attached by a GGGK linker to IRDye800CW (PLSWT7-DMI) or FITC (PLSWT7-FITC) to prevent steric hindrance. The peptide CQRSPIHDC was synthesized as a control for non-specific binding. The probe was purified to > 95% by HPLC using a C18 column (Waters Inc.) with a water (0.1% TFA)-acetonitrile (0.1% TFA) gradient. Further characterization was performed using either ESI (Waters Inc.) or MALDI-TOF mass spectrometry (Hitachi America, Ltd.). The excitation and emission spectra of the fluorescently labeled peptides were measured using a spectrophotometer (Ocean Optics). The peptide-binding assays and toxicology analysis are described in the Supplementary Materials and Methods.

Ex vivo imaging of human bladders

Fresh bladder specimens were collected from patients (n = 8) who underwent radical cystectomy. These patients were in the subgroup of high-risk NMIBC patients who underwent radical cystectomy according to cancer prevention guidelines. After radical cystectomy, whole bladder specimens were immediately removed and washed three times with 0.9% saline solution. The bladder specimens were first sprayed with the control (cPLSWT7-DMI) probe, then it was washed with 0.9% saline solution three times and images were obtained after 30 min using our in-house endoscopy system. After washing to remove the control probe, the bladders were resprayed with PLSWT7- DMI, and images were obtained. The mean fluorescent density was quantified using Image Pro Plus 6.0 (Media Cybernetics, Inc.).

Clinical evaluation of PLSWT7-DMI fluorescence endoscopy

Patients

From September 2017 to August 2018, 22 patients diagnosed with NMIBC were enrolled in the present study. Patient characteristics are provided in Table 1. All patients enrolled were female because the length of the in-house developed endoscope was only 19 cm, limiting access into the bladder via the urethra. The criteria for patient inclusion were the presence of a suspected bladder tumor on prior cystoscopy, ultrasound, or cytology, and no history of surgical or medical therapy for BC during the preceding 6 months. Patients with gross hematuria or a history of allergic reactions to proteins (such as milk, eggs, or beef) and patients who were pregnant, breastfeeding, or did not utilize adequate contraceptive measures were excluded. Ninety days follow up was conducted for subjects. Adverse effects occurred within 90 days post operation were collected.

PLSWT7-DMI-based NIR imaging of NMIBC in humans

An 18-French urinary catheter was inserted into each patient. The front part of the catheter was cut off to make the catheter a working channel, and 50 ml of PLSWT7-DMI solution (180 pmol/ml) was intravesically instilled. The catheter was clamped, and the bladder was incubated for 30 min, followed by washing

Table 1 Patient characteristics

Patients	No. patients
Age, mean ± SD (range), y	67 ± 10.9 (43–87)
Female	22
Tumor type	
TaG1	4
TaG2	9
TaG3	1
T1G1	3
T1G2	3
T1G3	1
Concomitant CIS	4
Solitary	9
Multifocal	13

Table 2 Tabular results of sensitivity/specificity tests of PLSWT7- DMI-based NIR fluorescence endoscopy of NMIBC

PLSWT7-DMI-based NIR fluorescence endoscopy	Pathological examination		Sum
	Positive	Negative	
Positive	TP, 62	FP, 4	66
Negative	FN, 6	TN, 36	42
Sum	68	40	

Sensitivity 91.2; specificity 90%; false negative rate 8.8%

with 200 ml of normal saline three times. Imaging was performed using an in-house developed NIR imaging endoscopy system, which is capable of both WL and NIR imaging. The endoscope was inserted into the bladder to obtain images of the entire mucosa under WL, followed by NIR imaging. The number of tumors detected under WL and NIR conditions was recorded. A biopsy instrument was inserted into the bladder via the catheter, and the illuminated lesions were biopsied. All biopsies were sent for H&E staining and were reviewed by a pathologist who was blinded to the imaging results.

Immunofluorescence analysis of PLSWT7 distribution

To assess the distribution and expression of PLSWT7 target sites, frozen NMIBC tissue and normal mucosa were sectioned into 5-μm thick slices, acetone fixed, and air dried for 30 min. The sections were then blocked with 1% BSA in PBS for 30 min, and incubated with PLSWT7-DMI and rabbit monoclonal anti-CK20 antibody overnight at 4 °C. The slides were washed three times with PBS, incubated with goat anti-rabbit antibody conjugated with rhodamine red-X for 30 min, and counterstained with DAPI for 5 min. Images were obtained using fluorescence microscopy (Olympus FV3000).

Imaging data analysis

The data is presented in TBR format. TBR is short for tumor background ratio. Due to the difference in the spatial distribution of the fluorescent contrast agent and the difference in the optical properties of the observed tissue, it is difficult to quantitatively analyze the results of fluorescence imaging. At present, many clinical studies of near-infrared (NIR) fluorescence imaging (NIR-FI) have adopted the TBR to characterize imaging results, such as the diagnostic study of intraoperative NIR fluorescence visualization of the lung tumor margin by Quan et al.[39]. Suspicious lesions (either under NIR or WL) were biopsied and sent to pathological examination. Suspicious lesions under NIR were identified as luminated lesions under NIR imaging. Suspicious lesions under WL were identified by surgeons only under WL and not illuminated under NIR. So, for NIR imaging detection, if a NIR suspicious lesion was found to be malignant by pathological examination, it was true positive (TP) as in Table 2. If a NIR suspicious lesion was found to be benign by pathological examination, it was false positive (FP) as in Table 2. If a WL suspicious lesion was found to be malignant by pathological examination, it was false negative (FN) as in Table 2. If a WL suspicious lesion was found to be benign by pathological examination, it was true negative (TN) as in Table 2.

Statistical analysis

Data were analyzed using SPSS version 20 (IBM Corp., Armonk, NY, USA). Results are presented as the mean ± standard deviation (SD) for experiments performed in triplicate. Two-tailed independent two-sample t-tests were used to assess the differences in fluorescence intensities and tumor-to-background ratios between the groups.

The detection rate was calculated as the number of tumors detected in one mode divided by the total number of detected tumors. Differences were considered to be statistically significant at $p < 0.05$. To determine the diagnostic accuracy of PLSWT7-DMI fluorescence endoscopy, sensitivity was calculated as TP / (TP + FN) and specificity was calculated as TN / (TN + FP), where TP indicates true positives, FN indicates false negatives, TN indicates true negatives, and FP indicates false positives.

Study design

This exploratory, single-center, open-label, prospective Health Insurance Portability and Accountability Act com- pliant study was approved by the MSK Institutional Review Board and conducted in accordance with the Declaration of Helsinki (Chinese Clinical Trials Database registration number: ChiCTR-DDD-17012616, registered on September 7, 2017). Written informed consent was obtained from all patients. Patients were aged 18–70 years, and pathologic diagnosis was obtained prior to surgical treatment. Patients were expected to survive ≥ 3 months with a KPS score ≥ 60. Patient organ function was normal based on the following laboratory test results (in the absence of continuous treatment, laboratory test results were obtained in the first week of enrollment): neutrophils > 1.5 × 10^9/L, blood platelets > 100 × 10^9/L, hemoglobin > 9.0 g/dl, bilirubin < 1.5 × UL, NAST (SGOT), ALT (SGPT) < 2.5 × ULN, and serum creatinine < 1.5 × ULN. Exclusion criteria were complications with cystitis or urological deformity and urethral stricture, allergy history, including medicaments and alimental allergy, patients with serious diseases of other systems, and the participation in other clinical studies in the past 30 days. The primary objective of the present study was to evaluate the safety and feasibility of PLSWT7-DMI imaging in patients with bladder cancer. We initially reported on the fluorescence signals in urothelial carcinoma and carcinoma in situ ex vivo tissue. Thereafter, 22 patients were enrolled in the study protocol. All patients completed the study. The study design and procedures are summarized in Fig. 1. We imaged small satellite tumors and carcinomas in situ and compared these with ulcers and inflammation. A biopsy was taken from the tumor and from the disease-free margin for fluorescence microscopy and histopathological correlation analysis.

Results

Peptide discovery and characterization

In vivo phage display technology was used to identify BC-

Eur J Nucl Med Mol Imaging. 2022. 49(9): 3033-3045 Published online: 21 February 2022

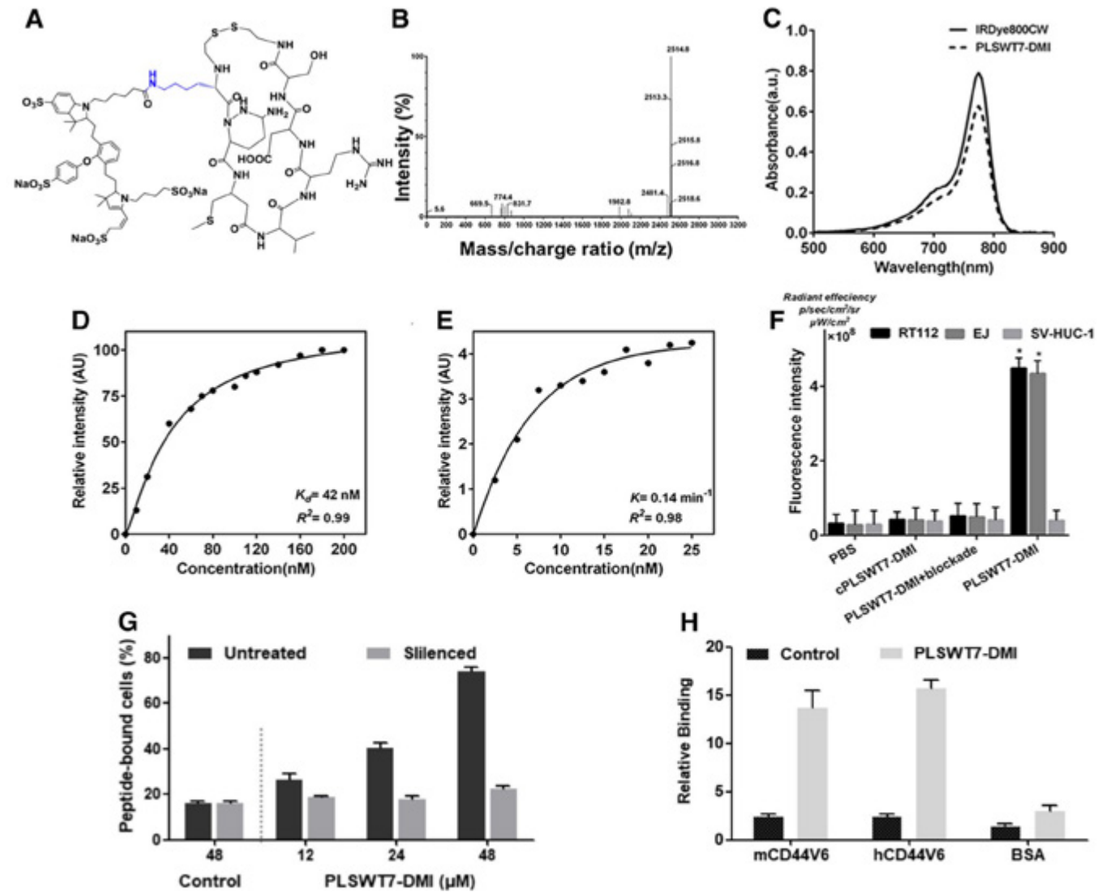


Fig.1 Fluorescently labeled peptides that are specific to NMIBC. **A** Chemical structure of the CSDRIMRGC peptide with a GGGK linker and an IRDye800CW label denoted PLSWT7-DMI. **B** Fluorescence emission spectra for PLSWT7-DMI and IRDye800CW with an excitation wavelength of 471 nm resulting in an emission peak of 519 nm. **C** Mass spectrum of PLSWT7-DMI. **D** Binding affinity (Kd) of PLSWT7-DMI to RT112 cells. **E** Binding kinetics (K) of ASY*- FITC to RT112 cells. Solid line represents the least-squares fit. **F** Fluorescence intensity (mean sores) of RT112, EJ, and SV-HUC-1 cells incubated with phosphate buffer saline (PBS), cPLSWT7-DMI, PLSWT7-DMI with blockade, or PLSWT7-DMI. The PLSWT7- DMI-treated group showed higher binding affinity than that of the other groups. *$p < 0.05$ versus cPLSWT7-DMI-treated cells. **G** Flow cytometry analysis of the binding of FITC-labeled cPLSWT7 and FITC-labeled cPLSWT7 + blockade at the indicated concentrations in RT112 cells. **, $p < 0.01$; data represents the mean ± SE of three independent experiments. ***, $p < 0.001$. **H** Binding of PLSWT7- DMI to recombinant human CD44V6 and mouse CD44V6. Bovine serum albumin (BSA) was used as the control protein. NMIBC, non- muscle invasive bladder cancer; cPLSWT7-DMI, scrambled labeled peptide control.

specific peptides in our previous study *(17)*. After three rounds of biopanning, phage clone P7 was selected based on its high affinity for RT112 (a BC cell line). P7 was isolated, sequenced, and translated into the corresponding peptide, CSDRIMRGC (PLSWT7), and labeled with IRDye800CW (PLSWT7-DMI) or fluorophore isothiocyanate (PLSWT7- FITC). The chemical structure is shown in Fig. 1A. Mass spectrometry was used to determine the mass/charge ratio (m/z) of PLSWT7-DMI, and its monoisotopic mass based on this was determined to be 2514.8 Da (Fig. 1B). The fluorescence spectra for PLSWT7-DMI and IRDye800CW in phosphate-buffered saline (PBS) at an excitation wavelength of 774 nm revealed an emission peak at 789 nm (Fig. 1C). Thus, no shift was observed after IRDye800CW labeling. The apparent dissociation constant (K_d) and association rate constant (K) of PLSWT7-FITC were 42 nm (Fig. 1D) and 0.14 min^{-1} (Fig. 1E), respectively. The results were determined using the least-squares fit of the data. To evaluate the specificity of the peptide in vitro, RT112, EJ, and SV-HUC-1 (a normal urothelium cell line) were incubated with the probes, and higher fluorescence intensity was observed in tumor cells incubated with PLSWT7-DMI, indicating efficient binding to RT112 and EJ cells. However, no fluorescence was observed

following incubation with cPLSWT7-DMI (scrambled peptide CQRSPIHDC, labeled with IRDye800CW) or PBS. Additionally, pretreatment with PLSWT7 prevented PLSWT7-DMI from binding (Fig. 1F), and minimal fluorescent signals were observed in SV-HUC-1 cells incubated with PLSWT7-DMI, suggesting that the binding of PLSWT7-DMI occurred via the targeting of specific sites on tumor cells. The binding of CD44v6 to RT112 cells also occurred in a dose-dependent manner. The level of PLSWT7-DMI binding was higher in non-transfected cells than in silenced cells (Fig. 1G). These peptides bind to RT112 mouse bladder tumor cells, which express murine CD44v6 of RT112 cells, and an anti-CD44v6 blocking antibody inhibited the cellular binding of CD44v6. These findings indicate that the binding of CD44v6 to CD44v6-overexpressing cells is specifically mediated by CD44v6. In addition, CD44v6 preferentially binds to plates coated with either human or mouse recombinant CD44v6 compared to control plates coated with albumin (Fig. 1H).

For pharmacological/toxicological analysis of PLSWT7-DMI, rats were administered four different doses of PLSWT7-DMI by oral gavage (n = 12 animals per dose). After 15 days, the rats showed no peptide-related acute adverse effects according to clinical signs, chemistries, or necropsy (Table S1).

Ex vivo endoscopic NIR imaging

Specific binding of PLSWT7-DMI to NMIBC was confirmed ex vivo using fresh human bladder specimens (n = 8) from patients who had undergone radical cystectomy. Multifocal tumors and CIS were present in the mucosa. After incubation with PLSWT7-DMI, tumors were clearly visible, but the normal mucosa was not, indicating specific targeting of the probe (Fig. 2A). Quantitative analysis showed that the fluorescence density was significantly higher in urothelial carcinoma and CIS tissue

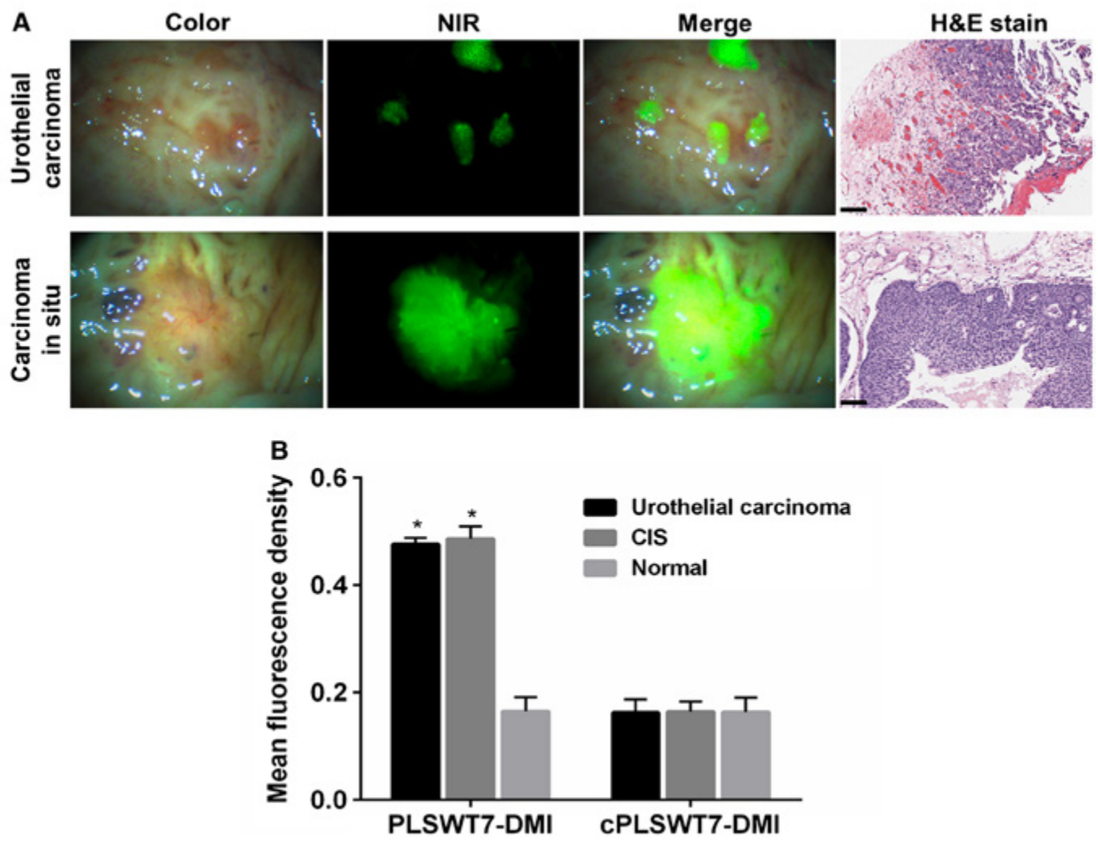


Fig.2 Ex vivo endoscopic NIR imaging of human bladder specimens. A The colocalization of PLSWT7-DMI binding and histopathology as shown by representative white and blue light images with corresponding hematoxylin and eosin (H&E) staining. PLSWT7-DMI binding was detected under NIR lighting on multifocal urothelial carcinomas and flat CIS. Scale bars, 50 μm. **B** Mean fluorescence density (mean ± SEM) in urothelial carcinoma, CIS, and normal tis- sues post administration of PLSWT7-DMI or the scrambled control cPLSWT7-DMI. *p < 0.05 vs. normal tissue treated with PLSWT7- DMI. WL, white light; NIR, near infrared; CIS, carcinoma in situ.

Eur J Nucl Med Mol Imaging. 2022. 49(9): 3033-3045 Published online: 21 February 2022

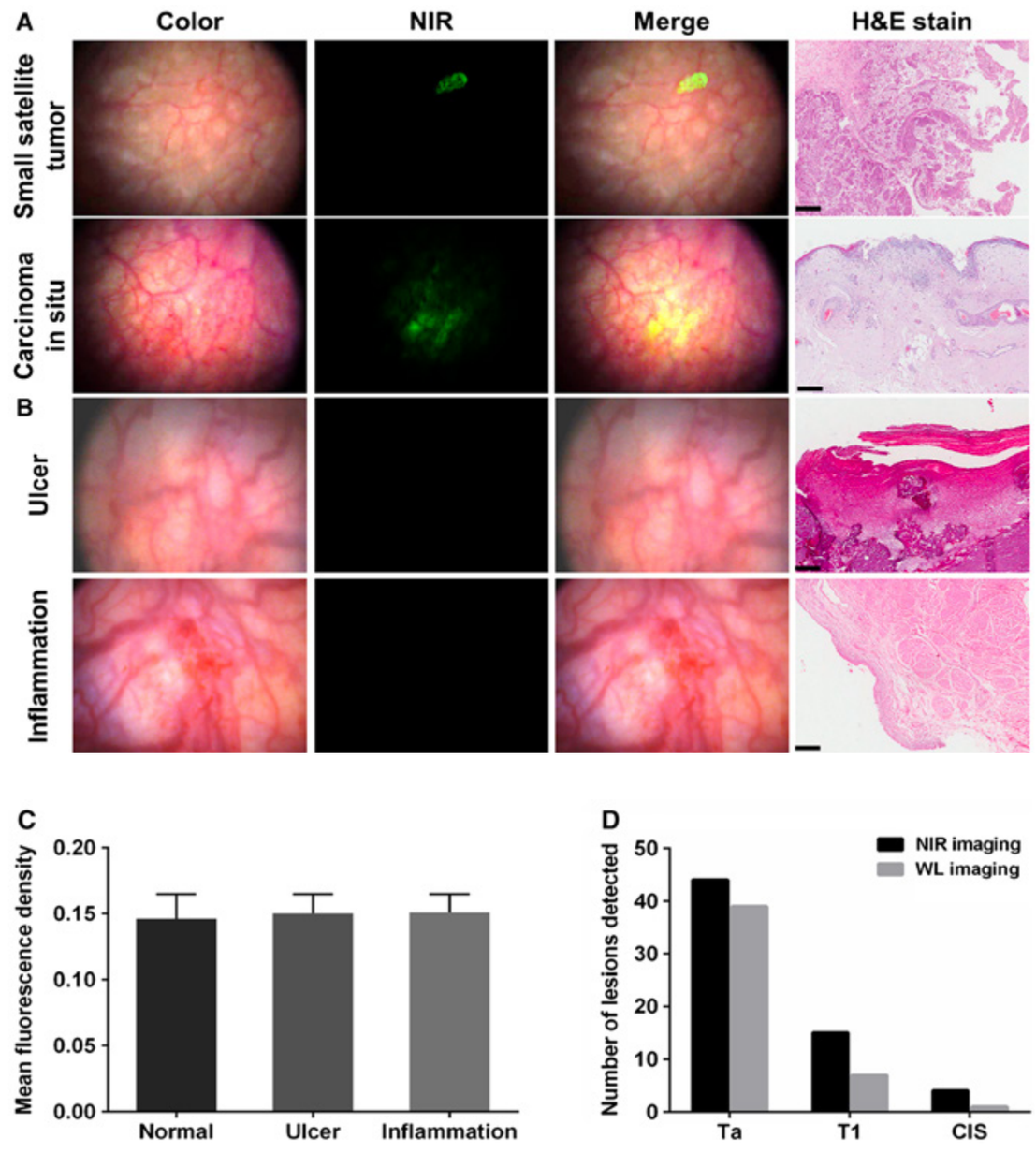


Fig.3 NIR fluorescence endoscopy of NIMBC in humans with the tumor-specific probe PLSWT7-DMI. A Representative images of WL and NIR imaging of stage Ta, T1 urothelial carcinoma and normal mucosa **(B),** with corresponding H&E staining to demonstrate the colocalization of PLSWT7-DMI binding and histopathology. Scale bars, 100 μm. **C** Quantification of the mean fluorescent density and **D** tumor-to-background ratio (TBR) in cancer and normal mucosa tissue post-administration of PLSWT7-DMI and cPLSWT7-DMI. Values are presented as the mean ± SEM. *p < 0.05 vs. urothelial carcinoma treated with PLSWT7-DMI. WL, white light; NIR, near infrared; cPLSWT7-DMI, scrambled control peptide. E The signal ratio between the lesion and margin in stage T1 (n = 8) and Ta (n = 14). F TBR for all patients stage T1 (n = 8) and Ta (n = 14).

than in the normal mucosa after incubation with PLSWT7-DMI, with no difference observed with cPLSWT7-DMI incubation (Fig. 2B). These results suggest that PLSWT7-DMI binds specifically to human BC tissue, and thus can be translated into clinical applications.

Endoscopic NIR imaging with PLSWT7-DMI in NMIBC patients

To determine whether PLSWT7-DMI specifically binds to NMIBC in vivo, we enrolled 22 NMIBC patients and compared the absolute fluorescence of tumor tissue with that of the adjacent normal tissue following intravesical probe administration. The bladders were washed and emptied, and intravesically instilled with a control probe (cPLSWT7-DMI), and images were obtained using an in-house developed endoscopy system. After washing to remove the control probe, bladders were re-instilled with PLSWT7-DMI and imaged again. With the control probe, no contrast was detected between the normal and apparent tumor mucosa (Fig. S1). After instillation with PLSWT7- DMI, urothelial carcinomas at stage Ta and T1 were clearly stained (Fig. 3A), but the normal mucosa was not (Fig. 3B). Quantitative analysis revealed that the mean fluorescence density was significantly higher in the tumor tissue than in the normal mucosa after incubation with PLSWT7-DMI, while no difference was observed with the control probe cPLSWT7-DMI (Fig. 3C), indicating that PLSWT7- DMI specifically binds to tumors. Moreover, the TBR of PLSWT7-DMI was 4.58-fold higher than that of cPLSWT7- DMI (Fig. 3D). After treatment with PLSWT7-DMI, the sig- nal ratio between the lesion and margin in stage Ta and T1 tumors was higher than that in the normal tissue (Fig. 3E). Furthermore, T1 urothelial carcinomas showed higher TBRs than the patient of Ta stage (Fig. 3F).

The illuminated lesions were biopsied using NIR imaging. Pathological examination confirmed that the probe- bound lesions corresponded to NMIBC tissue, while the lesions without probe binding were identified as normal mucosa.

Detection accuracy of PLSWT7-DMI fluorescence endoscopy for NMIBC

A total of 108 lesions (68 cancerous lesions and 40 benign lesions) were analyzed to compare PLSWT7-DMI fluorescence endoscopy and histopathological diagnosis (Table S2). For urothelial neoplasms, 20.6% (n = 14) were found only by NIR imaging, and 7.4% (n = 5) were found only by WL imaging. Small satellite tumors and CIS overlooked under WL imaging were identified using probe-based NIR imaging (Fig. 4A). Under WL imaging, 54 NMIBC lesions were detected, while nine additional lesions were detected by NIR imaging (Table S2), including six small foci and three CIS that were overlooked by WL endoscopy. These results indicate that PLSWT7-DMI-based NIR fluorescence endoscopy may reduce the number of overlooked NMIBC lesions, thus facilitating complete resection and reducing the recurrence rate of BC.

Suspicious benign lesions that were difficult to discriminate under WL, such as inflammation and ulcers, could be easily differentiated by PLSWT7-DMI-based NIR fluorescence endoscopy (Fig. 4B). The mean fluorescent density did not differ among normal mucosa, ulcers, and inflammation (Fig. 4C), indicating negligible probe binding to benign lesions. Ten out of thirteen inflammatory lesions and three out of three ulcers were invisible under NIR (Table S2), suggesting that mistaken resection of benign lesions would be minimized if our technique was used during tumor resection.

Overall, PLSWT7-DMI-based NIR fluorescence endos- copy resulted in a more thorough detection of urothelial neoplasms at different tumor stages than WL endoscopy (Fig. 4D). The sensitivity of probe-based NIR imaging was 91.2% (62/68), specificity was 90% (36/40), and the false positive rate was 10% (4/40), as shown in Table 2.

Distribution of PLSWT7-DMI in bladder tissue

We used immunofluorescence to further examine the distribution of PLSWT7-DMI in the tumor and normal tissue. Frozen sections of biopsies from the detected lesions and the adjacent normal mucosa were obtained during the pre- sent study. In representative images of NMIBC and normal mucosa, we found that the PLSWT7-DMI signal was higher in NMIBC tissue than in normal tissue and overlapped with CK20 expression (Fig. S2), indicating that PLSWT7-DMI was localized in NMIBC tissue but not in the normal urothelium. The tumor-selective distribution of PLSWT7-DMI may serve to illuminate tumor lesions during intraoperative imaging.

Safety and adverse effects

PLSWT7-DMI was well-tolerated by the study subjects, and no adverse pharmacological activity or allergic reactions occurred during the study. Three patients experienced surgical fevers within the first postoperative day (36.8–38.5 °C), which subsequently subsided. No damage to liver or renal function was observed. None of the patients complained of nausea, vomiting, or gross hematuria within 1 week after surgery. No symptoms of urinary tract infection were reported (Table S3).

Discussion

With a recurrence rate of up to 70% within 5 years, tumor recurrence is a major issue that affects the survival of patients that are treated for NMIBC. A substantial percent- age of tumor recurrences are likely to be caused by persistent tumors that were overlooked at the initial resection[40], despite urologists aiming to detect as many neoplastic lesions as possible to minimize the possibility of future relapse. In the present study, we present the first in-human assessment of the use of NIR fluorescence endoscopy with a specific probe, PLSWT7-DMI, to detect NMIBC lesions. We show that intravesical administration of PLSWT7-DMI is safe and effective in improving NMIBC detection, and successfully demonstrate its potential for detecting overlooked neoplastic lesions, which may minimize future relapse. Topical application of imaging probes is an effective method for tumor imaging[28]. The bladder is a storage organ, representing an established intravesical route for topical administration of pharmacological agents without significant systemic absorption. Compared with systemic delivery, topically administered probes are not diluted by the volume of distribution, thus requiring smaller quantities and decreasing the risk of toxicity and the cost of implementation[29, 30]. In the present study, no adverse effects were observed after intravesical administration of PLSWT-DMI, suggesting that the probe was well-tolerated in humans.

In a previous study, we used in vivo phage-display technology to identify the BC-specific peptide PLSWT7. Compared with antibodies, which are commonly used as targeting agents, peptides are easier to label and more cost-effective and have lower immunogenicity[41]. The peptide PLSWT7 had a high binding affinity with rapid onset in urothelial neoplasm cells. As urothelial neoplasms account for the majority of NMIBC cases, PLSWT7 was labeled with IRDye800CW to detect NMIBC endoscopically under NIR imaging in the present study. Before translating PLSWT7-DMI targeted imaging for clinical use, a rigorous validation process and focused regulatory strategy were applied. Mass spectrometry and high-performance liquid chromatography (HPLC) were used to elucidate the structure and synthesis of PLSWT7-DMI. In addition, toxicological tests were performed to confirm the safety of the probe in rats. To further evaluate the feasibility of PLSWT7-DMI for clinical use, ex vivo bladder specimens from high-risk NMIBC patients were used to assess probe-based imaging. Multifocal tumors and CISs were clearly visualized. Similar results were also reported by Pan et al.[42] and Golijanin et al.[43]. However, endoscopically-managed low-risk NMIBC accounts for many BC cases. Furthermore, real-time intraoperative endoscopy involves many challenges that are not encountered in ex vivo imaging, such as the limited range of motion of the endoscope, the length of the procedure, and increased background signal as a result of non-thorough bladder washing. Therefore, low-risk NIMIBC patients were enrolled in the present study, and NIR fluorescence endoscopy with PLSWT7-DMI was performed in vivo. PLSWT7-DMI showed positive binding to Ta and T1 urothelial neoplasms with 90% specificity and 91.2% sensitivity. However, these results need to be verified in a larger cohort with a wider range of pathological types of NMIBC. In particular, the sensitivity may be lower for other types of NMIBC (such as squamous cell carcinoma and adenocarcinoma), as target site expression may vary among tumor cells.

Overlooking small satellite tumors at TUR is one of the major obstacles in the successful treatment of patients with NMIBC, as it results in incomplete tumor control and a high rate of recurrence. CIS is a flat, high-grade NMIBC that poses a diagnostic challenge under WL imaging, and has a significant risk of recurrence and progression[35]. To detect as many NMIBC lesions as possible, the detection of both small multifocal lesions and CISs must be optimized. PLSWT7-DMI-based NIR fluorescence endoscopy detected a greater number of tumors, including three CISs and six small tumors that were not visualized under WL imaging. It is expected that an increase in tumor detection rates will reduce the early recurrence rate of NMIBC[44]. Accordingly, a reduction in the tumor recurrence rate is expected if PLSWT7-DMI fluorescence endoscopy is adopted as a standard procedure during NMBIC resection. Although further trials are needed to confirm these findings, we expect that its use will have a positive impact on the outcomes of patients with NMIBC in clinical practice.

During WL tumor resection, surgeons must remove all suspected lesions to ensure the complete removal of tumors, because the naked eye cannot differentiate malignant lesions from benign lesions[45]. Although the use of 5-aminole-vulinic acid (5-ALA) provides enhanced contrast, the non- specific accumulation of 5-ALA in benign lesions, including inflammation and ulcers, leads to high false-positive rates[33]. This can lead to unnecessary mucosal injury, which provides sites for tumor implantation and recurrence[4]. In contrast, PLSWT7-DMI-based NIR imaging clearly demarcated the tumors via positive binding of the cancer- specific probe. In contrast, benign lesions exhibited negligible fluorescence due to negative probe binding. Therefore, the application of PLSWT7-DMI should enable surgeons to easily discriminate between malignant and benign lesions. The false positive rate of PLSWT7-DMI (10%) was much lower than that of 5-ALA (~ 30%) reported in other studies[34, 46]. Thus, the risk of unnecessary mucosal injury, a critical factor in NMIBC recurrence, could be reduced with PLSWT7-DMI.

Conclusion

In the present study, we demonstrated that PLSWT7-DMI-based NIR fluorescence endoscopy is a feasible and safe approach for detecting NMIBC lesions. The method showed good specificity and sensitivity for the detection of NMIBC. Small satellite tumors and flat CISs that evaded detection under WL imaging were identified using probe-based NIR imaging, and benign lesions could be differentiated from malignant lesions. However, some of the limitations of this study include the exclusion of male patients due to the size of the endoscope and the limited number of patients that were included in the cohort. As a commercial NIR cystoscope is not currently available, a customized NIR endoscope system was developed for the present study. However, the customized endoscope could only be used in female patients because of its limited length. With improved endoscopes, the validity of the method may be evaluated in male patients with NMIBC in future studies. Furthermore, the present study was limited to only 22 patients with NMIBC, suggesting the need for these results to be verified in a larger cohort in future trials.

Author contribution

Wenting Shang and Li Peng wrote the manuscript, in addition to designing, performing, and analyzing all experiments. Wenting Shang synthesized and characterized the probe. Kunshan He designed the imaging system. Pengyu Guo assisted with collecting the information on NMIBC patients. Han Deng assisted with the manuscript modification. Yu Liu assisted with the data analysis. Jie Tian and Wanhai Xu designed, supervised, and analyzed all experiments, in addition to assisting with the manuscript preparation.

Conflict of interest

The authors declare no competing interests.

References

1. Siegel RL, Miller KD, Jemal A. Cancer statistics, 2018. CA Cancer J Clin. 2018;68(1):7–30.
2. Pasin E, Josephson DY, Mitra AP, Cote RJ, Stein JP. Superficial bladder cancer: an update on etiology, molecular development, classification, and natural history. Rev Urol. 2008;10(1):31–43.
3. Carson CC. World Health Organization classification of tumours: pathology & genetics of tumours of the urinary system and male genital organs. Urology. 2005;65(1):213–4.
4. Jichlinski P, Leisinger H. Fluorescence cystoscopy in the management of bladder cancer: a help for the urologist! Urol Int. 2005;74(2):97–101.
5. Oliva Encina J, Marco Valdenebro A, Pelegrí Gabarró J, Rioja SC. Beyond the photodynamic diagnosis: searching for excellence in the diagnosis of non-muscle-invasive bladder cancer.

Eur J Nucl Med Mol Imaging. 2022. 49(9): 3033-3045 Published online: 21 February 2022

Actas Urol Esp. 2010;34(8):657–68.
6. Sylvester RJ, van der Meijden APM, Oosterlinck W, Witjes JA, Bouffioux C, Denis L, et al. Predicting recurrence and progres- sion in individual patients with stage Ta T1 bladder cancer using EORTC risk tables: a combined analysis of 2596 patients from seven EORTC trials. Eur Urol. 2006;49(3):466–77.
7. Aboumarzouk O, Valentine R, Buist R, Ahmad S, Nabi G, Eljamel S, et al. Laser-induced autofluorescence spectroscopy: can it be of importance in detection of bladder lesions? Photodiagn Photodyn. 2015;12(1):76–83.
8. Babjuk M, Burger M, Compérat E, Gontero P, Mostafid AH, Palou J, van Rhijn BWG, Rouprêt M, Shariat SF, Sylvester R, Zigeuner R, Guidelines Associates: Capoun O, Cohen D, Dominguez Escrig JL, Peyronnet B, Seisen T, Soukup V. Guidelines on non- musclie invasive bladder cancer (TaT1 and CIS). EAU. 2020.
9. Babjuk M, Burger M, Compérat EM, Gontero P, Mostafid AH, Palou J, et al. European Association of Urology guidelines on non-muscle-invasive bladder cancer (TaT1 and carcinoma in situ) - 2019 update. Eur Urol. 2019;76(5):639–57.
10. Lykke MR, Nielsen TK, Ebbensgaard NA, Zieger K. Reducing recurrence in non-muscle-invasive bladder cancer using photo- dynamic diagnosis and immediate post-transurethral resection of the bladder chemoprophylaxis. Scand J Urol. 2015;49(3):230–6.
11. Fradet Y, Grossman HB, Gomella L, Lerner S, Cookson M, Albala D, et al. A comparison of hexaminolevulinate fluorescence cystoscopy and white light cystoscopy for the detection of carcinoma in situ in patients with bladder cancer: a phase III, multicenter study. J Urol. 2007;178(1):68–73.
12. Grimm M, Steinhoff C, Simon X, Spiegelhalder P, Ackermann R, Vögeli TA. Effect of routine repeat transurethral resection for superficial bladder cancer: a long-term observational study. J Urol. 2003;170(2):433–7.
13. Chai CA, Yeoh WS, Rajandram R, Aung KP, Ong TA, Kuppusamy S, Nazran A, Kumaran K, Razack AHA, Teoh JY. Com- paring CxBladder to urine cytology as adjunct to cystoscopy in surveillance of non-muscle invasive bladder cancer-a pilot study. Front Surg. 2021;8:659292.
14. Beji S, Lam GW, Ostergren PB, Toxvaerd A, Sonksen J, Fode M. Diagnostic value of probe-based confocal laser endomicroscopy versus conventional endoscopic biopsies of non-muscle invasive bladder tumors: a pilot study. Scand J Urol. 2021;55(1):36–40.
15. Rouanne M, Betari R, Radulescu C, Goubar A, Signolle N, Neu- zillet Y, et al. Stromal lymphocyte infiltration is associated with tumour invasion depth but is not prognostic in high-grade T1 bladder cancer. Eur J Cancer. 2019;108:111–9.
16. Daneshmand S, Bazargani ST, Bivalacqua TJ, Holzbeierlein JM, Willard B, Taylor JM, et al. Blue light cystoscopy for the diagnosis of bladder cancer: results from the US perspective multicenter registry. Urol Oncol. 2018;36(8):361.e1-361.e6.
17. Drejer D, Beji S, Oezeke R, Nielsen AM, Hoyer S, Johansen TEB, et al. Comparison of white light, photodynamic diagnosis, and narrow-band imaging in detection of carcinoma in situ or flat dysplasia at transurethral resection of the bladder: the DaBlaCa-8 study. Urology. 2017;102:138–42.
18. Rink M, Babjuk M, Catto JWF, Jichlinski P, Shariat SF, Stenzl A, et al. Hexyl aminolevulinate–guided fluorescence cystoscopy in the diagnosis and follow-up of patients with non–muscle-invasive bladder cancer: a critical review of the current literature. Eur Urol. 2013;64(4):624–38.
19. Schraml J, Silva JDC, Babjuk M. Current concept of transurethral resection of bladder cancer: from re-transurethral resection of bladder cancer to en-bloc resection. Curr Opin Urol. 2018;28(6):591–7.
20. Liu J, Droller MJ, Liao JC. New optical imaging technologies for bladder cancer: considerations and perspectives. J Urol. 2012;188(2):361–8.
21. Wiesner C, Jäger W, Salzer A, Biesterfeld S, Kiesslich R, Hampel C, et al. Confocal laser endomicroscopy for the diagnosis of urothelial bladder neoplasia: a technology of the future? BJU Int. 2011;107(3):399–403.
22. Gladkova N, Streltsova O, Zagaynova E, Kiseleva E, Gelikonov V, Gelikonov G, et al. Cross-polarization optical coherence tomography for early bladder-cancer detection: statistical study. J Bio- photonics. 2011;4(7–8):519–32.
23. Mahalingam SM, Dudkin VY, Goldberg S, Klein D, Yi F, Singhal S, et al. Evaluation of a centyrin-based near-infrared probe for fluorescence-guided surgery of epidermal growth factor receptor positive tumors. Bioconjug Chem. 2017;28(11):2865–73.
24. James ML, Gambhir SS. A molecular imaging primer: modalities, imaging agents, and applications. Physiol Rev. 2012;92(2):897–965.
25. Peng L, Shang W, Guo P, He K, Wang H, Han Z, et al. Phage display-derived peptide-based dual-modality imaging probe for bladder cancer diagnosis and resection postinstillation: a preclinical study. Mol Cancer Ther. 2018;17(10):2100–11.
26. Benias PC, Wells RG, Sackey-Aboagye B, Klavan H, Reidy J, Buonocore D, Miranda M, Kornacki S, Wayne M, Carr-Locke DL, Theise ND. Structure and distribution of an unrecognized interstitium in human tissues. Sci Rep. 2018;8(1):4947.
27. Bourn J, Rathore K, Donnell R, White W, Uddin MJ, Marnett L, Cekanova M. Detection of carcinogen-induced bladder cancer by fluorocoxib A. BMC Cancer. 2019;19(1):1152.
28. Schmidt A, Sommer F, Reiner M, Klotz T, Engelmann U, Addicks K, Bloch W. Differential endostatin binding to bladder, prostate and kidney tumour vessels. BJU Int. 2005;95(1):174–9.
29. Zupančič D, Kreft ME, Sterle I, Romih R. Combined lectin- and immuno-histochemistry (CLIH) for applications in cell biology and cancer diagnosis: analysis of human urothelial carcinomas. Eur J Histochem. 2020;64(3):3141.
30. Inoue K. 5-Aminolevulinic acid-mediated photodynamic therapy for bladder cancer. Int J Urol. 2017;24(2):97–101.
31. Feng Z, Yu X, Jiang M, Zhu L, Zhang Y, Yang W, Xi W, Li G, Qian J. Excretable IR-820 for in vivo NIR-II fluorescence cerebrovascular imaging and photothermal therapy of subcutaneous tumor. Theranostics. 2019;9(19):5706–19.
32. Huang J, Jiang Y, Li J, He S, Huang J, Pu K. A renal-clearable macromolecular reporter for near-infrared fluorescence imaging of bladder cancer. Angew Chem Int Ed Engl. 2020;59(11):4415–20.
33. Shen P, Yang J, Wei W, Li Y, Li D, Zeng H, et al. Effects of fluorescent light-guided transurethral resection on non-muscle- invasive bladder cancer: a systematic review and meta-analysis. BJU Int. 2012;110(6b):E209–15.
34. Witjes JA, Babjuk M, Gontero P, Jacqmin D, Karl A, Kruck S, et al. Clinical and cost effectiveness of hexaminolevulinate-guided blue-light cystoscopy: evidence review and updated expert recommendations. Eur Urol. 2014;66(5):863–71.
35. Burggraaf J, Kamerling IMC, Gordon PB, Schrier L, de Kam ML, Kales AJ, et al. Detection of colorectal polyps in humans using an intravenously administered fluorescent peptide targeted against c-Met. Nat Med. 2015;21(8):955–61.
36. Foersch S, Kiesslich R, Waldner MJ, Delaney P, Galle PR, Neurath MF, et al. Molecular imaging of VEGF in gastrointestinal cancer in vivo using confocal laser endomicroscopy. Gut. 2010;59(8):1046–55.
37. Hattori S, Kojima K, Minoshima K, Yamaha M, Horie M, Sawamura T, Kikuchi A, Deguchi T. Detection of bladder cancer by measuring CD44v6 expression in urine with real-time quantitative reverse transcription polymerase chain reaction. Urology. 2014;83(6):1443.
38. Goetz M, Wang TD. Molecular imaging in gastrointestinal endos- copy. Gastroenterology. 2010;138(3):828–33.
39. Quan YH, Oh CH, Jung D, Lim JY, Choi BH, Rho J, Choi Y, Han KN, Kim BM, Kim C, Park JH, Kim HK. Evaluation of intraoperative near-infrared fluorescence visualization of the lung tumor margin with indocyanine green inhalation. JAMA Surg. 2020;155(8):732–40.
40. Naselli A, Introini C, Bertolotto F, Spina B, Puppo P. Narrow band imaging for detecting residual/recurrent cancerous tissue during second transurethral resection of newly diagnosed non-muscle-invasive high-grade bladder cancer. BJU Int. 2010;105(2):208–11.
41. Sturm MB, Joshi BP, Lu S, Piraka C, Khondee S, Elmunzer BJ, et al. Targeted imaging of esophageal neoplasia with a fluorescently labeled peptide: first-in-human results. Sci Transl Med. 2013;5(184):184ra61.
42. Pan Y, Volkmer J, Mach KE, Rouse RV, Liu J, Sahoo D, et al. Endoscopic molecular imaging of human bladder cancer using a CD47 antibody. Sci Transl Med. 2014;6(260):260ra148.
43. Golijanin J, Amin A, Moshnikova A, Brito JM, Tran TY, Adochite R, et al. Targeted imaging of urothelium carcinoma in human bladders by an ICG pHLIP peptide ex vivo. Proc Natl Acad Sci U S A. 2016;113(42):11829–34.
44. Riedl CR, Daniltchenko D, Koenig F, Simak R, Loening SA, Pflueger H. Fluorescence endoscopy with 5-aminolevulinic acid reduces early recurrence rate in superficial bladder cancer. J Urol. 2001;165(4):1121–3.
45. Gosnell ME, Polikarpov DM, Goldys EM, Zvyagin AV, Gillatt DA. Computer-assisted cystoscopy diagnosis of bladder cancer. Urol Oncol. 2018;36(1):8. e99-8. e15.
46. Stenzl A, Penkoff H, Dajc-Sommerer E, Zumbraegel A, Hoeltl L, Scholz M, Riedl C, Bugelnig J, Hobisch A, Burger M, Mikuz G, Pichlmeier U. Detection and clinical outcome of urinary bladder cancer with 5-aminolevulinic acid-induced fluorescence cystoscopy: a multicenter randomized, double-blind, placebo-controlled trial. Cancer. 2011;117(5):938–47.

Urology

Letter to Editor

Intraoperative Near-Infrared II Window Fluorescence Imaging-Assisted Nephron-Sparing Surgery for Complete Resection of Cystic Renal Masses

Caiguang Cao,[1,2,*] Shaohui Deng,[3,*] Binshuai Wang,[3,*] Xiaojing Shi,[1,2] Liyuan Ge,[3] Min Qiu,[3] Fan Zhang,[3] Min Lu,[4] Lulin Ma,[3] Chongwei Chi,[1] Zhenhua Hu,[1,2] Jie Tian,[1,2,5,6] and Shudong Zhang[3]

[1] Beijing Key Laboratory of Molecular Imaging, The State Key Laboratory of Management and Control for Complex Systems, Institute of Automation, Chinese Academy of Sciences, Beijing China
[2] School of Artificial Intelligence, University of Chinese Academy of Sciences, Beijing China
[3] Department of Urology, Peking University Third Hospital, Beijing China
[4] Department of Pathology, Peking University Third Hospital, Beijing China
[5] Beijing Advanced Innovation Center for Big Data-Based Precision Medicine, School of Medicine, Beihang University, Beijing China
[6] Engineering Research Center of Molecular and Neuro Imaging of Ministry of Education, School of Life Science and Technology, Xidian University, Xi'an China
* These authors contributed equally to this work.

Dear Editor,

The resection of cystic renal masses (CRMs) represents a challenging process in terms of nephron-sparing surgery because the mostly fluid-filled growth pattern of renal cancers causes them easy to rupture.[1] As the malignant tumours rupture, cancer cells metastasize in the abdominal cavity, patients face a high risk of recurrence.[2] Meanwhile, studies have shown that more functional nephrons correlate with a better prognosis of patients.[3] Therefore, it is crucial to achieving accurate and complete tumour resection during partial nephrectomy (PN).

The near-infrared II (NIR-II, 1000–1700 nm) window fluorescence imaging is a highly promising strategy for medical applica-

Table 1 Characteristics and preoperative diagnosis of patients with CRM

Variable	Value
Patients, *n*	9
Age/year, M (range)	46 (35–65)
Gender, *n*	
Male	8
Female	1
Affected side, *n*	
Left	5
Right	4
Tumour diameter/mm, M (range)	48 (27–61)
Preoperative eGFR, M (range)	92 (68–113)
RENAL score, M (range)	8 (4–9)
Ischaemia time/min, M (range)	14 (10–25)
Blood loss/ml, M (range)	100 (10–400)
Hospital stay/day, M (range)	6 (3–6)
Pathology	
ccRCC	4
BRC	4
PKD	1
Postoperative eGFR, M (range)	72 (41–105)

Abbreviations: BRC, benign renal cyst; ccRCC, clear cell renal cell carcinoma; eGFR; estimated glomerular filtration rate; M, median; PKD, polycystic kidney disease.

tions. Based on our experience of image-guided surgery,[4] a novel NIR-II fluorescence imaging system was developed for helping the resection of CRM (Supplementary S1). From October 2019 to November 2020, nine patients who underwent PN for resection of CRM were enrolled (Table 1). After exposing tumours, indocyanine green (ICG, 0.5 mg/kg body weight) was injected intravenously, the NIR-II fluorescence imaging system was used for the visualization of tumours (Figure 1, Supplementary S2). Under the guidance of NIR-II fluorescence imaging, all tumours were completely resected without rupture, no recurrence or metastasis was found after 4–17 months of follow-up.

For a representative patient, the enhanced CT examination revealed a renal mass located at the right kidney (Figure 2A and B). After kidney exposure, the surgical region was first imaged under white light illumination (Figure 2C). One minute after ICG injection, NIR-II fluorescence was observed in renal parenchyma and partial of the tumour vessels. The boundaries between tumour and renal parenchyma were distinct in the NIR-II fluorescence images (Figure 2D and E), in which the renal parenchyma-to-tumour (RP/T, defined in Supplementary S3) fluorescence intensity ratio was 6.37 and the contrast-to-noise ratio (CNR, defined in Supplementary S3) was 5.25. Subsequently, tumour boundaries were marked by electrocautery guided by NIR-II imaging (Figure 2F). Fluorescence signal intensity extracted from the position of the black arrow in Figure 2E showed the intensity weakened sharply from renal parenchyma to tumour (Figure 2G).

The three-dimensional fluorescence distribution map of the imaged area in Figure 2D further showed the signal intensity of renal parenchyma was significantly higher than that of the tumour (Figure 2H), which again proved the efficacy of NIR-II imaging to detected tumour boundaries. After resection, the visual inspection did not detect residual tumours on the surgical margin (Figure 2I),

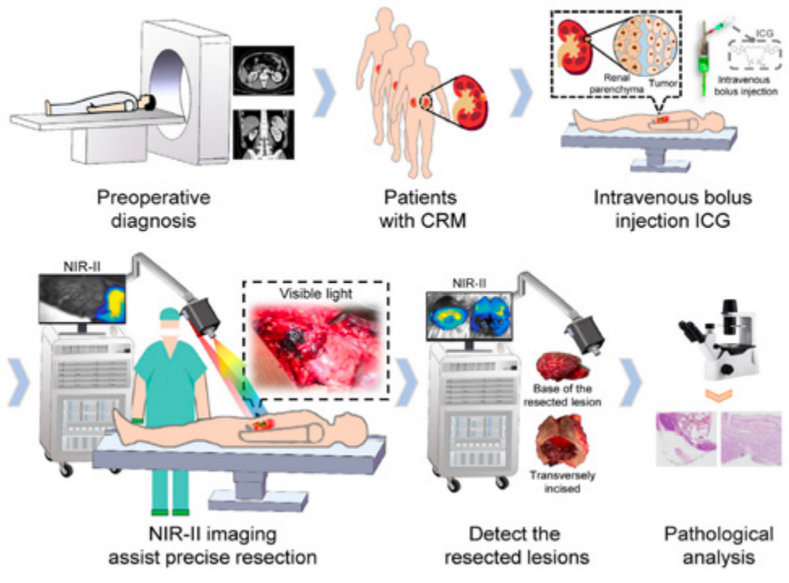


Fig.1 Flow diagram of the study protocol. Patients first received preoperative imaging examinations to determine whether eligible for the study. On the day of surgery, after laparotomy, ICG with a dose of 0.5 mg/kg body weight was administrated intravenously before blocking the renal artery. Then, the tumour boundaries were marked on the kidney surface under the guidance of the NIR-II images, which were followed by arteries clamping and tumour resection. After resection, images of the surgical margins and resected lesions in the white-light illumination and NIR-II region were acquired separately. Lastly, pathological examinations were carried out.

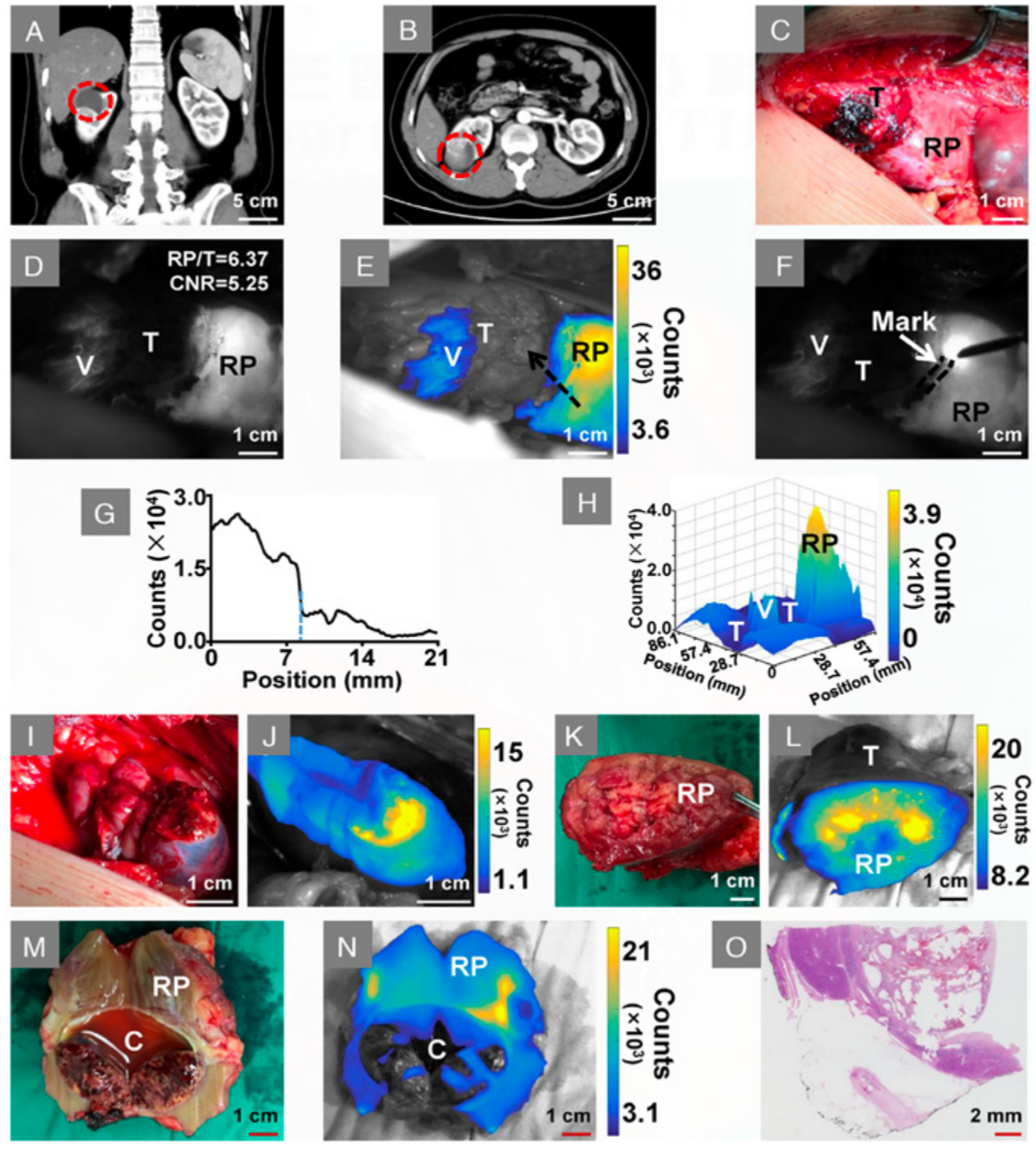


Fig.2 Intraoperative NIR-II image-assisted tumour resection. (A and B) Coronal-plane and transverse-plane of the enhanced CT image, red circle indicates a renal mass located at the right kidney. (C) Visible-light image of the tumour and renal parenchyma. (D) Fluorescence is observed in renal parenchyma and partial tumour vessels after ICG injection. (E) Overlay image of D, in which fluorescence is shown in pseudo-colour. (F) Tumour boundaries were marked by electrocautery on the kidney surface, the black dotted line showed the mark traces. (G) Cross-sectional fluorescence intensity, which was extracted from the position of the black arrow in E. The blue dotted line in G indicates the place where is the boundary between tumour and renal parenchyma. (H) Three-dimensional mapping of the fluorescence distribution of D. (I) White-light illumination image of the surgical margins. (J) NIR-II imaging shows intense fluorescence on the surgical margin. (K) Visible-light image of the tumour base. (L) Overlay image shows intense fluorescence on the base of the tumour. (M) Visible-light image of the tumour cavity, the intact internal fluid indicates the tumour is resected without rupture. (N) Overlay image of the tumour cavity. (O) Pathological examination with haematoxylin and eosin staining shows the tumour is ccRCC. Abbreviations: C, tumour cavity; RP, renal parenchyma; T, tumour; V, vessel

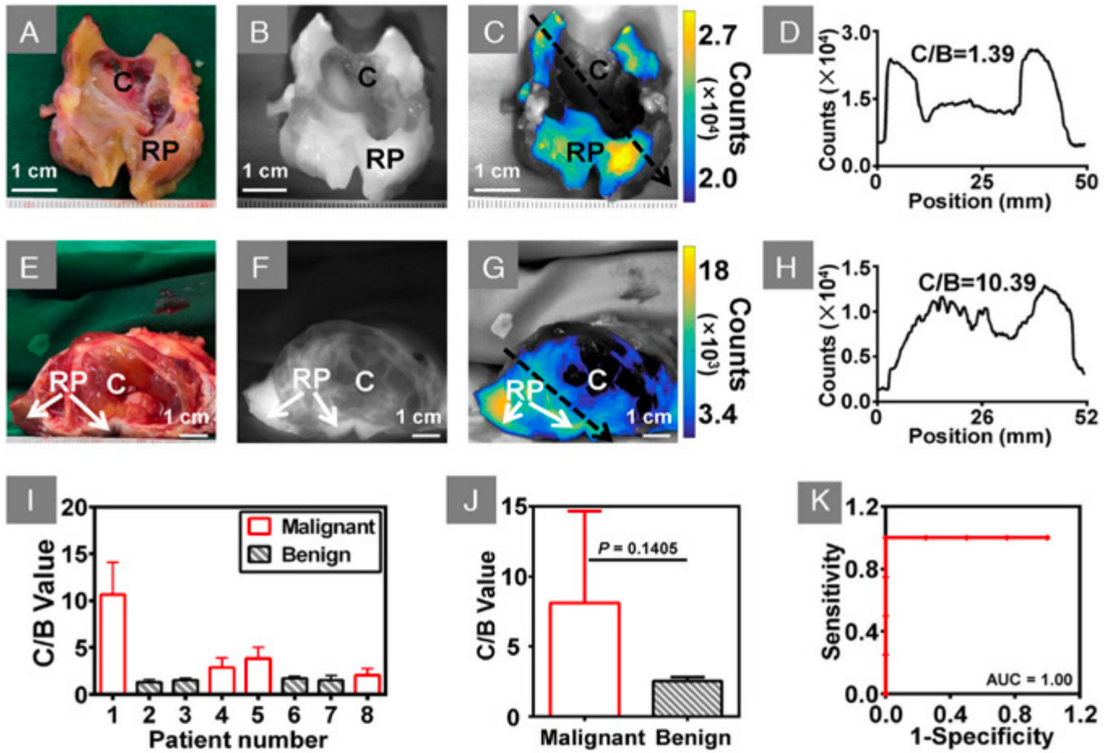


Fig.3 NIR-II imaging identified ccRCC from resected lesions. (A) A benign renal cystic tumour was dissected along the maximum axis. (B and C) NIR-II image and overlay image showed there was almost no fluorescence in the tumour cavity. (D) Cross-sectional fluorescence intensity corresponding to the location and direction of the black arrow in C, which also demonstrated the lower intensity in the cavity. (E) A ccRCC tumour was dissected along the maximum axis. (F and G) NIR-II image and overlay image showed some areas of the tumour cavity also appeared fluorescence. (H) Cross-sectional fluorescence intensity corresponding to the location and direction of the black arrow in G, which also showed the intense fluorescence presented in the tumour cavity. (I) Bar graph of the C/B ratio of each patient, the error bars indicate the standard deviation over all pixels within the region of interest of tumour cavity. (J) The comparison of the average ratio of C/B between benign and malignant tumours. (K) The ROC analysis about discriminating ccRCC by NIR-II imaging. Abbreviations: TC, tumour cavity; RP, renal parenchyma

the NIR-II imaging also exhibited intense fluorescence (Figure 2J). A similar fluorescence-guided surgery was conducted on other patients (Figure S1 and Video S1).

Subsequently, resected tissue of the patient was further inspected, intense fluorescence was detected on the base of the lesion (Figure 2K and L). Combining the NIR-II images of the surgical margin with the visual examination, the tumour was considered to be completely removed. The lesion was then dissected along its maximum axis, the internal fluid in the cavity indicated no rupture occurred during resection (Figure 2M and N). Finally, pathological examination showed the tumour was clear cell renal cell carcinoma (ccRCC) and was completely resected (Figure 2O).

The fluorescence images of the dissected lesions were further analysed. Quantitative analysis showed that NIR-II imaging was able to identify ccRCC from the resected lesions (Figure 3, Figure S2). For a benign renal cyst transversely incised, almost no fluorescence was exhibited in the tumour cavity (Figure 3A–C). The cross-sectional fluorescence intensity profile also showed a lower intensity in the tumour cavity (Figure 3D). Conversely, fluorescence was detected in some areas of the tumour cavity of ccRCC (Figure 3E–G), which was proved by the cross-sectional fluorescence intensity profile (Figure 3H). Eight of the nine resected lesions were dissected and all the tumour cavity-to-background (C/B, defined in Supplementary S3) fluorescence intensity ratio of ccRCCs was much higher than those of benign tumours (Figure 3I and J; 4.87 ±3.40 vs.1.53 ± 0.15, p = 0.1405). Besides, for each ccRCC, the C/B ratio was greater than 2.0, while the C/B

ratio was lower than 1.8 for benign tumours, the receiver operating characteristic analysis about categorizing resected lesions showed the area under the curve (AUC) was 1.00 (Figure 3K).

As shown in the above results, clinical benefits were brought with the use of NIR-II imaging. ICG-based traditional first near-infrared window (700–900 nm) fluorescence imaging of renal tumour is limited to reduce the positive margin rate.[5] The rate of positive surgical margins after nephron-sparing surgery is as high as nearly 10%.[6] One of the key obstacles is that those small residual tumours on the surgical margins are shadowed by the intense fluorescence of renal parenchyma during fluorescence imaging. In this study, surgical margins and base of the resected lesions received NIR-II imaging, only when both appeared intense fluorescence was the tumour considered completely removed. Our pilot clinical results demonstrate this approach is an effective method for detecting residual tumours in the condition where normal tissue exhibits higher intense fluorescence than tumours.

The ICG injection dose is an important influence fator of fluorescence imaging during PN. Briefly, different dose causes renal parenchyma appears inadequate fluorescence or otherwise tumours appear undesirable fluorescence.[7] Diverse injection doses have been reported, but not all tumours were successfully detected in the previous studies.[8,9] In this trial, ICG at a dose of 0.5 mg/kg body weight was administrated, benefited from the lower auto-fluorescence and less interfered from the ambient light in the NIR-II region, tumours were distinctly identified in all patients. The injection dose can be a reference for NIR-II imaging in other renal-related researches. Additionally, the ccRCC was identified based on the diversity of C/B ratios between different lesions. Although the relationship between the fluorescence in the tumour cavity and the ICG administration dose needed to be investigated. Our finding highlights the NIR-II imaging as a potential diagnostic technique that may alter the treatment of CRM.

In summary, the first clinical trial of NIR-II imaging for the resection of CRM was reported in this study. The novel technique brings benefits to patients, such as no positive surgical margins and no tumour ruptured during resection. In the future, other relevant benefits of the NIR-II imaging assists CRM resection can be explored.

Acknowledgements

This study was supported by the National Key Research and Development Program of China (2017YFA0205200), the National Natural Science Foundation of China (62027901, 81930053, 92059207, 81227901, and 82072828), Beijing Natural Science Foundation (JQ19027), the innovative research team of high-level local universities in Shanghai and the Zhuhai High-level Health Personnel Team Project (Zhuhai HLHPTP201703). We acknowledge the instrumental and technical support of the multi-modal biomedical imaging experimental platform, Institute of Automation, Chinese Academy ofSciences.

Conflict of Interests

The authors declare no conflict of interests.

References

1. Hindman NM. Imaging of cystic renal masses. Urol Clin North Am. 2018;45:331-349.
2. Pradere B, Peyronnet B, Delporte G, et al. Intraoperative cyst rupture during partial nephrectomy for cystic renal masses—does it increase the risk of recurrence? J Urol. 2018;200:1200-1206.
3. Tobis S, Knopf JK, Silvers C, et al. Robot-assisted and laparoscopic partial nephrectomy with near infrared fluorescence imaging. J Endourol. 2012;26:797-802.
4. Hu Z, Fang C, Li B, et al. First-in-human liver-tumour surgery guided by multispectral fluorescence imaging in the visible and near-infrared-I/II windows. Nat Biomed Eng. 2020;4:259-271.
5. Secil M, Elibol C, Aslan G, et al. Role of intraoperative US in the decision for radical or partial nephrectomy. Radiology. 2011;258:283-290.
6. Marszalek M, Carini M, Chlosta P, et al. Positive surgical margins after nephron-sparing surgery. Eur Urol. 2012;61:757-763.
7. Angell JE, Khemees TA, Abaza R. Optimization of near infrared fluorescence tumor localization during robotic partial nephrectomy. J Urol. 2013;190:1668-1673.
8. Veccia A, Antonelli A, Hampton LJ, et al. Near-infrared fluorescence imaging with indocyanine green in robot-assisted partial nephrectomy: pooled analysis of comparative studies. Eur Urol Focus. 2020;6:505-512.
9. Mitsui Y, Shiina H, Arichi N, et al. Indocyanine green (ICG)-based fluorescence navigation system for discrimination of kidney cancer from normal parenchyma: application during partial nephrectomy. Int Urol Nephrol. 2012;44:753-759.

Colorectal Surgery

Research Article

Blood Perfusion Assessment by Near-Infrared Fluorescence Angiography of Epiploic Appendages in Prevention of Anastomotic Leakage after Laparoscopic Intersphincteric Resection for Ultra-Low Rectal Cancer: A Case-Matched Study

Wenlong Qiu[1, *], Junguang Liu[2, *], Kunshan He[3, *], Gang Hu[1], Shiwen Mei[1], Xu Guan[1], Xishan Wang[1], Jie Tian[3], Jianqiang Tang[1] ✉

Abstract

Background: The role of intraoperative near-infrared fluorescence angiography with indocyanine green in reducing anastomotic leakage (AL) has been demonstrated in colorectal surgery, however, its perfusion assessment mode, and efficacy in reducing anastomotic leakage after laparoscopic intersphincteric resection (LsISR) need to be further elucidated.

Aim: Aim was to study near-infrared fluorescent angiography to help identify bowel ischemia to reduce AL after LsISR.

Material and methods: A retrospective case-matched study was conducted in one referral center. A total of 556 consecutive patients with ultra-low rectal cancer including 140 patients with fluorescence angiography of epiploic appendages (FAEA) were enrolled. Perfusion assessment by FAEA in the monochrome fluorescence mode. Patients were divided into two groups based on perfusion assessment by FAEA. The primary endpoint was the AL rate within 6 months, and the secondary endpoint was the structural sequelae of anastomotic leakage (SSAL).

Results: After matching, the study group (n = 109) and control group (n = 190) were well-balanced. The AL rate in the FAEA group was lower before (3.6% vs. 10.1%, P = 0.026) and after matching (3.7% vs. 10.5%, P = 0.036). Propensity scores matching analysis (OR 0.275, 95% CI 0.035–0.937, P 0.039), inverse probability of treatment weighting (OR 0.814, 95% CI 0.765–0.921, P 0.002), and regression analysis (OR 0.298, 95% CI 0.112–0.790, P = 0.015), showed that FAEA was an independent protector factor for AL. This technique can significantly shorten postoperative hospital stay [9 (6–13) vs. 10 (8–13), P = 0.024] and reduce the risk of SSAL (1.4% vs. 6.0%, P = 0.029).

Conclusions: Perfusion assessment by FAEA can achieve better visualization in LsISR and reduce the incidence of AL, subsequently avoiding SSAL after LsISR.

Keywords
Anastomoticn leakage, Near-infrared fluorescence angiography, Indocyanine green, Laparoscopic intersphincteric resection, Ultra-low rectal cancer

[1] Department of Colorectal Surgery, National Cancer Center/ National Clinical Research Center for Cancer/Cancer Hospital, Chinese Academy of Medical Sciences and Peking Union Medical College, Beijing 100000, China
[2] Department of General Surgery, Peking University First Hospital, Beijing 100034, China
[3] Key Laboratory of Molecular Imaging Chinese Academy of Sciences, Beijing Key Laboratory of Molecular Imaging. Key Laboratory of Big Data-Based Precision Medicine, Ministry of Industry and Information Technology, Beijing 100000, China
* Wenlong Qiu, Junguang Liu, and Kunshan He contributed equally to this work.

Introduction

Intersphincteric resection (ISR), is commonly performed in patients with ultra-low rectal cancer for whom anal preservation is desired. However, anastomotic leakage (AL) remains a major issue after ISR, with an incidence of 3%–20% [1–6]. Previous studies have shown that AL is a multifactorial process, commonly occurring in males and influenced by preoperative radiotherapy, nutritional status, anastomosis level, intraoperative blood loss, number of stapler firings, and bowel perfusion [7–9]. Traditionally, proximal bowel perfusion at the anastomosis site is assessed intraoperatively using experience-based judgment to check for active bleeding at the resection margins, palpable pulsation in the mesentery, and absence of discoloration [10, 11]. However, this measure is subjective and very unreliable.

Intraoperative pseudo-color fusion-based near-infrared fluorescence angiography (NIR-FA) of the mucosa with indocyanine green (ICG) provides sufficient visualization allowing for resection margin determination. A recent meta- analysis [12] revealed that NIR-FA significantly reduced AL and the need for surgical reintervention after colorectal surgery. A randomized clinical trial (EssentiAL trial) confirmed that the addition of ICG-FI significantly reduced the anastomotic leakage rate by 4.2%, although the actual reduction rate of anastomotic leakage in the

Surg Endosc. 2024. 38(9):5446-5456. Published online: 1 August 2024

ICG + group was lower than the expected reduction rate of 6% and the addition of ICG-FI was not superior to white light (ICG- group). However, the PILLAR III trial showed no significant difference in AL rates between NIR-FA and conventional imaging modalities [13]. Additionally, NIR-FA is susceptible to biological tissue scattering, resulting in the diffuse overall fluorescence signal near the anastomotic region [14]. Especially in the total laparoscopic era, surgeons still have to rely on subjective visual perception to determine the transection level. Therefore, the perfusion assessment mode and efficacy of NIR-FA need to be further optimized and established.

The promotion of laparoscopic surgery has raised higher requirements for intracorporeal anastomosis. However, the traditional ICG fluorescence judgment-based merged fluorescent image, which was easily affected by the background color. Here, we proposed a novel, monochrome fluorescence-based mode to dynamically determine bowel perfusion on the basis of fluorescence angiography of epiploic appendages (FAEA). This study aimed to investigate the feasibility and efficacy of the FAEA mode in reducing AL and structural sequelae of AL (SSAL) after laparoscopic intersphincteric resection (LsISR) for ultra-low rectal cancer. The primary endpoint was the AL rate within 6 months, and the secondary endpoint was the SSAL We hypothesized that FAEA could significantly reduce the AL incidence and avoid SSAL after laparoscopic intersphincteric resection (LsISR) for ultra-low rectal cancer.

Materials and methods

Patients

We retrospectively collected data of patients with LsISR from Cancer Hospital and the Chinese Academy of Medical Sciences between January 2012 and July 2023 (Fig. 1). The inclusion criteria were as follows: (1) patients with ultra- low

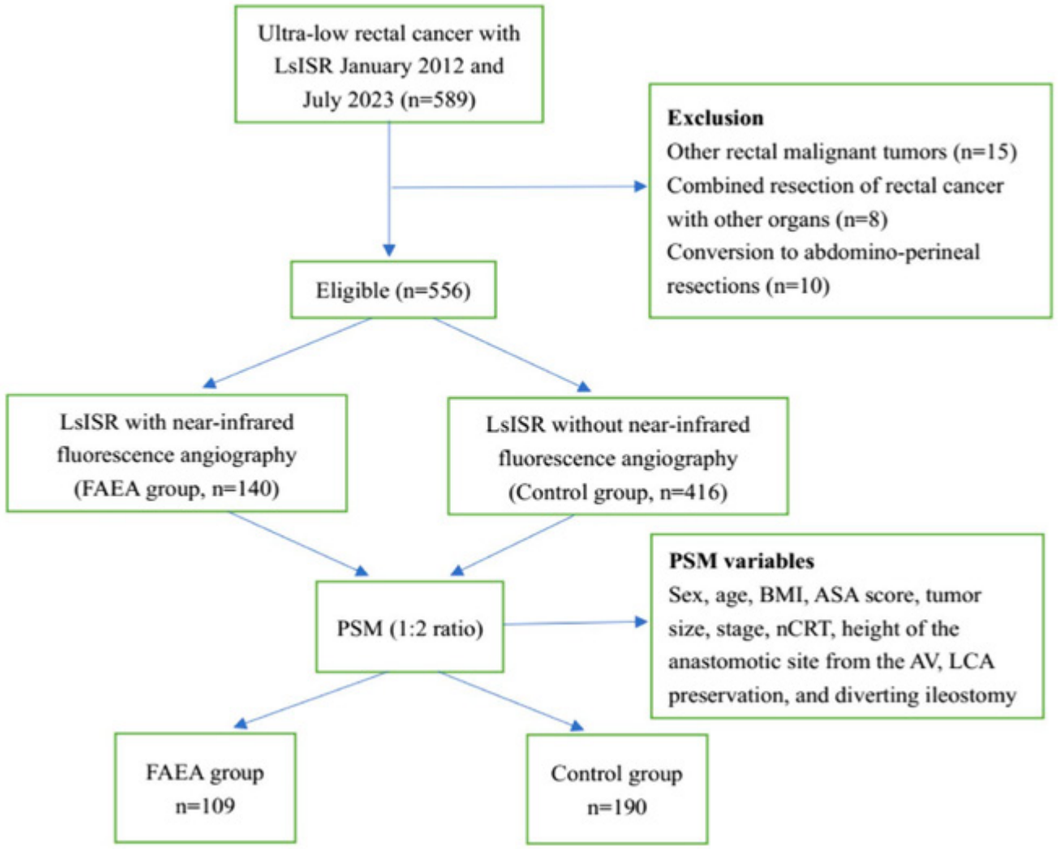


Fig.1 Flowchart of this study

rectal adenocarcinoma (≤ 5 cm from the anal verge);(2) LsISR. The exclusion criteria were (1) Other rectal malignant tumors, (2) Combined resection, (3) Conversion to abdomino-perineal resections. A multidisciplinary team meeting determined the treatment strategy and need for neo- adjuvant chemoradiotherapy (nCRT) for each patient. All the patients who received neoadjuvant chemoradiotherapy were treated with a long-course chemoradiation regimen. We used a standard long-course regimen of 5-fluorouracil (5-FU)-based chemotherapy and a total dose of 45 to 54 Gy of external beam radiation. Following nCRT, patients were reassessed by pelvic MRI. Surgery was performed approximately 8 to 12 weeks after nCRT. All patients enrolled in the study provided informed consent. The study protocol was approved by the Ethics Committee of Cancer Hospital, Chinese

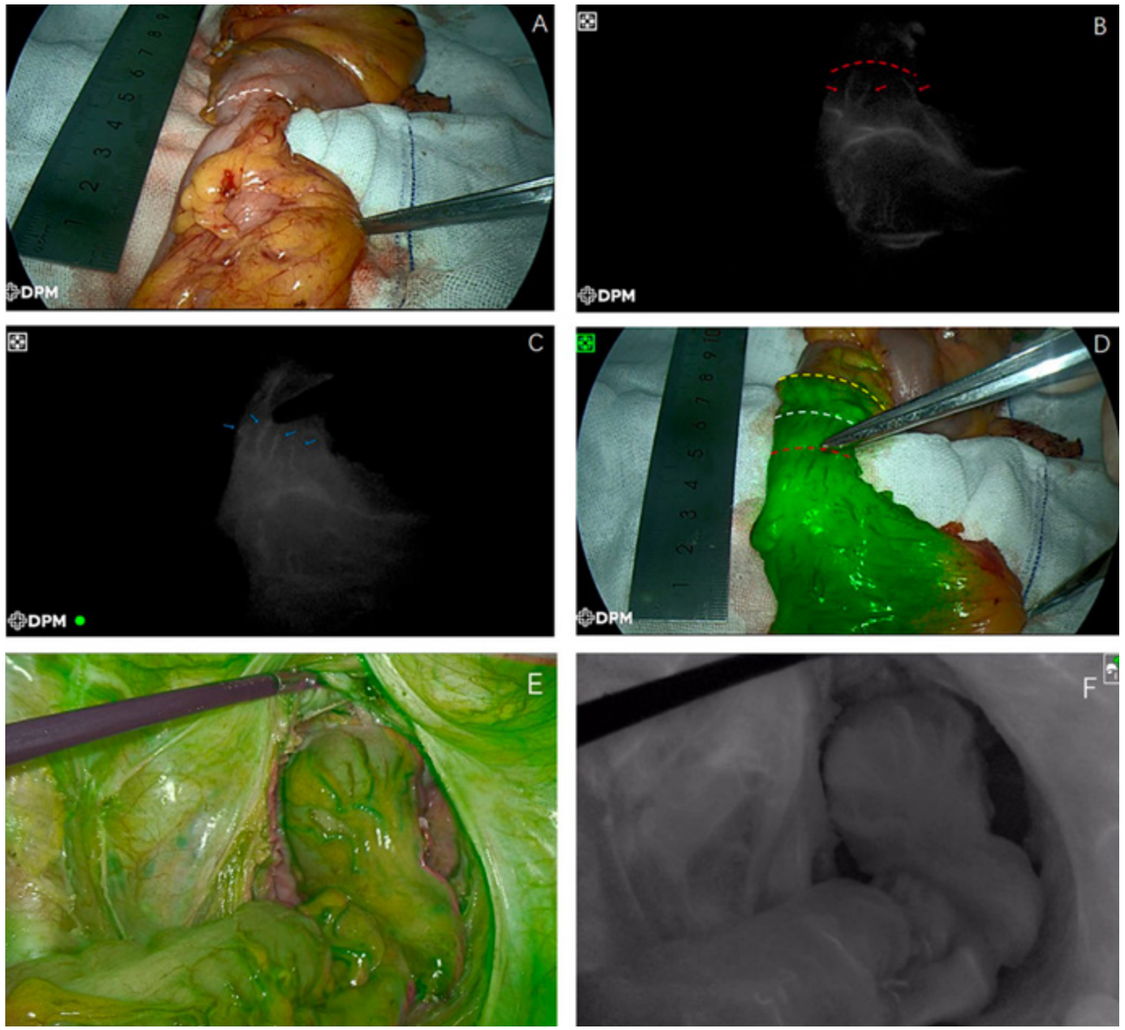


Fig.2 Clinical judgment of ischemic line in different near- infrared modes. After transection of the anal side of the rec- tum, the specimen was extracted through the incision. After the division of the mesentery at the level of planned transection, **A** the ischemic line was observed by using color vision mode (white line); **B** the micro- arterioles of epiploic appendage were dynamically observed using monochrome fluorescence mode after ICG was intravenously injected. The dissecting line (red line) based on the end of micro-arterioles in this mode was recorded; **C** the venules and the bowel wall gradually became visible; **D** changed the imaging to the merged mode, and marked the merging borderline (yellow line), this line is 1–2 cm distal to the dissecting line (red line) based on micro-arterioles of epiploic appendage; **E** before intra- corporeal anastomosis, the blood perfusion of bowel was observed under merged mode; **F** the blood perfusion of bowel was observed under monochrome fluorescence mode.

Academy of Medical Sciences.

NIR imaging system

We used a 4K ultra-HD laparoscopic NIR imaging system (DPM-ENDOCAM-03 and DPM-LIGHT-03, Zhuhai,

China) from Dipu Medical Technology Co. This system irradiates excitation light at 785 ± 5 nm and collects emission light at 830–900 nm. It employs a generative adversarial network-based image enhancement method to achieve multi-scale image detail boosting [15]. Furthermore, color, monochrome fluorescence, and pseudo-color fusion images can be displayed simultaneously or separately. All imaging results had a resolution of at least 3840 × 2160, and NIR images can be converted into different modes of heat maps according to surgical requirements. The imaging vision could be adjusted by manipulating the laparoscopic imaging adapter.

Surgical procedures

Radical rectal cancer surgery was routinely performed by two surgeons (XW and JT) with > 10 years of experience and who have handled ≥ 100 LsISR cases. A standard total mesorectal excision was performed, with careful preservation of the bilateral hypogastric nerve and neurovascular bundles. The intersphincteric plane between the puborectalis muscle and internal sphincter was carefully dissected under direct vision. The distal rectum was transected intracorporeally using a flexible linear stapler. When the distal resection margin was < 1 cm or was suspected to be positive, an intraoperative frozen section pathology was usually required for confirmation. The anastomosis was constructed manually. According to the distance from the anastomosis to the anus, the blood perfusion of the anastomotic bowel, the patient's willingness to stoma and surgical experience, we decided whether to stoma.

The details of ICG administration determination of ischemic line

The route of ICG administration for evaluating anastomotic blood perfusion in laparoscopic colorectal surgery was injection via peripheral vein or central vein, and then flushing venous catheter with 5 mL–10 mL normal saline. The dosage concentration of 2.5 mg/mL was recommended. The injection dose was calculated based on the body weight, and the dose was 0.1 mg/kg–0.5 mg/kg. The observation time duration of vascular perfusion was set to 10 s–60 s.

For the FAEA group, after dividing the mesentery at the level of the planned transection, the ischemic line was observed using color vision mode (Fig. 2a). Then, the 0.05 mg/kg of ICG was injected into the peripheral vein just before proximal bowel transection. We observed the micro-arterioles of the epiploic appendage dynamically observed using monochrome fluorescence mode, and recorded the dissecting line based on the end of micro-arterioles in this mode (Fig. 2b). The venules and the bowel wall were gradually visible in this procedure (Fig. 2c). We also changed the imaging to the merged mode, and marked the merging borderline (Fig. 2d). FAEA was performed in the monochrome fluorescence mode before serving the proximal bowel. Whether a stoma was performed according to above criteria. Before intracorporeal anastomosis, the blood perfusion of the bowel was observed under merged mode (Fig. 2e) and monochrome fluorescence mode (Fig. 2f). Under the merged mode, the diffusion of ICG stained peritoneum, and this green background color of peritoneum around the bowel seriously affects the observation and judgment of the blood perfusion of the anastomosis. The arterioles on the well blood perfusion bowel can be displayed with the FAEA method, and not affected by the background color under monochrome fluorescence mode. What's more, the blood perfusion of anastomotic bowel can be re-judged or confirmed by repeated injection of ICG. A video of FAEA is available as an online supplement (Video S1). After the anastomosis was completed, ICG was administered intravenously again. The anus was stretched open and the anastomosis was exposed by the anoscope, and the fluorescence intensity of the anastomosis was observed by the fluorescence laparoscopy.

For the control group, the color of the bowel wall was observed by naked eyes before cutting off the proximal bowel of the tumor. After anastomosis, the anus was retracted and the anastomosis was exposed, the color of the intestinal mucosa was judged by naked eyes.

The anastomotic leak was evaluated intraoperatively with ICG and underwater testing for FAEA group; and only underwater testing for control group after anastomosis.

Diagnosis of AL and definition of SSAL

The AL was classified into 3 categories, according to the degree of difference; grade A: radiological leakage (AL confirmed solely by diagnostic imaging of the anastomosis site, despite the lack of clinical symptoms. These cases do not require any active therapeutic intervention); grade B: symptomatic leakage without re-laparotomy (AL with clinical symptoms, which require therapeutic intervention by other means than surgery. It requires percutaneous or transanal drainage and antibiotic treatments); grade C: symptomatic leakage requiring re-laparotomy (AL with clinical symp- toms, which require surgical intervention).

The structural sequelae of anastomotic leakage (SSAL) were defined that AL developed into structural sequelae including prolonged fistula, sinus formation, or stricture. In the table of our manuscript, the types of SSAL were listed as stenosis, rectovaginal fistula, rectourethral fistula, presacral sinus.

The anastomotic leak was determined rectal contrast enema in all patients, and all patients underwent flex sig as a means of evaluating for leak.

Data collection and followup

Basic clinical and pathological characteristics were collected, including sex; age; body mass index (BMI); diabetes mellitus status; nCRT; American Society of Anesthesiologists (ASA) score; tumor distance from the anal verge (AV); differentiation status; maximal tumor diameter; (y)pT, (y)pN, and (y)pTNM stages (American Joint Committee on Cancer 8th edition); and serum hemoglobin, albumin, carcinoembryonic antigen (CEA) levels. Perioperative outcomes were also reviewed, including operative time, estimated blood loss, left colonic artery (LCA) preservation, height of the anastomotic site from the AV, AL, postoperative complications, and post- operative length of stay.

Follow-up was performed every 3 months for the first 2 years, every 6 months for the next 3 years, and annually thereafter. SSAL after LsISR was evaluated, including anastomotic stenosis, rectovaginal fistula, and chronic presacral fistula. In this

Surg Endosc. 2024. 38(9):5446-5456. Published online: 1 August 2024

Table 1 Comparison of patient characteristics in the baseline cohort before (n = 556) and after PSM (299)

	Before PSM		*P*	After PSM		*P*
	FAEA group ($n=140$)	Control group ($n=416$)		FAEA group ($n=109$)	Control group ($n=190$)	
Age (year)	62 (54–68)	60 (53–68)	0.307	61 (55–68)	62 (55–68)	0.357
<60	57 (40.7)	192 (46.2)		48 (44.0)	72 (37.9)	
≥60	83 (59.3)	224 (53.8)		61 (60.0)	118 (62.1)	
Sex			0.068			1
Female	64 (45.7)	152 (36.5)		67 (61.5)	116 (61.1)	
Male	76 (54.3)	264 (63.5)		42 (38.5)	74 (38.9)	
BMI (kg/m^2)	23.7 (22.0–25.9)	23.7 (21.7–25.9)	0.886	24.0(22.1–26.0)	23.7 (22.0–25.6)	0.811
<25	88 (62.9)	267 (64.2)		64 (58.7)	115 (60.5)	
≥25	52 (37.1)	149 (35.8)		45 (41.3)	75 (39.5)	
Smoking			0.120			0.517
No	127 (90.7)	356 (85.6)		99 (90.8)	168 (88.4)	
Yes	13 (9.3)	60 (14.4)		10 (9.2)	22 (11.6)	
Drinking						0.545
No	116 (82.9)	320 (76.9)	0.140	93 (85.3)	157 (82.6)	
Yes	24 (17.1)	96 (23.1)		16 (14.7)	33 (17.4)	
ASA			0.147			0.130
1–2	125 (89.3)	389 (93.5)		94 (83.5)	149 (78.4)	
3	15 (10.7)	27 (6.5)		15 (16.5)	41 (21.6)	
Diabetes						0.744
No	120 (85.7)	357 (85.8)		93 (85.3)	158 (83.2)	
Yes	20 (14.3)	59 (14.2)		16 (14.7)	32 (16.8)	
Preoperative Hb (g/L)			0.495			0557
≥120	124 (88.6)	347 (83.4)		99 (90.8)	167 (87.9)	
<120	16 (11.4)	69 (16.6)		10 (9.2)	23 (22.1)	
Preoperative CEA (g/L)			0.719			0.323
≤5	95 (67.9)	291 (70.0)		38 (34.9)	56 (29.5)	
>5	45 (32.1)	125 (30.0)		71 (65.1)	134 (70.5)	
Preoperative CA199 (kU/L)			0.964			0.629
≤37	125 (89.3)	372 (89.4)		98 (89.9)	171 (90.0)	
>37	15 (10.7)	44 (10.6)		11 (10.1)	19 (10.0)	
Maximal tumor size, mm, median	40.0 (29.0–50.0)	35.0 (27.0–48.0)	0.557	40.0(27.0–50.0)	35.0 (25.0–47.0)	0.256
Height of tumor from the anal verge, cm, median	4.0 (3.5–4.0)	4.0 (3.5–4.0)	0.465	4.0 (3.5–4.0)	4.0 (3.5–4.0)	0.809
Preoperative bowel obstruction	10 (7.1)	35 (8.4)	0.634	7 (6.4)	12 (6.3)	0.971
T stage			0.061			0.507
0–2	47 (33.6)	179 (43.0)		44 (40.4)	68 (35.8)	
3–4	93 (63.4)	237 (57.0)		65 (59.6)	122 (64.2)	
N stage			0.127			0.959
0	80 (57.1)	270 (64.9)		69 (63.3)	113 (59.5)	
1–2	60 (42.9)	146 (35.1)		40 (36.7)	77 (40.5)	
M stage			0.837			0.474
M0	138 (98.6)	408 (98.1)		108 (99.1)	186 (97.9)	
M1	2 (1.4)	8 (1.9)		1 (0.9)	4 (2.1)	
TNM stage			0.167			0.770
I, II	82 (58.6)	266 (63.2)		48 (44.3)	79 (41.6)	
III, IV	58 (41.4)	150 (36.8)		61 (56.0)	111 (58.4)	
Maximal tumor size (mm)						

Table 1 Comparison of patient characteristics in the baseline cohort before (n = 556) and after PSM (299) (continued)

	Before PSM		*P*	After PSM		*P*
	FAEA group (*n* = 140)	Control group (*n* = 416)		FAEA group (*n* = 109)	Control group (*n* = 190)	
≤ 35	61 (43.6)	216 (51.9)	0.534	32 (29.4)	69 (36.3)	0.316
> 35	79 (56.4)	200 (48.1)		41 (70.6)	66 (63.7)	
Differentiation			0.912			0.329
High-moderate	122 (87.1)	359 (86.3)		96 (88.1)	158 (83.2)	
Poor	18 (12.9)	57 (13.7)		13 (11.9)	32 (16.8)	
Preoperative therapy			0.016			0.808
No	111 (79.3)	366 (88.0)		91 (83.5)	162 (85.3)	
Yes	29 (20.7)	50 (12.0)		18 (16.5)	28 (14.7)	
Diverting ileostomy			0.829			1
No	25 (17.9)	69 (16.6)		20 (18.4)	35 (18.4)	
Yes	115 (82.1)	347 (83.4)		89 (81.6)	155 (81.6)	
Height of the anastomotic site from the anal verge, cm, median	2.0 (2.0–3.0)	2.0 (2.0–3.0)	0.657	2.0 (2.0–3.0)	2.0 (2.0–3.0)	0.742
LCA preservation			< 0.001			0.839
No	30 (21.4)	199 (47.8)		29 (26.6)	54 (28.4)	
Yes	110 (78.6)	217 (52.2)		80 (73.4)	136 (71.6)	

study, the primary endpoint was the AL rate within 6 months after primary resection, while the second- ary endpoint was the SSAL rate.

Statistical analysis

Chi-square or Fisher's exact test was used to analyze the differences between the primary and validation groups. Variables with P-values < 0.100 in univariate analyses were included in multivariate analyses. A greedy matching algorithm was used with a caliper width equal to 0.20 of the standard deviation of the log-transformed estimated propensity score (EPS) [16]. Propensity scores were estimated using sex, age, BMI, ASA score, tumor size, stage, preoperative treatment, height of the anastomotic site from the AV, LCA preservation, and diverting ileostomy. The FAEA group was appropriately matched to the control group (ratio, 1:2) using propensity score matching (PSM). Odds ratios (ORs) and their 95% confidence intervals (CIs) were calculated using univariable and multivariable logistic regression analyses, with the AL rate set as the outcome variable. Multivariable logistic regression analyses were performed with backward exclusion and stepwise selection methods at the 5% significance level. These were performed with the factors of AL as outcome variables and adjusted variables of EPS as explanatory variables. Subsequently, univariable logistic regression models were used for the PSM cohort, with the group as a covariate. Finally, inverse probability of treatment weighting (IPTW) with two different types of weights (i.e., standard and exposed) was used for EPS [17]. All statistical analyses were two-sided, and statistical significance was set at P < 0.05. Statistical analyses were performed using R software (version 4.0.5) and SPSS software (version 25.0).

Results

Patient characteristics

A total of 556 patients were finally analyzed, including 140 patients in the FAEA group and 416 patients in the control group (Fig. 1). The median ages were 62 (interquartile range [IQR], 54–68) and 61 (IQR, 55–68) years in the FAEA and control groups, respectively. The proportion of retained LCA was significantly higher in the FAEA group (78.6% vs. 52.2%, P < 0.001). After PSM, the FAEA and control groups respectively had 109 and 190 patients; 67 men and 42 women were in the FAEA group, with a median age of 61 [IQR, 55–68] years; 116 men and 74 women were in the control group, with a median age of 62 [IQR, 55–68] years), and all variables, including the percentage of LCA preservation, TNM stage and preoperative therapy in those two groups were well balanced (Table 1).

Shortterm results after LsISR

No ICG-related allergic reactions, such as fever, nausea, or rash, were observed. The AL rate (pre-PSM, 3.6% vs. 10.1%, P = 0.026; post-PSM, 3.7% vs. 10.5%, P = 0.036)and median postoperative length of stay (pre-PSM, 9 [6–13] vs. 10 [8–13], P = 0.024; post-PSM, 9 [6–13] vs. 10 [7–13], P = 0.036) in the FAEA group were all significantly lower than in the control group. None of the patients were converted to open surgery. The operative time, estimated blood loss, postoperative complications, AL grade, mortality, or reoperation showed no difference between the two groups. Only one patient with nCRT in the FAEA group developed anastomotic stenosis, significantly lower than that in the control group (1.4% vs. 6.0%, P = 0.029), and the latter included 9 patients with chronic presacral sinus, 8 with anastomotic strictures, 5 with rectovaginal fistula, 2 with anal fistula, and 1 with rectourethral fistula. A total of 14 patients underwent reoperation for major reasons including bleeding, obstruction and grade C AL. After PSM, the proportion of SSAL was still significantly lower in the FAEA group than in the control group (1.8% vs. 6.8%, P = 0.041). Specifically, 1 patient developed SSAL in the FAEA group, and 11 patients developed SSAL in the control group, including 4 with chronic presacral sinus, 4 with anastomotic stenosis, 2 with anal fistula, 1 with rectovaginal fistula. (Table 2).

Risk factors for AL

The regression analysis was used to explore the risk factors of AL. In the univariate logistic regression analysis, nCRT (OR 4.892, 95% CI2.584–9.260, P < 0.001)was risk factor for AL, while FAEA (OR 0.399, 95% CI 0.166–0.959, P = 0.004) reduced the incidence risk of AL. The AL-related variables with P < 0.2 from the univariate regression analysis were included in the final multivariate logistic regression analysis. Male sex (OR 3.120, 95% CI 1.379–7.062, P = 0.006), nCRT (OR 7.695, 95% CI 3.668–16.144, P < 0.001), and tumor height from the anal verge ≤ 4 cm (OR 4.038, 95% CI 1.534–10.630, P = 0.005)were independent risk factors for AL. As an independently favorable factors, diverting ileostomy (OR 0.485, 95% CI 0.107–0.676, P = 0.043) could reduce the AL risk by divert- ing stool, although it did not help the anastomosis heal. FAEA (OR 0.307, 95% CI 0.118–0.800, P = 0.016) and LCA preservation (OR 0.485, 95% CI 0.107–0.676, P = 0.043) were independently protective factors for AL (Table 3). We further analyzed the relationship between ICG evaluation of blood perfusion at anastomotic site and the incidence of AL (Table 3). In the group of good blood perfusion of the anastomotic site, 3 patients developed AL, which was sig- nificantly lower than that in poor perfusion group (2.2% vs. 50%, P < 0.001).

The advantages of FAEA in the evaluation of blood perfusion at anastomotic site

We analyzed the site of planned transection line in different modes (Table 4). Both in totally laparoscopic ISR and laparoscopic ISR with auxiliary incision, the planned transection lines under color vision mode (ΔM-FAEA = 1.74 ± 0.35, and 1.56 ± 0.33) and merged mode (ΔC-FAEA = 0.89 ± 0.24, and 0.92 ± 0.27) were more distal than the planned transection line determined by FAEA. What's more, under merged mode, the planned transection line in the group of totally laparoscopic ISR was more distal than the line in the group of laparoscopic ISR with auxiliary incision (P = 0.047), while the site of the transection line in above two groups had no difference under the FAEA (P = 1) and color vision mode (P = 0.272). The evaluation of FAEA for blood perfusion was more accurate than the other modes, especially in totally laparoscopic ISR.

FAEA efficacy in preventing AL

To further define the efficacy of FAEA in preventing AL, we compared several logistic regression analyses with anastomotic leakage as the outcome variable. In multivariate logistic regression analyses without backward exclusion, adjusting for the same covariates as those used to calculate EPS, FAEA was associated with significantly lower risk of AL (OR 0.298, 95% CI 0.112–0.790, P = 0.015). Similarly, stepwise selected multivariate logistic regression analysis showed that FAEA was associated with a significantly lower AL risk (OR 0.261, 95% CI 0.098–0.691, P = 0.007).In the PSM cohort, unconditional univariate logistic regression analysis also showed that FAEA was associated with a significantly lower AL risk (OR 0.275, 95% CI 0.035–0.937, P = 0.039). Finally, IPTW analysis using EPS for both weights likewise showed that FAEA was associated with a significantly lower AL risk (OR 0.814, 95% CI 0.765–0.921, P = 0.002). The magnitude of FAEA-related AL risk reduction was strong and consistent with the lower ORs (0.225–0.814) in all regression analyses described above (Table 5).

Discussion and conclusion

AL is one of the most serious complications after ISR for ultra-low rectal cancer, leading to reoperation, SSAL with permanent stoma, delayed further oncological treatment, and even worse oncological outcomes [5, 18–22]. Inadequate blood perfusion is considered as one of the most important risk factors for AL development. Routine ICG use to assess bowel perfusion in colorectal surgery has been proven as a safe and cost-effective method to reduce AL, without side effects [23–25]. Nonetheless, some challenges need to be addressed. The ICG dose and mode used for the evaluation of bowel perfusion vary widely. Moreover, the NIR-FA relies on a subjective evaluation of the mean fluorescence brightness of the anastomotic area, which is influenced by mucosal characteristics; thus, it is prone to biological tissue scattering and inter-observer variations in judgment [14]. Our study is the first to apply FAEA by dynamically observing intraoperative bowel perfusion in LsISR. We found that FAEA was effective in reducing AL by more accurate evaluation in blood perfusion of anastomotic bowel and determination of planned transection line, subsequently reducing postoperative hospital stay and SSAL incidence. To the best of our knowledge, this study included the largest LsISR sample to date and was the first to propose FAEA as an efficient AL prevention strategy.

Several patient-related factors negatively affect anastomosis healing, such as male sex, nCRT, low anastomosis level, high ligation, and tumor size [26, 27]. Nevertheless, Other factors are more directly influenced by technical failure that could be modified intraoperatively if detected, such as tension on the anastomosis, LsISR duration, insufficient integ- rity of the anastomosis and judgment of blood perfusion of anastomotic bowel [28–30]. Adequate blood perfusion is one of the most important in preventing AL. Our previously retrospective study revealed that male sex and nCRT were independent risk factors for AL,

Table 2 Perioperative outcomes of patients undergoing LsISR before and after PSM between NIR-FI group and control group

Variable	Before PSM		*P*	After PSM		*P*
	FAEA group ($n=140$)	Control group ($n=416$)		FAEA group ($n=109$)	Control group ($n=190$)	
Operative duration, median (IQR) min	172(130–215)	172 (135–211)	0.660	176(140–225)	180(150–230)	0.625
Estimated blood loss, median (IQR) mL	30 (20–70)	50 (20–100)	0.188	30 (20–80)	50 (20–100)	0.386
Conversion to open surgery (*n*, %)	0 (0)	0 (0)	–	0 (0)	0 (0)	–
Change in resection of proximal stump	23 (16.4)	15 (3.6)	<0.001	16 (14.7)	4 (2.2)	<0.001
AL (*n*, %)			0.026			0.036
No	135 (96.4)	374 (89.9)		105 (96.3)	170 (89.5)	
Yes	5 (3.6)	42 (10.1)		4 (3.7)	20 (10.5)	
AL grade (*n*, %)						
A-B	4 (2.9)	30 (7.2)	0.063	4 (3.6)	15 (7.9)	0.149
C	1 (0.7)	12 (2.9)	0.252	0 (0)	5 (2.6)	0.215
Complications (*n*, %)						
CD grade I–II	16 (11.4)	41 (9.9)	0.596	16 (14.7)	16 (8.4)	0.092
CD grade III–IV	5 (3.6)	20 (4.8)	0.541	3 (2.8)	8 (4.2)	0.744
Ileus (*n*, %)	4 (2.9)	14 (3.4)	0.996	3 (2.8)	7 (3.7)	0.923
Mortality (*n*, %)	0 (0)	3 (1.0)	0.733	0 (0)	2 (1.1)	0.736
Reoperation (*n*, %)	1 (0.7)	14 (3.4)	0.634	1 (0.9)	6 (3.2)	0.976
Postoperative hospital stay (day)	9 (6–13)	10 (8–13)	0.024	9 (6–13)	10 (7–13)	0.036
SSAL (*n*, %)	2 (1.4)	25 (6.0)	0.029	2 (1.8)	14 (7.4)	0.041
Stenosis (*n*, %)	1 (0.7)	8 (1.9)		1 (0.9)	4 (2.1)	
Rectovaginal fistula (*n*, %)	0 (0)	5 (1.2)		0 (0)	3 (1.6)	
Rectourethral fistula (*n*, %)	0 (0)	1 (0.2)		0 (0)	0 (0)	
Presacral sinus (*n*, %)	0 (0)	9 (2.2)		0 (0)	5 (2.6)	
Anal fistula (*n*, %)	1 (0.7)	2 (0.5)		1 (0.9)	2 (1.1)	

Table 3 The univariate analysis and multivariate analysis of anastomotic leakage

Variable	Univariate analysis		Multivariate analysis	
	Odds ratio (95% CI)	*P* value	Odds ratio (95% CI)	*P* value
Sex (Male vs. Female)	3.467 (1.590–7.558)	0.002	3.120 (1.379–7.062)	0.006
Age (≥60 years vs. <60 years)	0.726 (0.401–1.313)	0.289		
BMI (≥25 kg/m^2 vs. <25 kg/m^2)	1.546 (0.851–2.806)	0.152	1.443 (0.757–2.750)	0.265
Smoking (Yes vs. No)	0.668 (0.427–1.564)	0.239		
Drinking (Yes vs. No)	1.601 (0.879–3.291)	0.215		
Diabetes (Yes vs. No)	1.435 (0.642–3.208)	0.378		
nCRT (Yes vs. No)	4.892 (2.584–9.260)	<0.001	7.695 (3.668–16.144)	<0.001
LCA preservation (Yes vs. No)	1.535 (0.847–2.780)	0.158	0.485 (0.107–0.676)	0.043
Diverting ileostomy (Yes vs. No)	0.577 (0.288–1.157)	0.121	0.198 (0.085–0.459)	<0.001
TNM stage (III–IV vs.I–II)	1.001 (0.546–1.833)	0.998		
Maximal tumor size (≥36 mm vs. < 36 mm)	0.820 (0.453–1.485)	0.512		
Height of tumor from the anal verge (≤4 cm vs. > 4 cm)	2.236 (0.928–5.387)	0.073	4.038 (1.534–10.630)	0.005
FAEA (Yes vs. No)	0.399 (0.166–0.959)	0.004	0.307 (0.118–0.800)	0.016

Table 4 The planned transection line in different mode compared with FAEA

ICG mode	Totally laparoscopic ISR with intracorporeal anastomosis ($n=80$) Mean ± SD	Laparoscopic ISR with auxiliary incision ($n=60$) Mean ± SD	*P*
FAEA	0	0	1
ΔMerged mode-FAEA	1.74 ± 0.35	1.56 ± 0.33	0.047
ΔColor vision mode-FAEA	0.89 ± 0.24	0.92 ± 0.27	0.272

Table 5 Comparison of several logistic regression analyses with anastomotic leakage as the outcome variable

Models	N	Odds ratio (95% CI)	P value
Univariable logistic	556	0.399 (0.166–0.959)	0.004
Multivariable logistic (without backward elimination)	556	0.298 (0.112–0.790)	0.015
Multivariable logistic (with stepwise selection)	556	0.261 (0.098–0.691)	0.007
Univariable logistic for the PSM-matched cohort	299	0.275 (0.035–0.937)	0.039
IPTW logistic (standard and exposed weights)	556	0.814 (0.765–0.921)	0.002

while LCA preservation and diverting ileostomy independently protected against AL 9. Both nCRT and LCA preservation were associated with blood perfusion in the anastomotic site, which is consistent with the underlying mechanism of AL. Previous studies also evaluated the effect of nCRT on the blood supply to the proximal anastomotic bowel and suggested that nCRT may cause vascular endothelial damage and ultimately affect anastomotic blood perfusion [31, 32]. The risk of AL can be reduced by freeing the splenic flexure and expanding the length of radiation-induced proximal bowel resection [33, 34]. Recent studies analyzed the relationship between LCA preservation and fluorescence imaging, combined with artificial intelligence analysis, which showed that there was no difference in the maximum peak fluorescence; however, the time required to reach the peak was significantly shorter with LCA preservation. Unfortunately, these studies did not analyze the relationship between the time to reach the peak and AL[35].

A randomized control trial (RCT) failed to confirm the benefits of NIR-FA in reducing AL [13]. Some reasons need to be considered. Firstly, a large proportion of RCT participants had left-side colon and midand upper rectal cancer, with a lower AL incidence revealed by traditional imaging techniques, while the number of ultralow rectal cancer cases with a higher AL risk was relatively small. Secondly, NIR-FA was prone to biological tissue scattering, leading to inter-observer variations in judgment, Especially in the era of Totally laparoscopic ISR with intracorporeal anastomosis, the blood supply of the anastomotic bowel is often affected by the color of the surrounding tissue background, increases the missed judgment of ischemic bowel, which poses a challenge to total laparoscopic anastomosis. Whereas FAEA was based on dynamic observation of the micro-arterioles in epiploic appendages, the planned transection line was closer to the real ischemic line, and this evaluation method made perfusion assessment more objective, repeatable, and precise. We reviewed a case involving a patient with locally recurrent rectal cancer who underwent laparoscopic total hysterectomy and partial mesorectal resection. FAEA revealed that the mesenteric micro-arterioles were very weak, whereas they appeared normal using the pseudo-color fusion mode. The patient ultimately suffered ischemic proctitis and rectovaginal fistula. This case reflects the advantages of FAEA compared with NIR-FA, and further studies and more controlled cases are required to confirm the role of FAEA in AL prevention.

The blood perfusion at the anastomosis site also affects SSAL incidence. Hasegawa et al. reported SSAL rates of 1.4% (1/70) in the NIR-FA group and 10.4% (20/193) in the control group (P = 0.02). After PSM, the SSAL rates were 1.5% in the NIR-FA group and 11.7% in the control group (P = 0.02). Propensity score analyses revealed that NIR-FA was associated with a significantly lower SSAL risk (OR 0.10–0.13; P = 0.03–0.05) [36]. The findings of our study are consistent with this report. In our cohort, only one patient in the FAEA group developed SSAL (0.7% pre-PSM and 0.9% post-PSM), which is significantly less than that in the control group (6.0% pre-PSM and 6.8% post-PSM).

FAEA has some advantages in blood perfusion assessment over merged imaging in NIR-FA. Firstly, FAEA presents direct micro-arteriole angiography images of the anastomotic site, which is similar to our traditional test of bowel perfusion by using scissors to shear the epiploic appendages and detecting arterial bleeding. Secondly, the half-life of FAEA is shorter than that of NIR-FA, and it can be repeated over a short duration. Thirdly, FAEA is not easily affected by the scattering of adjacent fluorescence, especially when intracorporeal dissection is taken. Usually, the dissecting line in FAEA is closer to the proximal line compared with that in NIR-FA. When the bowel length is relatively limited, whether a 1–2-cm more proximal bowel removal affects anastomotic tension should be considered.

Our study has several limitations. Firstly, its retrospective design may lead to potential bias. Although propensity score adjustment may reduce some selection bias, residual or confounding factors may still be present. Secondly, with a low proportion of nCRT, the role of FAEA in the nCRT cohort needs further investigation. Thirdly, the sample size of the FAEA group was relatively small. Nevertheless, the FAEA technique might apply to all anastomosis related to colorectum, not only for ultralow anastomosis, and be effective in reducing ischemia-related AL. Further large-scale randomized prospective controlled trials should be conducted to validate our results.

Conclusions

Perfusion assessment by fluorescence angiography of epiploic appendages in the monochrome fluorescence mode can reduce AL incidence and subsequent post-LsISR SSAL.

Author contributions

Wenlong Qiu: Conceptualization, Methodology, Formal analysis, investigation, Writing—original draft. Junguang Liu: Resources, Data curation, Writing—review & editing. Kunshan He: Resources, Data curation, Writing—review & editing. Kunshan He: Resources, Data curation, Writing—review & editing. Gang Hu: Resources, Data curation, Writing—review & editing. Shiwen Mei: Resources, Data curation, Writing—review & editing, Project administration Xu Guan: Resources, Data curation, Writing—review & editing. Xishan Wang: Conceptualization, Writing—review & editing, Supervision. Jie Tian: Conceptualization, Writing—review & editing, Supervision. Jianqiang Tang: Conceptualization, Methodology, Writing—review & editing, Supervision, Project administration.

Funding

This study was supported by grants from the National Natural Science Foundation of China (No. 82072732) and Beijing Natural Science Foundation (L222054, 4232058).

Disclosures

Wenlong Qiu, Junguang Liu, Kunshan He, Gang Hu, Shiwen Mei, Xu Guan, Xishan Wang, Jie Tian, Jianqiang Tang have no conficts of interest or financial ties to disclose.

Ethical approval

All authors have approved the final version of the article.

References

1. Enomoto H, Ito M, Sasaki T, Nishizawa Y, Tsukada Y, Ikeda K, Hasegawa H (2022) Anastomosis-related complications after stapled anastomosis with reinforced sutures in transanal total meso- rectal excision for low rectal cancer: a retrospective single-center study. Dis Colon Rectum 65(2):246–253.
2. Zhang B, Zhuo GZ, Zhao K, Zhao Y, Gao DW, Zhu J, Ding JH (2022) Cumulative incidence and risk factors of permanent stoma after intersphincteric resection for ultralow rectal cancer. Dis Colon Rectum 65(1):66–75.
3. Martin ST, Heneghan HM, Winter DC (2012) Systematic review of outcomes after intersphincteric resection for low rectal cancer. Br J Surg 99(5):603–612.
4. Yamamoto S, Fujita S, Akasu T, Inada R, Takawa M, Moriya Y (2011) Short-term outcomes of laparoscopic intersphincteric resection for lower rectal cancer and comparison with open approach. Dig Surg 28(5–6):404–409
5. Liu J, Zheng L, Ren S, Zuo S, Zhang J, Wan Y, Wang X, Tang J (2021) Nomogram for predicting the probability of permanent stoma after laparoscopic intersphincteric resection. J Gastrointest Surg 25(12):3218–3229
6. Artus A, Tabchouri N, Iskander O et al (2020) Long term outcome of anastomotic leakage in patients undergoing low anterior resection for rectal cancer. BMC Cancer 20(1):780.
7. Tschann P, Weigl MP, Szeverinski P et al (2022) Are risk fac- tors for anastomotic leakage influencing long-term oncological outcomes after low anterior resection of locally advanced rectal cancer with neoadjuvant therapy? A single-centre cohort study. Langenbecks Arch Surg 407(7):2945–2957.
8. Costantini B, Vargiu V, Santullo F et al (2022) Risk factors for anastomotic leakage in advanced ovarian cancer surgery: a large single-center experience. Ann Surg Oncol 29(8):4791–4802.
9. Liu JG, Chen HK, Wang X, Tang JQ (2021) Analysis of risk fac- tors of anastomotic leakage after laparoscopic intersphincteric resection for low rectal cancer and construction of a nomogram prediction model. Zhonghua Wai Ke Za Zhi 59(5):332–337.
10. Ryu HS, Lim SB, Choi ET, Song I, Lee JL, Kim CW, Yoon YS, Park IJ, Yu CS, Kim JC (2021) Intraoperative perfusion assessment of the proximal colon by a visual grading system for safe anastomosis after resection in left-sided colorectal cancer patients. Sci Rep 11(1):2746.
11. Kudszus S, Roesel C, Schachtrupp A, Höer JJ (2010) Intraoperative laser fluorescence angiography in colorectal surgery: a noninvasive analysis to reduce the rate of anastomotic leakage. Langenbecks Arch Surg 395(8):1025–1030
12. Trastulli S, Munzi G, Desiderio J, Cirocchi R, Rossi M, Parisi A (2021) Indocyanine green fluorescence angiography versus standard intraoperative methods for prevention of anastomotic leak in colorectal surgery: meta-analysis. Br J Surg 108(4):359–372.
13. Jafari MD, Pigazzi A, McLemore EC et al (2021) Perfusion assessment in left-sided/low anterior resection (PILLAR III): a randomized, controlled, parallel, multicenter study assessing perfusion outcomes with PINPOINT near-infrared fluorescence imaging in low anterior resection. Dis Colon Rectum 64(8):995–1002.
14. Watanabe J, Ishibe A, Suwa Y, Suwa H, Ota M, Kunisaki C, Endo I (2020) Indocyanine green fluorescence imaging to reduce the risk of anastomotic leakage in laparoscopic low anterior resection for rectal cancer: a propensity score-matched cohort study. Surg Endosc 34(1):202–208.
15. Zhang C, Wang K, An Y, He K, Tong T, Tian J (2019) Improved generative adversarial networks using the total gradient loss for the resolution enhancement of fluorescence images. Biomed Opt Express 10(9):4742–4756.
16. Austin PC (2009) Some methods of propensity-score matching had superior performance to others: results of an empirical investigation and Monte Carlo simulations. Biom J 51(1):171–184.
17. Austin PC (2011) An introduction to propensity score methods for reducing the effects of confounding in observational studies. Multivariate Behav Res 46(3):399–424.
18. Ji WB, Kwak JM, Kim J, Um JW, Kim SH (2015) Risk factors causing structural sequelae after anastomotic leakage in mid to low rectal cancer. World J Gastroenterol 21(19):5910–5917.
19. Mongin C, Maggiori L, Agostini J, Ferron M, Panis Y (2014) Does anastomotic leakage impair functional results and quality of life after laparoscopic sphincter-saving total mesorectal excision for rectal cancer? A case-matched study. Int J Colorectal Dis 29(4):459–467.
20. Waa B, Westerduin E, Aukema TS, Bemelman WA, Tanis PJ (2017) Anastomotic leakage and chronic presacral sinus formation after low anterior resection: results from a large cross-sectional study. Ann Surg 266(5):870–877.
21. Dinnewitzer A, Jäger T, Nawara C, Buchner S, Wolfgang H, Öfner D (2013) Cumulative incidence of permanent stoma after sphincter preserving low anterior resection of mid and low rectal cancer. Dis Colon Rectum 56(10):1134–1142.
22. Kim MJ, Kim YS, Park SC, Sohn DK, Kim DY, Chang HJ, Oh JH (2016) Risk factors for permanent stoma after rectal cancer surgery with temporary ileostomy. Surgery 159(3):721–727.
23. Liu RQ, Elnahas A, Tang E, Alkhamesi NA, Hawel J, Alnumay A, Schlachta CM (2022) Cost analysis of indocyanine green fluorescence angiography for prevention of anastomotic leakage in colorectal surgery. Surg Endosc 36(12):9281–9287
24. Maione F, Manigrasso M, Chini A et al (2022) The role of indocyanine near-infrared fluorescence in colorectal surgery. Front Surg 9:886478.
25. Safiejko K, Tarkowski R, Kozlowski TP, Koselak M, Jachimiuk M, Tarasik A, Pruc M, Smereka J, Szarpak L (2022) Safety and efficacy of indocyanine green in colorectal cancer surgery: a sys- tematic review and meta-analysis of 11,047 patients. Cancers (Basel) 14(4):88.
26. Toyoshima A, Nishizawa T, Sunami E, Akai R, Amano T, Yamashita A, Sasaki S, Endo T, Moriya Y, Toyoshima O (2020) Narrow pelvic inlet plane area and obesity as risk factors for anastomotic leakage after intersphincteric resection. World J Gastro-intest Surg 12(10):425–434.
27. Pommergaard HC, Gessler B, Burcharth J, Angenete E, Haglind E, Rosenberg J (2014) Preoperative risk factors for anastomotic leakage after resection for colorectal cancer: a systematic review and meta-analysis. Colorectal Dis 16(9):662–671.
28. Tagart RE (1981) Colorectal anastomosis: factors influencing success. J R Soc Med 74(2):111–118.
29. Matthiessen P, Hallböök O, Andersson M, Rutegård J, Sjödahl R (2004) Risk factors for anastomotic leakage after anterior resection of the rectum. Colorectal Dis 6(6):462–469.
30. Bertelsen CA, Andreasen AH, Jørgensen T, Harling H (2010) Anastomotic leakage after anterior resection for rectal cancer: risk factors. Colorectal Dis 12(1):37–43.
31. Mu W, Hu N, Zhang LH et al (2022) Lonicerae japonicae flos ameliorates radiotherapy-induced mesenteric artery endothelial dysfunction through GTPCH1/BH4/eNOS pathway. Phytomedicine 102:154146.
32. El KA, Giles A, Czarnota GJ (2013) Dose-dependent response of tumor vasculature to radiation therapy in combination with Sunitinib depicted by three-dimensional high-frequency power Doppler ultrasound. Angiogenesis 16(2):443–454.
33. Kimose HH, Fischer L, Spjeldnaes N, Wara P (1989) Late radia- tion injury of the colon and rectum: surgical management and outcome. Dis Colon Rectum 32(8):684–689.
34. He Y, Zhou Z, Huang X et al (2022) Laparoscopic proximally extended colorectal resection with two-stage turnbull-cutait pull- through coloanal anastomosis for late complications of chronic radiation proctopathy. Front Surg 9:845148.
35. Han SR, Lee CS, Bae JH, Lee HJ, Yoon MR, Al-Sawat A, Lee DS, Lee IK, Lee YS (2022) Quantitative evaluation of colon perfusion after high versus low ligation in rectal surgery by indocyanine green: a pilot study. Surg Endosc 36(5):3511–3519.
36. Hasegawa H, Tsukada Y, Wakabayashi M, Nomura S, Sasaki T, Nishizawa Y, Ikeda K, Takeshita N, Teramura K, Ito M (2022) Impact of near-infrared fluorescence imaging with indocyanine green on structural sequelae of anastomotic leakage after laparoscopic intersphincteric resection of malignant rectal tumors. Tech Coloproctol 26(7):561–570.

Surg Endosc. 2024. 38(9):5446-5456. Published online: 1 August 2024

Colorectal Surgery

Research Article

Clinical Value of Fluorescence Laparoscopic Surgery on Anastomotic Leakage Prevention in Ultra-Low Rectal Cancer: Real-World Multicenter Retrospective Evidence with Neoadjuvant Chemoradiotherapy Stratification

W Qiu[1,#], G Hu[1,#], K He[2,#], S Mei[1], Z Xing[1], Y Li[1], J Tang[1,✉]

[1] Department of Colorectal Surgery, National Cancer Center/ National Clinical Research Center for Cancer/Cancer Hospital, Chinese Academy of Medical Sciences and Peking Union Medical College, Beijing 100021, China

[2] Beijing Key Laboratory of Molecular Imaging. Key Laboratory of Big Data-Based Precision Medicine, Ministry of Industry and Information Technology, Key Laboratory

* Wenlong Qiu, Gang Hu, and Kunshan He contributed equally to this work.

Abstract

Background: Neoadjuvant chemoradiotherapy (nCRT) is key for low rectal cancer but raises the risk of anastomotic leakage (AL). This study examines how fluorescence laparoscopic (FL) surgery reduces AL after intersphincteric resection (ISR), especially in nCRT patients.

Methods: This real-world multicenter cohort study included 533 patients undergoing laparoscopic ISR for ultra-low rectal adenocarcinoma from January 2012 to July 2023. Patients were categorized into FL and non-FL groups. Propensity score matching (PSM) was used at a 1:2 ratio to adjust for baseline differences. The primary endpoint was the incidence of AL within 6 months postoperatively. Secondary endpoints included anastomotic site perfusion, intraoperative blood loss, lymph node retrieval, perioperative complications, and postoperative recovery metrics. Subgroup analyses were conducted on the basis of nCRT status.

Results: After PSM, 393 patients were analyzed (131 FL versus 262 non-FL). The FL group showed a significantly lower AL incidence (3.1% versus 11.5%, P = 0.005), with fewer severe symptomatic AL cases (0.8% versus 6.1%, P = 0.014). Intraoperative blood loss was reduced (45.2 ± 58.9 mL versus 65.3 ± 73.1 mL, P = 0.004), and lymph node yield was higher (21.2 ± 11.4 versus 16.6 ± 7.3, P < 0.001) in the FL group. Postoperative recovery was accelerated, with earlier return of bowel function and shorter hospital stays (9.5 ± 3.1 versus 10.7 ± 3.8 days, P = 0.012). In subgroup analyses, FL significantly reduced AL rates in patients without nCRT (1.9% versus 7.2%, P = 0.045) and demonstrated a strong trend toward reduction in AL for patients receiving nCRT (13.0% versus 35.9%, P = 0.051). FL also increased the proportion of patients achieving benchmark lymph node retrieval, including those post-nCRT.

Conclusions: Fluorescence-guided laparoscopic surgery reduces anastomotic leakage and improves outcomes in low rectal cancer, especially after chemoradiotherapy, by enhancing surgical precision and recovery.

Keywords

Fluorescence laparoscopic surgery, Anastomotic leakage, Low rectal cancer, Neoadjuvant chemoradiotherapy, Intersphincteric resection, Indocyanine green

Introduction

Neoadjuvant chemoradiotherapy (nCRT) has long been recognized as a cornerstone in the treatment of low rectal cancer, especially for patients with advanced or locally invasive tumors[1, 2]. While this treatment modality improves oncologic outcomes, it is also associated with an increased risk of postoperative complications, particularly anastomotic leakage (AL) [3, 4]. The AL remains one of the most significant risk factors influencing both short-term recovery and oncological outcome in patients undergoing intersphincteric resection (ISR). Several studies have highlighted that the occurrence of AL is multifactorial, with both technical surgical factors and biological responses contributing to its onset and the blood supply at the anastomotic site as a critical factor that predisposes patients to this complication [5, 6].

Amid growing clinical concerns about AL, there has been an increasing focus on strategies to promote anastomotic healing and lower leak rates, especially in the context of neoadjuvant chemoradiotherapy (nCRT), which can aggravate tissue perfusion[7, 8]. Fluorescent laparoscopic (FL) surgery, employing indocyanine green (ICG), has emerged as a promising tool to enhance intraoperative decision-making by providing real-time, visual feedback on blood flow. This technique, particularly fluorescent laparoscopic angiography, has gained attention in colorectal surgery for its potential to improve the identification of crucial vascular structures and optimize anastomotic sites, ultimately reducing the risk of AL[9–11]. Nevertheless, despite its theoretical benefits, the application of FL in low rectal cancer surgery, particularly in patients undergoing nCRT, remains insufficiently explored.

Previous studies have predominantly focused on the role of FL in colorectal surgeries[12-14] without a specific emphasis on its utility in ultra-low rectal cancer after ISR or post-nCRT scenarios. Furthermore, while the potential of FL to improve the identification of blood vessels and lymph nodes has been demonstrated in various surgical contexts, its impact on reducing AL in low rectal cancer patients remains inadequately addressed in literature. This gap is particularly evident in the context of fluorescence guidance during laparoscopic ISR surgery, which is increasingly favored for its minimally invasive benefits. Moreover, few studies have evaluated the specific influence of FL in the challenging subset of

Tech Coloproctol. 2025. 29(1):165 Published online: 21 August 2025

patients who have undergone neoadjuvant chemoradiotherapy.

Above all, the primary aim of this study is to evaluate whether fluorescent laparoscopic (FL) surgery can reduce anastomotic leakage (AL) in patients with ultra-low rectal cancer, especially those who received neoadjuvant chemoradiotherapy (nCRT). Using propensity score matching (PSM), we aim to clarify the clinical benefits of fluorescence guidance in improving surgical safety, reducing blood loss, enhancing lymph node retrieval, and, ultimately, improving patient recovery and outcomes.

Materials and methods

Study design and patient enrollment

This real-world, multicenter retrospective cohort study was conducted across three tertiary hospitals in China, including the Cancer Hospital of the Chinese Academy of Medical Sciences and its affiliated regional centers, covering a study period from January 2012 to July 2023 (Fig.1). The number of enrolled patients was approximately balanced across the centers. There was no statistically significant difference in the distribution of FL and non-FL groups across the centers ($P > 0.05$), indicating a balanced distribution of patients and no systematic bias among centers. Patients with ultra-low rectal adenocarcinoma treated with laparoscopic intersphincteric resection (ISR) were included. Eligibility criteria included: (1) histologically confirmed adenocarcinoma ≤5 cm from the anal verge and (2) ISR treatment. Exclusion criteria were: (1) nonadenocarcinomatous rectal malignancies, (2) combined organ resections, or (3) conversion to abdominoperineal resection.

The neoadjuvant chemoradiotherapy (nCRT) was administered on the basis of multidisciplinary team (MDT) recommendations and prevailing clinical guidelines during the study period. Patients eligible for nCRT predominantly received long-course chemoradiotherapy, consisting of pelvic radiotherapy with a total dose of 45–50.4 Gy delivered over 25–28 fractions across 5–6 weeks, in combination with fluoropyrimidine-based chemotherapy (e.g., capecitabine or 5-fluorouracil). Short-course radiotherapy was not routinely employed. Patients who did not undergo nCRT were either diagnosed with early stage tumors that did not require preoperative treatment or were deemed unsuitable for nCRT on the basis of individualized assessment. Preoperative tumor evaluation was conducted using MRI 8–12 weeks after nCRT. Informed consent was obtained from all participants, and the study was approved by the institutional review board.

Near-infrared imaging system

Intraoperative tissue perfusion was assessed using a 4K ultra-high-definition near-infrared (NIR) laparoscopic system (DPM-ENDOCAM-03 and DPM-LIGHT-03; Dipu Medical Technology, Zhuhai, China). The system employs excitation wavelengths of 785±5 nm and detects fluorescence emission in the 830–900 nm range. Advanced image enhancement based on a generative adversarial network facilitated multiscale detail amplification.

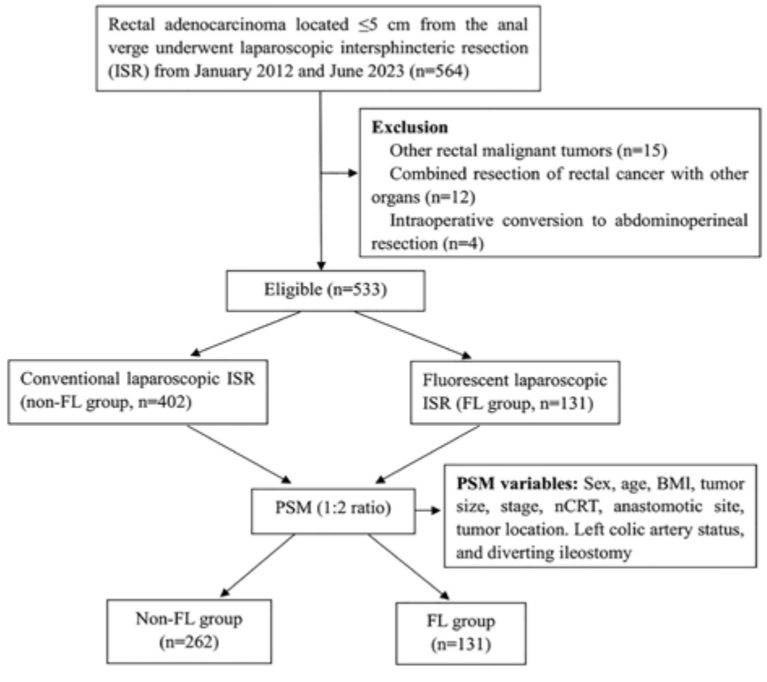


Fig.1 Flowchart of this study.

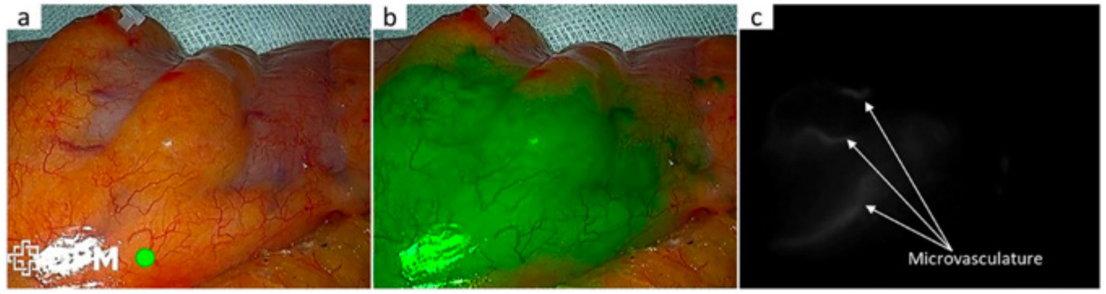


Fig.2 Clinical judgment of anastomotic blood perfusion in different near-infrared modes. a. the blood perfusion of bowel was observed under color vision mode; **b.** the blood perfusion status was observed by using merged mode; **c.** the microarterioles of epiploic appendage were dynamically observed using monochrome fluorescence mode to determined ischemic line.

Surgeons had the flexibility to switch between imaging modes—true color, monochrome fluorescence, and pseudo-color merged modes—either individually or in parallel (Fig. 2).

Surgical approach

Radical rectal cancer surgery was routinely performed by senior colorectal surgeons with more than 10 years of experience and a record of managing ≥100 laparoscopic intersphincteric resections (LsISR). A standard total mesorectal excision (TME) was conducted with meticulous preservation of the bilateral hypogastric nerves and pelvic autonomic nerve plexus. Dissection of the intersphincteric plane between the puborectalis muscle and the internal sphincter was carried out under direct vision. The distal rectum was transected intracorporeally using a flexible linear stapler.

In cases where the distal resection margin was less than 1 cm or suspected to be positive, intraoperative frozen section pathology was routinely performed for confirmation. Anastomosis was completed by hand-sewn technique. The decision to construct a diverting stoma was based on factors such as the distance from the anastomosis to the anal verge, perfusion status of the anastomotic bowel, the patient's preference, and the surgeon's clinical judgment.

Intraoperative assessment of anastomotic tension was based on the clinical judgment. A tension-free anastomosis was confirmed by ensuring that the proximal bowel could be delivered into the pelvis without undue traction. When necessary, additional mesenteric mobilization or splenic flexure mobilization was performed to reduce tension prior to anastomosis construction.

ICG fluorescence and perfusion assessment in the FL group

In the FL group, ICG was administered exclusively via intravenous injection at a dose of 0.25 mg/kg to assess bowel perfusion and anastomotic blood supply. Perfusion assessment was conducted intracorporeally under laparoscopy using fluorescence imaging system. Following ICG injection, fluorescence distribution within the bowel was observed in real time, typically within 10–60 s, to evaluate microvascular perfusion and ensure adequate blood supply at the planned transection and anastomotic sites, without exteriorizing the bowel.

Mesenteric division was performed at the planned transection level prior to ICG injection. Perfusion was primarily assessed using the monochrome fluorescence mode to visualize the microvasculature, with the transection line determined by the visible end of arterioles. Areas showing reduced or delayed fluorescence indicated poor perfusion and necessitated further proximal resection. If required, ICG was readministered to reassess vascular integrity. Merged imaging mode was deemed less reliable owing to diffuse fluorescence in the surrounding peritoneum.

After anastomosis construction, a second dose of ICG was administered, and the anastomotic site was examined under fluorescence with an anoscope to assess perfusion integrity. Leak testing in the FL group combined ICG fluorescence assessment and underwater testing, while the control group relied solely on gross inspection of bowel viability and underwater leak testing. Decisions regarding revision of transection margins or creation of diverting stomas were based on ICG findings, bowel viability, and patient risk factors.

Anastomotic leakage classification and definition of SSAL

Anastomotic leakage (AL) was classified into three grades: Grade A (radiologic leak without symptoms or intervention), Grade B (symptomatic leak requiring nonsurgical management), and Grade C (symptomatic leak requiring surgical reintervention). Structural sequelae of AL (SSAL) included chronic complications such as stenosis, rectovaginal fistula, rectourethral fistula, and presacral sinus. All patients underwent postoperative contrast enema and flexible sigmoidoscopy for leak detection.

2 Data collection and longitudinal follow-up

Data collected included patient demographics (age, sex, body mass index (BMI), and diabetes status), clinical parameters (surgical variabilities and nCRT), tumor characteristics (distance from anal verge, size, grade, and pathological stage), and laboratory indices (hemoglobin, albumin, and CEA levels). Perioperative

variables, such as operative duration, blood loss, left colic artery preservation, anastomotic level, postoperative complications, and hospitalization length, were also recorded. Patients were followed up regularly (every 3 months for 2 years, biannually for 3 years, and annually thereafter), with SSAL events documented. The primary endpoint was the incidence of AL within 6 months postoperatively, with SSAL as the secondary endpoint.

Statistical analysis

Intergroup differences were assessed using chi-squared or Fisher's exact tests. Variables with a P-value < 0.10 in univariate analysis were entered into multivariate logistic regression models. Propensity score matching (PSM) was performed using a 1:2 nearest-neighbor algorithm with a caliper of 0.2 standard deviations of the logit-transformed estimated propensity score (EPS). Matching covariates included age, sex, BMI, tumor size, location and stage, preoperative therapy, anastomotic height, LCA preservation, and diverting ileostomy status. To minimize temporal bias, patients were stratified by biennial surgical periods during PSM. Odds ratios (ORs) and 95% confidence intervals (CIs) were calculated for both univariate and multivariate analyses. A stepwise backward elimination method was used to identify independent predictors of AL. All statistical analyses were conducted using R (version 4.3.3) and SPSS (version 25.0), with statistical significance defined as $P<0.05$.

Results

Baseline characteristics before and after propensity score matching

A total of 533 patients undergoing low anterior resection were included in the study, with 402 patients in the non-FL group and 131 patients in the FL group before propensity score matching (PSM). After PSM with 1:2 ratio, 262 patients were successfully matched in the non-FL group to the 131 patients in the FL group. The demographic and clinical characteristics before and after PSM are summarized in Table 1.

Prior to matching, significant differences were observed between the groups, particularly in surgical strategy. The FL group had a markedly higher rate of left colic artery (LCA) preservation compared with the non-FL group (77.1% versus 48.0%, P < 0.001; SMD = 0.630), suggesting potential selection bias in operative planning. Although not statistically significant, the non-FL group tended to include a higher proportion of patients with smaller tumors (≤35 mm: 53.5% versus 43.5%, P = 0.060; SMD = 0.201) and early T-stage disease (T1–2: 44.3% versus 35.1%, P = 0.081; SMD = 0.188). These imbalances could potentially confound perioperative outcome comparisons.

Following PSM, baseline characteristics between the two cohorts were well balanced across all measured variables, with standardized mean differences (SMDs) falling below the conventional threshold of 0.20, indicating adequate covariate balance. Age (59.2 ± 10.9 versus 60.6 ± 10.1 years, P = 0.411; SMD = 0.089), BMI (24.0 ± 3.0 versus 23.9 ± 3.0 kg/m^2, P = 0.807; SMD = 0.026), and tumor size (38.4 ± 15.4 versus 39.0 ± 15.5 mm, P = 0.695; SMD = 0.056) were comparable between the non-FL and FL groups. Key oncological factors, including tumor stage (T3–4: 60.7% versus 64.9%, P = 0.485; SMD = 0.087) and nodal status (N+: 35.9% versus 40.5%, P = 0.439; SMD = 0.094), also showed no significant differences.

Importantly, the proportion of patients who received neoadjuvant chemoradiotherapy (nCRT) was similar between groups (14.9% versus 17.6%, P = 0.590; SMD = 0.073), supporting a balanced distribution of treatment-related factors that could influence postoperative outcomes. Furthermore, rates of LCA preservation and diverting ileostomy, both of which may impact anastomotic integrity, were comparable after matching (P = 0.486 and P = 0.570, respectively).

These results affirm that the PSM approach effectively minimized baseline imbalances, enabling a robust comparative analysis of surgical outcomes between patients undergoing conventional surgery versus those guided by fluorescent laparoscopy.

Operative findings

The mean operative time was comparable between the FL and non-FL groups overall (192.1 ± 66.2 min versus 183.8 ± 62.9 min, P = 0.232), as well as within the non-nCRT (P = 0.273) and nCRT subgroups (P = 0.863). However, blood loss during surgery was significantly lower in the FL group compared with the non-FL group overall (45.2 ± 58.9 mL versus 65.3 ± 73.1 mL, P = 0.004), as well as in the non-nCRT subgroup (41.2 ± 38.2 mL versus 61.9 ± 67.0 mL, P < 0.001), suggesting a potential benefit in terms of intraoperative hemostasis with the use of fluorescence laparoscopic surgery (Table 2).

The total number of lymph nodes (LNs) retrieved was significantly higher in the FL group (21.2 ± 11.4 versus 16.6 ± 7.3, P < 0.001), including among patients who did not receive nCRT (20.8 ± 11.1 versus 16.3 ± 7.0, P < 0.001). Although the difference was not statistically significant in the nCRT subgroup (P = 0.085), a trend toward higher LN retrieval was observed. Furthermore, a greater proportion of patients in the FL group met the benchmark for lymph node retrieval: ≥12 LNs (87.8% versus 77.5%, P = 0.014) and ≥25 LNs (30.5% versus 11.8%, P < 0.001). Notably, the FL group also demonstrated significantly higher retrieval of ≥25 LNs in the nCRT subgroup (34.8% versus 12.8%, P = 0.040).

Other perioperative complications

The incidence of intraoperative bleeding, ileus, and infection did not differ significantly between the FL and non-FL groups across all strata (Table 2). Specifically, intraoperative bleeding occurred in 2.3% of patients in the non-FL group and 3.1% in the FL group (P = 0.672), with similar rates observed in the non-nCRT (2.2% versus 2.2%, P = 0.852) and nCRT subgroups (7.7% versus 4.3%, P = 0.621).

Similarly, the occurrence of ileus was comparable between the FL and non-FL groups, with 3.8% of patients in the non-FL group and 4.2% in the FL group experiencing ileus (P = 0.887). This trend was consistent in the non-nCRT subgroup (2.7% versus 2.8%, P = 0.960) and the nCRT subgroup (12.8% versus 8.7%, P = 0.630). Infection rates were also similar across both groups, with 3.8% of non-FL patients and 5.3% of FL patients experiencing postoperative infections (P = 0.487). Again, there were no significant differences within the non-nCRT subgroup (3.6% versus 2.8%, P = 0.711) or the nCRT subgroup (15.4% versus 8.7%, P = 0.462).

While the differences did not reach statistical significance, the FL group consistently demonstrated lower rates of periopera-

Tech Coloproctol. 2025. 29(1):165 Published online: 21 August 2025

Table 1 Patient demographic characteristics and surgical procedures before and after the PSM

Clinical variables	Before PSM				After PSM			
	Non-FL ($n=402$)	FL ($n=131$)	P	SMD	Non-FL ($n=262$)	FL ($n=131$)	P	SMD
Age, years *	59.8 (11.3)	60.6 (10.1)	0.472	0.075	59.2 (10.9)	60.6 (10.1)	0.411	0.089
< 60	186 (46.3)	53 (40.5)	0.289	0.117	123 (46.9)	53 (40.5)		
≥ 60	216 (53.7)	78 (59.5)			139 (53.1)	78 (59.5)	0.266	0.131
Sex								
Male	251 (62.4)	70 (53.4)	0.084	0.183	160 (61.1)	70 (53.4)	0.180	0.155
Female	151 (37.6)	61 (46.6)			102 (38.9)	61 (46.6)		
BMI (kg/m^2)*	23.8 (3.2)	23.9 (3.0)	0.740	0.034	24.0 (3.0)	23.9 (3.0)	0.807	0.026
< 25	254 (63.2)	80 (61.1)	0.741	0.044	161 (61.5)	80 (61.1)		
≥ 25	148 (36.8)	51 (38.9)			101 (38.5)	51 (38.9)	1.000	0.008
Tumor status								
T1–2	178 (44.3)	46 (35.1)	0.081	0.188	103 (39.3)	46 (35.1)		
T3–4	224 (55.7)	85 (64.9)			159 (60.7)	85 (64.9)	0.485	0.087
Nodal stage								
N0	263 (65.4)	78 (59.5)	0.266	0.122	168 (64.1)	78 (59.5)	0.439	0.094
N+	139 (34.6)	53 (40.5)			94 (35.9)	53(40.5)		
Smoking								
No	346 (86.1)	120 (91.5)	0.138	0.174	232 (88.5)	120 (91.5)	0.462	0.099
Yes	56 (13.9)	11 (8.5)			30 (11.5)	11 (8.5)		
Drinking								
No	311 (77.4)	109 (83.2)	0.155	0.142	211 (80.5)	109 (83.2)	0.521	0.078
Yes	91 (22.6)	22 (16.8)			51 (19.5)	22 (16.8)		
Diabetes								
No	344 (85.6)	120 (91.5)	0.107	0.188	225 (85.9)	120 (91.5)	0.148	0.180
Yes	58 (14.4)	11 (8.5)			37 (14.1)	11 (8.5)		
Preoperative Hb (g/L)								
≥ 120	345 (85.8)	119 (90.8)	0.181	0.157	227 (86.6)	119 (90.8)	0.296	0.133
< 120	57 (14.2)	12 (9.2)			35 (13.4)	12 (9.2)		
Preoperative CEA (g/L)								
≤ 5	283 (70.4)	88 (67.2)	0.557	0.070	183 (69.8)	88 (67.2)	0.672	0.058
> 5	119 (29.6)	43 (32.8)			79 (30.2)	43 (32.8)		
Preoperative CA199 (kU/L)								
≤ 37	363 (90.3)	116 (88.5)	0.682	0.057	237 (90.5)	116 (88.5)	0.680	0.062
> 37	39 (9.7)	15 (11.5)	0.016	0.235	25 (9.5)	15 (11.5)	0.093	0.177
Tumor lower margin to anus (cm)*	4.0 (0.7)	3.8 (0.8)			3.9 (0.7)	3.8 (0.8)		
Anastomosis to anus (cm)*	2.2 (0.6)	2.2 (0.9)	0.566	0.052	2.3 (0.7)	2.2 (0.9)	0.281	0.109
Tumor size (mm)*	38.1 (15.6)	39.0 (15.5)	0.545	0.058	38.4 (15.4)	39.0 (15.5)	0.695	0.056
≤ 35	215 (53.5)	57 (43.5)	0.060	0.201	138 (52.7)	57 (43.5)	0.108	0.184
> 35	187 (46.5)	74 (56.5)			124 (47.3)	74 (56.5)		
LCA preservation			< 0.001	0.630				
No	209 (52.0)	30 (22.9)			70 (26.7)	30 (22.9)	0.486	0.088
Yes	193 (48.0)	101 (77.1)			192 (73.3)	101 (77.1)		
Diverting ileostomy								
No	66 (16.4)	25 (19.1)	0.568	0.070	58 (22.1)	25 (19.1)	0.570	0.076
Yes	336 (83.6)	106 (80.9)			204 (77.9)	106 (80.9)		
nCRT								
No	355 (88.3)	108 (82.4)	0.115	0.167	223 (85.1)	108 (82.4)	0.590	0.073
Yes	47 (11.7)	23 (17.6)			39 (14.9)	23 (17.6)		

Values in parentheses are percentages unless indicated otherwise; value in *mean (standard deviation)

SMD standardized mean differences, *FL* fuorescent lymphography, *BMI* body mass index, *AL* anastomotic leak, *LCA* left colic artery, *nCRT* neoadjuvant chemoradiotherapy

Table 2 Operative findings and short-term outcomes after PSM

Characteristics	All patients (n=)			Non-nCRT (n=331)			nCRT (n=62)		
	Non-FL (n=262)	FL (n=131)	P	Non-FL (n=223)	FL (n=108)	P	Non-FL (n=39)	FL (n=23)	P
Operative findings									
Operation time (min)*	183.8 (62.9)	192.1 (66.2)	0.232	176.6 (54.4)	184.5 (63.8)	0.273	224.5 (88.5)	228.3 (67.5)	0.863
Blood loss (ml)*	65.3 (73.1)	45.2 (58.9)	0.004	61.9 (67.0)	41.2 (38.2)	<0.001	84.6 (99.9)	63.9 (113.7)	0.457
Total LNs*	16.6 (7.3)	21.2 (11.4)	<0.001	16.3 (7.0)	20.8 (11.1)	<0.001	17.9 (8.7)	23.2 (12.8)	0.085
Retrieved LNs≥12	203	115	0.014	171	94	0.005	32	21	0.318
Retrieved LNs≥25	31	40	<0.001	26	32	<0.001	5	8	0.040
Complications (excluding AL)									
Intraoperative bleeding	8 (3.1%)	3 (2.3%)	0.672	5 (2.2%)	2 (1.9%)	0.852	3 (7.7%)	1 (4.3%)	0.621
Ileus incisional	11 (4.2%)	5 (3.8%)	0.887	6 (2.7%)	3 (2.8%)	0.960	5 (12.8%)	2 (8.7%)	0.630
Infection	14 (5.3%)	5 (3.8%)	0.487	8 (3.6%)	3 (2.8%)	0.711	6 (15.4%)	2 (8.7%)	0.462
Postoperative recovery									
Gas passing (days)*	2.9 (0.8)	2.6 (0.7)	0.008	2.8 (0.8)	2.5 (0.7)	0.011	3.4 (0.9)	3.0 (0.8)	0.047
Soft diet (days)*	4.2 (1.3)	3.8 (1.2)	0.002	4.0 (1.3)	3.7 (1.1)	0.022	4.9 (1.4)	4.4 (1.3)	0.088
Hospital stay (days)*	10.7 (3.8)	9.5 (3.1)	0.012	10.3 (3.6)	9.1 (3.0)	0.018	12.3 (4.1)	10.5 (3.6)	0.036

Values in parentheses are percentages unless indicated otherwise; value is *mean (standard deviation); *AL* anastomotic leak *FL* fuorescent lymphography, *BMI* body mass index, *nCRT* neoadjuvant chemoradiotherapy, *LN* lymph node

tive complications compared with the non-FL group, suggesting a potential trend towards reduced perioperative risks with the use of fluorescent laparoscopy.

Postoperative recovery

Furthermore, the length of postoperative hospital stay was significantly shorter in the FL group compared with the non-FL group (9.5±3.1 days versus 10.7±3.8 days, P=0.012). This was particularly evident in non-nCRT patients (9.1±3.0 days versus 10.3±3.6 days, P=0.018) and in the nCRT subgroup (10.5±3.6 days versus 12.3±4.1 days, P=0.036).

Patients in the FL group exhibited significantly faster recovery (Table 2). Time to first passage of gas was shorter in the FL group compared with the non-FL group (2.6±0.7 days versus 2.9±0.8 days, P=0.008), with similar trends observed in the non-nCRT (P=0.011) and nCRT subgroups (P=0.047). The FL group also transitioned to a soft diet earlier than the non-FL group (3.8±1.2 days versus 4.2±1.3 days, P=0.002), with a similar pattern noted in the non-nCRT subgroup (P=0.022). Although the difference was not statistically significant in the nCRT subgroup (P=0.088), a trend toward earlier diet progression was observed in the FL group.

Comparison of anastomotic leak rates and severity between fluorescent lymphography (FL) and non-FL groups

The comparison of AL rates between the FL and non-FL groups revealed a significant reduction in the incidence of AL in the FL group (Table 3). Among all patients, the overall AL rate was significantly lower in the FL group (3.1%) compared with the non-FL group (11.5%) (P=0.005). Similarly, when considering the severity of AL, patients in the FL group exhibited a significantly lower incidence of severe symptomatic anastomotic leaks (SSAL), with only 0.8% of FL patients experiencing SSAL, compared with 6.1% in the non-FL group (P=0.014). This underscores the advantage of fluorescence laparoscopic surgery in minimizing both the occurrence and severity of AL.

Regarding AL grade, the FL group had fewer grade A–B leaks (3.1% versus 8.4% in the non-FL group), and this difference approached statistical significance (P=0.045). However, the incidence of grade C AL did not differ significantly between the two groups (P=0.283), with only one case of grade C AL in the FL group (0.8%) compared with eight in the non-FL group (3.1%).

In the non-nCRT subgroup, the FL group demonstrated a significant reduction in the overall AL rate (1.9% in FL versus 7.2% in non-FL, P=0.045), indicating that fluorescence laparoscopic

Table 3 Comparison of AL rate after the PSM

	Non-FL group	FL group	P-value
All patients			
Patients number	262	131	
AL (n, %)			0.005
No	232 (88.5)	127 (96.9)	
Yes	30 (11.5)	5 (3.1)	
AL grade (n, %)			
A–B	22 (8.4)	4 (3.1)	0.045
C	8 (3.1)	1 (0.8)	0.283
SSAL (n, %)	16 (6.1)	1 (0.8)	0.014
Stenosis (n, %)	5 (1.9)	1 (0.8)	0.663
Rectovaginal fistula (n, %)	3 (1.1)	0 (0.0)	0.539
Rectourethral fistula (n, %)	2 (0.8)	0 (0.0)	0.316
Presacral sinus (n, %)	5 (1.9)	0 (0.0)	0.265
Anal fistula (n, %)	1 (0.4)	0 (0.0)	0.723
Non-nCRT			
Patients number	223	108	
AL (n, %)			0.045
No	207 (92.8)	106 (98.1)	
Yes	16 (7.2)	2 (1.9)	
AL grade (n, %)			
A–B	12 (6.3)	2 (1.9)	0.228
C	4 (1.8)	0 (0.0)	0.388
SSAL (n, %)	9 (4.0)	0 (0.0)	0.079
Stenosis (n, %)	2 (0.9)	0 (0.0)	0.315
Rectovaginal fistula (n, %)	2 (0.9)	0 (0.0)	0.315
Rectourethral fistula (n, %)	1 (0.5)	0 (0.0)	0.479
Presacral sinus (n, %)	3 (1.3)	0 (0.0)	0.218
Anal fistula (n, %)	0 (0.0)	0 (0.0)	1.000
nCRT			
Patients number	39	23	
AL (n, %)			0.051
No	25 (64.1)	20 (87.0)	
Yes	14 (35.9)	3 (13.0)	
AL grade (n, %)			
A–B	10 (25.6)	2 (8.7)	0.194
C	4 (7.7)	1 (4.3)	0.768
SSAL (n, %)	8 (20.5)	1 (4.3)	0.170
Stenosis (n, %)	3 (7.7)	1 (4.3)	0.637
Rectovaginal fistula (n, %)	1 (2.6)	0 (0.0)	0.437
Rectourethral fistula (n, %)	1 (2.6)	0 (0.0)	0.437
Presacral sinus (n, %)	2 (5.1)	0 (0.0)	0.379
Anal fistula (n, %)	1 (2.6)	0 (0.0)	0.437

Values in parentheses are percentages unless indicated otherwise;
Value in *mean (standard deviation)
FL fuorescent lymphography, *LN* lymph node, *BMI* body mass index, *AL* anastomotic leak, *SSAL* severe symptomatic anastomotic leaks, *nCRT* neoadjuvant chemoradiotherapy

surgery can reduce the incidence of AL even without the use of neoadjuvant chemoradiotherapy (nCRT). Furthermore, although the proportion of patients with grade A–B AL was lower in the FL group (1.9% versus 6.3%), this difference did not reach statistical significance (P=0.228), suggesting a trend toward reduced severity of AL in the FL group. The incidence of SSAL was also notably lower in the FL group, with no cases of SSAL compared with 4.0% in the non-FL group, though this difference was marginally non-significant (P=0.079).

In the nCRT subgroup, the FL group exhibited a trend toward lower AL rates (13.0% versus 35.9% in the non-FL group), approaching statistical significance (P=0.051). Although this difference did not reach conventional statistical significance, it suggests that fluorescence laparoscopic surgery may offer a protective effect in patients undergoing nCRT, who are typically at a higher risk for complications. The proportion of patients with grade A–B AL was lower in the FL group (8.7% versus 25.6%), but this difference was not statistically significant (P=0.194).

In this subgroup, the FL group also had fewer cases of SSAL (4.3% versus 20.5%), although this difference was, again, not statistically significant (P=0.170). The incidence of other complications, such as stenosis, rectovaginal fistula, and presacral sinus, was similar between the two groups, and none of these differences reached statistical significance.

The case in Fig. 3 demonstrates the use of multi-modal fluorescence imaging in a patient. Intraoperative color mode (Fig. 3A) and merged mode (Fig. 3B) showed acceptable perfusion, while monochrome fluorescence (Fig. 3C) identified a 3 cm×1 cm ischemic area near the anastomosis. Colonoscopy showed no ischemia in the colon mucosa (Fig. 3D). Postoperatively, the patient developed abdominal pain and fever, with emergent colonoscopy revealing necrosis at the ischemic site (Fig. 3E). On day 7, ulcers with white moss were observed (Fig. 3F), and the patient was discharged on day 14. Scar formation was noted on day 30 (Fig. 3G), and a rectovaginal fistula developed by day 60 (Fig. 3H). This example highlights the value of multimodal fluorescence for ischemia detection and monitoring.

Discussion

The results of this study highlight the potential benefits of fluorescence laparoscopic (FL) surgery in reducing the incidence of anastomotic leakage (AL) in patients with low rectal cancer, particularly those undergoing intersphincteric resection (ISR) after neoadjuvant chemoradiotherapy (nCRT). Our findings demonstrate that FL, utilizing indocyanine green (ICG) for real-time visualization of tissue perfusion, significantly lowers both the overall rate and severity of AL compared with traditional methods of assessing anastomotic integrity. What is more, the higher lymph node yield observed in the FL group may not be directly attributable to ICG fluorescence but rather to improved intraoperative visualization that facilitates precise dissection. Nonetheless, surgical variability and potential selection bias cannot be excluded. This study contributes valuable evidence to the ongoing search for strategies to optimize surgical outcomes and reduce postoperative complications in this high-risk population.

As established by numerous previous studies, nCRT is a standard preoperative treatment for locally advanced rectal cancer, aiming to downstage tumors and improve surgical resectability[15, 16]. However, despite its oncologic benefits, nCRT can also

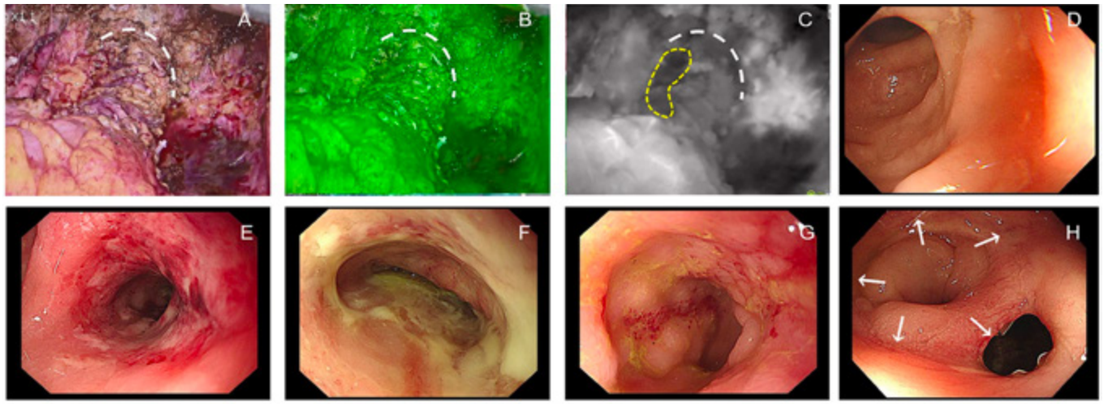


Fig.3 Multimodal fluorescence imaging for ischemia detection and monitoring in a patient. A. Intraoperative color mode showing the surgical site; **B.** merged mode displaying acceptable perfusion; **C.** monochrome fluorescence highlighting a 3 cm × 1 cm ischemic area near the anastomosis; **D.** colonoscopy showing no ischemia in the colon mucosa; **E.** emergent colonoscopy postoperatively revealing necrosis at the ischemic site; **F.** day 7 postsurgery showing ulcers with white moss at the ischemic location; **G.** scar formation observed on day 30; **H.** development of a rectovaginal fistula by day 60. This case underscores the utility of multimodal fluorescence for detecting and monitoring ischemia.

compromise the blood supply to the anastomotic site, leading to a heightened risk of AL. AL, a common and serious complication in low rectal cancer surgery, is known to increase postoperative morbidity and mortality, prolong hospital stays, and detract from long-term survival. The occurrence of AL is multifactorial, involving both technical aspects of surgery and biological changes induced by preoperative treatments such as nCRT[17–20]. Thus, understanding and mitigating the risk factors for AL remain critical challenges in colorectal surgery, especially for ultra-low rectal cancers treated with ISR.

In this context, FL surgery has emerged as a promising tool to improve intraoperative decision-making and potentially reduce complications such as AL. Several studies have demonstrated the utility of ICG fluorescence to enhance the identification of vascular structures and tissue perfusion during various colorectal surgeries[21–23]. While the application of fluorescence has been explored extensively in other colorectal surgeries, its specific role in low rectal cancer, particularly in post-nCRT scenarios, remains underexplored. Our study is one of the first to focus on the potential impact of fluorescence guidance in low rectal cancer surgery following nCRT, and it provides encouraging results.

The FL surgery group in our study had significantly lower rates of AL compared with the non-FL group, with a marked reduction in both grade A–B leaks and severe symptomatic anastomotic leaks (SSAL). This suggests that FL not only enhances the identification of critical vascular structures but also aids in optimizing anastomotic sites, thereby improving tissue perfusion and reducing the risk of AL. The lower incidence of SSAL in the FL group is particularly noteworthy, as SSAL is associated with chronic complications that can severely affect patient quality of life.

Furthermore, the subgroup analysis based on nCRT treatment showed that fluorescence guidance can reduce AL even in the more challenging cohort of patients who have received preoperative chemoradiation. While the difference did not reach statistical significance in the nCRT subgroup, the trend toward reduced AL rates in the FL group (13.0% versus 35.9%) underscores the potential protective effect of fluorescence laparoscopic surgery in these patients. This is consistent with the notion that nCRT-induced alterations in blood supply may be better addressed with real-time, precise perfusion visualization. To our knowledge, this is the first study to highlight that real-time perfusion assessment with fluorescence laparoscopic surgery contributes to improved outcomes in patients with high-risk low rectal cancer, especially those treated with nCRT.

In addition to its potential impact on AL, fluorescence guidance was associated with several other intraoperative and postoperative benefits. The FL group demonstrated lower blood loss, higher lymph node retrieval rates, and faster recovery times. These findings suggest that FL not only improves surgical precision but also enhances the overall quality of surgery, which may contribute to better long-term oncological outcomes. The ability to assess blood flow in real-time allows for more meticulous dissection, particularly in the critical mesenteric and anastomotic areas, which can result in less intraoperative bleeding and better lymph node retrieval. A key contribution of our work is the exploration of a dual-mode imaging strategy. While merged imaging offers significant advantages in anatomical orientation and lymphatic drainage mapping, it often encounters the challenge of background fluorescence interference. This can complicate accurate perfusion assessment, particularly in the complex pelvic environment. In our approach, utilizing a monochrome mode has proven especially effective in precisely delineating the microvascular supply to the bowel, a critical factor in ensuring anastomotic integrity. Our prior study similarly demonstrated that isolating the monochrome fluorescence signal enhances the assessment of bowel viability[24].

This retrospective study has inherent limitations. Although propensity score matching was employed to minimize baseline differences between groups, the possibility of selection bias cannot be entirely excluded. While fluorescence-guided surgery demonstrated benefits in both non-nCRT and nCRT subgroups, several results, particularly within the nCRT cohort, did not reach statistical significance. Larger prospective trials are warranted to validate these findings and to establish standardized protocols for ICG administration and fluorescence assessment. Additionally, known confounding factors such as smoking and diabetes were considered; however, other relevant variables including peripheral vascular disease and corticosteroid use were not systematically recorded and therefore not analyzed. The impact of these factors on outcomes remains unclear and should be addressed in future studies with more comprehensive data collection. Finally, long-term oncological outcomes were not evaluated owing to limited follow-up duration. Further investigations are necessary to determine whether the observed short-term improvements with fluorescence guidance translate into enhanced long-term survival and reduced recurrence.

In conclusion, fluorescence laparoscopic surgery using ICG shows considerable potential in reducing AL and improving other key surgical outcomes in patients with low rectal cancer, especially those who have undergone nCRT. The ability to assess tissue perfusion in real time provides surgeons with crucial information that can optimize anastomotic integrity and reduce postoperative complications. This technique may offer significant advantages over traditional methods, especially in high-risk populations, and warrants further investigation in future clinical trials to validate its role in improving surgical outcomes in low rectal cancer surgery.

Funding

This study was supported by grants from the National Natural Science Foundation of China (no. 82072732) and Beijing Natural Science Foundation (no. L222054 and 4232058).

Data availability

The datasets generated and/or analyzed during the current study are not publicly available due to confidentiality agreements with participants, but are available from the corresponding author on reasonable request.

Declarations

Conflict of interest: The authors declare no competing interests.

Ethical approval and consent to participate: Ethics reference number is NCC2022C-790, which is approved by Ethics Committee of the Clinical Trials Center of National Cancer Center (phone: +0086 010 87787112). The hyperlink to registration is here: http://cicams.ctims.com.cn/actmsf/index.action.

Informed consent: All participants gave their written informed consent to participate in this study.

Consent for publication: The authors have obtained consent from all participants for the publication of any data contained within the manuscript.

References

1. Yamashita K, Matsuda T, Hasegawa H, Mukohyama J, Arimoto A, Tanaka T et al (2019) Recent advances of neoadjuvant chemoradiotherapy in rectal cancer: future treatment perspectives. Ann Gastroenterol Surg 3(1):24–33
2. Khullar K, Patel NM, Anderson C, Chundury A, Carpizo D, Feingold D et al (2020) The evolving role of radiotherapy in locally advanced rectal cancer and the potential for nonoperative management. Oncol Hematol Rev 16(1):43–51
3. Tsalikidis C, Mitsala A, Mentonis VI, Romanidis K, Pappas-Gogos G, Tsaroucha AK et al (2023) Predictive factors for anastomotic leakage following colorectal cancer surgery: where are we and where are we going? Curr Oncol 30(3):3111–3137
4. Brisinda G, Chiarello MM, Pepe G, Cariati M, Fico V, Mirco P et al (2022) Anastomotic leakage in rectal cancer surgery: retrospective analysis of risk factors. World J Clin Cases 10(36):13321–13336
5. Koyama M, Murata A, Sakamoto Y, Morohashi H, Hasebe T, Saito T et al (2016) Risk factors for anastomotic leakage after intersphincteric resection without a protective defunctioning stoma for lower rectal cancer. Ann Surg Oncol 23(Suppl 2):S249-256
6. Lin L, Wang Y, Cai Y, Lei Y, Chen W, Liu G (2025) Intersphincteric resection for low-lying rectal cancer: analysis of risk factors and establishment of a preoperative assessment system for postoperative anal function. Tech Coloproctol 29(1):69
7. Shridhar R, Takahashi C, Huston J, Doepker MP, Meredith KL (2018) Anastomotic leak and neoadjuvant chemoradiotherapy in esophageal cancer. J Gastrointest Oncol 9(5):894–902
8. Gronnier C, Tréchot B, Duhamel A, Mabrut JY, Bail JP, Carrere N et al (2014) Impact of neoadjuvant chemoradiotherapy on postoperative outcomes after esophageal cancer resection: results of a European multicenter study. Ann Surg 260(5):764–770
9. Abdelrahman H, El-Menyar A, Peralta R, Al-Thani H (2023) Application of indocyanine green in surgery: a review of current evidence and implementation in trauma patients. World J Gastrointest Surg 15(5):757–775
10. Coco D, Leanza S (2024) Narrative review on the use of indocyanine green fluorescence in surgical oncology. Maedica (Bucur) 19(4):807–815
11. Jung JM, Park IJ, Park EJ, Son GM (2023) Fluorescence-guided colorectal surgery: applications, clinical results, and protocols. Ann Surg Treat Res 105(5):252–263
12. Watanabe J, Takemasa I, Kotake M, Noura S, Kimura K, Suwa H et al (2023) Blood perfusion assessment by indocyanine green fluorescence imaging for minimally invasive rectal cancer surgery (essential trial): a randomized clinical trial. Ann Surg 278(4):e688–e694
13. Pang HY, Chen XL, Song XH, Galiullin D, Zhao LY, Liu K et al (2021) Indocyanine green fluorescence angiography prevents anastomotic leakage in rectal cancer surgery: a systematic review and meta-analysis. Langenbecks Arch Surg 406(2):261–271
14. Lucarini A, Guida AM, Orville M, Panis Y (2024) Indocyanine green fluorescence angiography could reduce the risk of anastomotic leakage in rectal cancer surgery: a systematic review and meta-analysis of randomized controlled trials. Colorectal Dis 26(3):408–416
15. Nilsson PJ, van Etten B, Hospers GAP, Påhlman L, van de Velde CJH, Beets-Tan RGH et al (2013) Short-course radiotherapy followed by neo-adjuvant chemotherapy in locally advanced rectal cancer—The RAPIDO trial. BMC Cancer 13(1):279
16. Li Y, Wang J, Ma X, Tan L, Yan Y, Xue C et al (2016) A review of neoadjuvant chemoradiotherapy for locally advanced rectal cancer. Int J Biol Sci 12(8):1022–1031
17. Ju HE, Lee CS, Bae JH, Lee HJ, Yoon MR, Al-Sawat A et al (2022) High incidence of late anastomosis leakage in patients for rectal cancer after neoadjuvant chemoradiotherapy: a comparative study. Asian J Surg 45(10):1832–1842
18. Olivas AD, Shogan BD, Valuckaite V, Zaborin A, Belogortseva N, Musch M et al (2012) Intestinal tissues induce an SNP mutation in Pseudomonas aeruginosa that enhances its virulence: possible role in anastomotic leak. PLoS ONE 7(8):e44326
19. Babrowski T, Holbrook C, Moss J, Gottlieb L, Valuckaite V, Zaborin A et al (2012) Pseudomonas aeruginosa virulence expression is directly activated by morphine and is capable of causing lethal gut-derived sepsis in mice during chronic morphine administration. Ann Surg 255(2):386–393
20. Mima K, Sakamoto Y, Kosumi K, Ogata Y, Miyake K, Hiyoshi Y et al (2020) Mucosal cancer-associated microbes and anastomotic leakage after resection of colorectal carcinoma. Surg Oncol 32:63–68
21. De Simone B, Abu-Zidan FM, Boni L, Castillo AMG, Cassinotti E, Corradi F et al (2025) Indocyanine green fluorescence-guided surgery in the emergency setting: the WSES international consensus position paper. World J Emerg Surg 20(1):13
22. Guerra F, Coletta D, Greco PA, Eugeni E, Patriti A (2021) The use of indocyanine green fluorescence to define bowel microcirculation during laparoscopic surgery for acute small bowel obstruction. Colorectal Dis 23(8):2189–2194
23. Sugie T, Ikeda T, Kawaguchi A, Shimizu A, Toi M (2017) Sentinel lymph node biopsy using indocyanine green fluorescence in early-stage breast cancer: a meta-analysis. Int J Clin Oncol 22(1):11–17
24. Qiu W, Liu J, He K, Hu G, Mei S, Guan X et al (2024) Blood perfusion assessment by near-infrared fluorescence angiography of epiploic appendages in prevention of anastomotic leakage after laparoscopic intersphincteric resection for ultra-low rectal cancer: a case-matched study. Surg Endosc 38(9):5446–5456

Tech Coloproctol. 2025. 29(1):165 Published online: 21 August 2025

IEEE Trans Med Imaging. 2025. 44(3):1568-1580. Published online: 11 December 2024

Colorectal Surgery

Research Article

Prediction of Lymph Node Metastasis in Colorectal Cancer Using Intraoperative Fluorescence Multi-Modal Imaging

Xiaobo Zhu[1, 2], He Sun[3], Yuhan Wang[5], Gang Hu[5], Lizhi Shao[1, 2], Song Zhang[1, 2], Fucheng Liu[4], Chongwei Chi[1, 2], Kunshan He[1, 2], Jianqiang Tang[5] ✉, Yu An[3, #], Jie Tian[1, 2, 6] ✉, Zhenyu Liu[1, 2, 6] ✉

Abstract

The diagnosis of lymph node metastasis (LNM) is essential for colorectal cancer (CRC) treatment. The primary method of identifying LNM is to perform frozen sections and pathologic analysis, but this method is labor-intensive and time-consuming. Therefore, combining intraoperative fluorescence imaging with deep learning (DL) methods can improve efficiency. The majority of recent studies only analyze uni-modal fluorescence imaging, which provides less semantic information. In this work, we mainly established a multi-modal fluorescence imaging feature fusion prediction (MFI-FFP) model combining white light, fluorescence, and pseudo-color imaging of lymph nodes for LNM prediction. Firstly, based on the properties of various modal imaging, distinct feature extraction networks are chosen for feature extraction, which could significantly enhance the complementarity of various modal information. Secondly, the multi-modal feature fusion (MFF) module, which combines global and local information, is designed to fuse the extracted features. Furthermore, a novel loss function is formulated to tackle the issue of imbalanced samples, challenges in differentiating samples, and enhancing sample variety. Lastly, the experiments show that the model has a higher area under the receiver operating characteristic (ROC) curve (AUC), accuracy (ACC), and F1 score than the uni-modal and bi-modal models and has a better performance compared to other efficient image classification networks. Our study demonstrates that the MFI-FFP model has the potential to help doctors predict LNM and shows its promise in medical image analysis.

IEEE Trans Med Imaging. 2025. 44(3):1568-1580. Published online: 11 December 2024

Index Terms: Deep learning, multi-modal imaging, intra-operative fluorescence imaging, colorectal cancer, lymph node metastasis prediction.

[1] CAS Key Laboratory of Molecular Imaging and Beijing Key Laboratory of Molecular Imaging, Institute of Automation, Chinese Academy of Sciences, Beijing 100190, China

[2] School of Artificial Intelligence, University of Chinese Academy of Sciences, Beijing 100049, China

[3] Beijing Advanced Innovation Center for Big Data-Based Precision Medicine, School of Engineering Medicine, Bei-hang University, Beijing 100191, China

[4] Department of General Surgery, Beijing Fengtai Hospital, Beijing 100071, China

[5] Department of Colorectal Surgery, National Cancer Center/National Clinical Research Center for Cancer/Cancer Hospital, Chinese Academy of Medical Sciences and Peking Union Medical College, Beijing, 100021, China

[6] National Key Laboratory of Kidney Diseases, Beijing, 100853, China

* Xiaobo Zhu, He Sun, and Yuhan Wang contribute equally to the article

Introduction

Colorectal cancer (CRC) is the third most commonly diagnosed cancer and the third most common cause of cancer-related deaths worldwide [1]. The incidence of CRC has increased in recent years, and it accounts for about 10% of all cancers [2]. Complete resection of the primary tumor and regional lymph nodes is considered the most critical aspect of CRC treatment [3]. The lymph node metastasis (LNM) status significantly influences treatment decisions, including the choice of preoperative neoadjuvant radiotherapy versus surgery [4]. Preoperative conventional imaging methods such as computed tomography (CT) and magnetic resonance imaging (MRI) have some limitations in detecting LNM, such as the risk of radiation, low diagnostic efficiency that requires expert interpretation, etc., and need to be combined with other techniques to confirm the diagnosis [5-7]. Although, the utilization of lymph node biopsy can more accurately assess LNM; however, it leads to an expensive investment of time, labor, and other costs [8].

In CRC, Zhao et al. explored potential genomic phenotypes associated with deep learning (DL) features that facilitate LNM prediction [9]. Lennard et al. enhanced the prediction performance by utilizing a DL technique to analyze histological whole slide images (WSIs) to predict LNM in CRC [10]. Furthermore, Li and colleagues proposed improving the accuracy of LNM identification through the application of MRI in conjunction with a pre-trained Inception-v3 model on transfer learning [11]. However, the majority of studies on the prediction of LNM in CRC use either preoperative CT, MRI, or pathology imaging, or combine tissue genetic information with deep learning methods for prediction, which significantly raises implementation costs and reduces overall efficiency. Furthermore, these preoperative imaging techniques are incapable of visualizing the complete architecture of the lymph node, and their intraoperative utility is significantly restricted, leading to diminished detection efficiency and accuracy [12]. Nevertheless, intraoperative fluorescence navigation systems enable both surgical navigation during surgery and real-time imaging of multi-modal fluorescence images and real-time imaging of multi-modal fluorescence images to visualize tissues [13]. Due to the quick capture time and affordable nature of intraoperative multi-modal fluorescence imaging, the analysis of multi-modal fluorescence imaging not only decreases the time and cost of labor but also has the potential to assist in making clinical decisions during surgery. Hence, we propose integrating DL with intraoperative fluorescent multi-modal imaging to enhance the efficiency and accuracy of intraoperative LNM prediction significantly.

Indocyanine green (ICG) is considered to be more effective in CRC lymph node identification since ICG penetrates relatively deeply into the tissue of the colon compared to other fluorescent tracers [14]. When injected intravascularly, ICG binds to proteins and is transported through the lymphatic system, normally draining to the closest lymph node in 15 minutes or less. It is becoming more typical to employ near- infrared (NIR) fluorescence imaging (FI) to guide surgical guidance following ICG injection [15, 16]. Fluorescence- guided surgery offers advantages such as real-time imaging, high visualization, enhanced contrast, non-invasiveness, precise navigation, and broad applicability, all of which contribute to improved surgical safety, accuracy, and success rates. Typical fluorescence surgical imaging is available in three modes, white light imaging (WLI), fluorescence imaging (FI), and pseudo-color imaging (PCI). Most of the existing studies use DL to analyze FI, mainly for cancer diagnosis or image enhancement, etc., while few studies have been conducted to predict LNM.

Compared to machine learning-based radiomics approaches, DL offers the advantage of automatically learning hierarchical features from raw data, eliminating the need for manual feature extraction, and often achieving superior performance in tasks such as image classification, segmentation, and pattern recognition [17]. In the field of medical image analysis, DL has been widely utilized for analyzing multi-modal images, including CT and MRI.

However, most multi-modal medical imaging analysis methods employ the same feature extraction network, which is unable to take into account the specificity of distinct imaging features. In addition, most of the methods for multi- modal medical imaging feature fusion in the intermediate stage of the model directly integrate the features by dimensionally concatenating them or utilizing the Transformer structure [18], but this is not able to focus on the feature information at both the global and local levels.

Most studies have increasingly incorporated DL methods to process intraoperative FI for targeted medical tasks. Shen et al. developed an FL-CNN model to extract relevant information from glioma FI, enhancing the precision of intraoperative glioma diagnosis to assist surgeons in accurately identifying and removing gliomas [19]. Cahill et al. proposed a method combining artificial intelligence (AI) with intraoperative FI video analysis, which was utilized to improve the accuracy of tumor identification for intraoperative tissue classification of colorectal cancer [20]. The growing number of researchers leveraging AI to analyze intraoperative fluorescence imaging or video highlights the advantages of fluorescence-based surgical guidance [21-23]. Additionally, Xiao et al. developed a method for intraoperative glioma grading by combining various imaging features and introduced DLS-DARTS to fuse multi-modal near-infrared (NIR) fluorescence imaging, resulting in improved predictive outcomes [24]. Multi-modal medical imaging learning can take advantage of data from different medical imaging modalities to achieve comprehensive analysis and diagnosis. Most of the studies analyzed FI, while a few combined FI and WLI but lacked the analysis of PCI. Hence, three intraoperative modality imaging types, WLI, FI, and PCI, are utilized in our study to increase the information on lymph node features in CRC, which improves the prediction performance.

Here, we propose a multi-modal imaging learning frame work, called the multi-modal fluorescence imaging feature fusion prediction (MFI-FFP) model, to extract and integrate multi-modal intraoperative fluorescence information, including the three modalities of WLI, FI, and PCI, for LNM prediction in CRC. In this study, a CRC lymph node dataset is collected and prepared specifically for the three modalities of WLI, the first NIR fluorescence window (NIR-I, 700-900 nm) FI, and PCI. First, we design a feature extraction framework comprising three pre-trained branches to extract lymph node features from the tri-modal images: the Inverse Residual Network branch for white light image features, the Residual Network branch for fluorescence image features, and the Transformer Network branch for pseudo-color image features. Subsequently, the integration of global and local feature information from the three modal data is done by a multi- modal feature fusion (MFF) module, which then produces the fusion lymph node features. Moreover, LNM in cancer patients typically exhibit a more pronounced benign-malignant imbalance, with the benign-malignant ratio escalating to 10:1 in extreme instances [25-27]. Therefore, a novel loss function is tailored to the data characteristics to address the issue of class imbalance and the challenge of distinguishing between classes in the dataset. The main contributions of our work are summarized as follows:

To fully utilize the feature information from each imaging modality, we select three specialized feature extraction branches for the tri-modal images. This approach enhances the model's ability to capture and characterize features specific to each modality, and experimental results confirm the effectiveness of this design.

To comprehensively utilize the complementary information contained in different modal imaging and provide more comprehensive and accurate imaging characterization, we design a multi-modal feature fusion (MFF) module to enhance the model's ability to combine multi- modal imaging information for decision-making.

We propose a novel intra-class loss function based on the combination of label-distribution-aware margin (LDAM) loss and Focal loss, which increases the diversity of the data while reducing the impact of the sample imbalance problem.

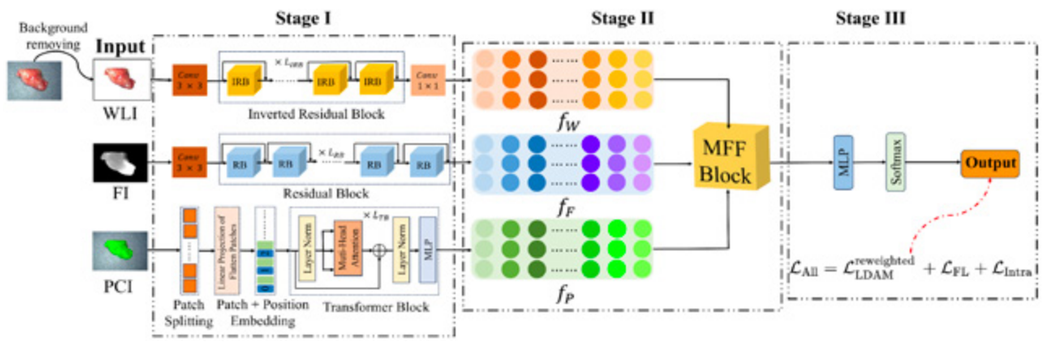


Fig.1 The overall framework of the MFI-FFP Model. Stage I. The features of the three modal data are extracted using the inverted residual, residual, and Transformer structures of the feature extraction branches, respectively. Stage II. The three extracted modal features are fused at the global and local levels through the MFF module. Stage III. Lymph node metastasis prediction based on fused features.

Methodology

Multi-modal Imaging Feature Extraction Branches

As demonstrated in Fig. 1, three feature extraction branches are built at the beginning of the entire MFI-FFP model to extract WLI, FI, and PCI image features. The advantage of extracting multiple modal images utilizing distinct feature extraction branches is that the feature information of each imaging modality can be fully utilized, potentially enhancing the model's characterization capacity. To ensure that the primary feature information is retrieved with the least amount of loss, we utilize a background removal method for the WLI data to eliminate superfluous background interference noise. Given that white light imaging (WLI) is characterized by high pixel density and numerous features, we employ an inverted residual structure to efficiently capture spatial details and structural features. This module enhances computational efficiency by reducing the number of operations in the bottleneck layer while preserving critical feature representations, enabling lightweight feature extraction. This makes it well-suited for WLI, which typically demands high-resolution and detailed spatial information. The inverted structure is particularly advantageous for processing high-dimensional images like WLI, as it balances accuracy with computational complexity.

In contrast, a conventional ResNet is used for fluorescence imaging, which has three-channel values resembling the characteristics of grayscale images. ResNet is effective at capturing both fine and coarse features across different depths. Since the spatial variability in fluorescence imaging is generally lower than that in WLI, a standard ResNet is sufficient for extracting the necessary hierarchical features without the need for additional computational optimizations.

PCI data, which includes tissue size, edge feature, and fluorescence intensity information is the result of mapping fluorescence feature information on tissue imaging. To avoid the WLI data losing some edge information during background removal, no background removal procedure is applied to the PCI data in this study. The Vision Transformer (ViT) structure is used for pseudo-color imaging (PCI) due to its ability to capture long-range dependencies within the data. Unlike convolutional networks, the ViT model establishes connections between local and global features, allowing it to focus on multiple parts of the image simultaneously. This capability enables effective capture of both local and global relationships in PCI, which is essential for accurate feature extraction. The extracted features from PCI can effectively complement the WLI and FL features, enhancing the overall feature representation and model performance.

In the feature extraction network branches, the WLI, FI, and PCI sample spaces are defined as $X_W = \{x^1_W, x^2_W, \dots, x^n_W\}$, $X_F = \{x^1_F, x^2_F, \dots, x^n_F\}$, and $X_P = \{x^1_P, x^2_P, \dots, x^n_P\}$, respectively, and x^i_W, x^i_F, and $x^i_P \in R^{C\times H\times W}$. The corresponding inverse residual, residual, and ViT feature extraction branches are defined as functions F_{IR}, F_R, and F_{ViT}, respectively. Thus, the procedure for extracting features is as follows in (1) to (3).

$$f^i_W = \mathbf{F_{IR}}(x^i_W) \tag{1}$$

$$f^i_F = \mathbf{F_R}(x^i_F) \tag{2}$$

$$f^i_P = \mathbf{F_{ViT}}(x^i_P) \tag{3}$$

where f^i_W, f^i_F, and f^i_P are the three modal imaging features corresponding to the lymph node with index i, respectively. In this case, the ViT model is calculated as follows in (4) to (7).

$$z_0 = \left[x_{\text{class}}; x^1_p E; x^2_p E \cdots x^N_p E\right], E \in \mathbb{R}^{(P^2\cdot C)\times D} \tag{4}$$

$$z'_\ell = \text{MSA}\left(\text{LN}\left(z_{\ell-1}\right)\right) + z_{\ell-1}, \ell \in [1, 2, \cdots, L] \tag{5}$$

$$z_\ell = \text{MLP}\left(\text{LN}\left(z'_\ell\right)\right) + z'_\ell \tag{6}$$

$$y = \text{LN}\left(z^0_L\right) \tag{7}$$

where x_{class} is the input PCI data, MLP represents the computational process of the multilayer perceptual machine, and MSA represents the computational process of the multi-head

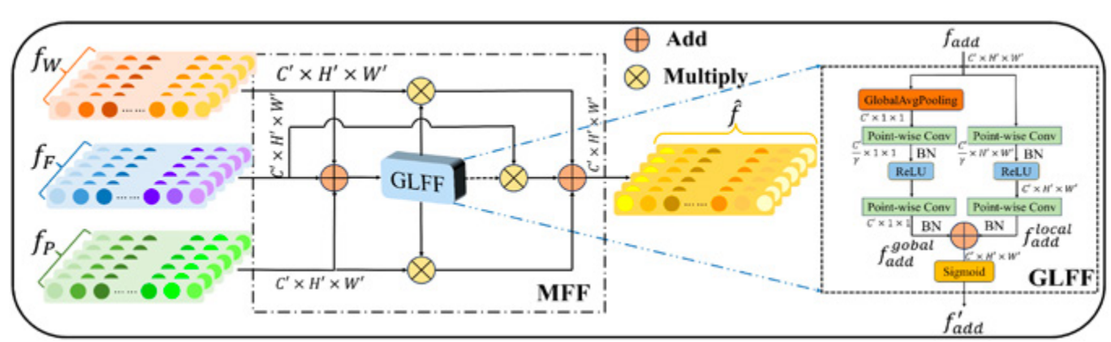


Fig.2 The overall structure of the MFF module. The extracted features from the three modal data are fused with the global and local hierarchical features through the GLFF module and a series of weighting operations are performed with the original features to produce the final fused features.

attention mechanism.

It is evident how the single-head attention mechanism is calculated for the MSA computation, as demonstrated in (8).

$$\text{Attention}(Q,K,V) = \text{soft}\max\left(\frac{QK^T}{\sqrt{d_k}}\right)V \tag{8}$$

where the value vector is V, the key vector is K, and the query vector is Q. The single-head attention mechanism extends the computation of the multi-head attention mechanism. The QKV vector matrix is mapped several times by the multi-head attention mechanism, which then combines the vector matrices. The equations (9) and (10) illustrate the computation procedure.

$$\text{MultiHead}(Q,K,V) = \text{Cat}\left(\text{head}_1,\cdots,\text{head}_h\right) \tag{9}$$

$$\text{head}_i = \text{Attention}\left(Q\cdot W_i^Q, K\cdot W_i^K, V\cdot W_i^V\right) \tag{10}$$

To validate the effectiveness of the designed feature ex-traction network, Section IV-A demonstrates the structure with experiments.

Multi-modal Imaging Feature Fusion

After extracting the features of the three modal, WLI, FI, and PCI data, feature fusion of the three modal features is required. The spatial alignment of the tri-modal data is ensured during acquisition, and the same size is maintained throughout feature extraction and in the resulting feature maps, ensuring that the features from each modality remain aligned. In the feature fusion module, after summing the dimensions of the tri-modal features, only weighting and multiplication operations are applied at corresponding positions, maintaining feature alignment throughout the entire process. Accordingly, we propose the MFF module to perform global and local-level feature fusion on the three modal features and finally output the fused feature $\hat{f}$, as illustrated in Fig. 2. Initially, an element-wise adding operation along the channel direction is applied to the three retrieved modal characteristics, f_w, f_F, and f_P, as shown in (11).

$$f_{add} = f_W \oplus f_F \oplus f_P \tag{11}$$

Additionally, f_{add} needs to be put into the global local feature fusion (GLFF) module. The GLFF module has two branches: the left branch handles global feature interaction, while the right branch handles local feature interaction. The Sigmoid function is subsequently utilized to output the results after the operation has been added together. Local features can capture specific details and unique information, whereas global features are typically able to capture the general global structure and semantic information of the image. To assist the model in comprehending the overall features, the left branch of the GLFF module implements a global average pooling layer to gather global information about the complete feature map. Furthermore, by using point-wise convolution to interchange and integrate data between various spatial locations or channels, both branches simultaneously alter the dimensionality of the feature maps. In this model, global features f^{gobal}_{add} are extracted through Global Average Pooling, summarizing the overall information from the input data and capturing the global context. On the other hand, local features f^{gobal}_{add} are obtained using Point-wise Convolution, which retains spatial details and local patterns in the data. The GLFF module integrates both global and local features, leveraging the summarization capability of global features and the detail-preserving nature of local features to enhance feature representation and improve model performance. The GLFF module process is as follows in (12) to (14).

$$f_{add}^{gobal} = BN(PWC(\xi(PWC(GAP(f_{add}))))) \tag{12}$$

$$f_{add}^{local} = BN(PWC(\xi(PWC(f_{add})))) \tag{13}$$

$$f_{add}^{'} = \sigma(f_{add}^{gobal} \oplus f_{add}^{local}) \tag{14}$$

where GAP is global average pooling, PWC is point-wise convolution, ξ is the Rectified Linear Unit (ReLU) activation function, σ is the Sigmoid function, and BN is the Batch Normalization (BN) layer. Here, the input feature tensor shape C′×H′×W′ is compressed to C′/γ ×1×1, then restored to C′×H′×W′ using point-wise convolution, which exchanges and integrates information.

The totals of the three modal features are subsequently weighed individually using f'_{add}, which is the fusion weight information obtained from the GLFF module's output. Finally, the adding operation is carried out to complete the fusion of the three modal features, as in

$$\widehat{f} = (f_{add}^{'} \otimes f_W) \oplus ((1 - f_{add}^{'}) \otimes f_F) \oplus (f_{add}^{'} \otimes f_P). \tag{15}$$

Additionally, to better adapt to various tasks and contexts, the relative prominence of certain modal elements can be dynamically changed. The GLFF output can assist the model in narrowing its focus to the most pertinent data, and by weighting and summing various modal features, the redundancy between features can be minimized. Moreover, the FI has fewer similar features to WLI and PCI, so a one-minus weighting operation is adopted. The MFF enhances the model's capacity for generalization, increases its efficiency, and prevents needless computational and storage overheads.

Loss Function

In colorectal cancer patients, metastatic lymph nodes constitute only a small fraction of the total lymph nodes, resulting in a significant imbalance between benign and malignant samples. To address this imbalance, LDAM Loss [8] is employed in this study. Additionally, due to the similarities between benign and malignant lymph nodes observed in intraoperative fluorescence imaging, distinguishing between them can be challenging. To tackle this issue, we use Focal Loss [29]. Finally, we design a novel intra-loss function to enhance sample diversity, further improving model performance by building on the combination of the previous losses. Thus, the new loss function consists of LDAM Loss, Focal Loss, and Intra-Loss, designed to enhance model prediction performance by combining the strengths of these three loss functions.

1) LDAM Loss: The LDAM loss aims to minimize generalization boundaries based on margin. To enhance the generalization performance of the minority class, the classification boundary can be shifted toward the majority class. This loss can be employed with a priori strategies for training with class- imbalanced data, including reweighting or resampling, in place of the traditional cross-entropy function during training [28]. The specific formula is shown in (16).

$$\mathcal{L}_{\text{LDAM}} = -\sum_{i=1}^{N}\log\left(\frac{e^{z_i^y-\Delta_y}}{e^{z_i^y-\Delta_y}+\sum_{j\neq y}e^{z_i^j}}\right) \tag{16}$$

$$where \Delta_j = \frac{\hat{C}}{n_j^{1/4}}, \quad for j \in \{1,\ldots,k\} \tag{17}$$

where $\hat{C}$ is the hyperparameter that needs to be adjusted, n_j of sample imbalance and differentiation difficulty while also is the class j sample size, k is the number of classes and z_i^y is the yth output of the model for the ith sample, which belongs to class y. Moreover, LDAM is reweighted by frequency in order to enhance its performance on class-imbalance learning. In our loss function, the reweighted LDAM is used, as in

$$\mathcal{L}_{\text{LDAM}}^{\text{reweighted}} = -\sum_{i=1}^{N}\omega_i\log\left(\frac{e^{z_i^y-\Delta_y}}{e^{z_i^y-\Delta_y}+\sum_{j\neq y}e^{z_i^j}}\right). \tag{18}$$

2) Focal Loss: Focal loss effectively suppresses the influence of easily classified samples on the loss by reducing their weight and increasing the weight of hard-to-classify samples, thus enhancing the model's focus on difficult-to-classify samples [29]. It addresses class imbalance issues and improves model performance on minority classes. The formula is shown blew

$$\mathcal{L}_{\text{FL}} = -\sum_{i=1}^{N}\omega_i\left(1-p_i\right)^{\kappa}\log\left(p_i\right) \tag{19}$$

where $(1\text{-}p_i)^K$ is a modulating factor, and is a hyperparameter needed to be setting. The higher value of $(1\text{-}p_i)^K$ means that the model will pay more attention to hard samples with small values of p_i.

3) Intra Loss: In order to bring the intra-class samples closer together and increase the diversity of the samples, we propose the Intra-loss. Initially, the Pearson correlation coefficient (PCC) is employed to determine the similarity between neighboring samples within a class, as shown in

$$\rho_{\mathbf{x}_i\mathbf{x}_{i+1}} = \frac{\text{Cov}\left(f\left(\mathbf{x}_i\right), f\left(\mathbf{x}_{i+1}\right)\right)}{\delta\left(f\left(\mathbf{x}_i\right)\right)\delta\left(f\left(\mathbf{x}_{i+1}\right)\right)} \tag{20}$$

where f (X_i) and f (X_i) represent the output of the model for samples x_i and x_{i+1}, respectively; Cov(·) is the covariance function; δ(·) is the standard deviation function. Therefore, the average similarity of each class defines the feature diversity ϕ_m of class m, as shown blew

$$\rho_m = \frac{\sum_{x_i\in\phi^m}\rho_{x_ix_{i+1}}}{n_m} \tag{21}$$

where n_m is the number of samples belonging to class m, and ϕ_m is the set of sample space on class m. As illustrated in (22), distinct classes are required to have similar data distributions in intra-class losses to concurrently tackle the class imbalance problem of data scarcity and data density.

$$\mathcal{L}_{\text{Intra}} = \sum_{m,k\in\phi \text{ and } m\neq k}\|\rho_m-\rho_k\|_2^2 \tag{22}$$

The final form of the loss function is shown below

$$\mathcal{L}_{\text{All}} = \mathcal{L}_{\text{LDAM}}^{\text{reweighted}} + \alpha\mathcal{L}_{\text{FL}} + \beta\mathcal{L}_{\text{Intra}}. \tag{23}$$

The proposed novel loss function has combined the afore-mentioned three loss functions, which will address the issues of sample imbalance and differentiation difficulty while also increasing the intra-class variety.

Experimental settings

Data

The intraoperative fluorescence dataset employed in this study contains three modalities of WLI, FI, and PCI data, where FI data are NIR-I fluorescence. The lymph node samples used in this study are isolated during colorectal cancer surgeries and imaged intraoperatively. For each lymph node, we capture three types of modality images: white-light imaging (WLI), fluorescence imaging (FI), and pseudo-color imaging (PCI) using the intra-operative fluorescence device (DPM-ENDOSCOPE-3D06 and DPM-0PENCAM-02, Zhuhai Dipu Medical Technology Co., Ltd.). The training and test datasets are provided by Beijing Fengtai Hospital, which supplied multi-modal fluorescence images of isolated lymph nodes from 49 patients. A total of 996 lymph nodes are analyzed, 87 of which are metastatic, while the remaining 909 are non-metastatic, resulting in a negative-to-positive sample ratio of approximately 10:1. In total, 2,988 multi-modal images are collected, with 996 images per modality. The dataset is split into train and test sets in the trials using a 7:3 ratio, and the three modal images adhere to the same dataset division guidelines.

To verify the model's generalization performance and robustness, we acquire multi-modal lymph node images from 19 colorectal cancer patients at the Cancer Hospital, Chinese Academy of Medical Sciences. This external validation set consists of 270 lymph nodes, yielding a total of 810 images, of which 76 nodes are metastatic. Intraoperative isolated lymph nodes are placed on medical placement cloths, in order to reduce the interference of the background on the WLI data, we sequentially perform the background removal operation on all WLI image data via the Photoshop software. To avoid inadvertent removal of the edge information of lymph nodes in the WLI, the background removal operation was not carried out on the PCI data so that the feature extraction network could perform the supplementation corresponding to the missing information during the model training. In the beginning, the image size is adjusted to 224 × 224, and random horizontal flip and random rotation operations are carried out.

IEEE Trans Med Imaging. 2025. 44(3):1568-1580. Published online: 11 December 2024

Implementation Details

The three modal imaging data sizes input to the model are (B, 3, 224, 224), where *B* is the batch size. In the feature extraction network, the branching structure for extracting the WLI data is a convolutional layer with an output dimension of 32, immediately followed by 17 inverted residual modules, and finally a convolutional and fully connected layer with an output feature map shape of (B, 512, 7, 7). All the above convolutional layers are immediately followed by the BN layer and the ReLU6 activation function. The branching structure of the extracted FI features uses the network structure of ResNet18 [30] throughout, and the shape of the output feature map is (*B*, 512, 7, 7). The feature branching structure of the extracted PCI is the ViT structure, which is firstly sliced and mapped to the data, then converted to the form of a long sequence of vectors, immediately followed by stacking of 12 Transformer modules, and finally outputting a feature map with the dimensions (*B*, 512, 7, 7). Pre-trained weights trained on the ImageNet dataset have been introduced into the complete feature extraction network to speed up model convergence and increase model accuracy.

The three modal feature dimensions C′ × H′ × W′ input to the MFF module are (*B*, 512, 7, 7), followed by element-wise addition, and the output feature dimensions after passing through the MFF module is (*B*, 512, 7, 7), where the hyperparameter γ in the GLFF module is 8. The final multi-layer perception (MLP) structure of the model is an adaptive pooling layer with an output dimension of (*B*, 512, 1, 1), followed by two fully connected (FC) layers mapping the feature dimensions from 512 to 2. Moreover, the two FC layers have a ReLU activation function applied and a dropout layer to prevent over-fitting.

The hyperparameters during model training are set as follows: learning rate (lr) is set to 0.001; weight decay (wd) is set to 0.003; batch size (*B*) is 32; and the dropout layer hyperparameter is set to 0.3. The Adam optimizer is chosen as the optimizer for model training. A total of 100 epochs are set up for the training process. The hyperparameter settings in the loss function align with those in references [28] and [29]. The hyperparameters in the loss function L_{ALL} are set as follows: the weight w_i of $L^{reweighted}_{LDAM}$ and L_{FL} are both set to 0.85; C in $L^{reweighted}_{LDAM}$ is set to 0.5; and κ in L_{FL} is set to 2.0. In Section IV-E, the sensitivity analysis of the hyperparameters indicates that α and β should be set to 1 for optimal model performance. The training process for all experiments is implemented using Pytorch-2.1.0 and is performed on the NVIDIA RTX 4090 GPU with 24 GB of memory.

Evaluation Metrics

To validate the performance of our proposed MFI-FFP model for the prediction of colorectal cancer, the main assessment metrics employed are the area under the receiver operating characteristic (ROC) curve (AUC), accuracy (ACC), and F1 score. The ROC curve is a curve with the true positive rate (TPR) as the y-axis and the false positive rate (FPR) as the x-axis. The AUC is the area under the ROC curve, which indicates the model's classification performance under different thresholds. The larger the AUC means the better the model's performance.

Results

Comparison of Different Feature Extraction Branches

To evaluate the performance of different network architectures as feature extraction branches for the three-modal imaging, we extracted WLI, FI, and PCI data features using the residual block (RB) structure, the inverted residual block (IRB) structure, and the ViT structure, respectively. As shown in Table I, the results of applying the same branching structure to the three modal data are also compared. Consequently, all comparison experiments are evaluated on the test dataset and external validation set across 5 runs. The median of these 5 runs of results is selected for presentation and 95% confidence intervals (CI) are calculated using 1000 trials of the Bootstrap approach.

The comparison results of the three modal imaging data extracted by different feature extraction branches show that extracting WLI data features using IRB structure, FI data features using RB structure, and PCI data features using ViT structure demonstrated the best performance, with the AUC of 0.8294 (95% CI 0.7813-0.8431), the ACC of 0.8669 (95% CI 0.8487-0.8967), and the F1 score of 0.4999 (95% CI 0.4612-0.5174) on the test set. Similarly, the model demonstrates strong performance on the external validation set, further confirming its generalization capability and robustness. Furthermore, there

is relatively high efficiency in the experimental results when exchanging the WLI and PCI data feature extraction branches, which achieves the AUC of 0.8054 (95% CI 0.7935-0.8283), the ACC of 0.8672 (95% CI 0.8462-0.8882), and the F1 score of 0.4236 (95% CI 0.3920-0.4542) on the test set. The ACC on the external validation set reaches 0.8296. The structure of the PCI data is similar to that of the WLI data, but it is mixed with some background noise and lacks some lymph node texture information after fluorescence information mapping. As a result, the global features cannot be effectively extracted using the IRB structure, which slightly reduces the overall performance of the model. Additionally, the last three rows of Table I demonstrate that even though similar features can be extracted using the same feature extraction structure in all three modalities, the unique features of each modality cannot be adequately represented.

Comparison of Single-Modal, Multi-Modal Imaging

To assess the effectiveness of fusing feature information from tri-modal imaging compared to fusing feature information from bi-modal or even uni-modal imaging, some comparative experiments using only bi-modal or uni-modal imaging are conducted in this study. As shown in Table II, the MFI-FFP model can more comprehensively learn the different feature information of the current corresponding lymph node by combining the feature information from the three-modal imaging, WLI, FI, and PCI, resulting in a more effective way to distinguish LNM. The experimental results demonstrate that the network learns best and the model performs optimally when the three modal imaging data serve as inputs, obtaining the ACC of 0.8782 (95% CI 0.8487-0.8967), the AUC of 0.8294 (95% CI 0.7813-0.8431), and the F1 score of 0.4999 (95% CI 0.4612-0.5174) on the test set. In the bi-modal imaging

IEEE Trans Med Imaging. 2025. 44(3):1568-1580. Published online: 11 December 2024

Table 1 Comparison of Results of Different Feature Extraction Branches for Extracting Three Modal Imaging Data. Numbers in Brackets Indicate 95% Confidence Intervals Using 1000 Trials of The Bootstrap Method.

Image mode	+Feature extraction branch		test set			External validation set		
			AUC	ACC	F1	AUC	ACC	F1
WLI+IRB	FI+RB	PCI+ViT	**0.8294** (0.7813,0.8431)	**0.8635** (0.8487,0.8967)	**0.4999** (0.4612, 0.5174)	**0.8437** (0.8006, 0.8769)	0.8111 (0.7630, 0.8356)	**0.6946** (0.6471, 0.7161)
WLI+RB	FI+IRB	PCI+ViT	0.7426 (0.7344,0.7709)	0.7970 (0.7721,0.8219)	0.3093 (0.2733,0.3411)	0.7569 (0.7283,0.7826)	0.7685 (0.7215, 0.7852)	0.5323 (0.5067,0.5562)
WLI+ViT	FI+RB	PCI+IRB	0.8054 (0.7935,0.8283)	0.8672 (0.8462,0.8882)	0.4236 (0.3920,0.4542)	0.8149 (0.7636, 0.8312)	**0.8296** (0.7407, 0.8407)	0.6290 (0.5928, 0.6548)
WLI+ViT	FI+IRB	PCI+RB	0.7691 (0.7517,0.8036)	0.8192 (0.7953,0.8431)	0.3544 (0.3271,0.3815)	0.7023 (0.6625, 0.7224)	0.7815 (0.7626, 0.8163)	0.5203 (0.4916, 0.5526)
WLI+IRB	FI+ViT	PCI+RB	0.7600 (0.7460,0.7915)	0.7934 (0.7683,0.8185)	0.3467 (0.3149,0.3804)	0.7792 (0.7582, 0.8180)	0.7556 (0.7237, 0.7837)	0.6118 (0.5974, 0.6402)
WLI+RB	FI+ViT	PCI+IRB	0.7853 (0.7510,0.8161)	0.8229 (0.7992,0.8466)	0.3688 (0.3422,0.4013)	0.7424 (0.7135,0.7765)	0.7481 (0.7167, 0.7704)	0.5211 (0.4902, 0.5457)
WLI+IRB	FI+ IRB	PCI+IRB	0.7089 (0.6704,0.7252)	0.7528 (0.7261,0.7795)	0.2708 (0.2437,0.3054)	0.7526 (0.7146, 0.7856)	0.7556 (0.7237, 0.7874)	0.5238 (0.4988, 0.5565)
WLI+RB	FI+RB	PCI+RB	0.6268 (0.6011,0.6544)	0.6753 (0.6463,0.7043)	0.2317 (0.2048,0.2573)	0.6681 (0.6402, 0.6912)	0.6778 (0.6470, 0.7031)	0.4710 (0.4416, 0.5189)
WLI+ViT	FI+ViT	PCI+ViT	0.6357 (0.6002,0.6603)	0.6827 (0.6539,0.7115)	0.2275 (0.1983,0.2592)	0.6719 (0.6389, 0.7007)	0.6926 (0.6741, 0.7278)	0.4645 (0.4327,0.4958)

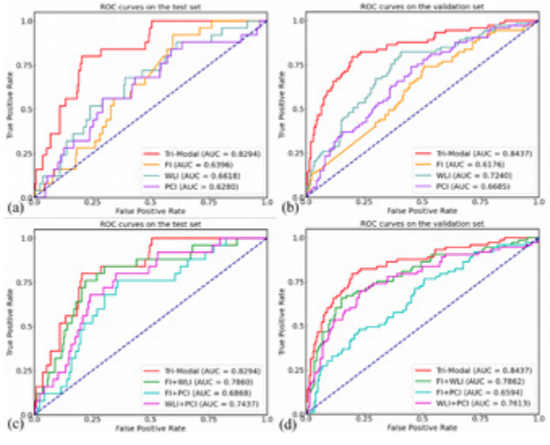


Fig.3 The ROC curves for comparison results of uni-modal and multi-modal images.
(a) The ROC curves for the results of the comparison between the tri-modal and uni-modal data on the test set. (b) The ROC curves for the results of the comparison between the tri-modal and uni-modal data on the validation set. (c) The ROC curves for the results of the comparison between the tri-modal and bi-modal data on the test set. (d) The ROC curves for the results of the comparison between the tri-modal and bi-modal data on the validation set.

data feature fusion experiments, the model effect of combining WLI and FI demonstrates better performance, achieving an AUC of 0.7860 (95% CI 0.7678-0.8174) and the ACC of 0.8192 (95% CI 0.8087-0.8561) on the test set, and an AUC of 0.7862 (95% CI 0.7501-0.8218) and the ACC of 0.7889 (95% CI 0.7407-0.8133) on the validation set, which indicates that the WLI and FI data contain minimal feature overlap and possess distinct information. Furthermore, the results from the unimodal imaging comparison reveal that the model trained on WLI data alone performed significantly better than those trained on the other two modalities. This not only demonstrates that the WLI data contains a substantial amount of valid lymph node feature information but also indirectly highlights the importance of background removal.

Fig.3 illustrates the ROC curves comparing the tri-modal imaging with the bi-modal and uni-modal imaging experiments on both the test set and validation set. It can be concluded that the classification performance of the tri-modal model is the most superior, and the uni-modal model performs the weakest. The results demonstrate that the characteristics of lymph nodes can be captured as comprehensively as possible using the information from the tri-modal imaging data, which is much more effective than the bi-modal and uni-modal imaging data and directly enhances the model performance and accuracy.

Table 2 Comparison Results of Single-Modal, Multi-Modal Imaging. Numbers in Brackets Indicate 95% Confidence Intervals Using 1000 Trials of The Bootstrap Method

Image mode	Params(M)	FLOPs(G)	test set			External validation set		
			AUC	ACC	F1	AUC	ACC	F1
Tri-modal	122.40	13.47	**0.8294** (0.7813,0.8431)	**0.8635** (0.8487,0.8967)	**0.4999** (0.4612, 0.5174)	**0.8437** (0.8006, 0.8769)	**0.8111** (0.7630, 0.8356)	**0.6946** (0.6471, 0.7161)
FI+WLI	45.80	2.19	0.7860 (0.7678,0.8174)	0.8192 (0.8087,0.8561)	0.3725 (0.3441,0.3982)	0.7862 (0.7501, 0.8218)	0.7889 (0.7407, 0.8133)	0.5512 (0.5244, 0.5952)
FI+PCI	88.03	13.13	0.6868 (0.6613,0.7175)	0.7726 (0.7365,0.7978)	0.2568 (0.2237,0.2854)	0.6594 (0.6271,0.6830)	0.6778 (0.6410, 0.7034)	0.4459 (0.4103, 0.4771)
WLI+PCI	111.22	11.67	0.7437 (0.7228,0.7725)	0.8376 (0.8007,0.8524)	0.3364 (0.3117,0.3753)	0.7613 (0.7407, 0.7935)	0.7815 (0.7541, 0.8178)	0.5426 (0.5147,0.5702)
FI	11.31	1.82	0.6396 (0.6194,0.6545)	0.7653 (0.7401,0.7942)	0.2049 (0.1865,0.2407)	0.6176 (0.5845,0.6411)	0.6110 (0.5762,0.6357)	0.3721 (0.3378,0.3941)
WLI	3.01	0.33	0.6618 (0.6507,0.6772)	0.7601 (0.7232,0.7897)	0.2574 (0.2235,0.2823)	0.7240 (0.6949,0.7526)	0.6926 (0.6724,0.7276)	0.5030 (0.4786,0.5317)
PCI	57.82	11.29	0.6280 (0.6057,0.6419)	0.7437 (0.7112,0.7617)	0.2016 (0.1783,0.2335)	0.6685 (0.6352,0.6974)	0.6593 (0.6352,0.6974)	0.4177 (0.3747,0.4435)

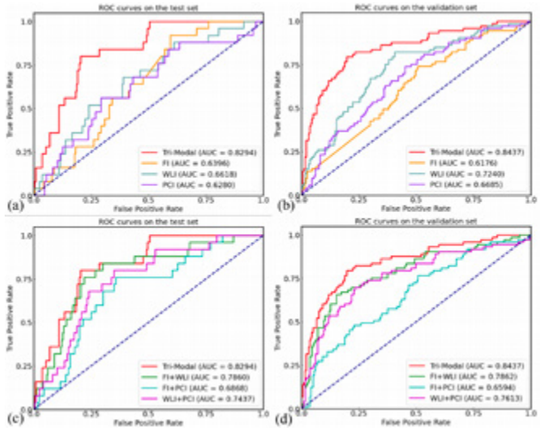


Fig.4 The ROC curves of the results of our model compared to other classification models.
(a) The ROC curves of the results of our model compared to other classification models with features concatenated in dimension on the test set. (b) The ROC curves of the results model compared to other classification models with features concatenated in dimension on the validation set. (c) The ROC curves of the results of our model compared to other classification models with attention-based features fusion method on the test set. (d) The ROC curves of the results of our model compared to other classification models with attention-based features fusion method on the validation set.

Comparison with Various Classification Models

Comparison of other superior classification models with our proposed MFI-FFP model on the task of intraoperative fluorescence LNM prediction in CRC can visually and efficiently illustrate the excellent performance of our model. Since there are no multi-modal models that specifically deal with intraoperative fluorescence data from lymph nodes in CRC, we choose some image classification models that exhibit superior performance on natural images as comparison models. Several outstanding research works have been conducted on natural image classification tasks; among these, the Resnet18 [30], the Swin-Transformer [31], the ConvNeXt [32], the Efficientnet-v2 [33], and the Mobilenet-v3 [34] are selected as comparison models.

All comparative models are pre-trained on the ImageNet dataset to boost the convergence of these models. The three modal features produced by the comparative models are fused for each of the two fusion methods, one for concatenating in the dimensional direction and one for attention-based fusion (WLI features serve as the query tensors, FI features as the key tensors, and PCI features as the value tensors). The experiment compares these two common fusion methods to prove our model's performance. The loss functions for all comparison models training are all set to a weighted cross-entropy loss function with weights of 0.85. The five comparison models include both the traditional convolutional network structure and the Transformer structure, which has been quite remarkable in recent years, and the final comparison results are shown in Tables III and IV. The results indicate that

the effect of our model works best on the intraoperative fluorescence tri-modal imaging dataset, followed by the training results of the Mobilenet-v3 model with attention-based fusion, which also demonstrated good results, achieving an AUC of 0.7712 (95% CI 0.7369-0.7915) and an ACC of 0.8266 (95% CI 0.8038-0.8559) on the test set, and an AUC of 0.7698 (95% CI 0.7257-0.7988) and an ACC of 0.7630 (95% CI 0.7315-0.7953) on the validation set. The floating point operations per second (FLOPs) of our model consume less computational resources compared to the pure Transformer structure model, but this is slightly worse than the convolutional network structure model, which is caused by the fact that the Transformer structure with a large number of parameters is also included in our model. Fig. 4 shows the ROC curves comparing the results of multiple models using different fusion methods, visually illustrating the superior performance of our model. All the above comparison experiments are trained on the dataset for 5 runs to avoid serendipity in the experimental results.

Ablation Experiments

In addition to conducting comparative experiments to validate the efficient performance of our model, we also design three ablation studies to evaluate the performance impact of the innovative part on the MFI-FFP model. The first ablation study is performed on each part of the losses in the designed loss function to verify the impact of each of these loss parts on the model training process, which is based on the presence of the fusion module MFF. In addition, the second ablation study is performed on the designed loss function and the fusion module MFF to verify the impact of each component on our model. The final ablation experiment demonstrates the effectiveness of different components by removing the feature extraction branch and the MFF module, confirming the significance of each in enhancing the model's overall performance.

Ablation Study for Analyzing the Loss Function: Table V presents the general results of the ablation experiment conducted on each of the three loss parts, $L^{reweighted}_{LDAM}$, L_{FL} and L_{Intra} in the first ablation study. The results indicated that all three loss components of the loss function L_{ALL} applied during model training performed the best, achieving the highest AUC and ACC. The ablation experiment with L_{Intra} alone as the entire loss function performs the worst, this is because the loss is the problem of difficulty in distinguishing between samples. Applying only the $L^{reweighted}_{LDAM}$ and L_{FL} losses can reach an AUC of 0.7576 (95% CI 0.7211-0.7841) on the test set and an AUC of 0.8005 (95% CI 0.7707-0.8373) on the validation set, and the result after adding the L_{Intra} loss shows that the L_{Intra} loss is effective in improving the diversity of the samples, which indirectly enhances the overall model effect. The sample imbalance issue in the validation set is not as pronounced as in the test set, and the model's performance on the validation set is superior to that on the test set. This indirectly highlights the effectiveness of the designed loss function in addressing sample imbalance. Additionally, the impact increase is more noticeable when a single $L^{reweighted}_{LDAM}$ or L_{FL} is combined with L_{Intra} loss, respectively.

Ablation Study for the Loss Function and the MFF module: Table VI demonstrates the results of the second ablation study, where the model that uses neither the newly designed loss function (applying a cross-entropy loss function with a weight of 0.85) nor the MFF has the worst performance, with the AUC of only 0.6933 (95% CI 0.6503-0.7241) on the test set and the AUC of 0.6518 (95% CI 0.6163-0.6789) on the validation set. Moreover, it is evident from the experimental results that the model has a significant performance improvement effect by applying the new loss function alone and the MFF fusion module alone. The simultaneous usage of the newly designed loss function and the fusion module MFF enables the model to reach its highest performance.

Ablation Study for the feature extraction branches and the MFF module: Table VII presents the results of the final ablation experiment, showing that the worst performance is observed when the MFF module is removed, while the three feature extraction branches maintain the same network structure. Once the MFF module was added, all models experienced a performance improvement, demonstrating its effectiveness. Furthermore, when our custom-designed feature extraction branches are used as the backbone network, the overall results surpass those of other branch designs. This validates the design of the inverse residual network for extracting WLI features, the residual network for FI features, and the ViT network for PCI features.

Hyperparameter sensitivity analysis

To verify the impact of the loss function hyperparameters on model performance, we set the values of α and β within the range [0.01, 0.05, 0.1, 0.5, 1.0] for hyperparameter sensitivity analysis. As shown in Fig. 6, small values for α and β negatively affect overall model performance, resulting in an AUC of only about 0.75 on the test set, with similar poor performance on the validation set. In contrast, the model performs better when α and β are close to 1, indicating improved results when the weights of the three individual losses in the total loss function are similar. This demonstrates that the model is sensitive to hyperparameters α and β, achieving optimal performance when both are set to 1.

Comparison with clinical experts

To assess the clinical value of the model, we invited five clinicians with experience in colorectal cancer treatment to evaluate lymph node metastasis based on multi-modal fluorescence images from the external validation set. This group included experts 1 and 4, who have less than 10 years of clinical experience, and experts 2, 3, and 5, who have more than 10 years of clinical experience. The clinicians provided a binary judgment on whether a lymph node is metastatic based on its tri-modal imaging. The evaluation metrics include sensitivity (SEN), specificity (SPE), accuracy (ACC), precision (PREC), and F1 score. As shown in Table VIII, the results demonstrate that our model outperforms the clinicians in sensitivity, accuracy, precision, and F1 score. Notably, expert 1 achieved a specificity of 0.9381, but a sensitivity of only 0.1447, which is attributed to his tendency to classify most lymph nodes as non-metastatic. Overall, the results demonstrate that our model is more effective at detecting potential features in model is more effective at detecting potential features in images compared to clinical experts, making it a more accurate and efficient approach than traditional imaging-based clinical judgment.

Interpretative Visualization

To increase the interpretability of our model network,

Table 3 Comparison Results of Various Classification Models with Our Model on The Test Set. Numbers in Brackets Indicate 95% Confidence Intervals Using 1000 Trials of The Bootstrap Method

Model	Params(M)	FLOPs(G)	Fusion mode					
			Concat			Attention		
			AUC	ACC	F1	AUC	ACC	F1
Swin-Transformer	103.08	17.28	0.6263 (0.5997,0.6672)	0.6826 (0.6384,0.6824)	0.2185 (0.1831,0.2476)	0.5710 (0.5576,0.6173)	0.6273 (0.5973,0.6415)	0.1985 (0.1744,0.2223)
ConvNeXt	152.25	26.09	0.6402 (0.6250,0.6654)	0.7159 (0.6974,0.7306)	0.2020 (0.1797,0.2351)	0.6406 (0.6023,0.6829)	0.6900 (0.6563,0.7127)	0.2174 (0.1812,0.2447)
Efficientnet v2	65.25	8.70	0.7525 (0.7231,0.7876)	0.8118 (0.7823,0.8450)	0.3103 (0.2811,0.3379)	0.7060 (0.6767,0.7426)	0.7232 (0.6908,0.7541)	0.3200 (0.2942,0.3518)
Mobilenet v3	16.44	0.23	0.7140 (0.6763,0.7318)	0.7675 (0.7454,0.7970)	0.3214 (0.2957,0.3528)	0.7712 (0.7369,0.7915)	0.8266 (0.8038,0.8559)	0.3434 (0.3120,0.3788)
Resnet18	36.3	5.47	0.7102 (0.6714,0.7418)	0.7860 (0.7601,0.8007)	0.2985 (0.2714,0.3211)	0.7187 (0.6860,0.7412)	0.7380 (0.7066,0.7712)	0.3063 (0.2714,0.3347)
Our model	122.40	13.47	AUC:**0.8294** (0.7813,0.8431)		ACC:**0.8635** (0.8487,0.8967)		F1:**0.4999** (0.4612, 0.5174)	

Table 4 Comparison Results of Various Classification Models with Our Model on The External Validation Set. Numbers in Brackets Indicate 95% Confidence Intervals Using 1000 Trials of The Bootstrap Method

Model	Params(M)	FLOPs(G)	Fusion mode					
			Concat			Attention		
			AUC	ACC	F1	AUC	ACC	F1
Swin-Transformer	103.08	17.28	0.6274 (0.5916, 0.6531)	0.6444 (0.5941, 0.6578)	0.4070 (0.3748, 0.4317)	0.6097 (0.5842,0.6593)	0.6259 (0.6078, 0.6415)	0.4094 (0.3877, 0.4383)
ConvNeXt	152.25	26.09	0.6339 (0.6141,0.6754)	0.6481 (0.5978, 0.6615)	0.4379 (0.3971, 0.4532)	0.6234 (0.5719, 0.6314)	0.6407 (0.6154, 0.6723)	0.4393 (0.4011, 0.4607)
Efficientnet v2	65.25	8.70	0.6609 (0.6303,0.6927)	0.6852 (0.6448, 0.7012)	0.4371 (0.3704, 0.4662)	0.7225 (0.6957, 0.7544)	0.7363 (0.7003, 0.7658)	0.5500 (0.5302, 0.5953)
Mobilenet v3	16.44	0.23	0.7475 (0.7232,0.7853)	0.7815 (0.7412, 0.8106)	0.5693 (0.6471, 0.7161)	0.7698 (0.7257, 0.7988)	0.7630 (0.7315, 0.7953)	0.5294 (0.3996, 0.5415)
Resnet18	36.3	5.47	0.7196 (0.6878,0.7421)	0.7370 (0.7141, 0.7742)	0.5103 (0.4917, 0.5564)	0.7180 (0.6867,0.7472)	0.7037 (0.6807, 0.7441)	0.5294 (0.4853, 0.5411)
Our model	122.40	13.47	AUC: **0.8437** (0.8006, 0.8769)		ACC: **0.8111** (0.7630, 0.8356)		F1: **0.6946** (0.6471, 0.7161)	

we utilize the Gradient-weighted class activation mapping (GCAM) method [35], known as a technology for the visualization and interpretation of deep learning models, to increase the understanding of the feature extraction and feature fusion layers of the model. Fig. 5 displays two samples: one with LNM and the other without. The first three columns display the three modal images of the lymph node samples. Columns 4 to 6 display the results of GCAM heat map mapping when the three modal imaging features are extracted on each of the three feature extraction layers, and the final column reveals the GCAM heat map mapped image on the WLI image on the fusion layer.

The results reveal that the feature extraction branch of the convolutional network structure pays more attention to information such as the surface texture of the image, while the feature extraction branch of the Transformer structure pays more attention to the global location information supplementing the lymph node edge feature information. Furthermore, the fused features are combined with modifications to the region of interest

Table 5 Ablation Experiments for Each Loss Component in The Loss Function. Numbers in Brackets Indicate 95% Confidence Intervals Using 1000 Trials of The Bootstrap Method

$\mathcal{L}_{\text{LDAM}}^{\text{reweighted}}$	$\mathcal{L}_{\text{FL}}$	$\mathcal{L}_{\text{Intra}}$	test set			External validation set		
			AUC	ACC	F1	AUC	ACC	F1
✓			0.7332 (0.7208,0.7463)	0.8044 (0.7897,0.8303)	0.3357 (0.3172,0.3617)	0.7744 (0.7481, 0.8084)	0.7370 (0.6989, 0.7526)	0.6120 (0.6006, 0.6587)
	✓		0.6452 (0.6390,0.6777)	0.7491 (0.7196,0.7749)	0.2548 (0.2214,0.2758)	0.6565 (0.6171,0.6833)	0.7037 (0.6704, 0.7215)	0.4521 (0.4278, 0.4713)
		✓	0.6238 (0.6143,0.6378)	0.7122 (0.1697,0.7417)	0.2015 (0.1829,0.2342)	0.5750 (0.5478,0.6063)	0.5519 (0.5204, 0.5852)	0.4265 (0.3947, 0.4512)
✓	✓		0.7576 (0.7211,0.7841)	0.7971 (0.7749,0.8450)	0.4020 (0.3787,0.4311)	0.8005 (0.7707,0.8373)	0.8011 (0.7754, 0.8215)	0.6250 (0.6010, 0.6567)
✓		✓	0.7403 (0.7278,0.7620)	0.8155 (0.7712,0.8229)	0.3664 (0.3305,0.3875)	0.7837 (0.7506,0.8173)	0.7926 (0.7663, 0.8211)	0.6216 (0.5851, 0.6439)
	✓	✓	0.6816 (0.6267,0.7059)	0.7528 (0.7269,0.7934)	0.3043 (0.28059,0.3274)	0.7276 (0.6808, 0.7503)	0.7778 (0.7415, 0.7952))	0.5714 (0.5317, 0.5908)
✓	✓	✓	**0.8294** (0.7813,0.8431)	**0.8635** (0.8487,0.8967)	**0.4999** (0.4612, 0.5174)	**0.8437** (0.8006, 0.8769)	**0.8111** (0.7630, 0.8356)	**0.6946** (0.6471, 0.7161)

Table 6 Ablation Experiments with Loss Function and Fusion Module MFF. Numbers in Brackets Indicate 95% Confidence Intervals Using 1000 Trials of The Bootstrap Method

$\mathcal{L}_{\text{All}}$	MFF	test set			External validation set		
		AUC	ACC	F1	AUC	ACC	F1
		0.6933 (0.6503,0.7241)	0.7380 (0.7085,0.7638)	0.3112 (0.2816,0.3384)	0.6518 (0.6163,0.6789)	0.6741 (0.6578, 0.7015)	0.4430 (0.4208,0.4745)
	✓	0.7539 (0.7272,0.7806)	0.8087 (0.7860,0.8376)	0.4153 (0.3847,0.4402)	0.7552 (0.7228, 0.7893)	0.7556 (0.7315, 0.7863)	0.5714 (0.5536, 0.6082)
✓		0.7472 (0.7284,0.7763)	0.7934 (0.7712,0.8192)	0.4094 (0.3882,0.4245)	0.7734 (0.7407,0.7962)	0.7852 (0.7641, 0.8015)	0.6329 (0.6102, 0.6647)
✓	✓	**0.8294** (0.7813,0.8431)	**0.8635** (0.8487,0.8967)	**0.4999** (0.4612, 0.5174)	**0.8437** (0.8006, 0.8769)	**0.8111** (0.7630, 0.8356)	**0.6946** (0.6471, 0.7161)

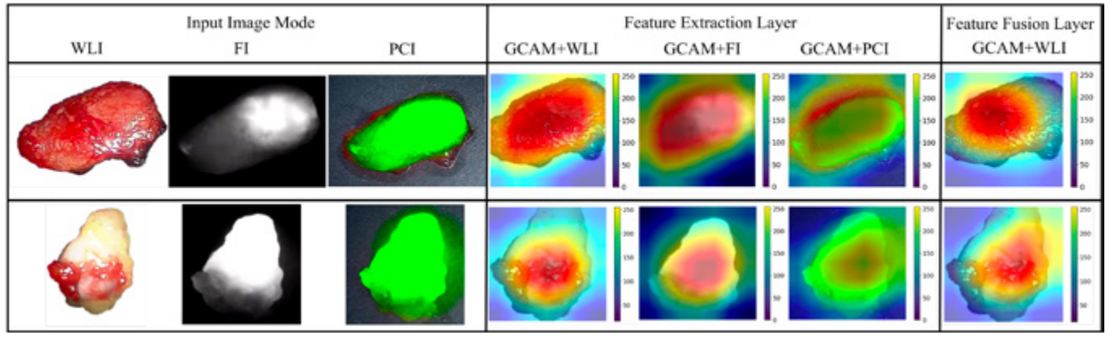


Fig.5 The schematic GCAM heatmap of lymph node samples. The first row shows the three modal images of the sample without lymph node metastasis, as well as the GCAM mapping heatmaps of the three modalities of the feature extraction layer and the GCAM heatmap mapping of the WLI of the fusion layer. The second row shows the three modality images of the sample where lymph node metastasis has occurred, as well as the GCAM mapping heatmap of the three modalities of the feature extraction layer and the GCAM heatmap mapping of the WLI of the fusion layer.

Table 7 Ablation Experiments with Feature Extraction Branches and Fusion Module MFF. Numbers in Brackets Indicate 95% Confidence Intervals Using 1000 Trials of The Bootstrap Method

Feature extraction branches	MFF	test set			External validation set		
		AUC	ACC	F1	AUC	ACC	F1
Tri-IRB		0.6810 (0.6553, 0.7067)	0.6974 (0.6785, 0.7233)	0.2407 (0.2125, 0.2732)	0.7013 (0.6706, 0.7218)	0.7037 (0.6842, 0.7221)	0.4407 (0.4385, 0.4704)
Tri-RB		0.6154 (0.5828, 0.6331)	0.6494 (0.6234,0.6615)	0.2180 (0.2025, 0.2323)	0.6281 (0.5979,0.6358)	0.6481 (0.6259,0.6728)	0.4379 (0.4124,0.4502)
Tri-ViT		0.6193 (0.6021,0.6454)	0.6531 (0.6215, 0.6752)	0.2074 (0.1895,0.2214)	0.6551 (0.6358,0.6765)	0.6852 (0.6549,0.7036)	0.4056 (0.2819,0.4276)
Tri-IRB	✓	0.7089 (0.6704,0.7252)	0.7528 (0.7261,0.7795)	0.2708 (0.2437,0.3054)	0.7526 (0.7146, 0.7856)	0.7556 (0.7237, 0.7874)	0.5238 (0.4988, 0.5565)
Tri-RB	✓	0.6268 (0.6011,0.6544)	0.6753 (0.6463,0.7043)	0.2317 (0.2048,0.2573)	0.6681 (0.6402, 0.6912)	0.6778 (0.6470, 0.7031)	0.4710 (0.4416, 0.5189)
Tri-ViT	✓	0.6357 (0.6002,0.6603)	0.6827 (0.6539,0.7115)	0.2275 (0.1983,0.2592)	0.6719 (0.6389, 0.7007)	0.6926 (0.6741, 0.7278)	0.4645 (0.4327,0.4958)
IRB_RB_ViT		0.7472 (0.7284,0.7763)	0.7934 (0.7712,0.8192)	0.4094 (0.3882,0.4245)	0.7734 (0.7407,0.7962)	0.7852 (0.7641, 0.8015)	0.6329 (0.6102, 0.6647)
IRB_RB_ViT	✓	**0.8294** (0.7813,0.8431)	**0.8635** (0.8487,0.8967)	**0.4999** (0.4612, 0.5174)	**0.8437** (0.8006, 0.8769)	**0.8111** (0.7630, 0.8356)	**0.6946** (0.6471, 0.7161)

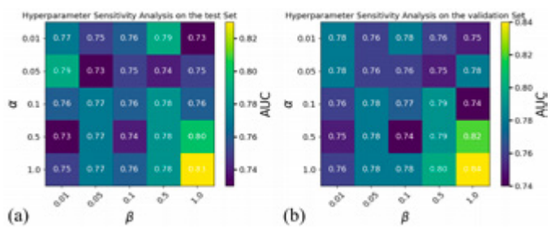


Fig.6 Hyperparameter sensitivity analysis. (a) Results of the sensitivity analysis of hyperparameters α and β in the loss function on the test set. (b) Results of the sensitivity analysis of hyperparameters α and β in the loss function on the validation set.

Table 8 Comparison Results of Clinical Experts with Our Model on The External Validation Set

Clinical Expert	SEN	SPE	ACC	PREC	F1
Expert 1	0.1447	**0.9381**	0.7148	0.4783	0.2222
Expert 2	0.4342	0.9021	0.7704	0.6346	0.5156
Expert 3	0.4211	0.8247	0.7111	0.4848	0.4507
Expert 4	0.2632	0.7371	0.6037	0.2817	0.2721
Expert 5	0.3947	0.8557	0.7259	0.5172	0.4478
Our model	**0.7632**	0.8299	**0.8111**	**0.6374**	**0.6946**

by the feature fusion layer, which highlights and concretizes the characteristics in crucial places. For images of lymph nodes that have metastasized, our model pays more attention to the weird irregular texture and shape features in the samples.

Discussion and conclusion

In this study, we propose the MFI-FFP model for LNM prediction in CRC using intraoperative fluorescence multi-modal imaging. Our model first extracts three modal data features, followed by the fusion of the extracted three modal features, and eventually performs LNM in CRC prediction based on the fused features. The suggested MFI-FFP model exhibited promise for real-time LNM diagnosis in the future by performing satisfactorily in the task of predicting LNM in CRC using intraoperative fluorescence multi-model imaging.

In the feature extraction part of our model, the corresponding special extraction branches are set according to the characteristics of the three modal data, respectively. Furthermore, experimental results indicate it is frequently more effective in building distinct feature extraction structures based on various modal imaging feature information than in using the same structure. The three modal features extracted in the previous stage are features fused in the MFF module in the model, which incorporates global and local features to boost model performance. Furthermore, there is a significant sample imbalance issue because the majority of the lymph nodes in the data sample are benign, and relatively few of them are malignant. According to the above problems, we design a novel loss function, in which the LDAM loss alleviates the sample imbalance problem, the focal loss reduces the difficulty in distinguishing the samples, and the proposed intra-loss increases the diversity of the samples and thus improves the performance of the model.

To predict LNM in CRC, our work leverages intraoperative fluorescence multi-modal imaging. By combining three modal imaging characteristics, the model can effectively learn lymph node feature information and exhibit outstanding prediction ability. Since little research has combined deep learning with intraoperative FI for identifying LNM, utilizing deep learning to analyze intraoperative FI for various downstream tasks has far-reaching implications and potential in the medical field.

Disclosure

This work is supported by the National Natural Science Foundation of China under Grant Nos. 62333022, 92259301, 81930053, and 62027901, the National Key R&D Program of China under Grant Nos. 2021YFF1201003, 2023YFC3402800, and 2022YFC2407400, and the Beijing Natural Science Foundation under Grant Nos. JQ23034, L234056, L232097, L222054, and 4232058. (Xiaobo Zhu, He Sun, and Yuhan Wang contribute equally to the article. Corresponding authors: Jianqiang Tang, Yu An, Jie Tian, and Zhenyu Liu.)

This work involved human subjects or animals in its research. Approval of all ethical and experimental procedures and protocols was granted by the study, which was approved by the Ethics Committee of Beijing Fengtai Hospital and Cancer Hospital, Chinese Academy of Medical Sciences.

Our code and model can be available at: https://github.com/Emibobo/MFI-FFP.

References

1. R. L. Siegel, N. S. Wagle, A. Cercek, R. A. Smith, and A. Jemal, "Colorectal cancer statistics, 2023," CA: a cancer journal for clinicians, vol. 73, no. 3, pp. 233–254, 2023.
2. E. Dekker, P. Tanis, J. Vleugels, P. Kasi, M. Wallace, and G. Dekker, "Colorectal cancer," The Lancet, vol. 394, pp. 1467–1480, 2019.
3. X. Guan, S. Jiao, R. Wen, G. Yu, J. Liu, D. Miao, R. Wei, W. Zhang, L. Hao, L. Zhou et al., "Optimal examined lymph node number for accurate staging and long-term survival in rectal cancer: a population-based study," International Journal of Surgery, vol. 109, no. 8, pp. 2241–2248, 2023.
4. G. J. Chang, M. A. Rodriguez-Bigas, C. Eng, and J. M. Skibber, "Lymph node status after neoadjuvant radiotherapy for rectal cancer is a biologic predictor of outcome," Cancer, vol. 115, no. 23, pp. 5432–5440, 2009.
5. Y. Erog˘lu, M. Yildirim, and A. C¸ inar, "Convolutional neural networks based classification of breast ultrasonography images by hybrid method with respect to benign, malignant, and normal using mrmr," Computers in biology and medicine, vol. 133, p. 104407, 2021.
6. J. Li, D. Dong, M. Fang, R. Wang, J. Tian, H. Li, and J. Gao, "Dual-energy ct–based deep learning radiomics can improve lymph node metastasis risk prediction for gastric cancer," European Radiology, vol. 30, pp. 2324–2333, 2020.
7. D. Dong, M.-J. Fang, L. Tang, X.-H. Shan, J.-B. Gao, F. Giganti, R.-P. Wang, X. Chen, X.-X. Wang, D. Palumbo et al., "Deep learning radiomic nomogram can predict the number of lymph node metastasis in locally advanced gastric cancer: an international multicenter study," Annals of oncology, vol. 31, no. 7, pp. 912–920, 2020.
8. M. Ahmed, A. D. Purushotham, and M. Douek, "Novel techniques for sentinel lymph node biopsy in breast cancer: a systematic review," The lancet oncology, vol. 15, no. 8, pp. e351–e362, 2014.
9. J. Zhao, H. Wang, Y. Zhang, R. Wang, Q. Liu, J. Li, X. Li, H. Huang, J. Zhang, Z. Zeng et al., "Deep learning radiomics model related with genomics phenotypes for lymph node metastasis prediction in colorectal cancer," Radiotherapy and Oncology, vol. 167, pp. 195–202, 2022.
10. L. Kiehl, S. Kuntz, J. Ho¨hn, T. Jutzi, E. Krieghoff-Henning, J. N. Kather, T. Holland-Letz, A. Kopp-Schneider, J. Chang-Claude, A. Brobeil et al., "Deep learning can predict lymph node status directly from histology in colorectal cancer," European Journal of Cancer, vol. 157, pp. 464–473, 2021.
11. J. Li, Y. Zhou, P. Wang, H. Zhao, X. Wang, N. Tang, and K. Luan, "Deep transfer learning based on magnetic resonance imaging can improve the diagnosis of lymph node metastasis in patients with rectal cancer," Quantitative Imaging in Medicine and Surgery, vol. 11, no. 6, p. 2477, 2021.
12. C. Chi, Y. Du, J. Ye, D. Kou, J. Qiu, J. Wang, J. Tian, and X. Chen, "Intraoperative imaging-guided cancer surgery: from current fluorescence molecular imaging methods to future multi-modality imaging technology," Theranostics, vol. 4, no. 11, p. 1072, 2014.
13. K. Wang, Y. Du, Z. Zhang, K. He, Z. Cheng, L. Yin, D. Dong, C. Li, W. Li, Z. Hu et al., "Fluorescence image-guided tumour surgery," Nature Reviews Bioengineering, vol. 1, no. 3, pp. 161–179, 2023.
14. T. Burghgraef, A. Zweep, D. Sikkenk, M. van der Pas, P. Verheijen, and E. Consten, "In vivo sentinel lymph node identification using fluorescent tracer imaging in colon cancer: a systematic review and meta-analysis," Critical Reviews in Oncology/Hematology, vol. 158, p. 103149, 2021.
15. S. H. Emile, H. Elfeki, M. Shalaby, A. Sakr, P. Sileri, S. Laurberg, and S. D. Wexner, "Sensitivity and specificity of indocyanine green near-infrared fluorescence imaging in detection of metastatic lymph nodes in colorectal cancer: Systematic review and meta-analysis," Journal of Surgical Oncology, vol. 116, no. 6, pp. 730–740, 2017.
16. S. R. Thammineedi, A. R. Saksena, S. Nusrath, R. R. Iyer, S. Shukla, S. C. Patnaik, R. P. Reddy, N. Boleneni, R. M. Sharma, L. Smith et al., "Fluorescence-guided cancer surgery—a new paradigm," Journal of Surgical Oncology, vol. 123, no. 8, pp. 1679–1698, 2021.
17. M. Avanzo, L. Wei, J. Stancanello, M. Vallieres, A. Rao, O. Morin, S. A. Mattonen, and I. El Naqa, "Machine and deep learning methods for radiomics," Medical physics, vol. 47, no. 5, pp. e185–e202, 2020.
18. O. Dalmaz, M. Yurt, and T. C¸ ukur, "Resvit: residual vision transformers for multimodal medical image synthesis," IEEE Transactions on Medical Imaging, vol. 41, no. 10, pp. 2598–2614, 2022.
19. B. Shen, Z. Zhang, X. Shi, C. Cao, Z. Zhang, Z. Hu, N. Ji, and J. Tian, "Real-time intraoperative glioma diagnosis using fluorescence imaging and deep convolutional neural networks," European Journal of Nuclear Medicine and Molecular Imaging, vol. 48, no. 11, pp. 3482–3492, 2021.
20. R. A. Cahill, D. F. O'Shea, M. Khan, H. Khokhar, J. P. Epperlein, P. Mac Aonghusa, R. Nair, and S. Zhuk, "Artificial intelligence indocyanine green (icg) perfusion for colorectal cancer intra-operative tissue classification," British Journal of Surgery, vol. 108, no. 1, pp. 5–9, 2021.
21. S. Zhuk, J. P. Epperlein, R. Nair, S. Tirupathi, P. Mac Aonghusa, D. F. O'Shea, and R. Cahill, "Perfusion quantification from endoscopic videos: learning to read tumor signatures," in Medical Image Computing and Computer Assisted Intervention–MICCAI 2020: 23rd International Conference, Lima, Peru, October 4–8, 2020, Proceedings, Part III 23. Springer, 2020, pp. 711–721.
22. S.-H. Park, H.-M. Park, K.-R. Baek, H.-M. Ahn, I. Y. Lee, and G. M. Son, "Artificial intelligence based real-time microcirculation analysis system for laparoscopic colorectal surgery," World Journal of Gastroenterology, vol. 26, no. 44, p. 6945, 2020.
23. Z. Ma, F. Wang, W. Wang, Y. Zhong, and H. Dai, "Deep learning for in vivo near-infrared imaging," Proceedings of the National Academy of Sciences, vol. 118, no. 1, p. e2021446118, 2021.
24. A. Xiao, B. Shen, X. Shi, Z. Zhang, Z. Zhang, J. Tian, N. Ji, and Z. Hu, "Intraoperative glioma grading using neural architecture search and multi-modal imaging," IEEE transactions on medical imaging, vol. 41, no. 10, pp. 2570–2581, 2022.
25. W. Steup, Y. Moriya, and C. Van de Velde, "Patterns of lymphatic spread in rectal cancer. a topographical analysis on lymph node metastases," European Journal of Cancer, vol. 38, no. 7, pp. 911–918, 2002.
26. J. Kang, Y. J. Choi, I.-k. Kim, H. S. Lee, H. Kim, S. H. Baik, N. K. Kim, and K. Y. Lee, "Lasso-based machine learning algorithm for prediction of lymph node metastasis in t1 colorectal cancer," Cancer Research and Treatment: Official Journal of Korean Cancer Association, vol. 53, no. 3, pp. 773–783, 2021.
27. S.-e. Kudo, K. Ichimasa, B. Villard, Y. Mori, M. Misawa, S. Saito, K. Hotta, Y. Saito, T. Matsuda, K. Yamada et al., "Artificial intelligence system to determine risk of t1 colorectal cancer metastasis to lymph node," Gastroenterology, vol. 160, no. 4, pp. 1075–1084, 2021.
28. K. Cao, C. Wei, A. Gaidon, N. Arechiga, and T. Ma, "Learning imbalanced datasets with label-distribution-aware margin loss," Advances in neural information processing systems, vol. 32, 2019.
29. T.-Y. Lin, P. Goyal, R. Girshick, K. He, and P. Dolla´r, "Focal loss for dense object detection," in Proceedings of the IEEE international conference on computer vision, 2017, pp. 2980–2988.
30. K. He, X. Zhang, S. Ren, and J. Sun, "Deep residual learning for image recognition," in Proceedings of the IEEE conference on computer vision and pattern recognition, 2016, pp. 770–778.
31. Z. Liu, Y. Lin, Y. Cao, H. Hu, Y. Wei, Z. Zhang, S. Lin, and B. Guo, "Swin transformer: Hierarchical vision transformer using shifted windows," in Proceedings of the IEEE/CVF international conference on computer vision, 2021, pp. 10 012–10 022.
32. Z. Liu, H. Mao, C.-Y. Wu, C. Feichtenhofer, T. Darrell, and S. Xie, "A convnet for the 2020s," in Proceedings of the IEEE/CVF conference on computer vision and pattern recognition, 2022, pp. 11 976–11 986.
33. M. Tan and Q. Le, "Efficientnetv2: Smaller models and faster training," in International conference on machine learning. PMLR, 2021, pp. 10 096–10 106.
34. S. Qian, C. Ning, and Y. Hu, "Mobilenetv3 for image classification," in 2021 IEEE 2nd International Conference on Big Data, Artificial Intelligence and Internet of Things Engineering (ICBAIE). IEEE, 2021, pp. 490–497.
35. R. R. Selvaraju, M. Cogswell, A. Das, R. Vedantam, D. Parikh, and D. Batra, "Grad-cam: Visual explanations from deep networks via gradient-based localization," in Proceedings of the IEEE international conference on computer vision, 2017, pp. 618–626.

Pediatric Surgery

Short Communication

Indocyanine Green Localization for Laparoscopic Duodenal Web Excision

Shuangshuang Li [1], Yong Zhao [1], Yanan Zhang [1], Junmin Liao [1], Kaiyun Hua [1], Yichao Gu [1], Dingding Wang [1], Jie Tian [2], Jinshi Huang [1] ✉

Abstract

Background: A duodenal web refers to partial or complete obstruction of the duodenum due to a membranous web. When looking at the serosal side of the intestine during duodenal web excision, especially during laparoscopic surgery, determining the web origin might be challenging. This study aimed to determine the efficacy of intraduodenum indocyanine green injection and near-infrared light during laparoscopic surgery in enhancing the ability to identify duodenal web localization.

Methods: We used intraduodenum indocyanine green injection to unequivocally recognize the duodenal web and facilitate laparoscopic excision. The clinical analysis was based on a male neonatal case with duodenal web admitted to our hospital. After the patient was placed in the supine position, 5 mL of ICG was injected via a 6-Fr nasogastric tube. The fluorescence was visualized in the white light and near-infrared light dual-mode of the camera system, localizing the duodenal precisely and in real-time.

Results: Laparoscopically, the duodenal web was accurately identified and removed with intraduodenum indocyanine green visualization under near-infrared light. The procedure was completed successfully, and the patient showed good postoperative outcomes.

Conclusions: Intraduodenum indocyanine green injection during laparoscopic surgery is a feasible adjuvant for duodenal web localization, showing improvements in terms of outcomes compared to previous methods of determining the duodenal web location.

Photodiagnosis Photodyn Ther. 2022. 38: 102842 Published online: 6 April 2022

[1] Department of Neonatal Surgery, Neonatal Center, Beijing Children's Hospital, National Center for Children's Health, Capital Medical University, Beijing 100045, China

[2] Key Laboratory of Molecular Imaging, Institute of Automation, Chinese Academy of Sciences, Beijing, 100190 China

Introduction

With a relative risk of 1 in 10,000–40,000, duodenal web is a prevalent pediatric gastrointestinal anomaly 1. For the definitive surgical treatment of a duodenal web, laparoscopic surgery can be used. Precise localization of the duodenal web is a key aspect of a successful laparoscopic management. In the laparoscopic setting, due to the lack of tactile feedback, these surgical principles can be very difficult to attain by visual signals. Techniques that improve the ability to visually detect the location of the duodenal web are therefore critical.

Indocyanine green is a fluorescent dye that allows for real-time imaging of a target structure when triggered by near-infrared light.

In this study, we hypothesized that intraduodenal injection of indocyanine green during laparoscopic surgery can enhance the ability to identify duodenal webs. This study aimed to verify the efficacy of this approach to precisely determine duodenal web localization during laparoscopic surgery.

Material and methods

Case presentation

A 13-day-old boy was admitted to our department because of repeated bilious vomiting for 13 days and malnutrition. Plain abdominal X-ray revealed a double bubble sign, and abdominal ultrasonography showing the water-refilling process of the duodenum detected a web at the junction of the 2nd and 3rd sections of the duodenum (Fig. 1).

Surgical technique

The patient was placed in the supine posture after general anesthesia induction. We used a 3-port (a 5-mm 30-degree laparoscope, a 3-mm right paraumbilical working port, and a 3-mm left upper quadrant working port) approach with an intra-abdominal insufflation pressure of 8 mmHg. The duodenum was opened at the duodenal web site. After confirmation of the site of the ampulla of Vater, the anterolateral side of the web was carefully resected. The traction suture was placed to lift the duodenum ventrally to the anterior abdominal wall and the duodenum was closed transversely with a running 5-0 absorbable suture.

Duodenal web localization procedure

Twenty-five mg of sterile indocyanine green (Dandong Yichuang Pharmaceutical Co., China) was dissolved in 10 mL distilled water (2.5 mg/mL) to prepare the ICG solution. Before usage, the ICG solution was diluted 20 times (0.125 mg/mL). Five milliliters of the diluted ICG solution was inserted through a preset 6 Fr nasogastric tube. The location of the duodenal web was accurately identified using a white light and near-infrared dual-channel laparoscopic system (DPM-ENDOCAM-01, DPM-LIHGT-01, Zhuhai Dipu Medical Technology Co., China). After the

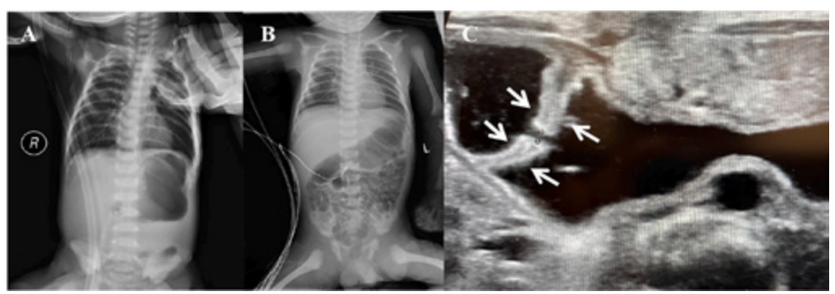


Fig.1 (A and B) Preoperative plain abdominal X-ray on the first and second day, respectively, after birth showing upper gastrointestinal incomplete obstruction. (C) Ultrasonography illustrating a web between the second and third portions of the duodenum (white arrows).

duodenal web was removed, another 5 mL of the diluted ICG solution was inserted to evaluate intestinal permeability.

Results

After exposing the duodenum, the genuine location of the duodenal web was confirmed using a fluoroscope. The margins of the duodenal web were identified based on the healthy duodenum that fluoresced green and the intestine lumen away from the nonviable tissue that remained non-florescent (Fig. 2). The whole process lasted 58 s. After the duodenal web was obliterated, 5 mL was injected through the nasogastric tube, and the ICG smoothly passed through the duodenum into the initial portion of the jejunum (Fig. 4) which took 44 s. The total time required for intraoperative fluorescence localization of duodenal web and intestinal patency detection was 1 min and 42 s.

The patient was administered liquids on the third day after surgery and achieved total enteral nutrition one week after surgery. At the one- month follow-up, the child was able to tolerate a full diet well without any complications. The upper gastrointestinal series at the follow-up revealed a much better proximal duodenal profile, with uninterrupted contrast passage over the location of the initial web blockage (Fig. 5).

Discussion

In this study, we described a novel method for accurately detecting the site of the duodenal web. This method is more accurate than direct visualization wherein the duodenal caliber can change.

The duodenal web is different from other duodenal obstructions in which the obstruction is located inside the duodenal lumen. Therefore, it is difficult to determine the exact location of the duodenal web on the serosal side. This is only possible through visual recognition under laparoscopy, especially for novices. Previous studies have suggested that the duodenal web is usually located at the position where the duodenum caliber changes 2,3, but this method often leads to a misleading location of web, especially when the duodenal web is wind-stock-like. Burns et al. have reported that intraoperative endoscopy has been utilized to precisely determine the site of the duodenal web during laparoscopic excision to give a safe and simple approach of duodenal web localization 4. However, endoscopy is still an invasive operation with potential risks, such as gastrointestinal perforation, aspiration risk, and lung compression in newborns. Therefore, a more non-invasive method for duodenal web localization during laparoscopic surgery is needed.

Our novel technique overcomes the difficulties in identifying the position of the duodenal web under laparoscopy and offers additional benefits. Firstly, our method is easy to operate. All operations were performed under general anesthesia without special additional anesthesia requirements. Moreover, ICG was injected through the routinely preset nasogastric tube without additional invasive manipulations and specialized tools. The whole process did not significantly increase the total operation time. Secondly, our approach

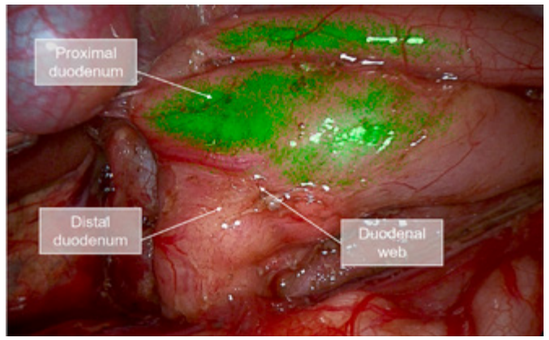


Fig.2 Laparoscopic real-time fluorescent visualization of the duodenum, allowing for general localization of the duodenal web.

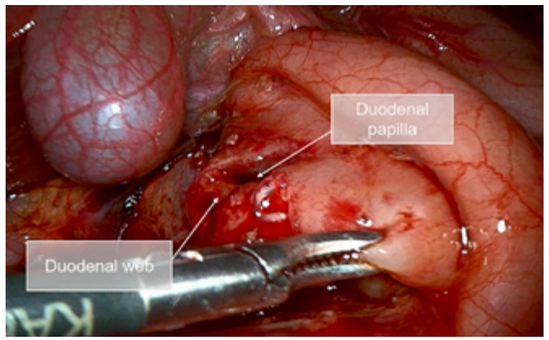


Fig.3 Area of the duodenal web where the ampulla of Vater is visible prox- imal to the septum.

enables accurate intra- operative duodenal web identification in real-time. The junction of green fluorescence, from the fluorescent duodenum proximal to the web to the non-florescent distal duodenum, is the position of the duodenal web. This optical difference is very easy to discern with the naked eye, and no additional training for the procedure was involved. Thirdly, after web resection, the whole duodenum and the first part of the jejunum were illuminated in bright green under dual light. This is extremely useful in confirming intestinal patency and detecting further blockages in the distal intestine. Finally, there were no negative consequences from inserting ICG into the duodenum. In rare situations, ICG has been associated with anaphylactic shock, bronchospasm, and cardiorespiratory arrest5. However, our approach prevents systemic ICG exposure, likely decreasing the risks of systemic ICG absorption. Moreover, although a small amount of indocyanine green leaked into the peritoneal cavity during the operation, this patient did not experience any perioperative complications, such as fever, abdominal pain, focal peritonitis, or adhesion. Miyoshi et al. 6 also reported that ICG leakage did not cause any complications, addressing the use of

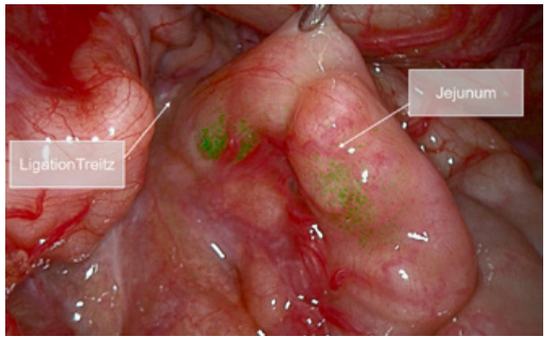


Fig.4 Fluoresced jejunum demonstrating patency of the duodenum after web resection.



Fig.5 Postoperative upper GI series showing duodenal patency, with no blockage or leak.

India ink.

Ding et al. 7 found that ICG is unstable and easily degraded under illumination, especially in acid conditions. After being irradiated with near-infrared light for 30 min, the absorption of the ICG solution in weak acidic environments was decreased significantly. In this study, although ICG interacted with gastric acid for a period of time, its fluorescence was still sufficient to help us locate the duodenal web. To minimize the effect of fluorescence degradation on duodenal web localization, in our future studies, we will postpone ICG injection until the duodenum is kocherized.

In conclusion, the use of ICG-guided surgery allows for a safe and straightforward duodenal web identification, while facilitating laparoscopic excision. A limitation of this study is that as this procedure was only used on one patient, more research is needed to fully understand these putative benefits.

Author Contributions

Shuangshuang Li: Conceptualization, Methodology, Visualization, Writing - original draft, Writing - review and editing. Yong Zhao: Methodology. Yanan Zhang: Methodology. Junmin Liao: Visualization. Kaiyun Hua: Visualization. Yichao Gu: Formal analysis. Dingding Wang: Writing - review and editing. Jie Tian: Conceptualization. Jinshi Huang: Conceptualization, Methodology, Validation, Funding acquisition, Supervision.

Human rights

All procedures were carried out in compliance with the ethical standards of the responsible committee on human experimentation (institutional and national), as well as the Declaration of Helsinki of 1975, as updated in 2008 (5). Ethical review approval was obtained from the Central Ethical Review Board of Beijing Children's Hospital ([2021]-E-150-Y).

Informed consent

Written informed consent was obtained from the guardian of the patient included in the study.

Funding

This work was supported by the Talent Founding of Beijing Children's Hospital of Capital Medical University [Grant number 2021-743].

CRediT authorship contribution statement

Shuangshuang Li: Writing – review & editing, Writing – original draft, Visualization, Methodology, Conceptualization. Yong Zhao: Methodology. Yanan Zhang: Methodology. Junmin Liao: Visualization. Kaiyun Hua: Visualization. Yichao Gu: Formal analysis. Dingding Wang: Writing – review & editing. Jie Tian: Conceptualization. Jinshi Huang: Validation, Supervision, Methodology, Funding acquisition, Conceptualization.

Declaration of Competing Interest

The authors have no conflicts of interest to declare.

Acknowledgement

We gratefully acknowledge the assistance of Beijing Children's Hospital Talent Funding, which supported the undertaking of this research. We would also like to thank the patient who participated in the current study.

References

1. M.H. Huang, H.Q. Bian, C. Liang, W.Q. Wei, X.F. Duan, J. Yang, Gastroscopic treatment of membranous duodenal stenosis in infants and children: report of 6 cases, J. Pediatr. Surg. 2015; 50:413–416,
2. Muensterer, E.N. Hansen, Resection of a duodenal web using single-incision pediatric endosurgery, J. Pediatr. Surg. 2011; 46:989–993.
3. Mahomed, B. D' hondt, K. Khan, A. Butt, Technical aspects of the laparoscopic management of a late presenting duodenal web, J. Laparoendosc. Adv. Surg. Tech A. 2009; 19:S175–S177.
4. N.E. Bruns, A.T. Gibbons, M.J. Wyneski, T.A. Ponsky, Endoscopic web localization for laparoscopic duodenal web excision, Surg. Laparosc. Endosc. Percutan. Tech. 2015; 25:e172–e174.
5. J. Meira, M.L. Marques, F. Falc˜ao-Reis, E. Rebelo Gomes, A˜. Carneiro, Immediate reactions to fluorescein and indocyanine green in retinal angiography: review of literature and proposal for patient's evaluation, Clin. Ophthalmol. 2020; 14:171–178.
6. N. Miyoshi, M. Ohue, S. Noura, et al., Surgical usefulness of indocyanine green as an alternative to India ink for endoscopic marking, Surg. Endosc. 2009; 23:347–351.
7. Y. Ding, C. Wang, B. Lu, Y. Yao, Enhancing the stability and photothermal conversion efficiency of icg by pillar[5]arene-based host-guest interaction, Front. Chem. 2021; 9:775436.

Fluorescence Imaging Standard

Research Article

Harmonized Technical Standard Test Methods for Quality Evaluation of Medical Fluorescence Endoscopic Imaging Systems

Bodong Liu [1,*], Zhaojun Guo [1,*], Pengfei Yang [1,*], Jian'an Ye [2,3,*], Kunshan He [3,4], Shen Gao [1], Chongwei Chi [3,4,✉], Yu An [2,3,✉], Jie Tian [2,3,4,✉]

[1] Center for Medical Device Evaluation, National Medical Products Administration, Beijing, 100081 China

[2] School of Engineering Medicine and School of Biological Science and Medical Engineering, Beihang University, Beijing, 100191 China

[3] The Key Laboratory of Big Data-Based Precision Medicine, Ministry of Industry and Information Technology of China, Beijing, 100191 China

[4] Key Laboratory of Molecular Imaging, Institute of Automation, Chinese Academy of Sciences, Beijing, 100191 China

* These authors contributed equally.

Abstract

Fluorescence endoscopy technology utilizes a light source of a specific wavelength to excite the fluorescence signals of biological tissues. This capability is extremely valuable for the early detection and precise diagnosis of pathological changes. Identifying a suitable experimental approach and metric for objectively and quantitatively assessing the imaging quality of fluorescence endoscopy is imperative to enhance the image evaluation criteria of fluorescence imaging technology. In this study, we propose a new set of standards for fluorescence endoscopy technology to evaluate the optical performance and image quality of fluorescence imaging objectively and quantitatively. This comprehensive set of standards encompasses fluorescence test models and imaging quality assessment protocols to ensure that the performance of fluorescence endoscopy systems meets the required standards. In addition, it aims to enhance the accuracy and uniformity of the results by standardizing testing procedures. The formulation of pivotal metrics and testing methodologies is anticipated to facilitate direct quantitative comparisons of the performance of fluorescence endoscopy devices. This advancement is expected to foster the harmonization of clinical and preclinical evaluations using fluorescence endoscopy imaging systems, thereby improving diagnostic precision and efficiency.

Keywords

Fluorescence endoscopy, Near-infrared, Image evaluation, Standardization

Introduction

Medical endoscopy technology is a seminal advancement in contemporary medicine that has significantly enhanced the efficacy and precision of disease diagnosis. As a high-fidelity, minimally invasive diagnostic instrument, medical endoscopy captures and relays real-time visual data from within the patient's anatomy to an external display. This is achieved by using a compact camera and light source apparatus, facilitating the unobstructed visual inspection of pathological tissues [1–3]. Consequently, clinicians can gain diagnostic insights that are both visually clear and clinically reliable. Moreover, endoscopes can be integrated with supplementary instruments such as biopsy forceps and therapeutic lasers, thereby enabling the sampling as well as in situ treatment of tissues within the body [4, 5].

The design of an endoscopic system must adhere to several critical requirements, as dictated by the definition of an endoscope. First, because endoscopes must access the human body via either natural orifices or surgical incisions, their design must accommodate diameter constraints and the need for enhanced flexibility. This ensures minimal invasiveness and maneuverability within the cavities of the body. Second, the endoscopic camera system must be complemented by an external light source to illuminate the internal body structures. The design of this light source must ensure that it does not cause thermal injury to the internal tissues, thereby maintaining patient safety. Third, the imaging quality must meet stringent standards to ensure that the clarity and resolution of the endoscopic images approximate the acuity of direct visual inspection. This is crucial for accurate diagnostic assessments and subsequent clinical decisions [6, 7].

Traditional white-light imaging employs xenon or light-emitting diode (LED) light sources, improving upon traditional fiber-optic imaging methods. Existing white-light endoscopes can achieve a resolution of 4K/8K UHD, providing physicians with higher-quality endoscopic images [8–10]. However, traditional white-light imaging relies on the natural reflection of light from the surface of tissues and lacks disease-specific optical characteristics, making it difficult to locate and visualize precancerous lesions [11]. In addition, some diseases may be unevenly distributed within the tissue, forming diffuse and patchy areas, which further hinders disease detection [12].

In contrast, fluorescence endoscopy technology is based on the biochemical properties and related reactions of biological tissues. It irradiates biological tissues by sending a light source of a specific wavelength through a laser (e.g., near-infrared (NIR)); this light source can be absorbed by fluorescent markers in the tissues and then released in the form of fluorescence, which is captured by the endoscopic camera and converted into a digital image for display [13, 14]. There is a significant difference between the fluorescence absorption and the emission spectra of diseased and normal tissues, and fluorescence endoscopy can capture unique fluorescence signals of the diseased area to realize the early detection of lesions and accurate diagnosis [15, 16]. In recent years, this technology has been used extensively in various clinical studies such as precise tumor localization and boundary identification, in vivo 3D visualization of gliomas, and surgical navigation [17–20]. In addition, fluorescence endoscopy technology can provide imaging using a multiple labeling strategy in combination with multiple fluorescent markers [21].

As medical expertise and public health consciousness continue to advance, expectations regarding the quality of fluorescence endoscopic imaging have increased. The design of the fluorescence endoscopic functional supply device and imaging outcomes produced by the fluorescence camera system exert an indirect or a direct influence on the diagnostic process for physicians. Numerous international consensus documents have been established, delineating standardized test methods based on the body mode for various medical imaging technologies. These techniques include magnetic resonance imaging [22], computed tomography [23], and positron emission tomography [24].

In 2009, the International Electrotechnical Commission (IEC) published technical standard IEC 60601-2-18:2009 for medical endoscopic equipment, which covers detailed requirements for the basic safety and essential performance of endoscopic devices [25]. In 2017, the Association of periOperative Registered Nurses

Vis Comput Ind Biomed Art. 2025. 8(1):2 Published online: 10 January 2025

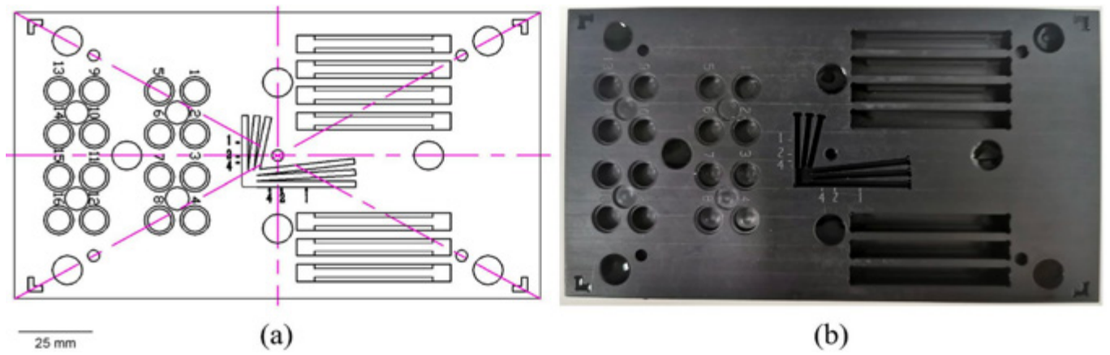


Fig.1 The structure of the imitation body used for the test and the physical drawing. a. Schematic of the fluorescence test phantom; **b.** photograph of the fluorescence test phantom prototype.

(AORN) proposed the AORN MAN-860C-2017 guidelines to assist healthcare professionals in performing care, cleaning, decontamination, and maintenance operations for flexible and rigid endoscopes and related accessories [26]. In 2019, the Pharmaceuticals and Medical Devices Agency approved the first native medical device that uses fluorescence endoscopy technology [27, 28]. In 2020, Kanniyappan et al. [29] published an article on a test method for NIR performance, but the method is not applicable to performance testing of fluorescent endoscopes and uses a phantom with a complex design that limits direct comparisons among different devices and studies. Moreover, the domain of NIR fluorescence (NIRF) endoscopy lacks established technical standards and guidance documents for the quantitative assessment of its imaging capabilities. Consequently, there is an urgent need to develop standardized criteria for evaluating the image quality of endoscopic camera systems. The establishment of unified and standardized protocols for fluorescence endoscopic instruments and the evaluation of fluorescence image quality are of significant practical and clinical importance. This initiative is crucial for enhancing the precision of medical diagnoses and efficacy of clinical applications.

We underscore the importance of developing technical standards for NIRF endoscopy, which are essential for the creation of standardized medical devices in this field. Enhancing the specifications for evaluating the quality of fluorescent images is paramount to ensure consistency and comparability across various devices and operators. It will also enable effective longitudinal comparisons of images that are captured at different time points. By implementing these standardization initiatives, we anticipate a marked enhancement in the performance of fluorescence endoscopy technology and the precision of its clinical applications. These advancements will provide medical professionals with more accurate and dependable diagnostic support. Ultimately, these efforts will benefit patients, elevate the standard of medical care, and improve the overall quality of health services.

Methods

Fluorescent endoscopic imaging system

In this study, we employed the commercially available NIRF thoracoscopic imaging system DPM-III-01 provided by Zhuhai Dipu Medical Technology Co., Ltd., to execute the experimental procedure [30, 31]. This system is equipped with real-time triple-window observation capabilities, enabling it to provide white-light (color), fluorescence (monochrome), and overlaid (pseudo-color) images according to the varying demands of different surgical stages. The design flexibility of the DPM-III-01 system allows it to display NIR images, white-light images, or their overlays, and even to present all three simultaneously, offering comprehensive visual information for surgery. This high degree of flexibility and multifunctionality endows the DPM-III-01 system with a crucial role in surgical procedures, significantly enhancing the precision and safety of the operations. During the experimental process, the endoscope camera system software (Version V1.1) was employed to acquire and post-process the camera images.

To select a fluorescent contrast agent, we used an ICG solution at a concentration of 2.5 mg/mL, blended with fetal bovine serum to create a fluorescent solution. ICG, which is recognized for its exceptional safety and fluorescent properties, has received approval from the US Food and Drug Administration, guaranteeing its safety and efficacy in clinical use. Consequently, ICG offered a secure and potent fluorescent labeling alternative for our experimental procedures, thereby reinforcing the dependability and scientific merits of the experiment.

Fluorescence test mimics

The fluorescence test simulator was made of black PTFE as the substrate material, and its size and shape were the same as those of the effective area of the transmission resolution test card [NQ/NE-10-50A(0.5X)] required by ISO 12233, i.e., 100 mm × 178 mm, with a thickness of 20 mm, as shown in Fig. 1. The design of the fluorescence test phantom included specific areas with standard test patterns and holes for capturing fluorescence images using the imaging system. By titrating the appropriate amount of fluorescent contrast agent into the designated test holes and patterns according to the testing protocol, image acquisition for the respective fluorescence testing items could be performed and the resulting images could be evaluated.

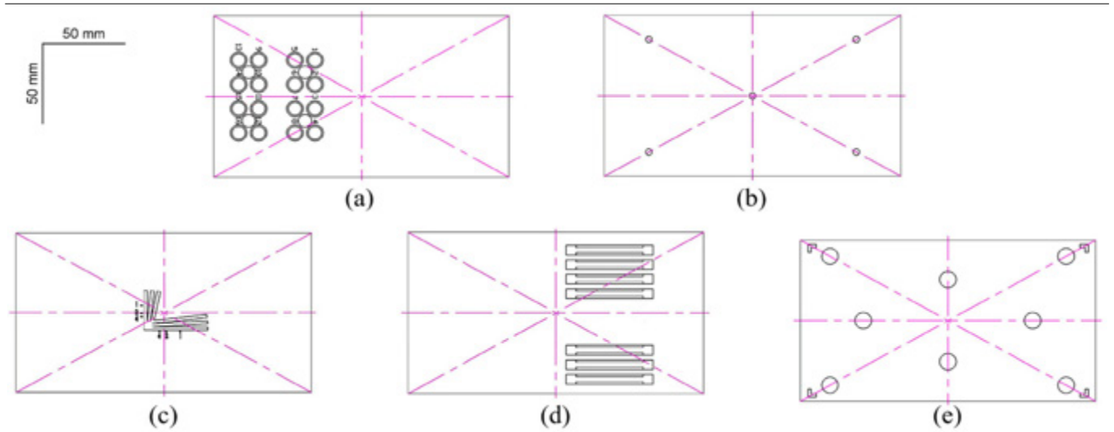


Fig.2 Schematic of the test phantom partitioning. a. Fluorescence sensitivity, SNR, and fluorescence dynamic range (DR) testing area; **b.** fluorescence imaging distortion and fluorescence image brightness uniformity testing area; **c.** fluorescence resolution resting area; **d.** fluorescence detection depth testing area; e. fusion accuracy testing area.

The partition layout of the test phantom is depicted in Fig. 2, with Fig. 2a showing the evaluation areas for the fluorescence sensitivity, signal-to-noise ratio (SNR), and dynamic response range. This section was composed of 16 numbered circular wells on the left and an interspersed set of four additional circular wells. The 16 numbered circular wells were intended to contain fluorescent contrast agents of different concentrations with dimensions of 8 mm × 5 mm. To prevent spillage of the contrast agent during the transfer process, which could affect the test by exceeding the upper surface, a concentric recess measuring 10 mm × 1 mm was also included. Four smaller circular wells were designated for the selection of background signals in the SNR testing, with dimensions of 8 mm × 2 mm.

Figure 2b depicts the fluorescence resolution testing area, which was composed of the central fork-like pattern shown in Fig. 1. The branches of the pattern (straight grooves) were 2 mm wide and 3 mm deep, with the spacing between adjacent straight grooves increasing gradually from 0 mm to 2 mm without exceeding a slope of 0.1.

Figure 2c shows the fluorescence detection depth testing area, which consisted of the seven different depths of straight slots shown on the right side of Fig. 1, forming the fluorescence detection depth test block. An appropriate slot size was selected based on the diameters of the quartz glass tubes and detection capabilities of the fluorescence imaging system.

Figure 2d shows the fluorescence image brightness uniformity testing area, which was composed of five 4 mm × 3 mm circular holes located at the center and at a 0.7 times field of view, as indicated in Fig. 1. These circular holes formed a test block for assessing fluorescence imaging distortion and the uniformity of the fluorescence image brightness.

Figure 2e shows the fusion accuracy testing area, featuring four L-shaped figures at the corners and eight circular blocks at various positions, which together formed the test block for evaluating the fusion accuracy. The four-corner L-shaped figures were designed to test whether the fluorescence image covers no less than 95% of the area of the color image, with the requirement that the tip of the angle of the L-shaped figure falls precisely at 0.95 of the maximum area of the color image. The other eight circular blocks, each with dimensions of 10 mm × 5 mm, were sunken and distributed at 0.25, 0.5, and 0.85 times the maximum field of view of the color image. These were used to test the fusion accuracy between the color and fluorescence images.

Fluorescence image resolution, focal plane uniformity

The spatial resolution or sharpness of an imaging system is a critical metric for assessing the image quality and is inherently linked to the capacity of the system to discern fine details. In the realm of NIRF imaging, the USAF 1951 resolution test chart has been a prevalent choice for evaluation, according to previous research [32]. Building on this, we employed the transmission resolution test card specified by the ISO 12233 standard issued by the International Organization for Standardization (ISO) to assess the resolution capabilities of endoscopic systems quantitatively. This standard method serves as a benchmark for evaluating the performance of fluorescence endoscopic imaging systems. The test card, depicted in Fig. 3, features an effective area enclosed by a thick black border.

The assessment of focus plane uniformity is a crucial metric for evaluating image clarity and focusing quality, exerting a significant influence in domains such as autofocus systems, image processing, and optical design. The evaluation methodology for

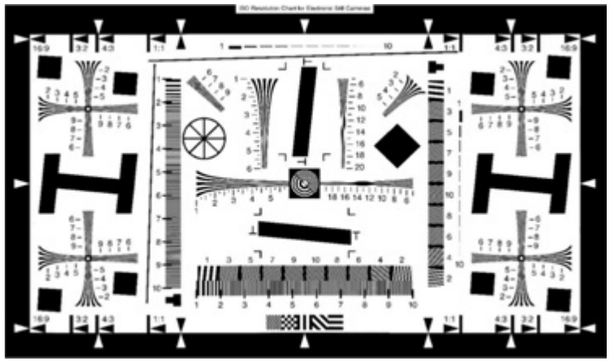


Fig.3 Resolution test card.

focus plane uniformity entails an integrated analysis of the images obtained throughout the entire field of view [33]. This process involves selecting suitable test subjects, capturing images, and using image processing techniques to assess the focus quality quantitatively. Within the scope of this research, we employed the resolutions of both fluorescence and white-light images to calculate the focus plane uniformity. The results derived from the following formula represent the uniformity of the focal plane:

$$\Delta d = \left| \frac{R_W - R_F}{R_F} \right| \tag{1}$$

where Δd is the focal plane uniformity, R_W is the white-light image resolution, and R_F is the fluorescence image resolution.

Fluorescence signal-to-background ratio, sensitivity, and dynamic response range

In fluorescence imaging techniques, the SNR and signal-to-background ratio (SBR) are key metrics for evaluating the performance of an imaging system, and are critical for ensuring the image quality and accuracy of the analyzed results [34]. The SNR measures the ratio of the signal strength to background noise and reflects the ability of an imaging system to distinguish between signal and noise. A high SNR indicates that the signal is much higher than the noise level, allowing for more accurate detection and quantification of fluorescent signals. In fluorescence imaging, the SNR directly affects the ability to detect weak signals, that is, the fluorescence sensitivity.

SNR is the imaging SNR, S is the average signal intensity in the measured fluorescence region, and N is the standard deviation of the signal in the measured fluorescence region. The SBR measures the ratio of the signal intensity to the background intensity and reflects the ability of the imaging system to extract the signal from the background. A high SBR helps to identify fluorescently labeled areas more clearly and reduces the impact of background interference on the image analysis. The SBR is calculated using the following formula:

$$SBR = S/B \tag{2}$$

where SBR is the imaging SBR, S is the average signal intensity of the measured fluorescence region, and B is the average signal intensity of the background region.

Fluorescence sensitivity usually refers to the ability of an imaging system to detect weak fluorescent signals. This indicator evaluates the response of a system to low concentrations of fluorescent markers or small signal changes. High fluorescence sensitivity means that the system can detect lower fluorescence intensities, thus playing a key role in applications such as biomarkers and the early diagnosis of diseases. In this system, the average signal gray value needs to be at least 30 to ensure that the lowest concentration of the fluorescent solution can be accurately detected; this concentration is defined as the fluorescence sensitivity (denoted as CL). The DR refers to the range of fluorescence signal intensities that can be distinguished by the imaging system and is usually expressed on a logarithmic scale. It ranges from the lowest detectable signal (fluorescence sensitivity) to the highest signal intensity that does not saturate. A high DR indicates that the system can simultaneously detect fluorescent signals ranging from very dark to very bright, which is critical for quantitative analysis and multi-marker imaging. When the average gray value of the fluorescent region is close to the saturation point, we identify it as the highest fluorescence concentration (denoted as CH). From this, we can calculate the fluorescence DR in decibels (dB).

$$DR = 20lg(CH/CL) \tag{3}$$

Fluorescence image brightness uniformity, fluorescence imaging aberration, and fluorescence resolution

Luminance uniformity reflects the consistency of the luminance distribution across the image field of view, implying that there are no significant local variations in the illumination or fluorescence signal intensity of the image across the field of view, which helps to prevent image interpretation errors caused by uneven luminance [35].

Experiments were conducted based on Fig. 2b, where images were captured and analyzed to measure the fluorescence average gray value of 90% of the area of the container hole diameter, with the image measurement at the center as F_1 and the image measurement around the edges as F_2–F_5. For fluorescence nudging, the fluorescence image luminance uniformity is the ratio of the average of the measurements around the edges to that at the center, G, with the following expression:

$$G = \frac{\bar{F}}{F_1} \tag{4}$$

where $\bar{F}$ is the average of the edge fluorescence image measurements of F_2–F_5. Aberrations are nonlinear distortions that appear in an image and can be caused by aberrations in the optical system, irregularities in the shape of the sample, or curvature of the imaging plane. They can cause straight lines in an image to appear curved or cause the actual size and shape of an object to not match the imaging results. Controlling and correcting aberrations are critical for maintaining image accuracy and performing precise measurements.

The radial dimensions of the diameter of the center circular spot (D_0) and diameters of the four surrounding circular spots (D_i, i=1,2,3,4) were measured and recorded separately, which was repeated three times.

A single measurement of the unit relative aberration $V_{u-\infty}$ is denoted by $V_{u-\infty,i}$ (i=1,2,3,4) and the calculation is given by

$$V_{U-\infty,i} = \frac{D_0 - D_i}{D_0} \tag{5}$$

The unit relative aberration of the Z field of view can be calculated from the unit relative aberration using the following equation:

$$V_{U-z} = \frac{\sum_{i}^{4} V_{U-\infty,i}}{4} \tag{6}$$

The measurement process was repeated three times, the arithmetic mean of the measurement results was obtained, and the unit relative aberration consistency was calculated.

$$U_{V\,rel} = \max \left| \frac{V_{U-z,i} - V_{U-z,j}}{2V_{U-z}} \right| \tag{7}$$

When taking absolute values,

$$U_V = \max |V_{U-z,i} - V_{U-z,j}|/2 \tag{8}$$

The final results are expressed as the arithmetic mean of the difference in agreement between the three measurements.

Fluorescence resolution is a measure of the ability of an imaging system to distinguish between adjacent objects or structures, which directly affects the clarity of the image and the visualization of details. It is usually defined in terms of the smallest distance that can be distinguished. A higher resolving power means that the system can capture finer structural features, which is critical for applications such as viewing fluorescent images and intracavitary tissues. Computer software was used to determine the limiting resolution distance (mm) of the sector line of the standard mimic resolution region, and the resulting resolution was the fluorescence resolution.

Fluorescence penetration depth

The fluorescence penetration depth is a key parameter in fluorescence imaging that determines the ability of an imaging technique to penetrate deep into biological tissues or materials. This metric is important for enabling three-dimensional visualization of deep tissue structures, performing multispectral imaging analyses and quantitative fluorescence concentration measurements, guiding clinical diagnosis and surgical navigation, and evaluating the internal properties of materials in materials science. The depth of fluorescence penetration is influenced by the optical properties of the fluorescent marker, optical absorption and scattering properties of the sample, and wavelength of light used. Therefore, careful consideration is required in the design of fluorescence endoscopes to ensure the accuracy and depth of imaging.

The fluorescence test mimic was the same as that shown in Fig. 2d. There were seven horizontal slots with different gradients in the detection depth region of the fluorescence test mimic. The bar groove in the middle of each gradient was the location for placing the fluorescent solution bar, and the center of each adjacent bar groove was equidistant from the center of the bar; the fluorescent solution bar (3 mm outside diameter) was covered with a fat emulsion solution (intralipid 10%). Each step represents a different depth gradient indicated by h, which is the distance from the upper surface of each step to the liquid surface of the fat emulsion solution. The image acquired in this area was analyzed, and the fluorescence gray value of the fluorescent solution rod area was measured when the number of imaging frames was not less than 60 and the SNR was not less than 10 B, as described above. The average signal gray value should not be less than 30, and the corresponding maximum value was the fluorescence detection depth.

Fluorescence fusion accuracy

Fluorescence image fusion accuracy ensures that information from different fluorescent channels is accurately represented in the synthesized image, thus providing a more comprehensive view of the sample. Moreover, high-precision image fusion enables researchers to observe and interpret the interactions and relative positions of different fluorescent markers more clearly, thereby contributing to an in-depth understanding of biological processes. If multiple fluorescent markers are used in an experiment, accurate image fusion ensures that the signals of each marker are correctly recorded and differentiated, thereby optimizing the experimental design. Therefore, fluorescence image fusion accuracy is a key factor that affects fluorescence images in fluorescence endoscopic photography systems.

The fluorescence test mimic was the same as that in Fig. 2e, and there were four L-shaped grooves in the corners and eight fusion accuracy test holes in the fusion accuracy area of the fluorescence test mimic. First, it was necessary to ensure that the frame rates of the white-light and fluorescence images were the same and perform a time synchronization test, followed by a field of view range test, and finally, the fusion shooting of white-light and fluorescence images was completed. The pixel coordinates of the center of the circle of the white-light color image are defined as (X_{i1}, X_{i1}), and the centroid pixel coordinates of the fluorescent image are defined as

(X_{i2}, Y_{i2})

i is defined as the number of sampling times and must be greater than 3. The fusion accuracy is calculated as follows:

$$\begin{aligned} JX_i &= |X_{i2} - X_{i1}|, \quad JX = \max JX_i \\ JY_i &= |Y_{i2} - Y_{i1}|, \quad JY = \max JY_i \end{aligned} \tag{9}$$

where JX_i is the x-axis image fusion accuracy calculated using the ith sampling, JX is the x-axis image fusion accura-

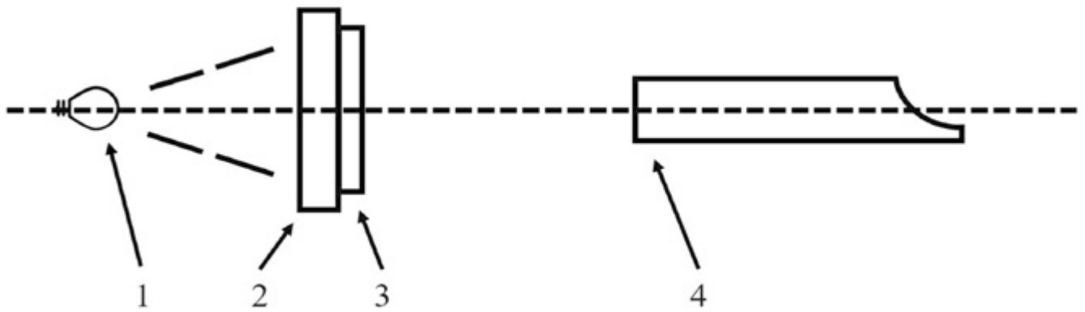


Fig.4 Schematic of the resolution test, where 1 is the test light source, 2 is the homogenizing device, 3 is the test plate, and 4 is the camera system.

cy, JY_i is the y-axis image fusion accuracy calculated using the ith sampling, and JY is the y-axis image fusion accuracy.

Results

Image resolution and focal plane uniformity experimental results

A uniform device was placed in front of the test light source with a wavelength range of 850 nm ± 30 nm so that the light was sufficient and uniformly irradiated in the resolution test card, and the illumination difference was less than 10%. The positions of the test light source, resolution test card, and lens are shown in Fig. 4; the resolution test card was perpendicular to the lens axis of view so that the center of the resolution test card was aligned with the center of the lens, and the length and width of the resolution test card were aligned with the horizontal and vertical directions of the lens screen, respectively. The corresponding effective area in the resolution test card was selected according to the aspect ratio that could be captured by the camera system, and the distance between the camera system lens and resolution test card was adjusted such that the effective area of the resolution test card filled the field of view. After the focus became clear, image acquisition was performed. Computer software was used to determine the limiting clear resolution of the wedge line in the J2 or K2 regions of the resolution test card, and the resolution result obtained was the fluorescence resolution. The value calculated by the system was 1400 lines.

The camera system was moved to an optically designed working distance and only the white-light band of the test light source was turned on. After the focus became clear, image acquisition was performed. The results are shown in Fig. 5. The test card wedge line limit resolution was visually determined and this value was recorded for the color image resolution, which was the white-light image resolution. At this time, the value of 2200 lines was determined. Subsequently, according to Eq. 1, the focal plane uniformity of the system was 0.57.

Experimental results of fluorescence SBR, sensitivity, and DR

Using the connection tooling, the light-guide beam and camera were mounted together, and the architecture is shown in Fig. 6. The center of the light-guide beam out of the light end face and the center of the lens end cap face to the imaging surface were the same distance, with a tolerance of ± 2 mm. The distance between the center of the light-guide beam out of the light end face and the center of the lens end cap face was A leq 50 mm, and the center of the light-guide beam illumination overlapped with the center of the imaging field of view on the imaging surface.

The fluorescent solution for testing was prepared with a two-fold gradient dilution method, using 1 mL ICG solution with 1 mL serum as the base solution, and the dilution of the fluorescent solution in other wells was configured according to the above method. We obtained 260 μL of the configured fluorescent solution in the order of concentration, and dropped it into the fluorescent test well plate container position in sequence, keeping the liquid surface level with the surface of the well plate.

As shown in Fig. 6, the height of the camera was adjusted so that the distance H1 from the lower face of the camera to the fluorescence test hole plate was 150 mm. The position of the container holes in the fluorescence test hole plate was moved so that the position of the container holes of the fluorescent solution of the concentration to be tested was in the center of the field of view. The fluorescence effect of the container holes of the various concentrations was observed individually, and images were collected. A stepwise normalization process was implemented on the acquired images according to the process in Fig. 2a. To ensure that the number of imaging frames was not less than 60 and that the SNR reached at least 10 B, we measured the fluorescence gray value of the region with 90% of the vessel pore diameter.

In this experimental assessment, we designated the circular region outlined by the dashed line in Fig. 7 as the background area and selected an area adjacent to the current test hole. The bright area corresponded to a concentric circle encompassing approximately 80% of the area of each test hole. The average signal intensity of the fluorescence region, denoted as S, for the brightest test hole was 241.80. Within this functional area, there

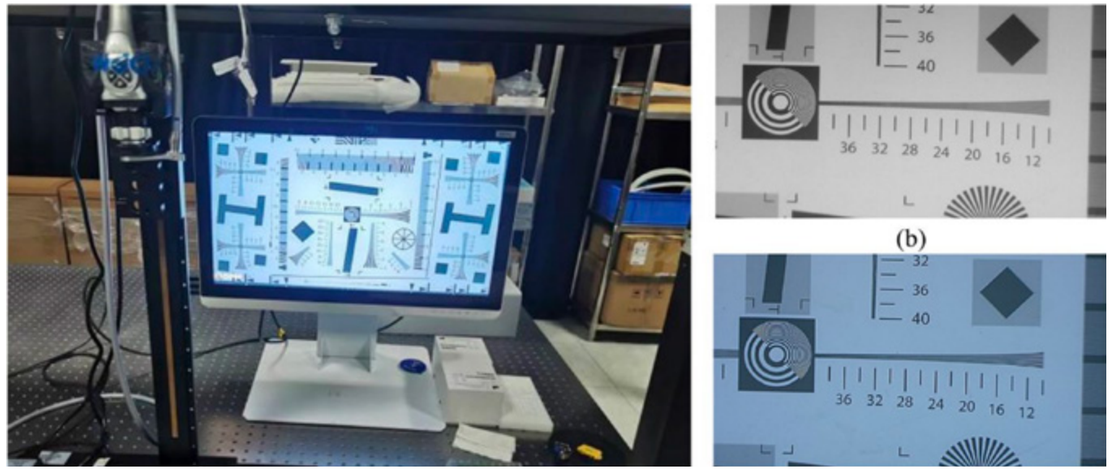


Fig.5 Resolution test experimental procedure. a. The overall image of the resolution test card; **b.** a fluorescence resolution image; and c a white-light resolution image.

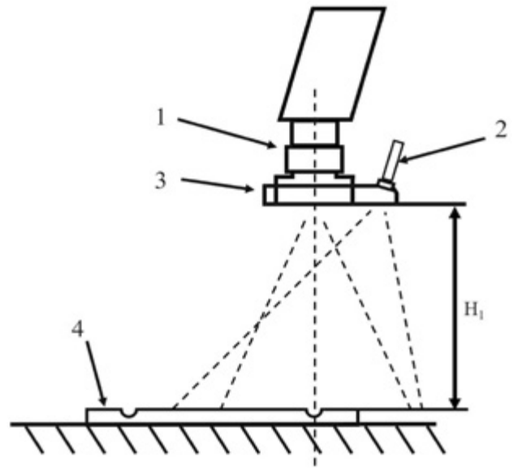


Fig.6 Schematic of the light-guide beam fixing tooling, where 1 is the camera system, 2 is the light-guide beam, 3 is the connection tooling, and 4 is the fluorescence test simulator.

were 16 test holes of varying concentrations, exhibiting gray values ranging from 10 to 241. The standard deviation of the signal in the fluorescence region, denoted as N, was 24.66, whereas the average signal intensity in the background region, denoted as B, was 1.046. After calculating the average signal intensity S, standard deviation N of the fluorescence region, and average signal intensity B of the background region using software, we employed Eq. 2 to determine the SNR of the fluorescence image, which was 19.83. Furthermore, using Eq. 3, we calculated the fluorescence image SBR of the system to be 253. Subsequently, the lowest fluorescent solution concentration CL that could be detected was 0.153 $\mu g/mL$, and the highest fluorescent concentration CH at the saturation point of the average gray value was 4.883 $\mu g/mL$, which could be calculated according to Eq. 4 as DR = 20*lg(CH / CL) = 20*lg(4.883/0.153) = 30.08 dB.

Experimental results of fluorescence image brightness uniformity, fluorescence imaging aberration, and fluorescence resolution

The fluorescence test mimic was placed in the same position as in Fig. 6. The height of the lens was adjusted so that the edge of the mimic coincided with the maximum field of view, and then focused clearly. The fluorescent solution with the highest fluorescence concentration (the concentration corresponding to the CH value) was pipetted and dropped into the five holes of the image brightness uniformity test block of the fluorescence test mimic, with the liquid level flush with the upper surface of the holes, and the images were captured. The results are shown in Fig. 8. The collected images were analyzed to measure the fluorescence average gray value of the 90% area of the diameter of the container holes and to calculate the fluorescence average gray value of the image measurements at the center and the image measurements around the edges. The results are shown in Table 1. The fluorescence image luminance uniformity G of the system was calculated to be 90.5%.

Subsequently, the radial dimensions of the diameter of the center circular spot (D_0) and diameters of the four surrounding circular spots (D_i, i=1,2,3,4) were measured and recorded separately, which was repeated three times. The result are shown in Table 2. The fluorescence imaging aberrations were calculated, and the results yielded a unit relative aberration $V_{u\text{-}z}$ = 12.3% for the Z field of view and an overall fluorescence imaging aberration

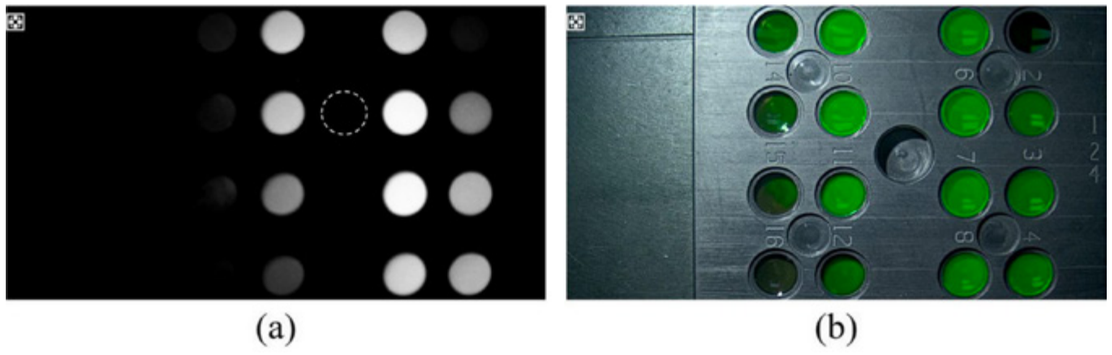


Fig.7 Fluorescent SBR, sensitivity, and DR result images. a Fluorescence mode image; b fluorescence fusion image.

parameter u_v = 2.3% for the system.

A drop of the fluorescent solution with the same concentration as the highest fluorescent concentration was pipetted into the linear groove of the fluorescent resolution test area of the fluorescent test mimic, with the level of the liquid flush with the upper surface of the mimic. Without changing the height of the lens, the mimic body was moved to use the resolution test area in the center of the field of view of the lens area, and image acquisition was performed, as shown in Fig. 9. Computer software was used to determine the standard mimic body resolving the power area sector line limit resolution distance (mm) and the minimum spacing of distinguishable neighboring straight lines was less than 0.25 mm. Therefore, the fluorescence resolving power index of the system was 0.25 mm.

Results of fluorescence penetration depth experiments

The fluorescence test mimic was the same as that in Fig. 1. There were seven horizontal slots with different gradients at the depth of the detection region of the fluorescence test mimic. The bar slots in the middle of each gradient were the locations where the fluorescent solution bars were placed, and each adjacent bar slot was equally spaced from the center of the bar. The fluorescent solution bars (3 mm outside diameter) were covered with a fat emulsion solution (intralipid 10%), with each step representing a different depth gradient, denoted by h, which was the distance from the upper surface of each step to the liquid surface of the fat emulsion solution. The same test platform as that shown in Fig. 6 was used, where the distance from the lens end cap surface of the camera system to the liquid surface of the fat emulsion solution was the common working distance. The fluorescent solution bar was placed in the step bar groove of the measured depth, and the fluorescence test mimic was moved so that the solution bar was in the center of the field of view. The depth position of the fluorescent solution bar was replaced one by one, and the above steps were repeated to observe the fluorescence image of each depth step, as shown in Fig. 10. The collected images were analyzed and the fluorescence gray value of the fluorescent solution bar area was measured. The depth of



Fig.8 Results of three samples of endoscopic fluoroscopy systems.

Table 1 Fluorescence average gray value.

	F_1	F_2	F_3	F_4	F_5	$\bar{F}$
Gray value	169.60	152.00	158.8	158.80	144.60	153.55

Table 2 Circular spot diameter.

Number	D_0	D_1	D_2	D_3	D_4
1	23 mm	21 mm	22 mm	22 mm	20 mm
2	23 mm	21 mm	22 mm	22 mm	20.5 mm
3	23 mm	21 mm	21 mm	22 mm	21 mm

detection was 3.5 mm, 4.5 mm, and 5.5 mm from top to bottom. The test result was a fluorescence detection depth of no less than 5.5 mm.

Results of fluorescence fusion accuracy experiments

First, the white-light and fluorescence images were detected to have the same frame rate, after which a stopwatch was placed in the field of view and the monitor was set to display the white-light and fluorescence images on a split screen. Using a camera or video camera, photos/videos of the white-light and fluorescent images were displayed on the monitor simultaneously. The difference between the stopwatch readings of the white-light and fluorescent images in the same photo/video frame image was examined, which should be less than 20 ms. The test results are shown in Table 3. Passing the test led to proceeding to the next test and vice versa for failing, and the fusion accuracy was out of specification.

After meeting the requirements of the time synchronization test, the fluorescent solution with the highest fluorescence concentration (the corresponding concentration of the CH value) was transferred to the four L-shaped grooves and eight test holes in the fusion accuracy test area of the fluorescence test simulator, and the liquid surface was flush with the upper surface of the holes. According to the test schematic shown in Fig. 6, the lens of the camera system was fixed on top of the fluorescence test mimic, which was adjusted to image clearly under white light, and the edge of the fluorescence test mimic was flush with the edge of the maximum field of view of the white light. The lens was maintained motionless and the fluorescence mode was turned on. In addition, it was determined whether the fluorescence image of the four L-shaped grooves at the corners of the fluorescence test simulator were all complete and visible, and that the image was not missing at the corners or other parts. The results are shown in Fig. 11. If the image was intact, the difference between the fluorescence imaging field of view and the white-light imaging field of view passed the test, and the next test could be performed.

Subsequently, white-light color images were obtained, following which the lens was kept still, the white-light camera was turned off, the fluorescence camera was turned on, fluorescence images were obtained, and the fusion of fluorescence and white-light images was performed. The fused image is shown in Fig. 12, and the fusion accuracy was calculated. The fusion accuracy of the x-axis image was calculated to be JX = 7 and that of the y-axis image was calculated to be JY = 5.



Fig.9 Fluorescence resolution result image. a Fluorescence pattern image; b fluorescence fusion image.



Fig.10 Fluorescence penetration depth test results. a. The experimental process image; **b.** the fluorescence pattern image; and c the fluorescence fusion image.

Discussion

This study proposes a set of technical criteria for evaluating the image quality of fluorescence endoscopic photography systems with the aim of improving the performance of imaging systems and the accuracy of clinical applications. These criteria are theoretically instructive; however, there are some potential shortcomings in their practical application. First, the testing conditions may be too ideal and fail to simulate the complexity of the clinical environment adequately, which may affect the generalizability of the standards. Second, the rapid development of technology means that existing standards must be updated continuously to accommodate emerging technologies and methods. In addition, despite our emphasis on the importance of standardization, the implementation of these standards in different healthcare settings may be challenged by differences in equipment and operators. Factors such as subjective differences in user operations, cost-effectiveness considerations, and individual patient differences may also affect the effectiveness of standards implementation. An inadequate assessment of long-term stability and reliability may limit the understanding of how devices are used in actual clinical settings. Specialty requirements for data interpretation and analysis may limit the involvement of a wider range of healthcare professionals. Finally, translating these standards from laboratory settings into clinical practice may face multiple barriers such as regulations, training, and workflow integration. Future research should focus on these shortcomings and explore solutions to ensure that fluorescence endoscopic photography systems can provide high-quality imaging in diverse clinical settings, while maintaining cost-effectiveness and ease of operation. In addition, further research should focus on improving the flexibility and adaptability of standards, as well as developing more advanced imaging techniques and analytical tools to meet changing clinical needs.

Table 3 Time synchronization test results.

Number	D_0	D_1	D_2	D_3	D_4
1	23 mm	21 mm	22 mm	22 mm	20 mm
2	23 mm	21 mm	22 mm	22 mm	20.5 mm
3	23 mm	21 mm	21 mm	22 mm	21 mm

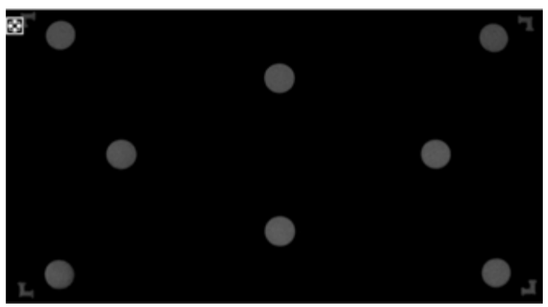


Fig.11 Fluorescence imaging field of view difference test passed with white-light imaging field of view difference test passed.

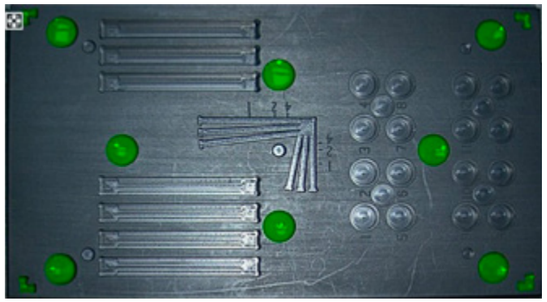


Fig.12 Fluorescence test mimic fusion accuracy test region for fluorescence fusion image results.

Conclusions

This study has thoroughly explored the standardized requirements that must be met by fluorescence endoscopy equipment before achieving widespread clinical application. It clarified the requirements for cold light sources containing NIR excitation light and provided detailed experimental methods to ensure the stable and reliable performance of the cold light source. This study sets forth clear requirements for various performance indicators of NIRF photography systems and provides the corresponding experimental methods to assess and ensure the performance of the imaging system. It stipulates the evaluation criteria and experimental methods for the image quality of medical endoscopy imaging systems, ensuring that the image quality meets clinical needs. To compare clinical outcomes effectively, assess the performance of imaging systems, and accurately quantify fluorescence signals during fluorescence endoscopy, it is crucial to establish unified standardization protocols.

Although the test methods in standards may not be appropriate for all medical devices with fluorescence technology, the study can serve as a guide for establishing performance evaluation tasks throughout the device life cycle, including design input, design output, product validation and verification, and clinical trial standardization. In addition, these methods may not be adaptable for novel system designs, but the standards in this study could be adopted in other medical observation devices with fluorescent imaging capabilities based on practicality.

In the realm of technical evaluation, multiple processes, such as preclinical assessment, clinical evaluation, and registration testing, are often performed to evaluate the security and effectiveness of medical devices. Various methods can be used to assess the fluorescence imaging quality, including the use of mimetic bodies, biological sample testing, animal trials, and other innovative approaches. The insights presented in this study offer an evaluation method for fluorescent endoscopic medical devices that can also be utilized to establish standardized research protocols.

Acknowledgements

We would like to thank Dipu Medical Technology Co., Ltd. for providing valuable experimental equipment for this study.

Abbreviations

LED: Light-emitting diode
NIR: Near-infrared
IEC: International Electrotechnical Commission
AORN: Association of periOperative Registered Nurses
NIRF: Near-infrared fluorescence
SNR: Signal-to-noise ratio
ISO: International Organization for Standardization
SBR: Signal-to-background ratio
DR: Dynamic range

Authors' contributions

BL contributed experimental ideas, designed methods, and drafted the paper; ZG focused on experimental design and organized data; PY contributed experimental design and visualization of results; JY organized data, created visualizations, and assisted in paper writing; KH conducted experiments and visualized results; SG validated experimental outcomes; CC designed methods, reviewed the paper, and supervised the research; YA and JT designed methods and experiments, reviewed the paper, validated experimental results, and were responsible for overseeing the research.

Funding

This article has been contributed to by the National Key Research and Development Program of China, No. 2023YFC3402800; Fundamental Research Funds for the Central Universities, No. YWF23Q1072; National Natural Science Foundation of China, Nos. 62027901, 81227901; Beijing Natural Science Foundation, No. L232097; Guangdong Key Research and Development Program of China, No. 2021B0101420005; Center for Medical Device Evaluation (CMDE) of the National Medical Products Administration (NMPA) of China; the NMPA's Regulatory Science Action Plan (RSAP).

Data availability

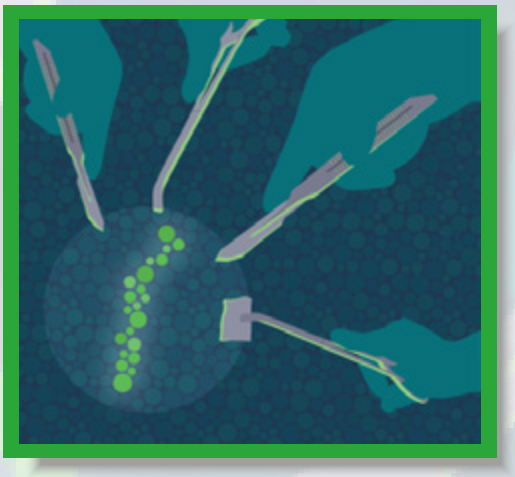
All data included in this study are available upon request by contact with the corresponding author Yu An.

Competing interests

The authors declare no conflicts of interest.

References

1. An Y, Wang HF, Li JQ, Li GH, Ma XP, Du Y et al (2023) Reconstruction based on adaptive group least angle regression for fluorescence molecular tomography. Biomed Opt Express 14(5):2225–2239. 10.1364/BOE.486451
2. An Y, Meng H, Gao Y, Tong T, Zhang C, Wang K et al (2020) Application of machine learning method in optical molecular imaging: a review. Sci China Inf Sci 63(1):111101. 10.1007/s11432-019-2708-1
3. Zhang ZY, Du Y, Shi XJ, Wang K, Qu QJ, Liang Q et al (2024) NIR-II light in clinical oncology: opportunities and challenges. Nat Rev Clin Oncol 21(6):449–467. 10.1038/s41571-024-00892-0
4. He KS, Hong XP, Chi CW, Cai CN, Wang K, Li PP et al (2020) A new method of near-infrared fluorescence image-guided hepatectomy for patients with hepatolithiasis: a randomized controlled trial. Surg Endosc 34(11):4975–4982. 10.1007/s00464-019-07290-z
5. Aylmore H, Dimitrakakis E, Carmichael J, Khan DZ, Stoyanov D, Dorward NL et al (2022) Specialised surgical instruments for endoscopic and endoscope-assisted neurosurgery: a systematic review of safety, efficacy and usability. Cancers 14(12):2931. 10.3390/cancers14122931
6. Choi S, El-Hayek K (2020) Endoscopic equipment-from simple to advanced. Surg Clin North Am 100(6):993–1019. 10.1016/j.suc.2020.08.002
7. Kampf B, Makowski T, Weiss H, Henn H, Hoeschen-Luemmen M, Brümmer T et al (2013) ESGE newsletter. Endoscopy 45(2):156–157. 10.1055/s-0032-1326183
8. D'Alessandris QG, Rigante M, Mattogno PP, La Rocca G, Romanello M, Auricchio AM et al (2022) Impact of 4K ultra-high-definition endoscope in pituitary surgery: analysis of a comparative institutional case series. J Neurosurg Sci 66(5):425–433. 10.23736/S0390-5616.20.04875-4
9. Uozumi Y, Taniguchi M, Nakai T, Kimura H, Umehara T, Kohmura E (2020) Comparative evaluation of 3-dimensional high definition and 2-dimensional 4-K ultra-high definition endoscopy systems in endonasal skull base surgery. Oper Neurosurg 19(3):281–287. 10.1093/ons/opz426
10. Ohigashi S, Taketa T, Shimada G, Kubota K, Sunagawa H, Kishida A (2019) Fruitful first experience with an 8K ultra-high-definition endoscope for laparoscopic colorectal surgery. Asian J Endosc Surg 12(3):362–365. 10.1111/ases.12638
11. He P, Su S, Fang C, He K, Chi CW, Xia XM et al (2019) Residual cancerous lesion and vein tumour thrombus identified intraoperatively using a fluorescence navigation system in liver surgery. ANZ J Surg 89(7-8):E308–E314. 10.1111/ans.15282
12. Li XS, Lovell JF, Yoon J, Chen XY (2020) Clinical development and potential of photothermal and photodynamic therapies for cancer. Nat Rev Clin Oncol 17(11):657–674. 10.1038/s41571-020-0410-2
13. Wang HF, Bian C, Kong LX, An Y, Du Y, Tian J (2021) A novel adaptive parameter search elastic net method for fluorescent molecular tomography. IEEE Trans Med Imaging 40(5):1484–1498. 10.1109/TMI.2021.3057704
14. Jaffer FA, Bhowmik JP (2022) Lighting up adherent LDL in plaques via near-infrared fluorescence molecular imaging. JACC Cardiovasc Imaging 15(8):1471–1472. 10.1016/j.jcmg.2022.04.013
15. Ye JZ, Chi CW, Xue ZW, Wu P, An Y, Xu H et al (2014) Fast and robust reconstruction for fluorescence molecular tomography via a sparsity adaptive subspace pursuit method. Biomed Opt Express 5(2):387–406. 10.1364/BOE.5.000387
16. An Y, Bian C, Yan DX, Wang HF, Wang Y, Du Y et al (2022) A fast and automated FMT/XCT reconstruction strategy based on standardized imaging space. IEEE Trans Med Imaging 41(3):657–666. 10.1109/TMI.2021.3120011
17. Wang K, Du Y, Zhang ZY, He KS, Cheng ZQ, Yin L et al (2023) Fluorescence image-guided tumour surgery. Nat Rev Bioeng 1(3):161–179. 10.1038/s44222-022-00017-1
18. Cheng ZQ, Jin YS, Li JQ, Shi GY, Yu LY, Shao B et al (2023) Fibronectin-targeting and metalloproteinase-activatable smart imaging probe for fluorescence imaging and image-guided surgery of breast cancer. J Nanobiotechnol 21(1):112. 10.1186/s12951-023-01868-5
19. Yan DX, An Y, Li GH, Li JQ, Du Y, Tian J (2023) High-resolution reconstruction of FMT based on elastic net optimized by relaxed ADMM. IEEE Trans Biomed Eng 70(1):296–306. 10.1109/TBME.2022.3190049
20. Zhang ZY, He KS, Chi CW, Hu ZH, Tian J (2022) Intraoperative fluorescence molecular imaging accelerates the coming of precision surgery in China. Eur J Nucl Med Mol Imaging 49(8):2531–2543. 10.1007/s00259-022-05730-y
21. Chi CW, Du Y, Ye JZ, Kou DQ, Qiu JD, Wang JD et al (2014) Intraoperative imaging-guided cancer surgery: from current fluorescence molecular imaging methods to future multi-modality imaging technology. Theranostics 4(11):1072–1084. 10.7150/thno.9899
22. Ihalainen TM, Lönnroth NT, Peltonen JI, Uusi-Simola JK, Timonen MH, Kuusela LJ et al (2011) MRI quality assurance using the ACR phantom in a multi-unit imaging center. Acta Oncol 50(6):966–972. 10.3109/0284186X.2011.582515
23. Weisser G, Lehmann KJ, Scheck R, Coppenrath E, Georgi M (1999) Dose and image quality of electron-beam CT compared with spiral CT. Invest Radiol 34(6):415. 10.1097/00004424-199906000-00005
24. Stabile A, Pellegrino A, Mazzone E, Cannoletta D, de Angelis M, Barletta F et al (2022) Can Negative Prostate-specific Membrane Antigen Positron Emission Tomography/Computed Tomography Avoid the Need for Pelvic Lymph Node Dissection in Newly Diagnosed Prostate Cancer Patients? A Systematic Review and Meta-analysis with Backup Histology as Reference Standard. Eur Urol Oncol 5(1):1–17. 10.1016/j.euo.2021.08.001
25. Grob A (2020) Setting Standards: the IEC 60601 series: quick-use guide. Biomed Instrum Technol 54(3):220–222. 10.2345/0899-8205-54.3.220
26. Marya NB, Muthusamy RV (2020) Methods for endoscope reprocessing. Gastrointest Endosc Clin N Am 30(4):665–675. 10.1016/j.giec.2020.06.002
27. Osumi W, Yamamoto M, Taniguchi K, Masubuchi S, Hamamoto H, Ishi M et al (2021) Clinical experience with near-infrared ray catheter, a fluorescent ureteral catheter, on laparoscopic surgery for colon diverticulitis: a case report. Medicine 100(21):e26085. 10.1097/MD.0000000000026085
28. Sterkenburg AJ, Hooghiemstra WTR, Schmidt I, Ntziachristos V, Nagengast WB, Gorpas D (2022) Standardization and implementation of fluorescence molecular endoscopy in the clinic. J Biomed Opt 27(7):074704. 10.1117/1.JBO.27.7.074704
29. Kanniyappan U, Wang BH, Yang C, Ghassemi P, Litorja M, Suresh N et al (2020) Performance test methods for near-infrared fluorescence imaging. Med Phys 47(8):3389–3401. 10.1002/mp.14189
30. Wang K, Huang WY, Chen XS, Li G, Li N, Huang XM et al (2023) Efficacy of near-infrared fluorescence video-assisted thoracoscopic surgery for small pulmonary nodule resection with indocyanine green inhalation: a randomized clinical trial. Ann Surg Oncol 30(9):5912–5922. 10.1245/s10434-023-13753-4
31. He KS, Hong XP, Chi CW, Cai CN, An Y, Li PP et al (2022) Efficacy of near-infrared fluorescence-guided hepatectomy for the detection of colorectal liver metastases: a randomized controlled trial. J Am Coll Surg 234(2):130–137. 10.1097/xcs.0000000000000029
32. Themelis G, Yoo JS, Soh KS, Schulz R, Ntziachristos V (2009) Real-time intraoperative fluorescence imaging system using light-absorption correction. J Biomed Opt 14(6):064012. 10.1117/1.3259362
33. Suo YK, Wu FX, Xu PF, Shi H, Wang TZ, Liu HG et al (2019) NIR-II fluorescence endoscopy for targeted imaging of colorectal cancer. Adv Healthc Mater 8(23):1900974. 10.1002/adhm.201900974
34. Qi J, Sun CW, Zebibula A, Zhang HQ, Kwok RTK, Zhao XY et al (2018) Real-time and high-resolution bioimaging with bright aggregation-induced emission dots in short-wave infrared region. Adv Mater 30(12):1706856. 10.1002/adma.201706856
35. Cai MS, Zhang ZY Shi XJ, Hu ZH, Tian J (2020) NIR-II/NIR-I fluorescence molecular tomography of heterogeneous mice based on Gaussian weighted neighborhood fused lasso method. IEEE Trans Med Imaging 39(6):2213–2222. 10.1109/TMI.2020.2964853



This book presents the recent research achievements of Professor Jie Tian's team in fluorescence image-guided surgery, covering interdisciplinary exploration as well as their clinical application. After comprehensive review, it is organized by department, highlighting the applications of this technology in various surgical specialties. As a testament to the team's dedication to advancing molecular fluorescence imaging technology, it marks a significant milestone in this field.